MATERIALI IN TEHNOLOGIJE

MATERIALS AND TECHNOLOGY

2

MATER. TEHNOL. | LETNIK 51 VOLUME 51 | ŠTEV. 2 NO. 2 | STR. 179-350 P. 179-350 | LJUBLJANA SLOVENIJA | MAR.-APR. 2017

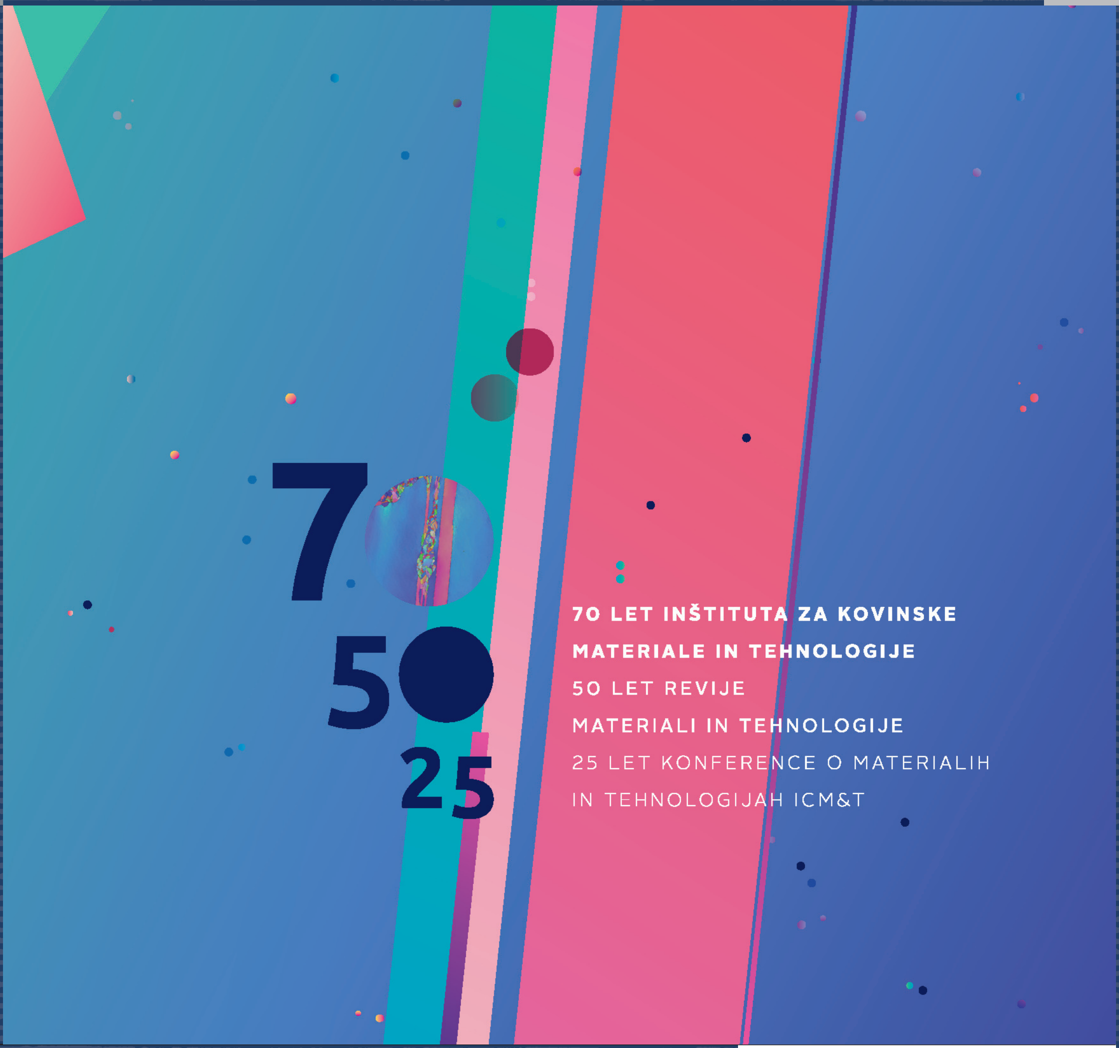

70 LET INŠTITUTA ZA KOVINSKE MATERIALE IN TEHNOLOGIJE

50 LET REVIJE MATERIALI IN TEHNOLOGIJE

25 LET KONFERENCE O MATERIALIH IN TEHNOLOGIJAH ICM&T

ISSN: 1580-2949
UDK: 669+666+678+53

MATERIALI IN TEHNOLOGIJE

MATERIALS AND TECHNOLOGY

2

MATER. TEHNOL. | LETNIK VOLUME 51 | ŠTEV. NO. 2 | STR. P. 179-350 | LJUBLJANA SLOVENIJA | MAR.-APR. 2017

MATERIALI IN TEHNOLOGIJE / MATERIALS AND TECHNOLOGY *so znanstvena serijska publikacija, ki objavlja izvirne in tudi pregledne znanstvene članke ter tehnične novice, ki obravnavajo teoretična in praktična vprašanja naravoslovnih ved in tehnologije na področjih kovinskih in anorganskih materialov, polimerov, vakuumske tehnike in v zadnjem času tudi nanomaterialov.*

The journal MATERIALI IN TEHNOLOGIJE / MATERIALS AND TECHNOLOGY *is a scientific journal, devoted to original scientific papers, reviewed scientific papers and technical news concerned with the areas of fundamental and applied science and technology. Topics of particular interest include metallic materials, inorganic materials, polymers, vacuum technique and lately nanomaterials.*

Izdajatelj (Published for):
Inštitut za kovinske materiale in tehnologije Ljubljana (IMT)

Soizdajatelji (Associated Publishers):
IMPOL Slovenska Bistrica, METAL Ravne, TALUM Kidričevo

Izdajanje **MATERIALI IN TEHNOLOGIJE** sofinancira: Javna agencija za raziskovalno dejavnost Republike Slovenije (ARRS)
(Journal **MATERIALS AND TECHNOLOGY** is financially supported by Slovenian Research Agency (ARRS))

Članki revije Materiali in tehnologije so indeksirani v/Articles published in Materials and Technology are indexed in: SCIENCE CITATION INDEX EXPANDED, MATERIALS SCIENCE CITATION INDEX® AND JOURNAL CITATION REPORTS/ SCIENCE EDITION.
Po bazi podatkov JCR15 ima Materiali in Tehnologije dejavnik vpliva 0,439. / In JCR15 Database Mater. Tehnol. has an impact factor of 0.439.

Članki objavljeni v periodični publikaciji MATERIALI IN TEHNOLOGIJE so indeksirani v mednarodnih sekundarnih virih: (Articles published in journal are indexed in international secondary periodicals and databases):

- DOAJ (Directory of Open Access Journals)
- Google Scholar
- SCIRUS
- CA SEARCH® – Chemical Abstracts®
- METADEX®
- TEME – Technology and management
- Inside Conferences
- Engineered Materials Abstracts®
- Aluminium Industry Abstracts
- SCOPUS
- Civil Engineering Abstracts
- Ceramic Abstracts/World Ceramic Abstracts
- Corrosion Abstracts
- Mechanical & Transportation Engineering Abstracts
- CSA Aerospace & High Technology Database
- Solid State and Superconductivity Abstracts
- Materials Business File
- Referativnyj žurnal: Metallurgija
- COBIB

Izhajanje: 6 številk letno / **Published:** 6 issues per year
Naročnina / Subscription: 42 EUR – **tujina / abroad:** 85 EUR

Naslov uredništva (Editorial Address):
MATERIALI IN TEHNOLOGIJE
IMT Ljubljana
Lepi pot 11
1000 Ljubljana, Slovenija
Telefon: +386 1 470 18 60
Telefax: +386 1 470 19 39
Podračun pri UJP št. 01100-6030344339

ISSN: 1580-2949
UDK: 669+666+678+53

Na INTERNET-u je revija MATERIALI IN TEHNOLOGIJE dosegljiva na naslovu (ELECTRONIC ACCESS):
http://mit.imt.si

Elektronska pošta (E-mail): mit@imt.si

Oblikovanje ovitka (Design): Ignac Kofol
Oblikovanje plakata na naslovnici (Poster on the Cover): Ajda Schmidt
Računalniški prelom in tisk (Prepress and Printed by):
NONPAREL grafične storitve d.o.o., Medvode
Naklada (Circulation): 400 izvodov/issues

MATERIALI IN TEHNOLOGIJE/MATERIALS AND TECHNOLOGY (1967–2017) – 50 LET/50 YEARS

UDK 669+666+678+53
ISSN 1580-2949
MTAEC9, 51(2)179–351(2017)

MATER. TEHNOL.	LETNIK VOLUME 51	ŠTEV. NO. 2	STR. P. 179–351	LJUBLJANA SLOVENIJA	MAR.–APR. 2017

VSEBINA – CONTENTS

PREGLEDNI ČLANEK – REVIEW ARTICLE

IZVIRNI ZNANSTVENI ČLANKI – ORIGINAL SCIENTIFIC ARTICLES

STROKOVNI ČLANKI – PROFESSIONAL ARTICLES

MATERIALI IN TEHNOLOGIJE/MATERIALS AND TECHNOLOGY (1967–2017) – 50 LET/50 YEARS

UDK 621.9.015:669.295:606:61
Review article/Pregledni članek

ISSN 1580-2949
MTAEC9, 51(2)181(2017)

A REVIEW OF THE SURFACE MODIFICATIONS OF TITANIUM ALLOYS FOR BIOMEDICAL APPLICATIONS

PREGLED MODIFIKACIJ POVRŠINE TITANOVIH ZLITIN ZA BIOMEDICINSKO UPORABO

Mallaiah Manjaiah, Rudolph Frans Laubscher
University of Johannesburg, Department of Mechanical Engineering Science, Kingsway Campus, Auckland Park,
2006 Johannesburg, South Africa
manjaiahgalpuji@gmail.com

Prejem rokopisa – received: 2015-12-18; sprejem za objavo – accepted for publication: 2016-03-02

doi:10.17222/mit.2015.348

Dental implants are mechanical components that are used to restore the mastication (chewing) function and/or aesthetic appeal because of tooth loss or degradation. They are affixed (screwed) into the upper or lower jaw and act as a base for single or bridge-type tooth replacements. They are mostly manufactured from titanium alloys. The surface integrity of the manufactured implant may have a significant effect on the functioning and success of the implant. A systematic review is described on the effect of engineered surface integrity on the performance of titanium dental implants as regards the implant fixation, mechanical performance, bone growth and cell response. The need for surface engineering of the implant is introduced first. This includes the mechanical, surface-integrity and biocompatibility-required properties. This is followed by introducing and discussing the dedicated surface-modification processes currently employed. These include: abrasive blasting, electrochemical processes, hybrid processes and laser modification. The mechanical and biocompatible properties of an implant are the most crucial factor for their application in biomedical use. Hence, the present review article focused on the latest improvements to dental implant design based on the mechanical and biocompatible properties. The physical contact of an implant with respect to its surface roughness is an important factor in dental implant design. The surface roughness of an implant on the macro, micro and nano scales have specific effects on the implant's contact with the surrounding tissue of the bone. In addition, the biocompitability of titanium material is very important to develop a sustainable dental implant. Looking into the importance of the above mechanical and biocompatible properties of bone implants, the authors review elaborately the development of titanium-based implants with reference to the above properties.

Keywords: implants, titanium, surface roughness, systematic review, surface engineering process, hybrid process, mechanical machining, chemical treatment

Zobni vsadki so mehanske komponente, ki se jih uporablja za obnovo funkcije žvečenja in/ali iz estetskih razlogov zaradi izgube ali poslabšanja zoba. Pritrjeni (privijačeni) so v zgornjo ali v spodnjo čeljust in služijo kot osnova za nadomestni zob ali za mostiček. Večinoma so izdelani iz titanovih zlitin. Integriteta površine izdelanih vsadkov lahko pomembno vpliva na delovanje in uspešnost vsadka. Opisan je sistematičen pregled o vplivu inženirske celovitosti površine na zmogljivost titanovega dentalnega vsadka glede na pritrditev vsadka, mehanske zmogljivosti, vraščanja kosti in odziva celic. Najprej je predstavljena potreba po obdelavi površine vsadka. To vključuje zahtevane mehanske lastnosti, celovitost površine in biokompatibilnost. Temu sledi predstavitev in razlaga trenutno uporabljanih postopkov za namensko spremembo površine. To vključuje: abrazivno peskanje, elektrokemijske procese, hibridne procese in modifikacijo z laserjem. Mehanske in biokompatibilne lastnosti vsadka so najbolj pomemben faktor pri njihovi uporabi v biomedicini. Zato ta članek predstavlja najnovejši razvoj za izboljšanje načrtovanja dentalnega vsadka na podlagi mehanskih in biokompatibilnih lastnostih. Fizični stik vsadka, glede na hrapavost površine, je pomemben faktor pri načrtovanju vsadka. Hrapavost površine vsadka ima na makro-, mikro- in nanonivoju specifičen vpliv na stik vsadka z obkrožujočim tkivom kosti. Poleg tega je biokompatibilnost titanovega materiala pomembna za razvoj trajnostnih dentalnih vsadkov. Zaradi pomembnosti mehanskih in biokompatibilnih lastnosti kostnih vsadkov avtorji prikazujejo, glede na te lastnosti, razvoj vsadkov na osnovi titana.

Ključne besede: vsadki, titan, hrapavost površine, sistematičen pregled, postopki spreminjanja površine, hibridni proces, mehanska, kemijska obdelava

1 INTRODUCTION

A significant portion of the population may have a need for implant dentistry to restore the mastication (chewing) function or aesthetic appeal after losing teeth because of disease or mechanical trauma. Dental implants are mechanical components that are affixed (screwed) into the jawbone and act as the base for single or bridge-type tooth replacement. They are mostly manufactured from titanium alloys. Dentists and dental specialists encounter various challenges regarding the placement of implants into the jawbone structure. They are continuously seeking new methods and alternative materials to solve the many challenges at hand while reducing the risks involved. Dental implants are the nearest equivalent replacement to a natural tooth that may be compromised by disease or trauma. A dental implant is a metal part and therefore a foreign body as far as the physiology of the patient is concerned. This may lead to several difficulties such as compatibility with the rest of the body. Successful application implies that the dental specialist industry considers all the relevant factors as related to dental reconstruction and restoration. These factors may include the implant geometric design, mechanical performance, aesthetic appeal, biocompatibility and osseointegration of the implant with the bone and surrounding tissues. Dental implants can be categorized into three widely used designs. These are subperoisteal, transosteal and the more recent and most popular of the three the endosseous implants. The endosseous types are placed deep within the mandible or maxilla, the lower and upper jawbone, respectively. Once the implant is placed (usually screwed) within the jaw and left to heal, the jawbone osseointegrates with the implant to create a secure interface between jaw and implant. Successful osseointegration, as far as mechanical performance is concerned, is assessed by the implant withstanding a certain minimum loosening torque, usually applied with a torque wrench.

Prosthetic and implant manufacture include various different types of designs, shapes and surface-engineered components made from various materials. Biocompatible materials that have been and are used include stainless steel, carbon, platinum, titanium, silver, cobalt chrome alloys, alumina, magnesium, sapphire, acrylic, porcelain, calcium phosphate compounds and zirconia.

Dental and orthopedic practitioners have previously used stainless steel and cobalt-chrome alloys for their implants. These materials have good mechanical properties such as high strength and good corrosion resistance. Furthermore, they have proven to be compatible with the human body. They demonstrated clinical success in many implant cases.[1] However, titanium and its alloys have largely superseded them because of similar and enhanced properties. Titanium is inert and has good biocompatibility. It resists a wide range of corrosive agents and has a superior strength-to-weight ratio when compared to that of steel. Today, dental practitioners mainly use commercially pure titanium as their material of choice. The clinical success of any biomedical orthopedic/dental implant depends on the surface interaction between the bone tissue and the implant (osseointegration). Hence, the dentists/orthopaedists must make use of an implant manufactured from a suitable material that also has a suitable surface integrity. In general, Ti alloys are more corrosion resistant and less toxic when used in the human body compared to steel, Co-Cr and tantalum.[2] The fact that titanium alloys also have a lower elastic modulus, more comparable with that of bone, helps with the load transfer and subsequent stress profile at the interface. Titanium-based alloys have therefore become the material of choice for many implant applications because of their outstanding characteristics, such as high tensile strength, corrosion resistance, lower modulus of elasticity, lower density and enhanced biocompatibility (osseointegration ability). Apart from these applications, titanium alloys have a wide range of applications in other commercial and aerospace industries.

1.1 Required mechanical and biocompatible properties of implant materials

The selection of a biomaterial for the intended application of bio parts is important. The material should have high durability without immunological rejection in the human body's environment and a good response with tissue cells. The mechanical properties of the materials should concurrently match with human bone properties like density, tensile strength, fatigue resistance, hardness, and a low modulus of elasticity, elongation wear resistance and corrosion resistance. It is difficult to get all the feasible properties in one material. Corrosion is the disintegration of an implant alloy that will spoil the implant material and surrounding tissues. For this reason, a material with a greater corrosion resistance and high strength for biomedical applications is preferred. These materials have replaced some of the parts of the human body, shoulders, knee, hips, elbows, and oro-dental structure.[3] Few materials are used in a very active role, like actuators, vascular stents, heart vertebras, orthodontic arch wires, etc. The authors reported that expedient materials for biomedical implants such as stainless steel AISI 316L, cobalt-based alloys, CoCrMo alloys, titanium alloys, TiNi shape-memory alloys and special alloys.[2]

The materials that are used for surgical implants in biomedical are listed in **Table 1**. In addition, all these biomaterials posses a higher modulus of elasticity than the bone. Among these materials, the titanium-based material is feasible and most appropriate for implantation. Due to the combination of outstanding characteristics compared to other materials such as enhanced biocompatibility, low modulus, high strength and good osseointegration.

These materials are highly non-toxic and do not cause any allergic reaction with the human body. Ti6Al4V is the long-term main medical alloy for implantation. However, these alloys have a possible toxic effect on the body, caused by the vanadium and aluminium. Due to this reason, vanadium- and aluminium-free titanium alloys are preferred for implant applications.[4] The surface properties of a metallic material play a role in the spontaneous build up of a stable and inert oxide layer to make it highly biocompatible. The responses induced by the material in the human body and degradation of the material are the two main factors in biocompatibility. Commercially pure Ti materials are preferred as they give bio-integration with the surrounding tissues, cells of the bone and healing, bone growth, etc. Material with a highly appropriate surface is required for the implant to assimilate with adjacent bone. Hence, surface engineering plays a major role in the development of good osseointegration. The success of a dental implant is highly dependent on the chemical, physical, mechanical and surface topography characteristics of the implants. Surface topography plays a vital role in osseointegration

Table 1: Bio-material and their mechanical properties[1,4]
Tabela 1: Biomateriali in njihove mehanske lastnosti[1,4]

Material	Yield strength (Mpa)	Ultimate tensile strength (MPa)	Modulus (GPa)	Elongation (%)	Density (g/cc)
316L steel	290	580	210	50	7.99
CoCrMo	275-1585	600-1795	200-230	8	8.3
CoCrNiMo	241	793	232	50	8.43
TiNi	195-690	895	80	25-50	6.45
CP Ti grade I	170	240	102	24	4.5
CP Ti grade II	275	345	102	20	4.5
CP Ti grade III	380	450	102	18	4.5
CP Ti grade IV	483	550	104	15	4.5
Ti-6Al-4V-ELI	795	860	113	10	4.4
Ti-6Al-4V	860	930	113	10	4.4
Ti-6Al-7Nb	880-950	900-1050	114	8-15	4.4
Ti-5Al-2.5Fe	895	1020	112	15	4.4
Ti-15Zr-4Nb-2Ta-0.2Pd	693-806	715-919	94-99	18-28	4.4
Ti-29Nb-13Ta-4.6Zr	864	911	80	13.2	4.4
Ti-13Nb-13Zr	900	973-1037	19-84	15	4.99
Ti-12Mo-6Zr-2Fe	1000-1060	1060-1100	74-85	18-22	5.0
Ti-35Nb-7Zr-5Ta	742-806	596	55	11-22	5.0
Ti-29Nb-13Ta-4.6Zr	715	911	65	22	5.0
Ti-35Nb-5Ta-7Zr-0.4O	590-1074	1010	66	21-27	5.0
Ti-15Mo-5Zr-3Al	1475	724-900	82	14	4.95

and shorter healing time from implant placement to restoration.[2]

1.2 The reason for surface modification

The biomedical applications of titanium alloys include replacement parts such as hip, knee, shoulder, screws, nuts, plates, nails, housing devises for pacemakers and artificial heart valves, surgical instruments and so on.[5–7] The goal of dentistry is to restore the normal function of a patient's speech, oral health and aesthetics, regardless of a weakened, diseased, or otherwise injured oral system. Although titanium alloys are extensively used in dental-implant manufacture, failure of the fixation may still occur because of insufficient early osseointegration, infection, surgical trauma, or premature overloading, improper surgical placement, fatigue and inadequate quality of the bone surrounding the implants.[8] Successful dental implantation is highly dependent on the biochemical, physical, mechanical and surface topography characteristics of the implant surface. The biocompatibility of the material is important and needless to say it must be non-toxic and should not cause any allergic reaction with the human body. Ti6Al4V has been extensively used for implant manufacture, but concerns have been raised about their long-term effects because of their vanadium and aluminium content. Due to this reason, commercially pure titanium alloys are preferred for implant applications.[4] The surface properties of metallic materials play a significant role in the spontaneous build up of a stable and inert oxide layer, which is usually highly biocompatible. The response induced by the implant material on the human body and the degradation thereof are the two main factors that contribute to biocompatibility. These commercially pure titanium alloys are preferred as they are bio-compatible with the surrounding tissue and bone cells and do not inhibit healing and bone growth. It does, however, also imply that a material with an appropriate surface is required for effective osseointegration with adjacent bone. Hence, surface engineering plays a significant role in the improvement of the implantation process. Surface topography has a significant effect on osseointegration and a shorter healing time from implant placement to restoration.[2] Hence, many studies tried to optimize dental and orthopedic implants by the modification of surface chemistry and surface topography by using many methods such as sandblasting, acid etching, electrochemical machining and anodizing to improve the aesthetic appearance.[9] However, the surface engineering of titanium improves the aesthetic appearance of the implant, the biocompatibility of the implant, the corrosion resistance, the fatigue life of the implant and to reduce the friction between the implant and abutments. The surface modification is also used to help osseointegration, a faster healing time, improved bone implantation contact and the life expectancy of titanium implants. Titanium dentures become dimmer, weakening its aesthetic aspect when being used for a long time in the oral environment. With the higher demand of dental implants not only for the restoration of oral function, such as chewing, pronunciation and durability, but also dental aesthetics, it is necessary to improve the titanium dental aesthetic for practical clinical uses.

The self-colouring of the anodisation of titanium has been patented[1] and the anodisation improves the aesthetic appearance. The uniform colours of the interference pattern can be obtained for any large surface area. From the practical point of view the surface treatment leads to producing uniform colours. This surface treatment improves the aesthetic appearance in dental implant application and other industrial uses such as jewellery and architectural purposes.[1] The surface treatment of titanium also improves the corrosion behaviour of the alloy. A. Karambakhsh et al.[10] have studied the effect of anodisation on the corrosion behaviour of a commercially pure (CP) titanium alloy. Anodising in sulphuric acid greatly reduced the corrosion resistance of the samples, which is due to the formation of a resistant anodic film. The greater film thickness increased the corrosion resistance. The corrosion resistance of the implant needs to be good because specific metal ions released from the implant can induce inflammation reaction with the surrounding tissues. Moreover, in the long term, it may be harmful to the human body. The porous oxide films formed by the anodic spark deposition, the porous oxide, predominantly consist of the TiO_2 phase. The crystalline structure of the film consists of anatase and rutile. The anodic oxidation improves the corrosion resistance of the CP titanium alloy.[11]

Titanium has excellent corrosion resistance, good fatigue strength and acceptable fracture toughness, but it has poor sliding characteristics. These alloys fail by galling and often exhibit high and unstable friction coefficients. To improve these properties, surface engineering techniques are required, such as hard coating, soft coating, diffusion treatment, and shot-peening. Diffusion treatments include oxygen diffusion, nitriding and carburizing.[12] The surface modification of titanium is also necessary to prevent the release of toxic elements from titanium such as aluminium and vanadium, which are known to cause toxicity.[13] Porous implants have an effect on the fatigue strength in a highly loaded application, such as the hip joint. These alloys experienced a drastic reduction in strength due to the porosity, and due to the stress intensity the pores are the major sources of weakness in the fatigue strength. To achieve a functionally strong implant, a porous implant design needs to account for these losses in metal strength. Hence, the surface engineering of these alloys is essential.

The bulk properties of biomaterials, such as non-toxicity, corrosion resistance or controlled degradability, modulus of elasticity, and fatigue strength have long been recognized as being highly relevant in terms of the selection of the right biomaterials for a specific biomedical application. The events after implantation include interactions between the biological environment and artificial material surfaces, the onset of biological reactions, as well as the particular response paths chosen by the body. The material surface plays an extremely important role in the response of the biological environment to artificial medical devices. In implants made of titanium, the normal manufacturing steps usually lead to an oxidized, contaminated surface layer that is often stressed and plastically deformed, non-uniform and rather poorly defined. Such native surfaces are clearly not appropriate for biomedical applications and some surface treatment must be performed. Another important reason for conducting surface a modification of titanium medical devices is that specific surface properties that are different from those in the bulk are often required. For example, in order to accomplish biological integration, it is necessary to have good bone formability. In blood-contacting devices, such as artificial heart valves, blood compatibility is crucial. In other applications, good wear and corrosion resistance are also required. The proper surface modification techniques not only retain the excellent bulk attributes of titanium and its alloys, such as a relatively low modulus, good fatigue strength, formability and machinability, but also improve specific surface properties required by different clinical applications. According to the different clinical needs, various surface modification schemes have been proposed and are shown in **Table 2**.

In the following sections, the surface modification of titanium implants to improve the bioactivity, biocom-

Table 2: Summary of surface-modification methods for titanium implants[15]
Tabela 2: Pregled metod za modifikacijo površine titanovih vsadkov[15]

Surface modification methods	Modified layer	Objectives
Mechanical methods: machining, grinding, polishing, blasting	Rough or smooth surface formed by subtraction process	Produce specific surface topographies; clean and roughen surface; improve adhesive in bonding
Chemical methods acid treatment	<10 nm of surface oxide layer	Remove oxide scales and contamination
Alkaline treatment	~1µm sodium titanate gel	Improve biocompatibility, bioactivity or bone conductivity
Hydrogen peroxide treatment	~5 nm of dense inner oxide and porous outer layer	Improve biocompatibility, bioactivity or bone conductivity
Sol-gel	~10 nm of thin film, such as calcium phosphate, TiO_2 and silica	Improve biocompatibility, bioactivity or bone conductivity
Anodic oxidation	~10 nm to 40 µm of TiO_2 adsorption and incorporation of electrolyte anions	Produce specific surface topographies; improved corrosion resistance; improve biocompatibility, bioactivity or bone conductivity

patibility, wear and corrosion resistance by the various surface modification technologies are discussed. These methods are classified into mechanical, electrochemical and hybrid processes according to the formation mechanism of the modified layer on the material surface.

2 ABRASIVE BLASTING

Abrasive blasting is one of the mechanical surface modification methods involving plastic treatment, shaping or the removal of materials from the surface. The objective of this mechanical modification process is to obtain a surface roughness, topography, removal of surface contamination and improve its surface-adhesion properties. The surface of titanium is abrasively sand blasted with hard ceramic particles to increase the surface roughness. Depending on the particle size to which the surface roughness can be produced, the surface roughness depends on the bulk material properties, ceramic particle material, particle size, particle shape, particle impact speed and the density of the particles. The surface may consist of craters, ridges and particles embedded on the surface. The surface roughness increases with an increase in ceramic particles of size 25 µm to 250 µm of TiO_2 or Al_2O_3. The blasted surface with a particle size of 25 µm has a higher surface roughness compared to machined surfaces, but smoother than 75 µm and 250 µm particles on blasted surfaces.[14] The authors also made comparisons between different particle sizes (25µm and 75µm) of Al_2O_3 blasted on the surface of titanium implants on the torque and surface topography. They concluded that more torque is required to remove an implant with the surface blasted with 75µm Al_2O_3 particles compared to 25µm particles. It is observed that the surface was blasted by different particle sizes, such as 25 µm and 75µm of Al_2O_3. It was characterized that two surfaces having different irregularities and different degrees of surface roughness have a greater surface roughness when blasted with a particle size of 75 µm (Sa-1.45 µm) compared to a surface blasted with 25 µm (Sa-1.11 µm), as shown in **Figure 1**. Titanium oxide particles can be used for the grit blasting of dental implants, which produces an average surface roughness of 1 µm to 2 µm. Many researchers reported that the torque force increases with surface roughness.[14,15] This indicates an improvement in the biocompatibility, cell activity and osseointegration of the titanium implant using the sandblasting method. The roughening of implants by titanium plasma spraying used to produce a rough surface of the implant can be obtained by a process known as grit blasting, which makes use of hard ceramic particles. The hard particle collides with the surface of the implant at a high velocity using compressed air. Different surface roughness can be obtained from the size of the ceramic particle and the type of particle. After blasting with a ceramic particle, cleaning the surface of the titanium is very important due to some of the residues of the alumina being embedded on the surface of the implant. The alumina ceramic particle is insoluble in acid. This does not, however, completely remove the osseointegration difficulties of the implant. A residue of particles may react with the surrounding tissue cells and cause failure in the implant fixation. The blasted surface has greater bone implant contact (BIC) compared to a machined implant. Titanium oxide particles can also be used for blasting the implant, which shows an improvement in the BIC compared to a machined surface.[16] The experimental demonstration of A. Abron et al.[17], shows a higher bone implant contact in the blasted surface implants compared to machined surface implants. These studies confirm that roughening of the titanium dental implants increases their mechanical fixation to the bone, but not their biological fixation.[18–20] A. Karacs et al.[21] investigated the morphology of machined, blasted and laser-treated surfaces of titanium. The Al_2O_3 blasted surface has a unique surface morphological characteristic that enhances the osseointegration process. Research conducted on animals indicates a 50 % improvement in the removal torque of an implant can be expected. The aforementioned indicates that the sand-blasting

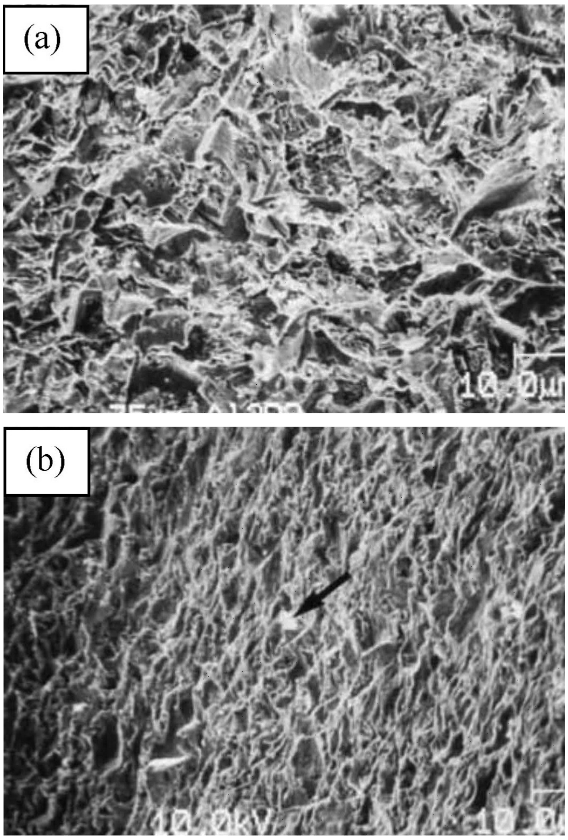

Figure 1: Sand-blasted titanium surface with different particle sizes: a) 25 µm and b) 75 µm[16]

Slika 1: Površina titana, obdelana s peskanjem z delci različne velikosti: a) 25 µm in b) 75 µm[16] preparation method is a promising technique for preparing titanium dental implant surfaces.

3 ELECTROCHEMICAL PROCESS

An electrochemical process of surface modification includes electro polishing, anodic oxidation, acid etching and electrochemical machining. Electro polishing is a controlled electrochemical dissolution of the surface. The process was carried out to obtain a mirror-like smooth surface finish that removes plastically deformed amorphous surface layer residues due to machining.[22]

3.1 Anodizing

Anodizing is an electrolytic chemical oxidation process whereby the oxide layer thickness is engineered to the aesthetic appearance (colour) of the titanium. A thin passive oxide layer is formed, which is usually more stable and thicker than the natural oxide layer that is formed when it first made contact with the air. Anodic titanium oxide has been used in various fields of advanced technologies and industries, e.g., an electrical component, resistive material for friction and wear, decorative coating, resistance to corrosion, as a reflective material and recently as photo electrode material and as well as to improve the aesthetic appearance of implants.[17,23] The anodic oxidation of the titanium surface for implant applications is relatively inexpensive and may produce a uniform thickness throughout the surface area.[24] The anodic oxidation is a simple and novel method for colouring titanium to improve the aesthetic appeal due to the high reactivity of titanium with oxygen. The anodization of titanium has been patented.[1]

Anodization is a surface-modification technique that has been proposed to minimize the rate of ion release from titanium alloys. There is an alternative method to produce surface modification that includes ion implantation, chemical passivation, and plasma spraying. All the common methods used to perform surface modifications lack the required layer thickness. However, the plasma spraying method can produce a thick coating of oxide layer. but is a difficult method for generating a uniform layer on the surface when applied to porous and non-regular substrates.[25]

Anodizing is an electrochemical oxidation process of thickening the oxide layer on the surface of titanium metals. Electrochemical anodizing is the most common method to control the colouring of titanium.[26] This process is a surface-modification process that is efficient in forming an uniform and stable oxide layer on the implant surface compared to other surface-modification processes. e.g., electrochemical, ion implantation and heat treatment, etc.[27] Titanium anodizing improves the surface properties which increases the lubricity, anti-galling and fatigue properties of the alloy. Because of the aforementioned properties, anodizing is becoming rapidly popular in treating components used in the medical industry, especially on orthopaedic implants. This process endows with an extensive formation of oxide coating under controlled conditions to offer the desired result. Due to this, it is biocompatible and non-toxic, resulting in a drastic improvement in performance purposes used for biomedical dental implants. The anodizing process will be carried out with either constant current (Galvonostat) or constant voltage (Potentiostat). Among the other surface-modification processes, the anodic oxidation process is easy to deposit the oxide film on the titanium surface by means of an electrochemical process. This process has various controlled variables such as the type of electrolyte used, the voltage applied across the electrodes and the current used for the process. A change in any of these variables can affect the surface morphology, chemical composition and film thickness of the titanium implant.[28] The thick oxide film formed during anodic oxidation at higher applied voltages leads to a high surface roughness, which provides a high bonding strength between the oxide and the titanium substrate. Moreover, the surface hardness is improved near the oxide layer due to anodic oxidation, which is caused by the incorporation of the oxide into the titanium alloy.[29,30] It is reported that the bioactivity of titanium can be improved by oxide film formation on the titanium surface by anodic oxidation. This oxide layer is either anatase or a mixture of anatase and the rutile crystal structure. Many researchers have reported that the bioactivity of titanium can be improved by varying the thickness of the oxide layer and the crystal structure. The anodization takes place in either galvanostatic or potentiostatic conditions with an increase in the voltage or current density leading to an increase in the oxide layer thickness. The manipulation of the oxide layer also affects the crystalline structure surface of the implant. The anodic oxidation process creates a porous surface structure on the titanium surface as shown in **Figure 2**. **Figure 2** shows how the oxidized dental implant morphology has volcano-shaped saliencies as the oxide form on the surface as a function of the anodic voltage,

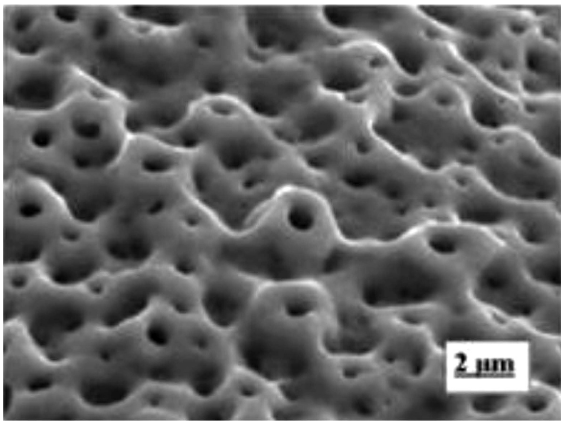

Figure 2: Anodized dental implant surface, resembling small volcanoes[34]

Slika 2: Anodizirana površina vsadka, podobna majhnim vulkanom[34] current, concentration of electrolyte and a change in the temperature. The titanium oxide (TiO_X), where ($1<X<2$) in the general form, depending on the X values 5 crystalline oxides are formed such as cubic (TiO, a_o = 0.424 nm), hexagonal (Ti_2O_3, a_o = 0.537 nm), tetragonal (TiO_2, Anatase, a_o = 0.378 nm, rutile, a_o = 0.458 nm), and orthorhombic (Brookite, a_o = 0.917 nm). There are also nonstoichiometric oxides and amorphous oxides. It is commonly understood that among these oxides, only the rutile and anatase phases are stable under normal conditions. The rutile and anatase oxide layer has different physical properties in terms of surface tension, the rutile condition is hydrophobic, and the anatase condition is hydrophilic. These oxide layers are the most important structure for the osseointegration of implants. K. Kim et al.[31] studied the surface properties and biological responses of anodized samples. The anodized surface has a porous and thick oxide layer of TiO_2. This exhibits better corrosion resistance and shows a significantly lower water contact angle compared to machined surfaces. The anodized surface showed enhanced alkaline phosphate activity compared to machined surfaces. The higher hydrophilic property and wettability is generally favourable for biocompatibility. Increased wettability promoted the interaction between the impact surface and biological environment. Cell activation was more rapid on hydrophilic surfaces. The hydrophilic surface promotes the adhesion of the relevant proteins.

The anodized implant surfaces were characterized by X-ray diffraction, as shown in **Figure 3**.[32] It indicates that the predominant anatase phase exists on the anodized surface. When compared with the machined, sandblasted and acid-etched surface, the main oxide layer is rutile. With respect to surface morphology, hydrophobicity was observed in the machined surface, but the SLA and acid etched had different surface morphologies. The anodized implant has volcano-like surface porous structures, having both rutile and anatase on the surface, as shown in **Figure 3**. The tissue healing process and bone growth is quick on the anodized and acid-etched implant surfaces compared to machined implants. B. C. de V. Gurgel et al.[33] studied the efficiency of anodized implants on animals. Dogs were used to perform implant testing. After 3 months the initial trauma, each wound was inspected and defects were observed, which measured 5 mm in height and 4 mm in width. Anodized implants were planted inside the root canal of the wound and were allowed to heal for an additional 3 months. The percentages of bone-to-implant contact and the bone density of the anodized implants were observed to be 57.03±21.86 % and 40.86±22.73 %, whereas the machined implants were 37.39±23.33 % and 3.52±4.87 %, respectively. Burgos et al.[34] also conducted experiments on rabbits. They observed an osseointegration rate for the anodized implants of 20 % (after 7 d), 23 % (14 d) and 46 % (28 d), compared to 15 % (in 7 d), 11 % (14 d), and 26 % (28 d) for the machined surface.

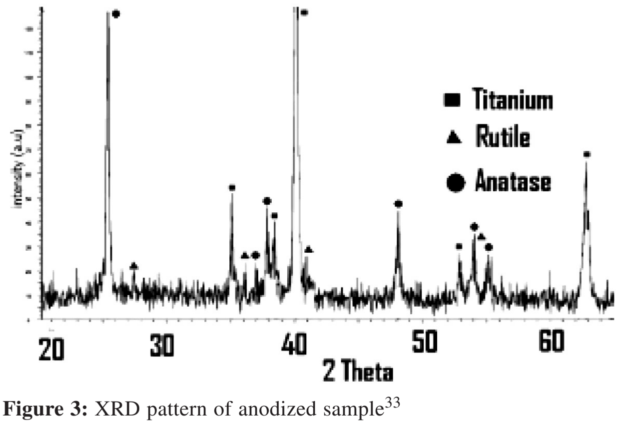

Figure 3: XRD pattern of anodized sample[33]
Slika 3: Rentgenogram (XRD) anodiziranega vzorca[33]

Despite titanium's biological compatibility, it is considered to be an inorganic material. This means that the metal does not form part of the human body. It has some properties that may require modifications to improve its integration into the jawbone, patient comfort, satisfaction and confidence. The potential problem in clinical application is that titanium dentures become dim, which impairs its aesthetic appearance after a long period of time. There is a higher demand for implant prostheses. This is not only for oral functions such as mastication, pronunciation and durability, but also dental aesthetics is also important. Several patients who have received titanium dental implants have complained about the decay of its aesthetic appearance. In most cases the gum covering the implant is thick enough to prevent implant visibility. But since implants have been used to replace or insert teeth, it was found that not all patients have the same gum thickness. Several cases have been reported where the dark metallic colour of titanium shown through the patient's gums. In cases where dissatisfaction was present of its aesthetic appeal, colour appearance was changed by an electrochemical anodic oxidation process which produces the interference of colours.

Titanium has an iron-dark appearance and is visible when it becomes exposed. In other cases the patient has thin gums and the titanium would appear beneath the skin. Many alternative measures have been sought ought to improve on its aesthetics. Some materials have been developed to replace titanium. Dentists would also use techniques to veneer the titanium with a white material or graft tissue over the visible part. However, mechanical methods are unmanageable, inexact and form contaminant particles on the titanium implant surfaces. Similarly, acid etching has no ability produce controllable surface topographies and it has the potential to form residual surface acids, which is harmful to bone growth. Implant surfaces formed through this process are nonuniform on the microscale or macroscale. However, osteoblast may accustom to a nanoscale topology rather than a microscale environment. As a result, more desirable methods to modify Ti surfaces are needed to promote tissue cells and bone growth.[35-37] The surface integrity of the Ti6Al4V alloy was studied by applying different surface treatment processes. The study focused on pickling and anodization.[38] An investigation of these processing techniques revealed no significant changes in the microstructure of the implant and surface oxygen and hydrogen superficial content were found to be unchanged. The roughness characteristics remained mostly unchanged. This surface-treatment technique revealed that compressive residual stresses significantly decreased and that internal stresses were mainly located on the oxide interface. Moreover, the fatigue resistance decreased after the application of either pickling or anodization on the Ti64 alloy. The effect of anodization time on the surface morphology, surface roughness, and crystal structure was studied by L. Wu et al.[39] The surface roughness increased with anodization time up to 20 min, and later dropped down, which is due to localized rapture of the compact inner layer and nucleation of the secondary oxide particles. The uniformity of the surface and the relative intensity of the anatase and rutile tended to increase with longer anodization times. Y. T. Sul[40] studied the electrochemical growth behaviour and surface behaviour of TiO_2 nanotubes fabricated on TiO_2 grit-blasted screw-shaped rough titanium implants. The potentiostatic anodization of blasted screw-shaped implants at 20 V in 1-M H_3PO_4 + 0.4 % of mass fractions HF for 30 min, 1 h and 3 h resulted in highly nanopore structures and vertical aligned nanotubes. The surface roughness value decreased with the reaction time and the results of the animal study provided significant evidence that the nature of nanotubes have superior bone responses compared to blasted implants. This indicates that TiO_2 nanotubes have the potential to be used in the field of bone implant and bone tissue engineering.

3.2 Acid etching

Acid etching is a chemical process used to modify the surface of titanium implants. It increases the retention between the implant surface and the bone by enhancing the surface properties of the implant such as osteoblast activity and quick bone growth. Strong acids used for acid etching include H_2SO_4, HNO_3, HCl and hydrofluoric acid. These acids produce micro pits on the titanium implant surface, as shown in **Figure 4**. The acid-etching process has been used to promote the osseointegration process beyond 3 years. There is no need to use any external reagents that contaminates the implant surface. The biological response of this surface in terms of bone apposition and bone-implant contact ratio is comparatively high. Compared to the machined surfaces, acid-etched surfaces have a higher bone implant contact.[16] A significantly higher torque is required to remove the acid-etched samples compared to the machined implants, but a lower torque compared to plasma-sprayed implants. The disadvantage of acid etching is that it reduces the mechanical properties of titanium implants, which is caused by hydrogen embrittlement. The presence of micro cracks is also observed on the surface of the implants, leading to a reduction in fatigue resistance. This hydrogen embrittlement forms the brittle phase in the titanium, leading to a reduction in ductility. The reduction in ductility leads to the occurrence of fracture in implants.[41] The influence of the implant surface on the primary stability is imperative.[42] The surface topography and roughness positively influences the healing process of the bone by favouring the cellular response and cell-surface interaction. Rough surfaces are considered to enhance the primary stability and allow firm mechanical fixation to the surrounding tissues.[43] **Figure 5** shows the primary stability of dental implants due to different surface-finishing techniques. The surface treatment process significantly alters the surface-roughness parameters, leading to a change in the cell-surface interaction, as indicated in **Figure 5**. The anodized surface (R_a-1.11 µm) has a greater surface roughness compared to the machined surface (R_a-0.74 µm) and acid etched surface (R_a-0.91 µm), which supports the healing process. It is clear that the improved surface roughness of the

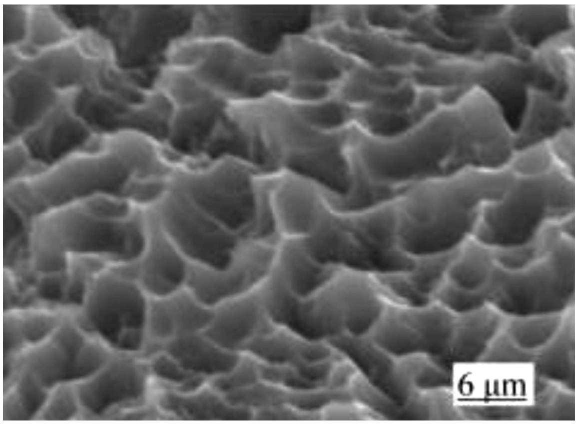

Figure 4: Acid etched surface of titanium[35]
Slika 4: S kislino jedkana površina titana[35]

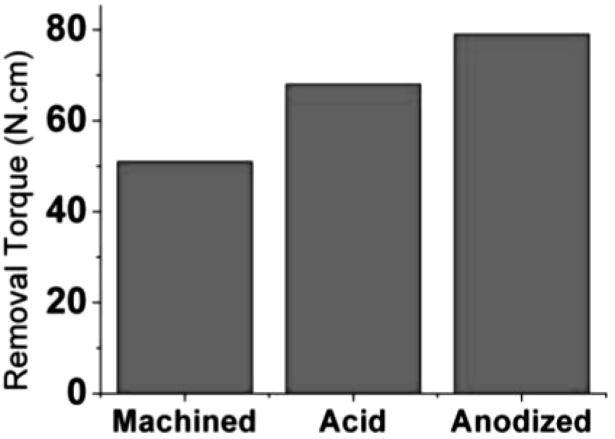

Figure 5: Effect of surface treatment on torque removal[34]
Slika 5: Vpliv obdelave površine na moment pri odstranitvi[34]

acid-etched surfaces has a positive effect on removal torque compared to machined samples. The anodized sample has remarkable improvement in the torque removal force over the machined and acid etched. The average surface roughness is highest for anodized samples, compared to other surface-treatment techniques.

M. V. D. Santos et al.[43] studied the implant surface finish and geometry on the primary stability of dental implants. Their results showed that the maximum torque insertion depends on the coefficient of friction between the implant surface and the placement of the wall, the implant design thread geometry and the surface-treatment technique. It was also found that the insertion torque varies as the geometry of the implants varies. As seen from **Figure 6**, the torque insertion is higher in a conical geometry compared to a cylindrical implant. This is due to the different thread geometries. The surface area of contact with host tissues is increased in a conical implant. As the surface area increases, the friction between the implant surface and the bone wall increases, leading to a higher insertion torque. The implants of the anodized surface have a higher roughness and a larger coefficient of friction than the machined one. They reported that the rough surface has greater significant success rates compared to the smoother surface implants. The surface treatment improves the primary stability of the implants. The anodized implants have a higher primary stability compared to the acid-etched and machined implants.[44]

4 HYBRID PROCESS

4.1 Sand blasted and acid etched (SLA)

This consists of dual processes to obtain both the surface roughness, as well as the removal of particles from the implant surface. Sand blasting is beneficial for removing the surface contaminants, roughening surfaces to increase effective surface area and can produce beneficial compressive residual stresses. The acid etching chemical process changes the surface structure and leads to the creation of a hydride layer thickness of 1–2 μm on the intermediate oxide layer and implant surface. Titanium implants are blasted with ceramic particles and then subsequently etched by acids. In the sand-blasting process, peaks and craters/pits are more commonly found. These peaks and pits can be reduced by acid etching and small pits will be formed, which reduces the surface roughness.[45] The different etching processes may also form the hydrides on the surface and the replacement of oxygen by the titanium hydrides, resulting in a slow transformation of the implant surface. This results in a nano-meter surface roughness, and helps in protein adhesion immediately after the implant is placed in the human body.[46] SLA increases the bone formation and amount of growth. The dual modified implants have improved torque removal force compared to the single modified process, like acid etching, machined and plasma sprayed surface.[47] Several studies have shown that SLA active implants have a better bone-contact ratio, stability and this reduces the healing time duration. J. K. Lee[9] has studied the bone implant contact ratio (BIC) of modified surfaces in titanium implants. In an vivo study of dental implants they were classified into machined surface implants, sand blasted with large grit sizes and acid etched (SLA) surface implants, TiO_2 nano tube array surface implants and TiO_2 nano tube surface implants with rhBMP-2. Histomorphometric analysis studies were performed and the

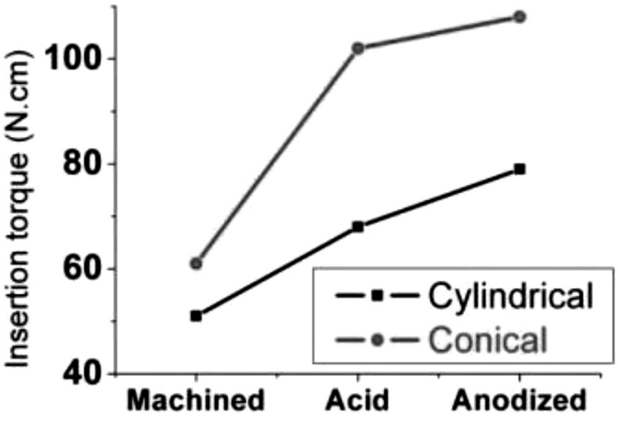

Figure 6: Effect of implant design and surface treatment on torque insertion[46]

Slika 6: Vpliv zgradbe vsadka in obdelave površine na moment pri obdelavi[46]

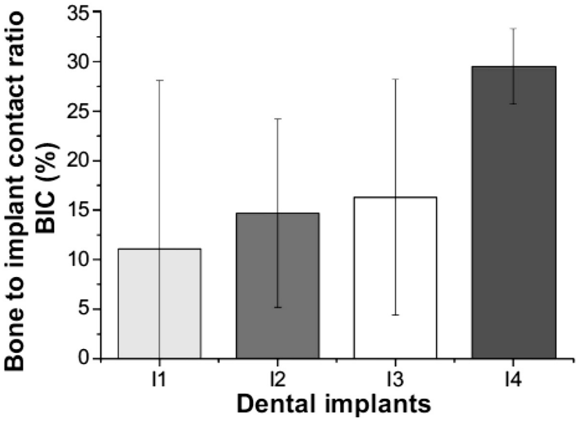

Figure 7: Bone-to-implant contact ratios of machined surface, SLA surface, TiO_2 nanotube array surface, and TiO_2 nanotube array surface with rhBMP-2, (I_1) machined surface implants, (I_2) SLA surface implants, (I_3) TiO_2 nanotube array surface implants, and (I_4) TiO_2 nanotube array surface implant with rhBMP-2

Abbreviations: BIC – bone-to-implant contact ratio, SLA – sandblasted large-grit and acid-etched, rhBMP-2 – recombinant human bone morphogenetic protein-2[9]

Slika 7: Razmerje stika kost-vsadek pri strojno obdelani površini, SLA-površina, TiO_2 matrika površine z nanocevkami in TiO_2 matrika površine z nanocevkami z rhBMP-2; (I_1) strojno obdelana površina vsadka, (I_2) SLA-površina vsadka, (I_3) TiO_2 matrika površine vsadka z nano cevkami in (I_4) TiO_2 matrika površine vsadka z nanocevkami in z rhBMP-2

Okrajšave: BIC – razmerje stika kost-vsadek, SLA – peskano z debelim peskom in jedkano s kislino, rhBMP-2 – rekombinantni morfogeni protein-2 človeške kosti[9] highest BIC of 29.5 % was obtained I_4 followed by I_3 (16.3 %), I_2 (14.7 %) and I_1(11.1 %) groups, as shown in **Figure 7**. The bone-volume ratio was also measured around the implant threads, which was found to be highest in the I_4 group (77.3 %) followed by I_3, I_2 and I_1 groups (67.2 %, 53.7 %, and 66.9 % respectively). The authors suggest that the nano tube array surfaces have improved osseointegration properties compared to machined and SLA-implant surfaces. TiO_2 nano tube implant surfaces have an enhanced bone formation, bone strength and cell adhesion compared to other modified surfaces.

4.2 Electro polished and anodized implants

The bone response in the early healing period and the bone responses to different types of titanium surfaces were studied. The responses of different surfaces were analysed; the electro polished implant surface has a low degree of bone-to-implant contact compared to the machined implant surface after 1 week. After 3 weeks post-implantation there were no major differences between the machined, machined plus anodized, electro polished and electro polished and anodized implant surfaces, as can be seen in **Figure 8**. As observed from **Figure 8**, after 6 weeks the electro polished implant surfaces had less bone contact compared to the other three groups. The electro polished plus anodized implant shows higher bone implant contact, but has less BIC in comparison to the machined and machined plus anodized surfaces. The reason is that the electro polishing removes a significant amount of material from the surface, which decreased the diameter of the implant. The reduction in diameter of implants caused a lower BIC ratio during the initial healing. After 6 weeks, the electro polished surfaces had less bone contact, which may be due to a slower rate of mineralization around the surfaces. This is because the electro polished surface is smooth and the amount of bone attachment to the implant is less compared to the machined implants. The bone response depends on two different types of surface roughness; the smooth surface expresses a lower degree of bone formation compared to the rough surface finish. The degree of a rough surface is adequate to furnish an overall response of the bone. However, the thick oxide on the bone formation was not practical when compared to two groups of machined implants. Thus, it seems that a combination of surface topography and thick oxide present on the electro polished plus anodized implant surfaces are the most encouraging type of surface roughness for bone growth and the rapid healing of interfacial tissues.[48]

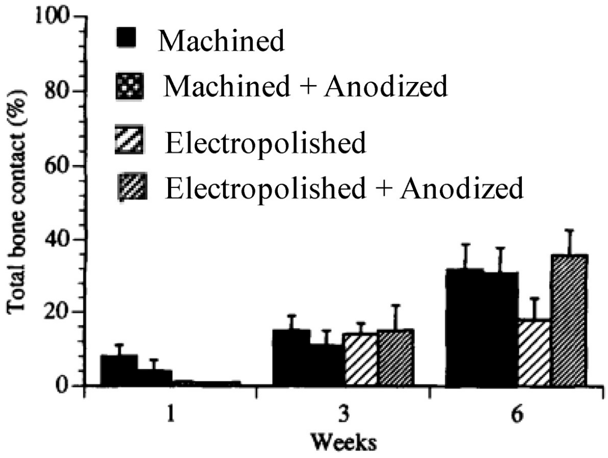

Figure 8: Total bone contact (%): after 1 week, 3 weeks and 6 weeks[51]
Slika 8: Celoten stik s kostjo (%): po 1 tednu, 3 tednih in 6 tednih[51]

5 LASER MODIFICATION

Laser is an emerging field in the manufacturing micro-components of complex surfaces of micro and nano levels. Laser surface engineering is advanced enough to modify the surface. This method becomes more popular method for resolving peri-implantitis. This technology claims a noncontact, no media and contamination-free method. The laser modification technique is very suitable for selective modification of surfaces and allows the generation of complex microstructures, this technique makes important in geometrically complex biomedical implants. The laser micromachining changes the micro and nano structured surface roughness of implant threads. The inner part of thread is more important than the outer part for bone formation and growth. The laser technique has advantage to treat only the inner part of the thread and leave the outer part machined. The pulsed laser melting of the titanium implant surface in a vacuum chamber is one of the surface-modification processes. The laser-treated surface morphology consists of more or less periodic wavelength of peaks with 50–100 µm between the elements.[16]

S. Cho et al.[49] studied laser treated, commercially pure titanium screws and inserted in right tibia metaphysics of white rabbits for 8 weeks. It was reported that the SEM of laser treated implants demonstrated a deep and regular honeycomb pattern with small pores and the removal torque was 23.58 N-cm for the controlled machined implants and 62.58 N-cm for the laser-treated implants. A. Gaggl et al.[50] made an comparative study on four different dental implant surfaces treated with machined roughness, titanium spray coating, treated by aluminium oxide and treated by laser. It is reported that the laser-treated surface has high purity and showed enough surface roughness for good osteointegration and had a regular pattern of micro pores with an interval of 10-12 µm, a diameter of 25 µm and a depth of 20 µm. Gill et al.[51] studied the influence of laser surface modifications on the mechanical and electrochemical behaviour of Ti and Ti6Al4V implants. When laser modification was carried out for each metal, the microstructural changes were observed:

a) melting zone with small grain size and martensitic structures in aforementioned metal and

b) the heat-affected zone (HAZ) with α-phase in CP Ti with a higher grain size and Widmanstatten structure in Ti6Al4V.

Positive tensile residual stress was determined by means of X-ray analysis in the zones marked by laser. Furthermore, corrosion behaviour was studied in a simulated body fluid at 37 °C. It was found that pitting was observed in different zones near the HAZ, and results showed that the corrosion resistance decreased in the laser-treated samples, and residual stresses and the martensitic microstructures favoured the decrease of the corrosion-fatigue life by around 20 % in both metals under physiological conditions. G. Romanos et al.[52] studied the osteoblast attachment on titanium surfaces after laser irradiation. It is reported that osteoblasts could be grown in all of the surfaces. The cell density is higher in the laser-irradiated surface than in the non-irradiated specimens because of the cleaner effect on superficial layer by the lasers. The laser irradiation on the titanium surface may promote the osteoblast attachment and further bone formation. Palmquist et al.[53] made an in-vivo study of laser modified titanium and nano-scale surface topographic features. The authors concluded that the torque removal significantly increased in the laser-modified implant and of clinical importance, the nano-structured surfaces supported long-term bone bonding and interface strength between the titanium implant and the bone. The removal torque is also substantially increased. S. S.-Y. L. Kang et al.[54] studied the biomechanical properties and inter-phase responses of machined and laser-treated stainless steel (SS) implant screws. The laser-treated implants have a higher surface roughness and no compromise in fracture resistance compared to the machined one. The surface roughnesses were increased due to repeated melting and solidification of the material. The bone implant's contact ratio was determined and there was no significant difference between laser-treated and machined micro-screw implants.

6 CONCLUSIONS

This article discussed the surface modification methods for titanium alloys in improving the biological properties and friction properties of implants. Based on the above survey, the research spotlight is especially focused on electrochemical anodizing. It can be used for the formation of an oxide layer on a commercially pure Ti surface for dental implants due to the high expectations regarding their applications. The anodization process is a simple and fast surface-modification technique to create a nano-structured TiO_2 on the Ti surface. It will improve the cell growth on the Ti surface. The degree of optimised geometry and surface roughness for implant fixation is still unknown. There is a contradiction in lthe iterature relating in-vivo and in-vitro studies with moderate surface roughness. Some of the researchers mentioned not only the degree of roughness is important; the textured surface of implant is also. There is scope for an evaluation of optimum surface roughness and surface morphology for dental implant applications. This is because the surface roughness plays a major role in quality, the coefficient friction and the rate of osseointegration in titanium dental implants. Aesthetics in this regard refers to the engineering of the surface colour for both marking and implant aesthetic reasons. There is no literature found which investigates the sliding friction behaviours of titanium on titanium with specific reference to the required torque for the axial preloading of titanium screws. Very little research has been conducted on laser surface-modification techniques that investigate its effect on biocompatibility.

7 FUTURE SCOPE

From this research gap one can perform research on the aesthetical appearance of dental implants by performing the anodizing process. However, there is no evidence on the statistical relationship between bone contact and surface roughness. Also there is a lack of appropriate measurement on the sliding friction between the titanium on titanium implants with specific reference to the required torque for the axial preloading of titanium screws. Hence, more studies are required to gain knowledge about the aesthetic appearance, surface topography on the bone growth and friction between the bone and titanium implants. The performance of titanium and its alloys can be improved intensely by developing a suitable surface-modification procedure that will lead to increased aesthetic appearance and wear, and frictional properties.

8 REFERENCES

[1] J.-L. Delplancke, M. Degrez, A. Fontana, R. Winand, Self-colour anodizing of titanium, Surf. Technol., 16 (**1982**), 153–162, doi:10.1016/0376-4583(82)90033-4

[2] M. Geetha, A. K. Singh, R. Asokamani, A. K. Gogia, Ti based biomaterials, the ultimate choice for orthopaedic implants - A review, Prog. Mater. Sci., 54 (**2009**), 397–425, doi:10.1016/j.pmatsci.2008.06.004

[3] M. V. Wise, D. L., Trantolo, D. J., Lewandrowski, K.-U., Gresser, J. D., Cattaneo, Biomaterials Engineering and Devices: Human Applications, 1st ed., Humana Press, 2000. http://www.springer.com/us/book/9780896038592

[4] C. N. Elias, J. H. C. Lima, R. Valiev, M. A. Meyers, Biomedical Applications of Titanium and its Alloys, J. Miner. Met. Mater. Soc., (**2008**), 46–49, doi:10.1007/s11837-008-0031-1

[5] K. Maehara, K. Doi, T. Matsushita, Y. Sasaki, Application of Vanadium-Free Titanium Alloys to Artificial Hip Joints, Mater. Trans., 43 (**2002**), 2936–2942, doi:10.2320/matertrans.43.2936

[6] M. Long, H. J. Rack, Titanium alloys in total joint replacement—a materials science perspective., Biomaterials., 19 (**1998**), 1621–1639, doi:10.1016/S0142-9612(97)00146-4

[7] M. Niinomi, M. Nakai, J. Hieda, Development of new metallic alloys for biomedical applications, Acta Biomater., 8 (**2012**), 3888–3903, doi:10.1016/j.actbio.2012.06.037

[8] K. Subramani, R. T. Mathew, Titanium Surface Modification Techniques for Dental Implants-From Microscale to Nanoscale, First Edit, Elsevier Inc., 2012, doi:10.1016/B978-1-4557-7862-1.00006-7

[9] J.-K. Lee, D.-S. Choi, I. Jang, W.-Y. Choi, Improved osseointegration of dental titanium implants by TiO_2 nanotube arrays with recombinant human bone morphogenetic protein-2: a pilot in vivo study, International Journal of Nanomedicine, 10 (**2015**), 1145–1154, doi:10.2147/IJN.S78138

[10] A. Karambakhsh, A. Afshar, S. Ghahramani, P. Malekinejad, Pure commercial titanium color anodizing and corrosion resistance, J. Mater. Eng. Perform., 20 (**2011**), 1690–1696, doi:10.1007/s11665-011-9860-0

[11] H. J. Song, M. K. Kim, G. C. Jung, M. S. Vang, Y. J. Park, The effects of spark anodizing treatment of pure titanium metals and titanium alloys on corrosion characteristics, Surf. Coatings Technol., 201 (**2007**), 8738–8745, doi:10.1016/j.surfcoat.2006.11.022

[12] D. G. Bansal, O. L. Eryilmaz, P. J. Blau, Surface engineering to improve the durability and lubricity of Ti-6Al-4V alloy, Wear., 271 (**2011**), 2006–2015, doi:10.1016/j.wear.2010.11.021

[13] A. Vadiraj, M. Kamaraj, Fretting fatigue behavior of surface modified biomedical titanium alloys, Trans. Indian Inst. Met., 63 (**2010**), 217–223, doi:10.1007/s12666-010-0030-0

[14] A. Wennerberg, T. Albrektsson, J. Lausmaa, Torque and histomorphometric evaluation of c.p. titanium screws blasted with 25- and 75—m-sized particles of Al_2O_3, J. Biomed. Mater. Res., 30 (**1996**), 251–260, doi:10.1002/(SICI)1097-4636(199602)30:2<251:AID-JBM16>3.0.CO;2-P

[15] G. Peto, A. Karacs, Z. Pászti, L. Guczi, T. Divinyi, A. Joób, Surface treatment of screw shaped titanium dental implants by high intensity laser pulses, Appl. Surf. Sci., 186 (**2002**), 7–13, doi:10.1016/S0169-4332(01)00769-3

[16] L. Le Guéhennec, A. Soueidan, P. Layrolle, Y. Amouriq, Surface treatments of titanium dental implants for rapid osseointegration, Dent. Mater., 23 (**2007**), 844–854, doi:10.1016/j.dental.2006.06.025

[17] A. Abron, M. Hopfensperger, J. Thompson, L. F. Cooper, Evaluation of a predictive model for implant surface topography effects on early osseointegration in the rat tibia model, J. Prosthet. Dent., 85 (**2001**), 40–46, doi:10.1067/mpr.2001.112415

[18] S. A. Novaes AB Jr, Souza SL, de Oliveira PT, Histomorphometric analysis of the bone-implant contact obtained with 4 different implant surface treatments placed side by side in the dog mandible, Int J Oral Maxillofac Implant., 17 (**2002**), 377–83

[19] M. Piattelli, A. Scarano, M. Paolantonio, G. Iezzi, G. Petrone, A. Piattelli, Bone response to machined and resorbable blast material titanium implants: an experimental study in rabbits, J. Oral Implantol., 28 (**2002**), 2–8, doi:10.1563/1548-1336(2002)028<0002:BRTMAR>2.3.CO;2

[20] W.-D. Müeller, U. Gross, T. Fritz, C. Voigt, P. Fischer, G. Berger, et al., Evaluation of the interface between bone and titanium surfaces being blasted by aluminium oxide or bioceramic particles., Clin. Oral Implants Res., 14 (**2003**), 349–356, doi:10.1034/j.1600-0501.2003.00791.x

[21] A. Karacs, A. Joob Fancsaly, T. Divinyi, G. Peto, G. Kovách, Morphological and animal study of titanium dental implant surface induced by blasting and high intensity pulsed Nd-glass laser, Mater. Sci. Eng. C., 23 (**2003**), 431–435, doi:10.1016/S0928-4931(02)00316-8

[22] C. Larsson, L. Emanuelsson, P. Thomsen, L. E. Ericson, B.-O. Aronsson, B. Kasemo et al., Bone response to surface-modified titanium implants: studies on the early tissue response to machined and electropolished implants with different oxide thicknesses, Biomaterials., 17 (**1996**) 605–616, doi:10.1016/0142-9612(96)88711-4

[23] H. Badekas, C. Panagopoulos, Titanium anodization under constant voltage conditions, Surface & Coatings Technology, 31 (**1987**), 381–388, doi: 10.1016/0257-8972(87)90164-2

[24] A. K. Sharma, Anodizing titanium for space applications, Thin Solid Films, 208 (**1992**), 48–54, doi:10.1016/0040-6090(92)90946-9

[25] M. Shirkhanzadeh, Electrochemical preparation of protective oxide coatings on titanium surgical alloys, J. Mater. Sci. Mater. Med., 3 (**1992**), 322–325, doi:10.1007/BF00705362

[26] Z. M. Yan, T. W. Guo, H. B. Pan, J. J. Yu, Influences of Electrolyzing Voltage on Chromatics of Anodized Titanium Dentures., Mater. Trans., 43 (**2002**), 3142–3145, doi:10.2320/matertrans.43.3142

[27] Z. Huan, L. E. Fratila-Apachitei, I. Apachitei, J. Duszczyk, Synthesis and characterization of hybrid micro/nano-structured NiTi surfaces by a combination of etching and anodizing., Nanotechnology, 25 (**2014**), 055602, doi:10.1088/0957-4484/25/5/055602

[28] H. Song, S. Park, S. Jeong, Y. Park, Surface characteristics and bioactivity of oxide films formed by anodic spark oxidation on titanium in different electrolytes, J. Mater. Process. Tech., 9 (**2008**), 864–870, doi:10.1016/j.jmatprotec.2008.02.055

[29] J. P. Schreckenbach, G. Marx, Characterization of anodic spark-converted titanium surfaces for biomedical applications, Journal of materials science: Materials in medicine, 10 (**1999**), 453–457, doi:10.1023/A:1008988706980

[30] A. Zhecheva, S. Malinov, W. Sha, Titanium alloys after surface gas nitriding, Surf. Coatings Technol., 201 (**2006**), 2467–2474, doi:10.1016/j.surfcoat.2006.04.019

[31] K. Kim, B. A. Lee, X. H. Piao, H. J. Chung, Y. J. Kim, Surface characteristics and bioactivity of an anodized titanium surface, J. Periodontal Implant Sci., 43 (**2013**), 198–205, doi:10.5051/jpis.2013.43.4.198

[32] C. N. Elias, Biomedical Applications of Titanium and its Alloys, Rev. Mater., 15 (**2010**), 138–142, doi:10.1007/s11837-008-0031-1

[33] B. C. de V. Gurgel, P. F. Gonçalves, S. P. Pimentel, F. H. Nociti, E. A. Sallum, A. W. Sallum et al., An Oxidized Implant Surface May Improve Bone-to-Implant Contact in Pristine Bone and Bone Defects Treated With Guided Bone Regeneration: An Experimental Study in Dogs, J. Periodontol., 79 (**2008**), 1225–1231, doi:10.1902/jop.2008.070529

[34] P. M. Burgos, L. Rasmusson, L. Meirelles, L. Sennerby, Early bone tissue responses to turned and oxidized implants in the rabbit tibia, Clin. Implant Dent. Relat. Res., 10 (**2008**), 181–190, doi:10.1111/j.1708-8208.2007.00074.x

[35] E. T. Uzumaki, A. R. Santos, C. S. Lambert, Titanium Oxide (TiO_2) Coatings Produced on Titanium by Oxygen-Plasma Immersion and Cell Behaviour on TiO2, Key Eng. Mater., 309–311 (**2006**), 367–370, doi:10.4028/www.scientific.net/KEM.309-311.367

[36] C. Yao, T. J. Webster, Anodization: a promising nano-modification technique of titanium implants for orthopedic applications., J. Nanosci. Nanotechnol., 6 (**2006**), 2682–92, http://www.ncbi.nlm.nih.gov/pubmed/17048475

[37] M. Sato, T. J. Webster, Nanobiotechnology: implications for the future of nanotechnology in orthopedic applications., Expert Rev. Med. Devices., 1 (**2004**), 105–14, doi:10.1586/17434440.1.1.105

[38] E. Vermesse, C. Mabru, L. Arurault, Surface integrity after pickling and anodization of Ti-6Al-4V titanium alloy, Appl. Surf. Sci., 285 (**2013**), 629–637, doi:10.1016/j.apsusc.2013.08.103

[39] L. Wu, J. Liu, M. Yu, S. Li, H. Liang, M. Zhu, Effect of Anodization time on Morphology and Electrochemical Impedance of Andic Oxide Films on Titanium Alloy in Tartrate Solution, Int. J. Electrochem. Sci., 9 (**2014**), 5012–5024

[40] Y. T. Sul, Electrochemical growth behavior, surface properties, and enhanced in vivo bone response of TiO_2 nanotubes on microstructured surfaces of blasted, screw-shaped titanium implants, Int. J. Nanomedicine., 5 (**2010**), 87–100, doi:10.2147/IJN.S8012

[41] K. Yokoyama, T. Ichikawa, H. Murakami, Y. Miyamoto, K. Asaoka, Fracture mechanisms of retrieved titanium screw thread in dental implant, Biomaterials., 23 (**2002**), 2459–2465, doi:10.1016/S0142-9612(01)00380-5

[42] F. Javed, G.E. Romanos, The role of primary stability for successful immediate loading of dental implants, A literature review, J. Dent., 38 (**2010**), 612–620, doi:10.1016/j.jdent.2010.05.013

[43] M. V. dos Santos, C. N. Elias, J. H. Cavalcanti Lima, The effects of superficial roughness and design on the primary stability of dental implants, Clin. Implant Dent. Relat. Res., 13 (**2011**), 215–223, doi:10.1111/j.1708-8208.2009.00202.x

[44] C. N. Eliasa, F. A. Rocha, A. L. Nascimento, P. G. Coelho, Influence of implant shape, surface morphology, surgical technique and bone quality on the primary stability of dental implants, J. Mech. Behav. Biomed. Mater., 16 (**2012**), 169–180, doi:10.1016/j.jmbbm.2012.10.010

[45] Y. Oshida, Surface modifications; Bioscience and Bioengineering of Titanium Materials, 2007, doi:10.1016/B978-008045142-8/50011-6

[46] H. Garg, G. Bedi, Implant Surface Modifications?: A Review, J. Clin. Diagnostic Res., 6 (**2012**), 319–324

[47] A. M. Ballo, O. Omar, W. Xia, A. Palmquist, Implant Dentistry – A Rapidly Evolving Practice, Implant Dent. - A Rapidly Evol. Pract., (**2011**), 19–56, doi:10.5772/706

[48] C. Larsson, P. Thomsen, B. O. Aronsson, M. Rodahl, J. Lausmaa, B. Kasemo et al., Bone response to surface modified titanium implants: Studies on the early tissue response to machined and electropolished implants with different oxide thicknesses, Biomaterials., 17 (**1996**), 605–616, doi:10.1016/0142-9612(96)88711-4

[49] S. Cho, S. Jung, A removal torque of the laser-treated titanium implants in rabbit tibia, Biomaterials., 24 (**2003**), 4859–4863, doi:10.1016/S0142-9612(03)00377-6

[50] A. Gaggl, G. Schultes, W. D. Mu, H. Ka, Scanning electron microscopical analysis of laser-treated titanium implant surfaces – a comparative study, Biomaterials., 21 (**2000**), 1067–1073, DOI:10.1016/s0142-9612(00)00002-8

[51] F. J. Gil, L. Delgado, E. Espinar, J. M. Llamas, Corrosion and corrosion-fatigue behavior of cp-Ti and Ti – 6Al – 4V laser-marked biomaterials, J Mater Sci Mater Med., 23 (**2012**), 885–890, doi:10.1007/s10856-012-4572-z

[52] G. Romanos, M. Dent, R. Crespi, D. D. S. A. Barone, D. D. S. U. Covani, Osteoblast Attachment on Titanium Disks After Laser Irradiation, Int. J. Oral Maxillofac. Implant., 21 (**2006**), 232–236

[53] A. Palmquist, O. M. Omar, M. Esposito, Titanium oral implants: surface characteristics, interface biology and clinical outcome, J. R. Soc. Interface., 7 (**2010**), 515–527, doi:10.1098/rsif.2010.0118.focus

[54] S. S.-Y. L. He-Kyong Kang, T.-M. Chu, P. Dechow, Kelton Stewart, H.-M. Kyung, Laser-treated stainless steel mini-screw implants_ 3D surface roughness, bone-implant contact, and fracture resistance analysis, Eur. J. Orthod., 37 (**2015**), doi:10.1093/ejo/cjv017

UDK 620.1:620.3:67.014
Original scientific article/Izvirni znanstveni članek

ISSN 1580-2949
MTAEC9, 51(2)195(2017)

ELECTROSPINNING OF BIODEGRADABLE POLYESTER URETHANE: EFFECT OF POLYMER-SOLUTION CONDUCTIVITY

ELEKTROPREDENJE BIORAZGRADLJIVEGA POLIESTER-URETANA: VPLIV PREVODNOSTI RAZTOPINE POLIMERA

Alena Pavelkova, Pavel Kucharczyk, Vladimir Sedlarik

Centre of Polymer Systems, University Institute, Tomas Bata University, Tr. Tomase Bati 5678, 76001 Zlín, Czech Republic
apavelkova@cps.utb.cz

Prejem rokopisa – received: 2015-06-29; sprejem za objavo – accepted for publication: 2016-02-10

doi:10.17222/mit.2015.139

This work deals with an investigation of fabrications of nanofibres based on biodegradable polylactic-acid/polyethylene-glycol-chain-linked copolymers, using the electrospinning technique. Crucial attention is paid to describing the effect of polymer-solution conductivity on the morphology of the resulting nanofibres. Nanofibre systems were studied with scanning electron microscopy and the subsequent image analysis of nanofibre diameters. Hydrolytical degradability of the investigated copolymers was studied using gel permeation chromatography. The results show a significant effect of polymer-solution conductivity on the quality of nanofibres.

Keywords: electrospinning, nanofibres, polylactide polyethylene glycol copolymer

To delo obravnava preiskavo izdelave nanovlaken na osnovi biorazgradljive, v verigo povezanih kopolimerov polimlečne kisline/polietilen glikola, z uporabo tehnike elektropredenja. Največja pozornost je usmerjena v opis vpliva prevodnosti raztopine polimera na morfologijo izdelanih nanovlaken. Sistem nanovlaken je bil proučevan z vrstično elektronsko mikroskopijo in analizo slik premerov nanovlaken. Hidrolitična degradacija preiskovanih polimerov je bila proučevana z gelsko permeacijsko kromatografijo. Rezultati kažejo močan vpliv prevodnosti raztopine polimera na kvaliteto nanovlaken.

Ključne besede: elektropredenje, nanovlakna, polilaktid polietilen glikol kopolimer

1 INTRODUCTION

Electrospinning products based on biodegradable polymers have been suitable materials for innovative tissue-engineering applications.[1]

Polylactic acid (PLA) is a biodegradable thermoplastic polymer with good properties and processability. Nevertheless, its properties can also be limiting in some of the applications.[2] An effective way of how to improve the PLA properties can be a modification of synthesis using a chain-linking reaction.[3] In this two-step process, a functionalized low-molecular-weight prepolymer is prepared first and then, in the second step, the chain linking through the reactive chain ends with a chain-linking agent (usually diisocyanate) is carried out.[4]

The research presented here focuses on the electrospinning of polyester urethane (PEU) based on PLA/polyethylene glycol (PEG) copolymer chain linked with diisocyanates. The morphology and characteristics of the prepared nanofibres are correlated with the conductivity of the polymer solution. Degradability of the studied PEU was studied under abiotic conditions in a phosphate-buffer medium.

2 EXPERIMENTAL PART

2.1 Materials

L-lactic acid, poly(ethylene glycol) (PEG, M_W = 400), hexamethylene diisocyanate (HMDI) and Tin(II)2-

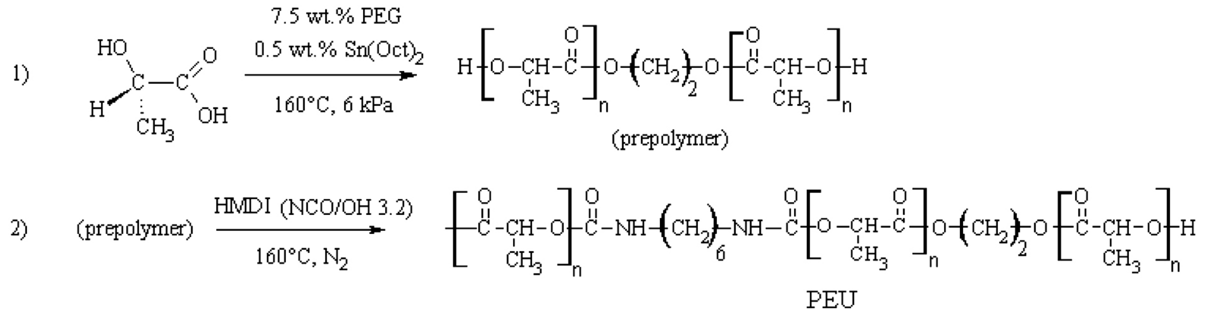

Figure 1: Scheme of the synthesis route: 1) preparation of prepolymer, 2) poly (lactic acid)-poly (ethylene glycol) chain-linking reaction
Slika 1: Shema poti sinteze: 1) priprava predpolimera, 2) poli (mlečna kislina)-poli - (etilen glikol) reakcija verižnega povezovanja

ethylhexanoate Sn(Oct)$_2$ (92.5–100.0 %) were purchased from Sigma-Aldrich; phosphate buffer (PB, 0.1 mol.L^{-1}, pH = 7, NaH_2PO_4 adjusted with NaOH) and tetrahydrofuran (HPLC-grade) were sourced from Chromspec, Brno, Czech Republic.

The synthesis of copolymers was conducted through a polycondensation reaction and, in the second step, a chain-linking reaction with hexamethylene diisocyanate (HMDI) was performed (**Figure 1**). In this study, a copolymer with a molar ratio of NCO and OH groups equal to 3.2 was used. The preparation of the studied PEU is described in detail in our previous work.[5]

2.2 Method

The molecular weight of PEU was examined with gel permeation chromatography under the conditions described in reference.[5] A hydrolysis test was performed on round-shaped samples (a diameter of 3.4 mm and a thickness of 1.5 mm) fully immersed in a liquid-buffer medium (pH = 7) at 37 °C and 55 °C.

The electrospinning process was carried out on an in-house constructed apparatus consisting of a jet and a target with a separation distance of 18 cm at 23 °C. The PEU solution (12 % of the mass fraction in DMF) was charged with DC 75 kV. The flow rate of the polymer solution was 0.086 mL min^{-1}. The conductivity of the polymer solution was adjusted with citric acid and sodium tetraborate (3:1, w/w) to 59.5, 107.9 and 150.9 μS cm^{-1}.

The morphology of the electrospun nanofibres was studied with scanning electron microscopy (Tescan Vega II LMU, Czech Republic). The morphology analysis of the nanofibres was carried out with an image analysis of SEM micrographs using the ImageJ software.

3 RESULTS

The values of the average molecular weight (M_w) of the studied PEU and their reduction during the degradation process at 37 °C and 55 °C are presented in **Table 1**. While M_w of PEU at the beginning of the degradation experiment was 300 kg.mol^{-1}, the samples showed a 99 % M_w reduction after 25 d.

Table 1: Molecular-weight loss of PLA-PEG copolymers during the degradation experiment
Tabela 1: Zmanjšanje molekulske mase PLA-PEG kopolimera, med preizkusom degradacije

Degradation time (days)	55 °C		37 °C	
	M_w (kg mol^{-1})	\	M_w (kg mol^{-1})	\
0	300	9.2	300	9.2
4	42	5.6	143	7.3
11	8.0	5.1	84	6.8
25	2.3	3.2	3.0	2.5
32	2.0	2.8	1.9	1.9
52	not detected	not detected	1.0	1.5

Diameter distributions of the nanofibre systems prepared from the PEU solutions with various conductivity values, together with inserted SEM micrographs, can be seen in **Figure 2**. **Table 2** presents the number (D_n), the weight average (D_w) and the polydispersity (D_w/D_n) of nanofibre diameters.

Table 2: Effect of PEU-solution conductivity on the fibre diameter
Tabela 2: Vpliv prevodnosti raztopine PEU na premer vlaken

Conductivity (μS cm^{-1})	D_n (μm)	D_w (μm)	*PDI*
59.5	0.24	0.36	1.50
107.9	0.18	0.28	1.55
150.9	0.29	0.42	1.42

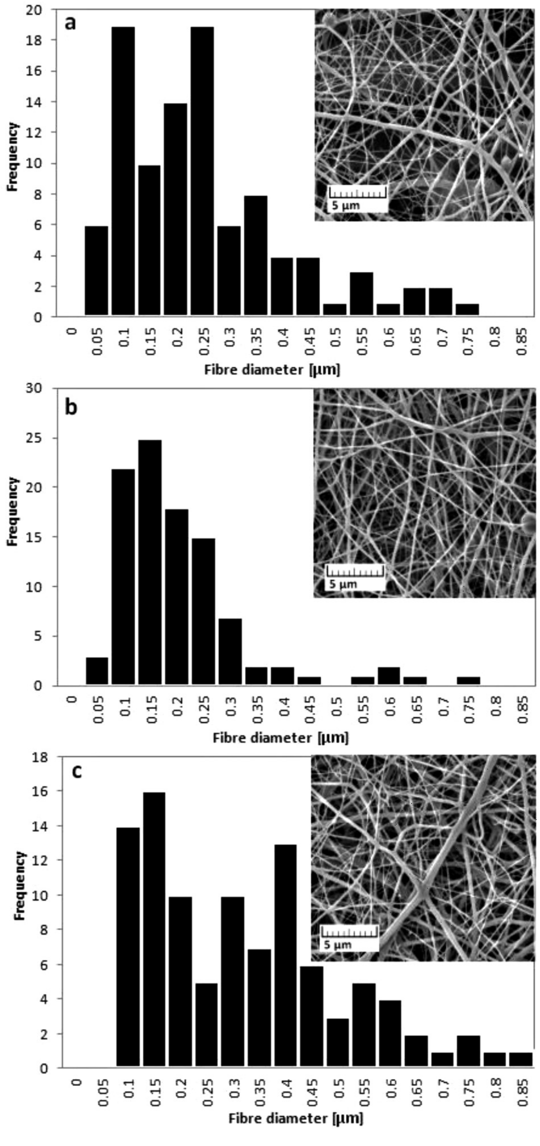

Figure 2: Histogram of PEU fibre-diameter distribution and corresponding SEM micrographs (inserted). The conductivity of PEU solutions was adjusted to: a) 59.5 μS cm^{-1}, b) 107.9 μS cm^{-1} and c) 150.9 μS cm^{-1}

Slika 2: Histogram razporeditve premera REU-vlaken in njihov SEM-posnetek. Prevodnost PEU raztopine je bila uravnana na: a) 59.5 μS cm^{-1}, b) 107.9 μS cm^{-1} in c) 150.9 μS cm^{-1}

4 DISCUSSION

The degradation behaviour of PEU is in accordance with the already published results.[5] The kinetics of the M_w reduction is interesting as it is strongly dependent on the temperature. A significantly faster degradation of PEU occurs at a temperature (55 °C) that is close to the glass-transition temperature. On the other hand, the degradation rate observed at 37 °C provides results comparable with the PLA-based polymers. The homogeneity of the electrospun PEU nanofibres was enhanced by increasing the conductivity of the polymer solution, unlike in the case of low-conductivity PEU solutions where an occurrence of the inhomogeneity of the electrospun products was observed. A combination of nano- and sub-microfibres was obtained for the PEU solutions with the lowest (59.5 µS cm^{-1}) and the highest conductivity (150.9 µS cm^{-1}) while a relatively narrow distribution of nanofibre diameters was found for the PEU solution with a medium conductivity (107.9 µS cm^{-1}). The non-uniformity of fibre diameters could have been caused by a broad molecular-weight distribution, whose relation to the fibre distribution was reported in the work of J. Lyons et al.,[6] though for a different type of material.

5 CONCLUSIONS

Biodegradable PEU nanofibres based on PLA/PEG chain-linked copolymers can be easily fabricated using the electrospinning process. The morphology of the resulting nanofibres can be significantly influenced by adjusting the polymer solution before the electrospinning process. PEU can provide a product with a mixture of nano- and sub-microfibres that can be potentially useful for specific filtration applications.

Acknowledgements

This work was financially supported by the Czech Science Foundation (grant No. 15-08287Y), the Ministry of Education, Youth and Sports of the Czech Republic (grant No. LO1504) and the Internal Grant Agency of TBU in Zlin (grant No. IGA/CPS/2015/003).

6 REFERENCES

[1] W. Jiang, B. Y. S. Kim, J. T. Rutka, W. C. W. Chan, Nanoparticle-mediated cellular response is size-dependent, Nature Nanotechnology, 3 (**2008**) 145–150

[2] A. P. Gupta, New emerging trends in synthetic biodegradable polymers – Polylactide: A critique, European Polymer Journal, 43 (**2007**), 4053–4074

[3] S. I. Moon, C. W. Lee, I. Taniguchi, M. Miyamoto, Y. Kimura, Melt/solid polycondensation of L-lactic acid: an alternative route to poly (L-lactic acid) with high molecular weight, Polymer, 42 (**2001**), 5059–5062

[4] J. Kylmä, J. Tuominen, A. Helminen, J. Seppälä, Chain extending of lactic acid oligomers. Effect of 2, 2?-bis (2-oxazoline) on 1, 6-hexamethylene diisocyanate linking reaction, Polymer, 42 (**2001**), 3333–3343

[5] A. Pavelkova, P. Kucharczyk, P. Stloukal, M. Koutny, V. Sedlarik, Novel poly (lactic acid)-poly (ethylene oxide) chain-linked copolymer and its application in nano-encapsulation, Polymers for Advanced Technologies, 25 (**2014**), 595–604

[6] J. Lyons, Ch. Li, F. Ko, Melt-electrospinning part I: processing parameters and geometric properties, Polymer, 45 (**2004**), 7597–7603

UDK 621.791.725:669.14.018.291:621.791.053
Original scientific article/Izvirni znanstveni članek

ISSN 1580-2949
MTAEC9, 51(2)199(2017)

LASER WELDING OF THE NEW GRADE OF ADVANCED HIGH-STRENGTH STEEL DOMEX 960

LASERSKO VARJENJE DOMEX 960 NOVEGA NAPREDNEGA JEKLA Z VISOKO TRDNOSTJO

Agnieszka Kurc-Lisiecka[1], **Aleksander Lisiecki**[2]
[1]University of Dąbrowa Górnicza, Rail Transport Department, Cieplaka 1C, 41-300 Dąbrowa Górnicza, Poland
[2]Silesian University of Technology, Faculty of Mechanical Engineering, Welding Department, Konarskiego 18A, 44-100 Gliwice, Poland
a.kurc@wp.pl, aleksander.lisiecki@polsl.pl

Prejem rokopisa – received: 2015-07-01; sprejem za objavo – accepted for publication: 2016-02-09

doi:10.17222/mit.2015.158

The article presents the results of investigations on autogenous laser welding of the new-generation advanced high-strength steels (AHSS) Domex 960, classified as thermomechanically rolled steel by the manufacturer. There is little information about welding this steel grade, relating only to arc-welding methods. Therefore, a modern disk laser was used for the butt-joint welding of 5.0 mm steel sheets. The results of a microstructure study, tensile tests, technological bending tests, impact-toughness tests and also microhardness measurements showed that a low heat input during the laser welding of the new Domex 960 grade steel is advantageous. A low heat input and thus a high cooling rate of the weld metal and the heat-affected zone (HAZ) led to the formation of a favourable fine-grained microstructure, providing also high mechanical properties of butt joints, comparable to the properties of the base metal. Despite the high cooling rates, there was no significant increase in the microhardness measured across the butt joints. Moreover, a slight decrease in the microhardness was observed in the HAZ.

Keywords: laserlaser welding, disk laser, thermomechanically rolled steel, advanced high-strength steel, fine-grained steel, properties of welded joints

Članek predstavlja rezultate preiskav avtogenega laserskega varjenja nove generacije naprednih visokotrdnostnih jekel (AHSS), jekla Domex 960, ki so ga proizvajalci opredeljujejo kot termomehansko valjano jeklo. Malo je informacij o varjenju te vrste jekla, nekaj le za metode obločnega varjenja. Za soležno varjenje 5 mm debelih pločevin je bil uporabljen modern diskasti laser. Rezultati študija mikrostrukture, nateznih preizkusov, tehnoloških upogibnih preizkusov, preizkusov udarne žilavosti in tudi meritev mikrotrdote, so pokazali, da je ugoden majhen vnos toplote med laserskim varjenjem nove vrste jekla Domex 960. Majhen vnos toplote in zato velika hitrost ohlajanja kovine v zvaru in v toplotno vplivani coni (HAZ), povzroči nastanek željene drobno zrnate mikrostrukture in tudi zagotavlja visoke mehanske lastnosti soležnega zvara, v primerjavi z lastnostmi osnovne kovine. Kljub velikim hitrostim ohlajanja, ni bilo občutnega povečanja mikrotrdote, izmerjene preko soležnega zvara. Poleg tega je bilo v HAZ opaženo rahlo zmanjšanje mikrotrdote.

Ključne besede: lasersko varjenje, diskasti laser, termomehansko valjano jeklo, napredna visokotrdnostna jekla, drobno zrnato jeklo, lastnosti zvarjenih spojev

1 INTRODUCTION

The constant trend to increase production efficiency, reduce energy consumption and material consumption, improve the durability and reliability has lead to an increasing use of advanced high-strength materials.[1–8] Depending on the application, working conditions and the type of load and wear, different metallic, bimetallic or composite materials are used.[9–12]

In the case of the manufacturing of building structures such as bridges, towers, industrial buildings and vehicles, particularly heavy vehicles such as trucks, trailers, semi-trailers, rail vehicles such wagons and tramcars, and also other utility vehicles and machines such as cranes, loaders, excavators, etc., the primary group of materials is structural steel.[13–18] The reason for this is the ease of forming and joining steel pieces, usually with welding technologies. Moreover, the use of high-strength steel (HSS) has been growing in the industry for many years. The dynamic development of high-strength steels has led to the introduction of modern advanced and ultra-high-strength steels (AHSS and UHSS), characterized by an extremely high yield point and tensile strength over 1000 MPa.[1–8] Steels of this type achieve high mechanical properties thanks to a very fine-grained structure and/or a sophisticated phase composition like in the case of dual-phase (DP), complex-phase (CP) and transformation-induced plasticity (TRIP) steels.[2,6,7]

A significant group of the modern structural steels currently used in the industry includes thermomechanically rolled fine-grained microalloyed steel classified by the EN 10149-2 standard and also the quenched and tempered low-alloy steel classified by the EN 10025-6 standard. The EN 10149-2 standard covers the thermomechanically rolled fine-grained microalloyed steel with a yield point of up to 700 MPa (e.g., S700MC). An example of the commercial name of this type of steel is Domex 700, manufactured by a Swedish company. On the contrary, the EN 10025-6 standard covers the low-alloy quenched and tempered steel with a yield point of up to 960 MPa (e.g., S960QL). An example of the commercial name in this case is Weldox 960.

Steels of the above groups differ in the chemical composition and manufacturing procedure, even if they have similar mechanical properties, as shown in **Table 1**. Differences in the chemical composition affect the carbon equivalent C_e, thus the hardenability and the associated susceptibility to cold cracking (hydrogen cracking).[15,20–22] Beside the chemical composition, structural constituents, especially the strengthening precipitations like carbides, borides or nitrides, also influence the requirements and specification of the welding procedure.

Table 1: Chemical composition of S700MC steel according to EN 10149-2

Tabela 1: Kemijska sestava jekla S700MC, skladno z EN 10149-2

C	Si	Mn	Al	Nb	V	Ti	Mo	B
0.12	0.6	2.1	0.015	0.09	0.2	0.22	0.5	0.005

CEV max = 0.38, CET max = 0.25

As a result of an intensive research and a dynamic development of modern steel grades, the world's largest steel manufacturers now offer steels with properties that go beyond the standards. Examples are steel grades Weldox 1100 or Weldox 1300 classified as quenched and tempered steel, suitable for welding. Additionally, new steel grades, such as Domex 960, are available in the market. The Domex 960 steel grade is classified by the manufacturer as a thermomechanically rolled steel even though the properties of this steel are at the level of quenched and tempered Weldox 960.

Thus, with the introduction of new grades of steel, the classification becomes more difficult.

The reason for this is a very sophisticated chemical composition, the combination of individual elements and also the sophisticated manufacturing process. It should also be noted that the chemical composition of these steels depends on their thickness. In addition, there are also significant differences between individual melts of steel. Moreover, the manufactures continue the research of how to modify the chemical composition in terms of the optimum combination of mechanical properties and weldability.

Such sophisticated steels also require sophisticated welding procedures and welding technologies.[19,23] Unfortunately, the manufactures provide only limited information about the welding, relating only to conventional arc-welding processes such gas metal arc (GMA), gas tungsten arc (GTA) or submerged-arc welding (SMAW).

At the same time, general guidelines for welding thermomechanically rolled fine-grained microalloyed steel grade such as Domex and low-alloy quenched and tempered steel such as Weldox are different. Generally, in the case of thermomechanically rolled fine-grained microalloyed steel, it is recommended not to exceed a certain heat input because it causes a drop in mechanical properties and impact toughness. On the other hand, in the case of low-alloy quenched and tempered steel, the heat input must be within a specific range. Too high a heat input causes a drop in the toughness, like in the case of the fine-grained microalloyed steel. On the other hand, too low a heat input can lead to cold cracking of a joint. Therefore, according to the manufacturer's instructions, the recommended cooling time $t_{8/5}$ between temperature ranges from 800 °C to 500 °C is 5 s to 15 s for Weldox 900 to 1300. As laser welding is of an increasing importance in the industry and the conditions of laser welding are radically different from arc welding, a research of the laser welding of new steel grade Domex 960 was undertaken in this work.[24,25]

2 EXPERIMENTAL PART

The steel chosen for the investigation was the new generation of advanced high-strength steel (AHSS) Domex 960, recently introduced to the industry by a Swedish company. The new grade of steel Domex 960 is included, by the manufacturer, in the group of thermomechanically rolled fine-grained microalloyed steels covered by the EN 10149-2 standard. However, the mechanical properties of steel Domex 960 go far beyond the steels specified in this standard. Additionally, details of the manufacturing process for the new steel grade are undisclosed. The investigated steel with the nominal chemical composition of 0.18 %C, 0.5 %Si, 2.1 %Mn and 0.018 %Al in % of mass fractions and balanced Fe has the minimum yield strength of 960 MPa and the minimum tensile strength of 980 MPa.

Specimens for the test involving laser welding were cut from a 5.0 mm steel plate into coupons with dimensions of 100.0 × 100.0 mm, using a 2D laser cutting machine with a CO_2 generator. Surfaces to be welded were sandblasted and then cleaned with acetone. The trials of welding were performed by means of a solid-state Yb:YAG disk laser emitted in the continuous-wave mode at a wavelength of 1.03 μm with the maximum output power of 3.3 kW. The laser beam was focused to a diameter of 200 μm.

First, the bead-on-plate welds were produced at the maximum output laser power of 3.3 kW and welding speeds of (0.5, 1.0, 1.5 and 2.0) m/min. The bead-on-plate welds were produced to simulate the process of butt-joint welding and to investigate the influence of welding parameters on the penetration depth and weld shape. Based on the bead-on-plate welding trials, the optimum parameters for butt joints were chosen. Butt joints were single-side autogenously laser welded at the maximum laser power of 3.3 kW and welding speeds of 1.0 m/min and 1.5 m/min, respectively. The specimens to be welded were mounted to a clamping device to be protect against distortions. The weld pool was protected by an argon flow via four cylindrical nozzles of 8.0 mm in diameter and set at an angle of 45° to the joint surface. The flow of argon was kept at 15 L/min. The laser beam was focused on the top surface of the specimens to be welded. When the laser-welding tests were completed, the first the visual inspections (VT) were performed according to the procedure of quality control in welding. Next, the metallographic and also mechanical examinations were done. The examination of the structure was carried out by means of optical microscopes (OM) and a scanning electron microscope (SEM). The chemical composition of the base metal was determined with a glow discharge spectrometer (GDS). On the other hand, mechanical tests included a technological bending test, a static tensile test and a Charpy V-notch test.

3 RESULTS AND DISCUSSION

The trials of bead-on-plate welding with a disk laser showed that the heat input required for a full penetration of a 5.0 mm plate of the Domex 960 steel is at least 100 J/mm, at a laser output power of 3.3 kW and a welding speed of 2.0 m/min. The width of a weld face produced at the minimum welding heat input is 2.15 mm, while the root width is 0.8–1.27 mm. In this case the depth/width ratio is over 2.3, indicating that the laser welding mode was the keyhole mode. Additionally, the shape of the fusion zone (FZ) in a columnar or hour-glass configuration (X shape) is characteristic for keyhole laser welding at a high power density of the laser beam. An increase in the heat input of laser welding, by lowering the welding speed at a constant laser power, increases the width of a single bead-on-plate weld and the width of the heat affected zone (HAZ).

The visual inspections (VT) of the test butt joints revealed a proper shape of the welds, and proper reinforcement of weld faces and roots. Macrographs of the test joints showed a proper shape of the fusion lines and no internal imperfections (**Figure 1a**). A high quality of the test joints was also confirmed with microscopic observations (**Figure 1b**) and mechanical tests. The technological bending test revealed no tendency to cracking of the welded joints, both in the weld and in the HAZ, even at the maximum angle of bending. On the other hand, the static tensile tests showed high strength of laser-welded joints at the level of the base metal (BM).

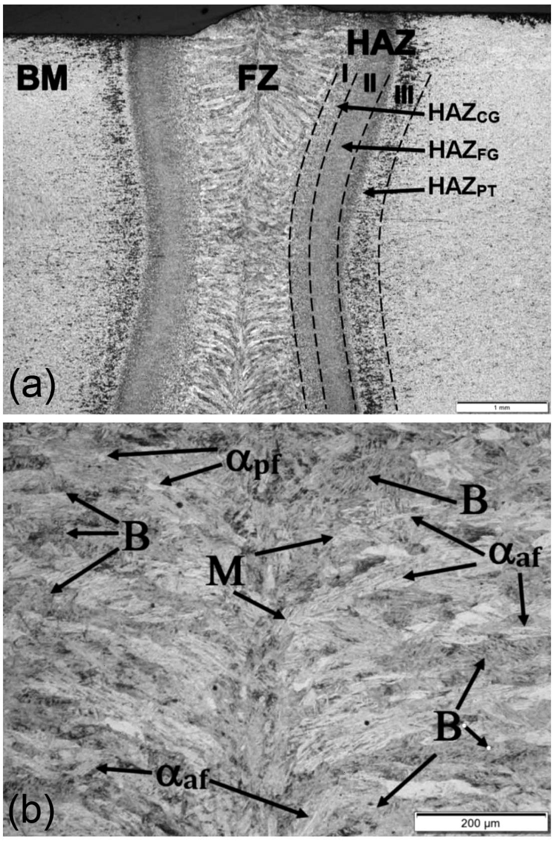

Figure 1: a) Macrostructure of the butt joint produced at the welding speed of 1.5 m/min, thus the heat input of 132 J/mm, b) and the microstructure of the weld metal (FZ)

BM – base metal, FZ – fusion zone, HAZ – heat-affected zone, HAZ_{CG} – coarse-grained region, HAZ_{FG} – fine-grained region, HAZ_{PT} – partially transformed region, B – bainite, M – martensite, α_{pf} – polygonal ferrite, α_{af} – allotriomorphic ferrite

Slika 1: a) Makrostruktura soležnega zvara, izdelanega s hitrostjo varjenja 1,5 m/min, vnos toplote 132 J/mm in b) mikrostruktura zvarjene kovine (FZ)

BM – osnovna kovina, FZ – področje taljenja, HAZ – toplotno vplivana cona, HAZ_{CG} – področje velikih zrn, HAZ_{FG} – področje drobnih zrn, HAZ_{PT} – delno transformirano področje, B – bainit, M – martenzit, α_{pf} – poligonalni ferit, α_{af} – alotriomorfni ferit

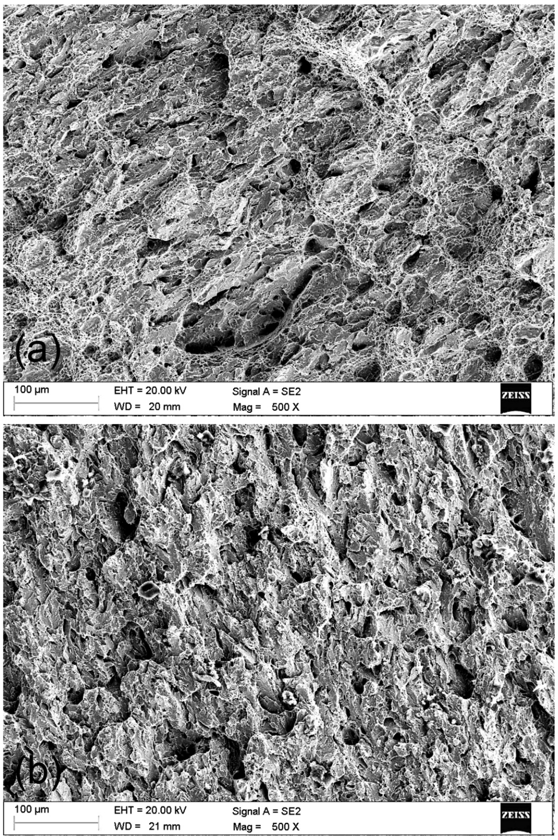

Figure 2: SEM micrographs of the fracture surface of the test joint produced at: a) the heat input of 198 J/mm and b) the heat input of 132 J/mm

Slika 2: SEM-posnetek površine preloma preizkusnega spoja izdelanega z vnosom toplote: a) 198 J/mm in b) vnosom toplote 132 J/mm

Table 2: Chemical composition of S690QL steel according to EN 10025-6
Tabela 2: Kemijska sestava jekla S690QL, skladno z EN 10025-6

C	Si	Mn	B	Cr	Cu	Mo	N	Nb	Ni	Ti	V	Zr
0.12	0.8	1.7	0.005	1.5	0.5	0.7	0.015	0.06	2.0	0.05	0.12	0.15

CEV max = 0.65, CET standard = 0.29

All of the tested samples broke out of the joint area in the base metal at a tensile strength of 1093MPa – 1017 MPa. The Charpy V-notch test, performed at room temperature, showed that the impact toughness of the test butt joints is clearly lower compared to the base metal. The results of the impact toughness determined for the base metal were very consistent, ranging from 128 J/cm^2 to 134 J/cm^2. The average value was 131.3 J/cm^2. The impact toughness of the test joint welded at a heat input of 198 J/mm was in a range of 82 J/cm^2 – 98 J/cm^2, at the average value of 90 J/cm^2. So, the impact toughness of this joint is as low as 68 % of the base-metal toughness. On the contrary, the impact toughness of the second test joint welded at a low heat input of 132 J/mm is 70.7 J/cm^2, so just 53 % of the base-metal toughness.

SEM micrographs of the fracture surfaces of the test joints are presented in **Figure 2**. As can be seen, the fracture surfaces indicate a typical ductile dimple fracture mode in both cases. So, although the impact toughness of the test joints is clearly lower compared to the base metal, the fracture mode is ductile. The results indicate that the impact toughness of the test butt joints depends directly on the heat input of autogenous laser welding within the investigated range of parameters, i.e., thermal conditions, cooling rates and the structures of the weld metal and the HAZ.

The cooling times $t_{8/5}$ between 800 °C and 500 °C were calculated for different heat inputs of laser welding by means of an equation adopted for the conditions of keyhole laser welding, as described in details in [4]. For the heat input of 198 J/mm for the butt laser welding of the 5.0 mm steel plates, the calculated cooling time $t_{8/5}$ was 1.299 s. However, the cooling time in the case of a lower heat input of 132 J/mm was just 0.577 s. For comparison, in both cases, cooling times $t_{8/5}$ are significantly lower than recommended for the quenched and tempered Weldox grade steel, being in the range of 5s –15 s. However, despite such short cooling times there was no tendency to cold (hydrogen) cracking of the test joints (**Figure 1**).

The microhardness profiles determined on the cross-sections of the welded butt joints show a clear increase in the microhardness values in the region of the weld metal, i.e., the fusion zone, compared to the microhardness of the base metal, which is about 370 HV0.2 (**Figure 3**). The microhardness distribution across the FZ is stable and maintained in a range of 360–440, while the mean value of microhardness in the FZ region is about 404 HV0.2. On the other hand, the distribution of microhardness in the HAZ is more complex, so the HAZ can be divided into at least two areas: the inner HAZ adjacent to the FZ and the outer HAZ adjacent to the BM. From the side of the base metal, roughly in the middle of the HAZ, the microhardness decreases gradually from 370 to the minimum value of 290–300 HV0.2 and then it rises sharply up to over 400 HV0.2 in the inner HAZ.

The microhardness in individual regions depends directly on the microstructure and this, in turn, depends on the chemical composition and the tendency to hardening. The GDS analysis showed that the investigated steel contains 0.161 % C, 0.31 % Si, 1.32 % Mn, 0.15 % Cr, 0.05 % Ni, 0.41 % Mo, 0.043 % Al, 0.01 % of V, Ti, Cu and 0.001 % Nb. Based on the determined compo-

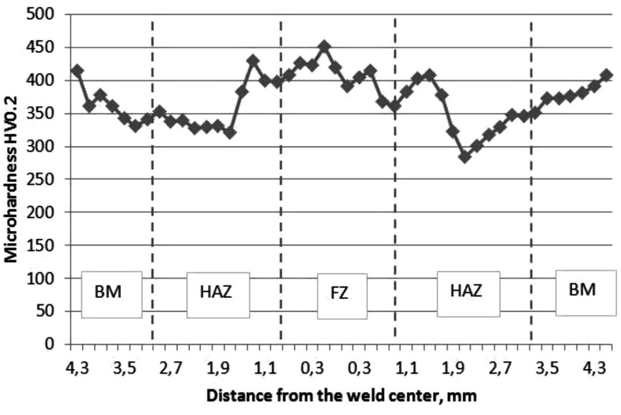

Figure 3: Microhardness distribution on the cross-section of the butt joint produced at the heat input of 132 J/mm
Slika 3: Razporeditev mikrotrdote po preseku soležnega spoja, izdelanega pri vnosu toplote 132 J/mm

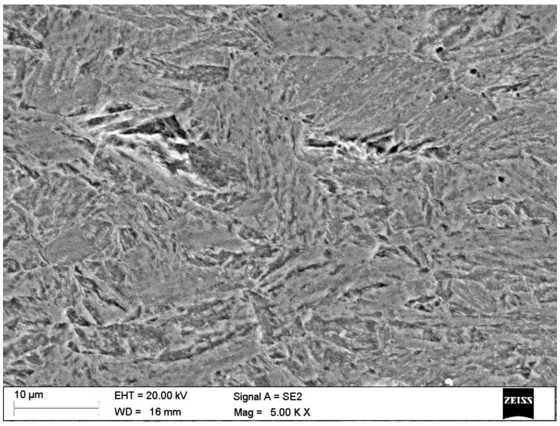

Figure 4: SEM micrograph showing the structure of the base metal of Domex 960 steel at a magnification of 5000×
Slika 4: SEM-posnetek strukture osnovne kovine jekla Domex 960 pri povečavi 5000×

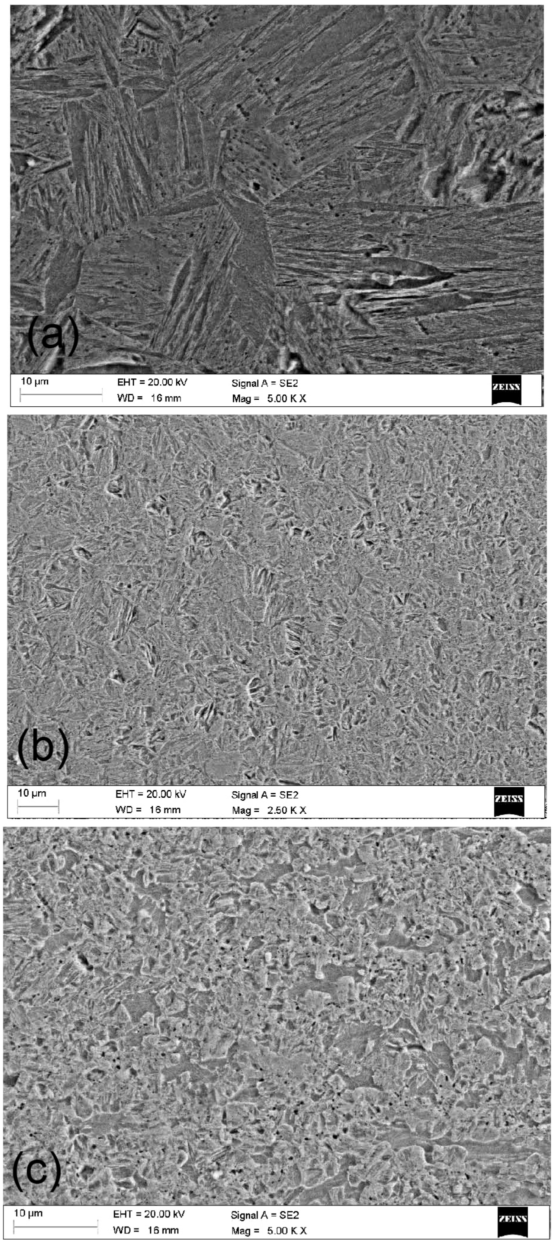

Figure 5: SEM micrographs showing the structure of the weld metal of the butt joint produced at the heat input of: a) 132 J/mm, b) the HAZ region adjacent to the fusion zone and c) the recrystallized fine-grained region of the HAZ

Slika 5: SEM-posnetek structure zvara soležnega spoja izdelanega z vnosom toplote: a) 132 J/mm, b) področje HAZ v bližini področja pretaljevanja in c) rekristalizirano drobnozrnato področje HAZ

sition, the martensitic transformation temperature was calculated according to the following equation: Ms (°C) = 561 – 474 (% C) – 33 (% Mn) – 17 (% Ni) – 17(% Cr) – 21 (% Mo). The calculated Ms temperature is 429.1 °**C**. Additionally, the carbon equivalent (CET) was determined according to the following equation: CET = C + (Mn + Mo)/10 + (Cr + Cu)/20 + Ni/40. The value of the calculated CET is 0.343. Both the high Ms temperature and the relatively low carbon equivalent indicate that the hardenability of the investigated steel is not very high.

The structure of the base metal of the Domex 960 steel is shown in **Figure 4**. In general, the investigated steel has a fine-grained bainitic-martensitic structure. A closer view at the structure exhibits quite a complex arrangement of different phases. The dominant structural constituent is bainite with a significant amount of needle-shaped low-carbon martensite. Beside the main structural constituents, ferrite and also traces of retained austenite can be identified. Additionally, small carbides with a high dispersion can be identified in the structure.

The structure of the HAZ depends on the distance from the fusion line and thus the thermal cycle and the related cooling rate. The thermal conditions during the liquid-metal solidification, especially in the HAZ, may be estimated on the basis of calculated cooling times $t_{8/5}$. The calculated cooling times in the range of 0.6–1.3 are very short and indicate that the solidification as well as the cooling rates were very high under the laser-welding conditions. The HAZ may be divided into three distinguishable regions with different structures (**Figure 1a**). The first characteristic region of the HAZ is adjacent to the fusion line. In this region, due to high temperatures, a slight grain growth occurs. In this region, the structure is bainitic with a higher share of ferrite compared to the BM (**Figures 1a, 5b**). Next, a recrystallized fine-grained region with fine-grained bainite as the dominant structural constituent may be distinguished, characterized by a microhardness in the range of 380–420 HV0.2, **Figure 3**. Finally, a partially transformed and tempered region with a bainitic-ferritic structure may be distinguished (**Figure 5c**). A relatively high share of ferrite in this region is responsible for a gradual microhardness decrease to 280–310 HV0.2, as shown in **Figure 3**.

The structure of the weld metal of the butt joint produced at a heat input of 132 J/mm is presented in **Figures 1b** and **5a**. The structure consists mainly of bainite, a smaller amount of fine martensitic islands and also of ferrite, mainly polygonal (α_{pf}) and allotriomorphic ferrite (α_{af}), as shown in **Figures 1b** and **5a**.

4 CONCLUSIONS

The investigated new steel grade Domex 960 is characterized by a low content of alloying elements (microalloyed steel), thus the low carbon equivalent (CET) is 0.343 and the relatively high temperature of martensitic transformation (Ms) is about 429 °C. Despite the low carbon equivalent, the base metal has a fine-grained bainitic-martensitic structure with a microhardness of 370–380 HV0.2. The calculated cooling times $t_{8/5}$ under the investigated laser-welding conditions are very short, being in a range of 0.6s –1.3 s, so significantly shorter than the recommended values for the quenched and tempered steel grades such as Weldox. Despite a very rapid solidification of the weld metal and cooling, the test joints exhibit a high tensile strength, being at the level of the BM. The impact toughness of the test joints clearly depends on the welding conditions (heat inputs). Although the impact toughness is lower compared to the BM, the fracture mode is ductile.

Acknowledgements

The article was financed by the University of Dąbrowa Górnicza in Poland. Special thanks are extended to Rafał Lis, a welding engineer from the WIELTON Company for providing the new steel grade and also to dr. Wojciech Pakieła for the experimental support.

5 REFERENCES

[1] J. Górka, Weldability of thermomechanically treated steels having a high yield point, Arch. Metall. Mater., 60 (**2015**), 469–475, doi:10.1515/amm-2015-0076,

[2] A. Grajcar, M. Różański, S. Stano, A. Kowalski, Microstructure characterization of laser-welded Nb-microalloyed silicon-aluminum TRIP steel, J. Mater. Eng. Perform., 23 (**2014**), 3400–3406, doi:10.1007/s11665-014-1118-1

[3] J. Górka, Changes in the structure and properties of the steel S700MC by heat treatment, Adv. Mat. Res., 1036 (**2014**), 111–116, doi:10.4028/www.scientific.net/AMR.1036.11

[4] A. Lisiecki, Welding of thermomechanically rolled fine-grain steel by different types of lasers, Arch. Metall. Mater., 59 (**2014**), 1625–1631, doi:10.2478/amm-2014-0276

[5] W. A. Swiatnicki, Modern steels: design-technologies-properties-applications (Guest Editorial), Mater. Sci. Technol., 31 (**2015**) 755–757, doi:10.1179/0267083615Z.000000000928

[6] A. Grajcar, M.Różański, M.Kaminska, B.Grzegorczyk, Study on non-metallic inclusions in laser-welded TRIP-adied Nb-microalloyed steel, Arch. Metall. Mater., 59 (**2014**), 1163–1169, doi:10.2478/amm-2014-0203

[7] A. Grajcar, M. Różański, S. Stano, A. Kowalski, B. Grzegorczyk, Effect of heat input on microstructure and hardness distribution of laser welded Si-Al TRIP-type steel, Adv. Mater. Sci. Eng., 2014 (**2014**), doi:10.1155/2014/658947

[8] A. Lisiecki: Diode laser welding of high yield steel, Proc. of SPIE Vol. 8703, Laser Technology 2012: Applications of Lasers, 87030S (January 22, **2013**), doi:10.1117/12.2013429

[9] L.A. Dobrzanski, M. Bonek, A. Klimpel, A. Lisiecki, Surface layer's structure of X40CrMoV5-1 steel remelted and/or WC alloyed with HPDL laser, Mater. Sci. Forum, 437-4 (**2003**), 69–72, doi:10.4028/www.scientific.net/MSF.437-438.69

[10] M. Bonek, The investigation of microstructures and properties of high speed steel HS6-5-2-5 after laser alloying, Arch. Metall. Mater., 59 (**2014**), 1647–1651, doi:10.2478/amm-2014-0280

[11] G. Moskal, A. Grabowski, A. Lisiecki, Laser remelting of silicide coatings on Mo and TZM alloy, Sol. St. Phenom., 226 (**2015**), 121–126, doi:10.4028/www.scientific.net/SSP.226.121

[12] D. Janicki, High Power Diode Laser Cladding of Wear Resistant Metal Matrix Composite Coatings, Sol. St. Phenom., 199 (**2013**) 587–592, doi:10.4028/www.scientific.net/SSP.199.587

[13] A. Lisiecki, Titanium matrix composite Ti/TiN produced by diode laser gas nitriding, Metals, 5 (**2015**), 54–69, doi:10.3390/met5010054

[14] A. Lisiecki, Welding of thermomechanically rolled fine-grain steel by different types of lasers, Arch. Metall. Mater., 59 (**2014**), 1625–1631, doi:10.2478/amm-2014-0276

[15] A. Kurc-Lisiecka, W. Ozgowicz, W. Ratuszek, J. Kowalska, Analysis of deformation texture in AISI 304 steel sheets, Sol. St. Phenom., 203–204 (**2013**), 105–110, doi:10.4028/www.scientific.net/SSP.203-204.105

[16] R. Burdzik, Ł.Konieczny, Z. Stanik, P. Folęga, A. Smalcerz, A. Lisiecki, Analysis of impact of chosen parameters on the wear of camshaft, Arch. Metall. Mater., 59 (**2014**), 957–963, doi:10.2478/amm-2014-0161

[17] R. Burdzik, T. Węgrzyn, Ł. Konieczny, A. Lisiecki, Research on influence of fatigue metal damage of the inner race of bearing on vibration in different frequencies, Arch. Metall. Mater., 59 (**2014**), 1275–1281, doi:10.2478/amm-2014-0218

[18] J. Kusiński, S. Kac, A. Kopia, A. Radziszewska, M. Rozmus-Górnikowska, B. Major, L. Major, J. Marczak, A. Lisiecki, Laser modification of the materials surface layer – a review paper, Bull. Pol. Acad. Sci. Tech. Sci., 60 (**2012**), 711–728, doi:10.2478/v10175-012-0083-9

[19] T. Węgrzyn, J. Piwnik, D. Hadryś, R. Wieszała, Car body welding with micro-jet cooling, J.Arch. Mater. Sci. Eng., 49 (**2011**), 90–94

[20] J. Slania, Influence of phase transformations in the temperature ranges of 1250-1000 °C and 650-350 °C on the ferrite content in austenitic welds made with T 23 12 LRM3 tubular electrode, Arch. Metall. Mater., 50 (**2005**), 757–767

[21] B. Slazak, J. Słania, T. Węgrzyn, A.P. Silva, Process stability evaluation of manual metal arc welding using digital signals, Mater. Sci. Forum, 730–732 (**2013**), 847–852, doi:10.4028/www.scientific.net/MSF.730-732.847

[22] K. Janerka, M. Pawlyta, J. Jezierski, J. Szajnar, D. Bartocha, Carburiser properties transfer into the structure of melted cast iron, J. Mat. Proc. Tech., 214(4) (**2014**), 794–801, doi:10.1016/j.jmatprotec.2013.11.027

[23] D. Janicki, Disk laser welding of Armor steel, Arch. Metall. Mater., 59 (**2014**), 1641–1646, doi:10.2478/amm-2014-0279

[24] J. Bodzenta, A. Kaźmierczak, T. Kruczek, Analysis of thermograms based on FFT algorithm, J. Phys. IV, 129 (**2005**), 201–206, doi:10.1051/jp4:2005129042

UDK 66.017:621.793:620.193.19
Original scientific article/Izvirni znanstveni članek

ISSN 1580-2949
MTAEC9, 51(2)205(2017)

PROPERTIES OF Al_2O_3/TiO_2 AND ZrO_2/CaO FLAME-SPRAYED COATINGS

LASTNOSTI PLAMENSKO NANEŠENIH PREMAZOV Al_2O_3/TiO_2 IN ZrO_2/CaO

Artur Czupryński
Silesian University of Technology, Faculty of Mechanical Engineering, The Welding Department,
Konarskiego 18A, 44-100 Gliwice, Poland
artur.czuprynski@polsl.pl

Prejem rokopisa – received: 2015-07-01; sprejem za objavo – accepted for publication: 2016-02-09

doi:10.17222/mit.2015.165

The article presents the results of a study on the exploitation properties of flame-sprayed ceramic coatings produced from an oxide ceramic material in the form of powder based on an aluminum oxide (Al_2O_3) matrix with an addition of 3 % titanium oxide (TiO_2) and also on a zirconium oxide (ZrO_2) matrix with 30 % of calcium oxide (CaO) on a substrate of unalloyed structural steel of grade S235JR. The buffer layer was produced from a metallic powder on the basis of Ni-Al-Mo. Plates with dimensions of (5 × 200 × 300) mm and also the front surfaces of ϕ40 × 50 mm cylinders were flame-sprayed. The buffer coatings were produced using a RotoTec 80 torch and external specific coatings were produced with a CastoDyn DS 8000 torch. Investigations of the coating properties were based on metallography tests, a phase-composition research, a measurement of microhardness, a research of the coating adhesion to the substrate, the abrasive-wear resistance (acc. to ASTM G65 standard), the erosion-wear resistance (acc. to ASTM G76-95 standard) and a thermal-stroke study. The coatings were characterized by a high adhesion to the substrate and also high erosion and abrasive-wear resistance and the resistance to cyclic thermal strokes.

Keywords: flame spray, coating, ceramic powder, abrasive-wear resistance, erosion-wear resistance, adhesion strength

Članek predstavlja rezultate študija uporabnih lastnosti plamensko nanešenih keramičnih premazov, izdelanih iz materiala oksidne keramike v obliki prahov na osnovi aluminijevega oksida Al_2O_3 z dodatkom 3 % titanovega oksida TiO_2 in tudi na osnovi cirkonovega oksida (ZrO_2) s 30 % kalcijevega oksida (CaO) na podlagi iz nelegiranega konstrukcijskega jekla S235JR. Tamponska plast je bila izdelana s kovinskim prahom na osnovi Ni-Al-Mo. Plošča dimenzij 5 mm × 200 mm × 300 mm in tudi čelna stran površine valjev ϕ40 mm × 50 mm sta bili plamensko nanešeni. Tamponski nanos je bil izdelan z gorilnikom RotoTec 80, zunanji specifični nanos z gorilnikom CastoDyn DS 8000. Preiskave lastnosti nanosov so bile izvršene z metalografijo, preiskavo sestave faz, meritvijo mikrotrdote, preiskavo prijemljivosti nanosa na podlago, z preizkusom odpornosti na abrazijsko obrabo, (v skladu z ASTM G65 standardom), odpornost na erozijsko obrabo, (v skladu z ASTM G76-95 standardom) in s preizkusom na termošok. Značilnost nanosov je bila velika oprijemljivost na podlago, tudi odpornost na erozijsko in abrazijsko obrabo ter odpornost na toplotne šoke.

Ključne besede: plamensko nanašanje, nanos, keramični prah, odpornost na abrazijsko obrabo, odpornost na erozijsko obrabo, adhezijska trdnost

1 INTRODUCTION

Thermal-spraying methods have developed significantly in the recent years by applying more and more technically advanced heat sources and new coating materials.[1–10] At present, this technology is used in about 70 % of industrial applications for manufacturing new parts or devices, for which high-quality workmanship and appropriate surface properties are required. An improvement in the operating parameters of machine and equipment parts associated with high loads and speeds, causing accelerated wear and the necessity of an effective regeneration, also contributed to the rapid advancement in the thermal-spraying technology.

The application of flame-sprayed coatings has not only been conducive to multifold enhancement in the durability of the protection of steel structures against a corrosive environment, but has also led to an extended service life of textile machinery parts, cast moulds, rollers for steel-industry conveyors, parts of pumps and stirrers, plastic-injection moulders, and has also improved the durability and reliability of power boilers.[11] Sprayed-ceramic coatings providing excellent thermal and electrical barriers have been manufactured more and more often due to high corrosion, erosion and wear resistance and hardness and high-temperature creep resistance. Ceramic-oxide materials based on aluminium oxide (Al_2O_3) and zirconium oxide (ZrO_2) are especially noteworthy. Thermal- and electric-barrier coatings flame-sprayed with such materials are applied in multiple cases, e.g., for electronic components, insulation parts of ignition plugs and power turbines, and high-temperature-resistant and heatstroke-resistant parts of combustion chambers in modern car and airplane engines.[12–14]

2 EXPERIMENTAL PROCEDURE AND RESULTS

The aim of the conducted investigations was to create technological conditions of flame powder spraying and to compare the operating properties of ceramic coatings produced with Al_2O_3- and ZrO_2-based powders on the structural unalloyed S235JR steel acc. to EN 10025-2:2004. A powder with a content of 97 % of Al_2O_3 and 3 % of TiO_2, and a powder with a content of 70 % of ZrO_2 and 30 % of CaO were selected for spraying. The binding powder (the buffer layer), i.e., a Ni-Al-Mo alloy, was employed as the primer coating.

Plates with dimensions of (5 × 200 × 300) mm and faces of ϕ40 × 50 mm cylinders were subjected to a manual flame-spraying operation using the two aforementioned powders. Prior to the spraying process, the surfaces of the plates and cylinders were cleaned with shot blasting including an abrasive blasting treatment in conformity with the EN 13507:2010 requirements. Surface shot blasting was performed using angular particles of cast iron. The spraying process consisted of the following operations:

- a 50–100 µm primer coating (buffer layer) including the Ni-Al-Mo powder sprayed with a RotoTec 80 torch (**Table 1**);
- an approx. 500 µm external specific coating including the powder of 97 % Al_2O_3 + 3 % TiO_2 and the powder of 70 % ZrO_2 + 30 % CaO using a CastoDyn DS 8000 torch (**Table 2**).

Following the spraying process, the plates with ceramic coatings were cut into samples intended for further examinations. Adhesion tests of the coatings sprayed onto the substrates were performed on cylindrical samples. Metallographic macroscopic examinations of the sprayed surfaces were undertaken with a stereomicroscope with a magnification of 4–25 times.

Table 1: Spraying parameters of the primer coating with Ni-Al-Mo powder

Tabela 1: Parametri pri napr̆sevanju podlage s prahom iz Ni-Al-Mo

Torch type:	RotoTec 80
Acetylene pressure:	0.7 (bar)
Oxygen pressure:	4.0 (bar)
Distance between the torch and the sprayed surface:	200 (mm)
12744 Preheating temperature:	40 (°C)
Change in the torch advancement angle relative to the next coating:	90°

Table 2: Spraying parameters of the external coating with aluminium oxide and zirconium oxide matrices

Tabela 2: Parametri pri nanašanju zunanjega nanosa z osnovo iz aluminijevega oksida in cirkonovega oksida

Torch type:	CastoDyn DS 8000
Torch tip:	SSM 30
Powder flow rate: for 97 % Al_2O_3 + 3 % TiO_2 powder for 70 % ZrO_2 + 30 % CaO powder	2 (setting acc. to the manual) 3 (setting acc. to the manual)
Acetylene pressure:	0.7 (bar)
Oxygen pressure:	4.0 (bar)
Assist. gas (compressed air) pressure:	3.0 (bar)

*The required primer coating made with Ni-Al-Mo powder

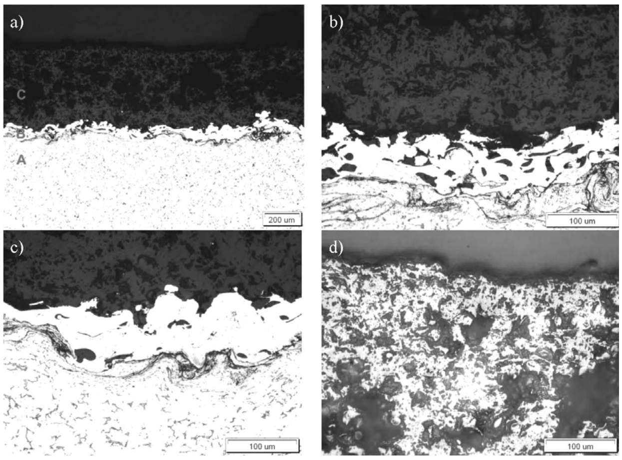

Figure 1: View after flame spraying with 97 % Al_2O_3 + 3 % TiO_2 powder: a) structure of specific external coating (C), primer Ni-Al-Mo coating (B) and base material (A), magn. of 100×; b) structure of external coating and image of binding zone of external coating with primer coating, magn. of 400×; c) structure of primer coating over the area of deformed steel with a developed surface line, magn. of 400×; d) structure of external coating, magn. of 400×

Slika 1: Izgled plamensko nanešenega prahu s 97 % Al_2O_3 + 3 % TiO_2: a) struktura posebnega zunanjega nanosa (C), nanos podlage iz Ni-Al-Mo (B) in osnovno jeklo (A), povečava 100×, b) struktura zunanjega nanosa in slika vezivnega področja zunanjega nanosa na vmesni nanos, povečava 400×, c) struktura vmesnega nanosa na deformiranem jeklu z razvito linijo površine, povečava 400×; d) struktura zunanjega nanosa, povečava 400×

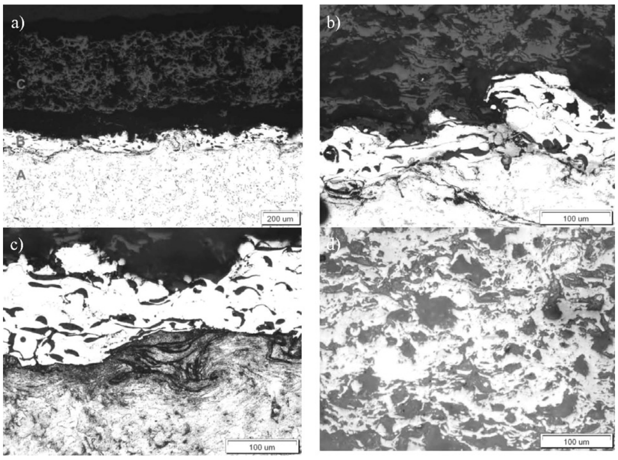

Figure 2: View after flame spraying with 70 % ZrO_2 + 30 % CaO powder: a) structure of specific external coating (C), primer Ni-Al-Mo coating (B) and base material (A), magn. of 100×; b) structure of external coating with microhollows and image of binding zone of external coating with primer coating, magn. of 400×; c) structure of primer coating over the area of deformed steel with a developed surface line, magn. of 400×; d) structure of external coating, magn. of 400×

Slika 2: Izgled plamensko nanešenega prahu s 70 % ZrO_2 + 30 % CaO: a) struktura posebnega zunanjega nanosa (C), nanos podlage iz Ni-Al-Mo (B) in osnovno jeklo (A), povečava 100×, b) struktura zunanjega nanosa z mikro prazninami in posnetek vezivnega področja zunanjega nanosa z nanosom podlage, povečava 400×, c) struktura nanosa podlage na deformiranem jeklu, z jasno linijo površine, povečava 400×, d) struktura zunanjega nanosa, povečava 400 ×

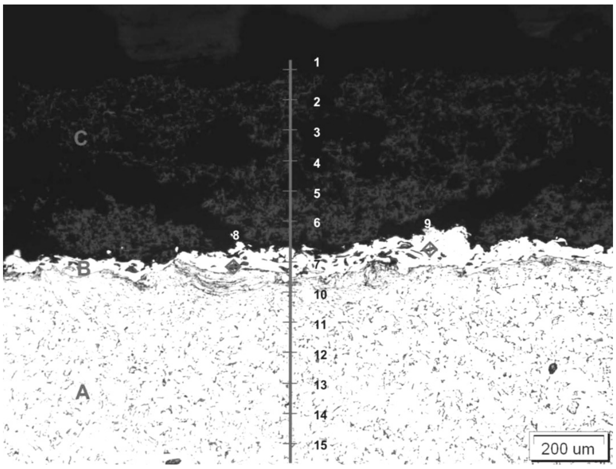

Figure 3: Diagram of hardness measurements at the cross-section of a sample after flame spraying: C – external specific coating, B – primer coating, A – substrate material

Slika 3: Prikaz meritve trdote na preseku vzorca po nanosu s plamenom: C – zunanji specifični premaz, B – nanos podlage, A – material osnove

Metallographic microscopic examinations were carried out on metallographic microsections perpendicular to the coating, cut from the plates after flame spraying with the powder matrix of aluminium oxide and zirconium oxide. The structure of the examined coatings was revealed on the microsections etched in a 4 % nitric acid solution (HNO_3) and ethyl alcohol solution (C_2H_5OH). Metallographic microscopic examinations were performed with a magnification of 100–1000×. The grain size in the plate structure was determined with the comparative method. The thickness of the coatings was determined with the metallographic method in compliance with ISO 1463 1997.

Table 3: Results of the hardness measurement on the cross-section of the sample after spraying it with 97 % Al_2O_3 + 3 % TiO_2 powder

Tabela 3: Rezultati meritve trdote na preseku vzorca po napršenem nanosu prahu s 97 % Al_2O_3 + 3 % TiO_2

Test area	Test point	Load (N)	HV hardness
External coating (C) (97 % Al_2O_3 + 3 % TiO_2)	1	5.0	747
	2	5.0	823
	3	5.0	910
	4	5.0	672
	5	5.0	762
	6	5.0	747
Primer coating (B) (Ni-Al-Mo)	7	0.1	469
	8	0.1	353
	9	0.1	458
Substrate material (A) (S235JR)	10	0.5	226
	11	0.5	189
	12	0.5	145
	13	0.5	131
	14	0.5	128
	15	0.5	110

Every result was represented by the average value of ten measurements. The results of the metallographic microscopic examinations allowed us to evaluate the structure of the base material, the primer coating and the specific external coating and their thickness after the flame-spraying operation (**Figures 1** and **2**).

The coating-hardness measurement was made with the Vickers method. The examinations were carried out in conformity with ISO 6507-1:2007. The load applied during the hardness measurement was between 0.1 and 5 N. The hardness measurement was made at the cross-sections of the samples with the ceramic coatings including the powders of 97 % Al_2O_3 + 3 % TiO_2 and 70 % ZrO_2 + 30 % CaO. Fifteen hardness measurements were made on the cross-sections of the samples, six measurements were made on the specific external coating (C), three on the primer coating (B) and six on the base material (A), in the micro-areas marked in **Figure 3**. The results of the measurements are presented in **Tables 3** and **4**.

Table 4: Results of the hardness measurement on the cross-section of the sample after spraying it with 70 % ZrO_2 + 30 % CaO powder

Tabela 4: Rezultati meritve trdote na preseku vzorca po napršenem nanosu prahu iz 70 % ZrO_2 + 30 % CaO

Test area	Test point	Load (N)	HV hardness
External coating (C) (70 % ZrO_2 + 30 % CaO)	1	5.0	705
	2	5.0	479
	3	5.0	549
	4*)	5.0	1176
	5	5.0	961
	6	5.0	449
Primer coating (B) (Ni-Al-Mo)	7	0.1	446
	8	0.1	397
	9	0.1	380
Substrate material (A) (S235JR)	10	0.5	231
	11	0.5	209
	12	0.5	245
	13	0.5	140
	14	0.5	126
	15	0.5	127

* The hardness measured on oxide precipitates with a larger area

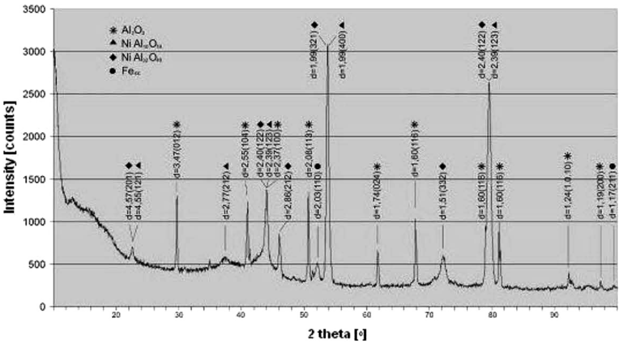

Figure 4: Diffraction pattern of the coating flame-sprayed with 97 % Al_2O_3 + 3 % TiO_2 powder

Slika 4: Rentgenogram plamensko nanešenega nanosa iz prahu s 97 % Al_2O_3 + 3 % TiO_2

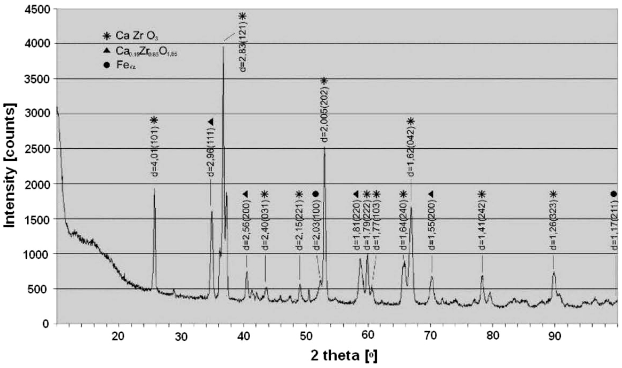

Figure 5: Diffraction pattern of the coating flame-sprayed with 70 % ZrO_2 + 30 % CaO powder

Slika 5: Rentgenogram plamensko nanešenega nanosa iz prahu s 70 % ZrO_2 + 30 % CaO

X-ray structure tests of the surfaces of the samples after flame spraying made with an X-ray diffractometer enabled us to determine the phase compositions of the external specific surfaces including the powders of aluminium oxide and zirconium oxide on the substrate of the primer coating created using the Ni-Al-Mo powder and the base material of the S235JR low-carbon steel. The results of the X-ray qualitative analysis are shown with diffraction patterns (**Figures 4** and **5**). Exact examinations of the structures of the coatings were carried out with an electronic scanning microscope. Metallographic microsections were viewed with a magnification of 250–5000×. The results of the examinations with the scanning microscope allowed us to determine the influence of the type of the powder used in the spraying process on the structure of an external specific coating and the concentration of the elements in the selected micro-areas. The examples of observing the microstructures of the external coating and the primer coating are shown in **Figures 6** and **7**.

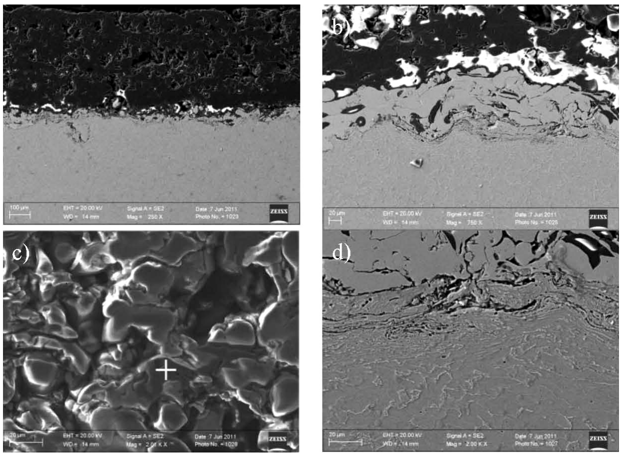

Figure 6: View of the coating after flame spraying 97 % Al_2O_3 + 3 % TiO_2 powder: a) structure of external coating with primer coating and base material with visible hollows of a varied size in the external coating of the sample; b) small amount of hollows in the external coating in the border area with primer coating; c) structure of external coating; d) area of base material and primer coating

Slika 6: Izgled nanosa po plamenskem nanašanju prahu s 97 % Al_2O_3 + 3 % TiO_2: a) struktura zunanjega nanosa z nanosom podlage in osnovnim jeklom, z različnimi vidnimi prazninami različne velikosti v zunanjem nanosu vzorca, b) malo praznin v zunanjem nanosu na mejnem področju z osnovnim nanosom, c) struktura zunanjega nanosa, d) področje osnovnega jekla in osnovnega nanosa

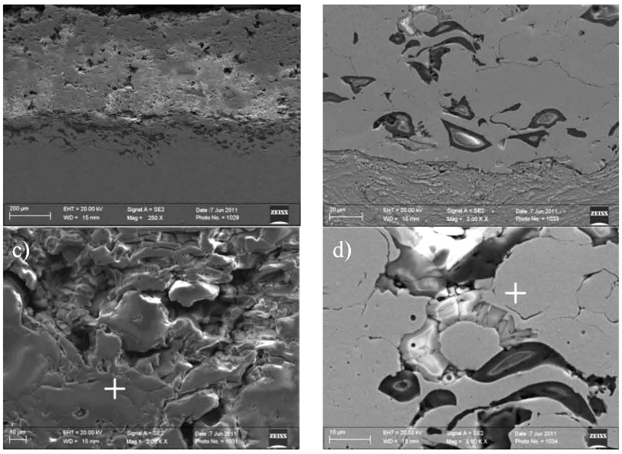

Figure 7: View of the coating after flame spraying 70 % ZrO_2 + 30 % CaO powder: a) external coating with a small amount of hollows, b) primer coating, c) structure of external coating, d) area of primer coating

Slika 7: Izgled nanosa po plamenskem nanašanju prahu s 70 % ZrO_2 + 30 % CaO: a) zunanji nanos z majhnim deležem praznin, b) osnovni nanos, c) struktura zunanjega nanosa, d) področje osnovnega nanosa

An abrasive-wear-resistance test of the mineral-mineral type of coatings involving the selected powders was performed on samples with dimensions of 5 mm × 25 mm × 75 mm in line with ASTM G65. The weight wear of a sample was determined as a result of the test, found after (100, 125, 250, 500 and 1500) revolutions of an abrasive pressure plate. The tests results allowed us to determine the abrasive-wear resistance of the deposited coatings. The measurement results of the abrasive-wear-resistance tests are presented in **Table 5**.

An erosion-resistance test was carried out in accordance with ASTM G76-95 on the samples with dimensions of 5 × 25 × 75 mm with the coatings involving the powders of 97 % Al_2O_3 + 3 % TiO_2 and 70 % ZrO_2 + 30 % CaO. Aluminium oxide (Al_2O_3) powder with a particle diameter of 45–70 µm was used as the erosion material. The test was undertaken at a molecular velocity of 70 ± 2 m/s, an erodent flow rate of approx. 2 g/min, a nozzle outlet-to-sample distance of 10 mm and incidence angles of the abrasive stream of (90, 60, 30 and 15)°. The test lasted for 10 min. The results are presented in **Table 6**.

The coating-adhesion test R_h (the stripping strength) was determined with the stripping method involving a static tensile test, in accordance with EN 582:1996, on cylindrical samples with a diameter of ϕ40 mm, flame-sprayed with the powders containing 97 % Al_2O_3 + 3 % TiO_2 and 70 % ZrO_2 + 30 % CaO. The face of a cylindrical sample with a coating deposited was bonded to the counter specimen with the Henkel Loctite Hysol 3478 A&B Superior Metal bonding agent with a tensile

Table 5: Results of the wear tests for the coatings made of 97 % Al_2O_3 + 3 % TiO_2 powder and 70 % ZrO_2 + 30 % CaO powder
Tabela 5: Rezultati preizkusov obrabe napršenih nanosov s prahom s 97 % Al_2O_3 + 3 % TiO_2 in 70 % ZrO_2 + 30 % CaO

Powder composition	Sample No.	Revolutions (n)	Test No.	Sample weight prior to the test (g)	Sample weight after the test (g)	Mass loss (g)	Average mass loss (g)	Volume loss (mm^3)
97%Al_2O_3+ 3%TiO_2	S 1.1	1500	1	75.8406	75.0086	0.8320	0.8314	207.85
			2	75.8396	75.0086	0.8310		
			3	75.8395	75.0084	0.8311		
	S 1.2	500	1	75.0825	74.6428	0.4397	0.4387	109.66
			2	75.0821	74.6431	0.4390		
			3	75.0802	74.6427	0.4375		
	S 1.3	250	1	75.4531	75.2617	0.1914	0.1840	92.00
			2	75.4524	75.2618	0.1906		
			3	75.4517	75.2816	0.1701		
	S 1.4	125	1	75.8165	75.6092	0.2073	0.2074	51.85
			2	75.8164	75.6091	0.2073		
			3	75.8167	75.6094	0.2073		
	S 1.5	100	1	73.8637	73.7352	0.1285	0.1283	32.07
			2	73.8635	73.7351	0.1284		
			3	73.8634	73.7355	0.1279		
70%ZrO_2+ 30%CaO	S 2.1	250	1	74.7266	74.0916	0.6350	0.6347	112.34
			2	74.7263	74.092	0.6343		
			3	74.7262	74.0915	0.6347		
	S 2.2	500	1	77.6013	76.638	0.9633	0.9633	170.49
			2	77.6014	76.6378	0.9636		
			3	77.6012	76.6381	0.9631		
	S 2.3	1500	1	76.9207	75.458	1.4627	1.4626	258.87
			2	76.9205	75.4578	1.4627		
			3	76.9206	75.4581	1.4625		
	S 2.4	125	1	76.8146	76.1956	0.6190	0.6190	109.56
			2	76.8148	76.1954	0.6194		
			3	76.8143	76.1958	0.6185		
	S 2.5	100	1	78.5391	77.8907	0.6484	0.6485	114.78
			2	78.5394	77.8905	0.6489		
			3	78.5391	77.891	0.6481		

Table 6: Mass-loss values in erosion tests for the coatings made of 97%Al_2O_3+3%TiO_2 and 70%ZrO_2+30%CaO powders
Tabela 6: Vrednosti masne izgube pri erozijskem preizkusu napršenega nanosa iz prahov s 97 % Al_2O_3 + 3 % TiO_2 in 70 % ZrO_2 + 30 % CaO

Erodent incidence angle (°)	Type of powder sprayed					
	97 % Al_2O_3 + 3 % TiO_2			70 % ZrO_2 + 30 % CaO		
	Sample mass prior to the test (g)	Sample mass after the test (g)	Mass loss (g)	Sample mass prior to the test (g)	Sample mass after the test (g)	Mass loss (g)
90°	73.8752	73.8703	0.0049	75.9886	75.9560	0.0026
45°	73.8703	73.8485	0.0218	75.9560	75.9118	0.0442
30°	73.8485	73.8206	0.0279	75.9118	75.8640	0.0378
15°	73.8206	73.8027	0.0179	75.8640	75.8020	0.0620

Table 7: Results of the adhesion tests for the coatings made of 97 % Al_2O_3 + 3 % TiO_2 and 70 % ZrO_2 + 30 % CaO powders
Tabela 7: Rezultati adhezijskih preizkusov nanosov napršenih s prahovi s 97 % Al_2O_3 + 3 % TiO_2 in 70 % ZrO_2 + 30 % CaO

Material of the external coating	Sample No.	Sample size		Maximum breaking load (N)	Adhesion of sprayed coating (N/mm^2)	
		Sample diameter (mm)	Cross-section field (mm^2)		R_h	$R_{h\ Av.}$*
97 % Al_2O_3 + 3 % TiO_2	1/1	39.4	1218.6	7614.0	6.0	6.5
	1/2	39.0	1193.9	6418.0	5.4	
	1/3	39.8	1243.5	10095.0	8.1	
70 % ZrO_2 + 30 % CaO	2/1	39.8	1243.5	4104.0	3.3	3.3
	2/2	39.8	1243.5	4376.0	3.5	
	2/3	39.5	1224.8	3735.0	3.1	

*average value

strength of 17 MPa. The samples, together with the fixing device, were placed in a tensile-testing machine and subjected to static stretching until rupture. Tensile test results allowed us to determine the values of the force detaching the coatings from the substrate and calculate the adhesion coefficient (**Table 7**).

A thermal-resistance test was carried out, in line with ISO 14923:2003, on the samples with the dimensions of 5 × 25 × 75 mm with an external coating including 97 % Al_2O_3 + 3% TiO_2 and an external flame-sprayed coating including 70 % ZrO_2 + 30 % CaO. Three stages of the test were determined as no detailed guidance concerning this type of test was available:

- the first stage – heating to 1050 °C and slow cooling, together with the oven, at a rate of 40 °C/h;
- the second stage – heating to 1050 °C and cooling the samples in a stream of compressed air at a rate of 25 °C/s, the cycle was repeated ten times;
- the third stage – heating to 1050 °C and a rapid cooling of the samples in water at a rate of 100 °C/s. The test result identified the number of the cycle, after which discontinuities and delamination were visible on the coating surface (**Figure 8**).

3 DISCUSSION

After carrying out the spraying process, the visual examinations did not reveal any sample-surface imperfections after flame spraying the 97 % Al_2O_3 + 3 % TiO_2 and 70 % ZrO_2 + 30 % CaO powdes. The metallographic examinations of the microsections perpendicular to the surface of the sample sprayed with the 97 % Al_2O_3 + 3 % TiO_2 powder showed that two coatings existed on the surface of the steel, with a developed surface line: the primer coating (B) and the external specific coating (C) (**Figure 1a**). The 30–110 μm primer coating (B) consisted of bright areas made of the Ni-Al-Mo alloy and dark oxide inclusions (**Figure 1c**); it was observed immediately above the base-material surface (A). A banded structure of the base material, distinctive for the strengthening of the steel surface during the shot blasting of the examined material, existed in the boundary area, along the primer coating. The external coating, sprayed on the first buffer coatings, had a thickness varying between 450 μm to 510 μm. The coating exhibited numerous voids with different sizes and a waved line of its external surface (**Figure 1d**).

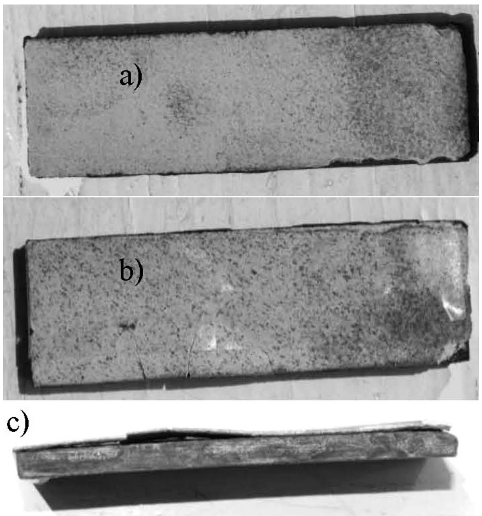

Figure 8: View of samples after the third stage of thermal-resistance tests: a) surface of the sample sprayed with 97 % Al_2O_3 + 3 % TiO_2 powder, b) cracks on the surface of the coating made of 70 % ZrO_2 + 30 % CaO powder, c) delamination of the coating made of 70 % ZrO_2 + 30 % CaO powder

Slika 8: Izgled vzorcev po tretji stopnji preizkusa toplotne odpornosti: a) površina vzorca z nanosom prahu s 97 % Al_2O_3 + 3 % TiO_2, b) razpoke na površini nanosa prahu s 70 % ZrO_2 + 30 % CaO, c) odstopanje nanosa iz prahu s 70 % ZrO_2 + 30 % CaO od površine

After the flame spraying of the steel surface with the 70 % ZrO_2 + 30 % CaO powder, the following individual layers were identified: the primer coating (B) and the external specific coating (C) (**Figure 2a**). A banded structure with a considerable plastic deformation, existing on the thickness of approx. 50 μm, was observed underneath the primer coating, in the steel. The primer coating consisted of bright areas of the elements forming the Ni-Al-Mo powder used for spraying and also of dark flattened oxides (**Figure 2c**). The coating was 50–160 μm thick. The external specific coating of about 600 μm exhibited numerous voids with a developed line of its external surface (**Figure 2d**).

The specific external coating sprayed with the 97 % Al_2O_3 + 3% TiO_2 powder had a hardness of 671.8–909.9 HV5. The hardness of the examined micro-areas in the primer coating was lower, i.e., 353–469 HV01. The hardness of the substrate material in the boundary zone along the primer coating was approx. 226 HV05, as confirmed by the occurrence of a narrow heat-affected zone (HAZ) or by steel-surface strengthening after shot blasting. The hardness of the external specific coating after the flame-spraying operation involving the 70 % ZrO_2 + 30 % CaO powder was different, ranging from approx. 449–961 HV5. The hardness measured on oxides with a larger area in the coating, in the places where oxide precipitates occurred, was even more than 1176 HV5. Different hardness results were due to a large number of voids in the coating. The hardness of the primer coating was from approx. 380 to approx. 446 HV01, and for the primer material, it was between 109–230 HV05.

X-ray structure tests allowed us to identify the phases existing in the structure of the coating after the flame spraying involving the 97 % Al_2O_3 + 3 % TiO_2 and 70 % ZrO_2 + 30 % CaO powders (**Figures 4** and **5**). There were mainly Al_2O_3, $NiAl_{10}O_{16}$ and $NiAl_{32}O_{49}$ phases; trace amounts of Fe-α were also identified after the spraying operation resulting in the external coating with an aluminium matrix (**Figure 4**). The examinations did not show any presence of a phase with titanium in this coating due to its small amount in the content of the powder for spraying (TiO_2 = 3 %). The phase can be identified with X-ray tests, provided it exists in the amount of more than 4 % of mass fraction.

Ten diffraction lines from the Al_2O_3 phase were shown in the diffraction pattern, including the maximum intensity values for planes (113), (116), (124), (030) and (1.0.10). Four diffraction lines for planes (121), (212), (400) and (123) of the $NiAl_{10}O_{16}$ phase and for planes (201), (321), (332), (122) of the $NiAl_{32}O_{49}$ oxide phase were also found. The existence of diffraction lines (100) and (211) with a small intensity, relating to Fe-α, was also confirmed. The presence of compound zirconium and calcium oxides was also revealed in the structure of the external surface obtained after the spraying operation involving the 70 % ZrO_2 + 30 % CaO powder. Ten peaks relating to the planes of the $CaZrO_3$ phase and four peaks relating to the planes of the $Ca_{0,15}Zr_{0,85}O_{1,85}$ phase occur in a diffraction pattern (**Figure 5**). The existence of peaks with a small intensity for planes (100) and (211), derived from the Feα steel surface, was also found.

The results of the wear-resistance test allowed us to conclude that the flame-sprayed 97 % Al_2O_3 + 3 % TiO_2 coating was more resistant than the coating made with the 70 % ZrO_2 + 30 % CaO powder within the tested range of revolutions of 100–1500 (**Table 5**).

It was confirmed, based on erosion-resistance tests, that the coating made with the 97 % Al_2O_3 + 3 % TiO_2 powder exhibits a higher erosion resistance (determined with the mass loss) than the coating made with the 70 % ZrO_2 + 30 % CaO powder, except in the case of testing it at the angle of 90°. In the cases of the erosion tests at the angles of (45, 30 and 15)°, the mass loss of the sample with the 93 % Al_2O_3 + 3 % TiO_2 coating was 0.0218, 0.0279 and 0.0179 g, respectively, while for the sample with the 70 % ZrO_2 + 30 % CaO coating, it was higher by about 50 % (**Table 6**).

The substrate adherence of the flame-sprayed coatings made with the 97 % Al_2O_3 + 3 % TiO_2 and 70 % ZrO_2 + 30 % CaO powders, determined with a static-stretching test, involving a detachment of the coating from the substrate, showed that the adherence of the coating made of the 97 % Al_2O_3 + 3 % TiO_2 powder was higher than that of the coating made of the 70 % ZrO_2 + 30 % CaO powder, being 6.5 MPa and 3.3 MPa, respectively (**Table 7**). The difference between the tensile-strength and adhesion values was confirmed by inhomogeneous microsections of the samples' surfaces after the tensile test.

The thermal resistance was investigated with the method of cyclic heating the samples coated on one side with the 97 % Al_2O_3 + 3 % TiO_2 coating and 70 % ZrO_2 +30 % CaO coating to 1050 °C and cooling them down at rates of 40 °C/h (in an oven), 25 °C/s (air cooling) and 100 °C/s (water cooling). After heating the samples to 1050 °C and cooling them down using an oven in the first cycle of the test, compressed air in the next nine cycles and water after the last cycle, the coating made of the 70 % ZrO_2 + 30 % CaO powder delaminated from the substrate and cracks were identified on it, along with the detached coating (**Figure 8c**). No damages in the form of delamination were identified for the coating made of the 97 % Al_2O_3 + 3 % TiO_2 powder; however, small cracks without broken-out sections were recorded (**Figure 8a**).

4 CONCLUSIONS

The following conclusions were formulated based on the investigations performed and the outcomes obtained and analysed:

1. Flame spraying with the 97 % Al_2O_3 + 3 % TiO_2 and 70 % ZrO_2 + 30 % CaO powders carried out within the range of the selected parameters allowed us to achieve high-quality ceramic coatings of approx. 500 µm applied to a steel substrate.
2. The structure of the coating flame-sprayed with the 97 % Al_2O_3 + 3 % TiO_2 powder consisted mainly of aluminium oxide and a small amount of the $NiAl_{10}O_{16}$ and $NiAl_{32}O_{49}$ phases, while the coating made of the 70 % ZrO_2 + 30 % CaO powder showed a structure of oxide zirconium phases with calcium.
3. The bonding of the primer coating made of the Ni-Al-Mo powder with the steel substrate and of the external coatings made of the 97 % Al_2O_3 + 3 % TiO_2 and 70 % ZrO_2 + 30 % CaO powders was of the mechanical adhesion nature. The ceramic coatings including the aluminium-matrix powder and zirconium-matrix powder were characterised by their adhesion to the substrate, being 6.5 MPa and 3.3 MPa, respectively.
4. The coatings achieved, consisting of the 97 % Al_2O_3 + 3 % TiO_2 powder and 70 % ZrO_2 + 30 % CaO powder, exhibited the average hardness values of approx. 780 and approx. 720 HV, respectively.
5. The abrasive-wear resistance of the coating made of the 97 % Al_2O_3 + 3 % TiO_2 powder was higher than the resistance of the coating made of the 70 % ZrO_2 + 30 % CaO powder, and the average erosion-wear resistance for an erodent incidence angle of less than 90° was higher by approx. 50 %.
6. The coating made of the 97 % Al_2O_3 + 3 % TiO_2 powder exhibited cyclical-heat-stroke resistance, while the coating made of the 70 % ZrO_2 + 30 % CaO powder, heated and cooled in the same conditions, revealed cracks, chippings and delamination.

5 REFERENCES

[1] D. Janicki, High Power Diode Laser Cladding of Wear Resistant Metal Matrix Composite Coatings, Solid State Phenomena, Mechatronic Systems and Materials V, 199 (**2013**), 587–592, doi:10.4028/www.scientific.net/SSP. 199.587

[2] A. Arcondéguy, G. Gasgnier, G. Montavon, B. Pateyron, A. Denoirjean, A. Grimaud, C. Huguet, Effects of spraying parameters onto flame-sprayed glaze coating structures, Surface and Coatings Technology, 202 (**2008**), 4444–4448

[3] A. Lisiecki, Titanium Matrix Composite Ti/TiN Produced by Diode Laser Gas Nitriding, Metals - Open Access Metallurgy Journal, 5 (**2015**) 1, 54–69, doi:10.3390/met5010054

[4] D. Janicki, Disk Laser Welding of Armor Steel, Archives of Metallurgy and Materials, 59 (**2014**), 1641–1646, doi:10.2478/amm-2014-0279

[5] A. Lisiecki, Welding of Thermomechanically Rolled FineGrain Steel by Different Types of Lasers, Archives of Metallurgy and Materials, 59 (**2014**), 1625–1631, doi:10.2478/amm-2014-0276

[6] A. Kurc-Lisiecka, W. Ozgowicz, W. Ratuszek, J. Kowalska, Analysis of deformation texture in AISI 304 steel sheets, Solid State Phenomena, 203–204 (**2013**), 105–110, doi:10.4028/www.scientific.net/SSP.203-204.105

[7] M. Adamiak, L. A. Dobrzański, Microstructure and selected properties of hot-work tool steel with PVD coatings after laser surface treatment, Applied Surface Science, 254 (**2008**) 15, 4552–4556

[8] L. A. Dobrzański, M. Adamiak, Structure and properties of the TiN and Ti(C,N) coatings deposited in the PVD process on high-speed steels, Journal of Materials Processing Technology, 133 (**2003**), 50–62

[9] J. Górka, Weldability of Thermomechanically Treated Steels, Having a High Yield Point, Archives of Metallurgy and Materials, 60 (**2015**), 469–475, doi:10.1515/amm2015-0076

[1] A. Czupryński, J. Górka, M. Adamiak: Examining properties of arc sprayed nanostructured coatings, Metalurgija, 55 (**2016**) 2, 173–176

[10] L. Pawlowski, The Science and Engineering of Thermal Spray Coatings, second ed., John Wiley & Sons, Chichester, UK, 2008

[11] K. Spencer, M. X. Zhang, Heat treatment of cold spray coatings to form protective intermetallic layers, Scripta Materialia, 61 (**2009**), 44–47

[12] F. Vargas, H. Ageorges, P. Fournier, P. Fauchais, M. E. López, Mechanical and Tribological Performance of Al2O3-TiO2 Coatings Elaborated by Flame and Plasma Spraying. Surface and Coatings Technology, 205 (**2010**), 1132–1136, doi:10.1016/j.surfcoat.2010.07.061

UDK 66.017:620.1:620.169.2
Original scientific article/Izvirni znanstveni članek

ISSN 1580-2949
MTAEC9, 51(2)213(2017)

ONE-DIMENSIONAL ELASTO-PLASTIC MATERIAL MODEL WITH DAMAGE FOR A QUICK IDENTIFICATION OF THE MATERIAL PROPERTIES

ENODIMENZIJSKI MODEL ELASTOPLASTIČNEGA MATERIALA S POŠKODBO ZA HITRO UGOTOVITEV LASTNOSTI MATERIALA

Tomáš Kroupa, Hana Srbová, Jan Klesa
University of West Bohemia, NTIS – New Technologies for the Information Society, Univerzitní 22, 306 14, Plzeň, Czech Republic
kroupa@kme.zcu.cz

Prejem rokopisa – received: 2015-07-01; sprejem za objavo – accepted for publication: 2016-02-10

doi:10.17222/mit.2015.173

Material parameters for elastic, plastic and damage behavior of low-molecular-weight epoxy resin CHS-EPOXY 520 hardened with CHS-P 11 are identified in the paper. Uniaxial cyclic static tests were performed on specimens in line with the ASTM standard D638 - 10 using a Zwick Roell/Z050 test machine with a BTC-Exaclbi.001 clip-on biaxial extensometer. Poisson's ratio and tensile strength were calculated directly from the test results. Other parameters were identified using a combination of a one-dimensional material model, which assumes the infinitesimal strain theory and takes into account elastic, plastic and damage behavior and the optimization method. The model is coded in *Python* and the values of the material parameters are identified using the optiSLang optimization software. The optimization process uses simple design improvement and gradient-based algorithms with the goal to minimize the difference between the force-elongation curves recorded during the tests and those calculated with the proposed model.

Keywords: epoxy, identification, optimization, elasticity, plasticity, damage

V članku so opredeljeni parametri epoksi smole z majhno molekulsko maso CHS-EPOXY 520, utrjeno z CHS-p 11, pri elastičnem, plastičnem obnašanju in pri poškodbi. Enoosni statični ciklični preizkusi so bili izvedeni na vzorcih, ki ustrezajo ASTM standardu D638-10, z uporabo Zwick Roell/Z050 preizkusnega stroja z nameščenim dvoosnim ekstenziometrom BTC-Exaclbi.001. Poissonov količnik in natezna trdnost sta bili izračunani neposredno iz rezultatov preizkusov. Drugi parametri so ugotovljeni s kombinacijo enodimenzijskega modela materiala, ki predpostavlja infinitezimalno teorijo napetosti in ki upošteva obnašanje v elastičnem, plastičnem in ob poškodbi ter metodo optimizacije. Model je kodiran v *Pythonu* in vrednosti parametrov materiala so ugotovljene z uporabo optiSLang programske opreme za optimizacijo. Proces optimizacije uporablja enostavno izboljšanje oblike in algoritme, ki temeljijo na gradientu, s ciljem po zmanjšanju razlike med krivuljo sila – raztezek zabeležene med preizkusom in izračunane z uporabo predlaganega modela.

Ključne besede: epoksi, identifikacija, optimizacija, elastičnost, plastičnost, poškodba

1 INTRODUCTION

A model simulating one-dimensional pure tensile, compressive or shear tests is proposed. This approach is able to predict a one-dimensional response of materials with elastic, plastic and damage behavior. The model is based on the idea to reduce the computational time necessary to identify characteristic parameters of the tested material. The presented model is not necessarily, or primarily, meant to be used for the final identification of material parameters; it can only be used for investigating the starting values or boundaries of the parameters in the subsequent identifications performed using, e.g., a finite-element model[1,2] or other models.[3] The model is written in free-licensed programing language Python using only widely used and common modules numpy, matplotlib, os and pickle. Pre-processing of the experimental results for the further identification process is also performed in Python. The paper presents results for pure epoxy resin; nevertheless, the model is not limited to such type of material.

2 SPECIMENS AND THE EXPERIMENT

Nine specimens shaped according to ASTM standard D638-10 (**Figure 1**) were cut from a rectangular plate with dimensions of approx. 140 mm × 250 mm. The specimens were made of low-molecular-weight epoxy resin CHS-EPOXY 520 hardened with CHS-P 11. The

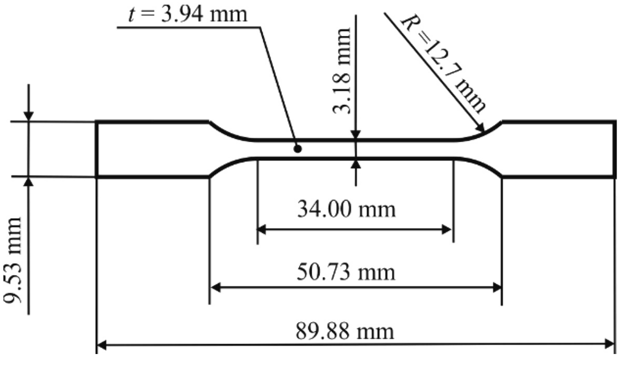

Figure 1: Dimensions of the specimens
Slika 1: Dimenzije vzorcev

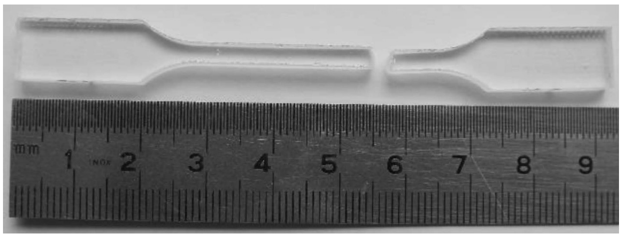

Figure 2: Cracked specimen
Slika 2: Prelomljen vzorec

air from the mixture was removed with a vacuum pump and the resin was then cured at atmospheric pressure, which increased the quality of the epoxy resin by reducing the number and volume of bubbles.

A ZWICK ROELL/Z050 test machine with a BTC-EXACLBI.001 clip-on biaxial extensometer was used for the experimental tests.

The specimens were subjected to cyclic tensile tests. During each cycle, unloading was started every time the elongation between the extensometer arms (the gage area) exceeded a multiple of $\Delta l = 0.02$ mm. During the corresponding cycle, loading started when the tensile force decreased below the multiple of 30 % of the force at the start of the unloading. All the tests were performed at room temperature of 22 °C. **Figure 2** shows a typically cracked specimen with a rupture.

3 MATERIAL MODEL

The free-energy-function method was used for the formulation of the model.[4,5] In this paper, the free-energy function ψ is proposed in the form of the sum of elastic, plastic and damage parts:

$$\psi = \frac{1}{\rho}\left[\frac{1}{2}E(1-D)(\varepsilon^{E})^{2} + \int_{0}^{\bar{\varepsilon}^{\mathrm{P}}} \mathrm{P}(\bar{\varepsilon}^{\mathrm{P}})\mathrm{d}\bar{\varepsilon}^{\mathrm{P}} + \int_{0}^{\beta} \mathrm{B}(\beta)\mathrm{d}b\right] \quad (1)$$

where ρ is the density of the material; E is Young's modulus; D is the damage factor; ε^{E} is the elastic strain; $\bar{\varepsilon}^{\mathrm{P}}$ is the equivalent plastic strain; R is the hardening-associated quantity; β is the damage variable; and B is the damage-associated quantity. Generalized forces are described in more detail below. The stress is calculated in Equation (2) as:

$$\sigma = \rho\frac{\partial\psi}{\partial\varepsilon^{\mathrm{E}}} = E(1-D)\varepsilon^{\mathrm{E}} \quad (2)$$

where stress σ is considered as the nominal stress acting in the whole area of the cross-section of a specimen. Stress ρ_{D} is the stress acting in the undamaged area of the cross-section of a specimen:[4]

$$\sigma_{\mathrm{D}} = \frac{\sigma}{(1-D)} = \frac{\sigma}{(1-D)}\frac{\partial\psi}{\partial\varepsilon^{\mathrm{E}}} = E\varepsilon^{\mathrm{E}} \quad (3)$$

The damage-associated energy, in this case identically equal to the strain energy density of the undamaged material, is

$$Y = -\rho\frac{\partial\psi}{\partial D} = \frac{1}{2}E(\varepsilon^{\mathrm{E}})^{2} \quad (4)$$

The hardening-associated quantity, which defines the plastic material behavior, is:

$$R(\bar{\varepsilon}^{\mathrm{P}}) = \rho\frac{\partial\psi}{\partial\bar{\varepsilon}^{\mathrm{P}}} \quad (5)$$

And the damage-associated quantity, which defines the damage material behavior, is:

$$B(\beta) = \rho\frac{\partial\psi}{\partial\beta} \quad (6)$$

The model is considered as a nonlinear material and the infinitesimal-strain theory is used in Equation (7):

$$\varepsilon = \frac{\Delta l}{l} \quad (7)$$

where ε is the total strain; Δl is the elongation of the gage area and l is the original length of the gage area. The elasto-plastic decomposition of the axial strain ε is also considered:[6,7]

$$\varepsilon = \varepsilon^{\mathrm{E}} + \varepsilon^{\mathrm{P}} \quad (8)$$

where ε^{P} is the plastic strain. The function of plasticity decides whether the plastic flow will be present. It is proposed in the following form:

$$F^{\mathrm{P}} = \sigma_{\mathrm{r}} - \sigma^{\mathrm{y}} = \sigma_{\mathrm{r}} - (R_{0} + R(\bar{\varepsilon}^{\mathrm{P}})) \le 0 \quad (9)$$

where $\sigma_{\mathrm{r}} = |\sigma_{\mathrm{D}}|$, which implies the assumption that the plastic flow is present only in the undamaged part of the cross-section and that the plastic flow will occur in tension as well as in compression; σ^{y} is the yield stress and R_0 is the initial yield stress. The function of damage is proposed in the following form:

$$F^{\mathrm{D}} = Y_{\mathrm{r}} - (B_{0} + B(\beta)) \le 0 \quad (10)$$

where $Y_{\mathrm{r}} \equiv Y$, therefore, as in the case of plasticity, no distinction between the tensile and compressive damage is considered; B_0 is the energy necessary for the damage initiation.

Rates of quantities are expressed below. Time derivatives ("·") are replaced by time step changes ("Δ") because all the analyses were performed as quasi-static. The change in the plastic strain $\Delta\varepsilon^{\mathrm{P}}$ is:

$$\Delta\varepsilon^{\mathrm{P}} = \Delta\lambda^{\mathrm{P}}\frac{\partial F^{\mathrm{P}}}{\partial\sigma} = \Delta\lambda^{\mathrm{P}}\mathrm{sign}(\sigma) \quad (11)$$

where $\Delta\lambda^{\mathrm{P}}$ is the plastic multiplier. The change in the equivalent plastic strain $\Delta\bar{\varepsilon}^{\mathrm{P}}$ is:

$$\Delta\bar{\varepsilon}^{\mathrm{P}} = -\Delta\lambda^{\mathrm{P}}\frac{\partial F^{\mathrm{P}}}{\partial R} = \Delta\lambda^{\mathrm{P}} \quad (12)$$

The change in the damage factor ΔD is:

$$\Delta D = -\Delta\lambda^{\mathrm{D}}\frac{\partial F^{\mathrm{D}}}{\partial Y} = \Delta\lambda^{\mathrm{D}} \quad (13)$$

where $\Delta\lambda^{\mathrm{D}}$ is the damage multiplier. The change in the damage variable is:

$$\Delta\beta = -\Delta\lambda^{\mathrm{D}}\frac{\partial F^{\mathrm{D}}}{\partial Y} = \Delta\lambda^{\mathrm{D}} \tag{14}$$

If inequalities (9) and (10) are fulfilled, the calculation of responses is simple. Otherwise, the changes of the unknown variables ($\Delta\varepsilon^{\mathrm{P}}$, $\Delta\bar{\varepsilon}^{P}$, ΔD, $\Delta\beta$, $\Delta\lambda^{\mathrm{P}}$, $\Delta\lambda^{\mathrm{D}}$) must be calculated. The following section shows the solution of this problem in the presented model.

4 CALCULATION OF RESPONSES

The calculation of the unknown variables is performed in several steps.

1. The so-called trial state is used. Firstly, the change in the total strain is considered only as a change in the elastic strain, which leads to:

$$\varepsilon^{\mathrm{E}}_{\mathrm{trial}} = \varepsilon^{\mathrm{E}}_{t} + \Delta\varepsilon \tag{15}$$

where $\varepsilon^{\mathrm{E}}_{\mathrm{trial}}$ is the trial value of the elastic strain; $\varepsilon^{\mathrm{E}}_{t}$ is the elastic strain at the end of the previous time step and $\Delta\varepsilon$ is the change in the total strain in the present time step. Trial values of the other quantities are considered as the values at time t. The values of the plasticity and damage functions are calculated using (9) and (10). If the inequalities in the mentioned equations are fulfilled, no plastic or damage quantities are changed and the trial values of strain and stress calculated using (2) are considered as the values in time $t+\Delta t$ and the calculations for the time step are finished. Otherwise the return mapping algorithm described in step 2 is used.

2. Using relations:

$$\Delta\varepsilon^{\mathrm{P}} = \varepsilon^{\mathrm{E}}_{\mathrm{trial}} - \varepsilon^{\mathrm{E}} \tag{16}$$

and

$$\Delta\bar{\varepsilon}^{\mathrm{P}} = \bar{\varepsilon}^{\mathrm{P}} - \bar{\varepsilon}^{\mathrm{P}}_{\mathrm{trial}} \tag{17}$$

and the fact obvious from relations (13) and (14) that $D = \beta = \lambda^{\mathrm{D}}$, the set of six equations from (9) to (14) can be transformed into the set of two equations with two unknowns (ε^{E} and D).

The first equation has the following form:

$$\left|E\varepsilon^{\mathrm{E}}\right| - R_0 - K_{\mathrm{R}}(\bar{\varepsilon}^{\mathrm{P}})^{n_{\mathrm{R}}} = 0 \tag{18}$$

where K_{R} and n_{R} are the shape parameters of the hardening function. The equivalent plastic strain $\bar{\varepsilon}^{\mathrm{P}}$ is calculated as:

$$\bar{\varepsilon}^{\mathrm{P}} = \bar{\varepsilon}^{\mathrm{P}}_{\mathrm{trial}} + (\varepsilon^{\mathrm{P}}_{\mathrm{trial}} - \varepsilon^{\mathrm{E}})\operatorname{sign}(E\varepsilon^{\mathrm{E}}) \tag{19}$$

where $\bar{\varepsilon}^{\mathrm{P}}_{\mathrm{trial}}$ is the trial value of the equivalent plastic strain. The term in the shape of the classical power law used in Equations (9) and (18):

$$\sigma^{y} = R_0 - K_{\mathrm{R}}(\bar{\varepsilon}^{\mathrm{P}})^{n_{\mathrm{R}}} \tag{20}$$

is the hardening function.

The second equation is:

$$\frac{1}{2}E(\varepsilon^{\mathrm{E}})^2 - (B_0 + B(D)) = 0 \tag{21}$$

where term ($B_0 + B(D)$) defines the damage behavior of the material.

Equations (18) and (21) can be solved separately. The first equation (18) needs to be solved numerically. In the present paper, ε^{E} is obtained with the golden-section method in the interval $\left\langle \bar{\varepsilon}^{\mathrm{P}}_{\mathrm{trial}} - \Delta\varepsilon, \bar{\varepsilon}^{\mathrm{P}}_{\mathrm{trial}} \right\rangle$. Other variables can be calculated from relations (16) and (19).

The solution of the second equation (21) can be written in the explicit form. It is not necessary to know the exact shape of function $B = B(\beta) = B(D)$ because it is only necessary to define inverse function $B^{-1} = B^{-1}(Y) = B^{-1}(\varepsilon^{\mathrm{E}})$. Then

$$D = B^{-1}\left(\frac{1}{2}E(\varepsilon^{\mathrm{E}})^2 - \frac{1}{2}E(\varepsilon^{\mathrm{E}}_{0})^2\right) \tag{22}$$

where $\varepsilon^{\mathrm{E}}_{0}$ is the initial strain for the damage evolution and B_0 is assumed in the following form:

$$B_0 = \frac{1}{2}E(\varepsilon^{\mathrm{E}}_{0})^2 \tag{23}$$

The exact shape of D is, in this paper, proposed in the following form:

$$D = D_{\mathrm{u}}\left\{K_{\mathrm{B}}\left[\frac{(\varepsilon^{\mathrm{E}})^2 - (\varepsilon^{\mathrm{E}}_{0})^2}{(\varepsilon^{\mathrm{E}}_{\mathrm{f}})^2}\right]^{n} + (1-K_{\mathrm{B}})\left[\frac{(\varepsilon^{\mathrm{E}})^2 - (\varepsilon^{\mathrm{E}}_{0})^2}{(\varepsilon^{\mathrm{E}}_{\mathrm{f}})^2}\right]^{m}\right\} \tag{24}$$

with

$$n = \left(\frac{\varepsilon_{\mathrm{r}}}{\varepsilon_{\mathrm{f}}}\right)^{a_1} \tag{25}$$

and

$$m = \left(\frac{\varepsilon_{\mathrm{f}}}{\varepsilon_{\mathrm{r}}}\right)^{a_2} \tag{26}$$

where D_{u} is the ultimate damage factor, for which the total failure of the material occurs; K_{B} and ε_{r} are the parameters of the damage-factor dependency defining the position of the inflection point of the damage curve; $\varepsilon^{\mathrm{E}}_{\mathrm{f}}$ is the strain at which failure occurs and a_1 and a_2 are the shape parameters.

3. Once the plastic strain, damage factor and all the other variables including the stress are known, the next time step can be solved.

The model includes 11 material parameters summarized in **Table 1**.

The calculation of the whole analysis of the cyclic tensile test with almost 3000 time steps is done in less than 1 second on the machine with Intel® Core™ I7-4790, a four-core CPU, running at the frequency of 3.60 GHz using Windows 7 operating system with an SSD disk.

Table 1: Material parameters
Tabela 1: Parametri materiala

Parameter	Units	Meaning
E	Pa	Elastic modulus
R_0	Pa	Initial yield stress
K_r	Pa	Shape parameter of the hardening curve
n_R	–	Shape parameter of the hardening curve
D_u	–	Maximum value of damage that the material can absorb before failure
K_B	–	Coefficient defining the position of the inflection point
ε_0^E	–	Initial elastic strain for damage
ε_f^E	–	Strain at which failure occurs
ε_r^E	–	Strain defining the position of the inflection point
a_1	–	Shape parameter of damage curve
a_2	–	Shape parameter of damage curve

5 IDENTIFICATION

Raw experimental data are pre-processed for the further identification. Important data points such as the maxima and minima of the loading cycles and cross points are found (**Figure 3**). Averaged values of these points serve as the target for the further identification.

In order to identify the material parameters, the difference between numerical and experimental results is minimized. Function r defining this difference is the so-called total residual. It is the sum of five particular residuals and it is minimized in the identification process.

The first residual is the difference between tensile curves r_L:

$$r_L = \frac{1}{N_L} \sum_{i=1}^{N_L} \left(\frac{F^E(\Delta l_i) - F^F(\Delta l_i)}{F_{\max}^E} \right)^2 \tag{27}$$

where superscripts E and N stand for the experimental and numerical analysis, respectively; N_L is the number of points, in which the curves are compared (the number of $P^{\max}$ points); Δl_i is the elongation of the specimen related to the point $P^{\max}$ and the denominator $F_{\max}^E$ is the maximum force in the target curve used as the weight coefficient.

According to **Figure 3**, the target for tensile curves in the experiment is considered as the connection of $P^{\max}$ points. Pure epoxy shows a negligible difference between points $P^{\max}$ and P^{int} unlike the other materials such as textile composites, rubber, etc. In a numerical analysis, if a model does not consider viscoelasticity (which is true of the presented model) these two points coincide. **Figure 4** shows the idea of a comparison of the tensile curves and the calculation of residual r_L.

The second residual r_K is the difference between the tangents of the unload-load cycles of the experimental data k^E and numerical data k^N:

$$r_K = \frac{1}{N_K} \sum_{i=1}^{N_K} \left(\frac{k^E(\Delta l_i) - k^N(\Delta l_i)}{k_{\max}^E} \right)^2 \tag{28}$$

where N_K is the number of the points, in which the curves are compared; Δl_i is the elongation of the specimen related to the point $P^{\max}$ and the denominator is the maximum value of the tangent in the experiment used as the weight coefficient. The tangents k are the first derivatives of the straight line connecting points $P^{\max}$ and $P^{\min}$ (**Figure 3**).

The third residual r_{mF} is the difference between the values of the maximum forces:

$$r_{mF} = \left(1 - \frac{F_{\max}^N}{F_{\max}^E} \right) \tag{30}$$

where $F_{\max}^N$ is the maximum force reached in the numerical analysis and $F_{\max}^E$ is the value from the target function.

The fourth residual r_{mD} is the difference between the values of the elongations related to the points of maximal forces:

$$r_{mD} = \left(1 - \frac{\Delta l_{\max F}^N}{\Delta l_{\max F}^E} \right) \tag{31}$$

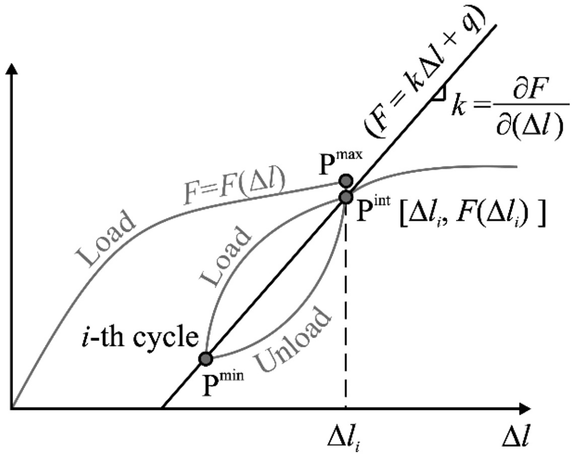

Figure 3: One unload-load cycle and important points
Slika 3: En cikel razbremenjeno – obremenjeno in pomembne točke

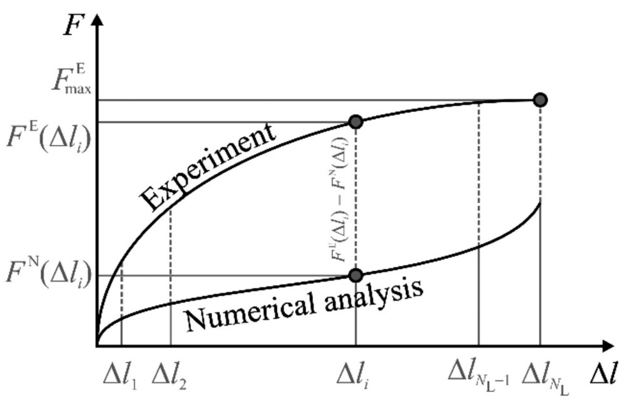

Figure 4: Comparison of the tensile curves
Slika 4: Primerjava nateznih krivulj

where $\Delta l^{\mathrm{N}}_{\max F}$ and $\Delta l^{\mathrm{E}}_{\max F}$ are the elongations related to the points where force-elongation curves reached their maxima of the force in the numerical analysis and in the experiment.

Finally, the fifth residual r_{E} is the difference between the values of the force measured after brittle crack (zero values) and the forces calculated in the numerical analysis, subsequent to the point where the curve reaches its maximum:

$$r_{\mathrm{E}} = \frac{1}{N_{\mathrm{E}}} \sum_{i=1}^{N_{\mathrm{E}}} \left(\frac{F^{\mathrm{N}}(\Delta l_i)}{F^{\mathrm{E}}_{\max}} \right)^2 \tag{32}$$

This particular residual is used to induce the model to get to the state where the brittle crack occurs.

Once the particular residuals are known, the total residual can be calculated as:

$$r = r_{\mathrm{L}} + r_{\mathrm{T}} + r_{\mathrm{mF}} + r_{\mathrm{mD}} + r_{\mathrm{E}} \tag{33}$$

Optimization software OptiSLang 3.2.3. was used. Gradient and simple design improvement algorithms were used.[8]

6 RESULTS

Figure 5 shows the force-elongation dependency. Note that the deviation of the maximum forces in the experiments is not negligible.

Considering the deviation of the experimental results, the identified dependency shows sufficient agreement; nevertheless, it is slightly more curved than the experimental target.

Figure 6 shows the comparison of the results for the calculated tangents of the unload-load cycles. The first cycle was ignored because of the influence of the inaccuracies of the experimental results for low loading forces. The comparison of the curves is performed within the interval where all the measured specimens provide the necessary data. The first specimen reached its strength limit at an elongation of about 0.25 mm. The justification for this choice is as follows: after reaching the mentioned elongation limit, significant jumps in the dependence of the averaged experimental results occur because of the disappearing data from each cracked specimen.

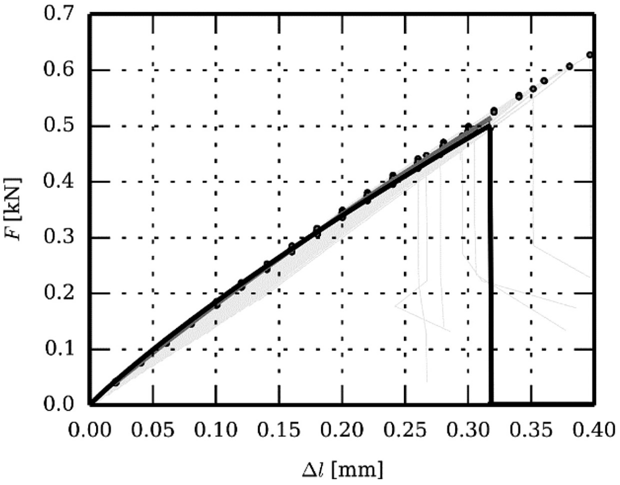

Figure 5: Force-elongation dependency. Dots represent points $P^{\max}$. Grey bold line is the target experiment; black bold line is the numerical analysis.

Slika 5: Odvisnost sile od raztezka. Točke predstavljajo $P^{\max}$. Siva, ojačana linija je cilj preizkusa, črna ojačana linija je numerična analiza.

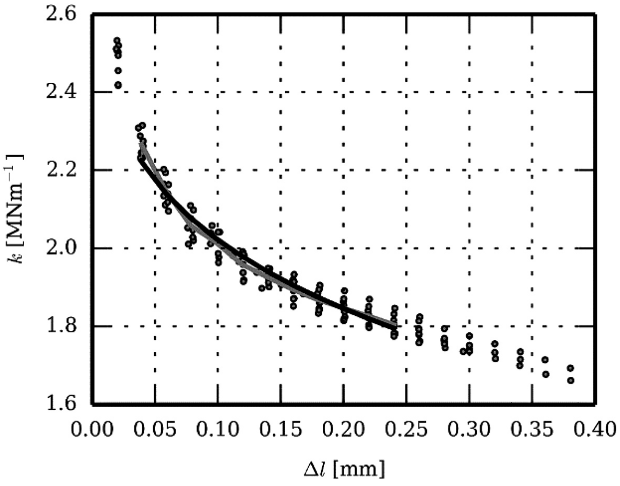

Figure 6: Tangent of unload-load cycle vs. elongation. Grey bold line is the target experiment; black bold line is the numerical analysis. Dots represent tangents k for each cycle in each experiment.

Slika 6: Tangenta na cikel obremenjeno – razbremenjeno, raztezek. Siva ojačana krivulja je cilj raziskave, črna debela krivulja je nume-

Figure 7 shows the identified hardening function.

Dependency of the damage factor on the elastic strain is shown in **Figure 8**. The modulus $E_{\mathrm{D}} = E(1 - D)$ occurs right before the brittle fracture and equals 3.55 GPa and the damage factor is $D = 0.47$ (see the gray circle in **Figure 8**).

The identified material parameters including those calculated directly from the experiment are given in **Table 2**.

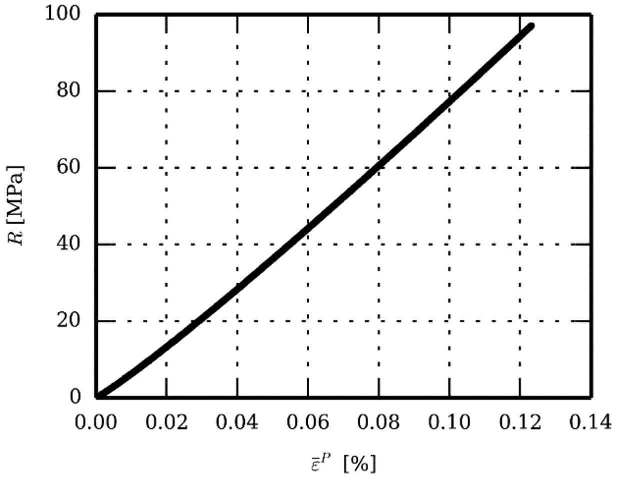

Figure 7: Hardening function

Slika 7: Funkcija utrjevanja

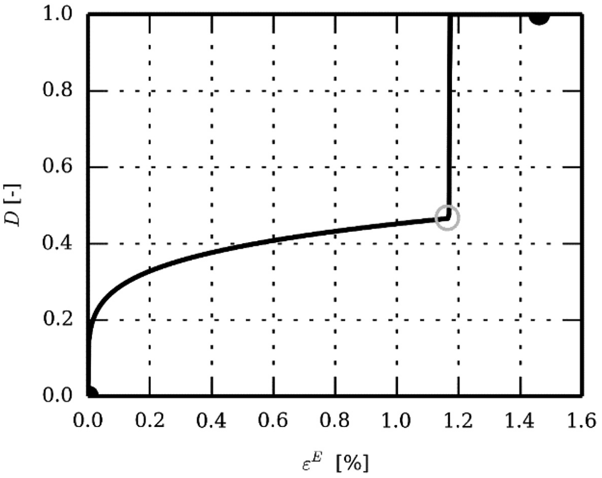

Figure 8: Damage function. Grey circle shows the initiation of brittle fracture and the final failure of the material.

Slika 8: Funkcija poškodb. Sivi krogi kažejo pričetke krhkega loma in končno porušitev materiala

Table 2: Identified parameters. Parameters with * were calculated directly from the experimental results.

Tabela 2: Ugotovljeni parametric. Parametri označeni z *, so bili izračunani neposredno iz eksperimentalnih rezultatov

Parameter	Value	Unit
E	6.64	GPa
R_0	0.00	MPa
K_R	149.19	GPa
n_R	1.10	-
D_u	0.76	-
K_B	0.62	-
ε_0^E	0.00	%
ε_r^E	0.46	%
ε_f^E	1.17	%
a_1	2.48	-
a_2	6.95	-
ν*	0.29	-
σ_S*	41.67	MPa

7 CONCLUSION

A relatively simple and effective algorithm for the calculation of the response of a material, showing elastic, plastic and damage behavior is proposed. The plastic and damage-flow problems are solved separately. A set of equations is transformed into a single nonlinear equation in the case of the plastic-flow problem and the equation is solved with the golden-section algorithm, which is extremely effective. The other set of equations that need to be solved in order to calculate the damage factor is transformed into one explicit formula for calculating the damage factor.

An appropriate identification process is proposed and its effectivity is shown in the case of the cyclic tensile tests of pure epoxy resin. The function that is minimized during the identification process is the sum of five independent residuals, each quantifying a difference between experimental and numerical results. These residuals express the differences between tensile-elongation dependencies and the values of the tangents of the unload-load cycles, the distance between the point of the maximum force reached in force and elongation directions and the value of the force after the brittle fracture of the specimen is minimized. The model and the identification process are robust and time effective.

Acknowledgement

This publication was supported by project LO1506 of the Czech Ministry of Education, Youth and Sports.

8 REFERENCES

[1] T. Kroupa, V. Laš, R. Zemčík: Improved nonlinear stress–strain relation for carbon–epoxy composites and identification of material parameters, Journal of Composite Materials, 45 **(2011)** 9, 1045–1057, doi:10.1177/0021998310380285

[2] R. Zemčík, R. Kottner, V. Laš, T. Plundrich, Identification of material properties of quasi-unidirectional carbon-epoxy composite using modal analysis, Mater. Tehnol., 43 (**2009**) 5, 257–260

[3] S. Ogihara, K. L. Reifsnider: Characterization of Nonlinear Behavior in Woven Composite Laminates, Applied Composite Materials, 9 **(2001)**, 249–263, doi:10.1023/A:1016069220255

[4] S. Murakami, Continuum damage mechanics, A continuum mechanics approach to the analysis of damage and fracture, Springer, 2012

[5] E. A. de Souza Neto, D. Perić, D. R. J. Owen, Computational Methods for Plasticity: Theory and Applications, Wiley, 2008

[6] V. Laš, R. Zemčík, Progressive Damage of Unidirectional Composite Panels, Journal of Composite Materials, 42 **(2008)** 1, 25–44, doi:10.1177/0021998307086187

[7] K. J. Bathe, Finite element procedures, Prentice Hall, Upper Saddle River, New Jersey 07458, USA, 2007

[8] J. S. Arora, Introduction to Optimum Design, Elsevier, 2004

UDK 66.017:544.424.2:662.613.12
Original scientific article/Izvirni znanstveni članek

ISSN 1580-2949
MTAEC9, 51(2)219(2017)

OPTIMIZING THE REACTIVITY OF A RAW-MATERIAL MIXTURE FOR PORTLAND CLINKER FIRING

OPTIMIZIRANJE REAKTIVNOSTI MEŠANICE SUROVIN PRI ŽGANJU PORTLAND KLINKERJA

Marcela Fridrichová, Dominik Gazdič, Karel Dvořák, Radek Magrla

Brno University of Technology, Faculty of Civil Engineering, Veveří 331/95, 602 00 Brno, Czech Republic
magrla.r@fce.vutbr.cz

Prejem rokopisa – received: 2015-07-01; sprejem za objavo – accepted for publication: 2016-03-16

doi:10.17222/mit.2015.187

On the basis of long-term chemical, mineralogical and granulometric analyses it was concluded that concrete recycled materials are usable for the production of Portland cement clinkers. However, they should be combined with high-calcium limestone, because even the finest undersize fraction has a relatively low CaO content, usually not exceeding 10 % of mass fractions. Furthermore, it was concluded that batching recycled materials with high-calcium limestone in a ratio of about 1:3 can produce Portland cement clinker of the same quality as common commercial clinker. However, there is an issue with the preparation of the cement clinker in the very low reactivity of the raw-material mixture containing high-calcium limestone and an increased content of silica in the concrete component. In order to improve the reactivity of the raw-material mixture modifications with fluxes for clinker production were proposed. An undersize fraction of recycled concrete of 0-8 mm and high-calcium limestone were used to prepare the raw-material mixtures. Gypsum, $CaSO_4 \cdot 2H_2O$, fluorite, CaF_2, and sodium fluorosilicate, Na_2SiF_6 were chosen as suitable additives. The prepared samples of raw-material mixtures were assayed for reactivity during the cement clinker firing process using the kinetic method. After the evaluation of the obtained results, a sample modified with the most effective grinding aid was burned in an operation rotary kiln. The effectiveness of the modifications was evaluated based on the phase composition of the burned cement clinker and by determining the technological properties.

Keywords: Portland clinker, high-calcium limestone, concrete recycled materials, gypsum, fluorite, sodium fluorosilicate

Na osnovi dolgotrajnih kemijskih, mineraloških in granulometrijskih analiz je mogoče zaključiti, da so reciklirani betonski materiali uporabni za izdelavo Portland cementnih klinkerjev. Vendar pa morajo biti kombinirani z apnencem z visoko vsebnostjo kalcija, ker ima tudi najdrobnejša frakcija relativno majhno vsebnost CaO, običajno pod 10 masnih %. Poleg tega je mogoče zaključiti, da so serije recikliranih materialov z apnencem z visoko vsebnostjo kalcija v razmerju okrog 1:3, primerne za izdelavo Portland cementnega klinkerja, enake kvalitete kot je običajen komercialni klinker. Vendar pa je vprašanje, kako pripraviti cementni klinker pri nizki reaktivnosti mešanice surovin, ki vsebuje apnenec z visoko vsebnostjo kalcija in povečano vsebnost kremena v betonski komponenti. Da bi izboljšali reaktivnost mešanice surovin za proizvodnjo klinkerja, so bile predlagane modifikacije mešanice s talili. Najdrobnejša frakcija recikliranega betona od 0–8 mm in apnenec z veliko vsebnostjo kalcija sta bili uporabljeni za pripravo mešanice surovin. Mavec, $CaSO_4 \cdot 2H_2O$, fluorit, CaF_2 in natrijev fluorosilikat, Na_2SiF_6 so bili izbrani kot primerni dodatki. Pripravljeni vzorci mešanice surovin so bili z uporabo kinetične metode preizkušeni na reaktivnost med postopkom žganja cementnega klinkerja. Po oceni dobljenih rezultatov je bil vzorec, modificiran z najbolj učinkovitim brušenjem, žgan v rotacijski peči. Učinkovitost modifikacije je bila ocenjena na osnovi sestave faz žganega cementnega klinkerja in z določitvijo tehnoloških lastnosti.

Ključne besede: Portland klinker, apnenec z veliko vsebnostjo kalcija, reciklirani betoni, mavec, fluorit, natrijev fluorosilikat

1 INTRODUCTION

The basic raw material used in the cement industry is limestone. It is a rock that together with dolomite constitutes four fifths of all the sediments on the Earth's surface. For this reason its deposits may appear virtually inexhaustible. In spite of this, the overview of limestone mining in the second half of the 20th century alone indicates that these large industrially-useable deposits are soon to shrink substantially with the current accelerating rate of mining. However, seeing as modern society produces a large amount of waste, such as FBC ashes and demolition waste, the possibility arises to process these as secondary raw-material resources for the production of building materials. As far as demolition waste is concerned, they are used mainly in the production of recycled materials that are well-established today as secondary aggregate. Only their finest, undersize fraction, typically from 0 mm to 8 mm, does not find sufficient use. It is this finest fraction that contains the highest content of the original cement mortar whose chemical composition can approach that of raw materials for clinker burning. Based on long-term, chemical-mineralogical analyses at our institute, the conclusion was reached that the recycled materials are applicable in the burning of Portland clinkers. However, they must be combined with high-calcium limestone. Based on laboratory and pilot plant burning in a model rotary kiln, the optimal batching ratio was determined at 1 : 3. This batching delivers Portland clinker of the same quality as common commercial clinker. Nevertheless, the issue with obtaining clinker in this way is in the very low reactivity of the raw-material mixture containing high-calcium limestone and increased silica content in the concrete component. For this reason it is necessary to address the improvement of reactivity of a mixture designed this way.[1–4]

One option is to use fluxes or mineralizers. These substances have the capacity to intensify the rate of clinker formation and have positive effects on the properties of the clinker.[5,6] Fluorides, sulfates, carbonates, chlorides, alkaline and metal oxides or various combinations have been widely studies and their favorable effect on the rate of clinkerization was reported.[7–12]

2 METHODOLOGY

The recycled material was made with recycled concrete of the undersize fraction of 0-8 mm and high-calcium limestone; their chemical analysis is in **Table 1**. The undersize fraction of recycled concrete was sorted in a ball mill 15 *w*/% remainder on a 0.09 mm screen. The high-calcium limestone was sorted in a similar way. Both the basic raw materials were then batched at the ratio recycled concrete : high-calcium limestone 1 : 3; this ratio was previously determined to be optimal. After batching and thorough homogenisation of both raw materials, ca. 100 g samples of recycled materials were prepared, modified by the chosen additives; i.e. gypsum, dosed at concentration of 1, 2, and 3 *w*/%, fluorite, tested at concentrations of (0.5, 1, 1.5 and 2) *w*/%, and sodium fluorosilicate dosed at (0.1, 0.5 and 1) *w*/%. The prepared samples were then tested for reactivity during clinker firing using the kinetic method. The effectiveness of the modifications was determined on the basis of the phase composition of the clinker.

Table 1: Chemical composition of input components
Tabela 1: Kemijska sestava vhodnih sestavin

Component	Component content (%)	
	Recycled concrete 0–8 mm	Limestone
SiO_2	63.29	1.02
TiO_2	0.38	0.05
Al_2O_3	9.87	0.57
Fe_2O_3	2.59	0.20
MnO	0.07	0.01
MgO	1.56	0.34
CaO	9.39	54.70
Na_2O	1,72	0.01
K_2O	3.38	0.13
loss on ignition	7.39	42.99
SO_3	0.43	0.05
Total	100.07	100.07

After the reactivity had been evaluated the clinker was burned in a laboratory model rotary kiln in an amount of 5 kg from the raw material of the highest reached reactivity. After burning, the clinker was put to phase analysis by means of microscopy point integration and X-ray diffraction analysis. Then it was sorted together with 5 w/% gypsum in a ball mill into cement at a specific surface of 375 $m^2 \cdot kg^{-1}$. The cement thus produced was tested for basic technological properties, i.e. granulometry, initial and final setting time and compressive and flexural strengths.

3 REACTIVITY DETERMINATION

The kinetic method of determining raw-material reactivity permits a separated evaluation of the influence of mineral resources and the influence of the means of raw-material preparation on the rate of clinker creation in the clinkering zone of the rotary kiln. The basis of the kinetic method is isothermal burning of the clinker at 1430 °C and its quantitative phase analysis by means of microscopy. Based on this analysis the rate constant *K* of the reaction producing alite ($C + C_2S = C_3S$) is calculated from the kinetic Equation (1):

$$K\ .\ t = [1 - \sqrt[3]{(1 - \alpha)}]^2 \qquad (1)$$

where:
α ….. conversion level CaO to C_3S
t ….. time of isothermal burning
K ….. rate constant

For the reactivity of raw material R_m it follows Equation (2):

$$R_m = K / K_s \qquad (2)$$

where: K_s ….. rate constant of comparative raw material.

The reactivity of the raw material R_m thus expressed constitutes the relative rate of isothermal formation of clinker from the raw material at a medium temperature in the clinkering zone of a rotary kiln. It includes the influence of all reactivity factors, which divided into uninfluenced factors of the raw resource (mineralogical composition and microstructure, the content of secondary oxides, etc.) and influenced factors of the raw-material preparation (composition, granulometry, homogeneity). The effect of the uninfluenced factors on reactivity can be determined during the standardization of the influenced factors, i.e., the preparation of raw materials with the same chemical and granulometric compositions. Because the practical implementation of this process is very difficult, it is carried out by calculation based on a knowledge of the mechanism and the kinetics of clinker production. In doing so, the results of the phase analysis of the determination R_m are used, supplemented by a screen analysis of the raw material. Thus, the following applies for the reactivity of the raw-material resource:

$$R_z = k / k_s \qquad (3)$$

where:
k ….. rate constant of raw the material with standardized parameters of preparation
k_s ….. rate constant of comparative raw material with standardized parameters of preparation

The results of the determination of the phase composition and reactivity are shown in **Table 2**, **Table 3** and **Table 4** for samples of the raw material with the individual modification additives. Besides these there are values determined for the reference sample of the raw material without additives.

Table 2: Raw material with added gypsum
Tabela 2: Surovina z dodatkom mavca

Raw material	Content of phase (*w*/%)			
	Reference sample	1 % gypsum	2 % gypsum	3 % gypsum
C_3S	25.6	25.0	21.5	19.5
C_2S	48.7	49.1	51.8	53.8
MH	17.2	16.6	17.4	16.9
C_{free}	8.5	9.3	9.2	9.8
pore	35.6	37.5	37.8	38.0
C_3S_{rov}	61.5	64.2	60.4	60.8
C_2S_{rov}	21.3	19.2	22.4	22.3
	Reactivity			
R_m	0.18	0.15	0.12	0.10
R_z	0.25	0.23	0.18	0.14

Table 3: Raw material with added CaF_2
Tabela 3: Surovina z dodatkom CaF_2

Raw material	Content of phase (*w*/%)				
	Reference sample	0.5 % CaF_2	1 % CaF_2	1.5 % CaF_2	2 % CaF_2
C_3S	25.6	35.2	38.4	40.8	42.2
C_2S	48.7	42.3	38.7	39.2	36.6
MH	17.2	15.7	16.3	15.0	15.7
C_{free}	8.5	6.8	6.6	5.0	5.5
pore	35.6	35.4	38.3	36.1	39.0
C_3S_{rov}	61.5	63.9	66.2	61.9	65.4
C_2S_{rov}	21.3	20.4	17.5	23.1	18.9
	Reactivity				
R_m	0.18	0.36	0.42	0.60	0.57
R_z	0.25	0.55	0.63	0.97	0.90

Table 4: Raw material with added Na_2SiF_6
Tabela 4: Surovina z dodatkom Na_2SiF_6

Raw material	Content of phase (*w*/%)			
	Reference sample	0.1 % Na_2SiF_6	0.5 % Na_2SiF_6	1 % Na_2SiF_6
C_3S	25.6	30.9	36.5	40.2
C_2S	48.7	45.3	42.4	38.1
MH	17.2	16.9	16.5	16.3
C_{free}	8.5	6.9	4.6	5.4
pore	35.6	34.3	36.8	39.0
C_3S_{rov}	61.5	60.0	55.9	63.0
C_2S_{rov}	21.3	23.1	27.6	20.7
	Reactivity			
R_m	0.18	0.30	0.59	0.55
R_z	0.25	0.43	0.89	0.85

The results presented in the tables show that the reactivity of the raw material of the reference non-modified sample is very low. The modification by gypsum influenced the reactivity of the raw material in the opposite way to what was assumed. Not only did it not increase the reactivity, it significantly reduced it at gypsum concentration of 2 *w*/%. Furthermore, an increased SO_3 content in the raw material caused an adverse increase of belite content at the expense of alite. On the other hand, fluorite had a very good influence on the reactivity of the raw material. With an increased content of this additive the values of the reactivity increased and the maximum was reached at 15 *w*/% dose. At the same time CaF_2 had a positive influence on the formation of alite and as its content increased, so did the alite content in the clinker. Na_2SiF_6 also had a positive effect on the reactivity of the raw material. The maximum values of the effectiveness were between 0.5 and 1 *w*/%, but the maximum values were a little lower than in the case of fluorite use. For a good reactivity of the raw material, the modification by fluorite with a concentration of 1.5 *w*/% was determined to be the optimum one and thus the raw material of this composition was used in further testing. It should be noted that this modification was very successful because reactivity afforded $R_m = 0.59$, respectively $R_z = 0.89$ is higher than, e.g., the reactivity of the raw material from the Mokra cement factory with its values $R_m = 0.52$, $R_z = 0.51$.

4 PILOT PLANT BURNING

For pilot-plant burning the raw material with the additive 1.5 *w*/% CaF_2 was converted into the form of compacted pieces by means of its homogenization with 1 % dextrin and water and subsequent processing using a plodder machine. The thus prepared and dried pieces were put in a model rotary kiln where they were burned at 1550 °C. Cooling in the conditions of this burning was performed by sudden free fall of the clinker in the air out of the heating end of the kiln.

A qualitative representation of each phase of the burnt clinker was observed by means of X-ray diffraction analysis. A dominant content of alite was identified as well as the presence of belite was apparent only through diffraction $d_{hkl} = 0.2403$ nm, diffractive lines C_3A and

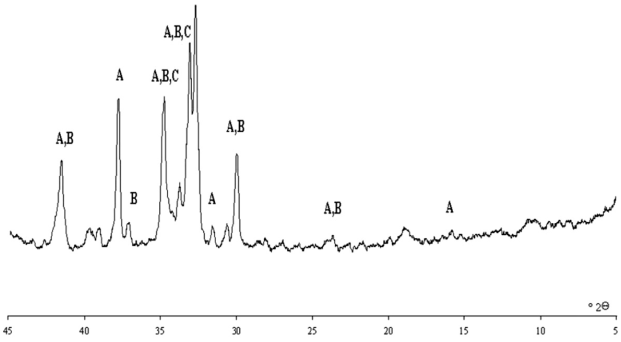

Figure 1: X-ray diffraction pattern of clinker: A – alite, B – belite, C – C_3A
Slika 1: Rentgenogram klinkerja: A – alit, B – belit, C – C_3A

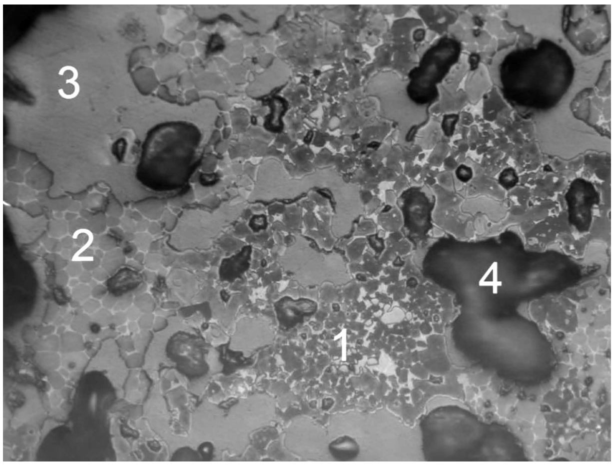

Figure 2: Microstructure of clinker: 1 – alite, 2 – belite, 3 – C_3A and C_4AF, 4 – pore

Slika 2: Mikrostruktura klinkerja; 1 – alit, 2 – belit, 3 – C_3A in C_4AF, 4 – pore

C_4AF were featureless, see the X-ray diffraction pattern in **Figure 1**.

The phase analysis carried out by means of microscopic point integration of the burnt sample identified it as a clinker with a dominant content of alite, a relatively high content of belite and C_3A, and, on the other hand, a reduced amount brown millerite a slight remainder of free CaO (**Figure 2**). Alite formed hypautomorphic to automorphic crystals with a high degree of mutual coalescence. The average size of the alite crystals ranged from 25 µm to 30 µm, while there were plentiful inclusions of alite in belite. Belite formed the usual oval agglomerates of grains with an average size of 15 µm to 20 µm. Free CaO occurred only sporadically in the form of clusters of globular grains in alite areas. Quantitative phase composition of the burnt clinker is in **Table 5**.

Table 5: Phase composition of burnt clinker determined microscopically

Tabela 5: Sestava faz žganega klinkerja, določena z mikroskopom

Phase	Content of phase (*w*/%)
C_3S	55.6
C_2S	25.9
C_3A	12.1
C_4AF	5.8
CaO_{free}	0.6
Total	100.0

5 TECHNOLOGICAL PROPERTIES OF THE BURNT CLINKER

The pilot-plant burnt clinker was milled with 5 *w*/% gypsum into cement with a specific surface of 375 m^2 kg^{-1}. Then it was tested for technological properties; the results together with the results of the properties of the reference cement are shown in **Table 6**. The reference cement was prepared using the same procedure as above with commercial clinker collected in the cement factory Mokra.

Table 6: Technological properties of alite cement

Tabela 6: Tehnološke lastnosti alit cementa

Observed property	Reference sample	Alite cement
Specific surface Blaine (m^2 kg^{-1})	375	375
Water-cement ratio (%)	26.1	29.0
Initial setting time (h min)	3:05	2:05
Final setting time (h min)	6:45	5:00
Compressive strength (MPa)		
1 d	23.2	28.6
3 d	45.5	54.8
7 d	46.6	63.8
28 d	56.1	76.5
Flexural strength (MPa)		
1 d	6.6	8.5
3 d	9.1	13.6
7 d	10.6	15.9
28 d	11.6	16.9

The results shown in the table indicate that at the same specific surface of the two compared cements, the reference cement showed a slightly lower value of water-cement ratio. The difference is probably connected with a slightly different phase composition of both clinkers. It is also evident that the tested cement, compared to the reference, has a shorter initial and setting time. This difference is related to the phase composition of the pilot-plant burnt clinker, respectively, with a relatively high proportion of C_3A. The compressive strength values of the tested cement were after all the observed hydration times higher than the reference sample's strength on average by 30 %, and even the flexural strength was higher by 50 %. The main cause of this phenomenon can probably be considered to be the higher hydraulicity of the burnt clinker, given its modification by fluorite.

6 CONCLUSIONS

The insufficiency of preparation and pilot-plant production of Portland clinker based on recycled concrete and high-calcium limestone, which lay in the low reactivity of the raw material, has been removed by modifying with fluorite. At a dose of 1.5 *w*/% of this additive in the raw material reactivity has improved so much that it even exceeded that of the normal raw material from the cement factory Mokra. It can be concluded that recycled concrete materials are utilizable for Portland cement burning in combination with high-calcium limestone. Because the resources of high-calcium limestone can also be found in existing waste materials, such as sugar factory sludge etc., their combination may represent not only the economic benefits, but particularly in the future, a contribution to the transition to non-waste technology too, and thus contribute to the protection of raw-material resources.

Acknowledgment

This work was financially supported by project number: GA14-32942S "Effect of fluidized bed ash on the thermodynamic stability of hydraulic binders" and project No. LO1408 "AdMaS UP – Advanced Materials, Structures and Technologies", supported by Ministry of Education, Youth and Sports under the "National Sustainability Programme I".

7 REFERENCES

[1] M. Fridrichová, J. Gemrich, Building recyclates as a partial material source for Portland clinker baking, Cement International, Verlag Bau + Technik GmbH, (2005)

[2] M. Fridrichová, J. Brauner, T. Stanìk, Recycled materials as a partial raw material for the production of Portland cement clinker, Ecology and new building materials and products, (2005), (in Czech)

[3] M. Fridrichová, D. Gazdič, K. Kulísek, Concrete recycled as sub-base raw material for burning of belite clinker, Materiálové inženýrství, 1 (**2009**), 63–66, BUT Brno, (in Czech)

[4] M. Fridrichová, J. Brauner, P. Zlámal, J. Novák, Rohmehlmodifikation zum Brennen des Belitklinkers, IBAUSIL, 1 (**2006**),147–154, Finger Institut Bauhaus-Univ. Weimar

[5] I. Odler, Improving energy effiency in portland clinker manufacturing, Cement and Concrete Science and Technology, Vol. 1, Part. 1, ABI Books Private Limited, (1991), 174–200

[6] G. K. Moir, Improvements in the early strength properties of Portland cement, Philos. Trans. R. Soc. Lond., A 310 (**1983**), 127–138

[7] G. K. Moir, Mineralised high alite cements, World Cem 10 (**1982**), 374–382

[8] Larbi Kacimi, Angélique Simon-Masseron, Abdelhamid Ghomari, Zoubir Derriche, Influence of NaF, KF and CaF2 addition on the clinker burning temperature and its properties, Comptes Rendus Chimie, 9 (**2006**) 1, 154–163, doi:10.1016/j.crci.2005.10.001.

[9] H. E. Borgholm, D. Herfort, S. Rasmusen, A new blended cement based on mineralised clinker, World Cement 8 (**1995**), 27–33

[10] A. Emanuelson, S. Hansen, E. Viggh, A comparative study of ordinary and mineralised Portland cement clinker from two different production units Part I: Composition and hydration of the clinkers, Cement and Concrete Research 33 (**2003**) 10, 1613–1621, doi:10.1016/S0008-8846(03)00115-7

[11] O. Dominguez, A. Torres-Castillo, L. M. Flores-Velez, R. Torres, Characterization using thermomechanical and differential thermal analysis of the sinterization of Portland clinker doped with CaF_2, Materials Characterization, 61 (**2010**) 4, 459–466, doi:10.1016/j.matchar.2010.02.002

[12] Joris Schoon, Anne Vergari, Klaartje De Buysser, Isabel Van Driessche, Nele De Belie, Fines extracted from porphyry and dolomitic limestone aggregates production: MgO as fluxing agent for a sustainable Portland clinker production, Construction and Building Materials, 43 (**2013**), 511–522, doi:10.1016/j.conbuildmat.2013.02.046

UDK 622.7.017:66.017:661.665.1
Original scientific article/Izvirni znanstveni članek

ISSN 1580-2949
MTAEC9, 51(2)225(2017)

EFFECT OF ADDING WATER-BASED BINDERS ON THE TECHNOLOGICAL PROPERTIES OF CERAMIC SLURRIES BASED ON SILICON CARBIDE

VPLIV DODATKA VODOTOPNEGA VEZIVA NA TEHNOLOŠKE LASTNOSTI SUSPENZIJE SILICIJEVEGA KARBIDA

Paweł Wiśniewski, Marcin Małek, Jarosław Mizera, Krzysztof Jan Kurzydłowski

Warsaw University of Technology, Faculty of Materials Science and Engineering, 141 Woloska street, Warszawe, Poland
p.wisniewski@inmat.pw.edu.pl

Prejem rokopisa – received: 2015-07-02; sprejem za objavo – accepted for publication: 2016-03-07

doi:10.17222/mit.2015.194

Presented is research work concerning the possibility of applying new materials for the preparation of ceramic shell moulds. Most of the methods for the fabrication of ceramic slurries for investment casting are based on alcohol binders. This is one of the first researches focused on the preparation of ceramic slurries using a new, ecological method based on water-soluble binders. The work presents the rheological properties of ceramic slurries based on silicon carbide and new binders, i.e., polyvinyl alcohol and two polyacrylic binders. The rheological properties of the investigated slurries were modified by the addition of 15 % of mass fractions of the binders in the solution form. The solid phase content in the ceramic slurries was 62.5 % of mass fractions. Standard industrial parameters such as pH, density, Zhan 4# Cup viscosity and apparent viscosity determined by a rheometer were studied. The grain size of the silicon carbide powder was determined by SEM observations. The ceramic slurries were fabricated using a mechanical mixer, and the mixing time was 96 h. The results showed that the ceramic slurries were stable vs. time and met standard industrial requirements. The ceramic slurries have very promising properties and they are very promising for future shell moulds fabrication.

Keywords: ceramic shell moulds, silicon carbide, binder, rheological properties, ceramic slurries

Predstavljeno je raziskovalno delo o možnostih uporabe novih materialov za pripravo keramičnih form. Večina metod priprave keramične suspenzije za precizijsko litje temelji na alkoholnih vezivih. To je ena od prvih raziskav usmerjenih v pripravo keramičnih suspenzij, z uporabo nove, ekološke metode na osnovi vodotopnih veziv. Delo predstavlja reološke lastnosti keramičnih suspenzij na osnovi silicijevega karbida in novih veziv, kot je polivinil alkohol in dve poliakrilni vezivi. Reološke lastnosti preiskovanih suspenzij so bile spremenjene z doatkom 15 masnih % veziv v obliki raztopine. Vsebnost trdne faze v keramični suspenziji je bila 62,5 masnih %. Proučevani so bili običajni industrijski parametri kot: pH, gostota, viskoznost z Zhan 4# Cup viskozimetrom in navidezna viskoznost, določena z reometrom. Velikost zrn silicijevega karbida je bila določena s SEM. Keramična suspenzija je bila izdelana s pomočjo mehanskega mešalnika, s časom mešanja 96 h. Rezultati so pokazali, da je suspenzija časovno stabilna in ustreza industrijskim zahtevam. Keramične suspenzije imajo obetajoče lastnosti in so zelo primerne za bodočo izdelavo školjkastih oblik.

Ključne besede: keramične školjkaste forme, silicijev karbid, vezivo, reološke lastnosti, keramične suspenzije

1 INTRODUCTION

Historically, investment-casting technology was mainly used for the casting of tools, weapons and ornaments. Nowadays, this technology is employed in many important manufacturing sectors, both industrial and artistic.[1] Investment castings fabricated by the lost-wax method are widely used in many fields of industry. Owing to their merits, including high quality, reliability, high Weibull modulus this method is the most popular in aircraft turbine parts manufacturing.[2] European environmental regulations press the precision-casting industry for elimination of to eliminate alcohol binders from the moulds production process. From the beginning the process was based on ethyl silicate binders. According to the European regulations they should be fully replaced by water-based binders. Water systems need to contain polymers to improve the "green" state properties. The application of polymer-modified binders decreases the strength of moulds after burnout, but increases their permeability and flexibility.[3–4]

In comparison with other techniques of casting, investment casting has many advantages:

- obtaining the highest dimensional accuracy and surface smoothness,
- replacing expensive machining methods to fabrication precision castings,
- possibility of obtaining castings with very complex shapes, which cannot be achieved by other methods,
- possibility of casting of any alloy (in mass production and high volume),
- thin-walled castings can be achieved.

Disadvantages of the process:

- difficult process for mechanization and automation,
- limited casting weight substantially to 1–2 kg, particularly to 10 kg.[5–7]

Silicon carbide is widely used in many industrial areas due to its properties and low cost. New research showed that its application in ceramic shell moulds improves the technological parameters of the shells, such as: mechanical strength, thermal conductivity and thermal shock resistance. Shell moulds containing SiC powder significantly shortened the process of the fabrication of the final cast, reduced grain size of the castings and improved its mechanical properties.[8–11]

2 EXPERIMENTAL PART AND METHODOLOGY

The studies were carried out on silicon carbide powder (Stanchem, Poland). In addition, three different water-soluble binders were used i.e., polyvinyl alcohol (26000 g/mol weight and 88 % hydrolysis content (PVAL), Moviol, Germany), and two polyacrylic binders with 20 % of mass fractions (PA) and 40 % of mass fractions (PA2) of vinyl acrylic copolymer (Ransom & Randolph, USA) as 10 % water solution. The main binder was a substance with nanoparticles of aluminium oxide (Evonik, Germany). The SiC powder content in the slurry was 62.5 % of mass fractions. SEM images of the SiC powder were taken using a SU70 Hitachi microscope (Japan). Grain size was measured on La-950 Horiba analyser (Japan). The ceramic slurries were fabricated in a reactor with a mechanical mixer. The ceramic slurries were characterized using a Zahn Cup 4#, aerometer, plate weight test (adhesion test) and pH meter. The plate weight test time (120 s) was elaborated by the authors and determined the stable properties of the researched ceramic slurries (experience from past studies). The apparent viscosity was determined using a DV II+ Brookfield rheometer (USA). The rheological properties were tested in the speed range 20–200–20 min^{-1}.

3 RESULTS AND DISCUSSION

Figure 1 presents the SEM image of the investigated silicon carbide power. SiC was characterized by sharp-edged particles typical for moldings powders. The average equivalent diameter of the SiC grains was 21.9 μm.

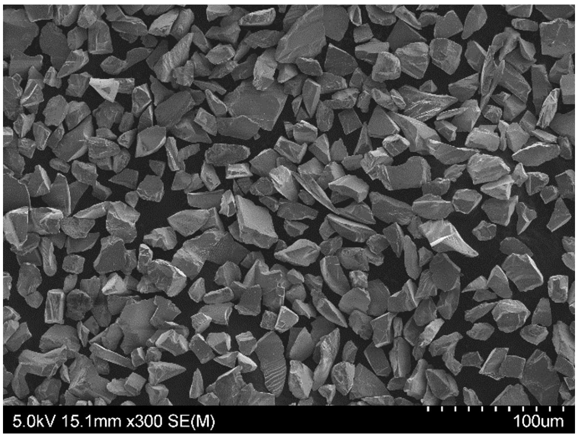

Figure 1: SEM image of investigated SiC powder
Slika 1: SEM-posnetek preiskovanega SiC prahu

Figures 2 to **4** presents adhesion test results of the ceramic slurries based on SiC. As seen in all the presented graphs, the highest weight loss occurred during the first day of the experiment. The rest of the curves were similar. A plateau was observed at 80 s for the PA- (**Figure 2**) for PA2 the plateau occured at 110 s (**Figure 3**) and for PVAL was also at 80 s (**Figure 4**). The time of the plateau's appearance depended on the viscosity and density of the ceramic slurries.

Figure 5 shows the apparent viscosity of the examined ceramic slurries. The highest viscosity was exhibited by a slurry with 15 % of mass fractions addition of

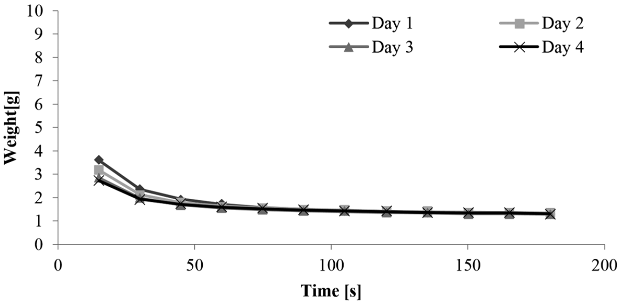

Figure 2: Results of plate weight test of slurry with 15 % of mass fractions of PA
Slika 2: Rezultati preizkusa adhezije suspenzije s 15 % masnih deležev PA

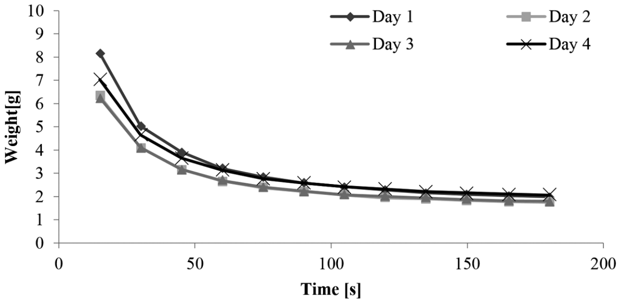

Figure 3: Results of plate weight test of slurry with 15 % of mass fractions of PA2
Slika 3: Rezultati preizkusa adhezije suspenzije s 15 % masnih deležev PA2

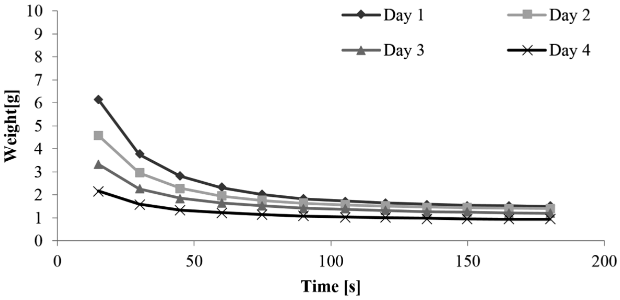

Figure 4: Results of plate weight test of slurry with 15 % of mass fractions of PVAL
Slika 4: Rezultati preizkusa adhezije suspenzije s 15 % masnih deležev PVAL

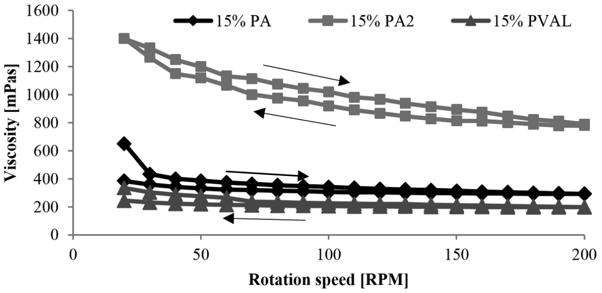

Figure 5: Apparent viscosity of the ceramic slurries
Slika 5: Navidezna viskoznost keramične suspenzije

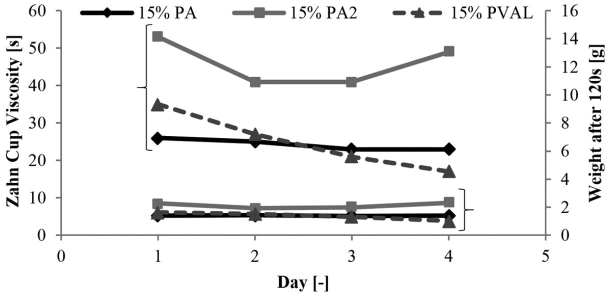

Figure 6: Rheological properties of the ceramic slurries
Slika 6: Reološke lastnosti keramičnih suspenzij

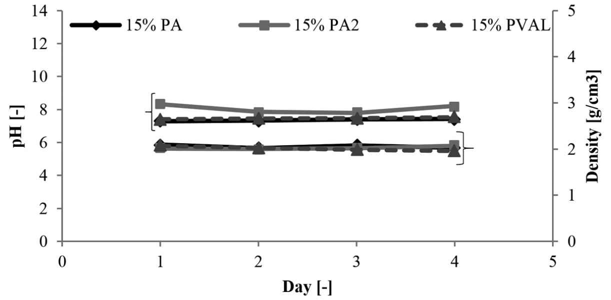

Figure 7: Density and pH of the ceramic slurries
Slika 7: Gostota in pH keramičnih suspenzij

PA2, while the lowest viscosity had the slurry with 15 % of mass fractions PVAL.

Figure 6 presents the basic rheological properties of the ceramic slurries. The addition of 15 % of mass fractions of PA2 and PVAL were inappropriate, because the viscosity of such slurries was high. A ceramic slurry with 15 % of mass fractions of PA met the standard industrial requirements. Its viscosity had the optimal value and slightly decreased with time. The results of the plate weight test made on daily basis were very comparable for all types of slurries.

Figure 7 shows the pH and density results of the examined ceramic slurries. The described properties were stable over time, and similar for all types of slurries.

4 CONCLUSIONS

According to the work assumption, with connection to the industrial requirements, these researches were focused on the rheological and technological properties of ceramic slurries based on silicon carbide powder. The main aim of this work was to fabricate ceramic slurries by using new water-soluble binders. The most desirable properties from the industry point of view were exhibited by the slurry with a 15 wt.% addition of PA binder. The slurries with PA binder were characterized by relatively low viscosity, the best adhesion and stability confirmed by the plate weight test. The research conducted in this work is the first in the world and has a very promising future in ceramic shell moulds fabrication.

Acknowledgments

Financial support of Structural Funds in the Operational Programme – Innovative Economy (IE OP) financed from the European Regional Development Fund – Project "Modern material technologies in aerospace industry", No. POIG.01.01.02-00-015/08-00 is gratefully acknowledged.

5 REFERENCES

[1] S. Rzadkosz, J. Zych, A. Garbacz-Klempka, M. Kranc, J. Kozana, M. Piekos, J. Kolczyk, L. Jamrozowicz, T. Stolarczyk, Copper alloys in investment casting technology, Metalurgia 54 (**2015**), 293–296

[2] J. Tomasik, R. Haratym, R. Biernacki, Investment casting or powder metallurgy- the ecological aspect, Archives of Foundry Engineering, 9 (**2009**) 2, 165–168

[3] A. Tyrek, J. Nawrocki, D. Sarek, Lost wax process – mould properties, Archives of Fundry and Engineering, 10 (**2010**) 1, 427–430

[4] M. Nadolski, Z. Konopka, M. Lagiewka, A. Zyska, Examining of slurries and production of moulds by spraying method in lost was technology, Archives of Fundry and Engineering, 8 (**2008**) 2, 107–110

[5] R. Haratym, R. Biernacki, D. Myszka, Ekologiczne wytwarzanie dokładnych odlewów w formach ceramicznych, Oficyna Wydawnicza Politechniki Warszawskiej, (**2008**), 25–47

[6] H. Matysiak, J. Ferenc, J. Michalski, Z. Lipinski, G. Jakubowicz, K. J. Kurzydlowski, Porosity and strength of ceramic shells used in Bridgman investment casting process, Materials Engineering 1 (**2011**), 17–21

[7] M. R. Ismael, R. D. dos Anjos, R. Salomao, V.C. Pandolfelli, Colloidal silica as a nostructured binder for refractory castables, Refractories Applications and News 11 (**2006**) 4, 16–20

[8] M. Malek, P. Wisniewski, H. Matysiak, R. Sitek, K. J. Kurzydlowski, Effect of polyethylene glycol addition on ceramic slurry properties used in investment casting, Polymer Processing 157 (**2014**) 20, 40–49

[9] M. Malek, J. Szymanska, P. Wisniewski, J. Mizera, K.J. Kurzydlowski, Technological properties of silicon carbide ceramic slurries for fabrication ceramic shell moulds, Proc. of the 5-th Aluminium 2000 Confeence, Florence, 2015, 1–8

[10] M. Malek, P. Wisniewski, J. Mizera, K.J. Kurzydlowski, Technological Technological properties of ceramic slurries based on silicon carbide for manufacturing ceramic shell moulds, Materials Engineering, 6 (**2015**) 208, 561–564

[11] M. Malek, P. Wisniewski, H. Matysiak, K.J. Kurzydlowski, Slurries for ceramic shell moulds fabrication, patent application no. P.406518, 2013

UDK 66.017:543.442.3:534.44
Original scientific article/Izvirni znanstveni članek

ISSN 1580-2949
MTAEC9, 51(2)229(2017)

PREPARATION OF BIO-POLYMERIC MATERIALS, THEIR MICROSTRUCTURES AND PHYSICAL FUNCTIONALITIES

PRIPRAVA BIOPOLIMERNIH MATERIALOV TER NJIHOVE MIKROSTRUKTURE IN FIZIČNE FUNKCIONALNOSTI

Xin-Li Chen, Ai-Juan Zhao, Hai-Jie Sun, Xian-Ru Pei

Zhengzhou Normal University, Institute of Environmental and Catalytic Engineering, College of Chemistry and Chenical Engineering, Zhengzhou 450044, China
katiloudy@163.com, sunhaijie406@zznu.edu.cn

Prejem rokopisa – received: 2015-07-09; sprejem za objavo – accepted for publication: 2016-05-13

doi:10.17222/mit.2015.211

In this work, three kinds of bio-based aromatic triols were prepared based on vegetable oils. Furthermore, PUs were synthesized using the three triols and 4,4'-methylenebis(phenyl isocyanate), 1,4-butanediol as a chain extender. The chemical structures, molecular characteristics, and physical functionalities were studied and compared using nuclear magnetic resonance (NMR) spectroscopy, Fourier-transform infrared (FTIR) spectroscopy, X-ray diffraction (XRD), differential scanning calorimetry (DSC), and thermogravimetry-differential thermal analysis (TG-DTA). Results showed that the poly-(oxypropylene)-based polyurethanes degrade in a single step, whereas the vegetable-oil-based polyurethane shows one-step decomposition. The present study therefore suggests a feasible synthesis route for the use of the biomaterials for the production of polyurethanes.

Keywords: polymers, microstructures, functionalities

V delu so bili iz bioolj prvič pripravljeni trije bioaromatični trioli. Poleg tega so bili sintetizirani PU, z uporabo treh triol in 4,4'-metilenbis(fenil izocianata) ter 1,4-butandiola kot podaljševalca verige. Študirane so bile kemijske strukture, molekularne značilnosti in fizične funkcionalnosti, ki so bile primerjane z uporabo spektroskopije jedrske magnetne resonance (NMR), spektroskopijo Fourierjeve infrardeče transformacije (NMR), rentgenske difrakcije (XRD), diferenčne vrstične kalorimetrije (DSC) in termogravimetrične diferenčne termične analize (TG-DTA). Rezultati so pokazali, da poliuretan na osnovi poli-oksipropilena razpade v enem koraku, medtem ko poliuretan na osnovi rastlinskih olj, kaže enostopenjski razpad. Predstavljena študija torej predlaga izvedljivo sintezo z uporabo biomaterialov za izdelavo poliuretanov.

Ključne besede: polimeri, mikrostrukture, funkcionalnosti

1 INTRODUCTION

In order to protect the environment and to reduce our dependence on fossil fuels, a great deal of research effort has been, and is still being, devoted to the development of innovative technologies using renewable resources.[1–7] Vegetable oils are abundant and cheap renewable resources that represent a major potential alternative source of chemicals suitable for developing safe, environmentally products.[8–10] The use of vegetable oils and natural fatty acids as starting raw materials offers numerous advantages: for example, inexpensive, abundant, low toxicity, and inherent biodegradability, thus they are considered to be one of the most important classes of renewable resources for the production of bio-based polymeric materials.[11–17] Polyurethanes (PUs) form a versatile class of polymers, which are used in a broad range of applications, for example, as elastomers, sealants, fibers, foams, coatings, adhesives, and biomedical materials. The industrial production of PUs is normally accomplished through the polyaddition reaction between organic isocyanates and compounds containing active hydroxyl groups, such as polyols. Comparing with polyurethanes derived from petrochemical polyols, the vegetable-oil-based polyols used to produce polyurethanes have been the subject of many studies.[9–12] Moreover, due to the hydrophobic nature of triglycerides, vegetable oils produce PUs that have excellent chemical and physical properties, such as enhanced hydrolytic, high tensile strength and elongation, high tear strength, and thermal stability.[13–18]

Vegetable oils are one of the most important sources of renewable raw materials for the chemical industry and provide versatile opportunities for a transformation to meet specific applications. In the 1980s, H. Baumann et al.[10] mainly focused on the carboxyl group of fatty acids, these include the hydrolysis of fats to make soaps, and synthesis of fatty amines from fatty acids. Recently, increasing interest in industrial and academic research has been focused on reactions on the hydrocarbon chains of fatty acids, especially on the double bonds of unsaturated fatty acids. Guo et al. applied the epoxidation of the double bonds of fatty acids, followed by nucleophilic ring opening of the epoxide to make polyols for producing polyurethanes.[19–23]

To further expand applications of the bio-based polymeric materials, previous studies were focusing on converting vegetable oils into useful PUs. Based on these studies, now it has become a main research field to functionalize vegetable oils by the introduction of aromatic co-monomers into the polymer structure, which could be suitable in the search for new viable polymeric materials.[12] The transition-metal-catalyzed trimerization of alkyne fatty acid compounds provides an alternative method for the preparation of highly functionalized aromatic polyols.[10,11]

In the present study, we have synthesized three kinds of bio-based aromatic triols prepared by oleic acid, 10-undecenoic acid, and erucic acid, which could be obtained from sunflower oil, castor oil, and rapeseed oil, respectively. PUs were synthesized by these aromatic triols and 4,4'-methylenebis(phenyl isocyanate), 1,4-butanediol as a chain extender. The chemical structures, molecular characteristics, physical properties, and thermal properties were studied and compared using nuclear magnetic resonance (NMR) spectroscopy, Fourier-transform infrared (FTIR) spectroscopy, X-ray diffraction (XRD), differential scanning calorimetry (DSC), and thermogravimetry-differential thermal analysis (TG-DTA).

2 EXPERIMENTAL PART

2.1 Materials

The following chemicals were obtained from the sources indicated: Oleic acid (AR, from Sinopharm) 10-undecenoic acid (from Sinopharm), erucic acid (from Aldrich), copper (II) chloride, $CuCl_2$ (99 %, from Sinopharm), palladium (II) chloride, $PaCl_2$ (AR, from Sinopharm), palladium on carbon, Pa/C (10 % of mass fractions, from Aldrich), potassium hydroxide, KOH (AR, from Kermel), n-propanol (AR, from Kermel), dimethyl sulfoxide, DMSO (AR, from Kermel), bromine (AR, from Xilong), chlorotrimethylsilane, TMSCl (CP, from Sinopharm), lithium aluminum hydride, $LiAlH_4$ (97 %, from Aldrich), 1,4-butandiol, BD (AR, from Bodi) and 4,4'-methylenebis(phenyl isocyanate), MDI (98 %, from Aldrich) were used as received.

2.2 Synthesis of aromatic triol 4 from oleic acid

2.2.1 Dibromide carboxylic acid

To a solution of oleic acid (10.6 g, 33.6 m/mol) in diethyl ether (150 mL) that was cooled to 0 °C in an ice-water bath, bromine (2.7 mL, 52.3 m/mol) was added dropwise over 30 min. Then the ice-water bath was removed and the solution was stirred for another 2 h at room temperature. A saturated sodium sulfite ($Na_2S_2O_3$) solution (20 mL) was added to reduce the excess bromine. The resulting organic phase was separated, washed with brine (20 mL) and dried over anhydrous magnesium sulfate ($MgSO_4$). The solvent was evaporated by reduced pressure to give a pale yellow powder 1 (yield 73 %).

IR (thin film): 3440 (OH), 1703 (C=O) cm^{-1}.

^{1}H NMR ($CDCl_3$/TMS, δ, 0.0001 %): 11.34 (s, 1H, COOH), 4.23-4.14 (m, 2H, CH-Br), 2.38-2.33 (t, 2H, CH_2-COOH), 2.06-1.99 (m, 2H, CH-CHBr), 1.88-1.80 (m, 2H, CHBr), 1.64-1.56 (m, 6H), 1.35-1.25 (m, 16H), 0.88 (t, 3H, CH_3).

2.2.2 Stearolic acid

The dibromide compound 1 (5.5 g, 15 m/mol) was dissolved in DMSO (18 mL, 250 mmol). KOH (20 g, 360 m/mol) and 1-propanol (150 mL) were added. The mixture was heated at 110 °C under reflux for 4 h. Then the solution was poured into 2N hydrochloric acid (HCl) (150 mL) at room temperature. The resulting organic layer was separated, washed with brine (20 mL) and dried over $MgSO_4$. The solvent was evaporated under reduced pressure to give a pale-yellow powder 2 (yield 76%).

IR (thin film): 3446 (OH), 2356 (C≡C), 1712 (C=O) cm^{-1}.

^{1}H NMR ($CDCl_3$/TMS, δ, 0.0001 %): 11.34 (s, 1H, COOH), 2.33 (t, 2H, CH_2-COOH), 2.12 (m, 4H, CH_2-CC), 1.26-1.62 (m, 22H), 0.88 (t, 3H, CH_3)

2.2.3 Stearoyl alcohol

Stearolic acid 2 (2.4 g, 8.6 m/mol) was dissolved in 50 mL diethyl ether and added dropwise to a dispersion of $LiAlH_4$ (0.4 g, 10.2 m/mol) in 100 mL of anhydrous diethyl ether. The mixture was stirred for 2 h at room temperature, and then the excess $LiAlH_4$ was decomposed by adding 20 mL of water dropwise. A 2N HCl (30 mL) aqueous solution was added until the pH was neutral. The resulting organic layer was separated, washed with brine (20 mL) and dried over $MgSO_4$. The solvent was evaporated under reduced pressure to give a pale-yellow oil 3 (yield 82 %).

IR (thin film): 3392 (OH), 2360 (C≡C) cm^{-1}.

^{1}H NMR ($CDCl_3$/TMS, δ, 0.0001 %): 3.65 (t, 2H, CH_2OH), 2.14 (t, 4H, CH_2-CC), 1.58-1.48 (m, 6H), 1.41-1.23(m, 18H), 0.90 (t, 3H, CH_3).

2.2.4 Aromatic triols

Stearoyl alcohol 3 (1.05 g, 4.0 m/mol) was dissolved in tetrahydrofuran (THF) (50 mL). 0.25 g of Pd/C (10 % of mass fractions) and TMSCl (0.75 mL, 6.0 m/mol) were added. The reaction mixture was heated at 65 °C refluxed for 8 h. The resulting mixture was cooled to room temperature and filtered to remove the Pd/C. The resulting organic layer was separated, washed with brine (20 mL) and dried over $MgSO_4$. The solvent was evaporated under reduced pressure to give a dark-yellow oil 4a and 4b (yield 58 %).

IR (thin film): 3438 (OH), 1652 (C=C of benzene) cm^{-1}.

^{1}H NMR ($CDCl_3$/TMS, δ, 0.0001 %): 3.56 (t, 6H, CH_2OH), 2.43 (m, 12H, CH_2Ph), 1.49-1.20 (m, 72H), 0.83 (t, 9H).

^{13}C NMR ($CDCl_3$/TMS, δ, 10^{-4} %): 136.77 (Ph-CH_2), 62.94 (CH_2OH), 31.94, 31.86, 29.68, 29.64, 29.57, 29.33, 29.26, 25.72, 22.68, 22.66, 14.12 (CH_3).

2.3 Synthesis of aromatic triol 4' from 10-undecenoic acid

2.3.1 Dibromide carboxylic acid 1'

10-Undecylenic acid (9.2 g, 50 m/mol) in diethyl ether (150 mL) was cooled to 0 °C in an ice-water bath. Bromine (4.2 mL, 81 m/mol) was added dropwise over 30 min. Then the ice-water bath was removed and the solution was stirred for another 2 h at room temperature. A saturated $Na_2S_2O_3$ solution (20 mL) was added to reduce the excess bromine. The resulting organic phase was separated, washed with brine (20 mL) and dried over $MgSO_4$. The solvent was evaporated under reduced pressure to give a gray solid 1' (yield 78 %).

IR (thin film): 3433 (OH), 1705 (C=O) cm^{-1}.

^1H NMR ($CDCl_3$/TMS, δ, 0.0001 %): 11.58 (s, 1H, COOH), 3.85-3.80 (q, 1H, CH-CHBr), 3.64-3.57 (t, 2H, CH-Br), 2.35-2.30 (t, 2H, CH_2-COOH), 2.17-2.05 (m, 3H), 1.84-1.50 (m, 3H), 1.30-1.23 (m, 8H).

2.3.2 10-Undecynic acid 2'

The dibromide compound 1' (5.2 g, 15 m/mol) was dissolved in DMSO (18 mL, 250 mmol). KOH (20 g, 360 m/mol) and 1-propanol (150 mL) were added. The mixture was heated at 110 °C under reflux for 4 h. Then the solution was poured into 2N HCl (150 mL) at room temperature. The resulting organic layer was separated, washed with brine (20 mL) and dried over $MgSO_4$. The solvent was evaporated under reduced pressure to give a white solid 2' (yield 63 %).

IR (thin film): 3440 (OH), 2360 (C≡C), 1710 (C=O) cm^{-1}.

^1H NMR ($CDCl_3$/TMS, δ, 0.0001 %): 11.54 (s, 1H, COOH), 2.31 (t, 2H, CH_2-COOH), 2.17-2.11 (m, 2H), 1.92 (t, 1H), 1.55-1.44 (m, 4H), 1.33-1.23 (m, 8H).

2.3.3 10-Undecyn-1-ol 3'

10-Undecynic acid 2' (1.6 g, 8.8 m/mol) was dissolved in 50 mL diethyl ether and added dropwise to a dispersion of $LiAlH_4$ (0.4 g, 10.2 m/mol) in 100 mL of anhydrous diethyl ether. The mixture was stirred for 2 h at room temperature, and then the excess $LiAlH_4$ was decomposed by adding 20 mL of water dropwise. A 2N HCl (30 mL) aqueous solution was added until the pH was neutral. The resulting organic layer was separated, washed with brine (20 mL) and dried over $MgSO_4$. The solvent was evaporated under reduced pressure to give a pale-yellow solid 3' (yield 72 %).

IR (thin film): 3335 (OH), 2358 (C≡C) cm^{-1}.

^1H NMR ($CDCl_3$/TMS, δ, 0.0001 %): 3.59 (t, 2H, CH_2OH), 2.20-2.14 (m, 4H), 1.76 (t, 1H, CH-C), 1.56-1.50 (m, 4H), 1.35-1.26 (m, 8H).

2.3.4 Aromatic triols 4'a and 4'b

10-Undecyn-1-ol 3' (0.68 g, 4.0 m/mol) was dissolved in n-butyl alcohol (9 mL) and benzene (150 mL). $PdCl_2$ (0.15 g, 0.85 m/mol) and $CuCl_2$ (2.05 g, 12 mmol) were added. The reaction mixture was heated at 40 °C and refluxed for 8 h. The resulting mixture was cooled to room temperature and filtered to remove the $PdCl_2$ and $CuCl_2$. The resulting organic layer was separated, washed with brine (20 mL) and dried over $MgSO_4$. The solvent was evaporated by reduced pressure to give a dark-yellow oil 4'a and 4'b (yield 68 %).

IR (thin film): 3456 (OH), 1639 (C=C of benzene) cm^{-1}.

^1H NMR ($CDCl_3$/TMS, δ, 0.0001 %): 6.40 (s, 3H, Ph), 3.64 (t, 6H, CH_2Ph), 2.29 (t, 6H), 1.61-1.24 (m, 42H).

^{13}C NMR ($CDCl_3$/TMS, δ, ppm): 138.22 (Ph-CH_2), 120.35 (Ph-H), 64.11 (CH_2OH), 39.86, 34.35, 30.68, 29.70, 29.08, 28.54, 27.46, 24.96.

2.4 Synthesis of aromatic triol 4" from erucic acid

2.4.1 Dibromide carboxylic acid 1"

Erucic acid (15.88 g, 33.6 mmol) in diethyl ether (150 mL) was cooled to 0 °C in an ice-water bath. Bromine (2.7 mL, 52.3 mmol) was added dropwise over 30 min. Then the ice-water bath was removed and the solution was stirred for another 2 h at room temperature. A saturated $Na_2S_2O_3$ solution (20 mL) was added to reduce the excess bromine. The resulting organic phase was separated, washed with brine (20 mL) and dried over $MgSO_4$. The solvent was evaporated under reduced pressure to give a gray solid 1'' (yield 78 %).

IR (thin film): 3425 (OH), 1706 (C=O) cm^{-1}.

^1H NMR ($CDCl_3$/TMS, δ, 0.0001 %): 11.89 (s, 1H, COOH), 4.27-4.18 (m, 2H, CH-Br), 2.35 (t, 2H, CH_2-COOH), 2.10-1.95 (m, 2H, CH-CHBr), 1.65-1.54 (m, 2H), 1.47-1.26 (m, 30H), 0.89 (t, 3H, CH_3).

2.4.2 Behenolic acid 2"

The dibromide compound 1'' (7.5 g, 15 mmol) was dissolved in DMSO (18 mL, 250 mmol). KOH (20 g, 360 mmol) and 1-propanol (150 mL) were added. The mixture was heated at 110 °C under reflux for 4 h. Then the solution was poured into 2N hydrochloric acid (HCl) (150 mL) at room temperature. The resulting organic layer was separated, washed with brine (20 mL) and dried over $MgSO_4$. The solvent was evaporated under reduced pressure to give a pale-yellow powder 2'' (yield 72 %).

IR (thin film): 3454 (OH), 2361 (C≡C), 1705 (C=O) cm^{-1}.

^1H NMR ($CDCl_3$/TMS, δ, 0.0001 %): 11.62 (s, 1H, COOH), 2.37 (t, 2H, CH_2-COOH), 2.15 (m, 4H, CH_2-CC), 1.69-1.23 (m, 30H), 0.90 (t, 3H, CH_3).

2.4.3 Behenolic ester 3"

To a solution of behenolic acid 2'' (4.5 g, 12.9 mmol) in methanol (100 mL) was added about 5 mL concentrated sulphuric acid. The reaction mixture was heated at

95 °C and refluxed for 3 h. The resulting organic layer was separated, washed with brine (20 mL) and

dried over $MgSO_4$. The solvent was evaporated under reduced pressure to give pale-yellow oil 3'' (yield 62 %).

IR (thin film): 2360 (C≡C), 1745 (C=O), 1170 (C-O) cm^{-1}.

^{1}H NMR ($CDCl_3$/TMS, δ, 0.0001 %): 3.66 (s, 3H, CH_3-O), 2.30 (t, 2H, CH_2-$COOCH_3$), 2.13 (m, 4H, CH_2-CC), 1.68-1.20 (m, 30H), 0.88 (t, 3H, CH_3).

2.4.4 Aromatic triester 4''a and 4''b.

Behenolic ester 3'' (2.8 g, 8.0 mmol) were dissolved in n-butyl alcohol (9 mL) and benzene (150 mL). $PdCl_2$ (0.15 g, 0.85 mmol) and $CuCl_2$ (2.05 g, 12 mmol) were added. The reaction mixture was heated at 40 °C and refluxed for 12 h. The resulting mixture was cooled to room temperature and filtered to remove the $PdCl_2$ and $CuCl_2$. The resulting organic layer was separated, washed with brine (20 mL) and dried over $MgSO_4$. The solvent was evaporated under reduced pressure to give a yellow oil 4''a and 4''b (yield 68 %).

IR (thin film): 1745 (C=O), 1641 (C=C of benzene), 1174 (C-O) cm^{-1}.

^{1}H NMR ($CDCl_3$/TMS, δ, 0.0001 %): 3.68 (s, 9H, CH_3-O), 2.54-2.43 (m, 12H, CH_2Ph), 2.32 (t, 6H, CH_2-$COOCH_3$), 1.70-1.26 (m, 90H), 0.90 (t, 9H, CH_3)

^{13}C NMR ($CDCl_3$/TMS, δ, 0.0001 %): 174.41 (C=O), 136.71 (Ph-CH_2), 51.48 (CH_3-O), 34.13, 33.76, 31.96, 31.46, 30.69, 30.17, 29.71, 29.52, 29.42, 29.36, 29.31, 29.10, 24.97, 22.72, 14.16 (CH_3).

2.4.5 Aromatic triols 5''a and 5''b.

Aromatic triester 5'' (2.1g, 2.0 mmol) were dissolved in 50 mL diethyl ether and added dropwise to a dispersion of $LiAlH_4$ (0.4 g, 10.2 mmol) in 100 mL of anhydrous diethyl ether. The mixture was stirred for 2 h at room temperature, and then the excess $LiAlH_4$ was decomposed by adding 20 mL of water dropwise. A 2N HCl (30 mL) aqueous solution was added until the pH was neutral. The resulting organic layer was separated, washed with brine (20 mL) and dried over $MgSO_4$. The solvent was evaporated under reduced pressure to give a pale-yellow oil 5''a and 5''b (yield 88 %).

IR (thin film): 3430 (OH), 1465 (C=C of benzene) cm^{-1}.

^{1}H NMR ($CDCl_3$/TMS, δ, 0.0001 %): 3.63 (t, 6H, CH_2OH), 2.56-2.40 (m, 12H), 1.64-1.26 (m, 96H), 0.89 (t, 9H, CH_3).

^{13}C NMR ($CDCl_3$/TMS, δ, 0.0001 %): 136.71 ($PhCH_2$), 63.06 (CH_2OH), 34.12, 32.81, 32.61, 31.96, 31.49, 30.68, 29.70, 29.51, 29.42, 29.26, 25.75, 24.97, 22.70, 22.70, 19.15, 14.13(CH_3).

2.5 Synthesis of polyurethanes

Polyurethane powders were prepared by reacting aromatic triol with diisocyanate at different molar ratios of the OH group to the NCO group. The desired OH/NCO molar ratio satisfies Equation (1):

$$M_{\text{ratio}} = \frac{W_{\text{polyol}} / EW_{\text{polyol}}}{(W_{\text{PU}} - W_{\text{polyol}}) / EW_{\text{diisocyanate}}} \quad (1)$$

where W_{polyol} is the weight of the polyol, EW_{polyol} is the equivalent weights of polyol, W_{PU} is the total weight of polyurethane, and $EW_{\text{diisocyanate}}$ is the equivalent weight of the diisocyanate.

The equivalent weight for the diisocyanate was calculated based on the molar mass and was $EW_{\text{diisocyanate}}$ = 250 g/mol. The equivalent weights of aromatic triol were determined using Equation (2):

$$EW_{\text{polyol}} = \frac{\text{molecular weight of KOH} \times 1000}{\text{OH Number}} = \quad (2)$$

$$= \frac{56110}{\text{OH Number}} \text{ g per mole of hydroxyl group}$$

The weights of the polyol and diisocyanate were calculated using the above-calculated equivalent weight.

Polyurethane elastomers are block copolymers and their domain structure can be controlled through the selection of the materials and their relative proportions. The polyurethanes were prepared using a single-stage process. In our investigation the hard-segment composition was controlled by the molar ratios of polyol/diisocyanate/diol and aromatic triol used in the synthesis.[18] The molar ratios of the OH group to the diisocyanate (NCO) group chosen for the formulations were 0.9. The $OH_{\text{diol}}/OH_{\text{aromatic triol}}$ molar ratio used was 1.0/2.0 in each of the synthesized polyurethane samples. After 10 min of mixing the appropriate amount of aromatic triols and chain extender (BD) at 75 °C, diisocyanate at the OH/NCO ratio of 0.9 was added. The mixture was cured for 2 h at 75 °C and then post-cured at 110 °C for 16 h.

2.6 Measurements and analysis

The X-ray diffraction (XRD) patterns obtained on an X-ray diffractometer (type Bruker AXS D8) using Cu-$K\alpha1$ radiation at a scan rate (2θ) of 0.02° s^{-1} were used to determine the identity of any phase present and the crystallite size. The accelerating voltage and the applied current were 15 kV and 20 mA, respectively.

The Fourier-transform infrared spectroscopy (FTIR) spectra were recorded on a Bruker Tensor 27 spectrometer in the range 400-4000 cm^{-1} using KBr disks. ^{1}H NMR and ^{13}C NMR were recorded on Bruker Advance III 300MHz spectrometers with $CDCl_3$ as a solvent.

DSC measurements were carried out on a Diamond DSC instrument (TA instruments, DE, USA), equipped with a refrigerated cooling system. The samples were heated at a rate of 10 °C/min from 25 °C to 200 °C to erase the thermal history and cooled down to -65 °C at cooling rate of 5 °C/min. The DSC experiments were carried out with a liquid-nitrogen cooler under a dry-nitrogen atmosphere.

For thermal stability analysis, 10 mg of the dried polyurethanes powders were used in TG-DTA thermal analyzer (type PerkinElmer Diamond TG/DTA, America) at a heating rate of 10 °C/min from 20 °C to 800 °C in an inert-gas atmosphere.

3 RESULTS AND DISCUSSION

3.1 Synthesis of bio-based aromatic triols

The synthesis of triol monomers from oleic acid, erucic acid and 10-undecenoic through a cyclotrimerization reaction yielded a mixture of asymmertrical and symmetrical molecules (Chart 1). Bio-based aromatic triols oleic acid-based aromatic triols (O-BAT), erucic acid-based aromatic triols (E-BAT) and 10-undecenoic-based aromatic triols (U-BAT) were synthesized by two different methods. Alkyne alcohol derivatives were obtained in moderate yields from the corresponding fatty acids by bromation, dehydrobromination, and reduction of carboxylic acid using well-established procedures (Scheme1). Alkyne fatty derivatives were obtained in moderate yields from the corresponding fatty acids by bromation, dehydrobromination, and esterification using well-established procedures (Scheme1).[9,12] Cyclotrimerization of the 10-undecyn-1-ol 3' and behenolic ester 3'' were carried out using $PdCl_2$ as a transition-metal catalyst. However, when cyclotrimerization of stearoyl alcohol 3 was carried out under the same conditions, some side products were slowly generated or no indication of the trimer formation was obtained. The reaction was then carried out using Pd/C as a transition-metal catalyst, and the expected product was obtained in moderate yields.[10,11]

Transition-metal-catalyzed cyclotrimerization of alkynes can be considered as one of the most powerful and general methodologies used to assemble arene rings, and a large number of transition-metal catalysts have been developed for alkyne cyclotrimerization in organic media.[12,24–25] A simple method utilizes a heterogeneous Pa/C catalyst in a nitrogen atmosphere with refluxing THF as the solvent and commercial grade chlorotrimethylsilane.[10,26] Cyclotrimerization of Stearoyl alcohol 3 was carried out following this procedure, and the symmetric and asymmetric isomers, such as aromatic triols 4a and 4b, have almost identical IR or ^{13}C NMR spectra in $CDCl_3$. The formation of the aromatic derivative was confirmed by the appearance of the signal at 0.013677 % in the ^{13}C NMR spectrum corresponding to the aromatic core. The two compounds could not be separated by flash chromatography due to their similar polarities. Therefore, the presence of two compounds could not be ruled out.

The preparation of benzene derivatives via the palladium-chloride-catalyzed cyclotrimerization of alkynes in the presence of $CuCl_2$ has been described as a smooth and regioselective method.[12] When the cyclotrimerization of 10-undecyn-1-ol 3' was carried out using $PdCl_2$ and $CuCl_2$ as transition-metal catalysts, a 1,3,5-trisubstituted benzene derivative was obtained regioselectively in a moderate yield. The appearance of signals at 0.000639 % in the ^1H NMR spectrum and 0.012035 % and 0.013763 ppm in the ^{13}C NMR spectrum confirms the formation of the symmetric product.

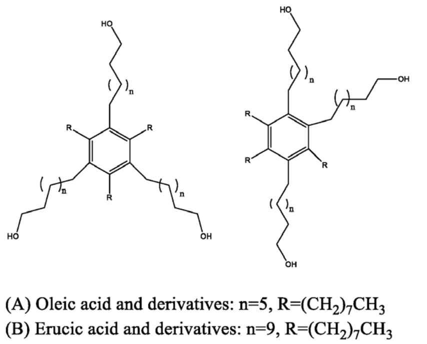

(A) Oleic acid and derivatives: n=5, R=$(CH_2)_7CH_3$
(B) Erucic acid and derivatives: n=9, R=$(CH_2)_7CH_3$
(C) 10-undecenoic acid and derivatives: n=6, R=H

Chart 1: Chemical structures of aromatic triols monomers obtained by oleic acid, erucic acid and 10-undecenoic, respectively

Grafikon 1: Kemijske strukture aromatičnih triol monomerov, dobljenih z oleinsko kislino, eruka kislino in 10-undekenojsko kislino

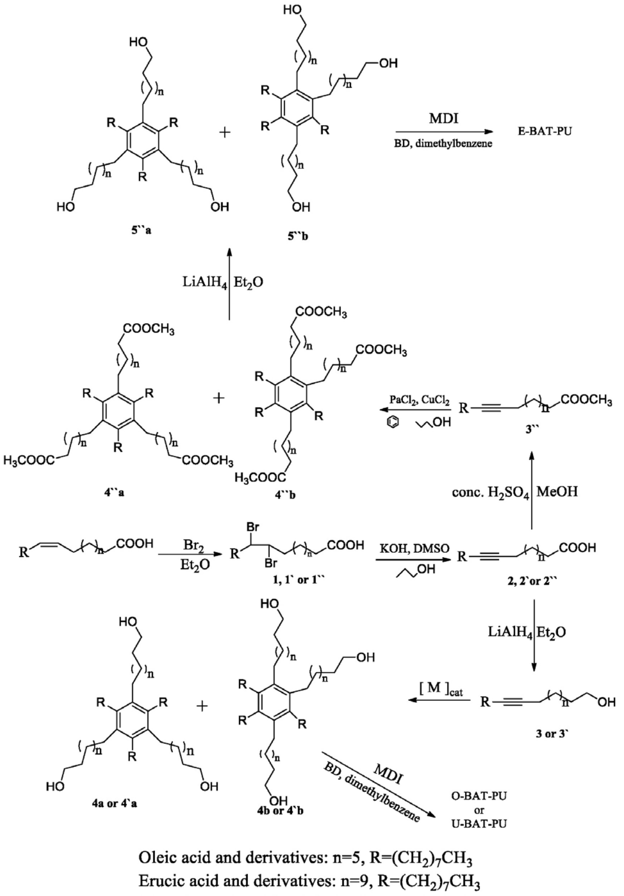

Oleic acid and derivatives: n=5, R=$(CH_2)_7CH_3$
Erucic acid and derivatives: n=9, R=$(CH_2)_7CH_3$
10-undecenoic acid and derivatives: n=6, R=H

Scheme 1: Synthesis of aromatic triols from oleic acid, erucic acid and 10-undecenoic acid, respectively

Shema 1: Sinteza aromatičnih triol iz oleinske kisline, eruka kisline in 10-undekenojske kisline

The attempt to cyclotrimerize behenolic ester 3'' via Pa/C catalyst in nitrogen atmosphere with refluxing THF as the solvent and chlorotrimethylsilane, some side products were slowly generated. The preparation of benzene derivatives via the palladium-chloride-catalyzed cyclotrimerization of alkynes in the presence of $CuCl_2$ has been described as a smooth and regioselective method.[12,27–28] When we applied the reaction to behenolic ester 3'', the symmetric and asymmetric isomers, such as aromatic triols 4''a and 4''b, have almost identical IR or ^{13}C NMR spectra in $CDCl_3$. The formation of the aromatic derivative was confirmed by the appearance of the signal at 0.013671 % in the ^{13}C NMR spectrum corresponding to the aromatic core. The two compounds could not be separated by flash chromatography due to their similar polarities. Therefore, the presence of two compounds could not be ruled out. The reaction can also proceed with behenolyl alcohol. However, when cyclotrimerization of the behenolyl alcohol was carried out in the same conditions, a lot of side products were slowly generated and the yields of aromatic triester 4''a and 4''b were lower. So, aromatic ester derivatives were used as a starting material for the reduction of the carboxylate groups to synthesize two triols with primary hydroxyl groups.

3.2 Synthesis and characterization of polyurethanes

Vegetable-oil-based polyols have been widely used to produce segmented and non-segmented polyurethanes.[19–22] Segmented polyurethanes are elastomeric block copolymers that generally exhibit a phase-segregated morphology made up of soft rubbery segments and hard glassy or semi-crystalline segments.[23,24] The soft segment usually consists of polyether or polyester diols, whereas the hard segment consists of the diisocyanate component and a low molecular weight consists of the diisocyanate component and a low-molecular-weight chain extender. The advantage of segmented polyurethanes is that their segmental and domain structure can be controlled over a considerable range through the selection of the materials, their relative proportions, and the processing conditions.[12]

In the study, bio-based polyurethanes were prepared using the one-shot technique from O-BAT, E-BAT or U-BAT, BD as a chain extender, and MDI as a coupling agent. The bio-based aromatic triols/MDI part is considered as the soft phase, even though its glass transition is above room temperature (**Table 1**). These hard segments are polar, crystallizable and likely to form a separate phase if the hard-segment content is high enough. The chemical composition and hard-segment content of the synthesized polyurethanes are also shown in **Table 1**. The OH/NCO molar ratio was kept at 1.5. Reactants were mixed at 75 °C and cured at this temperature for 2 h and post-cured at 110 °C for 18 h to give the polyurethanes.

Table 1: Formulations and hardness of the polyurethanes obtained
Tabela 1: Formulacija in trdota dobljenega poliuretana

Sample code	Ratio (OH:NCO)	Ratio (Polyol/BD/MDI)	% Hard segment*
O-BAT-PU	0.9	1:3:3	56.9
E-BAT-PU	0.9	1:3:3	52.1
U-BAT-PU	0.9	1:3:3	67.6

*The hard-segment percentage is calculated as the *w*/% of BD and MDI per total material weight

To investigate the molecular structure of polyurethanes WAXD and FTIR were employed. The amorphous character of both the asymmetric and symmetric polyurethanes was verified by WAXD (**Figure 1**). All the samples show similar WAXD curves with a broad peak at about $2\theta \approx 22°$. This broad peak is a typical characteristic of amorphous polymers[12,13,15–17], which confirms that there are no crystals in O-BAT-PU, E-BAT-PU and U-BAT-PU.

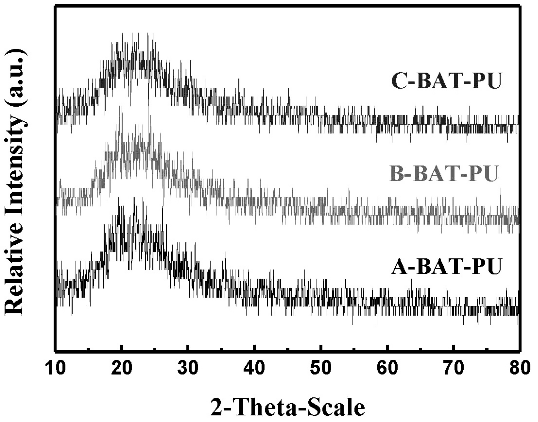

Figure 1: Wide-angle X-ray diffraction patterns of: a) O-BAT, b) E-BAT and c) U-BAT polyurethane
Slika 1: Širokokotna rentgenska difrakcija: a) O-BAT, b) E-BAT in c) U-BAT poliuretana

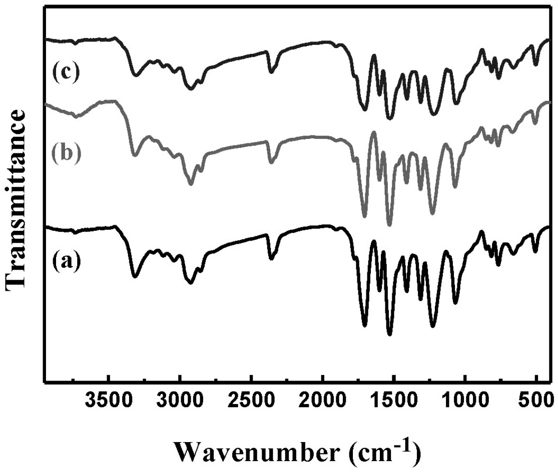

Figure 2: FTIR spectra of: a) O-BAT-PU, b) E-BAT-PU, and c) U-BAT-PU
Slika 2: FTIR-spektri: a) O-BAT-PU, b) E-BAT-PU in c) U-BAT-PU

The FTIR spectra for O-BAT-PU, E-BAT-PU, and U-BAT-PU are shown in **Figure 2**. From **Figure 2**, it is clear that the spectra are similar for the PUs prepared from the same diisocyanate but different aromatic triols sources. The unreacted diisocyanate (NCO group) is clearly shown by a peak centered at 2362 cm^{-1}. A strong stretching band located at around 3317 cm^{-1} characteristic of the N-H group and a stretching vibration band centered around 1708 cm^{-1} characteristic of the C=O group are present in the FTIR spectra.[7,8,15] There are also two stretching regions attributed to the C=O group. The band centered at around 1768cm^{-1} corresponds to the free carbonyl group. These results indicated that the three kinds of PU materials undergo physical bonding.[16,18]

3.3. Thermal stability of polyurethanes

Thermal analysis of the polyurethanes obtained was performed to provide insights into the morphological structure of the material. **Figure 3** shows the DSC thermogram for the polyurethanes. There were two endothermic peaks at about 45–50 °C and 175–190 °C. The glass-transition temperature of the samples measured by DSC was 45–50 °C. The transition appeared in the region from 45 °C to 50 °C and were attributed to the soft-segment glass-transition temperature (T_g). The T_g value is a measure of relative purity of the soft-segment regions; when there are hard segments dispersed in the soft domains, the T_g is raised.[12] The addition of bifunctional components such as MDI/BD reduces the cross-linking density, but increases the phenyl ring content. In principle, a reduced cross-linking density should decrease the T_g, but an increased aromatic content should have the opposite.[12] The peak in the region from 175 °C to 190 °C was ascribed to the melting point of hard-segment domains, which supports the development of a phase-separated morphology and indicates that the hard-segment content is high enough to achieve phase separation.[12]

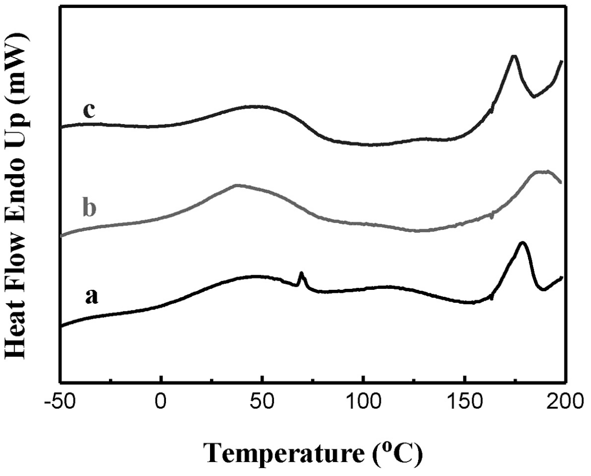

Figure 3: DSC thermograms (10 °C/min) of: a) O-BAT-PU, b) E-BAT-PU, and c) U-BAT-PU

Slika 3: DSC-termogrami (10 °C/min): a) O-BAT-PU, b) E-BAT-PU in c) U-BAT-PU

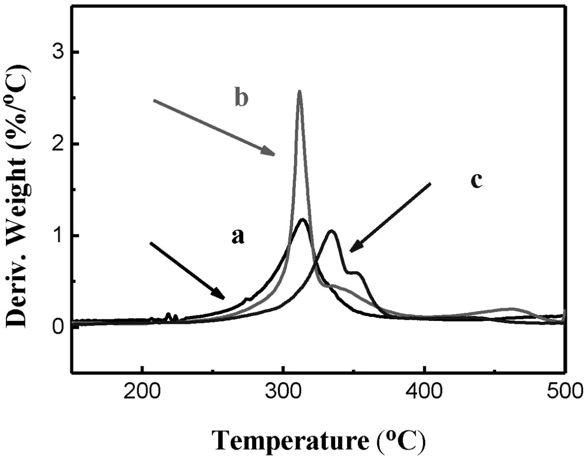

Figure 4: DTG curves of: a) O-BAT-PU, b) E-BAT-PU, and c) U-BAT-PU

Slika 4: DTG-krivulje: a) O-BAT-PU, b) E-BAT-PU in c) U-BAT-PU

TGA is the most favored technique for the evaluation of the thermal stability of polymers. Polyurethanes have a relatively low thermal stability, mainly because the presence of urethane bonds. From the DTG curves it can be seen that in nitrogen only one process occurs during thermal degradation. G. Lligadas et al.[12] observed a similar behavior in the case of vegetable-oil-based polyurethanes. They showed that poly-(oxypropylene)-based polyurethanes degrade in a single step, whereas vegetable-oil-based polyurethane shows one-step decomposition.[4,7,15] **Figure 4** shows the DTG curve and **Figure 5** shows the TGA curves of different polyurethanes, which reveals a degradation stage at temperatures between 300 °C and 400 °C. The results are similar to the three bio-based polyurethanes systems. That can be associated with the decomposition of urethane bonds, which takes place through the dissociation to diisocyanate and alcohol, the formation of primary amines and olefins, or the formation of secondary amines.[16,18]

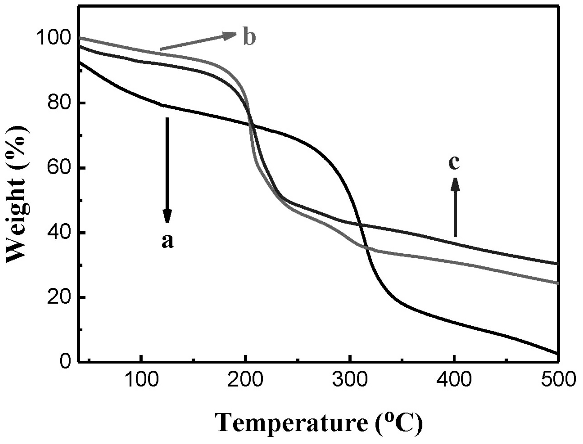

Figure 5: TGA curves of: a) O-BAT-PU, b) E-BAT-PU, and c) U-BAT-PU

Slika 5: TGA-krivulje: a) O-BAT-PU, b) E-BAT-PU in c) U-BAT-PU

4 CONCLUSIONS

Bio-based aromatic triols, O-BAT, E-BAT and U-BAT have been synthesized using two different methods. It is demonstrated that alkyne alcohol derivatives can be obtained in the moderate yields from the corresponding fatty acids by bromation, dehydrobromination, and reduction of carboxylic acid, and alkyne fatty derivatives can also be obtained in moderate yields from the corresponding fatty acids by bromation, dehydrobromination, and esterification. Such a synthesis methodology has indicated a practical feasibility of utilizing the new bio-based aromatic triols for the production of bio-based polyurethanes. The crystalline structure and thermal stability of these polyurethanes have been compared to their counterparts made from a similar O-BAT, E-BAT, and U-BAT, respectively. The corresponding polyurethane networks with hard-segment have been further prepared by the reaction of the polyol, BD, and MDI. The synthesized materials have been characterized using the spectroscopic techniques, WAXD, DSC and TG-DTA. The results have showed that it is possible to exploit renewable resources to achieve environment-friendly green materials.

5 REFERENCES

[1] L. Hu, A. Zhang, Y. Yu, Z. Zheng, S. Du, X. Cheng, Synthesis of hybrid crosslinked polyphosphazenes and investigation of their properties, Iran. Polym. J., 23 (**2014**), 689–698

[2] A. S. Singha, H. Kapoor, Effects of plasticizer/cross-linker on the mechanical and thermal properties of starch/PVA blends, Iran. Polym. J., 23 (**2014**), 655–662

[3] S. J. Li, L. Bouzidi, S. S. Narine, Synthesis and physical properties of triacylglycerol oligomers: examining the physical functionality potential of self-metathesized highly unsaturated vegetable oils, Ind. Eng. Chem. Res., 52(**2013**), 2209–2219

[4] L. Raghunanan, S. S. Narine, Influence of structure on chemical and thermal stability of aliphatic diesters, J. Phys. Chem. B 117(**2013**), 14754–14762, doi:10.1021/jp409062k

[5] L. Raghunanan, J. Yue, S. S. Narine, Synthesis and characterization of novel diol, diacid and di-isocyanate from oleic acid, J. Am. Oil Chem. Soc. 91(**2014**), 349–356, doi:10.1007/s11746-013-2376-z

[6] M. Desroches, M. Escouvois, R. Auvergne, S. Caillol, B. Boutevin, From vegetable oils to polyurethanes: synthetic routes to polyols and main industrial products. Polym Rev 52 (**2012**): 38–79, doi:10.1080/15583724.2011.640443

[7] P. C. Blasco, J. M. M. Martinez, I. V. Antoniac, Synthesis and characterization of polyurethane sealants containing rosin intended for sealing defect in annulus for disc regeneration, Int. J. Adhes. 42 (**2013**), 11–20, doi:10.1016/j.ijadhadh.2012.11.011

[8] D.V. Palaskar, A. Boyer, E. Cloutet, J. F. L. Meins, B. Gadenne, C. Alfos, C. Farcet, H. Cramail, Original diols from sunflower and ricin oils: synthesis, characterization, and use as polyurethane building blocks, J. Polym. Sci. Pol. Chem., 50 (**2012**) 1766–1782, doi:10.1002/pola.25944

[9] G. Lligadas, J. C. Ronda, M. Galia, V. Cadiz, Plant oils as platform chemicals for polyurethane synthesis: current state-of-the-art, Biomacromolecules, 11 (**2008**) 2825–2835

[10] H. Baumann, M. Bühler, H. Fochem, Natural Fats and Oils – Renewable Raw Materials for the Chemical Industry, Angewandte Chemie International Edition in English, 27 (**1988**), 41–62

[11] J. Yue, S.S. Narine, Synthesis of aromatic triols and triacids from oleic and erucic acid: separation and characterization of the asymmetric and symmetric isomers, Chem. Phys. Lipids, 152 (**2008**), 1–8, doi:10.1016/j.chemphyslip.2007.11.002

[12] G,. Lligadas, J. C. Ronda, M. Galia, V. Cadiz, Polyurethane networks from fatty-acid-based aromatic triols: synthesis and characterization. Biomacromolecules , 8 (**2007**), 1858–1864, doi:10.1021/bm070157k

[13] M. J. Dumont, S. S. Narine, Physical properties of new polyurethanes foams from benzene polyols synthesized from erucic acid, J. Appl. Polym. Sci., 118 (**2010**), 3211–3217, doi:10.1002/app.32542

[14] G,. Ligadas, J. C. Ronda, M. Galia, V. Cadiz, Oleic and undecylenic acids as renewable feedstocks in the synthesis of polyols and polyurethanes, Polymers 2 (**2010**), 440–453, doi:10.3390/polym2040440

[15] L. Hojabri, X. H. Kong, S. S. Narine, Fatty acid-derived diisocyanate and biobased polyurethane produced from vegetable oil: synthesis, polymerization, and characterization, Biomacromolecules, 10 (**2009**), 884–891, doi:10.3390/polym2040440

[16] M. J. Dumont, X. Kong, S. S. Narine, Polyurethanes from benzene polyols synthesized from vegetable oils: dependence of physical properties on structure, J. Appl. Polym. Sci., 117 (**2010**), 3196–3203

[17] L. Hojabri, X. H. Kong, S. S. Narine, Novel long chain unsaturated diisocyanate from fatty acid: synthesis, characterization, and application in bio-based polyurethane, J. Polym. Sci. Pol. Chem., 48 (**2010**), 3302–3310, doi:10.1002/pola.24114

[18] S. Oprea, Synthesis and properties of polyurethane elastomers with castor oil as crosslinker, J. Am. Oil Chem. Soc., 87 (**2010**), 313–320, doi:10.1007/s11746-009-1501-5

[19] J. H. Li, Y. Liang, Y. X. Xie, Mild and selective palladium-catalyzed dimerization of terminal alkynes to form symmetrical (Z,Z)-1,4-dihalo-1,3-dienes, J. Org. Chem., 69 (**2004**), 8125–8127, doi:10.1021/jo0486645

[20] J. H. Li, S. Tang, Y. X. Xie, General and selective synthesis of (Z)-3-haloacrylates via palladium-catalyzed carbonylation of terminal alkynes, J. Org. Chem., 70 (**2005**), 477–479, doi:10.1021/jo048358r

[21] J. H. Li, H. F. Jiang, M. C. Chen, $CuCl_2$-Induced regiospecifical synthesis of bezene derivatives in the palladium-catalyzed cyclotrimerization of alkynes, J. Org. Chem., 66 (**2001**), 3627–3629, doi:10.1021/jo0017382

[22] H. Dietl, H. Reinheimer, J. Moffat, P. M. Maitlis, Reactions of acetylenes with noble-metal halides, VIII, The palladium chloride catalyzed trimerization of 2-butyne and 1-phenyl-1-propyne, J. Am. Chem. Soc., 92 (**1970**), 2276–2285, doi:10.1021/ja00711a013

[23] J. S. Cheng, H. F. Jiang, Palladium-catalyzed regioselective cyclotrimerization of acetylenes in supercritical carbon dioxide, Eur. J. Org. Chem., 3 (**2004**), 643–646, doi:10.1002/ejoc.200300299

[24] M. A. R. Meier, J. O. Metzger, U. S. Schubert, Plant oil renewable resources as green alternatives in polymer science, Chem. Soc. Rev., 36(**2007**), 1788–1802, doi:10.1039/b703294c

[25] L. M. D. Espinosa, M. A. R. Meier, Plant oils: the perfect renewable resource for polymer science?!, Eur. Polym. J., 47 (**2011**), 837–852, doi:10.1016/j.eurpolymj.2010.11.020

[26] A. Gandini, The irruption of polymers from renewable resources on the scene of macromolecular science and technology, Green Chem., 13 (**2011**), 1061–108, doi:10.1039/c0gc00789g

[27] Y. Xia, R. C. Larock, Vegetable oil-based polymeric materials: synthesis, properties, and applications, Green Chem., 12 (**2010**), 1893–1909, doi:10.1039/c0gc00264j

[28] A. K. Jhingan, W. F. Maier, Homogeneous catalysis with a heterogeneous Pd catalyst, An effective method for the cyclotrimerization of alkynes, J. Org. Chem., 52 (**1987**), 1161–1165, doi:10.1021/jo00382a039

MATERIALI IN TEHNOLOGIJE/MATERIALS AND TECHNOLOGY (1967–2017) – 50 LET/50 YEARS

UDK 67.017:620.191.3:621.74.047
Original scientific article/Izvirni znanstveni članek

ISSN 1580-2949
MTAEC9, 51(2)237(2017)

STUDY OF MACRO-SEGREGATIONS IN A CONTINUOUSLY CAST BILLET

ŠTUDIJ MAKROIZCEJ V KONTINUIRNO ULITI GREDICI

Ladislav Socha[1], Vlastimil Vodárek[2], Karel Michalek[1], Hana Francová[3], Karel Gryc[1], Markéta Tkadlečková[1], Ladislav Válek[4]

[1]VŠB – Technical University of Ostrava, FMME, Department of Metallurgy and Foundry, 17. listopadu 15/2172, 708 33 Ostrava – Poruba, Czech Republic
[2]VŠB – Technical University of Ostrava, FMME, Department of Material Engineering, 17. listopadu 15/2172, 708 33 Ostrava – Poruba, Czech Republic
[3]VŠB – Technical University of Ostrava, FMME, Department of Physical Chemistry and Theory of Technological Processes, 17. listopadu 15/2172, 708 33 Ostrava – Poruba, Czech Republic
[4]ArcelorMittal Ostrava a.s., Research, Vratimovská 689, 707 02 Ostrava-Kunčice, Czech Republic
ladislav.socha@vsb.cz

Prejem rokopisa – received: 2015-07-13; sprejem za objavo – accepted for publication: 2016-02-09

doi:10.17222/mit.2015.220

This paper is devoted to the study of macro-segregations on the longitudinal section of a continuously cast billet Ø 160 mm destined for the production of seamless pipes. Its evaluation comprised a visual inspection of macro-etching, microstructure characterisation and a quantitative X-ray microanalysis by means of an energy-dispersive X-ray microanalysis (EDX) in the selected areas. Furthermore, segregation parameters were calculated using combustion-analysis data. The results given in this paper present the basic information about the interior structure of a continuously cast billet. The results will be used, beside other things, for the verification of the results of the numerical modelling of continuously cast billets.

Keywords: steel, macro-segregation, continuous casting, round billet

Ta članek obravnava študij makro-izcej na vzdolžnem prerezu kontinuirno ulite gredice Ø 160 mm namenjene za proizvodnjo brezšivnih cevi. Ocena je sestavljena iz vizuelnega pregleda po makrojedkanju, iz ocene in kvantitativne rentgenske mikroanalize s pomočjo energijsko disperzijske rentgenske analize (EDX) izbranih področij. Izračunani so bili tudi parametri izcejanja s pomočjo podatkov zgorevne analize. Rezultati, prikazani v tem članku, predstavljajo osnovno informacijo o notranji strukturi v kontinuirno uliti gredici. Rezultati bodo uporabljeni, poleg drugega, tudi za preverjanje rezultatov numeričnega modeliranja kontinuirno ulitih gredic.

Ključne besede: jeklo, makro-izceja, kontinuirno ulivanje, okrogla gredica

1 INTRODUCTION

Steel crystallization occurs during the casting and subsequent solidification of continuously cast billets. Material solidification, the grain size, chemical heterogeneity and the existence of incompactness can have negative influences on the properties of the final material.[1] A relatively big homogeneity of the distribution of sulphur and other elements and also the absence of thick segregate areas in the whole cross-section are due to the fast solidification of the billet. The range and removal of impurities are mainly connected with the contents of phosphorus and sulphur in the steel, the steel temperature and also the intensity of the billet cooling.[2] The local chemical heterogeneity appears in the billet axis, especially for the steels with higher contents of carbon where the possibility of internal-hollow creation is higher.[3,4]

The paper presents the results of the study of macro-segregation on the longitudinal section of a continuously cast billet Ø 160 mm. Samples were taken during the casting of a high-quality billet destined for the production of seamless pipes without the usage of the MEMS technology. First, a visual inspection of the longitudinal section of the billet was made for the study of macro-segregation in a continuously cast billet. Then a micro-structural analysis using a quantitative X-ray microanalysis with the help of EDX in SEM (Quanta 450 FEG) was carried out. The results of the microstructural analysis were subsequently supplemented with an analysis of the contents of carbon and sulphur with the aim to evaluate the chosen segregation parameters for the micro-samples taken from particular areas of macro-etching. The obtained original results will be, beside other things, used for verifying the results of numerical modelling of casting continuously cast billets.

2 MACRO-STRUCTURAL ANALYSIS OF THE BILLET

First, a visual inspection of the longitudinal section of the billet was made for the study of macro-segregation in the continuously cast billet, which is given in **Figure 1a**.

It is evident in **Figure 1a** that the surface area of equiaxed crystals (the chill zone) penetrates into a depth

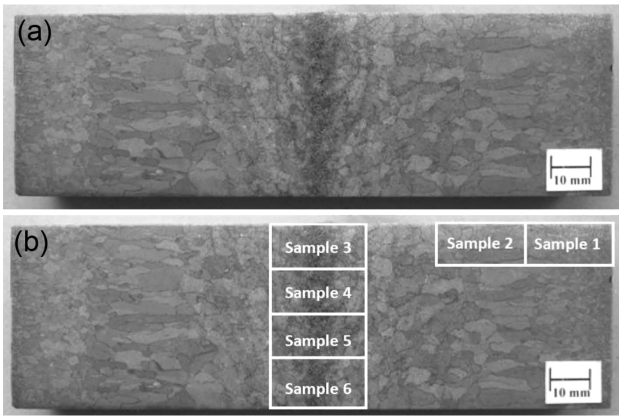

Figure 1: Longitudinal section through Ø 160 mm billet: a) macro-etching of the studied billet, b) positions of the samples taken for a microstructure characterisation

Slika 1: Vzdolžni prerez skozi gredico Ø 160 mm: a) makrojedkana gredica, b) položaj vzorcev, vzetih za karakterizacijo mikrostrukture

of approx. 18 mm. This is followed by an area of columnar crystals with a thickness of approx. 35 mm and, in the middle of the longitudinal section, there is an area of equiaxed grains.

In the axial area of the billet, there is shrinkage porosity that is a consequence of the casting conditions during the final period of the billet solidification. The darker contrast in the area of shrinkage porosity is related to the processes of chemical segregation during the solidification.

3 MICROSTRUCTURAL ANALYSIS OF THE BILLET

After the visual inspection of macro-etching, the sample was cut into smaller parts, evident in **Figure 1b**. The samples were prepared for a microstructural analysis aimed at evaluating the characterisation of the microstructure and chemical heterogeneity using the EDX technique. A few samples – sample 2, sample 4 and sample 5 – were chosen for the analysis. The following elements were chosen for the X-ray microanalysis (EDX): silicon, phosphorus, chromium, manganese, iron and molybdenum. The results of a semi-quantitative X-ray microanalysis were normalized to 100 %.

The microstructure of sample 2 presenting areas of columnar crystals is given in **Figure 2**. Previous austenite grain boundaries are decorated with fine grains of allotriomorphic ferrite. Nodules of the pearlite component usually grow up along the networks of allotriomorphic ferrite. The microstructure inside the austenitic grains consists of a mixture of acicular ferrite and a small fraction of pearlite, as it is evident in **Figure 3**.

Subsequently, a quantitative X-ray microanalysis (EDX) was made. A spectral RTG microanalysis of the matrix was made in the randomly chosen areas of sample 2 and the results are given in **Table 1**.

Table 1: Results of the EDX microanalysis – sample 2

Tabela 1: Rezultati EDX mikroanalize – vzorec 2

Analysis	Analysed elements (*w*/%)				
	Si	Cr	Mn	Fe	Mo
1	0.30	0.72	1.01	97.47	0.50
2	0.40	0.75	1.21	97.24	0.40
3	0.36	0.78	0.90	97.66	0.30
AVE	**0.35**	**0.75**	**1.04**	**97.46**	**0.40**
STD	0.05	0.03	0.16	0.21	0.10

Note: AVE – arithmetic mean, STD – standard deviation

The microstructure of sample 4 in the axial area of the billet, which shows an increased fraction of the pearlite component in the surroundings of the shrinkage porosity, is shown in **Figure 4**. Networks of allotriomorphic ferrite decorate the prior austenite grain boundaries. Austenite decomposed into a mixture of acicular ferrite and pearlite inside the original austenitic grains.

Fine shrinkage porosity, surrounded by narrow bands exhibiting a limited etching response, is evident in **Figure 5**. Further, an increased amount of non-metallic inclusions (manganese sulphide) and the bainite observed in these areas proves that these are the last solidified areas of enriched melt where the largest segregation can be expected.

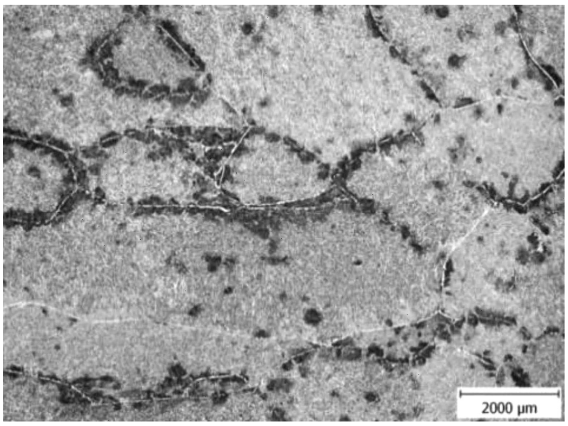

Figure 2: Microstructure in the area of columnar crystals

Slika 2: Mikrostruktura področja s stebrastimi kristalnimi zrni

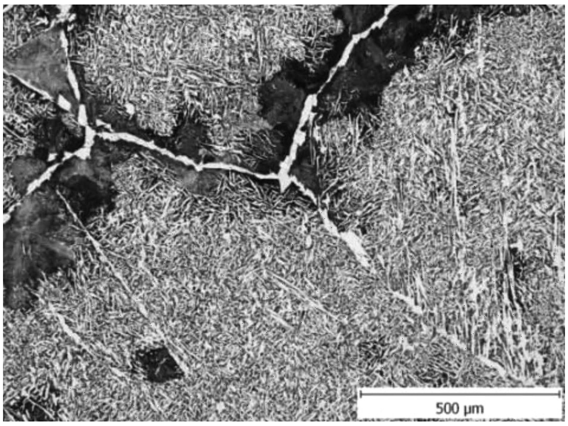

Figure 3: Detail of the microstructure in the area of columnar crystals

Slika 3: Detajl mikrostrukture v področju stebrastih kristalnih zrn

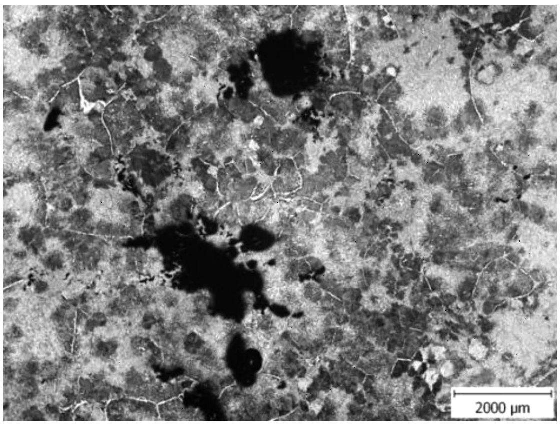

Figure 4: Microstructure in the axial area of the billet
Slika 4: Mikrostruktura na sredini gredice

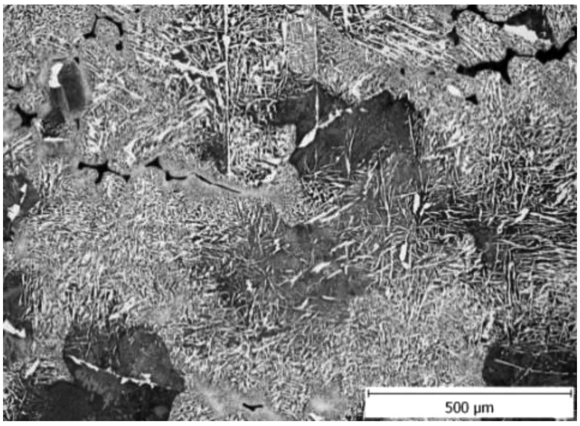

Figure 5: Detail of the microstructure in the axial area of the billet
Slika 5: Detajl mikrostrukture na sredini gredice

Results of a semi-quantitative X-ray microanalysis of *sample 4* are given in **Table 2**. When comparing them with the results given in **Table 1**, it is evident that the metal matrix in the studied area with a different etching response was enriched by all the evaluated substitution solutes and, in addition, a significant concentration of phosphorus was found here.

Table 2: Results of the EDX microanalysis – sample 4
Tabela 2: Rezultati EDX-mikroanalize – vzorec 4

Analysis	Analysed elements (wt. %)					
	Si	*P*	Cr	Mn	Fe	Mo
1	0.40	*0.33*	1.22	1.46	95.84	0.75
2	0.35	*0.19*	1.30	1.33	95.96	0.87
3	0.42	*0.21*	1.26	1.42	95.98	0.71
AVE	**0.39**	***0.24***	**1.26**	**1.40**	**95.93**	**0.78**
STD	0.08	*0.08*	0.07	0.08	0.08	0.08

Note: AVE – arithmetic mean, STD – standard deviation

The microstructure of sample 5 (the axial part of the billet) with an increased fraction of pearlite adjacent to the shrinkage porosity is shown in **Figure 6**.

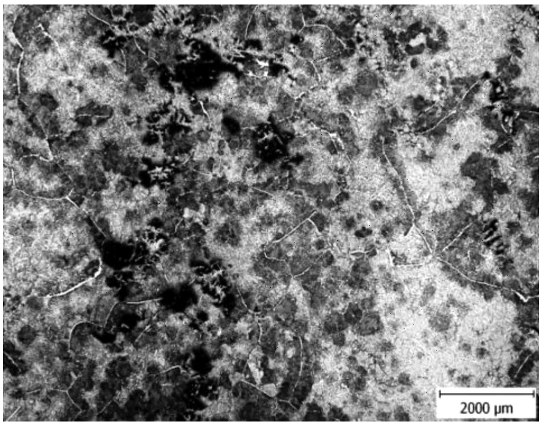

Figure 6: Microstructure in the axial area of the billet
Slika 6: Mikrostruktura na sredini gredice

Similar to sample 4, bands with a different etching response were found in the surroundings of the shrinkage porosity where the microstructure was made of bainite, and a large amount of sulphide inclusions was observed, as seen in **Figure 7**.

In the case of sample 5, a semi-quantitative X-ray microanalysis was also made and its results are given in **Table 3**.

Table 3: Results of the EDX microanalysis – sample 5
Tabela 3: Rezultati EDX-mikroanalize – vzorec 5

Analysis	Analysed elements (*w*/%)					
	Si	*P*	Cr	Mn	Fe	Mo
1	0.49	*0.34*	1.53	1.35	95.21	1.08
2	0.55	*0.22*	1.27	1.49	95.75	0.72
3	0.54	*0.00*	1.46	1.31	95.77	0.92
AVE	**0.53**	***0.19***	**1.42**	**1.38**	**95.58**	**0.91**
STD	0.03	*0.17*	0.13	0.09	0.32	0.18

Note: AVE – arithmetic mean, STD – standard deviation

4 SEGREGATION PARAMETERS

On the basis of the X-ray microanalysis results, it was decided to carry out also a carbon and sulphur analysis of the micro-samples taken from individual

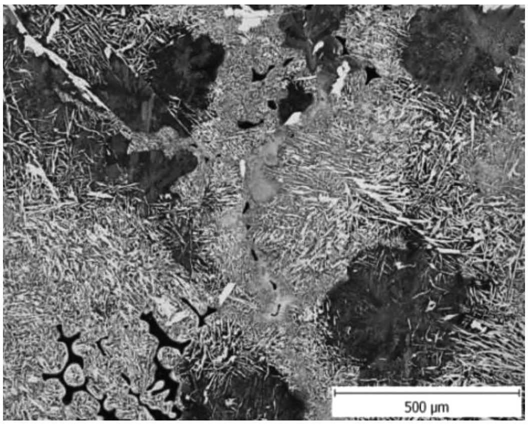

Figure 7: Detail of the microstructure in the axial area of the billet
Slika 7: Detajl mikrostrukture na sredini gredice

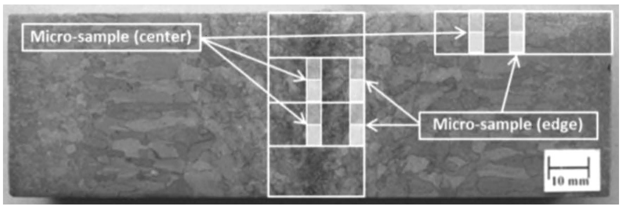

Figure 8: Positions of micro-samples taken for the combustion analysis
Slika 8: Položaji mikrovzorcev za analizo z zgorevanjem

areas of the macro-etching. Sample 2, sample 4 and sample 5 were chosen for a proper analysis. The samples were cut into the micro-samples for an evaluation of individual areas, as seen in **Figure 8**.

The analysis was carried out in an ELTRA CS 2000 combustion analyser and the results obtained for individual micro-samples are given in **Table 4**.

Table 4: Results of the combustion analysis of micro-samples
Tabela 4: Rezultati analize z zgorevanjem mikro vzorcev

Sample	Place of sampling	Elements (*w*/%)		Average values (*w*/%)	
		C	S	Ø carbon	Ø sulphur
2	Edge	0.304	0.0083	0.301	0.0081
		0.297	0.0078		
	Centre	0.300	0.0087	0.302	0.0087
		0.304	0.0086		
4	Edge	0.269	0.0071	0.278	0.0074
		0.287	0.0077		
	Centre	0.328	0.0101	0.347	0.0098
		0.365	0.0095		
5	Edge	0.287	0.0089	0.285	0.0090
		0.283	0.0090		
	Centre	0.318	0.0090	0.321	0.0098
		0.325	0.0105		

It is evident from **Table 4** that the micro-samples taken from the centre show higher contents of carbon, by 0.045 % of mass fractions (sample 4) and by 0.021 % of mass fractions (sample 5), than in the area of columnar crystals (sample 2). It can be stated, in the case of sulphur, that its contents are in the range from 0,0074 % to 0,0098 % of mass fractions for all the micro-samples. On the basis of the obtained results, the micro-samples from the central area were evaluated by means of the chosen segregation parameters[5] and their relations are given in Equations (1), (2) and (3).

$$Ih = \frac{SX}{XS} \tag{1}$$

where *Ih* – is heterogeneity index, (-), *SX* – standard deviation, (-), *XS* – mean value, (-).

$$Is = \frac{MAX}{XS} \tag{2}$$

where *Is* – is segregation index, (-), *MAX* – maximum value, (-), *XS* – mean value, (-).

$$k_{ef} = \frac{1}{Is} \tag{3}$$

where k_{ef} – is efficient partition coefficient, (-), *Is* – segregation index. (-).

Chemical compositions of the analysed micro-samples were used for determining the segregation parameters, which were completed by the basic statistical parameters, and the results for carbon are given in **Table 5,** while the results for sulphur are in **Table 6**.

Table 5: Results of segregation parameters for carbon
Tabela 5: Rezultati parametrov izcejanja pri ogljiku

Sample	Place of sampling	Segregation parameters		
		Ih	*Is*	k_{ef}
2	Edge	0.019	1.024	0.977
	Centre	0.020	1.020	0.980
4	Edge	0.034	1.029	0.972
	Centre	0.094	1.115	0.897
5	Edge	0.010	1.012	0.988
	Centre	0.048	1.044	0.958

Table 6: Results of segregation parameters for sulphur
Tabela 6: Rezultati parametrov izcejanja pri žveplu

Sample	Place of sampling	Segregation parameters		
		Ih	*Is*	k_{ef}
2	Edge	0.0695	1.0779	0.9277
	Centre	0.0962	1.0741	0.9310
4	Edge	0.0422	1.0590	0.9443
	Centre	0.1519	1.1374	0.8792
5	Edge	0.1108	1.0832	0.9232
	Centre	0.1639	1.1895	0.8407

On the basis of the calculated segregation parameters from **Tables 5** and **6**, the following rows were determined. Individual substitutional solutes segregate in conformity with the decreasing value in the efficient partition coefficient (k_{ef}):

- sample 2: Mo-Si-Mn-Cr
- sample 4: P-Mo-Cr-Si-Mn
- sample 5: P-Mo-Cr-Si-Mn

Considering the values of the efficient partition coefficient (k_{ef}), the phosphorus in sample 5 segregates extremely significantly, the phosphorus of sample 4 segregates significantly, while carbon, sulphur, silicon, chromium, molybdenum and manganese segregate into an interdendritic melt. Molybdenum segregates with the highest intensity ($k_{ef.}$ = 0.685) in sample 2, phosphorus segregates with the highest intensity ($k_{ef.}$ = 0.365) in sample 4, phosphorus segregates with the highest intensity (k_{ef} = 0.169) in sample 5, carbon segregates with the lowest intensity (k_{ef} = 0.979) in sample 2, carbon segregates with the lowest intensity (k_{ef} = 0.935) in sample 4 and carbon segregates with the lowest intensity (k_{ef} = 0.973) in sample 5.

An identical order of segregation follows from the obtained values of the efficient partition coefficients (k_{ef})

and from the data index of element segregation (*Is*) when, in both cases, the process is finished by carbon.

5 CONCLUSIONS

A study of macro-segregations on the longitudinal sections of continuously cast billets Ø 160 mm was made without the usage of the MEMS technology. The evaluation was aimed not only at a macro-structural analysis of the longitudinal section of a billet but also at an evaluation of the microstructure, a quantitative X-ray microanalysis (EDX) and an evaluation of the segregation parameters on the chosen samples. Based on the results of the structure characterisation, the following conclusions can be stated:

- macro-etching revealed three typical areas (the chill zone, columnar crystals and the central area of equiaxed crystals) of the structure of a cast billet. In the axial area, there was shrinkage porosity with a diameter of approx. 2 mm. Local changes in the etching response in that area were explained as the consequence of the effect of the chemical segregation during the billet solidification.
- the microstructure of the whole section of the billet consisted of networks of allotriomorphic ferrite grains along the previous austenite-grain boundaries, needles of acicular ferrite and nodules of the pearlite component. Immediately under the billet surface and in the centre of the longitudinal section of the billet, higher fractions of pearlite were observed. This proved that carbonization occurred in these areas. In the under-the-surface areas, it was probably due to the reaction of steel with the cast powder. In the centre of the longitudinal section of the billet, the microstructural changes are connected with the effects of the chemical segregation during solidification.
- during the microstructural analysis of the axial area of the billet, bands with different etching responses, together with sulphide inclusions, were found in the surroundings of the shrinkage porosity. The last portions of the segregated melt were solidified in these areas. As a result of the chemical segregation, austenite decomposed into bainite in these areas.
- in the areas with a modified etching response, an enrichment due to all the substitutional solutes, including a significant increase in the phosphorus concentration, was proved with an X-ray microanalysis. Apart from phosphorus, a high degree of segregation was proved in the cases of molybdenum, chromium and manganese.
- on the basis of a metallographic and micro-analytic evaluation, a carbon analysis of the micro-samples taken from individual bands of the macro-etching was carried out by means of a combustion analyser to perform a complex evaluation.
- it is evident from the distribution of the maximum and minimum values of the segregation indexes (Is) of individual elements that the highest values were determined (for most of the analysed elements) in the centre of the longitudinal section of the billet. On the contrary, the lowest values of the segregation indexes (Is) of individual elements were found (for most of the analysed samples) in the area of columnar crystals. This confirmed the precondition that the highest tendency to segregation can be expected along the billet axis, while the lowest tendency to segregation can be expected in the area of columnar crystals and in the chill zone.
- it is obvious that phosphorus is the most segregating element because its value of the efficient partition coefficient (k_{ef}) is lower than for the other analysed elements. It was proved that the segregation index for phosphorus (Is) reached the highest values.
- the obtained results made it possible to describe and evaluate the material properties of the continuously cast billet Ø 160 mm, which can be used for a result verification and solidification-model development by means of numerical modelling.

Acknowledgements

This paper was carried out with the support of the project of Student Grant Competition, numbers SP2015/78 and SP2015/70.

This work was created at the Faculty of Metallurgy and Materials Engineering within Project No. LO1203 Regional Materials Science and Technology Centre – Feasibility Program funded by the Ministry of Education, Youth and Sports of the Czech Republic.

6 REFERENCES

[1] M. Žaludová, B. Smetana, S. Zlá, J. Dobrovská, A. Watson, J. Vontorová, S. Rosypalová, J. Kukutschova, M. Cagala, Experiment study of Fe_C-O based system above 1.000 A degrees C, Journal of Thermal Analysis and Calorimetry, 112 (**2013**) 1, 465–471, doi:10.1007/s10973-012-2847-8

[2] M. C. Flemings, Solidification Processing, 1st ed., McGraw -Hill College, New York, 1974, 364

[3] W. R. Irving, Continuous Casting of Steel, Cambridge University Press, (**1993**), 207

[4] K. Schwerdtfeger, Metalurgie des Stranggießens, Verlag Stahl und Eisen GmbH, Düseldorf, **1992**, 640

[5] M. N. Gungor, A statistically significant experimental technique for investigating microsegregation in cast alloys, Metallurgical Transactions A: Physical Metallurgy and Materials Science, 20 (**1989**) 11, 2529–2533, doi:10.1007/ BF02666687

UDK 67.017:621.742.48:62-97-022.171
Original scientific article/Izvirni znanstveni članek

ISSN 1580-2949
MTAEC9, 51(2)243(2017)

CHANGES IN THE COMPOSITE STRUCTURE AND PARAMETERS AFTER AN EXPOSURE TO A SYNERGIC ACTION OF VARIOUS EXTREME CONDITIONS

SPREMINJANJE STRUKTURE IN PARAMETROV KOMPOZITOV IZPOSTAVLJENIH SINERGISTIČNI AKTIVNOSTI RAZLIČNIH EKSTREMNIH POGOJEV

Tomáš Melichar, Ámos Dufka, Jiří Bydžovský

Brno University of Technology, Faculty of Civil Engineering, Institute of Technology of Building Materials and Components,
Veveří 331/95, 602 00 Brno, Czech Republic
melichar.t@fce.vutbr.cz

Prejem rokopisa – received: 2015-08-14; sprejem za objavo – accepted for publication: 2016-03-01

doi:10.17222/mit.2015.256

The research presented in this paper is aimed at studying the properties of composites designed for a redevelopment of reinforced concrete structures where it is possible to expect an increased risk of fire, i.e., shock actions of extreme temperatures. Such conditions may occur, for example, in transport constructions, particularly in tunnels. We have developed two recipes (formulas) for materials based on a polymer-cement matrix and a porous filler. These materials were subjected to cyclic freezing and de-freezing in combination with a water action. In terms of a long-term durability, we monitored the characteristics after 50 and 100 cycles. The impact of an increased humidity was not considered in this phase of the research. After testing the frost resistance, the bodies were dried up. Then, temperature shocks of (400, 600 and 1000) °C followed. The bodies were cooled down under control, with gradual temperature decreases. The reason for assessing the impact of these two exposure conditions on the properties of designed materials was mainly the use of the porous filler. This filler has a favourable effect on the temperature resistance. On the other hand, however, the frost resistance can be negatively affected in combination with water. Studying the influence of the above two exposures was carried out using the basic physico-mechanical and also physico-chemical methods. We also utilized analytical methods for assessing the microstructure. The structure was also examined using an innovative imaging technique allowing a three-dimensional visual assessment, which was primarily aimed at identifying faults of the structure.

Keywords: composite, polymer-cement matrix, cementitious supplementary material, high temperature, frost resistance, synergic, microstructure

Namen predstavljene raziskave je študij lastnosti kompozitov namenjenih obnovi betonskih zgradb, kjer je možno pričakovati povečano nevarnost požara in delovanje ekstremnih temperatur. Taki pogoji se lahko pojavijo, na primer, v prometnih konstrukcijah, posebno v tunelih. Razvili smo dva recepta (formuli) materialov, ki temeljijo na mešanici polimer-cement in poroznega polnila. Ti materiali so bili izpostavljeni cikličnemu zamrzovanju in odtajanju, v kombinaciji z delovanjem vode. V smislu dolge zdržljivosti, smo pregledali značilnosti po 50 in 100 ciklih. Vpliv povečanja vlažnosti v tem delu raziskav ni bil obravnavan. Po preizkušanju odpornosti na mraz, so bila telesa osušena. Sledili so temperaturni šoki na (400, 600 in 1000) °C. Telesa so bila kontrolirano ohlajena, s postopnim zmanjšanjem temperature. Razlog za ocenjevanje učinka teh dveh pogojev izpostavitve na lastnosti materiala, je bila predvsem uporaba poroznega polnila. To polnilo ima ugoden vpliv na temperaturno obstojnost. Po drugi strani pa je lahko odpornost na zmrzal manjša v kombinaciji z vodo. Študij vpliva obeh načinov izpostavitve je bil izveden z uporabo osnovnih fizikalno-mehanskih in tudi fizikalno-kemijskih metod. Za ocenjevanje mikrostrukture smo uporabili tudi analitične metode. Struktura je bila preiskana z uporabo inovativne slikovne tehnike, ki omogoča tridimenzionalno vidno oceno, katere prvotni namen je bil identifikacija napak v strukturi.

Ključne besede: kompozit, mešanica polimer-cement, cementni nadomestni material, visoka temperatura, odpornost na zmrzal, sinergija, mikrostruktura

1 INTRODUCTION

Durability of building materials is one of the key aspects of their smooth function in a given structure. There are many factors that could realistically affect engineering constructions. These may include exterior climatic conditions, the presence of aggressive media as well as accidental exposure to high temperatures. In practice, consequently, we can even come across situations where the structure is loaded with cyclic exposures to water and frost followed by fire. When developed, the building materials intended for the environments with the said potential risks of random factors must therefore be verified in laboratories. The primary reason is the use of non-traditional raw materials. With regard to the environmental situation and price, these raw materials often come from alternative resources. Alternative raw materials are more or less characterized by the variability of parameters, including their composition. The choice of suitable compositions of polymer-cement composites destined for demanding exposure conditions is one of the basic prerequisites of their sufficient resistance and the expected building lifetime.

The development of cement composites for unfavourable environments was addressed by more authors, for example in studies.[1–7] Regarding the use of a porous aggregate for cement composites, very interesting and significant findings were published in study.[8] Here, the research focuses on the contact zone (or surface transition zone) of the porous aggregates and the cement matrix. The issue is dealt with in terms of both experimental research and numerical simulation. It is shown that this zone is less porous when using a lightweight aggregate with a smaller thickness than in the case of conventional dense aggregates. Depending on the water-cement ratio and the structure of the aggregate surface layer or aggregate porous system, this matrix/aggregate transition zone is characterized by different parameters. For example, this zone disappears in the case of a very low water-cement ratio and the use of microsilica.

While exploring scientific literature and scientific articles, we did not find any publications that would present a research aimed at the synergistic effects of frost and subsequent high temperatures (simulating fire) on the composites containing a lightweight aggregate. The issue was only addressed separately. Interesting findings of authors dealing with the effects of high temperatures on cement composites are presented, inter alia, in studies.[9–11]

The parameters of a lightweight aggregate produced in self-firing processes from secondary energy products are studied in article.[12]

2 METHODOLOGY OF THE EXPERIMENTAL WORK

The research tested two recipes of repair materials based on a polymer-cement composite matrix. Specific formulations of recipes are given in the following table (**Table 1**).

Table 1: Compositions of tested mixtures
Tabela 1: Sestava preizkušenih mešanic

Component	Unit	Mixture	
		RMS	RMA
Cement	kg m^{-3}	435	435
Blast furnace slag	kg m^{-3}	234	–
Fly ash	kg m^{-3}	–	234
Vinyl acetate copolymer	% (w_{cem})	3	3
Microsillica	% (w_{cem})	5	5
Amphibolite 0-1 mm	kg m^{-3}	837	837
Porous aggregate 1-2 mm	kg m^{-3}	632	632
Polypropylene fibres	kg m^{-3}	1,0	1,0
Water	kg m^{-3}	187*	187*

* The porous aggregate was saturated with water before preparing the mixtures. The aggregate has a water-absorption ability of about 35 %. So, a certain amount of water was leached from the porous aggregate during the mixing.

The polymeric additive based on a copolymer of vinyl acetate and ethylene in an amount of 3 % of the cement weight was used in order to improve the cohesion in the fresh as well as hardened state, and the plasticity of the fresh mixture. The filler was an amphibolite-aggloporite mixture, which is an artificially produced porous sintered aggregate (hereinafter referred to as aggloporite).

Since these materials were fine-grained mortars, the testing was performed on bodies with dimensions of (40 × 40 × 160) mm. The first group of these bodies was exposed to 50 freezing cycles with a subsequent thermal load, followed by a definition of the essential characteristics according to [13–15]. The second group of the bodies was exposed to 100 freezing cycles followed by a thermal load and an assessment of the parameters. The exposure under the conditions of alternating freezing and de-freezing was carried out according to [16]. Cycling was implemented so that the tests of the characteristics were conducted after 70 d or 120 d. In these ages, we also tested reference bodies that had been only exposed to extreme temperatures.

The thermal exposure was carried out in steps of (400, 600 and 1000) °C. The cooling took place gradually in furnaces with a decreasing gradient of about 1 °C min^{-1}. Laboratory-stored bodies were exposed continuously to about 22 °C. In addition to the basic material properties and microstructure, the mortars were also visually assessed.

3 RESULTS

A comparison of the achieved outputs is shown in the graphs below (**Figures 1** to **6**). An emphasis was placed on the assessment of the bulk density (designated as

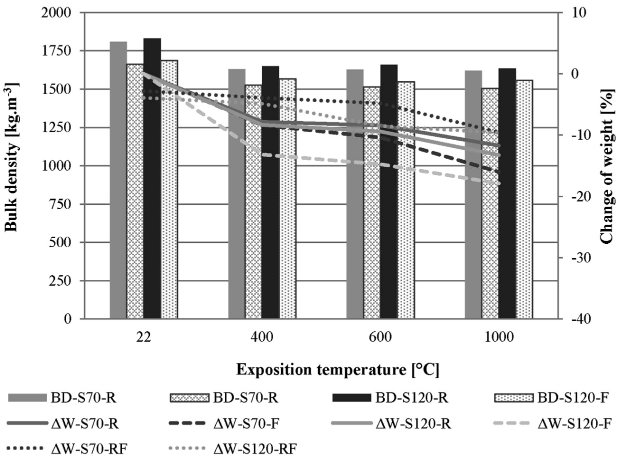

Figure 1: Bulk density and weight change of mixture RMS containing blast furnace slag (BD – bulk density; W – weight; S70(120)-R – reference composite after 70 (120) days and thermal exposure; S70(120)-F – composite after 70 (120) days or 50 (100) frost cycles and thermal exposure; S70(120)-RF – difference between reference and frost-exposed specimens)

Slika 1: Gostota osnove in spreminjanje teže mešanice RMS, ki vsebuje plavžno žlindro (BD – gostota osnove, W – teža; S70(120)-R – referenčni kompozit po 70 (120) dneh toplotne izpostavitve; S70(120)-F – kompozit po 70 (120) dnevih ali 50 (100) ciklih zamrzovanja in toplotne izpostavitve; S70(120)-RF – razlika med referenčnim vzorcem in vzorcem izpostavljenem zamrzovanju)

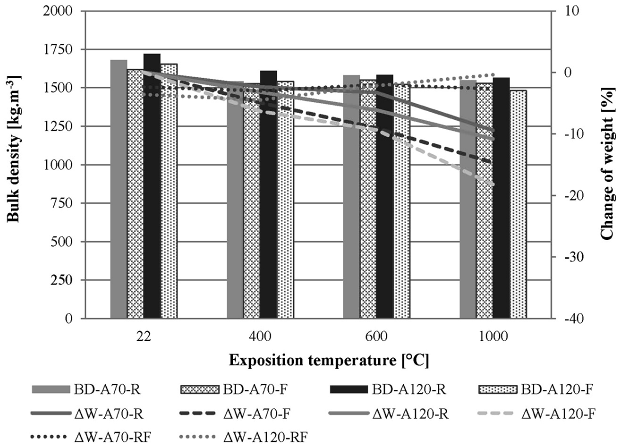

Figure 2: Bulk density and weight change of mixture RMA containing fly ash (BD – bulk density; W – weight; A70(120)-R – reference composite after 70 (120) days and thermal exposure; A70(120)-F – composite after 70 (120) days or 50 (100) frost cycles and thermal exposure; A70(120)-RF – difference between reference and frost-exposed specimens)

Slika 2: Gostota osnove in spreminjanje teže RMA, ki vsebuje leteči pepel (BD – gostota osnove, W – teža; A70(120)-R – referenčni kompozit po 70 (120) dneh toplotne izpostavitve; A70(120)-F – kompozit po 70 (120) dneh ali 50 (100) ciklih zamrzovanja in toplotne izpostavitve; A70(120)-RF – razlika med referenčnim vzorcem in vzorci po toplotni izpostavitvi)

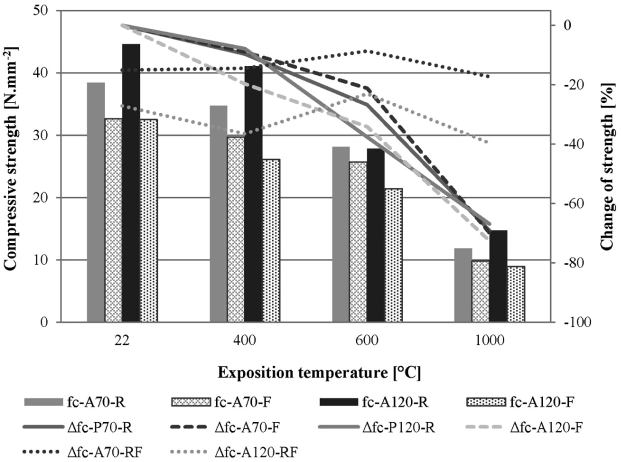

Figure 4: Compressive strength of mixture RMA containing fly ash (A70(120)-R – reference composite after 70 (120) days and thermal exposure; A70(120)-F – composite after 70 (120) days or 50 (100) frost cycles and thermal exposure; A70(120)-RF – difference between reference and frost-exposed specimens)

Slika 4: Tlačna trdnost mešanice RMA, ki vsebuje leteči pepel (A70(120)-R – referenčni kompozit po 70 (120) dneh toplotne izpostavitve; A70(120)-F – komozit po 70 (120) dneh ali 50 (100) ciklih zamrzovanja in toplotne izpostavitve; A70(120)-RF – razlika med referenčnim in zamrzovanju izpostavljenim vzorcem)

BD), weight (designated as W) and strength characteristics (designated as fc – compressive strength and ff – bending tensile strength). The courses of each recipe and parameter are evaluated separately. Each graph always contains a comparison of one recipe and the studied characteristic at the ages of 70 d and 120 d. Courses of percentage changes (parameters designated as Δ) of a given characteristic due to the exposure to the alternating freezing and de-freezing with a subsequent thermal shock are plotted on the secondary axis (solid and dashed curves). Furthermore (shown with a dotted curve), the graphs indicate differences in the reference parameters (designated as R) for the frozen (designated as F) bodies after each temperature exposure (difference – designated as RF).

Fluctuations of negative temperatures in combination with a saturation of the material with water and the

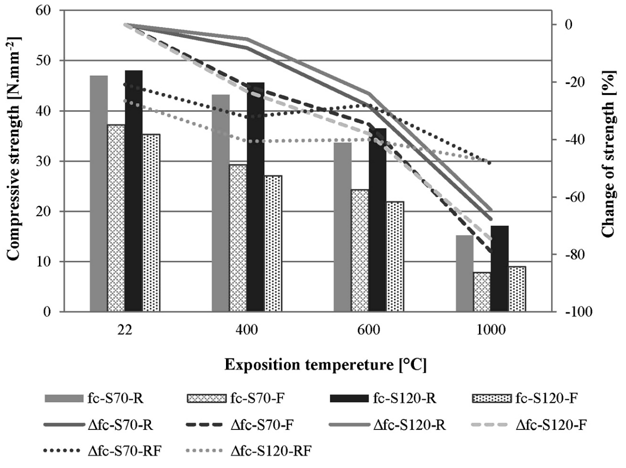

Figure 3: Compressive strength of mixture RMS containing blast furnace slag (S70(120)-R – reference composite after 70 (120) days and thermal exposure; S70(120)-F – composite after 70 (120) days or 50 (100) frost cycles and thermal exposure; S70(120)-RF – difference between reference and frost-exposed specimens)

Slika 3: Tlačna trdnost mešanice RMS, ki vsebuje plavžno žlindro (S70(120)-R – referenčni kompozit po 70 (120) dneh toplotne izpostavitve; S70(120)-F – kompozit po 70 (120) dneh ali 50 (100) ciklih zamrzovanja in toplotni izpostavitvi; S70(120)-RF – razlika med referenčnim in zamrzovanju izpostavljenim vzorcem)

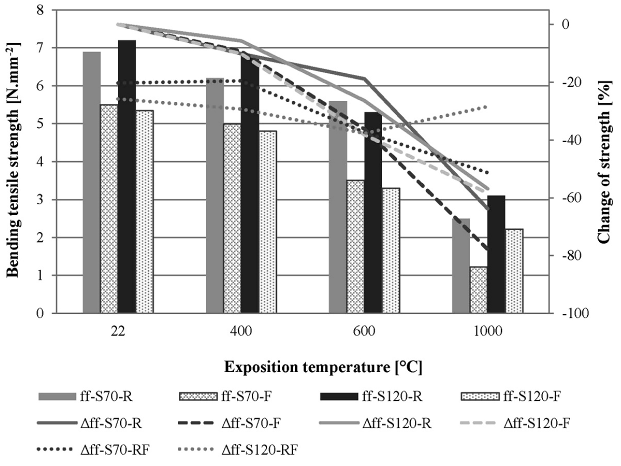

Figure 5: Flexural strength of mixture RMS containing blast furnace slag (S70(120)-R – reference composite after 70 (120) days and thermal exposure; S70(120)-F – composite after 70 (120) days or 50 (100) frost cycles and thermal exposure; S70(120)-RF – difference between reference and frost-exposed specimens)

Slika 5: Upogibna trdnost mešanice RMS, ki vsebuje plavžno žlindro (S70(120)-R – referenčni kompozit po 70 (120) dneh toplotne izpostavitve; S70(120)-F – komozit po 70 (120) dneh ali 50 (100) ciklih zamrzovanja in toplotne izpostavitve; S70(120)-RF – razlika med referenčnim in zamrzovanju izpostavljenim vzorcem)

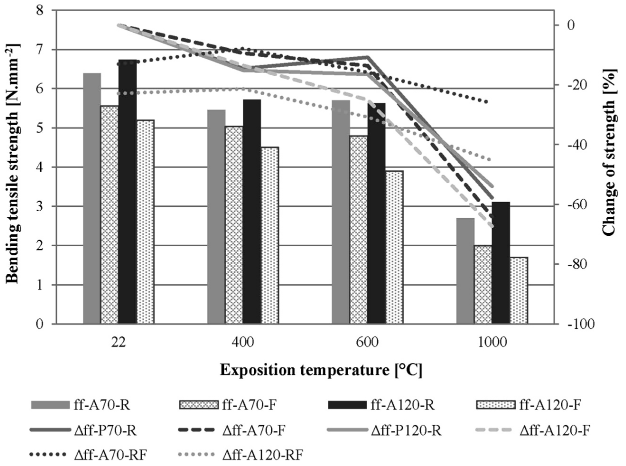

Figure 6: Flexural strength of mixture RMA containing fly ash (A70(120)-R – reference composite after 70 (120) days and thermal exposure; A70(120)-F – composite after 70 (120) days or 50 (100) frost cycles and thermal exposure; A70(120)-RF – difference between reference and frost-exposed specimens)

Slika 6: Upogibna trdnost mešanice RMA, ki vsebuje plavžno žlindro (A70(120) – R – referenčni kompozit po 70 (120) dneh toplotne izpostavitve; A70(120) – F – kompozit po 70 (120) dneh ali 50 (100) ciklih zamrzovanja in toplotne izpostavitve; A70(120) – RF – razlika med referenčnim in zamrzovanju izpostavljenim vzorcem)

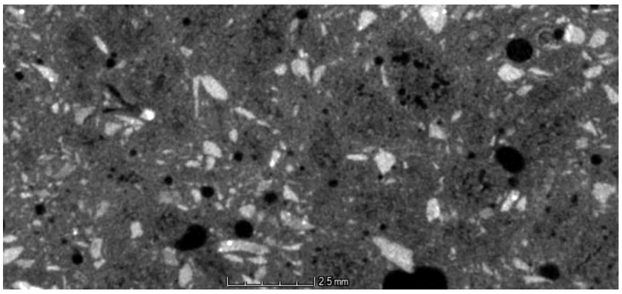

Figure 7: CT image – slice of RMA, 120 days, R – reference sample (without freezing cycles), exposure to 1000 °C

Slika 7: CT-posnetek rezine RMA, 120 dni, R – referenčni vzorec (brez ciklov zamrzovanja), izpostavljen na 1000 °C

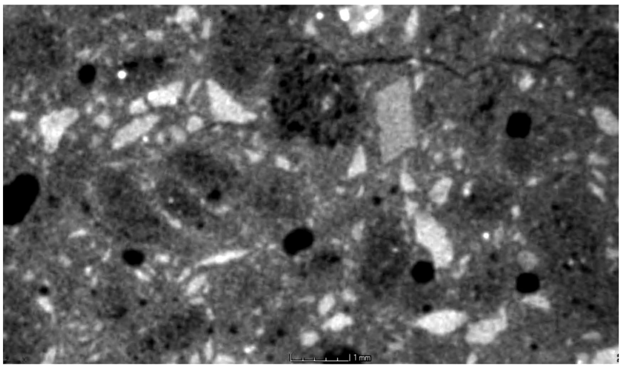

Figure 8: CT image – slice of RMA, 120 days, R – reference sample, 100 freezing cycles, exposure to 1000 °C

Slika 8: CT-posnetek rezine RMA, 120 dni, R – referenčni vzorec po 100 ciklih zamrzovanja, izpostavljen na 1000°C

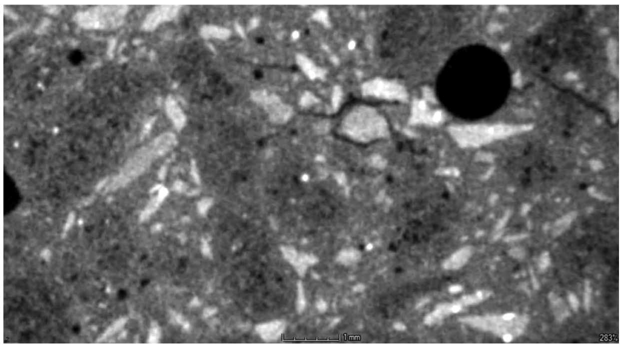

Figure 9: CT picture – slice of RMS, 120 days, R – reference sample, 100 freezing cycles, exposure to 1000 °C

Slika 9: CT-posnetek rezine RMS, 120 dni, R – referenčni vzorec po 100 ciklih zamrzovanja, izpostavljen na 1000 °C

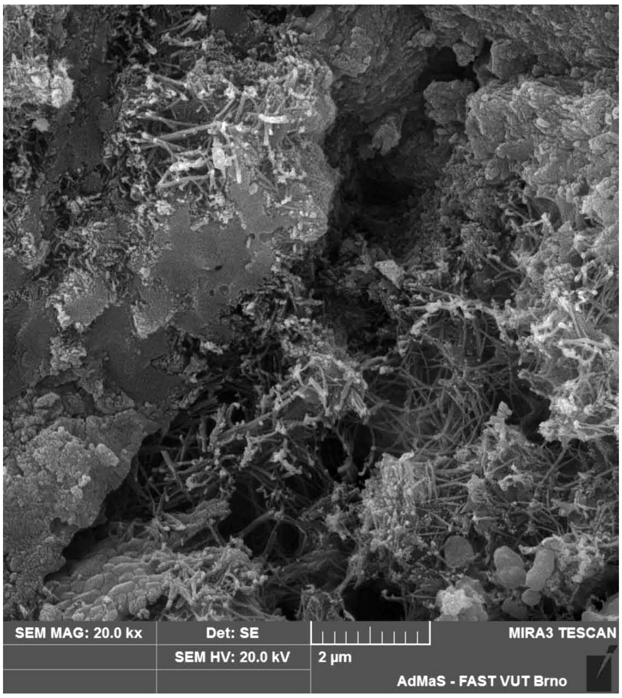

Figure 10: Microstructure of RMS, exposure temperature of 1000 °C (without freezing), mag. 20.000×; detail of structure degradation

Slika 10: Mikrostruktura RMS, temperature izpostavitve 1000 °C (brez zamrzovanja), pov. 20,000×; detajl degradacije strukture

subsequent thermal load may lead to cracks or microcracks. For this reason, one of the key included analytical methods was computer tomography (hereinafter referred to as CT). Figures below present selected images of the bodies loaded with a temperature of 1000 °C including the reference bodies (**Figures 7** to **9**). Another substantial analysis was electron microscopy (hereinafter referred to also as SEM). Here, the attention was focused on the faults of the matrix itself as well as on any microscopic cracks, mainly in the matrix-filler interface (**Figures 9** and **10**).

4 DISCUSSION

The RMS formula gave us bulk-density values (**Figure 1**) of 1810 kg.m^{-3} and 1830 kg.m^{-3} after 70 d or 120 d, respectively. Therefore, an almost negligible growth was observed. For a proper evaluation (in terms of requirements of normative documents), the graph (**Figure 1**) also contains curves characterizing the weight loss. The course of the curves indicates that the resistance to high temperatures gradually gently decreased due to the frost cycles. After 100 cycles and exposure to an ambient temperature of 1000 °C, we observed a weight loss of 17.9 % while the reference material showed a decrease of about 13.3 %. Differences between the weight losses (RF curve, **Figure 1**) after 100 frost cycles were identified as slightly higher. After exposure to 1000 °C, however, the differences in the weight loss (RF curve, **Figure 1**) after 50 and 100 cycles became equal.

The RMA formula was characterized by bulk-density values of 1680 kg.m^{-3} and 1720 kg.m^{-3} after 70 d and 120 d, respectively (**Figure 2**). As in the case of the RMS recipe, this parameter increases very slightly. The courses of weight decreases are different in comparison with the RMS formula. The R and F curves can be characterized by a more uniform and more gradual decline than in the case of the RMS. Nevertheless, the weight losses after 100 frost cycles followed by the thermal exposure of 1000 °C are comparable for both recipes (about 18 %), i.e., the influences of fly ash and slag are similar (with a negligible difference of 0.3 % in favour of the slag). The RF curves show a relatively balanced course.

In comparison with the weight, the declines in strength characteristics were much more noticeable. In the case of the RMS recipe, 50 frost cycles led to a decrease in the compressive strength by about 21 % (from the original value of about 47 N.mm^{-2}) and 100 cycles resulted in a decrease by 26.5 % (from the original value of 48 N.mm^{-2}; **Figure 3**). According to the relevant technical standard,[16] the essential criterion for a decrease is 25 %; this criterion was slightly exceeded after 100 cycles. When comparing the R and F curves characterizing the loss of strength due to the thermal stress or frost stress, it is evident that the influence of the cyclic frost was manifested by pronounced declines. The difference between the exposures at 50 or 100 cycles is not very noticeable. The graph clearly shows that 100 frost cycles followed by a thermal load at the age of 120 d caused a decrease in the compressive strength to 74.6 %, i.e., the residual strength of 24.4 % (or 9 N mm^{-2}). Exposure to the temperature of 1000 °C resulted in virtually identical residual strengths (**Figure 3**, RF curves).

In the RMA recipe, the trends of the compressive strength are not so clear (**Figure 4**). The values show a significant increase in the strength owing to a longer ripening time. This was partly expected due to the nature of fly ash because of its involvement in the hydration process occurring after a prolonged period of time. Due to the frost stress (without the temperature exposure), the compressive strength decreased by 15.1 % and 27.1 % after 50 cycles and 100 cycles, respectively. The difference is thus slightly greater than for the RMS recipe. The R and F curves follow a similar pattern; after the exposure at 1000 °C, it is possible to record almost the same values of the residual compressive strength, i.e., around 30 % (9–10 N.mm^{-2}). Regarding the compressive strength, therefore, the resistance of the composite matrix based on fly ash can be evaluated better compared to the case of using slag.

The bending tensile strength of the RMS recipe reached 6.9 N.mm^{-2} and 7.2 N.mm^{-2} after 70 d and 120 d, respectively (**Figure 5**). Due to the frost cycles, the strength decreased by 20 % and 25.8 % after 50 cycles and 100 cycles, respectively (without the thermal load). Except for the 70-day exposure to frost with a subsequent thermal load, the residual strengths (after 1000 °C) ranged around the value of 40 %.

The bending tensile strength of the RMA recipe was around 6.4 N.mm^{-2} after 50 cycles and 6.7 N.mm^{-2} after 100 freezing and de-freezing cycles. The residual strengths after the frost cycles with a subsequent high temperature load were determined in a range of 33–36 %. The bodies loaded only thermally retained 42–46 % of the bending strength. The results show that the residual bending tensile strengths in the RMS and RMA recipes do not differ significantly. Only the courses of the RF curves are distinctly different.

The CT analysis focused on the structure degradation, both in the individual components and their

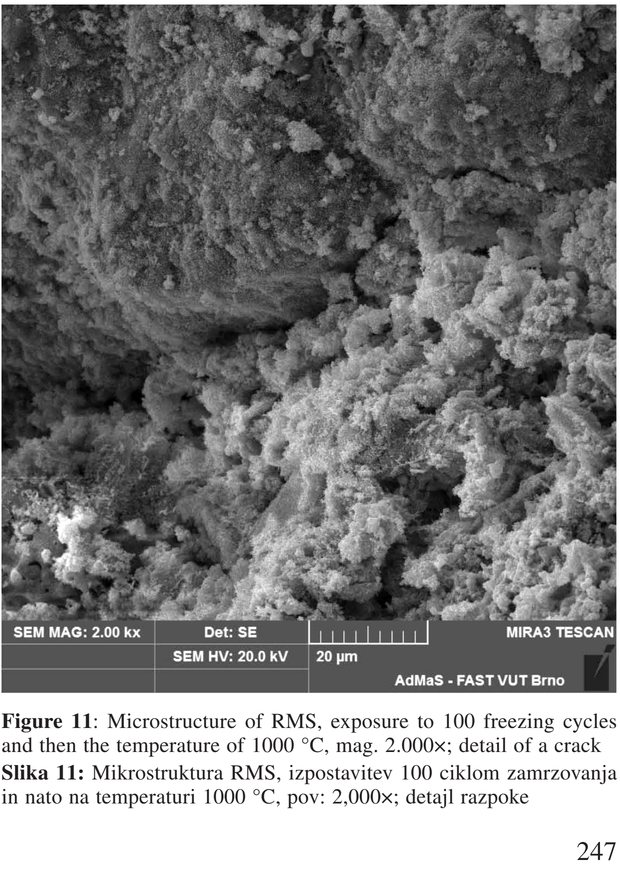

Figure 11: Microstructure of RMS, exposure to 100 freezing cycles and then the temperature of 1000 °C, mag. 2.000×; detail of a crack

Slika 11: Mikrostruktura RMS, izpostavitev 100 ciklom zamrzovanja in nato na temperaturi 1000 °C, pov: 2,000×; detajl razpoke contact zones. It was found that the bodies exposed to frost and then to high temperatures show a slightly increased incidence of cracks. In comparison with the bodies exposed to a high temperature without the cyclical freezing, however, the difference was not too pronounced. Identified cracks were located primarily in the matrix, at the interface of the dense aggregate and the matrix, and – to a lesser extent – in the porous aggregate (**Figures 7** to **9**). As for the incidence of cracks, the differences between the RMA and RMS recipes were almost negligible.

The microstructural method was mainly used to identify the matrices gradually degrading with the increasing temperature (**Figures 10** and **11**). No differences between the bodies exposed and not exposed to frost were observed. Likewise, there was no significant difference in the microstructure of the samples after 70 d and 120 d or after 50 and 100 frost cycles. It is therefore evident that the frost is more likely to distort the structure on the "macroscopic" scale without microstructural changes, while the thermal exposure also supports the decomposition of hydration complexes and possibly the emergence of new products. This could particularly occur in the case of fly ash, which might act as a flux if the contents of iron or alkalis are increased.

Hydration of fly ash or its involvement in the hydration reactions during the silica-matrix ripening requires longer times. According to normative documents, the influence of fly ash applied to the concrete is tested after 28 d and 90 d. In the case of a shorter time period, it is therefore possible that the greater portion of fly ash could act as a flux without any significant contribution to shaping the silicate-matrix structure. After a longer period, conversely, the greater portion of fly ash could hydrate, which would theoretically reduce its ability as a flux. Alternatively, if the ability as a flux remained while the participation in hydration reactions was demonstrable, the positive effect of fly ash would be clear. In this case, however, it would be necessary to verify the specific amounts of fly ash depending on its chemical composition in order to avoid the melting of the composite at a certain temperature to an extent that would cause the loss of its carrying capacity. For this reason, it would be appropriate to supplement the performed analyses with heat microscopy.

5 CONCLUSIONS

With regard to the achieved results, we can say that both developed recipes are resistant to the action of extreme temperature conditions, i.e., the combination of frost and the subsequent high temperatures. However, this only applies to 50 frost cycles. After an exposure to 100 cycles, the limit criterion of 25 % (the minimum residual strength of 75 %) was slightly exceeded. Frost resistance is partially limited by the use of lightweight porous aggregates. Within the following research, it would be useful to focus on optimizing the composition of recipes in terms of a long-term resistance to frost. Taking into account the conditions of the application of the developed materials, however, it would also be possible to consider secondary protection, i.e., surface treatment by painting. This could increase the resistance to frost. It is important to find that the temperature resistance was not affected to a striking extent despite the decline in the strengths in the order of about 15–27 % due to frost – the trend of the residual strengths.

Higher strengths (without exposures to extreme conditions) were reached in the recipe containing slag, i.e., the RMS. In the case of the RMA recipe, a pronounced incidence of strength characteristics was more apparent in the longer term. The RMA recipe showed improved temperature resistance. This is demonstrated by the determined residual strengths, especially the compressive strengths at 1000 °C, where we observed residual strengths of almost 30 %. This fact is not so explicit in the case of bending strengths. The benefit of the presented research, among other things, is the composition of the recipes. It was a combination of commercially produced (i.e., available) primary as well as alternative raw materials – in terms of both matrix and filler.

To clarify the behaviour of fly ash in the given matrix under extreme conditions, it would be appropriate to include other additional analyses. Studying properties of the developed composites under simultaneous effects of extreme temperatures and their mechanical stress (compression or tensile bending) seems to be very interesting. This could prove whether the an increasing temperature and the related structural changes including degradation of the matrix or other components lead to a total loss of the carrying capacity of the respective material before it becomes cold.

Acknowledgements

This article was made with the financial support of The Czech Science Foundation (GAČR) project 14-25504S "Research of Behaviour of Inorganic Matrix Composites Exposed to Extreme Conditions", as well as under the project No. LO1408 "AdMaS UP – Advanced Materials, Structures and Technologies", supported by Ministry of Education, Youth and Sports under the "National Sustainability Programme I".

6 REFERENCES

[1] N. U. Kockal, T. Ozturan, Durability of lightweight concretes with lightweight fly ash aggregates, Construction and Building Materials, 25 (**2011**) 3, 1430–1438, doi:10.1016/j.conbuildmat.2010.09.022

[2] B. Kucharczyková, Z. Keršner, O. Pospíchal, P. Misák, P. Daněk, P. Schmid, The porous aggregate pre-soaking in relation to the freeze-thaw resistance of lightweight aggregate concrete, Construction and Building Materials, 30 (**2012**) 761–766, doi:10.1016/j.conbuildmat.2011.12.067

[3] H. Garbalińska, A. Wygocka, Microstructure modification of cement mortars: Effect on capillarity and frost-resistance, Construction and Building Materials, 51 (**2014**), 258–266, 10.1016/j.conbuildmat.2013.10.091

[4] S. Rahman, Z. Grasley, A poromechanical model of freezing concrete to elucidate damage mechanisms associated with substandard aggregates, Cement and Concrete Research, 55 (**2014**), 88–101, doi:10.1016/j.cemconres.2013.10.001

[5] S. Chandra, L. Berntsson, 10 – Freeze-Thaw Resistance of Lightweight Aggregate Concrete, in Lightweight Aggregate Concrete, edited by Satish Chandra and Leif Berntsson, William Andrew Publishing, Norwich, NY, 2002, 321–368, doi:10.1016/B978-081551486-2.50013-4

[6] M. B. Karakoç, R. Demirboğa, İ. Türkmen, İ. Can, Modeling with ANN and effect of pumice aggregate and air entrainment on the freeze-thaw durabilities of HSC, Construction and Building Materials, 25 (**2011**) 11, 4241–4249, doi:10.1016/j.conbuildmat.2011.04.068

[7] S. Chandra, J. Aavik, L. Berntsson, Influence of polymer microparticles on freeze-thaw resistance of structural lightweight aggregate concrete, International Journal of Cement Composites and Lightweight Concrete, 4 (**1982**) 2, 111–115, doi:10.1016/0262-5075(82)90015-X

[8] Y. Ke, S. Ortola, A. L. Beaucour, H. Dumontet, Identification of microstructural characteristics in lightweight aggregate concretes by micromechanical modelling including the interfacial transition zone (ITZ), Cement and Concrete Research, 40 (**2010**) 11, 1590–1600, doi:10.1016/j.cemconres.2010.07.001

[9] J.-P. Won, H.-B. Kang, S.-J. Lee, S.-W. Lee, J.-W. Kang, Thermal characteristics of high-strength polymer–cement composites with lightweight aggregates and polypropylene fiber, Construction and Building Materials, 25 (**2011**) 10, 3810–3819, doi:10.1016/j.conbuildmat.2011.03.023

[10] F. Koksal, O. Gencel, M. Kaya, Combined effect of silica fume and expanded vermiculite on properties of lightweight mortars at ambient and elevated temperatures, Construction and Building Materials, 88 (**2015**), 175–187, doi:10.1016/j.conbuildmat.2015.04.021

[11] S. Aydın, Development of a high-temperature-resistant mortar by using slag and pumice, Fire Safety Journal, 43 (**2008**) 8, 610–617, doi:10.1016/j.firesaf.2008.02.001

[12] V. Černý, Š. Keprdová, Usability of fly ashes from Czech Republic for sintered artificial aggregate, Advanced Materials Research, (**2014**), 805–808, doi:10.4028/www.scientific.net/AMR.887-888.805

[13] ČSN EN 12190. Products and systems for the protection and repair of concrete structures - Test methods - Determination of compressive strength of repair mortar. ČNI, 1999

[14] ČSN EN 196-1. Methods of testing cement - Part 1: Determination of strength. ČNI, 2005

[15] ČSN EN 1504-3. Products and systems for the protection and repair of concrete structures - Definitions, requirements, quality control and evaluation of conformity - Part 3: Structural and non-structural repair. ČNI, 2006

[16] ČSN 73 1322, including Z1. Determination of frost resistance of concrete. ČNI, 2003

UDK 669.017.13:620.164:543.428.3
Original scientific article/Izvirni znanstveni članek

ISSN 1580-2949
MTAEC9, 51(2)251(2017)

SELECTIVE LEACHING AND SURFACE PROPERTIES OF TiNiFe SHAPE-MEMORY ALLOYS

SELEKTIVNO IZPIRANJE IN POVRŠINSKE LASTNOSTI ZLITIN TiNiFe S SPOMINOM

Shih-Hang Chang, Jyun-Sian Liou, Bo-Yen Huang

National I-Lan University, Department of Chemical and Materials Engineering, I-Lan 260, Taiwan
shchang@niu.edu.tw

Prejem rokopisa – received: 2015-09-02; sprejem za objavo – accepted for publication: 2016-04-21

doi:10.17222/mit.2015.269

This study investigated the selective leaching and surface characteristics of $Ti_{50}Ni_{50-x}Fe_x$ (x = 1, 2, and 3) shape-memory alloys using inductively coupled plasma-mass spectrometry, X-ray diffractometry, electrochemical tests and X-ray photoelectron spectroscopy. According to our results, the concentrations of Ni and Fe ions selectively leached from each specimen were considerably higher than that of Ti ions. Electrochemical tests revealed a gradual deterioration in the corrosion resistance of the $Ti_{50}Ni_{50-x}Fe_x$ SMAs as the Fe content in the alloys was increased. X-ray photoelectron-spectroscopy results indicate that the surface of each specimen is primarily made up of a passive TiO_2 film. NiO and Fe_2O_3 oxides, which also formed on the surfaces of the $Ti_{50}Ni_{50-x}Fe_x$ SMAs, caused a deterioration of the uniformity, undermining the protective effect of the TiO_2 films, resulting in a highly selective leaching of the Ni and Fe ions. The $Ti_{50}Ni_{50-x}Fe_x$ SMAs exhibit a number of favourable properties compared to the other SMAs; however, high concentrations of selectively leached Ni and Fe ions may pose a risk in biomedical applications, particularly when used as implant materials.

Keywords: TiNiFe shape-memory alloys, biomaterials, selective leaching, corrosion, X-ray photoelectron spectroscopy

V študiji je proučevano selektivno izpiranje in značilnosti površine zlitine s spominom $Ti_{50}Ni_{50-x}Fe_x$ (x = 1, 2, in 3), z uporabo masne spektrometrije z induktivno sklopljeno plazmo, rentgensko difrakcijo, elektrokemijskimi preizkusi in rentgensko fotoelektronsko spektroskopijo. Rezultati kažejo, da je bila koncentracija selektivno izpranih Ni in Fe ionov iz vsakega vzorca veliko večja kot pa Ti ionov. Elektrokemijski preizkusi so pokazali postopno zmanjšanje korozijske odpornosti $Ti_{50}Ni_{50-x}Fe_x$ SMA, ko je vsebnost Fe v zlitinah naraščala. Rezultati rentgenske fotoelektronske spektroskopije kažejo, da je površina vseh vzorcev predvsem sestavljena iz pasivnih TiO_2 plasti. NiO in Fe_2O_3 oksidi, ki so tudi nastali na površini $Ti_{50}Ni_{50-x}Fe_x$ SMAs, poslabšajo enotnost in ogrožajo varovalno plast iz TiO_2 prevlek, kar ima za posledico bolj selektivno izpiranje ionov Ni in Fe. $Ti_{50}Ni_{50-x}Fe_x$ SMAs vsebuje številne ugodne lastnosti v primerjavi z drugimi SMA; vendar pa velika koncentracija selektivno izpranih Ni in Fe ionov lahko predstavlja tveganje pri biomedicinski uporabi, posebno pri implantiranih materialih.

Ključne besede: TiNiFe zlitine s spominom, biomateriali, selektivno izpiranje, korozija, rentgenska fotoelektronska spektroskopija

1 INTRODUCTION

Nickel-titanium shape-memory alloys (TiNi SMAs) are widely used in advanced engineering applications due to their favourable shape memory and superelastic properties.[1] Most TiNi SMAs further exhibit a low cytotoxicity and a good biocompatibility[2–4] and thus they are also suitable for biomedical applications, such as laparoscopic surgery, stents, shape-memory microvalves, and osteosynthesis devices.[5–7] It was reported that substituting Fe for Ni in TiNi SMAs induces the formation of the R-phase during the martensitic transformation and leads to some advanced mechanical properties superior to those of typical TiNi SMAs.[8,9]

W. J. Moberly et al.[10] investigated the deformation, twinning and thermo-mechanical strengthening of $Ti_{50}Ni_{47}Fe_3$ SMAs. Their results demonstrated that cold-worked and annealed $Ti_{50}Ni_{47}Fe_3$ SMAs had a refined subgrain size, a high yield strength, and a good ductility. In addition, several studies reported on TiNiFe SMAs with ultra-high internal-friction properties, which are excellent candidates for high-damping applications.[11–13] Recently, D. Wang et al.[14] established a complete temperature-composition phase diagram that included the pre-martensitic state, martensite and strain glass. They also reported that strain glass forms in TiNiFe SMAs when the Fe doping exceeds the critical value.

Several articles reveal that TiNiFe SMAs are candidate materials for biomedical applications. C. Li and Y. F. Zheng[15] investigated the electrochemical behaviours of $Ti_{50}Ni_{47}Fe_3$ SMAs and found that the surface of a $Ti_{50}Ni_{47}Fe_3$ SMA mainly consists of TiO_2, which is responsible for the good biocompatibility and anti-corrosion properties of the alloys. T. A. Tabish et al.[16] further performed an *in-vivo* cytotoxic evaluation of TiNiFe SMAs and found that they do not exhibit any appreciable cytotoxic or systematic reactions to living systems. However, when SMAs are used as implant materials, interactions between the alloys and the living tissue can lead to the corrosion of the surface oxide layer, thereby increasing the risk of metal ions being released into the body. These metallic ions pose a potential health hazard capable of inducing allergic reactions or even promoting the onset of cancer.[17–19]

Several researches had previously investigated the selective leaching behaviour of TiNi and TiNiCu SMAs[20–23]; however, the selective leaching of Ti, Ni, and Fe ions released from TiNiFe SMAs has not been studied. Therefore, this study investigated the selective leaching and surface properties of $Ti_{50}Ni_{50-x}Fe_x$ (x = 1, 2, and 3) SMAs using inductively coupled plasma mass spectrometry (ICP-MS), an X-ray diffraction (XRD) analysis, electrochemical tests, and X-ray photoelectron spectroscopy (XPS).

2 EXPERIMENTAL PART

The $Ti_{50}Ni_{50-x}Fe_x$ (x = 1, 2, and 3) SMAs used in this study were prepared from pure raw titanium (a purity of 99.9 % mass fraction), nickel (a purity of 99.9 % mass fraction), and iron (a purity of 99.98 % mass fraction). The raw materials were re-melted using conventional vacuum arc remelting to form ingots in an argon atmosphere. Each ingot was hot-rolled at 900 °C using a rolling machine (DBR150x200 2HI-MILL, Daito Seiki Co, Japan) to form a 2 mm plates, which were then solution-heat-treated at 900 °C for 1 h and quenched in water. The surface oxide layer of a plate was removed using an etching solution of $HF:HNO_3:H_2O$ at a volume ratio of 1:5:20. Each plate was then cut into bulk samples with dimensions of (30.0 × 4.0 × 2.0) mm for characterization.

The crystallographic features of each $Ti_{50}Ni_{50-x}Fe_x$ SMA were determined using a Rigaku IV XRD instrument with Cu-$K\alpha$ radiation (λ = 0.154 nm) at room temperature. The selective leaching properties of $Ti_{50}Ni_{50-x}Fe_x$ SMAs were evaluated by immersing samples in test flasks containing 500 mL of Ringer's solution. Ringer's solution was used in selective-leaching tests because it is an isotonic solution similar to bodily fluids and is widely used in *in-vitro* experiments. Each test flask was maintained at 37 °C in an orbital shaker incubator for 80 d. We then measured the concentrations of the released Ti, Ni, and Fe ions in Ringer's solution using ICP-MS (Agilent 7500ce).

Electrochemical measurements of the $Ti_{50}Ni_{50-x}Fe_x$ SMAs were performed using an electrochemical workstation (ECW-5600, Jiehan) to determine the cathodic and anodic polarization Tafel curves, where a platinum plate was used as the counter electrode, a saturated calomel electrode (SCE) was used as the reference electrode and Ringer's solution was used as the test solution. The average corrosion potential (E_{corr}) and the average corrosion current density (i_{corr}) values of each specimen were calculated from seven Tafel curves, for which the maximum and minimum values were deleted. The surface chemical composition of the $Ti_{50}Ni_{50-x}Fe_x$ SMAs was analysed using an XPS device (Thermo Scientific (VGS) K-Alpha) with a monochromatic Al-$K\alpha$ radiation source of 1468.6 eV. The survey spectrum of each specimen was measured over a range of 200–1200 eV in 1-eV steps. High-resolution Ti, Ni, and Fe 2p spectra for each specimen were determined in 0.05-eV steps. The XPSPeak 4.1 software was used for the analysis of XPS spectra.

3 RESULTS

3.1 XRD results

Figure 1 presents the XRD results of the $Ti_{50}Ni_{50-x}Fe_x$ SMAs, where each $Ti_{50}Ni_{50-x}Fe_x$ SMA sample exhibits diffraction peaks related to $(110)_{B2}$, $(200)_{B2}$, and $(211)_{B2}$ at approximately 2θ = 42.2°, 61.3°, and 77.5°, respectively. Figure 1 further reveals that all of the $Ti_{50}Ni_{50-x}Fe_x$ SMAs used in this study were in the parent phase at room temperature, indicating that the surface relief, which is normally observed at the R-phase, or the B19' martensite of TiNi-based SMAs, had no influence on the selective leaching.

3.2 Selective leaching behaviours

Figures 2a to **2c** present the concentrations of the Ti, Ni, and Fe ions, respectively, which were selectively leached from the $Ti_{50}Ni_{50-x}Fe_x$ SMAs in Ringer's solution as a function of the immersion time. **Figure 2a** shows that the concentration of the Ti ions selectively leached from the specimens was extremely low (< $1\cdot10^{-8}$) throughout the 80 d of the immersion. **Figure 2b** shows that the concentrations of the Ni ions selectively leached from the $Ti_{50}Ni_{50-x}Fe_x$ SMAs were also extremely low during the first 30 d; however, these concentrations increased significantly to above $1.5\cdot10^{-6}$ ppb by day 80. This feature indicates that the selective leaching rate of the Ni ions from the $Ti_{50}Ni_{50-x}Fe_x$ SMAs is considerably high. As shown in **Figure 2c**, the concentrations of the Fe ions selectively leached from the $Ti_{50}Ni_{50-x}Fe_x$ SMAs

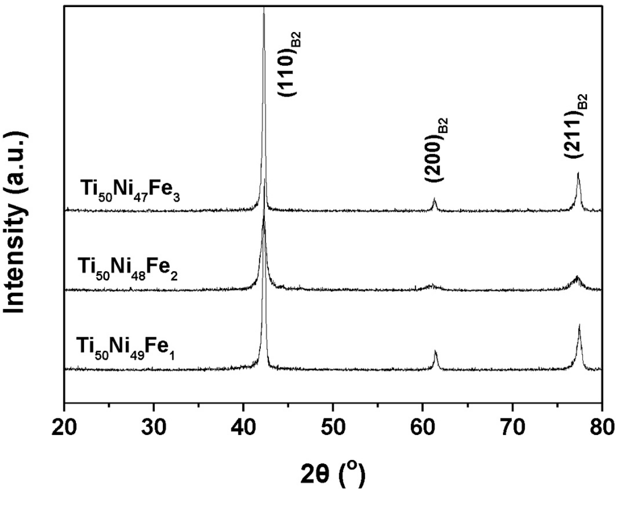

Figure 1: XRD pattern for $Ti_{50}Ni_{50-x}Fe_x$ SMAs
Slika 1: Rentgenogram $Ti_{50}Ni_{50-x}Fe_x$ SMA

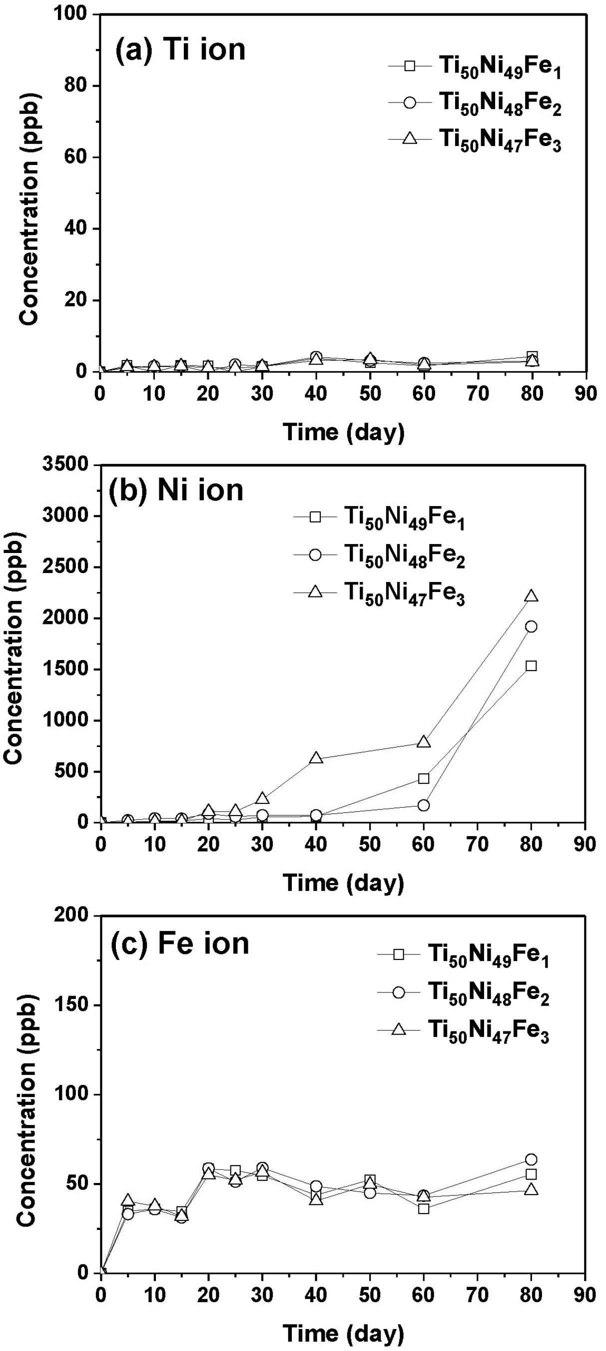

Figure 2: Concentrations of: a) Ti, b) Ni, and c) Fe ions selectively leached from $Ti_{50}Ni_{50-x}Fe_x$ SMAs

Slika 2: Koncentracije: a) Ti, b) Ni in c) Fe ionov, selektivno izpranih iz $Ti_{50}Ni_{50-x}Fe_x$ SMA

were approximately $5\cdot10^{-8}$ after 80 d. No obvious differences in the concentration of the Fe ions were observed among alloys with different chemical compositions. According to the results shown in **Figure 2**, the concentration of the Ni ions selectively leached from each of the specimens was considerably higher than that of the Ti and Fe ions, indicating that Ni ions are more easily released from the surface of $Ti_{50}Ni_{50-x}Fe_x$ SMAs than the Ti or Fe ions.

3.3 Electrochemical properties

Figure 3 presents the selected cathodic and anodic polarization Tafel curves obtained from Ringer's solution containing $Ti_{50}Ni_{50-x}Fe_x$ SMAs. The average corrosion potential (E_{corr}) and corrosion-current density (i_{corr}) of each sample are listed in **Table 1**. The E_{corr} values of $Ti_{50}Ni_{50-x}Fe_x$ SMAs gradually decreased from approximately –0.379 V to –0.433 V when the Fe content in the alloys was increased from 1 to 3. This indicates that, when immersed in Ringer's solution, the $Ti_{50}Ni_{50-x}Fe_x$ SMAs with a lower Fe content exhibit a better corrosion resistance, superior to that of the other SMAs. **Table 1** also shows that, in the presence of an elevated Fe content, the i_{corr} values of the $Ti_{50}Ni_{50-x}Fe_x$ SMAs gradually increased from $(3.27\pm0.86)\times10^{-7}$ A/cm² to $(5.52\pm1.05)\times10^{-6}$ A/cm², demonstrating a gradual increase in the corrosion rate of the$Ti_{50}Ni_{50-x}Fe_x$ SMAs when alloys had a higher Fe content.

Table 1: The average E_{corr} and I_{corr} values determined according to the cathodic and anodic polarization Tafel curves from **Figure 3**

Tabela 1: Srednje vrednosti E_{corr} in I_{corr} določene pri katodni in anodni polarizaciji iz Taflovih krivulj iz **Slike 3**

Sample	Avg. E_{corr} (V)	Avg. I_{corr} (A/cm²)
$Ti_{50}Ni_{49}Fe_1$	-0.379±0.017	$(3.27\pm0.68)\times10^{-7}$
$Ti_{50}Ni_{48}Fe_2$	-0.394±0.006	$(3.54\pm0.66)\times10^{-6}$
$Ti_{50}Ni_{47}Fe_3$	-0.433±0.007	$(5.52\pm1.05)\times10^{-6}$

3.3 X-ray photoelectron spectroscopy

Figures 4a to **4c** present the XPS survey spectra of the $Ti_{50}Ni_{49}Fe_1$, $Ti_{50}Ni_{48}Fe_2$, and $Ti_{50}Ni_{47}Fe_3$ SMAs, respectively. Each specimen exhibited significant characteristic peaks associated with Ti (a Ti 2p peak at approximately 460 eV), Ni (a Ni 2p peak at approximately 853 eV), O (an O 1s peak at approximately 531 eV), and contamination C (a C 1s peak at approximately 285 eV).

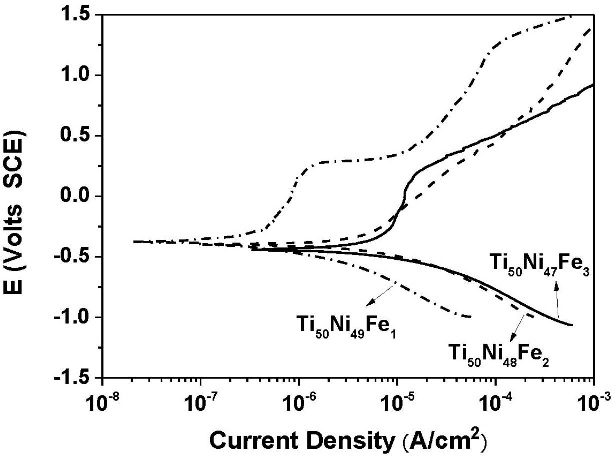

Figure 3: Cathodic and anodic polarization Tafel curves for $Ti_{50}Ni_{50-x}Fe_x$ SMAs

Slika 3: Taflova krivulja katodne in anodne polarizacije $Ti_{50}Ni_{50-x}Fe_x$ SMAs

(a) $Ti_{50}Ni_{49}Fe_1$ Survey

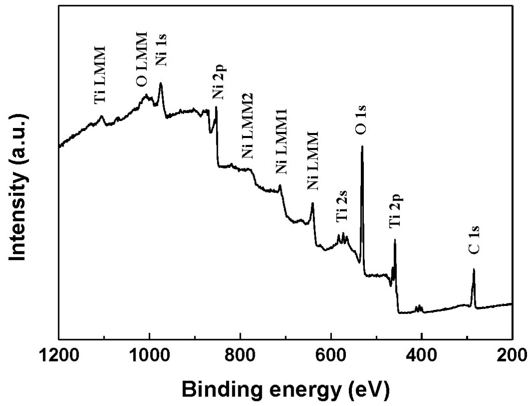

(b) $Ti_{50}Ni_{48}Fe_2$ Survey

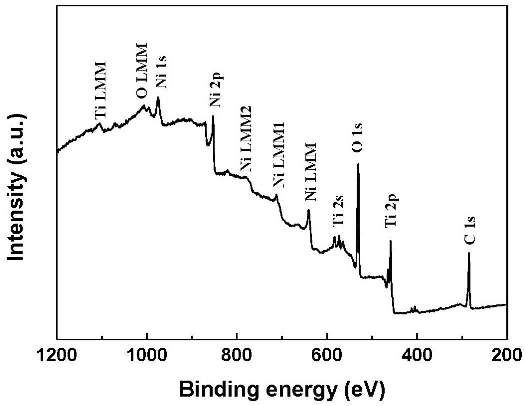

(c) $Ti_{50}Ni_{47}Fe_3$ Survey

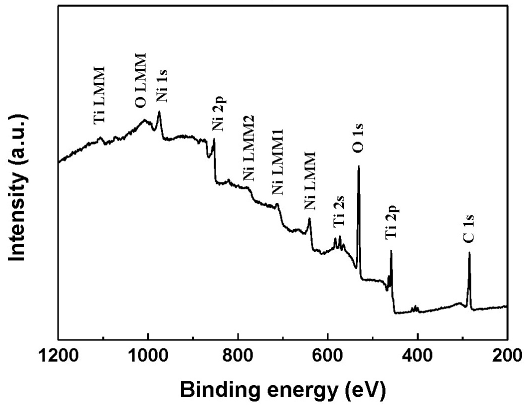

Figure 4: XPS survey spectra of the surfaces of: a) $Ti_{50}Ni_{49}Fe_1$, b) $Ti_{50}Ni_{48}Fe_2$, and c) $Ti_{50}Ni_{47}Fe_3$ SMAs

Slika 4: XPS-spektri površin: a) $Ti_{50}Ni_{49}Fe_1$, b) $Ti_{50}Ni_{48}Fe_2$ in c) $Ti_{50}Ni_{47}Fe_3$ SMAs

(a) $Ti_{50}Ni_{49}Fe_1$ Ti2p

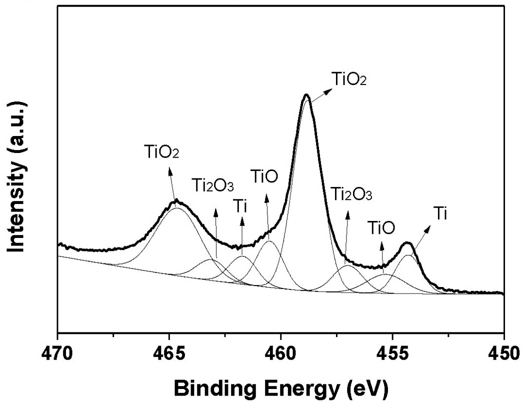

(b) $Ti_{50}Ni_{48}Fe_2$ Ti2p

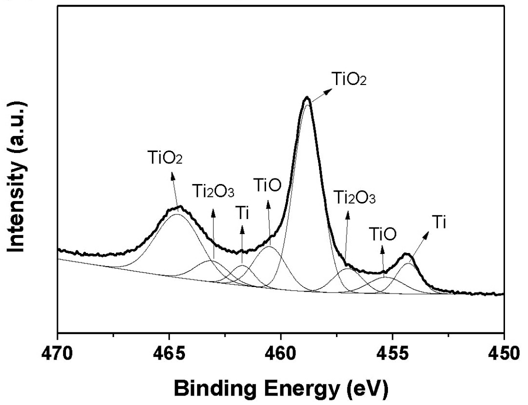

(c) $Ti_{50}Ni_{47}Fe_3$ Ti2p

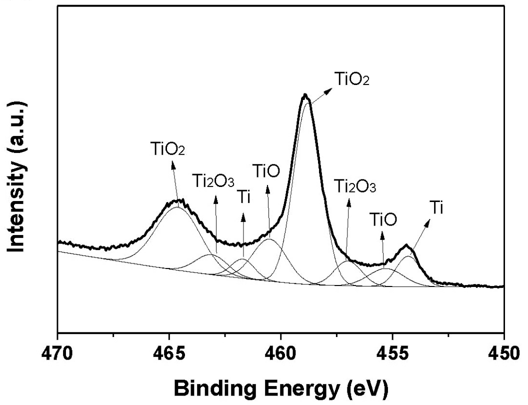

Figure 5: Ti 2p XPS spectra of the surfaces of: a) $Ti_{50}Ni_{49}Fe_1$, b) $Ti_{50}Ni_{48}Fe_2$, and c) $Ti_{50}Ni_{47}Fe_3$ SMAs

Slika 5: Ti 2p XPS spektri površin: a) $Ti_{50}Ni_{49}Fe_1$, b) $Ti_{50}Ni_{48}Fe_2$ in c) $Ti_{50}Ni_{47}Fe_3$ SMAs

Figure 4 also reveals an insignificant Fe 2p peak at approximately 710 eV for each specimen.

Figures 5a to **5c** present the Ti 2p XPS spectra of the $Ti_{50}Ni_{49}Fe_1$, $Ti_{50}Ni_{48}Fe_2$, and $Ti_{50}Ni_{47}Fe_3$ SMAs, respectively. **Figure 5a** shows that the Ti 2p characteristic peaks of the $Ti_{50}Ni_{49}Fe_1$ SMA can be divided into four oxidation states, Ti^{4+}, Ti^{3+}, Ti^{2+}, and Ti^0, corresponding to TiO_2, Ti_2O_3, TiO, and metallic Ti, respectively.[24–26] As shown in **Figure 5a**, the TiO_2 peak was more prominent than the other peaks, indicating that TiO_2 was the dominant oxide layer on the surface of the $Ti_{50}Ni_{49}Fe_1$ SMA. **Figures 5b** and **5c** show that the Ti 2p XPS spectra of the $Ti_{50}Ni_{48}Fe_2$ and $Ti_{50}Ni_{47}Fe_3$ SMAs were very similar to that of the $Ti_{50}Ni_{49}Fe_1$ SMA shown in **Figure 5a**. This suggests that the surfaces of the $Ti_{50}Ni_{48}Fe_2$ and $Ti_{50}Ni_{47}Fe_3$ SMAs were also primarily composed of a TiO_2 oxide layer.

Figures 6a to **6c** present the Ni 2p XPS spectra of the $Ti_{50}Ni_{49}Fe_1$, $Ti_{50}Ni_{48}Fe_2$, and $Ti_{50}Ni_{47}Fe_3$ SMAs, respectively. **Figure 6a** shows that the Ni 2p characteristic

(a) $Ti_{50}Ni_{49}Fe_1$ Ni2p

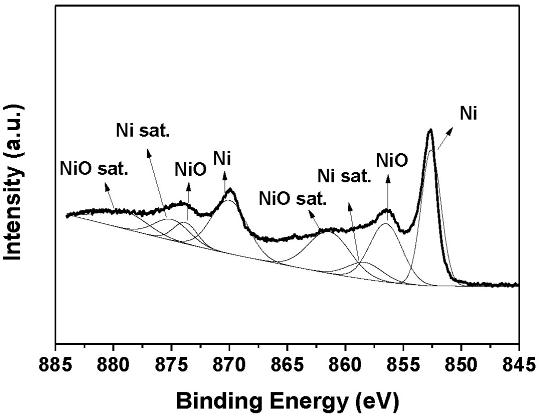

(b) $Ti_{50}Ni_{48}Fe_2$ Ni2p

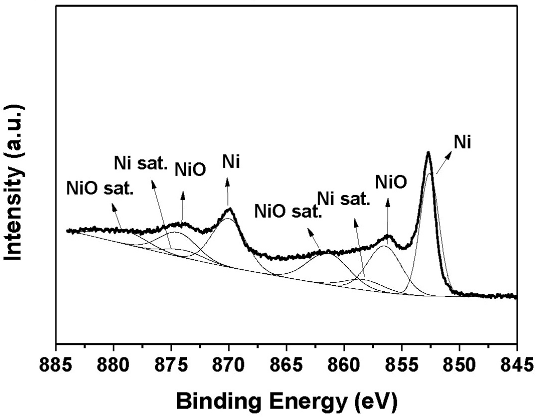

(c) $Ti_{50}Ni_{47}Fe_3$ Ni2p

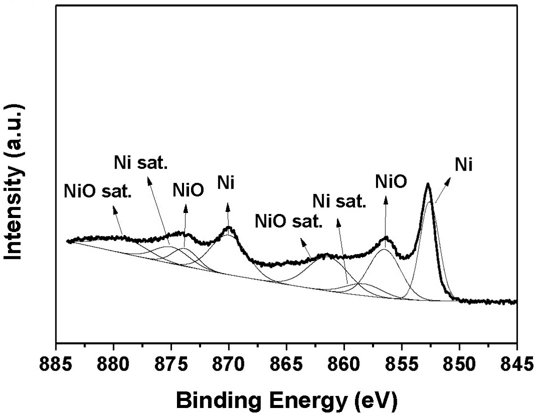

Figure 6: Ni 2p XPS spectra of the surfaces of: a) $Ti_{50}Ni_{49}Fe_1$, b) $Ti_{50}Ni_{48}Fe_2$, and c) $Ti_{50}Ni_{47}Fe_3$ SMAs

Slika 6: Ni 2p XPS-spektri površin: a) $Ti_{50}Ni_{49}Fe_1$, b) $Ti_{50}Ni_{48}Fe_2$ in c) $Ti_{50}Ni_{47}Fe_3$ SMA

(a) $Ti_{50}Ni_{49}Fe_1$ Fe 2p

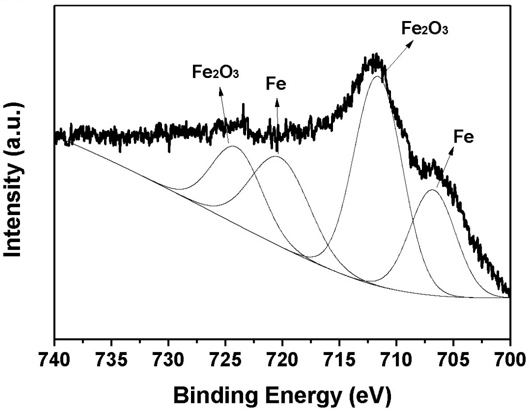

(b) $Ti_{50}Ni_{48}Fe_2$ Fe 2p

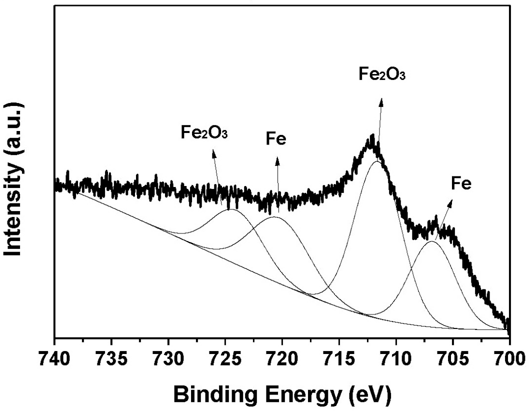

(c) $Ti_{50}Ni_{47}Fe_3$ Fe 2p

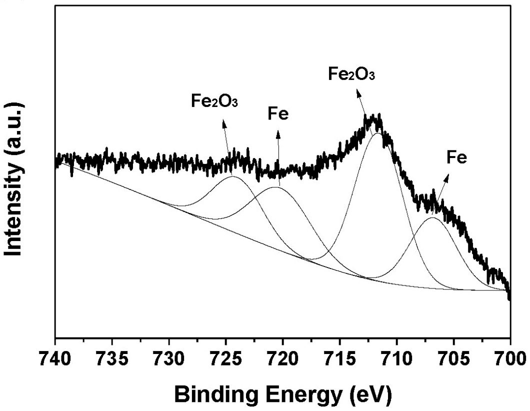

Figure 7: Fe 2p XPS spectra of the surfaces of: a) $Ti_{50}Ni_{49}Fe_1$, b) $Ti_{50}Ni_{48}Fe_2$, and c) $Ti_{50}Ni_{47}Fe_3$ SMAs

Slika 7: Fe 2p XPS-spektri površin: a) $Ti_{50}Ni_{49}Fe_1$, b) $Ti_{50}Ni_{48}Fe_2$ in c) $Ti_{50}Ni_{47}Fe_3$ SMA

peaks of the $Ti_{50}Ni_{49}Fe_1$ SMA can be divided into the metallic-Ni and NiO-oxidation states. We also observed two small shoulders corresponding to the satellite (sat.) peaks of the metallic Ni and NiO near the characteristic peaks. **Figures 6b** and **6c** show that the Ni 2p XPS spectra of the $Ti_{50}Ni_{48}Fe_2$ and $Ti_{50}Ni_{47}Fe_3$ SMAs were nearly identical to that of the $Ti_{50}Ni_{49}Fe_1$ SMA, suggesting an abundance of metallic Ni atoms on the surfaces of $Ti_{50}Ni_{50-x}Fe_x$ SMAs. **Figures 7a** to **7c** present the Fe 2p XPS spectra of the $Ti_{50}Ni_{49}Fe_1$, $Ti_{50}Ni_{48}Fe_2$, and $Ti_{50}Ni_{47}Fe_3$ SMAs, respectively. Compared to the XPS spectra of Ti 2p and Ni 2p in **Figures 5** and **6**, the intensity of the Fe 2p XPS spectrum was relatively low. **Figures 7a** to **7c** show that the Fe 2p characteristic peaks of the $Ti_{50}Ni_{50-x}Fe_x$ SMAs can be divided into Fe_2O_3 and metallic Fe peaks, in which Fe_2O_3 is the dominant oxide characterizing the surfaces of $Ti_{50}Ni_{50-x}Fe_x$ SMAs.

4 DISCUSSION

According to the Ti 2p XPS spectra in **Figure 5**, the Ti atoms near the surfaces of the $Ti_{50}Ni_{50-x}Fe_x$ SMAs were covered mainly with a film of a TiO_2 oxide. This result can be explained with a high thermodynamic stability of TiO_2.[27–30] Furthermore, the TiO_2 films that formed on the surfaces of $Ti_{50}Ni_{50-x}Fe_x$ SMAs are highly corrosion resistant, which leads to extremely low selective leaching of the Ti ions, as demonstrated in **Figure 2a**. In contrast, **Figure 2b** shows that comparatively higher concentrations of Ni ions were leached from the $Ti_{50}Ni_{50-x}Fe_x$ SMAs, indicating that the selective leaching rate of the Ni ions was much higher than that of the Ti ions, which was, in turn, due to an abundance of metallic Ni atoms on the surfaces of the $Ti_{50}Ni_{50-x}Fe_x$ SMAs, as shown in **Figure 6**. **Figure 2b** also reveals that the concentrations of the Ni ions selectively leached from the $Ti_{50}Ni_{50-x}Fe_x$ SMAs gradually increased with an increase in the Fe content in the $Ti_{50}Ni_{50-x}Fe_x$ SMAs. This corresponds to the fact that the corrosion resistance of the $Ti_{50}Ni_{50-x}Fe_x$ SMAs gradually deteriorated with an increase in the Fe content of the alloys, as revealed by **Figure 3**. As shown in **Figure 2c**, the concentration of the Fe ions selectively leached from the $Ti_{50}Ni_{50-x}Fe_x$ SMAs was approximately 50 ppb, which is much lower than that of the Ni ions. This is a direct consequence of the fact that the Fe content in the $Ti_{50}Ni_{50-x}Fe_x$ SMAs was below 3 atomic percent. As shown in **Figure 7**, this finding also corresponds to the fact that most Fe atoms on the surface of a specimen were in the form of Fe_2O_3 oxides, rather than metallic Fe.

A previous study found that extremely low concentrations of Ti and Ni ions were selectively leached from $Ti_{50}Ni_{50}$ SMAs and attributed this to a passive TiO_2 surface film inhibiting the ion movement.[23] However, during the current study, we observed high concentrations of selectively leached Ni and Fe ions. This suggests that the NiO and Fe_2O_3 oxides that formed on the surfaces of the $Ti_{50}Ni_{50-x}Fe_x$ SMAs caused a deterioration of the uniformity of the TiO_2 oxide films and, therefore, of their protective effect. Thus, despite the fact that the $Ti_{50}Ni_{50-x}Fe_x$ SMAs exhibit a number of properties not found in the other SMAs, the high concentrations of selectively leached Ni and Fe ions may pose a health risk in biomedical applications. A further surface modification is necessary if the $Ti_{50}Ni_{50-x}Fe_x$ SMAs are to be considered as implantation materials in human bodies.

5 CONCLUSION

All of the $Ti_{50}Ni_{50-x}Fe_x$ SMAs used in this study were in the parent phase during the selective leaching tests. The concentrations of the Ti ions selectively leached from the $Ti_{50}Ni_{50-x}Fe_x$ SMAs were extremely low because the Ti atoms near the surface of the alloys underwent oxidization to form passive TiO_2 films. The concentration of the Ni ions selectively leached from the $Ti_{50}Ni_{50-x}Fe_x$ SMAs gradually increased with an increase in the Fe content in the $Ti_{50}Ni_{50-x}Fe_x$ SMAs, which can be explained with the fact that the corrosion resistance inversely correlated with the Fe content in the alloys. The concentrations of the Fe ions selectively leached from the $Ti_{50}Ni_{50-x}Fe_x$ SMAs were approximately 5× higher than those of the Ti ions. The high concentrations of the Ni and Fe ions released from the $Ti_{50}Ni_{50-x}Fe_x$ SMAs were probably caused by the fact that the NiO and Fe_2O_3 oxides, formed on the surfaces of the $Ti_{50}Ni_{50-x}Fe_x$ SMAs reduced the uniformity of the TiO_2 oxide films and thereby compromised the protective effect of the films. Selectively leached Ni and Fe ions may pose a risk in biomedical applications; therefore, a surface modification is required if the $Ti_{50}Ni_{50-x}Fe_x$ SMAs are to be used as implant materials.

Acknowledgements

The authors gratefully acknowledge the financial support for this research provided by the Ministry of Science and Technology (MOST), Taiwan, Republic of China, under Grant No. MOST103-2221-E-197-007.

6 REFERENCES

[1] K. Otsuka, X. Ren, Physical metallurgy of Ti–Ni-based shape memory alloys, Progress in Materials Science, 50 (**2005**) 5, 511–678, doi:10.1016/j.pmatsci.2004.10.001

[2] M. Assad, N. Lemieux, C. H. Rivard, L'H. Yahia, Comparative in vitro biocompatibility of nickel-titanium, pure nickel, pure titanium, and stainless steel: genotoxicity and atomic absorption evaluation, Bio-Medical Materials and Engineering, 9 (**1999**) 1, 1–12

[3] M. Es-Souni, M. Es-Souni, H. F. Brandies, Assessing the biocompatibility of NiTi shape memory alloys used for medical applications, Analytical and Bioanalytical Chemistry, 381 (**2005**) 3, 557–567, doi:10.1007/s00216-004-2888-3

[4] M. Assad, A. Chernyshov, M. A. Leroux, C. H. Rivard, A new porous titanium-nickel alloy: Part 1, Cytotoxicity and genotoxicity evaluation, Bio-Medical Materials and Engineering, 12 (**2002**) 3, 225–237

[5] P. Filip, J. Lausmaa, J. Musialek, K. Mazanec, Structure and surface of TiNi human implants, Biomaterials, 22 (**2001**) 15, 2131–2138, doi:10.1016/S0142-9612(00)00404-X

[6] K. Kuribayashi, K. Tsuchiya, Z. You, D. Tomus, M. Umemoto, T. Ito, M. Sasaki, Self-deployable origami stent grafts as a biomedical application of Ni-rich TiNi shape memory alloy foil, Materials Science and Engineering, A 419 (**2006**) 1–2, 131–137, doi:10.1016/j.msea.2005.12.016

[7] J. Y. Xiong, Y. C. Li, X. J. Wang, P. D. Hodgson, C. E. Wen, Titanium–nickel shape memory alloy foams for bone tissue engineering, Journal of the Mechanical Behavior of Biomedical Materials, 1 (**2008**) 3, 269–273, doi:10.1016/j.jmbbm.2007.09.003

[8] E. Goo, T. Duerig, K. Melton, R. Sinclair, Mechanical twinning in $Ti_{50}Ni_{47}Fe_3$ and $Ti_{49}Ni_{51}$ alloys, Acta Metallurgica, 33 (**1985**) 9, 1725–1733, doi:10.1016/0001-6160(85)90167-1

[9] C. M. Hwang, C. M. Wayman, Phase transformations in TiNiFe, TiNiAl and TiNi alloys, Scripta Metallurgica, 17 (**1983**) 11, 1345–1350, doi:10.1016/0036-9748(83)90230-2

[10] W. J. Moberly, J. L. Proft, T. W. Duerig, R. Sinclair, Deformation, twinning and thermo-mechanical strengthening of $Ti_{50}Ni_{47}Fe_3$, Acta Metallurgica et Materialia, 38 (**1990**) 12, 2601–2612, doi:10.1016/0956-7151(90)90272-I

[11] G. Fan, Y. Zhou, K. Otsuka, X. Ren, Ultrahigh damping in R-phase state of Ti–Ni–Fe alloy, Applied Physics Letters, 89 (**2006**) 16, 161902, doi:10.1063/1.2363173

[12] I. Yoshida, D. Monma, T. Ono, Damping characteristics of $Ti_{50}Ni_{47}Fe_3$ alloy, Journal of Alloys and Compounds, 448 (**2008**) 1–2, 349–354, doi:10.1016/j.jallcom.2007.04.217

[13] G. Fan, Y. Zhou, K. Otsuka, X. Ren, T. Suzukib, F. Yin, Comparison of the two relaxation peaks in the $Ti_{50}Ni_{48}Fe_2$ alloy, Materials Science and Engineering, A, 521–522 (**2009**) 15, 178–181, doi:10.1016/j.msea.2008.09.086

[14] D. Wang, Z. Zhang, J. Zhang, Y. Zhou, Y. Wang, X. Ding, Y. Wang, X. Ren, Strain glass in Fe-doped Ti–Ni, Acta Materialia, 58 (**2010**) 18, 6206–6215, doi:10.1016/j.actamat.2010.07.040

[15] C. Li, Y. F. Zheng, The electrochemical behavior of a $Ti_{50}Ni_{47}Fe_3$ shape memory alloy, Materials Letters, 60 (**2006**)13–14, 1646–1650, doi:10.1016/j.matlet.2005.11.097

[16] T. A. Tabish, T. Z. Butt, M. Ali, M. Ali, R. S. Shaikh, S. Atiq, L. Draghi, In vivo cytotoxic evaluation of Ti–Ni–Fe shape memory alloys, Materials Technology: Advanced Performance Materials, 29 (**2014**) 3, 139–143, doi:10.1179/1753555713Y.0000000091

[17] K. Takamura, K. Hayashi, N. Ishinishi, T. Yamada, Y. Sugioka, Evaluation of carcinogenicity and chronic toxicity associated with orthopedic implants in mice, Journal of Biomedical Materials Research, 28 (**1994**) 5, 583–589, doi:10.1002/jbm.820280508

[18] H. Takahashi, M. Kinbara, N. Sato, K. Sasaki, S. Sugawara, Y. Endo, Nickel allergy-promoting effects of microbial or inflammatory substances at the sensitization step in mice, International Immunopharmacology, 11 (**2011**) 10, 1534–1540, doi:10.1016/j.intimp.2011.05.010

[19] V. D'Antò, A. Eckhardt, K. A. Hiller, G. Spagnuolo, R. Valletta, L. Ambrosio, G. Schmalz, H. Schweikl, The influence of Ni(II) on surface antigen expression in murine macrophages, Biomaterials, 30 (**2009**) 8, 1492–1501, doi:10.1016/j.biomaterials.2008.12.004

[20] C. L. Chu, C. Guo, X. B. Sheng, Y. S. Dong, P. H. Lin, K. W. K. Yeung, P. K. Chu, Microstructure, nickel suppression and mechanical characteristics of electropolished and photoelectrocatalytically oxidized biomedical nickel titanium shape memory alloy, Acta Biomaterialia, 5 (**2009**) 6, 2238–2245, doi:10.1016/j.actbio.2009.01.046

[21] E. Espinar, J. M. Llamas, A. Michiardi, M. P. Ginebra, F. J. Gil, Reduction of Ni release and improvement of the friction behaviour of NiTi orthodontic archwires by oxidation treatments, Journal of Materials Science, Materials in Medicine, 22 (**2011**), 1119–1125, doi:10.1007/s10856-011-4292-9

[22] F. J. Gil, E. Espinar, J. M. Llamas, J. M. Manero, M. P. Ginebra, Variation of the superelastic properties and nickel release from original and reused NiTi orthodontic archwires, Journal of the Mechanical Behavior of Biomedical Materials, 6 (**2012**), 113–119, doi:10.1016/j.jmbbm.2011.11.005

[23] S. H. Chang, W. C. Chiu, Selective leaching and surface properties of $Ti_{50}Ni_{50-x}Cu_x$ (x = 0–20 % of amount fractions) shape memory alloys for biomedical applications, Applied Surface Science, 324 (**2015**), 106–113, doi:10.1016/j.apsusc.2014.10.030

[24] Y. W. Gu, B. Y. Tay, C. S. Lim, M. S. Yong, Characterization of bioactive surface oxidation layer on NiTi alloy, Applied Surface Science, 252 (**2005**) 5, 2038–2049, doi:10.1016/j.apsusc.2005.03.207

[25] R. M. Wang, C. L. Chu, T. Hu, Y. S. Dong, C. Guo, X. B. Sheng, P. H. Lin, C.Y. Chung, P. K. Chu, Surface XPS characterization of NiTi shape memory alloy after advanced oxidation processes in UV/H_2O_2 photocatalytic system, Applied Surface Science, 253 (**2007**) 20, 8507–8512, doi:10.1016/j.apsusc.2007.04.018

[26] C. L. Chu, C. Guo, X. B. Sheng, Y. S. Dong, P. H. Lin, K. W. K. Yeung, P. K. Chu, Microstructure, nickel suppression and mechanical characteristics of electropolished and photoelectrocatalytically oxidized biomedical nickel titanium shape memory alloy, Acta Biomaterialia, 5 (**2009**) 6, 2238–2245, doi:10.1016/j.actbio.2009.01.046

[27] C. L. Chu, C.Y. Chung, P. K. Chu, Surface oxidation of NiTi shape memory alloy in a boiling aqueous solution containing hydrogen peroxide, Materials Science and Engineering A, 417 (**2006**) 1–2, 104–109, doi:10.1016/j.msea.2005.11.010

[28] D. Vojtěch, M. Voděrová, J. Fojt, P. Novák, T. Kubásek, Surface structure and corrosion resistance of short-time heat-treated NiTi shape memory alloy, Applied Surface Science, 257 (**2010**) 5, 1573–1582, doi:10.1016/j.apsusc.2010.08.097

[29] S. A. Shabalovskaya, G. C. Rondelli, A. L. Undisz, J. W. Anderegg, T. D. Burleigh, M. E. Rettenmayr, The electrochemical characteristics of native Nitinol surfaces, Biomaterials, 30 (**2009**) 22, 3662–3671, doi:10.1016/j.biomaterials.2009.03.034

[30] S. A. Shabalovskaya, H. Tian, J. W. Anderegg, D. U. Schryvers, W. U. Carroll, J. Van Humbeeck, The influence of surface oxides on the distribution and release of nickel from Nitinol wires, Biomaterials, 30 (**2009**) 4, 468–477, doi:10.1016/j.biomaterials.2008.10.014

UDK 66.017:549.324/.326(234.32)(497.4)
Original scientific article/Izvirni znanstveni članek

ISSN 1580-2949
MTAEC9, 51(2)259(2017)

TEMPERATURE-INITIATED STRUCTURAL CHANGES IN FeS_2 PYRITE FROM POHORJE, EASTERN ALPS, NORTH-EASTERN SLOVENIA

S TEMPERATURO POVZROČENE STRUKTURNE SPREMEMBE FeS_2 PIRITA IZ POHORJA, VZHODNE ALPE, SEVEROVZHODNA SLOVENIJA

[1]Blaž Leskovar, [2]Mirijam Vrabec, [2]Matej Dolenec, [1]Iztok Naglič, [2]Tadej Dolenec,
[3]Evgen Dervarič, [1]Boštjan Markoli

[1]University of Ljubljana, Faculty of Natural Sciences and Engineering, Department of Materials and Metallurgy, Ljubljana, Slovenia
[2]University of Ljubljana, Faculty of Natural Sciences and Engineering, Department of Geology, Ljubljana, Slovenia
[3]University of Ljubljana, Faculty of Natural Sciences and Engineering, Department of Mining and Geotechnology, Ljubljana, Slovenia
leskovarblaz@gmail.com

Prejem rokopisa – received: 2015-11-02; sprejem za objavo – accepted for publication: 2016-03-31

doi:10.17222/mit.2015.328

X-ray phase analysis (XRD), differential thermal analysis (DTA) and X-ray fluorescence spectroscopy (XRF) of pyrite samples in a protective (Ar) and an oxidative atmosphere (air) at different temperatures (200, 300, 500, 700) °C and times (1, 2, 4) h were made. A graphical representation of the unit cell of magnetic pyrrhotite and diffraction patterns of the individual crystal structures of pyrite, which occur in the sample at selected temperatures, atmosphere, and exposure times were analyzed with X-ray diffraction software (CrystalMaker). The results show that FeS_2 exhibited temperature-dependent changes in the crystal structure that are not included in current Fe-S phase diagrams.

Keywords: Pohorje, Eastern Alps, structural changes, FeS_2 pyrite, XRD, XRF, DTA

Vzorci pirita so bili analizirani s pomočjo rentgenske fazne analize (XRD), diferenčne termične analize (DTA) in rentgenske fluorescentne spektroskopije (XRF) po žarjenju v zaščitni (Ar) in oksidativni atmosferi (zrak) pri različnih temperaturah (200, 300, 500 in 700) °C in časih (1, 2 in 4) h. S programsko opremo (CrystalMaker) je grafično predstavljena osnovna celica magnetnega pirotita. Analizirani so tudi rentgenogrami posameznih kristalnih struktur pirita, ki se pojavijo v vzorcu pri določenih temperaturah, atmosferi in časih žarjenja. Rezultati kažejo, da pirit izkazuje temperaturno odvisne spremembe v kristalni strukturi, ki niso vključene v dosedanje fazne diagrame Fe-S.

Ključne besede: Pohorje, Vzhodne Alpe, strukturne spremembe, pirit (FeS_2), XRD, XRF, DTA

1 INTRODUCTION

Pyrite is the most common and widespread of the sulfide minerals, found in a wide variety of geological formations. It occurs as magmatic segregations, as an accessory mineral in igneous rocks, in contact metamorphic deposits, in large hydrothermal veins and in many sedimentary rocks. In these rocks the pyrite is usually found associated with other sulfides or oxides and is often mined for the gold or copper associated with it. Despite a high Fe content (46.55 % of mass fractions), pyrite has never been used as a significant source of iron. Because of the large amount of sulfur present in the mineral, it is used as an iron ore only in those countries where oxide iron ores are not available. Iron is produced from pyrite by roasting, causing complete oxidation and removal of the sulfur; the latter is the reason for the brittleness in iron and its alloys.[1,2] During the early years of the 20th century, pyrite was used as a mineral detector in radio receivers, and is still used by 'crystal radio' hobbyists. Pyrite detectors occupied a midway point between galena detectors and the more mechanically complicated perikon mineral pairs.[3,4] Pyrite is a semiconducting material with band gap of 0.95 eV.[5] It has been proposed as an abundant, inexpensive material in low-cost photovoltaic solar panels.[6] Pyrite still remains in commercial use for the production of sulfur dioxide, in the paper industry, and in the production of sulfuric acid. It is also a source of sulfur, for the production of tires, explosives, disinfectants, medicines, ink, wood preservatives, dyes and matches.[1] Pyrite is also used as the cathode material in the Energizer brand of non-rechargeable lithium batteries.[7]

Although pyrite is the principal constituent of many ore bodies, it is absent in some high-temperature deposits formed from liquids and gases, suggesting clear dependency of the pyrite crystallization under restricted temperature conditions.[8] In this paper, the phase transformation of pyrite as a function of temperature, time and atmosphere are studied in order to clarify its stability and changes in crystal structure in the range of 33 % of mass fractions to 60 % of mass fractions of S in an inert atmosphere and the path of pyrite decomposition in the oxidative atmosphere.

2 GEOLOGICAL BACKGROUND AND SAMPLE LOCATIONS

The Pohorje Mountains are located at the south-eastern margin of the Eastern Alps in north-eastern Slovenia. They represent ultrahigh-pressure metamorphic terrane and are built up of three Eo-Alpine nappes that belong to pre-Neogene metamorphic sequences of Austroalpine units of the Eastern Alps. Structurally, the lowest nappe represents the Lower Central Austroalpine and consists of medium- to high-grade metamorphic rocks, predominantly micaschists, gneisses and amphibolites with marble and quartzite lenses. It also contains several eclogite lenses and a body of metaultrabasic rocks. The Pohorje nappe is overlain by nappe composed of weakly metamorphosed Paleozoic rocks, mainly low-grade metamorphic slates and phyllites. The uppermost nappe is built up of Permo-Triasic clastic sedimentary rocks, mainly sandstones and conglomerates. The two latter nappes represent the Upper Central Austroalpine.[9,10] The entire nappe stack is overlain by Early Miocene sediments that belong to the svn-rift basin fill of the Pannonian Basin.[11] The central part of Pohorje is occupied by granodioritic to tonalitic intrusion of Miocene age (18-19 Ma).[12,13]

Pyrite mines in Zgornja Polskava are located along the creek where several exploratory tunnels were dug in a sequence of metapelitic rocks. The GPS geographic coordinates of the mines are as follows: N 46°25’54.8’’, E 15°35’40.0’’.

Pyrite crystals occur within tremolite forming more than 50-cm-thick layers or veins in metapelitic country rocks.[14,15] These are mostly gneisses and micaschists that formed under high-pressure and high-temperature conditions of 2.2–2.7 GPa and 700–800 °C. They are medium-grained rocks with a granoblastic texture composed mostly of quartz, mica, biotite, garnet, kvanite, plagioclase and K feldspar. Metapelitic rocks in the investigated area are more or less intensively limonitized.[9,10,16]

3 FORMATION OF PYRITE AND SAMPLE DESCRIPTION

The samples of pyrite that were used for the analyses were taken from the mine in Zgornja Polskava, which was operational from 1916 to 1920. The ore was mainly used for the production of sulfuric acid. In abandoned mine tunnels, pyrite cubes from 2 mm to 20 mm in size and more can still be found today.[15,17] From **Figure 1** it is clear that analyzed samples are brass yellow modified cubes with typical pyrite striations on the surface. In places pyrite crystals are limonitized and contain rare quartz veins. The size of the samples is approximately (20 × 20 × 20) mm.

Pyrite forms in high-temperature veins at temperatures from 300 °C to 400 °C.[16] The rock around the veins is characterized by a red color, which is due to the presence of hematite dispersed in the sequence of metapelitic rocks. For hydrothermal ore deposits of this type it is characteristic that sulfides are found in the green, gray and black layers, which alternate with the red layer.[18]

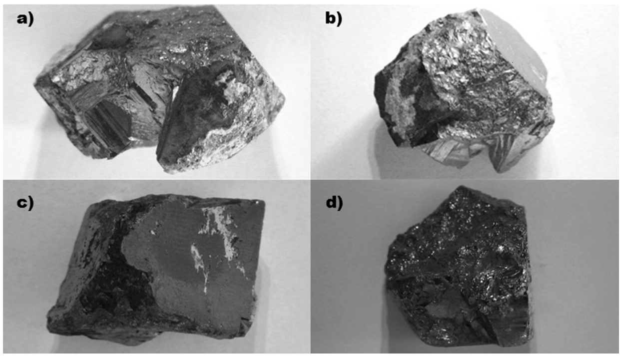

Figure 1: Analyzed samples of pyrite
Slika 1: Vzorci pirita uporabljeni za analize

The binary phase diagram Fe-S reported by Kubaschewski[19] is shown in **Figure 2**. The crystal structure of pyrite (α, β) transforms into the pyrrhotite (α, β, γ) when the sulfur concentration is decreasing or the temperature is rising. With increasing temperature the pyrite decomposes into pyrrhotite (γFeS) and liquid at a temperature of 743 °C. Because of the low boiling point of sulfur (444.6 °C) at atmospheric pressure the free bonded atoms evaporate (irreversible reaction). With decreasing temperature the crystal structures of γFeS ($P6_3/mmc$) transform to βFeS ($P\bar{6}2c$) at 315 °C and then βFeS into αFeS (unknown crystal structure by Kubaschewski).

4 MATERIALS AND METHODS

4.1 X-ray powder diffraction (XRD)

A Philips X-ray diffractometer with a PW3830 generator was used for the XRD analyses. The patterns were recorded with the following parameters: voltage 40 kV,

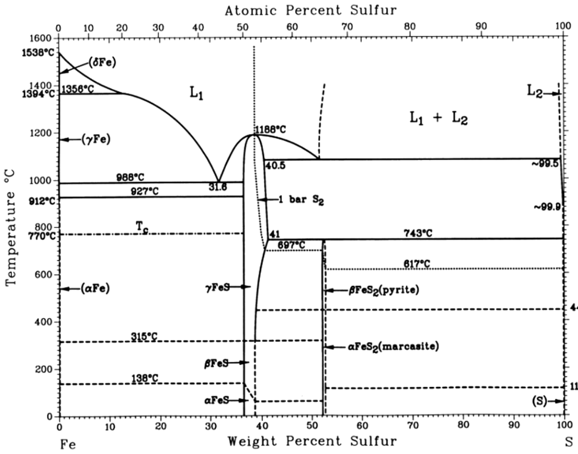

Figure 2: Phase diagram Fe-S[19]
Slika 2: Fazni diagram Fe-S[19]

current 30 mA, wavelength of light used X-ray Cu–$K\alpha$ 0.15418 nm, secondary graphite monochromator and proportional counter. The angle 2θ was recorded in the range of 0° to 70°, at a rate of 1.2° 2θ/min. The limit of detection of the minerals in the sample is 1–3 %.

4.2 X-ray fluorescent spectroscopy (XRF)

A portable (field) X-ray fluorescence analyzer NITON (model XL3t + GOLDD-900S He) was used to determine the quantity of each element in the sample. The method allows a quantitative analysis of more than 80 elements, from magnesium to uranium. When measuring, we used the module "Mining". During the measurement the sampling site was pumped with helium gas for the better detection of light elements (Mg, Si, Al, P). The measurement time for each sample was 210 s.

4.3 Differential thermal analysis (DTA) and differential scanning calorimetry (DSC)

DSC was performed on a STA 449 Jupiter device by NETZSCH. All the analyses were carried out in a protective argon atmosphere or air. The experiments were conducted at heating/cooling rates of 10 °C/min, according to the Heat Flux mode. In this mode the investigative and comparative sample are heated with the same heat source.

5 RESULTS AND DISCUSSION

The phase transformations of pyrite are defined as a function of temperature, time and atmosphere. The crystal structures of the phases that occur in the sample at various temperatures and times in the presence of a protective (Ar) or the oxidizing atmosphere (air) were determined by means of X-ray structural analysis. The purity of each sample was identified using X-ray fluorescence spectroscopy. The presence of the chemical reactions or changes in the crystal structure was traced by DSC. The temperatures of the heating were (300, 500 and 700) °C. At each temperature we held the samples for (1, 2 and 4) h. The DSC experiments were carried out according to a temperature program of 10 °C min^{-1} to 800 °C to trace changes in FeS$_2$ that were not found in Fe-S phase diagram. The crystal structure of the sample was defined with the help of a computer program CrystalMaker and Atlas of Crystal Structure Types for Intermetallic Phases.[20,21]

5.1 Annealing pyrite in air at 300 °C

In the crystal structure of pyrite no changes occurred after annealing at a temperature of 300 °C for 4 h. The sample consisted of pyrite and quartz. The diffraction pattern for the sample after annealing at 300 °C for 4 h is shown in **Figure 3**.

The unit cell of pyrite is a cubic crystal lattice with a point symmetry by Hermann-Mauguin notation (HM) $m\overline{3}$ (there is mirror plane in the direction of a and 3-fold rotational axis with inversion ($\overline{3}$) in the direction of b axis), and a space group Pa$\overline{3}$, that illustrates the primitive lattices (P), a glide plane in the direction of the a axis and the 3-fold rotational axis with the inversion ($\overline{3}$) in the direction of the b axis. The unit cell of α-quartz represents a trigonal crystal system with a point symmetry (HM) 32 (which illustrates the 3-fold axis in the direction of the a axis and 2-fold rotational axis in the direction of the b axis) and the space group P$3_2$21 (primitive lattice (P), the screw axis with the 3-fold rotation in the direction of a axis (triad) and a 2-fold rotational axis in the direction of the b axis).

5.2 Annealing pyrite in air at 500 °C

Already after one hour of annealing at 500 °C a change in the crystal structure appeared. It can be seen that the intensity of the peaks representing the crystal structure of pyrite decreased (the amount of the crystalline structure of pyrite decreased) and new peaks arose, which represented new crystal structures. With the help of diffraction patterns it was found that along with the

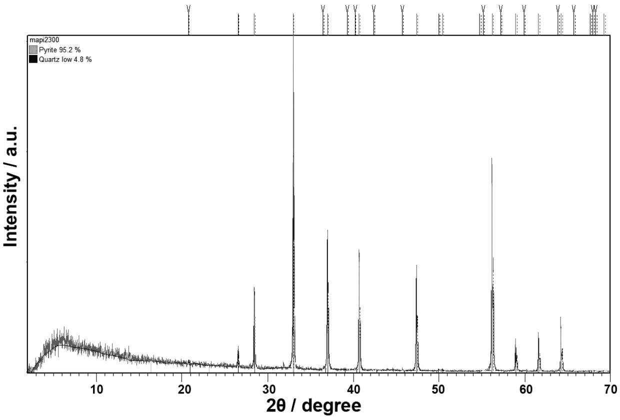

Figure 3: XRD analysis of a sample annealed at 300 °C for 4 h
Slika 3: Rentgenogram vzorca žarjenega 4 h na temperaturi 300 °C

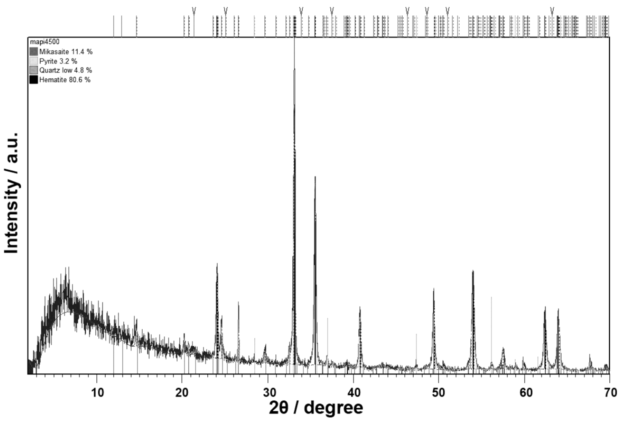

Figure 4: XRD analysis of a sample annealed at 500 °C for 4 h
Slika 4: Rentgenogram vzorca žarjenega 4 h na temperaturi 500 °C

crystal structure of pyrite and the quartz crystal structure of hematite (Fe_2O_3) and mikasaite or iron(III)sulfate ($Fe_2(SO_4)_3$) appeared. The amount of hematite increased with the annealing time, while the amount of pyrite and iron(III)sulfate decreased. The amount of quartz was equal during the time of annealing. **Figure 4** has the diffraction pattern of a sample made after annealing at 500 °C for 4 h.

The unit cell of the iron(III)sulfate belongs to the trigonal crystal system with a point symmetry (HM) $\overline{3}$ (3-fold rotation axis with inversion in the direction of *a* axis), and a space group $R\overline{3}$ (rhombohedral lattice R and the 3-fold rotation with the inversion in the direction of the *a* axis). The basic cell of hematite (α-hematite) belongs to the trigonal crystal system with a symmetry point (HM) $\overline{3}2/m$ (which represents a 3-fold rotational axis with the inversion in the direction of the *a* axis and a 2-fold rotational axis with the mirror plane in the direction of the b axis) and space group $R\overline{3}c$ (rhombohedral lattice R, 3-fold rotation axis with inversion in the direction of the *a* axis, and a glide plane in the direction of the *c* axis).

5.3 Annealing pyrite in air at 700 °C

Already after one hour of annealing at 700 °C the sample consisted of the crystal structure of hematite with only a small amount of quartz. The temperature was so high that the sulfur evaporated and reacted with the oxygen in the atmosphere to form sulfur dioxide. Oxygen from the atmosphere diffused into the sample and formed hematite. **Figure 5** shows the diffraction pattern of the sample made after annealing at 700 °C for 4 h.

5.4 The X-ray fluorescent spectroscopy

Table 1 presents the weight percentages of the chemical elements and the relative error in the calculation of weight fraction of the chosen elements. Presented are the three samples that were heated to 300 °C, 500 °C and 700 °C and exposed for 4 h to air.

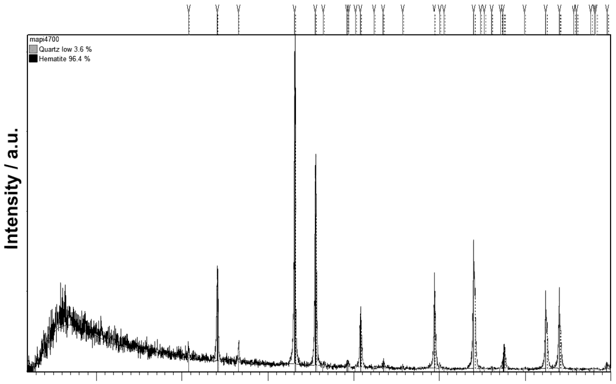

Figure 5: XRD analysis of a sample annealed at 700 °C for 4 h
Slika 5: Rentgenogram vzorca žarjenega 4 h na temperaturi 700 °C

The sample annealed at 300 °C had about 37 % of mass fractions of Fe, and approximately 60 % of mass fractions of S. Due to the fact that the chemical composition of pyrite corresponds to 46.55 wt. % Fe and 53.45 % of mass fractions of S, it can be concluded that some atoms of sulfur are free and bonded to the surface of the sample. It can also be assumed that a small amount of tremolite $Ca_2Mg_5Si_8O_{22}(OH)_2$ is present (in which one can find pyrite) and some metamorphic rocks, specifically gneiss (location of exploratory tunnels of pyrite), due to the presence of other chemical elements.

Table 1: Chemical composition of samples annealed at (300, 500 and 700) °C in air (X-ray fluorescent spectroscopy, *w*/%)
Tabela 1: Kemična sestava vzorcev žarjenih na zraku pri temperaturah (300, 500 in 700) °C (rentgenska fluorescentna spektroskopija, *w*/%)

Temperature	Chemical element					
	Fe	Fe Error	S	S Error	Si	Si Error
300 °C	37.49	0.14	60.77	0.13	0.01	0.02
500 °C	53.72	0.46	17.63	0.11	4.37	0.05
700 °C	71.82	0.75	0.18	0.01	6.65	0.07
	Al	Al Error	Ca	Ca Error	Cl	Cl Error
300 °C	0.04	0.07	0.02	0.01	0.97	0.02
500 °C	2.98	0.11	0.13	0.02	0.14	0.01
700 °C	1.03	0.06	0.19	0.02	0.23	0.01
	Mg	Mg Error	P	P Error	As	As Error
300 °C	0.24	0.24	0.14	0.03	0.22	0.00
500 °C	0.94	0.22	0.13	0.02	0.33	0.01
700 °C	0.00	0.11	0.12	0.01	0.07	0.01

5.5 Differential scanning calorimetry (DSC)

To determine the beginning of the phase transformations in air, differential scanning calorimetry was used. **Figure 6** has a DSC heating curve for a run carried out using a heating/cooling rate of 10 °C/min on a sample of pure pyrite.

Pyrite was first transformed into an iron(III)sulfide, which then further dissociated into hematite. We believe that the disintegration process took place according to the following chemical reactions in Equations (1), (2) and (3):

$$2FeS_2(s) + 7O_2(g) \rightarrow Fe_2(SO_4)_3(s) + SO_2(g) \qquad (1)$$

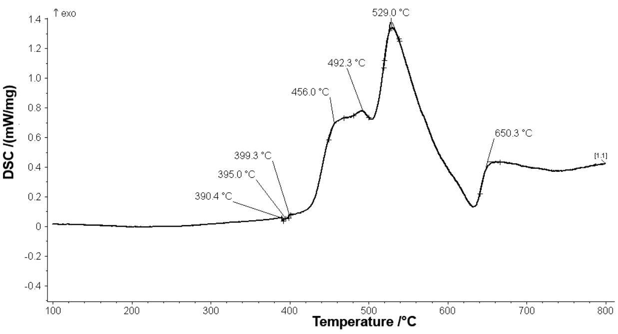

Figure 6: DSC heating curve for pyrite in air
Slika 6: DSC-krivulja segrevanja pirita na zraku

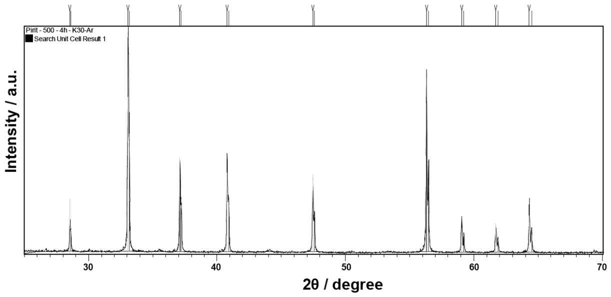

Figure 7: XRD analysis of a sample annealed at 500 °C for 4 h
Slika 7: Rentgenogram vzorca žarjenega 4 h na temperaturi 500 °C

$$Fe_2(SO_4)_3(s) \Leftrightarrow Fe_2O_3(s) + 3SO_3(g) \qquad (2)$$

$$SO_2(g) + 0{,}5O_2(g) \Leftrightarrow SO_3(g) \qquad (3)$$

Apparently, the disintegration of iron(III)sulfide is obviously complicated as it involves three partial reactions. So, the total rate of disintegration or conversion of iron(III)sulfide into hematite depends on the partial rate of each individual reaction listed above.

5.6 Annealing pyrite in a protective atmosphere (argon) at 200 °C, 300 °C and 500 °C

Annealing in a protective atmosphere at 500 °C does not lead to the transformation of pyrite. The **Figure 7** shows a diffraction pattern of a sample after annealing at 500 °C for 4 h.

5.7 Annealing pyrite in a protective atmosphere (argon) at 700 °C

Already after one hour of sample annealing at 700 °C it can be observed that the crystalline structure of pyrite transformed to the magnetic pyrrhotite Fe_7S_8. **Figure 8** has a diffraction pattern of magnetic pyrrhotite and the corresponding unit cell as generated by CrystalMaker. Additionally, there is the diffraction pattern of a sample made after annealing at 700 °C for 4 h.

The basic cell of magnetic pyrrhotite Fe_7S_8, **Figure 8c**, belongs to the trigonal crystal system, point group (HM) $\overline{3}$ (3-fold axis with the inversion in the direction of the *a* axis), and the space group $R\overline{3}$ (rhombohedral lattice R, and the 3-fold axis with the inversion in the direction of the *a* axis).

5.8 The X-ray fluorescent spectroscopy (argon)

Table 2 presents the weight percentages of chemical elements and the relative error in the calculation of the weight fraction of each element. Presented are the three samples that were heated to (300, 500 and 700) °C and exposed for 4 h in argon.

Table 2: Chemical composition of samples annealed at (300, 500 and 700) °C in argon (X-ray fluorescent spectroscopy, w/%)
Tabela 2: Kemijska sestava vzorcev žarjenih v zaščitni atmosferi (Ar) pri temperaturah 300 °C, 500 °C in 700 °C (rentgenska fluorescenčna spektroskopija, w/%)

Temperature	Chemical element					
	Fe	Fe Error	S	S Error	Si	Si Error
300 °C	35.47	0.03	32.25	0.02	0.71	0.07
500 °C	35.41	0.07	32.12	0.01	0.78	0.11
700 °C	47.18	0.02	23.29	0.02	2.98	0.07
	Al	Al Error	Ca	Ca Error	Cl	Cl Error
300 °C	-	0.07	0.02	0.07	0.04	0.06
500 °C	0.16	0.13	0.02	0.03	0.05	-
700 °C	0.33	0.03	0.07	0.05	0.05	-
	Cr	Cr Error	Mg	Mg Error	As	As Error
300 °C	0.02	0.00	-	0.09	0.08	-
500 °C	0.02	0.00	0.88	0.05	0.08	0.00
700 °C	0.03	0.00	0.01	0.00	0.00	0.00

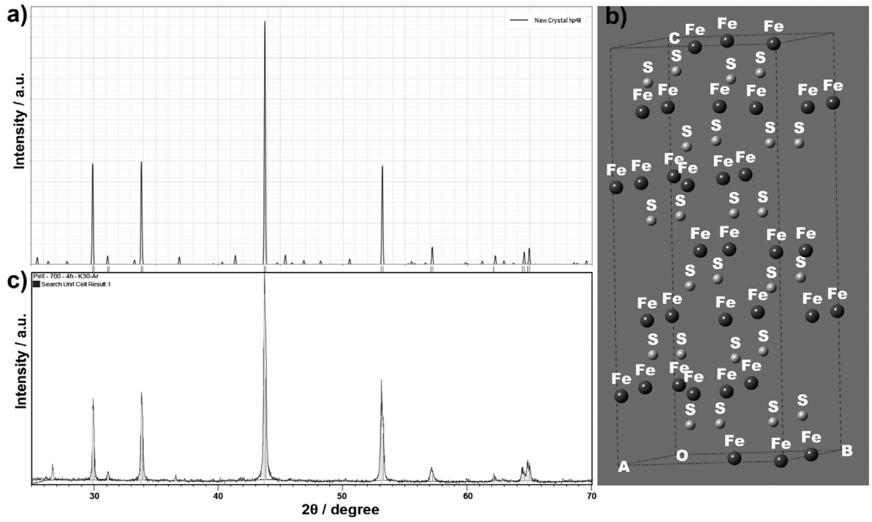

Figure 8: XRD analysis of a sample annealed at 700 °C for 4 h: a) diffraction pattern of magnetic pyrrhotite, b) with its unit cell and c) the diffraction pattern of the sample
Slika 8: Rentgenogram vzorca žarjenega 4 h pri temperaturi 700 °C: a) generiran rentgenogram magnetnega pirotita, b) z osnovno celico in c) rentgenogram žarjenega vzorca

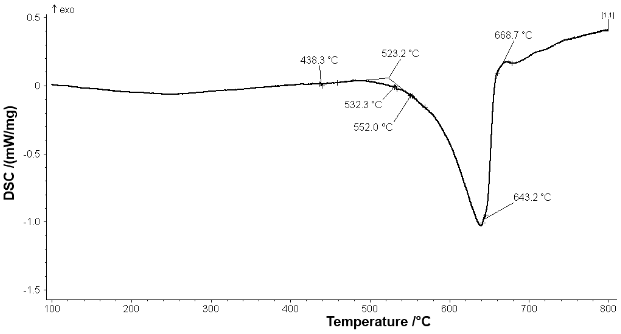

Figure 9: DSC heating curve of pyrite in argon
Slika 9: DSC-krivulja segrevanja pirita v zaščitni atmosferi (Ar)

As can be seen from **Table 2**, we have a sample of about 35 wt. % of Fe and about 32 wt. % of S. Since the X-ray fluorescence spectroscopy cannot detect light chemical elements, from H to Na, these could have not been analyzed. Hence, the mass percentages of the remaining chemical elements do not sum up 100 wt. %. The difference can be attributed to the presence of light elements.

5.9 Differential scanning calorimetry (DSC)

To determine the beginning of the phase transformations in a protective atmosphere we again turned to differential scanning calorimetry. In **Figure 9** the DSC heating curve for the sample of pyrite was carried out using a temperature program of 10 °C/min in argon.

From the heating DSC curve we can see that the change in the crystalline structure of pyrite ($Pa\bar{3}$) into the magnetic pyrrhotite ($R\bar{3}$) started at about 530 °C. The transformation of pyrite in a protective atmosphere takes place according to the following chemical reaction in Equation (4):

$$7FeS_2(s) \Leftrightarrow Fe_7S_8(s) + 3S_2(g) \qquad (4)$$

6 CONCLUSIONS

Based on the results of the X-ray fluorescence spectroscopy, X-ray phase analysis and differential thermal analysis, we can conclude the following:

- The largest amount of impurities in the pyrite samples was represented by quartz and some heavier elements, but these were present with a very low content.
- The process of pyrite decomposition in the oxide atmosphere depends heavily on the temperature.
- The transformation of pyrite at a temperature of 500 °C takes place gradually by the formation of iron(III)sulphate, which is further oxidized into the crystal structure of hematite.
- At a temperature of 700 °C and the oxidizing atmosphere pyrite directly decomposed into hematite after only 1 h.
- The result of the dissolution of pyrite in a protective atmosphere is the formation of magnetic pyrrhotite Fe_7S_8. Direct transformation occurred already after 1 h of annealing at 700 °C.
- Finally, we established that pyrite is not stable up to 744 °C, as predicted by the Fe-S phase diagram, but rather undergoes changes into magnetic pyrrhotite.

Acknowledgement

I would like to thank all in the Dept. of Materials and Metallurgy and the Dept. of Geology who helped me in this project, especially in the preparation of samples and the interpretation of results.

7 REFERENCE

[1] T. Rosenqvist, Principles of extractive metallurgy, Tapir academic press, 2004

[2] B. Leskovar, B. Markoli. Spremembe kristalne strukture z?elezovega disulfida s temperaturo = Change in crystal structure of iron disulphide with temperature: diplomsko delo, Ljubljana, 2013

[3] T. H. Lee, The Design of CMOS Radio-Frequency Integrated Circuits, Cambridge University Press, 2004, 4-6

[4] United States Army Signal Corps, Radio Communication Pamphlet, U.S. Government Printing Office, 1919, 302-305

[5] T. H. Ellmer K., Iron Disulfide (Pyrite) as Photovoltaic Material: Problems and Opportunities, Proceedings of the 12th Workshop on Quantum Solar Energy Conversion – (QUANTSOL) 2000

[6] C. Wadia, A. P. Alivisatos, D. M. Kammen, Materials availability expands the opportunity for large-scale photovoltaics deployment, Environmental Science & Technology, 43 (**2009**) 6, 2072-7, doi:10.1021/es8019534

[7] Energizer Corporation, Lithium Iron Disulfide Handbook and Application Manual. Energizer Battery Manufacturing Inc., http://www.ruedespiles.com/images/PDFmedia/Fiche_technique_Pile_ENERGIZER_LR6_AA_Lithium.pdf, 28. 10. 2015

[8] G. Kullerud, H. S. Yoder, Pyrite stability relations in the Fe-S system, Economic Geology, 54 (**1959**) 4, 533-72, doi:10.2113/gsecongeo.54.4.533

[9] M. Janák, N. Froitzheim, B. Lupták, M. Vrabec, E. J. K. Ravna, First evidence for ultrahigh-pressure metamorphism of eclogites in Pohorje, Slovenia: Tracing deep continental subduction in the Eastern Alps, Tectonics, 23 (**2004**) 5, 1-10, doi:10.1029/2004TC001641

[10] M. Janak, N. Froitzheim, M. Vrabec, E. Krogh Ravna, J. Hoog, Ultrahigh-pressure metamorphism and exhumation of garnet peridotite in Pohorje, Eastern Alps, Journal of metamorphic Geology, 24 (**2006**) 1, 19-31, doi:10.1111/j.1525-1314.2005.00619.x

[11] L. Fodor, K. Balogh, I. Dunkl, Z. Pécskay, B. Koroknai, M. Trajanova, et al., Structural evolution and exhumation of the Pohorje-Kozjak Mts., Slovenia, Annales Universitatis Scientarum Budapestinensis, Sectio Geologica, 35 (**2003**) 118-9, doi:10.2478/v10096-010-0027-y

[12] N. Zupančič, Petrografske značilnosti in klasifikacija pohorskih magmatskih kamnin, Rudarsko-metalurški zbornik, 12 (1994) 101

[13] M. Trajanova, Z. Pecskay, T. Itaya, K-Ar geochronology and petrography of the Miocene Pohorje Mountains batholith (Slovenia), Geologica carpathica 59 (**2008**) 3, 247

[14] D. Preisinger, A. Novak, M. Jeršek, M. Chvatal, Rudniki : opuščeni rudniki v Sloveniji, Turistika, Golnik (**2010**), 122-123

[15] Pajtler F., Minerali občin Slovenska Bistrica in Oplotnica (nahajališče Janezov graben pri Polskavi), Zavod za kulturo Slovenska Bistrica, Slovenska Bistrica, (**2003**) 33-7

[16] R. Vidrih, M. Grm, Svet mineralov, Tehniška založba Slovenije, Ljubljana, 2002, 6-42

[17] F. Tućan, Mineralogija: Specijalna mineralogija, Školska knjiga, 1957, 8-10, 118-121

[18] J. Zavašnik, T. Dolenec, A. Rečnik. Nahajališče pirita pri Katarini nad Ljubljano = Pyrite occurance close to Katarina mountain near Ljubljana, 2009

[19] H. Okamoto, Phase diagrams of binary iron alloys, ASM International, 1993

[20] CrystalMaker Software Limited Centre for Innovation and Enterprise, Oxford University Begbroke Science Park, http://www.crystalmaker.com/, 20. 10. 2015

[21] J. L. C. Daams, P. Villars, J. H. N. Vucht, Atlas of Crystal Structure Types for Intermetallic Phases, ASM International, 1991

UDK 67.017:666.96:620.173
Original scientific article/Izvirni znanstveni članek

ISSN 1580-2949
MTAEC9, 51(2)267(2017)

LIGHTWEIGHT AGGREGATES MADE FROM FLY ASH USING THE COLD-BOND PROCESS AND THEIR USE IN LIGHTWEIGHT CONCRETE

LAHKI AGREGATI IZDELANI IZ ELEKTROFILTRSKEGA PEPELA S POSTOPKOM HLADNEGA VEZANJA IN NJIHOVA UPORABA ZA LAHKE BETONE

Ana Frankovič[1], Violeta Bokan Bosiljkov[1], Vilma Ducman[2]
[1]University of Ljubljana, Faculty of Civil and Geodetic Engineering, Jamova 2, 1000 Ljubljana, Slovenia
[2]Slovenian National Building and Civil Engineering Institute, Dimičeva 12, 1000 Ljubljana, Slovenia
vilma.ducman@zag.si

Prejem rokopisa – received: 2015-12-06; sprejem za objavo – accepted for publication: 2016-02-10

doi:10.17222/mit.2015.337

Aggregates made from fly ash have been developed by means of the cold-bonding process, with the addition of Portland cement as a binder at (10, 20, and 30) % of mass fractions, and by pouring the mixtures into moulds. After curing for 28 d the samples were processed into aggregate by crushing and sieving. An aggregate containing a weight percentage of 10 % of cement was additionally produced by pelletization on a granulating plate. The density, water-adsorption capacity, porosity, compressive strengths, and frost resistance of the samples were determined. The aggregates prepared by both routes were then used to make concrete samples, whose properties were then compared to those of conventional concrete made using limestone aggregate. The compressive strength of the concrete made with the granulated aggregate reached 16.0 MPa after 28 d, whereas that of the concrete made with crushed aggregate amounted to 24.1 MPa, and that of the conventional concrete was 34.6 MPa.

Keywords: fly ash, lightweight aggregates, density, compressive strength, frost resistance

Agregati izdelani iz elektrofiltrskega pepela so bili razviti s postopkom hladnega vezanja, z dodatkom (10, 20 in 30) % masnega deleža Portland cementa kot veziva in z ulivanjem mešanice v modele. Po 28 dnevnem strjevanju vzorcev so bili vzorci predelani v agregat z drobljenjem in sejanjem. Sestava, ki je vsebovala 10 masnih % cementa, je bila še dodatno peletizirana na plošči za granuliranje. Določene so bile: gostota, kapaciteta absorpcije vode, poroznost, tlačna trdnost in odpornost na zamrzovanje. Sestave, izdelane na oba načina, so bile uporabljene za izdelavo betonskih vzorcev, katerih lastnosti so bile primerjane z lastnostmi običajno izdelanega betona z uporabo sestave apnenca. Tlačna trdnost betona, izdelanega z granulirano sestavo, je dosegla 16,0 MPa po 28 dneh, medtem, ko je pri betonu izdelanem iz drobljenega agregata, znašala 24,1 MPa, pri običajnem betonu pa je bila 34,6 MPa.

Ključne besede: elektrofiltrski pepel, lahki agregati, gostota, tlačna trdnost, odpornost na zamrzovanje

1 INTRODUCTION

Although, if it has a suitable composition, fly ash can be added to cement to form a "blended cement", much of this ash is still deposited on landfill sites, causing an environmental burden. Apart from this, according to the European Waste Catalogue[1] fly ash is labelled as hazardous waste, so that even higher costs are incurred for landfilling. Because of these facts, more and more scientists have been trying to find new ways in which such ash could be used, e.g., for the development of alkali-activated materials, which are frequently named geopolymers[2,3], but also for the production of artificial aggregates.[4–13] Artificial aggregates can be obtained simply by the crushing and grinding of industrial waste if the basic starting material is bulk waste. If, however, the basic starting material is a fine powder, such as fly ash, such aggregate can be produced by several different routes, as follows:

1) by high-temperature procedures, e.g., foaming and/or sintering at elevated temperatures of approx. 1200 °C,
2) by a hydrothermal process at a temperature of approx. 250 °C (autoclaving),
3) by the cold bonding process, where consolidation takes place at room temperature.

In the last case a binding agent needs to be added to the mixture in order to achieve such consolidation. This agent is usually cement and/or water glass.[14–18]

In the first two processes a lot of energy is consumed, so that recently more effort has been put into investigations of cold-bonding processes.

The most common method for the preparation of aggregates from dust waste (e.g., fly ash) is granulation on a pelletization plate. The efficiency of granulation depends on the fineness of the fly ash, speed and time of rotation of the plate, as well as its inclination and the diameter of the plate [8,12,15,19]. From the point of view of costs, another more favourable method exists, in which there is no need for a pelletization plate, or for dry waste powder. This alternative method consists of mixing the raw material with a binder, and pouring the mixture into models. After the consolidation, setting, and hardening processes have been completed, the samples are crushed and sieved into different fractions.

Aggregates obtained in the above-described ways (especially granulation) almost always have lower densities. According to the definitions given in the standard EN 13055-1:2002 [20], lightweight aggregates (LWAs) are those whose maximum particle density does not exceed 2000 kg/m^3, and whose loose bulk density does not exceed 1200 kg/m^3.

For some decades lightweight aggregates have been used in concrete instead of ordinary aggregates, mainly because of their contribution to the improvement of thermo-insulation properties. Apart from this, if LWAs are used, then a reduction can be achieved in the concrete's own weight, which can be important in earthquake-prone areas, as well as in cases where the subsoil beneath the foundations has a low bearing capacity. During the last decade much attention has been paid to the role of LWAs with open porosity in the internal curing of concrete. This is because lightweight aggregates with such porosity can serve as water reservoirs, which are available for later hydration, thus leading to higher compressive strengths.[21–23] Many authors used lightweight aggregates made of fly ash in concreate to investigate the strength and durability of hardened concrete, and the influence of a lightweight fly-ash aggregate microstructure on the properties of concrete.[24–29] As expected, the compressive strength of LWAC is lower than the one produced by natural aggregate, even though LWAC can anyway serve as a structural concrete.[25] If fly-ash aggregate is sintered, it reaches a higher compressive strength of the aggregate itself, and consequently a higher compressive strength of the concrete is achieved.[26] For cold bonded (non fired) aggregate it is also reported that chloride penetration could be somewhat higher.[27] It is well recognized that by applying a sintering process the properties of LWAs are improved significantly,[27,29] but it shall be noted that the firing process contributes to a much higher production cost, and on the other hand it negatively influences the environmental impacts (contributing to higher CO$_2$ footprints).

The aim of the present work was to verify the usability of locally available fly ash (which due to the high loss on ignition is not suitable as an additive for cement) for the production of a lightweight aggregate, and to compare the results of the aggregate obtained by the granulation process to those obtained in the case when fly ash, together with a binding agent, is first poured into moulds and later crushed. The frost resistance of such an aggregate was also tested and optimised. The behaviour of both types of aggregate in the concrete matrix was also investigated.

Figure 1: The sieving curve corresponding to the investigated fly ash
Slika 1: Sejalna krivulja preiskovanega elektrofiltrskega pepela

2 EXPERIMENTAL PART

2.1 Basic starting materials

The basic starting material that was used to develop the investigated LWAs was fly ash, which was obtained as a by-product in the combustion of brown Indonesian coal. This particular type of fly ash contains only low amounts of sulphur. The results of a chemical analysis showed that this fly ash contains the following chemical components in the stated mass percentages: SiO$_2$ 27.57 %, Al$_2$O$_3$ 8.3 7%, Fe$_2$O$_3$ 16.24 %, MgO 7.06 %, CaO 22.99 %, Na$_2$O 0.67 %, K$_2$O 2.67 %, and TiO$_2$ 0.5 %. The loss on ignition amounts to 12.57 %. Because of its chemical composition, this type of fly ash is classified, according to EN 450-1[30], as an alumino-silicate fly ash. According to the results of a mineralogical analysis, it consists of a glassy phase (67 %), brownmillerite (9.1 %), quartz (8.3 %), lime (6.1 %), anhydrite (3.2 %), calcite, portlandite, and hematite.

The particle size distribution was determined by sieving the ash through sieves with diameters of 1.8 mm, 0.5 mm, 0.125 mm, 0.063 mm and 0.04 mm, as is shown in **Figure 1**. Most of the particles in the fly ash were smaller than 1 mm, 40 % of them being smaller than 0.04 mm. The Blaine finesse was determined according to EN 196-6 and it amounted to 2989 cm^2/g.

Table 1: Composition of mixtures for the preparation of the LWA
Tabela 1: Sestava mešanic za pripravo LWA

Composition	Mixture	Fly Ash (g)	Cement (g)	Water (g)
PT1	90 % FA + 10 % CEM	3600	400	2000
PT2	80 % FA + 20 % CEM	3200	800	2000
PT3	70 % FA + 30 % CEM	2800	1200	2000
GT1	90 % FA + 10 % CEM	3600	400	Added as necessary for the needs of the granulation process

The binding agent cement CEM I was added in different proportions, as shown in **Table 1**. A Cementol Hiperplast 179 superplasticizer was also used.

For the frost-resistance improvement a commercial air entraining admixture Cementol ETA S was added.

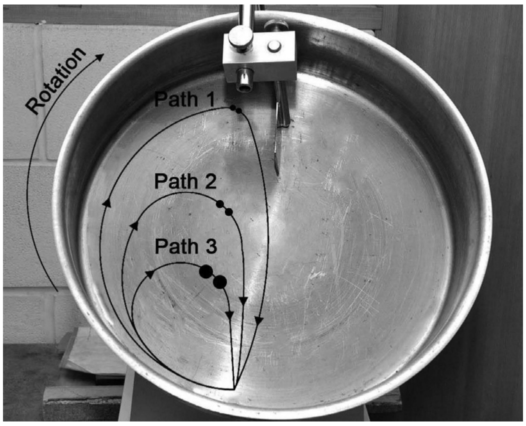

Figure 2: The granulating plate with a schematic presentation of the granulation process

Slika 2: Krožnik za granuliranje s shematskim prikazom procesa granulacije

2.2 Procedures for the production of the investigated LWA

The aggregates were produced by means of two different methods.

The aggregate that was designated "PT" was produced from prisms, which were made by first mixing the fly ash with the selected binder and water, and then pouring the mixture into standard mortar moulds. After curing in a climatic chamber at a temperature of 21 °C and a relative humidity of 94 % for 28 d, the prisms were crushed and then sieved into fractions of 0–1 mm, 1–2 mm, 2–4 mm, and 4–8 mm. The aggregate that was designated "GT" was produced by the pelletization procedure[31], using a rotating plate (**Figure 2**).

During the granulation phase the tilting angle was fixed at 60°, the mixer speed was 48 min^{-1}, and the mixing time was 2 min. The fly ash had been previously mixed with cement, and was then poured slowly onto the plate. During the granulation process, water droplets were added by spraying.

Both types of aggregate are shown in **Figure 3a** (the PT aggregate) and **3b** (the GT aggregate).

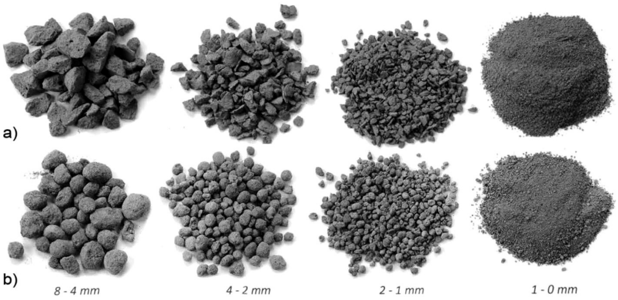

Figure 3: The final products: a) PT- made from crushed aggregate and b) GT- made from granulated aggregate

Slika 3: Končni proizvodi: a) PT – izdelan iz zdrobljenega agregata in b) GT – izdelan iz granuliranega agregata

Normal-weight aggregate, i.e., dense limestone aggregate from the Laže quarry in SW Slovenia, was used for the preparation of the blank concrete samples.

2.3 Characterization of the investigated aggregates

The porosity, pore size distribution, apparent density, and bulk density of the prepared aggregates were determined by means of mercury intrusion porosimetry (MIP). Particles having a size of approximately 1 cm^3 for each of the prepared artificial aggregates were dried in an oven for 24 h at 110 °C, and then analysed by means of MIP Autopore IV 9500 equipment (Micrometrics).

The microstructure of the polished cross-sections of the aggregate samples were examined using the backscattered electron (BSE) image mode of a low-vacuum scanning electron microscope (SEM) using JEOL 5500 LV equipment.

The water absorption of all three types of crushed aggregate (PT1, PT2, PT3) and of the granulated aggregate was determined by measuring the dry mass m_{dry} and the wet mass after immersion for 24 h in water (this is the saturated surface-dry mass m_{sat}). It was calculated from Equation (1):

$$W = \frac{m_{\text{sat}} - m_{\text{dry}}}{m_{\text{dry}}} \cdot 100 \tag{1}$$

The mechanical properties of the prisms were evaluated according to EN 196-1:2005[32], whereas the compressive strength of the granules was determined after curing the granulates in a climatic chamber at 21 °C and a relative humidity of 94 % for 28 d, according to the procedure described by C. R. Cheeseman[5], where individual granules are loaded to failure between two parallel plates. For the calculation of the compressive strength the following Equation (2) was used:

$$R_{\text{c}} = \frac{2{,}8 \cdot F_{\text{c}}}{h^2 \cdot \pi} \tag{2}$$

where F_{c} is the load causing failure (i.e., fracture), h is the spherical diameter of the granule, and the value of 2.8 is a shape factor.

The frost resistance of the aggregate was determined according to EN 13055-1:2002 [20] on two parallels, where in each parallel 400 g of dry samples (mass M_1) of the fraction 4–8 mm was immersed in water for 4 h. After that the samples were exposed to 20 cycles of freezing-thawing, from –18 °C to +18 °C. After 20 cycles the samples were dried and sieved through a sieve with apertures of 2 mm. The remains on the sieve represent the mass M_2. The percentage of mass loss due to the freezing action (F) is calculated using Equation (3):

$$F = \frac{M_1 - M_2}{M_2} \cdot 100 \tag{3}$$

The mechanical properties of the prisms were determined by means of a 300-kN ToniNorm compression testing machine.

The bulk densities and strength tests of the concrete samples were determined on standard prisms for mortars of (4 × 4 × 16) cm.

2.4 Preparation of the fly-ash aggregate concrete mixes

The compositions of the concrete mixes that were prepared from the two different types of artificial aggregate (PT1-C, and GT1-C), and that of the mix made using natural limestone aggregate (LMS-C), are shown in **Table 2**.

Table 2: Composition of the concrete specimens made by different types of aggregate

Tabela 2: Sestava betonskih vzorcev, izdelanih z različnimi vrstami agregatov

Sample designation	PT1-C	GT1-C	LMS-C
Type of aggregate	crushed	granulated	crushed
Mass (g)			
Aggregate	5188	3269	9595
Cement	1505	1505	1505
Fly ash	645	645	645
Water in the aggregate	917	1531	0
Added water	1110	769	1227
Super plasticizer	7.5	7.5	7.5
w/c ratio			
w/c ratio (with water in the aggregate)	0.94	1.07	0.57
w/c ratio (without water in the aggregate)	0.52	0.36	0.57

The contents of the individual fractions of the aggregates were determined according to the curves specified in the standard SIST 1026:2008 [33] (curve B for the crushed aggregate, and curve A for the granulated aggregate (**Figure 4**)).

Because of the high water absorption of the lightweight aggregates, prior to mixing they were immersed in water for 30 min and then drained in order to remove the surface water. Taking into account the k-value concept for the fly ash (according to EN 206: 2013[34]), a maximum of 30 % of the cement binder was replaced by fly ash as an additive. Compressive strength tests according to the standard EN 196-1:2005[32], as well as density tests, were performed on hardened test specimens after (7, 28, and 90) days. In all cases the test specimens were cured in a climatic chamber at a temperature of 21 °C and a relative humidity of 94 %.

3 RESULTS

3.1 Characterization of the aggregates

The densities and porosities of the investigated aggregates, determined by MIP, are shown in **Table 3**. The pore size distributions for the artificial aggregates are shown in **Figure 5**.

Table 3: Density and porosity of the investigated aggregates, as determined by MIP

Tabela 3: Gostota in poroznost preiskovanih agregatov, določene z MIP

Sample designation	Total intrusion volume (cm^3/g)	Total pore area (m^2/g)	Average pore diameter (µm)	Bulk density (g/cm^3)	Apperent density (g/cm^3)	Porosity (%)
PT1	0.3899	33.171	0.047	1.182	2.1923	46.08
PT2	0.3710	46.925	0.0316	1.258	2.359	46.67
PT3	0.3178	50.231	0.0253	1.333	2.313	42.37
GT1	0.6429	31.4	0.0819	0.9195	2.2487	59.11

If the results obtained for the aggregates PT1, PT2, and PT 3 are compared, it can be seen that in the case of a higher amount of added binder (cement), the density of the aggregate is higher, and the porosity is lower. It can be further seen, comparing GT1 and PT1, that the granulated aggregate has a lower density and higher porosity than the crushed aggregate.

For instance the density of the granulated aggregate was 0.9 g/cm^3, whereas that of the aggregates obtained by crushing was significantly higher, i.e., 1.2 g/cm^3. However, both of these two aggregates, i.e., PT1 and

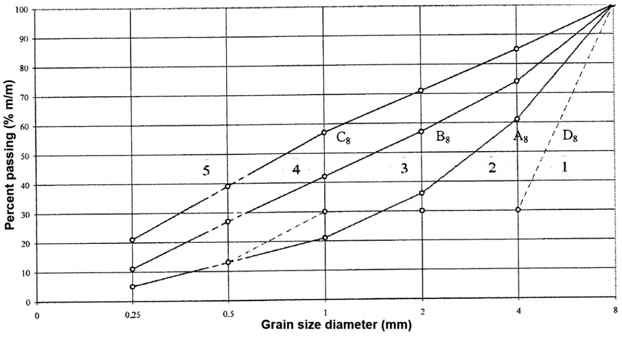

Figure 4: Recommended sieve curves for 0/8 mm aggregate mixtures taken from SIST 1026:2008[33]

Slika 4: Priporočene sejalne krivulje za 0/8 mm mešanico agregatov, vzeta iz SIST 1026:2008[33]

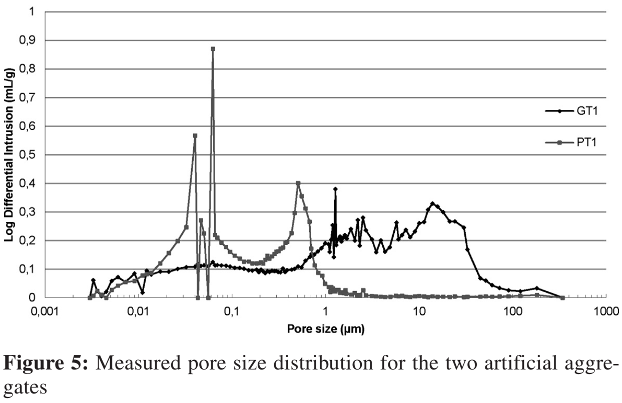

Figure 5: Measured pore size distribution for the two artificial aggregates

Slika 5: Izmerjena razporeditev velikosti por v dveh izdelanih agregatih

GT1, can be classified as lightweight aggregates according to EN 13055-1:2002.[20] The measured porosity of the aggregate PT1 was found to be equal to 46.1 %, whereas that of the aggregate GT1 amounted to 59.1 %.

From **Figure 5** it can be seen that, in the case of aggregate PT1, almost all the pores have sizes of less than 1 μm, the average pore size being 0.047 μm, whereas in the case of aggregate GT1, the pore sizes ranged between 0.003 μm and 100 μm. The average pore size of aggregate GT1 was 0.082 μm.

The measured water absorption of the crushed aggregate was, as expected from the density of the aggregates, less than that of the granulated aggregate. In the case of the aggregate sample PT1 the water absorption amounted to 38.4 % (in the case of the samples PT2 and PT3: 35.9 % and 30.7 % respectively), whereas in the case of aggregate sample GT1 it amounted to 57.8 %. According to these results the porosity of the aggregates can be classified as being open. It is clear that the content of the binder has an effect on the water absorption of the aggregate.

The results of the tensile and compressive strength tests performed on the aggregates are presented in **Table 4**. As could be expected, the results show that the crushing strength increases with the binder content. The tensile strength of the crushed aggregates (samples PT1, PT2, PT3) ranged between 2.2 MPa and 4.6 MPa, whereas their compressive strengths ranged between 12.6 MPa and 30.6 MPa. In the case of the granulated aggregate granules (sample GT1) only the compressive strength was determined, by measurements that were performed on single granules. For this reason the value cannot be directly compared to the values obtained in the case of the PT samples. It amounted to 0.96 MPa.

Table 4: Crushing strengths of the aggregate samples
Tabela 4: Trdnost vzorcev agregatov pri drobljenju

	Bending strength		Compressive strength	
Sample designation	after 7 d curing at 94 % humidity (MPa)	after 28 d curing at 94 % humidity (MPa)	after 7 d curing at 94 % humidity (MPa)	after 28 d curing at 94 % humidity (MPa)
PT1	2.1	2.2	6.8	12.6
PT2	2.9	3.2	11.1	18.6
PT3	4.1	4.6	19.5	30.6
GT1	/	/	/	0.96

The results of the SEM investigation confirmed the differences in the microstructure between the crushed aggregate and the granulated aggregate. The microstructure of sample PT1 was found to be more homogeneous than that of sample GT1 (**Figure 6**). In both figures grains of fly ash can still be seen. In the case of sample GT1 several smaller granules are bonded together to form a larger granule, with large associated air pores inside, which contributes to the higher porosity of the granulated aggregate.

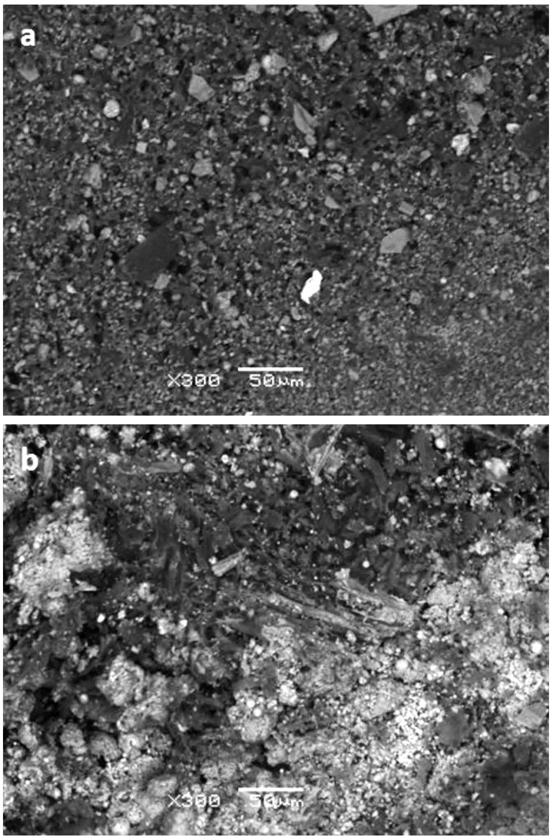

Figure 6: BSE SEM images of samples: a) PT1 and b) GT1of the investigated aggregates, shown at the same magnification
Slika 6: BSE SEM-posnetek vzorcev: a) PT1 in b) GT1, preiskovanih agregatov, prikazanih pri enaki povečavi

Comparing the properties of the granulated aggregate to the properties of the crushed aggregate it can be noted that the crushed aggregate has better mechanical properties and a lower porosity, which could be partially ascribed to the process of pelletization (if not all the parameters are optimal), but also to the fact that during pelletization the *w/c* factor is not uniformly distributed throughout the single granules of aggregate, which introduce weak points at the microstructural level. By the mixing, pouring and crushing process of aggregate production a more uniform w/c and microstructure of aggregate is obtained.

3.2 Characterization of the hardened concrete test specimens

In **Table 5**, the results for the compressive and bending strengths are presented for hardened test specimens of the concrete mixes, which were made from LWAC, whose preparation is defined in **Table 2**. The strength of the concrete made with limestone aggregate is higher than that of the concrete made using the artificial LW crushed or granulated aggregate, despite the highest water-to-cement ratio. However, when crushed aggregate is used, the bending and compressive strengths of the hardened concrete made from them are considerably higher than those that can be achieved with granulated aggregate. This is confirmed by the results that are shown in Table 5, where, despite the much lower water-to-cement ratio of test specimen GT1-C (0.36), the obtained strengths are still much lower than those corresponding to test specimen PT1-C, which had a water-to-cement ratio of 0.52.

Table 5: Determined compressive and tensile strengths of the concrete test specimens

Tabela 5: Določene tlačne in upogibne trdnosti preizkušanih vzorcev betona

Test specimen designation		PT1-C	GT1-C	LMS-C
Tensile strength (MPa)	after 7 d curing at 94 % humidity	2.9	2.6	5.6
	after 28 d curing at 94 % humidity	3.5	2.7	6.4
	after 90 d curing at 94 % humidity	3.6	2.8	7.4
Compressive strength (MPa)	after 7 d curing at 94 % humidity	19.0	13.5	28.7
	after 28 d curing at 94 % humidity	24.1	16.0	34.6
	after 90 d curing at 94 % humidity	25.3	17.1	40.5

The density of the concrete made with crushed aggregate amounted to 1610 kg/m^3, whereas that of the concrete made with granulated aggregate was 1490 kg/m^3. As expected, the density of the concrete made with natural limestone aggregate (LMS-C) was much higher, and amounted to 2290 kg/m^3 (Table 6).

Generic values for the thermal properties can be obtained from the standard EN 1745:2012[34,35] (**Table A.9** for lightweight aggregate concrete, and **Table A.2** for dense aggregate concrete) – the assigned values for the different types of concrete prepared within the scope of this investigation are also given in **Table 6**.

Table 6: Density of the different types of concrete together with the corresponding thermal properties, based on the generic values given in the standard EN 1745[35]

Tabela 6: Gostota različnih vrst betonov skupaj z njihovimi toplotnimi lastnostmi, na osnovi generičnih vrednosti danih v standardu EN 1745[35]

Sample designation		PT1-C	GT1-C	LMS-C
Density (kg/m^3)	After 90 d curing	1610	1490	2290
$\lambda_{10,dry}$ (W/mK)	Acc. to EN 1745	0.84	0.73	1.36

According to the properties obtained in the case of test specimen PT1-C (a tensile strength of 3.5 MPa, a compressive strength of 24.1 MPa, and a density of 1610 kg/m^3), this type of concrete can be classified as a medium-strength concrete with a low density and improved thermal insulation properties.

SEM investigations of the concrete did not show significant differences in the microstructures of the concrete that had been made with crushed aggregate or granulated aggregate (**Figure 7**). The observed cement matrix is homogeneous with relicts of portlandite, and adhered well to the aggregate. Interlocking of the cement matrix with the porous crushed aggregate (PT1), where the cement paste entered the crushed grains, was more pronounced than in the case when the rounded granulated aggregate (GT 1) was used.[36]

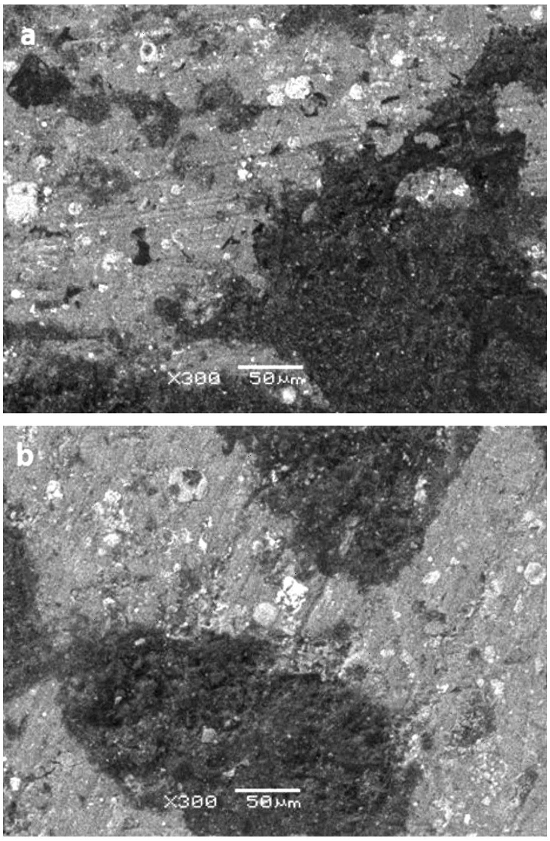

Figure 7: BSE SEM-images of: a) the test specimens PT1-B and b) GT1-B, shown at the same magnification

Slika 7: BSE SEM-posnetek preizkusnih vzorcev: a) PT1 – B in b) GT1 – B, prikazan pri enaki povečavi

3.3 Determination and optimization of aggregate frost resistance

The frost resistance of an aggregate depends to a large extent on the pore structure of its grains. It is well-known that aggregates with a lower porosity and a greater proportion of fine pores possess better frost resistance.[37]

The results of the tests that were performed in order to determine the frost resistance of the investigated aggregate indicated a significant loss of mass upon freezing (**Table 7**), which was especially severe in the case of the granulated aggregate (GT1), where the loss of mass amounted to 96.7 %. The very high loss of mass (96.7 %) on freezing of the granulated fly ash aggregates could be ascribed to the very high porosity (water absorption of 57.8 %) and the very low crushing strength (0.96 MPa).

Samples that were obtained by pouring the mixtures into moulds, and after that crushing and sieving (they were designated PT), resulted in a somewhat improved frost resistance due to the lower initial porosity, as well as better mechanical properties. However, in this case, too, the loss of mass was significant (from 19.1 % to 31.5 %). In the case of sample PT 1 improvements in the frost resistance were searched for in two directions. In the first test (sample PT 1a), the fly ash was additionally sieved onto a 0.125 mm sieve (in this way the majority of the organic particles were removed; loss on ignition decreased from the original value of 10.17 % to 3.3 %), and then processed in the same way as PT 1. In second test (sample PT 1+ ETA S) the sample of fly ash was not additionally processed by sieving, but instead a commercially available air entraining admixture (normally used for the improvement of the frost resistance of concrete) was added, whose mass amounted to 0.1 % of the mass of the cement. Both approaches significantly improved the frost resistance of the aggregate. The sieving away of particles above 0.125 mm resulted in a mass loss of 8.1 % after freezing thawing , whereas the adding of an air-entrapping agent resulted in a mass loss of 1.8 % after freezing.

Table 7: Loss of mass after 20 cycles of freezing-thawing
Tabela 7: Izguba mase po 20 ciklih zmrzovanja-taljenja

Sample designation	Loss of mass (%)
GT1	96.7
PT1	19.1
PT1a	8.1
PT2	31,5
PT3	25,9
PT1+ETA S	1,8

4 CONCLUSIONS

Based on the results of the performed investigations, it can be concluded that in the case of pouring and crushing (PT), aggregates of higher density and strength can be obtained in comparison with aggregates that can be obtained by granulation (GT). In the case of crushing, polygonally shaped aggregates are obtained, which can improve the interlocking effect with the cement matrix.

Both of the two types of investigated aggregate (PT and GT) were highly porous (with porosities of 38.4 %, and 57.8 %, respectively), and their porosity was of the open type. In such cases water can be stored within the aggregate grains, which can then be available for subsequent hydration. Open porosity can also contribute to a stronger interfacial zone between the aggregate and the cement matrix.

The frost resistance of such aggregates is influenced by their content of organic particles, but it can be significantly improved by removing part of the organic particles and /or by adding a commercially admixture for frost-resistance improvement.

The application of such aggregates in concrete has confirmed their usability in the construction sector by the utilization of nearly 80 % of fly ash in concrete (partly as an additive to cement, with its main share in the aggregate).

The methodology described in the paper for the use of fly ash could also be used for other kinds of waste dust that are generated, for example, in the construction industry, in agriculture, and in the refractory industry.

Acknowledgements

This work was financially supported by the Slovenian Research Agency Programme Group P2-0273.

5 REFERENCES

[1] Environmental Protection Agency, European waste catalogue and hazardous waste list (valid from 1 January 2002), http://www.nwcpo.ie/forms/EWC_code_book.pdf/

[2] A. Palomo, M. W. Grutzeck, M. T. Blanco, Alkali-activated fly ashes: A cement for the future, Cement and Concrete Research, 29 (**1999**), 1323–1329, doi:10.1016/S0008-8846(98)00243-9

[3] J. L. Provis, J. S. J. Van Deventer, Alkali activated materials, State of the art report, RILEM TC 224-AAM, 2014

[4] R. Cioffi, F. Colangelo, F. Montagnaro, L. Santoro, Manufacture of artificial aggregate using MSWI bottom ash, Waste management, 31 (**2010**), 281–288, doi:10.1016/j.wasman.2010.05.020

[5] C. R. Cheeseman, A. Makinde, S. Bethanis, Properties of lightweight aggregate produced by rapid sintering of incinerator bottom ash. Resources, Conservation and Recycling, 43 (**2005**), 147–162, doi:10.1016/j.resconrec.2004.05.004

[6] F. Colangelo, C. Ferone, F. Messina, R. Cioffi, MSWI fly ash cementation by means of cold-bonding pelletization, 34th Cement and Concrete Science Conference and Workshop on Waste Cementation, Sheffield, September 14–17, 2014

[7] F. Colangelo, F. Messina, R. Cioffi, Recycling of MSWI fly ash by means of cementitious double step cold bonding pelletization: Technological assessment for the production of lightweight artificial sggregates, Journal of Hazardous Materials, 299 (**2015**), 181–191, doi:10.1016/j.jhazmat.2015.06.018

[8] G. Baykal, A. G. Dovan, Utilization of fly ash by pelletization process: theory, application areas and research results, Resources Conservation and Recycling, 30 (**2000**), 59–77, doi:10.1016/S0921-3449(00)00042-2

[9] S. Shanmugasundaram, S. Jayanthi, R. Sundararajan, C. Umarani, K. Jagadeesan, Study of utilization of fly ash aggregates in concrete, Modern Applied Science, 4 (**2010**) 5, 44–57

[10] C. Vengatachalapathy, S. Thirugnanasambandam, Fly ash – based lightweight aggregate concrete containing steel fibers and polyesters fibers, The IUP journal of structural engineering, 7 (**2014**) 2, 15

[11] N. U. Kockal, T. Ozturan, Characteristics of lightweight fly ash aggregates produced with different binders and heat treatments, Cement and Concrete Composites, 33 (**2011**), 61–67, doi:10.1016/j.cemconcomp.2010.09.007

[12] M. Gesoglu, E. Guneyisi, H. O. Oz, Properties of light weight aggregates produced with cold-bonding pelletization of fly ash and ground granulated blast furnace slag, Materials and Structures, 45 (**2012**), 1535–1546, doi:10.1617/s11527-012-9855-9

[13] C. Ferone, F. Colangelo, F. Messina, F. Iucolano, B. Liguori, R. Cioffi, Coal combustion wastes reuse in low energy artificial aggregates manufacturing, Materials, 6 (**2013**), 5000–5015, doi:10.3390/ma6115000

[14] J. M. J. M. Bijen, Manufacturing processes of artificial lightweight aggregates from fly ash, International Journal of Cement Composites and Lightweight Concrete, 8 (**1986**) 3, 191–199, doi:10.1016/0262-5075(86)90040-0

[15] S. Geetha, K. Ramamurthy, Reuse potential of low-calcium bottom ash as aggregate through pelletization. Waste Management, 30 (**2010**) 8–9, 1528–1535, doi:10.1016/j.wasman.2010.03.027

[16] K. Ramamurthy, K. I. Harikrishnan, Influence of binders on properties of sintered fly ash aggregate, Cement and concrete cmposites, 28 (**2006**), 33–38, doi:10.1016/j.cemconcomp.2005.06.005

[17] K. I. Harikrishnan, K. Ramamurthy, Influence of pelletization process on the properties of fly ash aggregates, Waste management, 26 (**2006**), 846–852, doi:10.1016/j.wasman.2005.10.012

[18] R. Manikandan, K. Ramamurthy, Effect of curing method on characteristics of cold bonded fly ash aggregates, Cement and concrete composites, 30 (**2008**), 848–853, doi:10.1016/j.cemconcomp.2008.06.006

[19] R. Manikandan, K. Ramamurthy, Influence of fineness of fly ash on the aggregate pelletization process, Cement and concrete composites, 29 (**2007**), 456–464, doi:10.1016/j.cemconcomp.2007.01.002

[20] EN 13055-1:2002, Lightweight aggregates, Part 1, Lightweight aggregates for concrete, mortar and grout

[21] K. Kovler, Internal curing of Concrete- Effect of internal curing on autogenous deformation, RILEM TC 196-ICC: State-of-the-Art Report, RILEM Publications, S.A.R.L. (2007), 71–104

[22] O. M. Jensen, Internal curing of Concrete - Mechanisms of internal water curing, RILEM TC 196-ICC: State-of-the-Art Report, RILEM Publications, S.A.R.L., (2007), 15–27

[23] P. Lura, O. M. Jensen, S. I. Igarachi, Internal curing of concrete - Experimental methods to study internal water curing, RILEM TC 196-ICC: State-of-the-Art Report, RILEM Publications, S.A.R.L., (2007), 57–69

[24] A. Elsharief, M. D. Cohen, J. Olek, Influence of lightweight aggregate on the microstructure and durability of mortar, Cement and concrete research, 35 (**2005**), 1368–1376, doi:10.1016/j.cemconres.2004.07.011

[25] M. Gesoglu, T. Ozturan, Shrinkage cracking of lightweight concrete made with cold-bonded fly ash aggregates, Cement and concrete research, 34 (**2004**), 1121–1130, doi:10.1016/j.cemconres.2003.11.024

[26] N. U. Kockal, T. Ozturan, Durability of lightweight concrete with lightweight fly ash aggregates, Construction and building materials, 25 (**2011**), 1430–1438, doi:10.1016/j.conbuildmat.2010.09.022

[27] N. U. Kockal, T. Ozturan, Effects of lightweight fly ash aggregate properties on the behaviour of lightweight concretes, Journal of hazardous materials, 197 (**2010**), 954–965, doi:10.1016/j.jhazmat.2010.03.098

[28] R. Wasserman, A. Bentur, Effect of lightweight fly ash aggregate microstructure on the strength of concretes, Cement and concrete research, 27 (**1997**) 4, 525–537, doi:10.1016/S0008-8846(97)00019-7

[29] A. Terzić, L. Pezo, V. Mitić, Z. Radojević, Artificial fly ash based aggregates properties influence on lightweight concrete performances, Ceramics international, 41 (**2015**), 2714–2726, doi:10.1016/j.ceramint.2014.10.086

[30] EN-450-1, Fly ash for concrete, Part 1, Definition, specifications and conformity criteria, 2013

[31] A. Sivakumar, P. Gomathi, Pelletized fly ash lightweight aggregate concrete: A promising material, Journal of Civil Engineering and Construction Technology, 3 (**2012**), 42–48, doi:10.5897/JCECT11.088

[32] EN 196-1:2005, Methods of testing cement, Part 1: Determination of strength

[33] SIST 1026:2008, Concrete, Part 1: Specification, performance, production and conformity – Rules for the implementation of SIST EN 206-1

[34] EN 206:2013, Concrete, Specification, performance, production and conformity

[35] EN 1745:2012, Masonry and masonry products, Methods for determining thermal properties

[36] C.G. Rocco, M. Elice, Effect of aggregate shape on the mechanical properties of a simple concrete, Engineering Fracture Mechanics, 76 (**2009**) 2, 286–2987, doi:10.1016/j.engfracmech.2008.10.010

[37] J. Mao, K. Ayuta, Freeze – Thaw Resistance of Lightweight Concrete and Aggregate at Different Freezing Rates, Journal of Materials in Civil Engineering, (2008) 78–84, doi:10.1061/(ASCE)0899-1561(2008)20:1(78)

UDK 67.017:621.039.532.2:669.11
Original scientific article/Izvirni znanstveni članek

ISSN 1580-2949
MTAEC9, 51(2)275(2017)

EFFECT OF INOCULATION ON THE FORMATION OF CHUNKY GRAPHITE IN DUCTILE-IRON CASTINGS

VPLIV MODIFIKACIJE NA NASTANEK GRUDASTEGA GRAFITA V ULITKIH IZ GNETLJIVEGA ŽELEZA

Ivana Mihalic Pokopec[1], Primož Mrvar[2], Branko Bauer[1]
[1]University of Zagreb, Faculty of Mechanical Engineering and Naval Architecture, Ivana Lucica 5, 10002 Zagreb, Croatia
[2]University of Ljubljana, Faculty of Natural Science and Engineering, Lepi pot 11, 1000 Ljubljana, Slovenia
branko.bauer@fsb.hr

Prejem rokopisa – received: 2015-12-23; sprejem za objavo – accepted for publication: 2016-02-22

doi:10.17222/mit.2015.355

Chunky graphite is one of the most deleterious graphite degenerations in thick-walled ductile-iron castings. This defect normally appears in the thermal center of a casting and dramatically decreases the mechanical properties. Chunky-graphite formation is primarily caused by a reduction in the cooling rate and melt composition. An addition of subversive elements (Bi, Sb, Pb, Sn,...) associated with a small amount of Ce is known to be beneficial to avoid chunky graphite. In this study, the effects of Bi and Ce additions at different cooling rates on the graphite morphology and mechanical properties of ductile-cast iron EN-GJS-400-18-LT were investigated. Y-blocks with wall thicknesses of 25 mm and 75 mm and cylindrical blocks with a diameter of 200 mm and a height of 300 mm were cast. The presence of chunky graphite in the thermal center of the cylindrical blocks and a decrease in the mechanical properties were revealed, regardless of the presence of Bi.

Keywords: chunky graphite, cooling rate, graphite morphology, thick-walled ductile-iron castings

Grudast grafit je ena od najbolj škodljivih degeneracij grafita v debelostenskih ulitkih iz gnetljivega železa. Ta napaka se običajno pojavi v toplotnem središču ulitka in močno zmanjša mehanske lastnosti. Nastanek grudastega grafita je posledica zmanjšanja hitrosti ohlajanja in sestave taline. Dodatek škodljivih elementov v sledovih (Bi, Sb, Pb, Sn,...) v povezavi z majhnim dodatkom Ce je poznan kot ugoden za preprečitev nastanka grudastega grafita. V tej študiji je bil proučevan vpliv dodatka Bi in Ce pri različnih hitrostih ohlajanja na morfologijo grafita in mehanske lastnosti gnetljivega litega železa EN-GJS-400-18-LT. Uliti so bili Y-kosi z debelino stene 25 mm in 75 mm ter cilindrični kosi s premerom 200 mm in visoki 300 mm. Odkriti sta bili prisotnost grudastega grafita v toplotnem središču cilindričnih kosov ter zmanjšanje mehanskih lastnosti, neodvisno od prisotnosti Bi.

Ključne besede: grudast grafit, hitrost ohlajanja, morfologija grafita, debelostenski ulitki iz gnetljivega železa

1 INTRODUCTION

Chunky graphite, CHG, is one of the most deleterious graphite degenerations in thick-walled ductile-iron castings. CHG normally appears in the thermal center of large castings, and decreases the mechanical properties, in particular the tensile and fatigue strength and elongation. Local, cell-type accumulations of compact graphite forms are characteristic for CHG.[1] On the macro-scale, it is optically visible on cut or machined surfaces as a black spot. Microscopic observation shows that CHG consists of large cells of highly branched and interconnected graphite strings. A graphite nodule can usually be observed at the end of these strings. CHG grows along the c-axis with a spiral growth mechanism. Although the mechanism of growth is the same as with spheroidal graphite, its driving forces are different.[2]

A great number of studies have been conducted to describe the CHG formation, but a clear understanding of its appearance and a safe mastering of the metal preparation to avoid CHG are not yet available.

The main causes of a CHG formation are a slower cooling rate and the melt composition.[3,4] With slower cooling rates and increasing section thicknesses, the size of the spherulites increases and their count per unit of area decreases. In such zones, CHG frequently develops as a result of graphite degeneration.[1,5] A high carbon equivalent, approx. >4.1 % of mass fractions, and increasing contents of the elements such as Ni, Si, Cu, Ce, Ca, Al, P, Mg promote the formation of CHG.[1,2,6,7]

The CHG formation is also affected by the presence of low-level elements in the melt. It has been well documented that the presence of either subversive elements, such as Pb, Bi, Sb and As, or excessive RE amounts cause the degeneration of graphite spheriods, i.e., the CHG formation. However, the co-existence of subversive elements and RE in appropriate ratios will result in the retention of spheroidal graphite.[8,9]

It was found that small amounts of bismuth added to the melt promote the formation of spheroidal graphite. However, when its content exceeds the critical value, Bi is known as a detrimental element, which can cause degeneration of a good nodular graphite structure. This effect was attributed to the interaction between Bi and Mg, which blocks the spheroidization effect of Mg to a certain extent. This negative effect of Bi is mostly neutralized with RE additions, especially Ce. The interaction effect between RE and Bi is achieved with the formation of various types of intermetallic compounds, e.g., Bi_3Ce_4, $BiCe_3$, etc. Intermetallic compounds delete the effect of subversive elements, and also serve as nuclei for the graphite formation.[5,9,10] According to reference[11], adding 0.002–0.006 % of mass fraction of Bi with a certain amount of Ce, increases the nodule count and prevents the CHG formation in thick sections. But, when the amount of RE exceeds the value required for neutralization of the subversive elements, CHG may form.[5]

In reference[10], it was found that a Ce/Bi ratio of 0.8–1.1 was sufficient to achieve a complete neutralization of the castings with a relatively long solidification time (e.g., 3200 s), while Ce/Bi ratios in excess of 1.1 were required for the castings with very short solidification times (e.g., 100 s).

P. Ferro et al.[5] studied the effects of an inoculant sequence and inoculant chemical composition on a casting heavy-section microstructure. An in-stream inoculation with an inoculant containing RE and Bi was found to drastically reduce the formation of CHG. This result was attributed to the major fading resistance of such an inoculant compared to the standard ones. They found that Bi is suppressing or reducing the CHG formation by reducing the undercooling, which is considered the main reason for the CHG formation. In this case, Bi behaves in a similar way like Sb, whose effect was confirmed by P. Larrañaga et al.[12] Bismuth also has the function to remove the oxygen absorbed at the interface between graphite and liquid iron, thus reducing the oxygen absorption and preventing the formation of CHG.[5]

Although it is known that the correlation between the ratio of RE/subversive elements and the appearance of chunky graphite in thick-walled ductile-iron castings exists, this area is still not fully investigated. More work is needed to provide a correct balancing of the RE/Bi ratio that would prevent the formation of chunky graphite.

In the present work, the solidification behavior of large ductile-iron blocks with or without an addition of Bi and the same amount of Ce are compared by means of a microstructure observation and measuring of mechanical properties. Bi and Ce were supplied from different inoculants.

2 EXPERIMENTAL PART

The test castings used in this study were Y blocks, 25 mm and 75 mm in size and cylindrical blocks with a diameter of 200 mm and a height of 300 mm, **Figure 1**, to enable the investigation of the influence of different solidification times on the chunky graphite formation. The thermal modulus, i.e., the relation between the volume and the cooling surface area (V/A) of a cylinder was 3.75 cm.

Two moulds (M1, M2), with the same test castings, were produced from sodium silicate bonded sand.

With the aim to limit the number of the parameters, all the samples were cast using the same melt. The melt was produced in a 5.6 t capacity medium-frequency induction furnace. The charge material consisted of grey pig iron (Sorelmetal®), steel scrap and returns as listed in **Table 1**. In order to increase the carbon and silicon content and the nucleation ability of the melt, SiC (~92 % of the mass fractions of SiC) was added into the furnace with the metallic charge. Once the melting was finished, the chemical composition of the metal was adjusted according to the carbon and silicon evaluation obtained with a thermal analysis and spectrometric analysis carried out on the coupon for the other elements.

Table 1: Charge materials used for melting

Tabela 1: Vložki, uporabljeni za pretaljevanje

total mass (kg)	pig iron (kg)	steel scrap (kg)	returns (kg)	SiC (kg)
5600	4026	448	1120	6
	72 (*w*/%)	8 (*w*/%)	20 (*w*/%)	0.1 (*w*/%)

For both moulds, the spheroidising treatment was carried out in a dedicated ladle with a capacity of 200 kg by adding ~2 % of the mass fractions of the FeSiMg alloy (44–48 % of the mass fraction of Si, 3.5–3.8 % of mass fraction of Mg, 0.9–1.1 % of the mass fraction of Ca, 0.5–1.2 % of the mass fraction of Al, 0.6–0.8 % of the mass fractions of RE, and Fe bal.) using the sandwich method at ~1480 °C. The FeSiMg alloy was positioned at the bottom of the casting ladle and then covered with steel scrap before pouring the iron from the furnace. 0.7 % of the mass fraction of Ni was also added to the casting ladle. The source of Ni is 99.9 % of the mass fractions of the Ni pure metal. In this type of industrial alloy, it is not possible to sustain the requested 95 % of the mass fraction of the ferritic matrix in the as-cast state, so it has to be heat treated. Ni is added to assure the requested tensile strength (above 400 N/mm^2) and to improve the low-temperature ductility after the heat treatment of this alloy.

Simultaneously with the spheroidising treatment, the first inoculation (preconditioning) was carried out by adding 0.2 % of the mass fraction of commercial inoculant I1. After the treatment, slag was removed from the melt surface and the melt was poured into the mould. The holding time was ~3 min. The second inoculation (in-stream) during the pouring of the mould was performed by adding 0.2 % of the mass fraction of inoculant I2, containing Ce, at ~1380 °C. The Mg recovery was about 75 %.

In order to investigate the influence of the Bi-containing inoculant in the second mould, inoculation was additionally performed by adding commercial inoculant I3, in the form of a block fixed with the foundry adhesive to the bottom of the downsprue, as indicated in **Figure 1**.

Figure 1: Pattern used in the experiment
Slika 1: Vzorec, uporabljen pri preizkusu

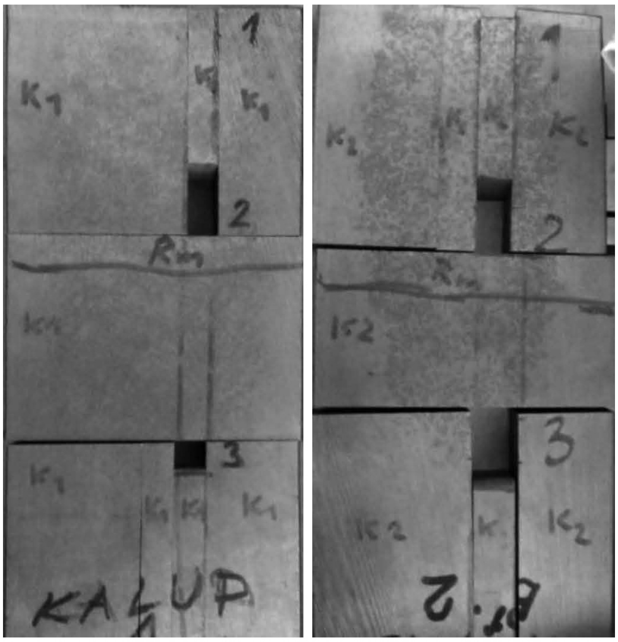

M1 block M2 block

Figure 2: Central sections of cast cylindrical blocks M1 and M2 (zones 1, 2 and 3)
Slika 2: Sredinski del cilindričnih kosov M1 in M2 (področja 1, 2 in 3)

The chemical composition of the used inoculants is reported in **Table 2**. The pouring temperature for both moulds was 1380 °C and the pouring time was 27 s.

Just before pouring the melt to the mould, the chilled coupon was analysed with an optical emission spectrometer (ARL 3460). The C and Si contents were determined from the results of the thermal analysis using the ATAS® system. The chemical compositions are listed in **Table 3**.

Each cylindrical block was afterwards sectioned along the vertical symmetry plane to evaluate the zone affected by CHG. As illustrated in **Figure 2**, the zone affected by CHG was easily located as the darker zone in the thermal center of the casting. Zones 1 and 2 were from the CHG area and zone 3 was from the border of the CHG area. Also, the samples obtained from these zones were prepared for the metallographic analysis; samples S1, S2 and S3 as shown in **Figure 2**. The metallographic analysis was done with an optical microscope (Olympus GX 51), equipped with a system for automatic image processing (Analysis® Materials Research Lab). All the metallographic parameters such as nodularity, nodule count, nodule size, area fraction of graphite, graphite particle size class distribution, graphite shape classification and ferrite/pearlite ratio were evaluated according to the Standard EN-ISO 945-1 2010. Finally, tensile-test bars were machined out from the core of each cylindrical block as indicated in **Figure 2**.

Y blocks of 25 mm and 75 mm were also machined to obtain tensile-test bars. The samples for the metallographic analysis of the Y blocks were collected from the heads of the tensile-test bars.

The microstructure in the vicinity of the fracture surface of the tensile-test bars was investigated under an optical microscope.

The samples for the metallographic analysis were prepared with the standard methods of grinding, polishing and etching in 5 % nital. The microstructures

Table 2: Chemical compositions of inoculants
Tabela 2: Kemijska sestava modifikatorjev

Inoculant	Chemical composition, (*w*/%)										
	Si	Mg	Ca	Al	Ce	Ba	RE	Bi	S	O	Fe
I1	64–70	–	1.0–2.0	0.8–1.5	–	2.0–3.0	–	–	–	–	bal.
I2	70–76	–	0.75–1.25	0.75–1.25	1.5–2.0	–	–	–	(<1%)	(<1%)	bal.
I3	71.33		0.79	3.96				1.20			

Table 3: Chemical compositions of the melts, (*w*/%)
Tabela 3: Kemijska sestava talin, (*w*/%)

	C	Si	Mn	P	S	Mg	Ni
M1	3.68	1.65	0.13	0.034	0.01	0.049	0.741
M2	3.67	1.62	0.13	0.032	0.011	0.043	0.761

were analysed according to the Standard EN ISO 945-1:2008.

Tensile tests were carried out on a tensile-testing machine (Fritz Heckert ZD-20) at room temperature on five samples taken from the Y blocks and two samples taken from the cylindrical blocks. The yield strength, tensile strength and elongation were determinated according to the Standard EN 1563.

3 RESULTS

3.1 Macro- and microstructures

Usually CHG is easily detected after sectioning a casting. The presence of CHG is visible as a localized darkening of the surface, often revealed without any need of chemical etching. In **Figure 2**, the CHG macrostructures of the cross-sections of the cylindrical blocks are clearly visible. CHG appeared in the thermal centers due to the slowest cooling rates, in both blocks, with and without Bi. The solidification time in the centre was 5140 s, determined from the results of the simulation in the ProCAST® software. Evident differences in the proportion of the areas affected by CHG in these two cast blocks were observed, as shown in **Figures 2** and **3**.

The diameter of the area affected by CHG at the top of zone 1 for M1 was 129 mm, and 78 mm for M2, **Figure 3**. The area affected by CHG appeared in an ellipsoid shape in the cross-section along the vertical symmetry plane, for both blocks. The CHG zone for M1 starts 58 mm from the bottom of the block, and 87 mm for M2, as can be seen in **Figure 2**.

An addition of Bi caused a significant reduction of the CHG-affected zone, at the lower cooling rates in the centre of a block.

The microscopic observation showed that CHG occurred locally, having typical cell-type structures, **Figure 4**. These cells were relatively large, with the apparent diameter in the range of 0.5–1.5 mm, with a sharp transition between the non-affected and the affected zones, **Figures 4** and **5**. Inside the CHG area, zones with spherical graphite were found. Distribution of CHG is generally not uniform within the affected zone.

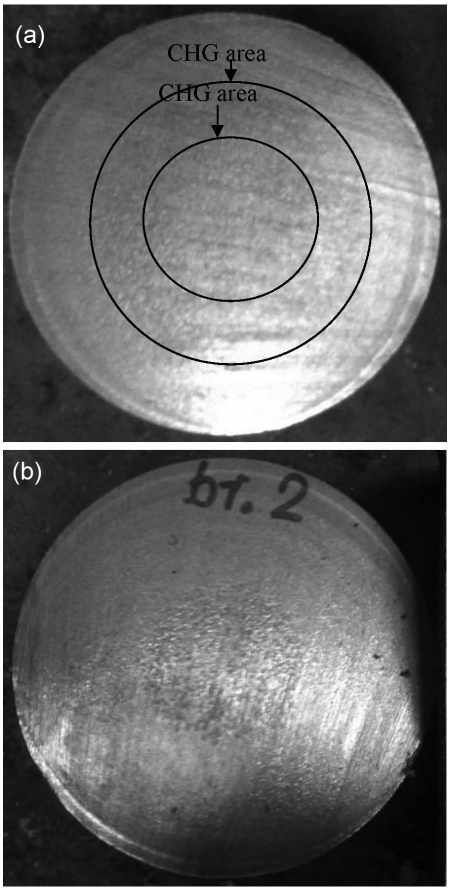

Figure 3: Cross-sections of cast blocks at the top of zone 1: a) M1 without Bi, b) M2 with Bi
Slika 3: Prerez ulitega kosa na vrhu področja 1: a) M1 brez Bi, b) M2 z Bi

The samples with a Bi addition showed a pronounced eutectic growth in zones 1 and 3, while in the samples without a Bi addition, it was more difficult to distinguish specific cells in zones 1 and 2, **Figure 4**. The nodules around the CHG area in zones 1 and 2 showed a regular shape, while in zone 3 more degenerated nodules were found.

As can be seen from **Table 4**, after long solidification times, from 3670 s to 5140 s, a significant graphite deterioration occurred with the graphite nodularity in the vicinity of 50 %, and a very low nodule count, below 50

Table 4: Graphite-microstructure data for cylindrical blocks in CHG area according to EN-ISO 945-1
Tabela 4: Podatki o mikrostrukturi grafita v cilindričnih kosih v področju CHG, skladno z EN-ISO 945-1

Mould	Zone (**Figure 2**)	Shape	Size	Nodularity (%)	Nodule count (mm^{-2})	Area frac. of graphite (%)	Size distribution					
							3 (max. 500 µm)	4 (max. 250 µm)	5 (max. 120 µm)	6 (max. 60 µm)	7 (max. 30 µm)	8 (max. 15 µm)
M1	1	V,III(35 %)	6	47	65	10.7	0	3	107	426	789	1284
	2	V,II (35 %)	5	48	38	10.8	2	11	87	330	473	741
	3	IV	6	51	47	11.1	1	8	67	392	753	1287
M2	1	V,II (40 %)	6	45	25	10.4	0	5	105	472	729	807
	2		6	49	42	8.9	0	12	99	365	463	396
	3	V,II (45 %)	6	40	43	10.3	0	10	135	459	788	694

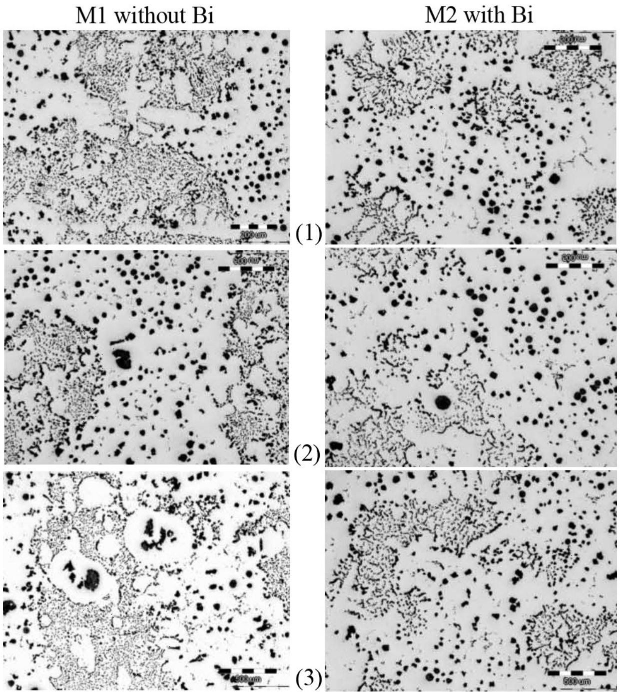

Figure 4: Microstructures from zones 1, 2, 3 from blocks M1 and M2
Slika 4: Mikrostrukture iz različnih področij 1, 2, 3, iz kosov M1 in M2

nodules/mm^2 (except in zone 1 of M1). The obtained nodule count was substantially below the recommended minimum nodule count for heavy-section castings, which is more than 60 nodules/mm^2. The results were slightly inferior for the samples with the Bi addition. The results of the nodule count cannot be related with the solidification time. The lowest nodule count was observed for cylindrical block M2. With the decrease in the nodule count for the cylinders, the size of the nodules increased, **Figure 4**. Also, the Bi addition reduced the amount of ferrite, from approx. 90 to 80 %, **Table 5**.

Table 5: Ferrite/pearlite ratio of cylindrical blocks in CHG area according to EN-ISO 945-1
Tabela 5: Razmerje ferit/perlit v cilindričnih kosih v področju CHG, skladno z EN-ISO 945-1

Mould	Zone (**Figure 2**)	Ferrite area %	Pearlite area %
M1	1	91.4	8.6
	2	91.8	8.2
	3	90.6	9.4
M2	1	85.3	14.7
	2	81.4	18.6
	3	79.8	20.2

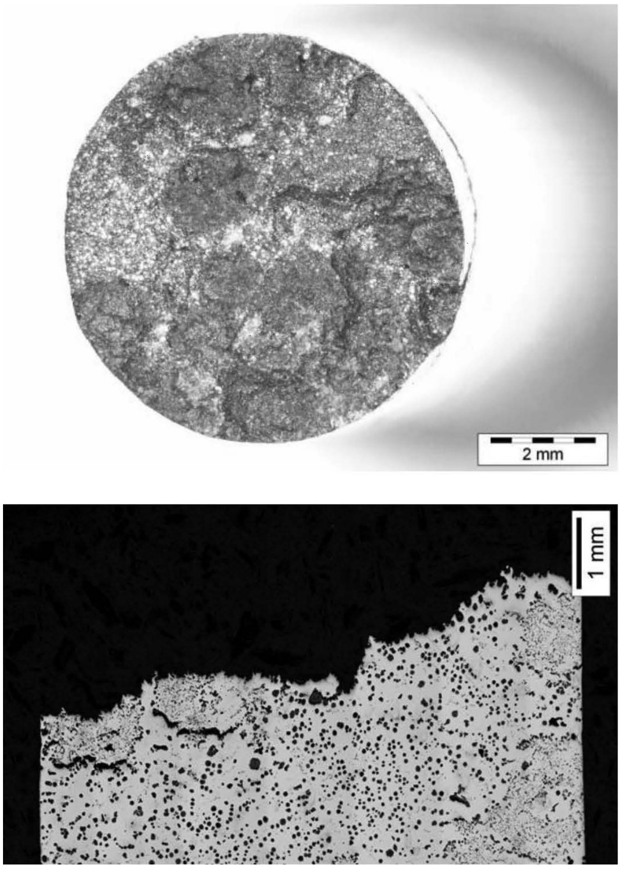

Figure 5: Fracture surface of a test bar (M1-2)
Slika 5: Prelom preizkusne palice (M1-2)

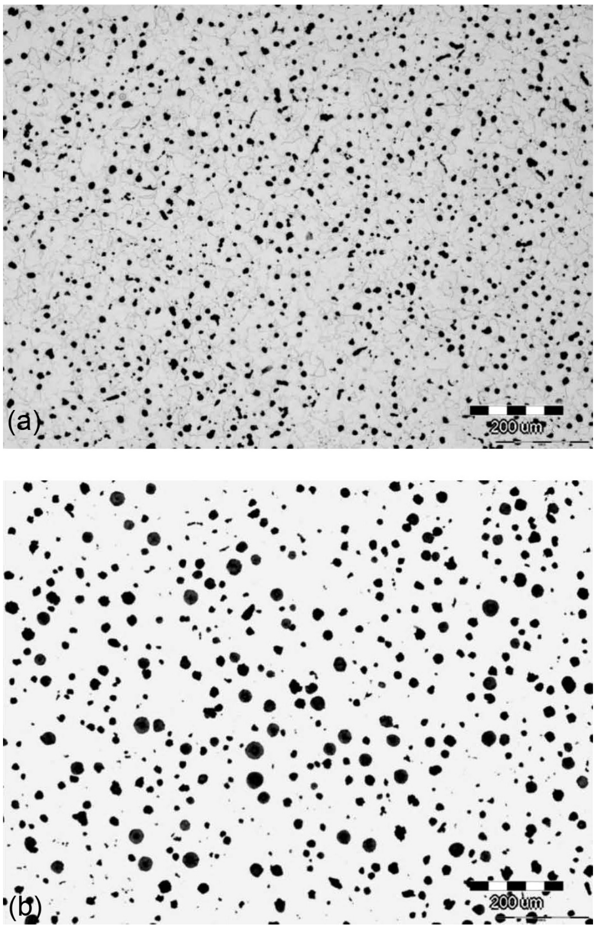

Figure 6: Microstructures of Y-blocks, 25 mm: a) M1 without Bi, b) M2 with Bi
Slika 6: Mikrostrukturi Y-kosa, 25 mm: a) M1 brez Bi, b) M2 z Bi

In the Y blocks of 25 mm and 75 mm, CHG did not appear, **Figure 6**. The nodule count of the Y blocks was in a range from 74 to 405 nodules/mm^2. The nodularity was from 60 % to 73 %. The bismuth addition negatively affected the microstructure regarding the nodule count, while the nodularity was positively affected.

3.2 Tensile test

Table 6 gives the tensile-test results for the CHG area in the cylindrical blocks. The samples containing CHG were characterized by a significant reduction in the elongation and tensile strength compared to the CHG-free samples from the Y blocks. The samples from the Y blocks showed elongation values in the vicinity of 18 %, while the samples containing CHG achieved elongation values in a range of 3.5–7.5 %. The tensile strength values for the CHG area were reduced by 20–25 %, while the yield strength was reduced by 10 %. Hardness was hardly affected at all.

Table 6: Mechanical properties in the CHG area
Tabela 6: Mehanske lastnosti v področju CHG

Mould	Specimen	R_m N/mm^2	$R_{p0,2}$ N/mm^2	A_5 %	HB
M1	1	323	269	4.2	140
	2	317	269	3.5	-
M2	1	345	249	7.5	123
	2	331	259	5.5	-

The effect of the Bi addition on the mechanical properties can be seen. In the CHG area, the Bi addition resulted in better elongation and tensile-strength properties, while the yield strength and hardness were slightly reduced, **Table 6**. In the Y blocks, the Bi addition positively influenced the elongation properties, while the strength properties were reduced.

Visual testing of the fracture surfaces of the tensile-test bars pointed out local dark areas of various sizes. The macroscopic observation of CHG corresponded very well with the microscopic observations, **Figure 5**. On the fracture surface, eutectic cells of chunky graphite surrounded with normal spheroidal graphite were detected.

4 DISCUSSION

High concentrations of Ce, Ca, Si and Ni are the usual reasons of the CHG formation. Excessive Ce, in the absence of subversive elements in heavy-section ductile iron will almost always cause a CHG formation. In thin-section castings, the risk of a CHG formation is minimum due to short solidification times.

Most MgFeSi alloys contain some level of RE, especially Ce, to promote a high nodule count, improve nodularity and counteract the effects of anti-nodularising elements. This is usually good for thin-section parts, but it is a problem for the sections thicker than 50 mm. There is a unified opinion found in the literature that an addition of Bi (up to about 0.003 % of mass fraction) can prevent the formation of degenerated graphite in thick-section castings.[14] To eliminate the detrimental effect of RE, the most important task to do is to achieve the right balance between the presence of RE and the subversive elements.[1,7] Note also that the amount of Bi required to counteract the detrimental effect of RE (Ce) is casting section-size dependent.

In this study the Bi addition did not totally suppress the CHG formation, but the added amount reduced the area affected with CHG. The amount of Bi was too low and the presumption is that the right balance between Ce and Bi would prevent the formation of CHG.

The microstructure analysis of the CHG area in the cylindrical blocks showed similar results with and without a Bi addition. The present results indicate that the addition of Bi to heavy-section ductile-iron castings exhibited a beneficial effect of a decreasing CHG area as reported in other works.[5,13,14]

5 CONCLUSION

Based on the results obtained in this study, the following main conclusions can be drawn:

- CHG occurred in the thermal center of a heavy-section ductile-iron casting;
- a Bi addition has a positive influence on the CHG suppression in thick-section areas, while maintaining good mechanical properties in thin-section areas;
- the Bi addition also improved the tensile strength and elongation in the CHG area;
- for the investigated section size, the addition of Bi was too low to totally suppress the CHG formation.

Acknowledgements

This work was partially supported by the foundry MIV d.d., Varaždin.

6 REFERENCES

[1] H. Löblich, Effect of nucleation conditions on the development of chunky graphite in heavy ductile iron castings, Giessereiforschung, 58 (**2006**) 3, 28–41

[2] O. Knustad, L. Magnusson Åberg, Chunky graphite, effects and theories on formation and prevention, 14th Inter. Foundry Conference, Opatija, Croatia, 2014

[3] R. Källbom, K. Hamberg, M. Wessen, L.-E. Björkegren, On the solidification sequence of ductile iron castings containing chunky graphite, Materials Science and Engineering A, 413–414 (**2005**), 346–351, doi:10.1016/j.msea.2005.08.210

[4] J. Lacaze, L. Magnusson, J. Sertucha, Review of microstructural features of chunky graphite in ductile cast irons, Keith Millis Symp. on Ductile Cast Iron, Nashville, USA, 2013, 360–368

[5] P. Ferro, A. Fabrizi, R. Cervo, C. Carollo, Effect of inoculant containing rare earth metals and bismuth on microstructure and mechanical properties of heavy-section near-eutectic ductile iron castings, Journal of Materials Processing Technology, 213 (**2013**), 1601–1608, doi:10.1016/j.jmatprotec.2013.03.012

[6] K. Hartung, O. Knustad, K. Wardenaer, Chunky graphite in ductile cast iron castings – Theories and examples, Indian Foundry Journal, 55 (**2009**), 25–29

[7] R. Källbom, K. Hamberg, L. E. Björkegren, Chunky Graphite - Formation and Influence on Mechanical Properties in Ductile Cast Iron, Proc. of Gjutdesign 2005, Espoo, Finland, 2005

[8] S. Mendez, D. Loper, I. Asenjo, P. Larrañaga, J. Lacaze, Improved analytical method for chemical analysis of cast iron, Application to castings with chunky graphite, ISIJ International, 51 (**2011**), 242–249

[9] P. C. Liu, C. R. Loper Jr., T. Kimura, H. K. Park, Study of chunky graphite in heavy section ductile iron, AFS Transactions, 83–51 (**1983**), 119–126

[10] E. N. Pan, C. Y. Chen, Effects of Pb and solidification conditions on the graphite structure of heavy-section ductile cast iron, AFS Transactions, 103 (**1995**), 265–273

[11] M. Koch, Chunky Graphite, Effects and theories on formation and prevention, 2013 Keith Millis Symp. on Ductile Cast Iron, Nashville, USA, 2013

[12] P. Larrañaga, I. Asenjo, J. Sertucha, R. Suarez, I. Ferrer, J. Lacaze, Effect of Antimony and Cerium on the Formation of Chunky Graphite during Solidification of Heavy-Section Castings, Metallurgical and Materials Transactions A, 36A (**2009**), 654–661, doi:10.1007/s11661-008-9731-y

[13] E. N. Pan, C. Y. Chen, Effects of Bi and Sb on graphite structure of heavy-section ductile cast iron, AFS Transactions, 104 (**1996**), 845–858

[14] J. Riposan, M. Chisamera, S. Stan, Performance of heavy ductile iron castings for windmills, China Foundry, 7 (**2010**) 2, 163–170

UDK 67.017:620.1:66.095.26
Original scientific article/Izvirni znanstveni članek

ISSN 1580-2949
MTAEC9, 51(2)283(2017)

COPOLYMERIZATION OF POLY (O-PHENYLENEDIAMINE-CO-O/P-TOLUIDINE) VIA THE CHEMICAL OXIDATIVE TECHNIQUE: SYNTHESIS AND CHARACTERIZATION

KOPOLIMERIZACIJA POLI (O-FENILENDIAMINA-CO-O/P-TOLUIDINA) S TEHNIKO KEMIJSKE OKSIDACIJE: SINTEZA IN KARAKTERIZACIJA

Omar Melad, Mariam Jarour
Al-Azhar University Gaza, Chemistry Department, P.O.Box 1277, Gaza, Palestine
omarmelad@yahoo.com

Prejem rokopisa – received: 2016-01-23; sprejem za objavo – accepted for publication: 2016-03-16

doi:10.17222/mit.2016.023

Chemical oxidative copolymerization of *o*-phenylenediamine -co-*o*/*p*-toluidine at different molar ratios of monomer was performed using potassium dichromate as an oxidant. The resulting copolymers were investigated using Fourier transform infrared spectroscopy (FTIR) and UV-visible spectroscopy. In the copolymer, the intensity of the band at 1005 cm^{-1} is substantially decreased due to the -CH_3 bending vibrations. A hyposochromic shift is observed in UV-visible spectroscopy. The electrical-conductivity values obtained for the *o*-toluidine copolymers are higher than those for the *p*-toluidine copolymers.

Keywords: *o*-phenylenediamine, *o*-toluidine, *p*-toluidine, conductivity, chemical oxidativeness, FTIR

Izvedena je bila kemijska oksidativna kopolimerizacija *o*-fenilendiamina-co-*o*/*p*-toluidina pri različnih molarnih razmerjih monomera, z uporabo kalijevega dikromata kot oksidanta. Nastali kopolimeri so bili preiskovani z uporabo infrardeče spektroskopije s Fourierjevo transformacijo (FTIR) in UV-vidno spektroskopijo. V kopolimeru je intenziteta pasu pri 1005 cm^{-1} občutno zmanjšana zaradi upogibnih vibracij -CH_3. V UV vidnem spektru je opažen zamik v spektralnem pasu. Vrednosti električne prevodnosti dobljene pri *o*-toluidin kopolimerih so višje kot pri *p*-toluidin kopolimerih.

Ključne besede: *o*-fenilendiamin, *o*-toluidin, *p*-toluidin, prevodnost, kemijska oksidativnost, FTIR

1 INTRODUCTION

Intrinsically conductive polymers have become an efficient alternative to inorganic conductors in many practical applications in the recent decade.[1] Polyaniline, poly toluidine, polypyrrole, poly aminopyridine, polythiophene and poly phenylenediamine are examples of conductive polymers, showing high conductivity. Polyaniline is an important member of the intrinsically conductive polymers because of the ease of its preparation, an excellent environmental stability, interchangeable oxidation states, electrical and optical properties, economic costs,[2–4] and because they can be used for chemical sensors,[5,6] electromagnetic shielding,[7] electrochemical and corrosion devices.[8–9] Polymerization of a conducting polymer may be performed with chemical[10] or electrochemical[11] methods. Different chemical oxidizing agents such as potassium dichromate,[12–14] potassium iodate,[15] hydrogen peroxide,[16] ferric chloride or ammonium persulphate[17] can be used. The application of polyaniline is limited because of its poor processability,[18] which is true for most conducting polymers.

A good method to obtain soluble conductive polymers is the polymerization of aniline derivatives. Poly phenylenediamine homopolymer has attracted attention because it has been reported to be a high aromatic polymer containing a 2,3-diamino phenazine or quinoxaline repeat unit and exhibiting an unusually high thermostability.[19–21] In recent years, copolymerization has been developed as one of the most essential and alternative strategies for modifying physical and chemical properties of conducting polymers. These copolymers show characteristics reasonably different from those of the homo polymer.[22,23] Thus, copolymerization can be a convenient synthetic method and a process for preparing new conducting materials with improved properties. However, the conductivity and solubility of the phenylenediamine homopolymer are low.[19–21] Copolymerization of o-phenylenediamine with o/p toluidine might be one of the best methods. A close analysis of the literature shows a large number of reports on the chemical and electrochemical synthesis of polytoluidine and its copolymer with aniline and other substituted anilines.[24–33] Electrochemical copolymerization of o-phenylenediamine with *o*-toluidine has been reported.[34] So far, there has been no report on copolymerization of o-phenylenediamine with *o*/*p* toluidine using the chemical oxidative method. Toluidines are derivatives of aniline where a – CH_3 group is substituted in the aromatic ring at the *o*-, *m*- or *p*- positions. In this work, a chemical oxidative copolymerization of o-phenylenediamine with *o*/*p* toluidine at different molar ratios of monomer was synthesized and characterized using FTIR, UV-visible spectroscopy and conductivity measurements.

2 EXPERIMENTAL PART

2.1 Materials

o-phenylenediamine (*o*-PD), o-touidine (*o*T), p-toluidine (*p*T) (ADWIC, Egypt), potassium dichromate ($K_2Cr_2O_7$), ammonium persulfate ($(NH_4)_2S_2O_3$) (Merk, Germany), hydrochloric acid (HCl 32 %), formic acid (HCOOH 98 %) and glacial acetic acid (CH_3COOH 99.5 %) (Merk-Germany), dimethylsulfoxide (DMSO) and N,N-dimethylformamide (DMF) were used for the UV-visible and conductivity measurements, respectively. All the chemicals, acids and solvents were used as received without any further purification.

2.2 Measurements

The FTIR spectra were recorded with a FTIR 8201PC (SHIMADZU) instrument using KBr pellets techniques. For measuring the UV-visible absorption spectra, a spectrophotometer (UV-1601 SHIMADZU) was used. Conductivity measurements were made at room temperature using a conductivity meter (CM-30V).

2.3 Synthesis of poly (o-phenylenediamine – Co –o/p-toluidine)copolymer

2.3.1 Synthesis of poly o-phenylenediamine

The polymer of *o*-phenylenediamine was synthesized by dissolving 1.622 g of *o*-phenylenediamine in 100 mL of 0.1M HCL in a stirred ice bath to produce a homogenous solution. 4.413 g of potassium dichromate was dissolved in 50 mL of 0.1M HCL and added to the first solution for 30 min while being constantly stirred, then it was left at room temperature for 24 h. After this the solution was filtered, washed with acetone and distilled water and the polymer was left to dry in an oven at 60 °C for 24 h.

2.3.2 Synthesis of poly o- and p- toluidine

Poly (*o*- and *p*- toluidine) were synthesized with chemical oxidative polymerization of *o*- and *p*- toluidine in an acidic media. 5 mL of *o*T was dissolved in 300 mL of 1M formic acid and kept at 0 °C; 11.4 g of $K_2Cr_2O_7$ was dissolved in 200 mL of 1M formic acid also at 0 °C and added dropwise under constant stirring to the (*o*T/HCOOH) solution over a period of 20 min. The resulting dark green solution was maintained under constant stirring for 24 h. The solution was filtered and then washed with distilled water; the black powder of poly *o*-toluidine was left to dry in air for one week, while 2.5 mL of *p*T was dissolved in 150 mL of 1M HCL and kept at 0 °C; 5.7 g of $K_2Cr_2O_7$ was also dissolved in 100 mL of 1M HCL at 0 °C and added dropwise under constant stirring to the (*p*T/HCL) solution over a period of 20 min. The resulting dark red solution was maintained under constant stirring for 24 h. The solution was filtered and then washed with distilled water, and the black red powder of poly *p*-toluidine was left to dry in air for one week.

2.3.3 Synthesis of poly (o-phenylenediamine – Co – o-/p- toluidine)copolymer

1.54 g *o*PD and 0.5133 mL *o*T/*p*T were added to 150 mL of 1M glacial acetic acid in a 500 mL single-neck glass flask at 40 °C . 13.68 g ($(NH_4)_2S_2O_8$) was dissolved separately in 14 mL distilled water to prepare an oxidant solution. The monomer solution was then stirred and treated with the oxidant solution added dropwise at an adding rate of one drop every three seconds for 30 min at 40 °C. Immediately after the first few drops, the reaction solution turned violet in the case of *o*T and blackish green in the case of *p*T. After 1 h, the copolymer acetate was isolated from the reaction mixture with filtration and washed with the excess of distilled water to remove the oxidant and oligomers. A whitish

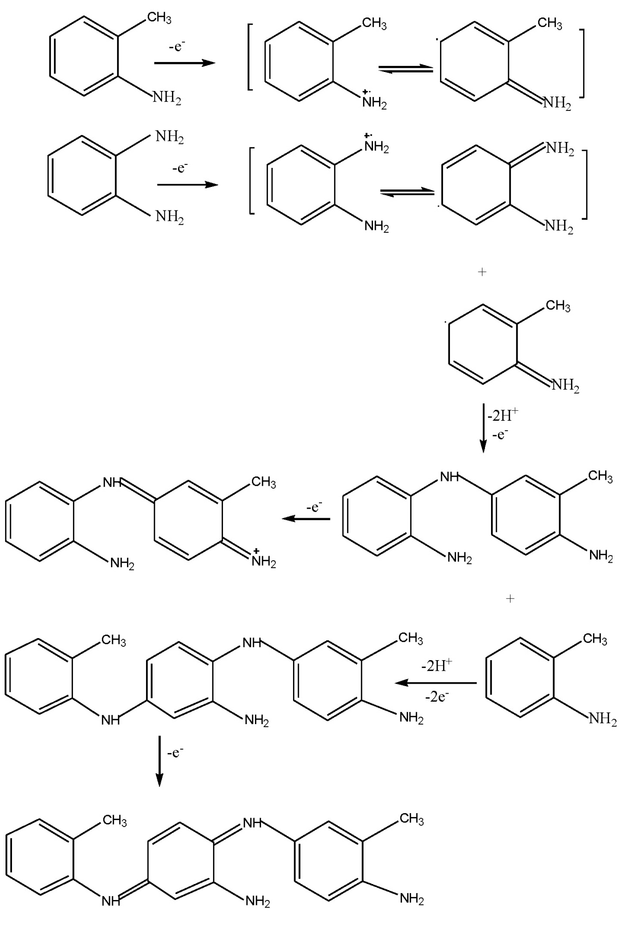

Figure 1: Scheme of copolymerization mechanism of poly (*o*-phenylenediamine-Co-*o*-toluidine) copolymer

Slika 1: Shema mehanizma kopolimerizacije poli (*o*-fenilendiamin in *o*-toluidin) kopolimera violet solid powder and a greenish brown solid powder for *o*T and *p*-T copolymers, respectively, were left to dry in the oven at 118 °C for 48 h and then dry in air for one week. The above procedure was repeated at various molar ratios of the monomers *o*T and *p*T at the feeds of 0.50 and 0.25 molar of *o*PD, respectively.

3 RESULTS AND DISCUSSION

3.1 Synthesis of poly (o-phenylenediamine – Co – o-/p-toluidine)copolymer

Toluidines are derivatives of aniline where a $–CH_3$ group is substituted in the aromatic ring at the *o*-, *m*- or *p*- positions. Schemes in **Figures 1** and **2** represent the copolymerization mechanism of poly (*o*-phenylenediamine-Co-*o*-/*p*-toluidine)copolymer, respectively.

3.2 FTIR spectra of poly (o-phenylenediamine – Co - o / p- toluidine) copolymer

Figure 3 shows the FTIR spectra of poly *o*-phenylenediamine, poly *o*-toluidine and poly *p*-toluidine, respectively.

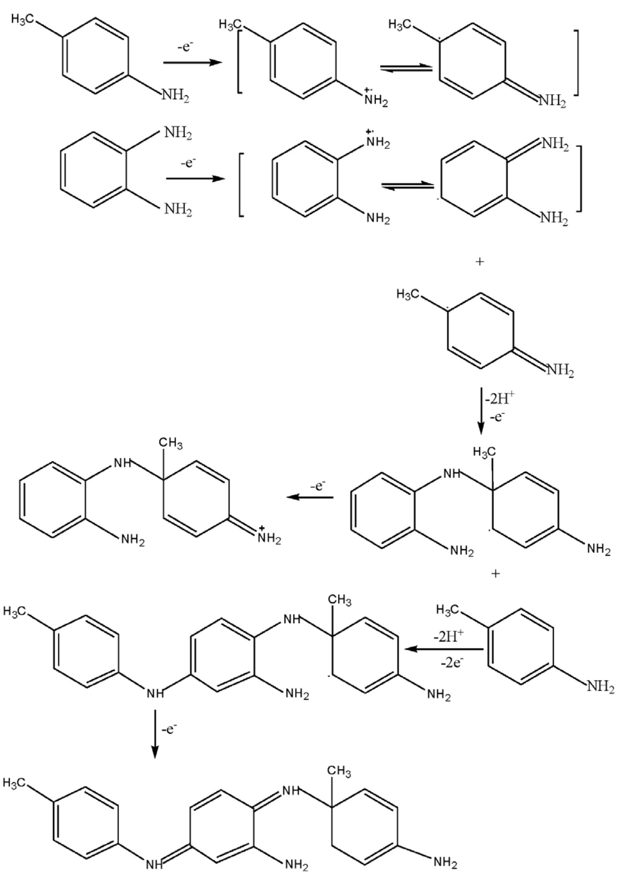

Figure 2: Scheme of copolymerization mechanism of poly (*o*-phenylenediamine-Co-*p*-toluidine) copolymer

Slika 2: Shema mehanizma kopolimerizacije poli (*o*-fenilendiamin in *p*-toluidin) kopolimera

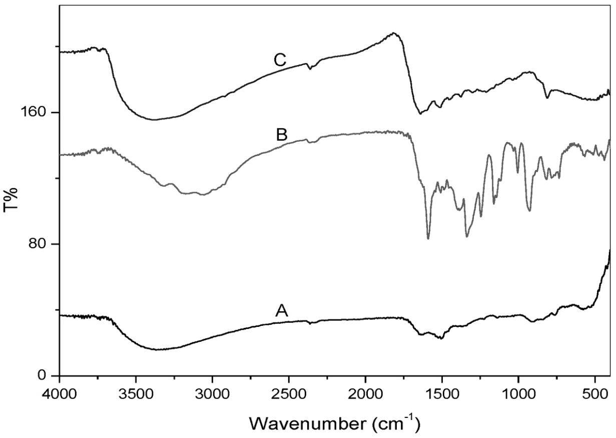

Figure 3: FTIR spectra of: A) poly *o*-phenylenediamine, B) poly *o*-toluidine and C) poly *p*-toluidine

Slika 3: FTIR-spekter: A) poli *o*-fenilendiamina, B) poli *o*-toluidina in C) poli *p*-toluidina

A weak band is observed at 3326–3391 cm^{-1} characteristic of the $–NH_2$ and N-H stretching, another one is observed at 1640–1525 cm^{-1} assigned to the quinoid and benzenoid phenyl ring for poly o-phenylenediamine (**Figure 3** (A), the signal due to the C-H in-plane bending vibratio is observed at 1161 cm^{-1}. **Figure 3** (B and C) shows the frequency peaks at (2917, 1638, 1450, 1301, 1207, 1157, 920) cm^{-1} that are attributed to the C-H stretching of the substituent methyl group, C=C stretching vibrations of quinoid rings, C=C stretching vibrations of benzoid rings, C-N stretching vibrations of quinoid rings, C-N stretching vibrations of benzoid rings, C-H in-plane bending vibrations and 1, 2, 4- tri substituted aromatic rings, respectively. The signal at 567 cm^{-1} is due to the C-H out-of-plane bending vibration. The peak at 3063 cm^{-1} in **Figure 3** (B and C) is caused by the C-H stretch modes of the substituent methyl group. **Figure 4** shows the FTIR spectra of poly

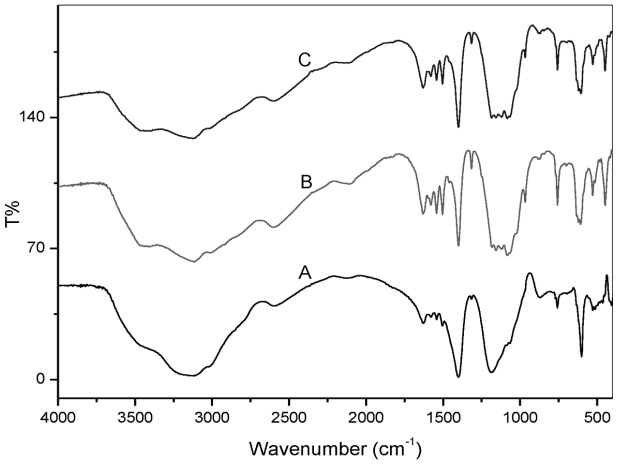

Figure 4: FTIR spectra of poly (*o*PD-Co-*o*T) copolymer with different molar ratios of *o*PD: A) 0.25, B) 0.50, C) 0.75

Slika 4: FTIR-spektri poli (*o*PD in *o*T) kopolimera z različnimi molskimi razmerji *o*PD: A) 0,25, B) 0,50, C) 0, 75 (*o*PD-Co-*o*T) copolymer with different molar ratios of *o*PD.

Most of the bands show variations in the intensity and position. The spectra of the copolymer show the main bands corresponding to the N-H stretching vibrations and ring stretching vibrations of quinoid and benzeoid structures. The intensity of the N-H stretching vibrations in the region between 3470–3010 cm^{-1} increases with the increasing *o*PD feed concentration, indicating an increase in the number of primary and secondary amino groups in the copolymer structure. The band at 1590 cm^{-1} (**Figure 3** (B)) and the band at 1627 cm^{-1} (**Figure 3** (C)) correspond to the C=C stretching vibrations of the aromatic rings. This signal is shifted to 1630 cm^{-1} in the copolymer, **Figure 4**. The intensity of the two bands centered at 1497 cm^{-1} and 600 cm^{-1} greatly increases with the increasing *o*PD feed concentration (**Figure 4**), while the 1497 cm^{-1} band in the copolymer indicates the presence of phenazine-type structures in the copolymer backbone. These cyclic structures in the copolymer are either due to the presence of *o*PD blocks or may result from the cyclization of the adjacent *o*PD and *o*T units in the copolymer chain. On the other hand, the intensity of the band at 1005 cm^{-1}, due to the –CH_3 bending vibrations, substantially decreases in the copolymer. This is indicative of a gradual decrease in the *o*T units in the copolymer structure with the increasing *o*PD feed concentration.

Figure 5 shows the FTIR spectra of poly(*o*PD-Co-*p*T) copolymer with different molar ratios of *o*PD.

In general, with some exceptions, the spectral characteristics of the copolymers are very similar to those of P*o*PD. The intensity of the broad band, in the region of 3000–3353 cm^{-1} increases with the increasing *o*PD feed concentration. The band corresponding to the quinoid stretching vibrations occurs at 1616 cm^{-1} for the copolymer. The intensity of this band was also found to increase with the increasing *o*PD feed concentration. The incorporation of the p-toluidine moiety in the copolymer was indicated by the appearance of the characteristic C-H stretching of the substituent methyl group, which was observed as a very weak band at 2917 cm^{-1}. As in o-toluidine, the intensity of the band at 1029 cm^{-1}, due to the -CH_3 bending vibrations, substantially decreases in the copolymer.

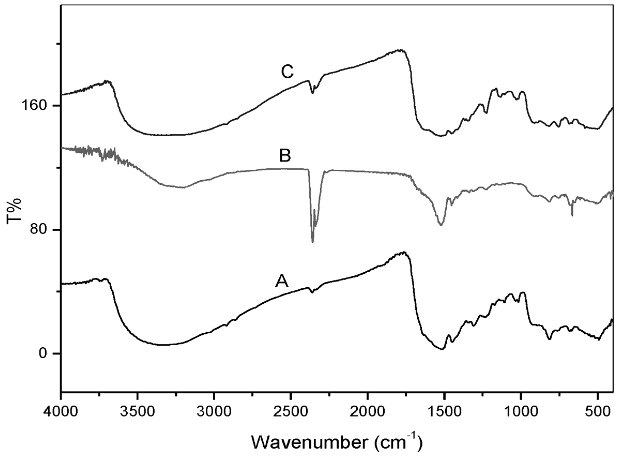

Figure 5: FTIR spectra of poly (*o*PD-Co-*P*T) copolymer with different molar ratios of *o*PD: A) 0.25, B) 0.50, C) 0.75

Slika 5: FTIR-spektri poli (*o*PD in PT) kopolimera z različnimi molskimi razmerji *o*PD: A) 0,25, B) 0,50 in C) 0,75

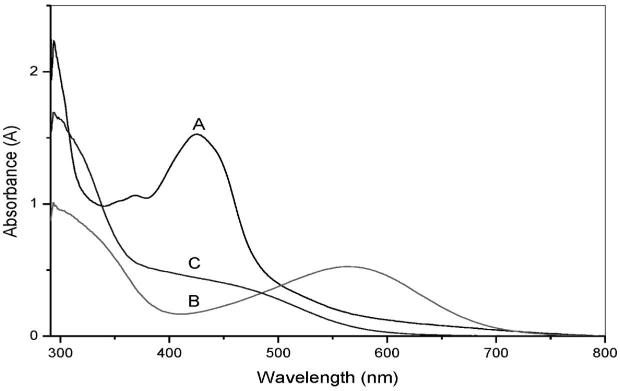

Figure 6: UV-VIS spectra of: A) poly *o*-phenylenediamine, B) poly *o*-toluidine and C) *p*-toluidine

Slika 6: UV-VIS spektri: A) poli *o*-fenilendiamin, B) poli *o*-toluidin in C) *p*-toluidin

3.3 *UV-visible spectra of poly (o-phenylenediamine – Co - o / p- toluidine) copolymer*

Figure 6 shows the UV-visible spectra of poly *o*-phenylenediamine, poly *o*-toluidine and poly *p*-toluidine, respectively.

Figures 7 and **8** show the UV-visible spectra of poly (*o*PD-Co-*o*T) and poly (*o*PD-Co-*p*T)copolymers, respectively, with different molar ratios of *o*PD. In **Figures 6**, **7** and **8**, for UV-visible spectra of homopolymers and copolymers, two characteristic absorption peaks were found at around 290 nm and in a range of 417–563 nm corresponding to the benzene π-π* electronic transition and n-π* electronic transition. A hyposochromic shift from 550 nm in the o-toluidine copolymer to 450 nm in

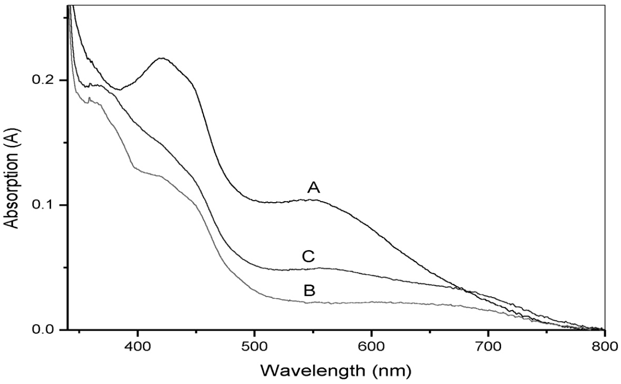

Figure 7: UV-VIS spectra of poly (*o*PD-Co-*o*T) copolymer with different molar ratios of *o*PD: A) 0.25, B) 0.50 and C) 0.75

Slika 7: UV-VIS spektri poli (*o*PD in *o*T) kopolimera z različnimi molskimi razmerji *o*PD: A) 0,25, B) 0,50 in C) 0,75

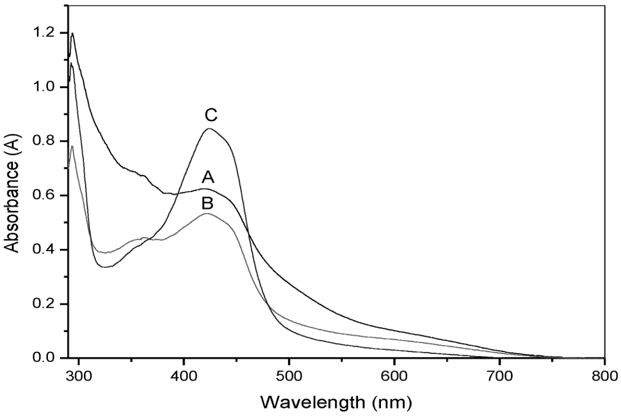

Figure 8: UV-VIS spectra of poly (*o*PD - Co- *p*T) copolymer with different molar ratio of *o*PD: A) 0.25, B) 0.50 and C) 0.75.

Slika 8: UV-VIS spektri poli (*o*PD in *p*T) kopolimera z različnimi molskimi razmerji *o*PD: A) 0,25, B) 0,50 in C) 0,75

the p-toluidine copolymer implies a decrease in the extent of conjugation and an increase in the band gap. These bands correspond to the excitation transition of the quinoid rings. It can be observed that these bands increase when the o-phenylenediamine in the copolymer is increased. This blue shift with the increasing o-phenylenediamine in the copolymer is due to the steric effect of the substituents, indicating a successful copolymerization.

3.4 Electrical conductivity

Table 1: shows electrical conductivity of poly (*o*-phenylenediamine –Co-*o*/*p*-toluidine) copolymer at room temperature in DMF

Tabela 1: Električna prevodnost poli (*o*-fenilendiamina in *o*/*p*-toluidin) kopolimera pri sobni temperaturi v DMF

Polymer	Conductivity (S/cm)
P*o*PD	2.23
P*o*T	1.43
P*p*T	2.04
P(*o*PD-Co-*o*T)25	3.39
P(*o*PD-Co-*o*T)50	3.42
P(*o*PD-Co-*o*T)75	4.65
P(*o*PD-Co-*p*T)25	1.615
P(*o*PD-Co-*p*T)50	1.878
P(*o*PD-Co-*p*T)75	1.898

It can be seen that the conductivity increases as the amount of *o*-phenylenediamine increases in the copolymers. In general, o-isomer gives higher conductivity values than the other isomers; the small values of the conductivity in the case of poly (*o*-phenylenediamine–Co-*p*-toluidine) copolymer compared with the conductivity value of *o*-phenylenediamine may indicate that *p*-toluidine is not a good enough polymer to make a copolymer with *o*-phenylenediamine.

5 CONCLUSION

The synthesis of the copolymerization of *o*-phenylenediamine with *o* / *p*-toluidine was characterized using FTIR and UV-Vis spectroscopy. The intensity of the band at 1005 cm^{-1} that is due to the -CH$_3$ bending vibrations, substantially decreases in the copolymer. A hypsochromic shift from 550 nm in the *o*-toluidine copolymer to 450 nm in the *p*-toluidine copolymer implies a decrease in the extent of conjugation and an increase in the band gap. In general, ortho-isomers give higher conductivity values than the other isomers; so the obtained conductivity values that are higher for the *o*-toluidine copolymer than for the *p*-toluidine copolymer, indicate that *p*-toluidine is not a good enough polymer able to make a copolymer with *o*-phenylenediamine.

6 REFERENCES

[1] E. Hrehorova, V. N. Bliznyuk, A. A. Pud, V. V. Shevchenko, K. Y. Fatyeyeva, Electrical properties and fractal behavior of polyurethane elastomer/polyaniline composites under mechanical deformation, Polymer, 48 (**2007**), 4429–4437, doi:10.1016/j.polymer.2007.05.065

[2] P. Wang, L. Liua, D. A. Mengistiec, B. Wen, T. Liue, C. Chuf, Transparent electrodes based on conducting polymers for display applications, Displays, 34 (**2013**), 301–314, doi:10.1016/j.displa.2013.05.003

[3] M. Jaymand, Recent progress in chemical modification of polyaniline, Prog.Polym.Sci., 38 (**2013**), 1287–1306, doi:10.1016/j.progpolymsci.2013.05.015

[4] X. Guo, M. Baumgarten, K. Mullen, Designing π-conjugated polymers for organic electronics, Prog.Polym.Sci., 38 (**2013**), 1832–1908, doi:10.1016/j.progpolymsci.2013.09.005

[5] Y. Zhao, S. Si, C. Liao, A single flow zinc//polyaniline suspension rechargeable battery, J. Power Sources, 241 (**2013**), 449–453, doi:10.1016/j.jpowsour.2013.04.095

[6] C. Steffens, A. Manzoli, J. E. Oliveira, F. L. Leite, D. S. Correa, P. Herrmann, Bio-inspired sensor for insect pheromone analysis based on polyaniline functionalized AFM cantilever sensor, Sensors and Actuators, B191 (**2014**), 643–649, doi:10.1016/j.snb.2013.10.053

[7] L. Wang, E. Hua, M. Liang, C. Ma, Z. Liu, S. Sheng, Liu Min, G. Xie, W. Feng, Biosensors, 51C (**2014**), 201–207, doi:10.1016/j.bios.2013.07.049

[8] Y. Moon, J. Yun, H. Kim, Synergetic improvement in electromagnetic interference shielding characteristics of polyaniline-coated graphite oxide/γ-Fe2O3/BaTiO3 nanocomposites, J. Ind. Eng. Chem., 19 (**2013**),493–497, doi:10.1016/j.jiec.2012.09.002

[9] G. Gupta, N. Birbilis, A. B. Cook, A. S. Khanna, Polyaniline-lignosulfonate/epoxy coating for corrosion protection of AA2024-T3, Corros. Sci. 67 (**2013**), 256–267, doi:10.1016/j.corsci.2012.10.022

[10] K. Gopodinova, L. Terlemezyan, Conducting polymers prepared by oxidative polymerization: polyaniline, Progress in Polym. Sci., 38 (**1998**), 1832–1908

[11] K. Gurunathan, A. V. Murugan, R. Marimuthu, U. P. Mulik, D. P. Amalnerkar, Electrochemically synthesised conducting polymeric materials for applications towards technology in electronics, optoelectronics and energy storage devices, Materials Chem. and Phys., 61 (**1999**), 173–191, doi:10.1016/S0254-0584(99)00081-4

[12] P. Chowdhury, B. Saha, Indian J. Chem. Tech., 12 (**2005**), 671–675

[13] S. M. Sayyah, A. B. Khaliel, A. A. Aboud and S. M. Mohamad, Chemical Polymerization Kinetics of Poly-O-Phenylenediamine and Characterization of the Obtained Polymer in Aqueous Hydrochloric

Acid Solution Using K2Cr2O7 as Oxidizing Agent, Int. J. Polym. Sci., (**2014**), 1–16, doi:10.1155/2014/520910

[14] O. Melad, Chemical Oxidative Synthesis and Characterization of Poly (o-phenylenediamine) Doped With Different Acids, Eur. J. Chem., 7 (**2016**) 4, 463–467, doi:10.5155/eurjchem.7.4.463-467.1449

[15] R. Hirase, T. Shikata, M. Shirai, Selective formation of polyaniline on wool by chemical polymerization, using potassium iodate, Synth. Met., 146 (**2004**), 73–77, doi:10.1016/j.synthmet.2004.06.009

[16] K. Gopalakrishnan, M. Elango, M. Thamilsevan, Optical studies on nano-structured conducting Polyaniline prepared by chemical oxidation method, Archives of Phys. Research, 3 (**2012**), 315–319

[17] K. Molapo, P. M. Ndangili, R. F. Ajayi, Electronics of Conjugated Polymers (I): Polyaniline, Int. J. Electrochem. Sci., 7 (**2012**), 11859–11875

[18] Y. Cao, P. Smith, A. Heeger, Counter-ion induced processibility of conducting polyaniline and of conducting polyblends of polyaniline in bulk polymers, Synth. Met., 48 (**1992**), 91–97

[19] A. H. Premasiri, W. B. Euler, Syntheses and characterization of poly(aminophenazines), Macromol. Chem. Phys., 196 (**1995**), 3655

[20] H. S. O. Chan, S. C. Nig, T.S.A. Hor, J. Sun, K. L. Tan, B. T. G. Tan, Poly(*m*-phenylenediamine): Synthesis and characterization by X-ray photoelectron spectroscopy, Eur. Polym. J., 27 (**1991**), 1303

[21] F. Cataldo, On the polymerization of p-phenylenediamine, Eur. Polym. J., 36 (**1996**), 2593

[22] A. Malinauskas, M. Bron, R. Holze, Electrochemical and Raman spectroscopic studies of electrosynthesized copolymers and bilayer structures of polyaniline and poly(o-phenylenediamine), Synthetic metals, 92 (**1998**), 127–137, doi:10.1016/S0379-6779(98)80102-1

[23] X. G. Li, L. X. Wang, Y. Jin, Z. L. Zhu, Y. L. Yang, Preparation and identification of a soluble copolymer from pyrrole and o-toluidine, Journal of applied polymer science, 82 (**2001**), 510–518

[24] Y. Wei, R. Hariharan, S. A. Patel, Chemical and electrochemical copolymerization of aniline with alkyl ring-substituted anilines, Macromolecules, 23 (**1990**), 758, doi:10.1021/ma00205a011

[25] N. Pekmez - Ozcicek, K. Pekmez, R. Holze, A.Yildiz, Increased stability of polythiophene in the presence of aniline in acetonitrile, J. Appl. Polym. Sci., 89 (**2003**), 862, doi:10.1002/app.12291

[26] Y. Sahin, S. Percin, M. Sahin, G. Ozkan, Electrochemical polymerization of fluoro- and chloro-substituted anilines and copolymers with aniline, J. Appl. Polym. Sci., 91 (**2004**), 2302, doi:10.1002/app.133677

[27] P. Savita, D. N. Sathyanarayana, Copolymers of aniline withoandm-toluidine: synthesis and characterization, Polym. Int., 53 (**2004**), 106, doi:10.1002/pi.1316

[28] P. Savita, D. N. Sathyanarayana, Synthesis and characterization of soluble conducting poly(o-/m-toluidine-co-o-nitroaniline), Synth. Met., 145 (**2004**), 113, doi:10.1016/j.synthmet.2004.04.024

[29] H. Tang, A. Kitani, S. Maitani, H. Munemura, M. Shiotanti, Electropolymerization of aniline modified by para-phenylenediamine, Electrochim. Acta, 40 (**1995**), 849, doi:10.1016/0013-4686(94)00370-G

[30] R. Mazeikiene, A. Malinauskas, Electrochemical copolymerization of aniline with m-phenylenediamine, Synth. Met., 92 (**1998**), 259

[31] M. Probst, R. Holze, A systematic spectroelectrochemical investigation of alkyl-substituted anilines and their polymers, Macromol. Chem. Phys., 198 (**1997**), 1499, doi:10.1002/macp.1997.021980515

[32] O. Melad, H. Alhendawi, M. Fayyad, Research and Reviews: J. Material Sci., 2 (**2014**), 27–34

[33] O. Melad, M. Esleem, Copolymers of Aniline with O-Anthranilic Acid: Synthesis and Characterization, Open J. Org. Polym. Materials, 5 (**2015**), 31–36, doi:10.4236/ojopm.2015.52003

[34] S. Bilal, R. Holze, Electrochemical copolymerization of o-toluidine and o-phenylenediamine, J. Electroanalytical Chem., 592 (**2006**), 1–13, doi:10.1016/j.jelechem.2006.03.039

67.017:669.721.5:621.78
Original scientific article/Izvirni znanstveni članek

ISSN 1580-2949
MTAEC9, 51(2)289(2017)

THE EFFECT OF THERMO-MECHANICAL PROCESSING ON THE STRUCTURE, STATIC MECHANICAL PROPERTIES AND FATIGUE BEHAVIOUR OF PURE Mg

VPLIV TERMOMEHANSKE PREDELAVE ČISTEGA MAGNEZIJA NA STRUKTURO, STATIČNE MEHANSKE LASTNOSTI IN OBNAŠANJE PRI UTRUJANJU

Jiří Kubásek, Dalibor Vojtěch, Drahomír Dvorský

University of Chemistry and Technology, Department of Metals and Corrosion Engineering, Prague, Technická 5,
166 28 Prague 6, Czech Republic
kubasek.jiri@gmail.com

Prejem rokopisa – received: 2016-02-03; sprejem za objavo – accepted for publication: 2016-04-06

doi:10.17222/mit.2016.029

Magnesium alloys find important applications in automotive, aircraft and space industries. Magnesium itself is also a key component in biodegradable metallic materials considered for applications in medicine. Although there are many studies that include the mechanical behaviour of pure Mg and its alloys after different thermomechanical processing, there is a huge impact of the processing method on the observed properties. Based on these facts, predicting the final properties is difficult. This paper deals with the preparation of pure Mg using a classic extrusion method with a low extrusion ratio, slow extrusion rate and low temperature. These parameters were selected to prevent an excessive grain size and to obtain optimal mechanical properties. The prepared materials were subsequently heat treated under different conditions and the relations between the grain size, texture strength and mechanical properties were studied. As well as static mechanical tests in tension and compression, fatigue tests were also performed. Finally, the obtained data were fitted using the Hall-Petch relation and the results were compared with the literature. The observed results confirmed the significant effect of processing on the mechanical properties with a strong impact on the Hall-Petch behaviour.

Keywords: magnesium, mechanical properties, texture, Hall-Petch relation

Magnezijeve zlitine so pomembne za uporabo v avtomobilski, letalski in vesoljski industriji. Magnezij je tudi ključna komponenta v biorazgradljivih kovinskih materialih za uporabo v medicini. Čeprav obstaja mnogo študij, ki vključujejo mehansko obnašanje čistega Mg in njegovih zlitin po različnih termomehanskih obdelavah, je velik vpliv metode obdelovanja na opazovane lastnosti. Na osnovi tega je težko napovedovati končne lastnosti. Ta članek obravnava pripravo čistega Mg s klasično metodo ekstruzije z majhnim razmerjem ekstruzije, majhno hitrostjo ekstruzije pri nizki temperaturi. Ti parametri so bili izbrani, da se prepreči prekomerna rast zrn in da se doseže optimalne mehanske lastnosti. Pripravljeni material je bil pozneje toplotno obdelan pri različnih pogojih in študirane so bile odvisnosti med velikostjo zrn, teksturo in mehanskimi lastnostmi. Razen statičnih mehanskih preizkusov, nateznih in tlačnih, so bili izvedeni tudi preizkusi utrujanja. Na koncu so bili dobljeni podatki primerjani s Hall-Petchevim razmerjem in dobljeni rezultati so bili primerjani s podatki iz literature. Dobljeni rezultati so potrdili močan vpliv obdelave na mehanske lastnosti, z močnim vplivom na Hall-Petchevo razmerje.

Ključne besede: magnezij, mehanske lastnosti, Hall-Petchevo razmerje

1 INTRODUCTION

Magnesium is an essential matrix element of many materials used in the traffic industry and also of some biodegradable materials that can be used for medical applications. Both these groups are characterized by high demands on the mechanical properties. These properties are strongly affected by many material factors. One of the very well-known factors is strengthening by grain boundaries, which is simply described by the Hall-Petch Equation (1):

$$\sigma = \sigma_0 + k \cdot d^{-1/2} \qquad (1)$$

In this equation "σ_0" and "k" are the constants representing the intercept and the slope of the Hall-Petch line, respectively. Magnesium as well as other metals with *hcp* structures have already been the subjects of many studies which showed that "σ_0" is related to the critical resolved shear stress (CRSS) for the easy slip system operating within the grain volume or in other words it represents the friction stress of mobile dislocations on the slip plane[1,2], and "k" is related to the CRSS for the more difficult slip/twinning systems required to operate near grain boundaries in order to maintain the continuity of strain[3] or in other words "k" represents the stress-concentration factor.[2] Both these constants ("σ_0" and "k") are texture dependent.

Material texture can be significantly affected by different processing methods such as rolling, extrusion, forging and of course by the parameters of those processes.

Another Equation (2), which characterizes the dependence of polycrystalline strength "σ" on the critical shear strength "τ_0" and the stress concentration required to propagate slip across a grain boundary "k_s" has to be modified if we consider textured materials since the orientation constants relating "σ_0" and "k" to the corresponding single-crystal resolved shear stresses will be different and depend on the intensity of the respective textures. In such case, Equation (2) can be modified to Equation (3), where "M" is the orientation factor relating "σ_0" to the CRSS for an easy slip, and "N" is the orientation factor relating "k" to "k_s":

$$\sigma = m \cdot (\tau_0 + k_{s\,.}\, l^{-1/2}) \tag{2}$$

$$\sigma = M \cdot \tau_0 + N \cdot k_{s\,.}\, l^{-1/2} \tag{3}$$

On the basis of the pile-up model, the Hall-Petch slope "k" is related to the resolved shear stress "τ_c" for the difficult slip system controlling plastic flow in the grain-boundary regions, Equation (4):

$$k = N \cdot k_S = C \cdot N \cdot [m \cdot \mathrm{G}b/2\tau \mathrm{a}]^{1/2} \cdot \tau_c^{\ 1/2} \tag{4}$$

In this Equation (4) "C" is a constant, "m*" is the Sach's orientation factor that takes into account the differences in the grain-to-grain orientation, "a" is a numerical constant depending on the screw or edge character of the dislocation pile-up, "G" is the shear modulus, and "b" is the Burgers vector. Therefore, "k" is related to the CRSS for prismatic slip and the {10-10} texture can be expected to affect the value of the slope "k". It is evident that the material properties are strongly texture dependent and the Hall-Petch behaviour can be different for materials prepared by different processing routes.

Due to the limited number of slip systems in *hcp* structures, other mechanisms such as twinning also play an important role in the deformation behaviour of magnesium and magnesium-based alloys. It has been shown that twin boundaries act as strong barriers to dislocation motion.[4] Therefore, in practice, the mean free path of the dislocations should incorporate terms representing the effects of both the grain size and the presence of any twins. Several types of single- and double-twinning such as $\{10\bar{1}1\}$, $\{10\bar{1}2\}$, $\{10\bar{1}3\}$, $\{10\bar{1}1\}$–$\{10\bar{1}2\}$ and $\{10\bar{1}3\}$–$\{10\bar{1}2\}$ are formed in magnesium and its alloys,[5–7] and the crystallographic relation of the lattice rotates around the $\langle 1\bar{1}20\rangle$ direction by 56°, 86° and 64° for these types of single twinning formation. Among these types of twinning, the {10–12}-type (‹*c*›-axis tension) twins form easily at the beginning of plastic deformation, since its CRSS is the lowest and has a similar order as that in the basal plane.[5,6] The twinning is formed by the concentrated stress due to the dislocation pile-up, as reported in [3]. When the magnitude of the stress concentration is larger than the nucleation stress, twinning is thought to form at an adjacent grain.[8] It has also been reported that twinning tends to form at grain boundaries with lower misorientation angles, which are characterized by a higher grain-boundary energy in magnesium.[9,10]

Different methods can be used for the manufacture of magnesium alloys with a low grain size, and different textures are prepared during these processes. The main examples of such methods are extrusion, ECAP (equal channel angular pressing) and HPT (high pressure torsion). Material prepared by original straight extrusion has a typical texture consisting of $\langle 10\bar{1}0\rangle$ and $\langle 11\bar{2}0\rangle$ fibres (i.e., basal poles perpendicular to the extrusion axis). ECAP textures and its strength are dependent on ECAP routes and also on the number of ECAP passes.

Final texture affects measured mechanical properties. After extrusion, if the tensile axis lies within the basal plane of the majority of grains, the grains are forced to deform by either non-basal cross-glide of basal dislocations or pyramidal slip of large Burgers vector ‹*c*+*a*› dislocations.[11] These hard deformation modes possess a high critical resolved flow stress, and ultimately result in the premature failure of properly oriented samples. In contrast, if the basal axes are oriented close to the tensile stress axis, there is very strong signature of the $\{10\bar{1}2\}$ tensile twinning $[11\bar{1}3]$. Twinning re-orients a portion of the crystallites, and only a small plastic strain is required to ensure that a major volume fraction of grains becomes poorly oriented for slip or twinning. Therefore, the anisotropy of the mechanical properties observed in magnesium alloys with specific texture and both tensile and compressive properties are a distinctive base on the tests' orientation.

The present work is focused on a classic extrusion process with a low extrusion ratio equal to 10 and an extrusion rate only 5 mm/min. Together with a low temperature (200 °C), such conditions were selected to obtain fine-grained structures and proper mechanical properties.

2 MATERIALS AND METHODS

2.1 Materials

In this study, pure Mg (99.9 %) in an extruded state was investigated. Cylindrical ingots of Mg were prepared by melting pure Mg (99.9 %) in an induction furnace under a protective argon atmosphere (99.996 %). The melt was homogenised at 750 °C for 15 min and cast into a brass mould of 100 mm in length and 20 mm in diameter. Magnesium was directly extruded at a temperature of 200 °C, an extrusion rate of 5 mm/min, and an extrusion ratio of 10:1 to prepare rods of 6 mm in a diameter. Such specimens were annealed at temperatures of (200, 300 and 400) °C for different times to prepare magnesium with different grain sizes and properties.

2.2 Structure

The microstructure of the Mg was studied by optical microscopy (Olympus PME3) and scanning electron microscopy (SEM – TescanVega3 LMU) equipped with an energy-dispersive spectrometer (EDS, Oxford Instruments Inca 350) and an EBSD detector – NordlysMax and AZtecHKL software. For SEM analysis, the samples were mechanically grinded using SiC abrasive papers P180–P4000, polished by diamond pastes with 2 μm and 0.7 μm particles and etched in a 2 % Nital solution. For EBSD additional mechanical polishing was performed on a neutral alumina suspension (OP-AN Suspension). Finally, samples were prepared by electro-polishing in 15 % nitric acid in ethanol at 12 V for 15 s.

2.3 Mechanical properties

The mechanical studies were performed using Vickers hardness measurements with a loading of 5 kg (HV5). The mechanical properties were also characterised by tensile tests and compression tests (LabTest 5.250SP1-VM). For the tensile tests of the as-cast alloys, rod samples of 4 mm in diameter and 60 mm in length were used. The strain rate during the tensile tests was set to 0.001 s^{-1}. Compression tests were performed on rod samples of 6 mm in a diameter and 12 mm height at a strain rate of 0.001 s^{-1} as was used for the tensile tests.

Fatigue tests were performed on a device SCHNCK PHG. Smooth fatigue specimens with a diameter of 6 mm and a gauge length of 18.7 mm were machined from the extruded materials. Before the fatigue test they were mechanically polished using progressively finer grades of emery paper and buff-finished. The fatigue tests were performed at a frequency of 50 Hz in laboratory air at ambient temperature.

3 RESULTS AND DISCUSSION

3.1 Structure

Typical examples of microstructures of pure Mg obtained by different thermomechanical processing are given in **Figure 1**. Magnesium after the extrusion at 200 °C (**Figure 1a**) was fully recrystallized with the grain size ranging from 2 μm to 18 μm and with the dominant equivalent grain diameter of 4 μm. No elongated grains were observed in the structure. Different thermal treatment leads to an obvious grain coarsening. **Figure 2** shows the distribution of grain sizes for pure Mg treated at different conditions – extruded material and extruded material exposed to the subsequent thermal treatment at 200, 300 and 400 °C for 1 h and 2 h. It is clear that the coarsening of Mg is strongly dependent on both temperature and time. However, it seems that at lower temperatures such as 200 °C coarsening is not so significant with prolonged time on the temperature. At higher temperatures (300 °C, 400 °C) the grain size is increased significantly, also with a prolonged exposure time. **Figure 3a** shows EBSD maps of pure Mg extruded at 200 °C. The analysis was performed on the surface parallel to the extrusion direction. As can also be seen in **Figure 4**, the majority of grains is oriented in the structure with the basal planes parallel to the extrusion direction, which is a known effect of the extrusion process on magnesium-based alloys. Texture orientation and strength are evident in **Figure 4a**. A specimen subjected to the subsequent annealing at 400 °C for 2 h was analysed using EBSD (**Figures 3b** and **4b**) for a comparison with the extruded Mg. The grain size ranged from 20 μm to 160 μm and the dominant equivalent grain diameter reached about 40 μm. It can be clearly seen that texture was maintained similar to the extruded condition and only texture strength was slightly reduced from 10.2 to 10 for extruded Mg and extruded + annealed Mg, respectively (**Figure 4**). This confirms that the texture created during thermomechanical treatment is maintained also during the subsequent thermal treatment.

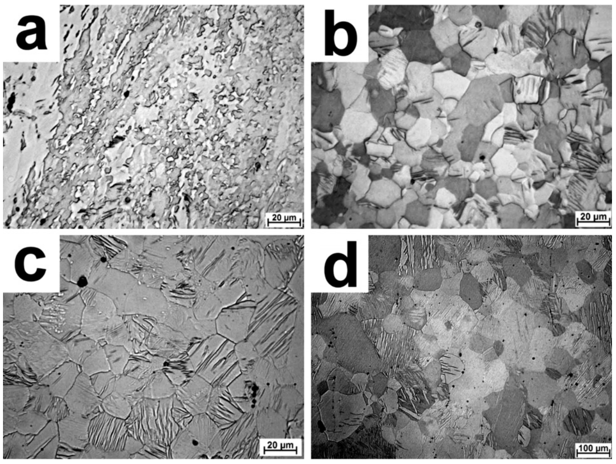

Figure 1: Structure of Mg after different thermo-mechanical processing: a) extruded at 200 °C, b) extruded at 200 °C and annealed at 200 °C for 1 h, refer to extrusion direction, c) extruded at 200 °C and annealed at 200 °C for 2 h, refer to extrusion direction, d) extruded at 200 °C and annealed at 400 °C for 2 h, refer to extrusion direction

Slika 1: Mikrostruktura v smeri ekstrudiranja Mg po različnih termomehanskih obdelavah: a) ekstrudirano pri 200 °C, b) ekstrudirano pri 200 °C in 1 h žarjeno na 200 °C, c) ekstrudirano pri 200 °C in žarjeno 2 h na 200 °C, d) ekstrudirano pri 200 °C in žarjeno 2 h na 400 °C

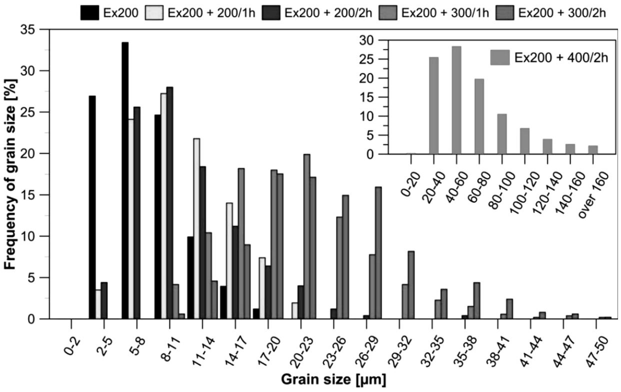

Figure 2: Grain size distribution in the Mg treated under different conditions

Slika 2: Razporeditev velikosti zrn v Mg, obdelanem pri različnih pogojih

Dynamic recrystallization is supposed to manage the recrystallization process during the hot extrusion. In this case, new fine grains are formed at the original grain boundaries and subsequent nucleation occurs at the recrystallized grains.

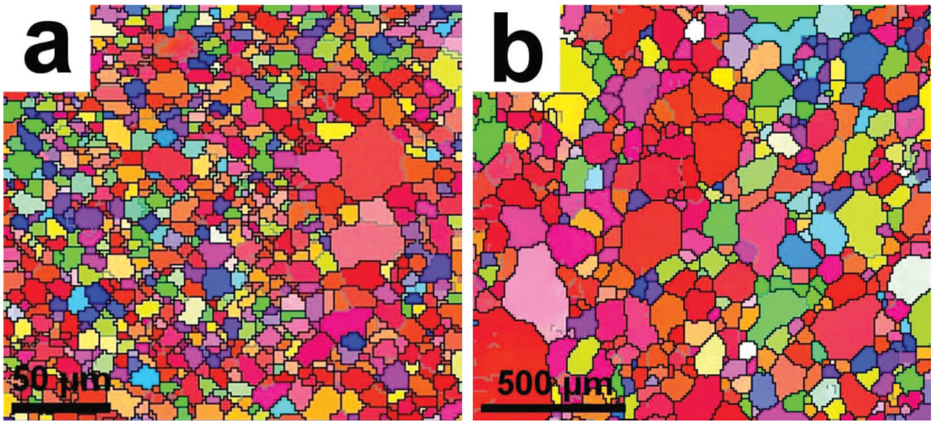

Figure 3: IPF maps of pure Mg: a) extruded at 200 °C, b) extruded at 200 °C and annealed at 400 °C for 2 h, refer to extrusion direction
Slika 3: IPF-mape pri čistem Mg v smeri ekstruzije: a) ekstrudirano pri 200 °C, b) ekstrudirano pri 200 °C in 2 h žarjeno na 400 °C

Discontinuous and continuous dynamic recrystallization (DDRX, CDRX) are considered for magnesium depending on the initial grain size and also the temperature. DDRX is operative when the initial grain size of magnesium alloys is large enough for the crystallographic slip to be heterogeneous, which is the case of the as-cast Mg. Pure magnesium in the as-cast sate was characterized by the grains with about 100 µm in thickness and nearly 1 mm in length. It is known that extrusion ratio (ER) has a significant effect on the grain size. Although an ER equal to 10 seems to be low, it is possible to reach a very fine-grained structure after extrusion at 200 °C. According to the empirical Equation (5), strain during extrusion process corresponds only to 2.3:

$$\varepsilon = \ln(\mathrm{ER})^{14} \tag{5}$$

Therefore, other important factors, such as temperature and extrusion velocity, have to affect the final grain size significantly. In this case the extrusion velocity is only 2 mm/min. At a lower extrusion velocity, a lower strain rate can lead according to the Zener–Hollomon parametre to the coarsening of the structure. Moreover, it means prolonged times at temperature during the extrusion process and subsequent cooling, which can also lead to the coarsening. However, a lower strain rate also means only a smaller temperature increase in the material during deformation, which prevents an excessive grain growth.[15]

Texture development is global process that includes slip in the basal system and also other slip systems and

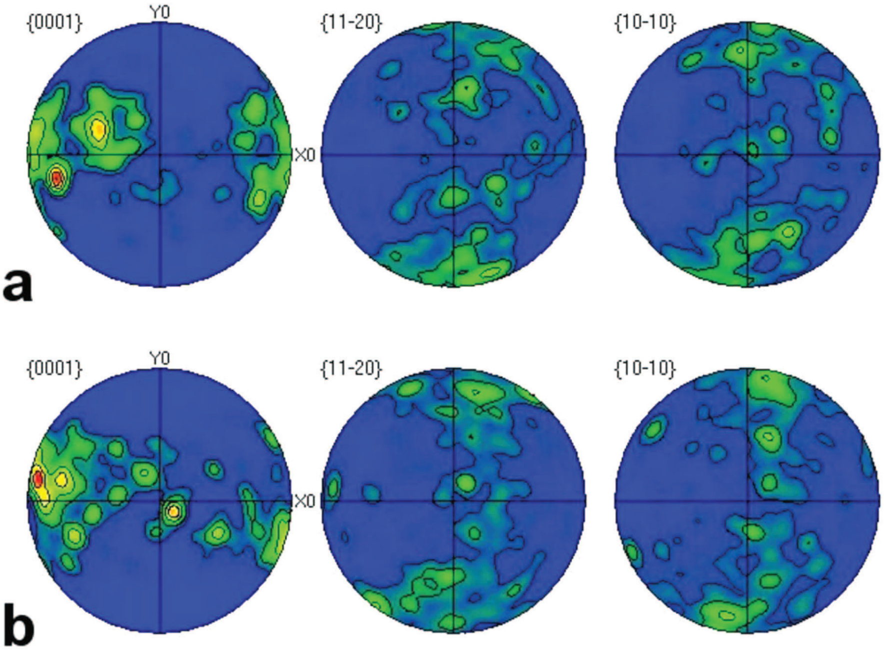

Figure 4: Pole figures of pure Mg: a) extruded at 200 °C (max mud = 10.14), b) extruded at 200 °C and annealed at 400 °C for 2 h (max mud = 9.91), X0–Y0 area is parallel to the extrusion direction and Y0 represents the extrusion direction
Slika 4: Slike polov za čisti Mg: a) ekstrudirano pri 200 °C (max mud = 10,14), b) ekstrudirano pri 200 °C in 2 h žarjeno na 400 °C (max mud = 9,91), X0-Y0 je področje, ki je vzporedno s smerjo ekstruzije, Y0 predstavlja smer ekstruzije

twinning. At low temperatures, the dominate slip system is basal slip. Tensile twinning also plays an important part in the accommodation of strain during the deformation, especially in the coarse-grained magnesium alloys. Due to the fact that coarse grains are presented in the structure especially at the beginning of deformation process, tensile twining is favoured at this stage and helps to reorient the grains to a basal orientation. It was also proved that other mechanisms, such as double twinning and shear and kink banding, also operate to accommodate c-axis compression when non-basal slip is limited at low temperature.[16] Texture can be partially suppressed by the slip in non-basal slip systems; however, the critical resolved shear stresses (CRSS) of non-basal slip systems for Mg are significantly higher compared with the basal slip system. This can be partially compensated by stress concentration at the grain boundaries, which is effective for the activation of non-basal slip. A higher extrusion ratio can be partially responsible for the activation of non-basal slip and finally also a weaker texture. Also, a higher temperature can lead to an easier activation of non-basal slip, which can significantly affect the texture evolution.

The DRX process itself does not lead to the texture change in the case of magnesium-based alloys exposed to the extrusion or a combination of extrusion and annealing (**Figure 4**); conversely, it serves to strengthen the basal texture. Due to the low temperature of the extrusion process, the low extrusion velocity and the extrusion ratio, it is really difficult for non-basal slip to be activated. There are only signs of twins in the structure, which can be responsible for a slight texture weakening. Overall, all the samples were characterized by similar and strong textures.

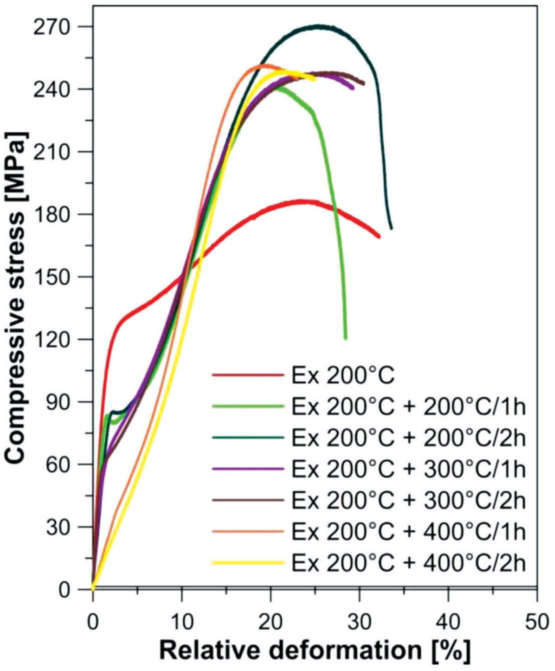

Figure 5: Compressive curves of Mg processed by extrusion and different subsequent heat treatments

Slika 5: Tlačne krivulje za Mg izdelan z ekstruzijo in z različnimi toplotnimi obdelavami po njej

3.2 Mechanical properties

Mechanical properties in both compression and tension were measured. Based on the conditions of thermal treatment, magnesium is characterized by different compressive yield strength (CYS) and ultimate compressive strength (UCS) and also different behaviour after the onset of plastic deformation (**Figure 5**). The CYS of extruded Mg reached the maximum value of nearly 130 MPa. After that, the deformation strengthening is obvious; however, the ultimate tensile strength reaches a value as low as 190 MPa. On the contrary, magnesium exposed to the subsequent thermal treatment is characterized by lower values of CYS. Moreover, CYS is decreased with increased temperatures and prolonged times at these temperatures. When the CYS is overcome, strong deformation strengthening take place and finally, UCS reaches values between 240 MPa and 270 MPa (**Figure 5**).

The significant strain hardening in compression for materials with a coarse-grained structure is known and can be ascribed to the formation of $\{10\bar{1}2\}$ twins.[8,17] The formation of deformation twins causes a significant strain-hardening tendency, because the twins block the propagation of dislocations. With a decrease in the grain size the decrease in the strain hardening is caused because the twinning cannot develop in the same manner as for materials with larger grains.[18]

The TYS and UTS increased gradually with grain refinement (**Table 1**), because magnesium has a large Taylor factor due to the lack of slip systems.[19] It is also clear that uniform elongation is decreased with subsequent thermal treatment, in other words with increased grain size.

Table 1: Mechanical properties of magnesium in different states estimated from the tensile tests

Tabela 1: Z nateznimi preizkusi določene mehanske lastnosti magnezija v različnih stanjih

	Proof stress 0.2 % (TYS) (MPa)	UTS (MPa)	Elongation (%)
Mg Ex 200 °C	108±10	173±10	6.7±0.8
Mg Ex 200 °C + 200/2 h	91±8	168±7	6.2±0.8
Mg Ex 200 °C + 300/2 h	79±5	160±5	5.3±1.1
Mg Ex 200 °C + 400/2 h	72±5	150±7	3.6±0.9

Although there are many studies about the effect of texture and related effect on the Hall Petch behaviour, the obtained values were properly fitted by linear function, because all the samples seems to be characterized by a very similar texture and also its strength. **Figures 6**

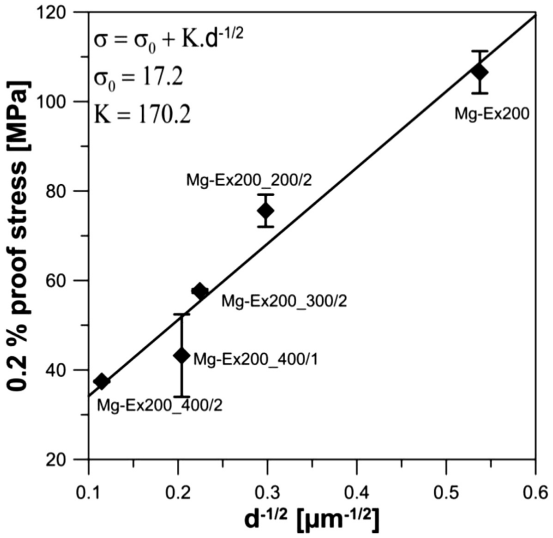

Figure 6: Experimental change of the compressive yield strength (CYS) with the grain size
Slika 6: Spreminjanje tlačne meje plastičnosti z velikostjo zrn

to **8** show the Hall-Petch relations based on the compressive tests, tensile tests and hardness measurements for pure Mg. It is worth mentioning that in all cases the deviation of different points from linear behaviour was negligible. Based on these facts it seems that the measured mechanical properties are dependent on the grain size according to the Hall-Petch relation. The obvious differences in the estimated constants for different measurement methods are connected with different types of mechanical loading and also texture of the material. It is known that during the extrusion or hot-rolling process, the basal planes are strongly oriented parallel to the rolling direction. In the case of extrusion, the texture strength is often weaker compared to the rolling; however, it is still there, as can be seen from **Figure 4**. The observed mechanical properties are then strongly dependent on the direction of loading during the mechanical testing. If the basal planes are parallel to the axis of tension, so the directions $(10\bar{1}0)$ are parallel to the extrusion direction, the slip on basal planes is complicated. Therefore, a high tensile strength is observed along the extrusion direction.[20]

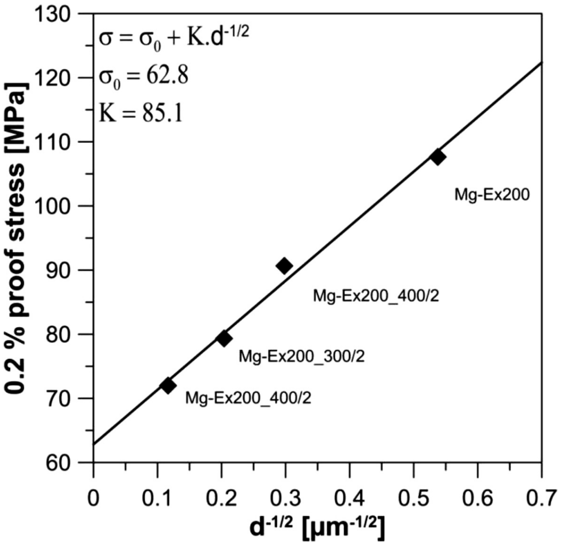

Figure 7: Experimental change of the tensile yield strength (TYS) with the grain size
Slika 7: Spreminjanje natezne meje plastičnosti z velikostjo zrn

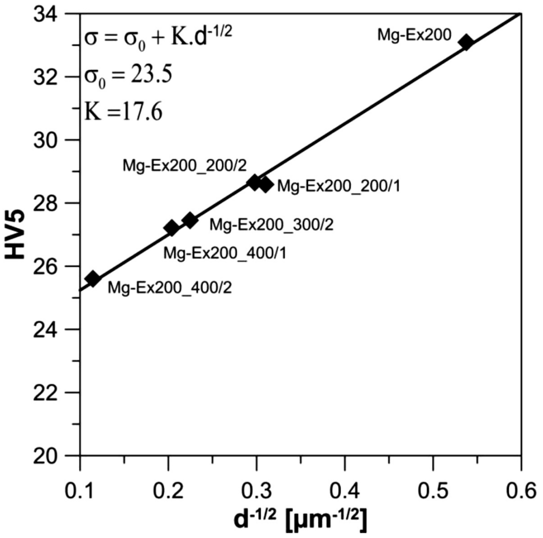

Figure 8: Experimental change of the Vickers hardness (HV5) with the grain size
Slika 8: Spreminjanje trdote po Vickersu (HV5) z velikostjo zrn

The flow stress of Mg strongly depends on the grain size; although there is also a strong texture dependence due to the large difference in critical shear stress between the basal planes and the non-basal planes. Such differences are decreased with increased temperature. The effect of texture on the Hall-Petch slope or in other words the grain size dependence of "*K*" is significant.[21] It is known that the misorientation of grain boundaries affects the grain size dependence of the flow stress. As a result, the value of "*K*" is lower for low-angle grain boundaries. Based on these facts, extruded Mg is characterized by a stronger dependence of the yield strength on the grain size compared to the Mg with a weaker texture.

Different works study the Hall-Petch behaviour of Mg after different thermomechanical processing. Some results are indicated in **Figure 9**. N. Ono et al.[1] used rolled Mg sheets as a starting material for a determination of the Hall-Petch relation using tensile tests. G. S. Rao et al.[3] studied the Hall-Petch behaviour on tensile specimens from a hot rolled sheet in the longitudinal and transverse directions and also from hot-rolled square rods. H. Somekawa et al.[8] prepared magnesium plates using extrusion with an extrusion ratio of 10 at 200 °C. The compression tests on these samples were performed with the compression axis parallel to the extrusion direction, which is the same as in the present research. A. Yamashita et al.[22] studied magnesium and magnesium alloys prepared by ECAP with an internal angle of 90° at

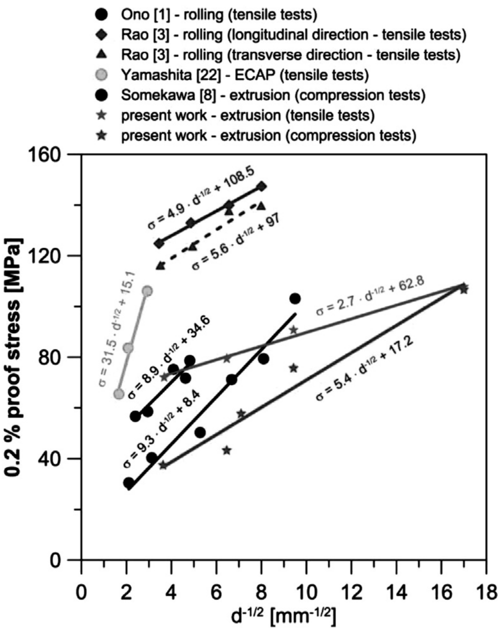

Figure 9: Hall Petch of pure magnesium after different preparation conditions

Slika 9: Hall Petch relacija pri čistem magneziju po različnih pogojih priprave

200–400 °C. The Hall-Petch behaviour was subsequently studied using tensile tests. Compared to our experiments, it is seen that Mg prepared by rolling is characterized by a higher value of σ_0 (**Figure 9**). Moreover, this value is dependent on the intensity of the rolling, which has a direct effect on texture strength.[1, 3] The same reason can be considered in the case of the difference between the properties of extruded Mg. From all these studies it is clear that there is no general Hall-Petch relation, which could cover different conditions. Instead, it is necessary to include grain size, texture and also other phenomena (basal, non-basal slip and twinning), which are affected by the grain size and texture in a general consideration for the final behaviour of the Mg material.

In **Figure 10,** stress versus the number of cycles fatigue curves are shown for two extreme states of the studied Mg. Magnesium extruded at 200 °C is characterized by an improved fatigue life. The maximum value of the stress amplitude for a service life longer than 8×10^7 cycles is 30 MPa for extruded Mg and about 25 MPa for Mg with a subsequent thermal treatment at 400 °C. Such a difference is connected with grain refinement, which is very effective for improving the fatigue strength.[23] Another fact that plays an important role during fatigue testing is the texture. Due to the preferential orientation of the basal planes parallel to the extrusion direction, there is an anisotropy between hardening for tensile and compressive loading.[24] During tensile loading, twinning is very challenging due to the initial orientation. Pyramidal ‹*a*› and ‹*c*+*a*› pyramidal slips are characterized by higher values of the Schmidt factors (0.33 and 0.49 respectively[24]). Also, ‹a› prismatic slip is problematic and a value of Schmidt factor equal to 0.35 has been postulated. As a consequence, especially basal slip with a low Schmidt factor of 0.17 takes place during this stage. In contrast, during the compressive step, $(10\bar{1}2)$ ‹1101› twinning and also basal slip are active. Different twin types have been observed during cycling, although some types are presented in the structure after a number of cycles. During cycling, a hardening effect was observed and more stress is concentrated in the structure. As a consequence, more complicated twinning processes and also non-basal slip take place with an increasing number of cycles.[25]

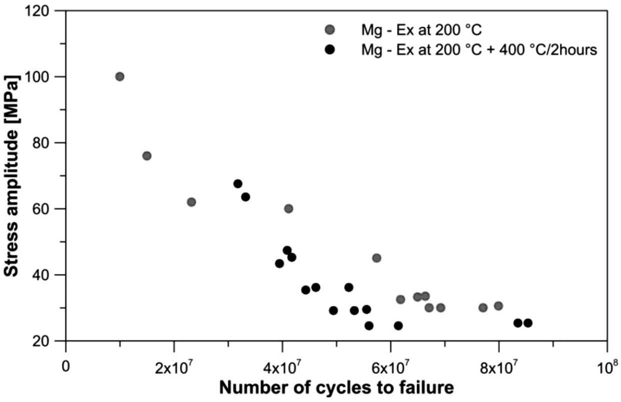

Figure 10: Fatigue behaviour of magnesium extruded at 200 °C and subsequently annealed at 400 °C for 2 h

Slika 10: Utrujanje magnezija, ekstrudiranega pri 200 °C in nato žarjenega 2 h na 400 °C

Tension twinning occurs when the resolved shear stress exceeds the critical resolved shear stress (CRSS). The values of 2.2–3.0 MPa were measured for such behaviour in a single crystal by Q. Yu et al.[25] and also the value of 2.4 MPa was published by the same author for a different monocrystal orientation.[26]

Due to such limitations, complex dislocation structures are rather unlikely in magnesium under cyclic loading.[24,27] In the case of pure Mg, cyclic hardening is expected as has already been proved in [28].

4 CONCLUSION

The present paper is focused on a study of the mechanical properties of pure Mg prepared by an extrusion process at 200 °C with an extrusion ratio equal to 10. Our results confirmed the significant effect of both grain size and texture on the mechanical properties. Both these main characteristics affect the slip and twinning activity. The anisotropy in mechanical properties is documented by different Hall-Petch behaviour based on compressive and tensile testing in the same direction and also by a comparison with literature. It is shown that both σ_0 and k from the Hall-Petch relation are strongly dependent on the mechanical processing. Fatigue tests performed at laboratory temperature confirm the increase in the fatigue life with a decreased grain size. The effect of texture strength can be, in this case, neglected due to the similar texture strength of the measured samples.

Acknowledgement

Jiří Kubásek wishes to thank for financial support of this research (project no. GA16-08963S) and Drahomír Dvorský wishes to thank the Czech Science Foundation for financial support (project no. P108/12/G043).

5 REFERENCES

[1] N. Ono, R. Nowak, S. Miura, Effect of deformation temperature on Hall–Petch relationship registered for polycrystalline magnesium, Materials Letters, 58 (**2004**) 1–2, 39–43, doi:10.1016/s0167-577x(03)00410-5

[2] W. Yuan, S. K. Panigrahi, J. Q. Su, R. S. Mishra, Influence of grain size and texture on Hall–Petch relationship for a magnesium alloy, Scripta Materialia, 65 (**2011**) 11, 994–997, doi:10.1016/j.scriptamat.2011.08.028

[3] G. S. Rao, Y. V. R. K. Prasad, Grain-Boundary Strengthening in Strongly Textured Magnesium Produced by Hot-Rolling, Metallurgical and Materials Transactions A, 13 (**1982**) 12, 2219–2226, doi: 10.1007/Bf02648393

[4] Y. Zhang, N. R. Tao, K. Lu, Effect of stacking-fault energy on deformation twin thickness in Cu-Al alloys, Scripta Materialia, 60 (**2009**) 4, 211–213, doi:10.1016/j.scriptamat.2008.10.005

[5] R. E. Reedhill, W. D. Robertson, additional modes of deformation twinning in magnesium, Acta Metallurgica, 5 (**1957**) 12, 717–727, doi:10.1016/0001-6160(57)90074-3

[6] B. Wonsiewi, W. A. Backofen, Plasticity of magnesium crystals, Transactions of the Metallurgical Society of Aime, 239 (**1967**) 9 1422–1431

[7] E. W. Kelley, W. F. Hosford, Plane-strain compression of magnesium and magnesium alloy crystals, Transactions of the Metallurgical Society of Aime, 242 (**1968**) 1, 5

[8] H. Somekawa, T. Mukai, Hall–Petch relation for deformation twinning in solid solution magnesium alloys, Materials Science and Engineering, A, 561 (**2013**) 0, 378–385, doi:10.1016/j.msea.2012.10.040

[9] J. Wang, I. J. Beyerlein, C. N. Tome, An atomic and probabilistic perspective on twin nucleation in Mg, Scripta Materialia, 63 (**2010**) 7, 741–746, doi:10.1016/j.scriptamat.2010.01.047

[10] J. T. Chou, K. Ikeda, H. Nakashima, Energy and structure of 1(1)over-bar00 symmetric tilt grain boundaries in magnesium, Journal of the Japan Institute of Metals, 69 (**2005**) 3, 303–307, doi:10.2320/jinstmet.69.303

[11] S. R. Agnew, C. N. Tome, D.W. Brown, T. M. Holden, S. C. Vogel, Study of slip mechanisms in a magnesium alloy by neutron diffraction and modeling, Scripta Materialia, 48 (**2003**) 8 1003–1008, doi:10.1016/s1359-6462(02)00591-2

[12] S. R. Agnew, D. W. Brown, S. C. Vogel, T. M. Holden, In-situ measurement of internal strain evolution during deformation dominated by mechanical twinning, A. M. Dias, J. Pina, A. C. Batista, E. Diogo (Eds.), Ecrs 6, Proceedings of the 6th European Conference on Residual Stresses, Trans. Tech. Publications Ltd., Stafa-Zurich, 2002, 747–752

[13] A. A. Salem, S. R. Kalidindi, R. D. Doherty, Strain hardening regimes and microstructure evolution during large strain compression of high purity titanium, Scripta Materialia, 46 (**2002**) 6, 419–423, doi:10.1016/s1359-6462(02)00005-2

[14] W. Tang, S. Huang, S. Zhang, D. Li, Y. Peng, Influence of extrusion parameters on grain size and texture distributions of AZ31 alloy, Journal of Materials Processing Technology, 211 (**2011**) 7, 1203–1209, doi:http://dx.doi.org/10.1016/j.jmatprotec.2011.01.014

[15] Govind, K. S. Nair, M. C. Mittal, R. Sikand, A. K. Gupta, Effect of extrusion parameters on microstructure and mechanical properties of ZK30 Mg Alloy, Materials Science and Technology, 24 (**2008**) 4, 399–405, doi:10.1179/174328408X276224

[16] L. W. F. Mackenzie, M. Pekguleryuz, The influences of alloying additions and processing parameters on the rolling microstructures and textures of magnesium alloys, Materials Science and Engineering, A, 480 (**2008**) 1–2, 189–197, doi:10.1016/j.msea.2007.07.003

[17] M. R. Barnett, Z. Keshavarz, A. G. Beer, D. Atwell, Influence of grain size on the compressive deformation of wrought Mg-3Al-1Zn, Acta Materialia, 52 (**2004**) 17, 5093–5103, doi:10.1016/j.actamat.2004.07.015

[18] H. J. Choi, Y. Kim, J. H. Shin, D. H. Bae, Deformation behavior of magnesium in the grain size spectrum from nano- to micrometer, Materials Science and Engineering, A, 527 (**2010**) 6, 1565–1570, doi:10.1016/j.msea.2009.10.035

[19] R. Armstrong, I. Codd, R. M. Douthwaite, N. J. Petch, The plastic deformation of polycrystalline aggregates, Philosophical Magazine, 7 (**1962**) 73, 45–58, doi:10.1080/14786436208201857

[20] Y. N. Wang, J. C. Huang, Texture analysis in hexagonal materials, Materials Chemistry and Physics, 81 (**2003**) 1, 11–26, doi:10.1016/S0254-0584(03)00168-8

[21] M. Mabuchi, Y. Chino, H. Iwasaki, T. Aizawa, K. Higashi, The Grain Size and Texture Dependence of Tensile Properties in Extruded Mg-9Al-1Zn, Materials Transactions, 42 (**2001**) 7, 1182–1188, doi:10.2320/matertrans.42.1182

[22] A. Yamashita, Z. Horita, T. G. Langdon, Improving the mechanical properties of magnesium and a magnesium alloy through severe plastic deformation, Materials Science and Engineering, A, 300 (**2001**) 1–2, 142–147, doi:10.1016/S0921-5093(00)01660-9

[23] Y. Uematsu, K. Tokaji, M. Kamakura, K. Uchida, H. Shibata, N. Bekku, Effect of extrusion conditions on grain refinement and fatigue behaviour in magnesium alloys, Materials Science and Engineering, A 434 (**2006**) 1–2 131–140, doi:10.1016/j.msea.2006.06.117

[24] C. Guillemer, M. Clavel, G. Cailletaud, Cyclic behavior of extruded magnesium: Experimental, microstructural and numerical approach, International Journal of Plasticity, 27 (**2011**) 12, 2068–2084, doi:10.1016/j.ijplas.2011.06.002

[25] Q. Yu, Y. Jiang, J. Wang, Cyclic deformation and fatigue damage in single-crystal magnesium under fully reversed strain-controlled tension–compression in the [10-11] direction, Scripta Materialia, 96 (**2015**) 0, 41–44, doi:10.1016/j.scriptamat.2014.10.020

[26] Q. Yu, J. Zhang, Y. Jiang, Direct observation of twinning-detwinning–retwinning on magnesium single crystal subjected to strain-controlled cyclic tension–compression in [0?0?0?1] direction, Philosophical Magazine Letters, 91 (**2011**) 12, 757–765, doi:10.1080/09500839.2011.617713

[27] C. Potzies, K. U. Kainer, Fatigue of Magnesium Alloys, Advanced Engineering Materials, 6 (**2004**) 5, 281–289, doi:10.1002/adem.200400021

[28] R. Kwadjo, L. M. Brown, Cyclic hardening of magnesium single crystals, Acta Metallurgica, 26 (**1978**) 7, 1117–1132, doi:10.1016/0001-6160(78)90139-6

UDK 620.1:66.017:621.791
Original scientific article/Izvirni znanstveni članek

ISSN 1580-2949
MTAEC9, 51(2)297(2017)

MICROSTRUCTURAL EVOLUTION AND MECHANICAL CHARACTERIZATIONS OF AL-TiC MATRIX COMPOSITES PRODUCED VIA FRICTION STIR WELDING

KARAKTERIZACIJA RAZVOJA MIKROSTRUKTURE IN MEHANSKIH LASTNOSTI KOMPOZITA Al-TiC IZDELANEGA S TORNIM VARJENJEM Z MEŠANJEM

Oluwatosin Olayinka Abegunde, Esther Titilayo Akinlabi, Daniel Madyira

University of Johannesburg, Faculty of Engineering and Built Environment, Department of Mechanical Engineering Science,
Auckland Park Kingsway Campus, 2006 Johannesburg, South Africa
oabegunde@uj.ac.za

Prejem rokopisa – received: 2016-02-09; sprejem za objavo – accepted for publication: 2016-03-21

doi:10.17222/mit.2016.033

A study was conducted on the material characterization of aluminium (Al) and titanium carbide (TiC) metal-matrix composites produced via friction stir processing. Different process parameters were employed for the welding process. Rotational speeds of 1600 min^{-1} to 2000 min^{-1}, at an interval of 200 min^{-1} and traverse speeds of 100 mm/min to 300 mm/min, at an interval of 100 mm/min were employed for the welding conducted on an Intelligent Stir Welding for Industry and Research (I-STIR) Process Development System (PDS) platform. The characterizations carried out include light microscopy and the scanning electron microscopy analyses combined with Energy-Dispersive Spectroscopy (SEM/EDS) techniques to investigate the particle distribution, microstructural evolution and the chemical analysis of the welded samples. Vickers microhardness tests were used to determine the hardness distribution of the welded zone and tensile testing was conducted to quantify the strength of the welded area compared to the base metal in order to establish the optimal process parameters. Based on the results obtained from the characterization analysis, it was found that the process parameters played a major role in the microstructural evolution. A homogenous distribution of the TiC particles was observed at a high rotational speed of 2000 min^{-1} and a low traverse speed of 100 mm/min. The highest hardness value was measured at the stir zone of the weld due to the presence of the TiC reinforcement particles. The tensile strength also increased as the rotational speed increased and 92 % joint efficiency was recorded in a sample produced at 2000 min^{-1} and 100 mm/min. The EDS analysis revealed that Al, Ti and C made up the composition formed in the stir zone. The optimum process parameter setting was found to be at 2000 min^{-1} and 100 mm/min and can be recommended.

Keywords: aluminium, friction stir welding, mechanical properties, metal matrix composite, microstructural evolution, titanium carbide

V tem raziskovalnem delu je bila izvedena obsežna študija karakterizacije kovinskega kompozita aluminija (Al) in titanovega karbida (TiC) izdelanega z mešalno tornim varjenjem. Za postopek varjenja so bili uporabljeni različni procesni parametri. Rotacijski hitrosti 1600 min^{-1} do 2000 min^{-1}, v razmaku po 200 min^{-1}, in prečnih hitrostih od 100 mm/min do 300 mm/min, v intervalu 100 mm/min, je bilo uporabljeno za varjenje na industrijski platformi za razvoj in raziskave (PDS) sistema inteligentnega varjenja z mešanjem (I-Stir). Izvedena karakterizacija vključuje svetlobno mikroskopijo in vrstično elektronsko mikroskopijo v kombinaciji z energijo disperzijsko spektroskopijo (SEM/EDS), za preiskavo porazdelitve delcev, razvoja mikrostrukture in kemijsko analizo zvarjenih vzorcev. Za določitev optimalnih procesnih parametrov je bil uporabljen Vickers preizkus mikrotrdote, s katerim je bila določena porazdelitev trdote na področju zvara, z nateznim preizkusom pa je bila določena trdnost zvara v primerjavi z osnovnim materialom. Na osnovi rezultatov, dobljenih z analizo, je bilo ugotovljeno, da so procesni parametri igrali pomembno vlogo pri razvoju mikrostrukture. Homogena porazdelitev TiC delcev je bila opažena pri visokih hitrostih vrtenja (2000 min^{-1}) in nizki prečni hitrosti (100 mm/min). Največja vrednost trdote je bila izmerjena v mešalni coni zvara zaradi prisotnosti delcev TiC za ojačanje. Natezna trdnost se je povečala tudi pri povečanju hitrosti vrtenja in 92 % skupne učinkovitosti spoja je bila zabeležena pri vzorcu, izdelanem pri 2000 min^{-1} in prečni hitrosti 100 mm/min. EDS-analiza je pokazala, da Al, Ti in C povzročijo sestavo kompozita, ki je nastal v področju mešanja. Priporočljiva in optimalna nastavitev procesnih parametrov je 2000 min^{-1} in prečna hitrost 100 mm/min.

Ključne besede: aluminij, torno varjenje z mešanjem, mehanske lastnosti, kompozit s kovinsko osnovo, mikrostruktura, titan karbid

1 INTRODUCTION

Metal-matrix composites (MMCs) reinforced with ceramic phases exhibit high stiffness, high elastic modulus, improved resistance to wear, creep and fatigue, which make them promising structural materials for the aerospace and automobile industries compared to monolithic metals. However, these composites also suffer from a significant loss in ductility and toughness due to the incorporation of non-deformable ceramic reinforcements, which limit their application, especially where the ductility of the material is a determinant factor in the material selection.[1] Aluminium metal-matrix composites (AMCs) are variants of MMCs that have the potential to replace many conventional engineering materials. AMCs have already found commercial applications in the defence, aerospace, automobile and the marine industries due to their favourable metallurgical and mechanical properties.[2–5] The metal matrix is aluminium, while the reinforcement can be any ceramic particles compatible with the metal matrix.

In recent years, several techniques have been reported for manufacturing AMCs, these include; plasma air spraying, stir casting, squeeze casting, molten metal infiltration and powder metallurgy. These techniques have been reported for producing bulk composites, while high-energy laser melt injection, plasma spraying, cast sinter and electron beam irradiation have been used for producing surface AMCs.[6,7] Nevertheless, it should be pointed out that most of these existing processing techniques for forming composites are generally based on liquid-phase processing at high temperatures. In this case, it is hard to avoid the interfacial reaction between the reinforcement and the metal matrix and the formation of some detrimental phases.[1]

Friction stir welding (FSW) is a solid-state welding process developed by TWI for welding aluminium and its alloys.[8] It has been used to successfully weld aluminium alloys[9–11] and also used to weld other metals like magnesium, copper and titanium.[12–14] FSW is an emerging potential technique that can be employed for producing AMCs.[15–18] Since the process is a solid-state welding process, it is envisaged to alleviate the problems associated with interfacial reaction, the melting of ceramics and the formation of detrimental phases during the manufacture of AMCs.

Research studies have been reported on the friction stir processing (FSP) of aluminium matrix composites.[19–22] These studies concluded that grain refinement was achieved using the FSP process. An improved particle distribution and better mechanical properties were also observed. Also reported is that the process parameters used for welding and the tool geometry played a major role in the final outcome. Based on the available literature, previous research studies have been limited to surface composites using the FSP process for a modification of the surface properties.

In this study, AMCs were produced using FSP and titanium carbide (TiC) particles were used as the reinforcement. The addition of the TiC ceramic particles is due to its favourable mechanical properties, which include a high melting point, favourable fracture and tribological properties. The preference of FSP for the production of Al-TiC composite is to avoid delamination (a failure when laminated material becomes separated, perhaps due to poor processing during production, impact on service, or some other factors that may lead to the separation of layers of reinforcement), debonding (when two materials stop adhering to each other), incompatible mixing of base materials and filler materials, the presence of porosity, inhomogeneous distribution (clustering), the segregation of grains at boundaries, the wetting of the particles, excess eutectic formation, melting of ceramic particles and the formation of undesirable deleterious phase usually experienced in other techniques. FSP is also advantageous due to the rapid removal of reaction products from the interface, which enhances further reaction

The effect of process parameters on the stir zone's microstructure, microhardness and tensile behaviour was studied and the optimal process parameters were established.

2 EXPERIMENTAL PART

2.1 Preparation, dimensions and composition of workpieces

Aluminium 1050 alloy sheets of dimensions 300 mm × 200 mm × 3 mm with a smooth surface finish were used for this research work. The chemical composition of the aluminium as per manufacturer Material Safety Data Sheet (MSDS) is shown in **Table 1**.

Before the welding process, V grooves with depth of 1.5 mm and a width of 3 mm were made on all the aluminium sheets using a milling machine and the titanium carbide particles were filled and compacted into the grooves using a tool with only the shoulder, as illustrated schematically in **Figure 1**.

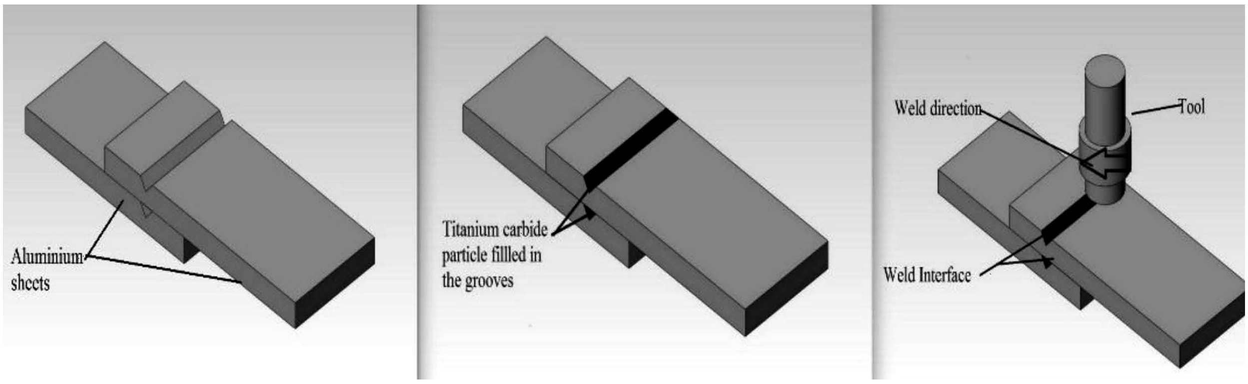

Figure 1: Schematic illustration of FSW of Al/TiC
Slika 1: Shematski prikaz FSW Al / TiC

Figure 2: FSW Tool
Slika 2: Orodje za FSW

2.2 FSW tool

The FSW tool used is a cylindrical H13 steel tool hardened to 52 HRC shown in **Figure 2**.

A basic tool geometry was used with a tool length of 5.7 mm and a tool diameter of 6 mm. The tool shoulder diameter is three times the pin diameter (18 mm) and with a concave geometry to exert pressure on the workpiece during welding.

2.3 Friction stir welding platform

The experimental setup of the samples properly positioned and firmly clamped on the backing plate is shown in **Figure 3**. The process was performed on an Intelligent Stir Welding for Industry and Research (I-STIR) Process Development System (PDS) at the eNtsa of Nelson Mandela Metropolitan University, Port Elizabeth, South Africa. **Table 1** summarizes the different welding parameters used to produce the welds. A tilt angle of 3° was kept constant and used for all the different welding parameters.

Table 1: FSW process parameters
Tabela 1: FSW-procesni parametri

Weld number	Rotational speed (min^{-1})	Traverse speed (mm/min)	Weld Interface	Weld pitch (mm/ min^{-1})
A1	1600	100	With TiC	0.063
A2	1600	200	With TiC	0.125
A3	1600	300	With TiC	0.188
B1	1800	100	With TiC	0.056
B2	1800	200	With TiC	0.111
B3	1800	300	With TiC	0.167
C1	2000	100	With TiC	0.050
C2	2000	200	With TiC	0.100
C3	2000	300	With TiC	0.150
D1	1600	200	Without TiC	0.125
D2	1800	200	Without TiC	0.111
D3	2000	200	Without TiC	0.100

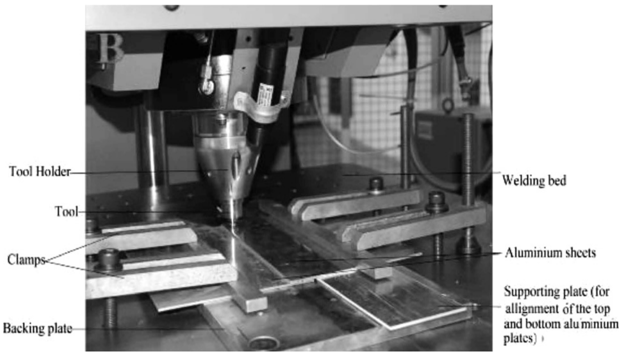

Figure 3: Experimental weld setup of FSW platform
Slika 3: Eksperimentalna postavitev FSW platforme za varjenje

A backing plate made of mild steel was positioned between the bed of the FSW platform and the workpiece. The choice of the backing plate is for a proper dissipation of heat during the welding process. A supporting sheet of the same thickness was placed underneath the upper plate to help align and stabilize the sheets to be joined during welding.

2.4 Metallographic sample preparation and mechanical testing

Before sectioning the samples for various characterizations with a water-jet cutting machine, the flashes created during welding were removed from the weld seams. The metallographic sample preparation was done in accordance with ASTM E3-95 for microstructure analyses.[23] The samples were sectioned perpendicular to the weld direction. Grinding and polishing were carefully done on the samples to obtain mirror-finished samples. Keller's reagent was used to etch the samples for the proper observation of the grains. A DP25 Olympus optical microscope and a scanning electron microscope with energy-dispersive spectrometry (SEM + EDS) were used for the microstructural analysis. To evaluate the mechanical properties, Vickers microhardness and Instron tensile testing were used. The Vickers hardness was done in accordance with the ASTM E92-82E3 standard.[24] A load of 100 g and a dwell time of 10 seconds were used. The tensile tests were carried out using a load cell capacity of 100 kN at a crosshead rate of 1 mm/min. No fewer than three lap tests were made for each process parameter. Since there is no test standard for friction stir lap joints, ASTM E8/E8M-13a and ASTM D1002[25,26] for shear strength of a single lap joint adhesively bonded metal specimen (tension loading of metal-to-metal) were used as the reference test standard for the lap shear tests. Fractography was performed on the fractured surface of the tensile samples to determine the mode of failure.

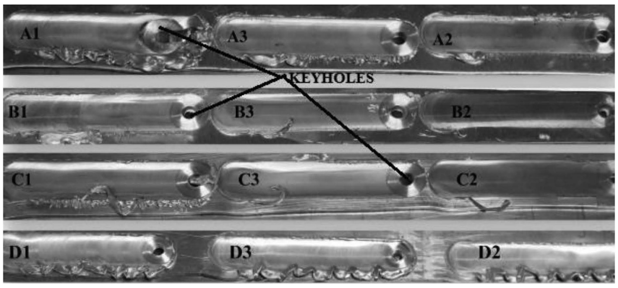

Figure 4: Top view of the processed FSW welds
Slika 4: Pogled od vrha na FSW-zvare

3 RESULTS AND DISCUSSION

3.1 Weld surface visual observation

The top surfaces of the welded samples under different welding process parameters are shown in **Figure 4**. The samples are labelled according to the designations indicated in **Table 1**. The visual assessment of the weld surfaces show no typical physical defects like wormholes, cracks or voids.

Table 2: Macrostructural features for different process parameters
Tabela 2: Izgled makrostrukture pri različnih procesnih parametrih

Weld number	Macrostructure	Nugget shape
A1		Elliptical
A2		Basin
A3		Basin
B1	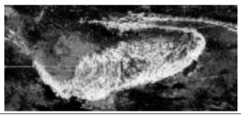	Elliptical
B2		Elliptical
B3		Basin
C1		Elliptical
C2	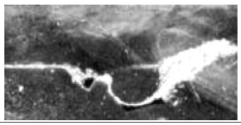	Basin
C3	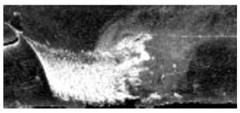	Basin

The shape of the weld seam is slightly convex in nature, which is caused by the design of the tool shoulder. A semi-circular ripple effect caused by the action of the tool shoulder was also observed. This effect is referred to as the wake effect. Keyholes were seen at the end of the weld seam. The depth of these keyholes shows the extent of the penetration of the pin from the top to the bottom sheet. Flashes were observed for all the process parameters used and more on the welds produced without reinforcement particles. Most of the flashes were located on the retreating side of the weld due to the movement of the materials from the advancing side of the weld to the retreating side.

3.2 Microstructural evolution

Macrostructure

Table 2 summarizes the macrostructure pictures at the cross-section of the weld zone for different process parameters.

From **Table 2** it is clear that the process parameters have a significant effect on the orientation of the FSP macrostructure. As the traverse speed increased from 100 mm/min to 300 mm/min using the same tool geometry, the geometry of the nugget zone changed from an elliptical shape to a basin-like shape. It is important to note that the formation of the basin shape is due to the effect of thermal heat transfer from the shoulder of the tool to the sheets. At a high traverse speed of 300 mm/min, the heat generated is lower and most of the heat built up at the top sheet with a minimal proportion of the heat sink into the bottom sheet. This makes the top sheet undergo more thermal cycles by direct contact with the tool shoulder and severe plastic deformation than the bottom sheet, causing the basin-like shape to form. The intense plastic deformation and high-temperature exposure experienced at the lower traverse speed resulted in the elliptical shape.

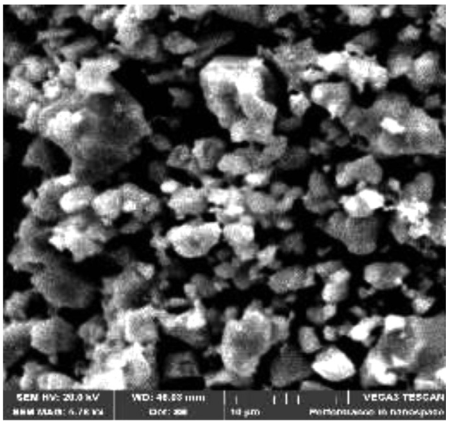

Figure 5: SEM photomicrograph of TiC Powder
Slika 5: SEM-posnetek prahu TiC

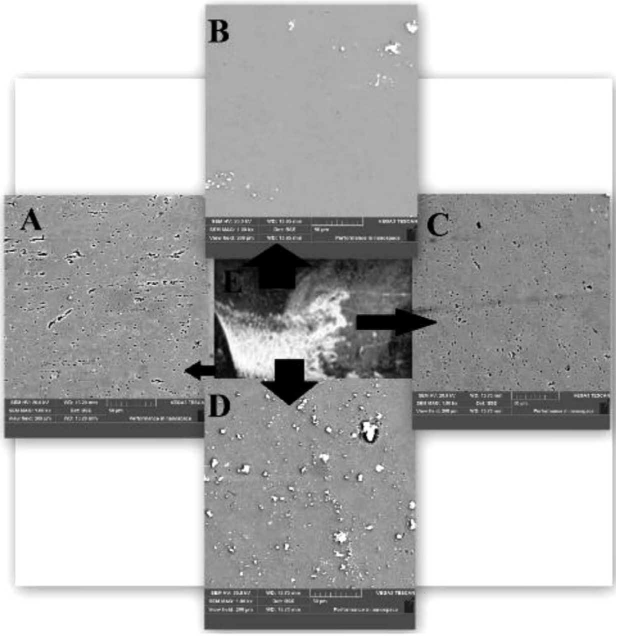

Figure 6: Microstructural evolution at different zones: A) thermo-mechanical affected zone, B) upper stir zone, C) heat-affected zone, D) lower stir zone E) macrostructure of the weld zone at 2000 min^{-1} and 300 mm/min

Slika 6: Razvoj mikrostrukture na različnih področjih: A) termo-mehansko vplivano področje, B) zgornje mešalno področje, C) toplotno vplivano področje, D) spodnje mešalno področje, E) makro-struktura zvara pri 2000 min^{-1} in prečni hitrosti 300 mm/min

TiC Powder

The micrograph of the TiC powder under the SEM of the TiC powder used as the reinforcement in this research study is illustrated in **Figure 5**.

The morphology of the TiC powder is irregular shaped ball milled powder with a grain size of about 2 microns.

Microstructure

The pictorial overview of the microstructural evolution across different zones after FSP is presented in **Figure 6**. All the four zones, namely the base metal (BM) close to the heat-affected zone (HAZ), the HAZ that is sandwiched by the BM and the thermo-mechanically affected zone (TMAZ), TMAZ found on both sides of the stir zone (SZ) and the SZ were exhibited in the micrographs taken from the processed zones. The BM retains its original microstructural features. The TMAZ and HAZ were formed on both the retreating and advancing sides of the welds. The grain structure in the HAZ shows elongated grain growth that is slightly different from the base material. The temperature experienced in the HAZ was enough to thermally activate the grain growth, but not sufficient to plastically deform the grain. In TMAZ, severely deformed grains are found, which are induced by drastic plastic deformation of the SZ during the FSP. In the SZ, the microstructure is characterized by dynamically recrystallized fine equiaxed grains owing to the drastic deformation induced by the sufficient stirring during welding of the top and bottom sheets. The distribution of the TiC reinforcement particles is a salient feature observed between the top and the bottom sheets around the SZ. At the top SZ, the presence of TiC is negligible and scanty, but a significant distribution was found at the bottom of the sheet. This indicates that during the welding process, the reinforcement particles experienced both downward and horizontal flow around the stir zone. Grains in the upper SZ are coarser than those in the bottom SZ. The heat during the FSP mainly originates from the tool shoulder friction with the surface of the top sheet. Additionally, the heat in the bottom SZ can easily transfer into the bottom sheet and the backing plate. Therefore, the heat cycle of the bottom SZ is relatively lower. The grains in the upper SZ have more time to grow due to the higher heat input.

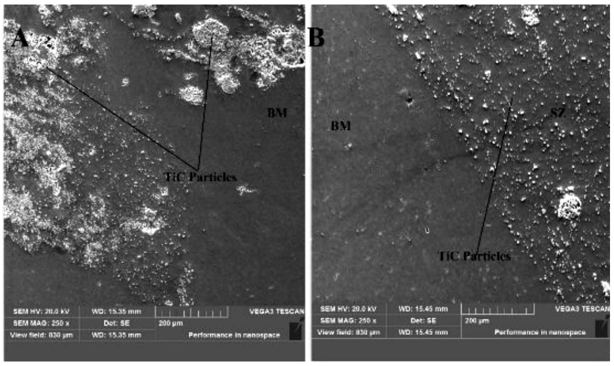

Figure 7: Transition zone: A) retreating side and B) advancing side

Slika 7: Prehodno področje: A) umikajoča stran in B) napredujoča stran

Another observation from the microstructure is the transition region on the advancing side (AS) and the retreating side (RS), which is illustrated in **Figure 7**. On the AS, the transition region is sharper and well defined and on the RS, the transition region diffuses into the parent material. On the AS, the plastic deformation direction of the processed zone and the BM are in opposite directions, which resulted in an enormous relative deformation and the homogenous distribution of the TiC particles between the BM and the processed zone at the AS, but the BM distorted and diffused smoothly together with the processed zone at the RS, resulting in clustering of the reinforcement.

It can be observed that the TiC reinforcement within the processed zone had undergone intense mixing and stirring, resulting in breakup of the coarse TiC morphology. As the rotational speed of the weld increased from 1600 min^{-1} to 2000 min^{-1}, the distribution of TiC becomes more homogenous, as shown in **Figure 8**. At a rotational speed of 1600 min^{-1}, the particles clustered together around the bottom sheet and at 2000 min^{-1}, the particles were uniformly distributed around the stir zone.

The contribution of intense deformation and high-temperature exposure within the stir zone resulted in

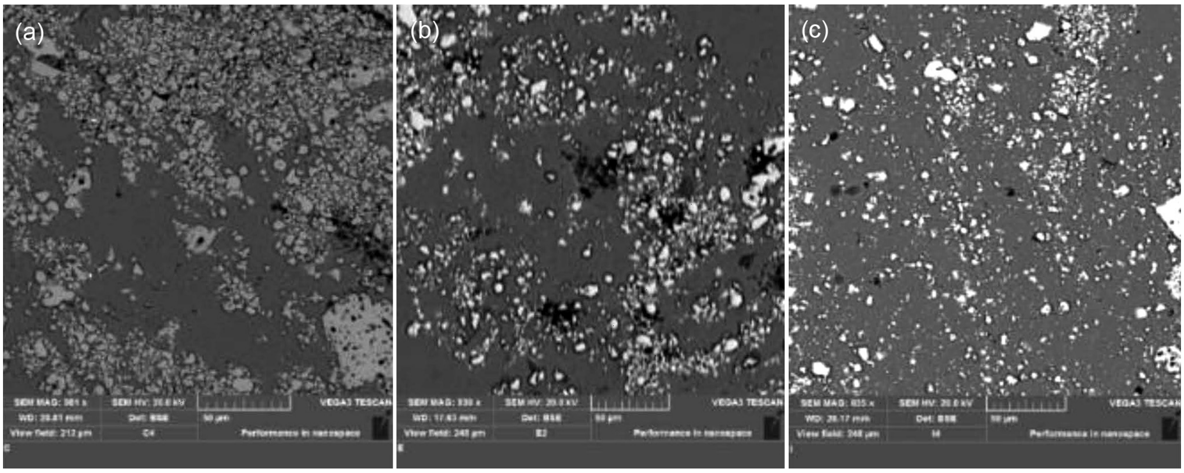

Figure 8: SEM micrograph at a traverse speed of 100 mm/min and rotational speeds of: a) 1600 min^{-1} b) 1800 min^{-1} and c) 2000 min^{-1}
Slika 8: SEM posnetek pri prečni hitrosti 100 mm/min in hitrosti vrtenja: a) 1600 min^{-1}, b) 1800 min^{-1} in c) 2000 min^{-1}

fragmentation, recrystallization and the development of refined texture within and around the stir zone at a rotational speed of 2000 min^{-1}. In addition, an increase in the traverse speed caused the particles to agglomerate in the stir zone. As the traverse speed decreased, the grain size also decreased in the composite but increased in the pure aluminium samples without the reinforcement. This might be due to the high heat input associated with the low traverse speed. The significant effect of particle reinforcement on the grain size refinement of the matrix is reported as a pinning effect. According to the pinning effect, the grain refinement by reinforcement particles increases with a decrease in the particle size and an increase in the volume fraction of the particles. Sufficient heat input and stirring are responsible for the deformation and recrystallization of the matrix with the reinforcement. At a higher rotational speed of 2000 min^{-1} and a traverse speed of 100 mm/min, a more uniform distribution of the TiC particles was found.

Energy Dispersive Spectroscopy Results

EDS analyses were performed on all the welds with reinforcement. The uniformly distributed particles were confirmed to be titanium and carbon, as shown in **Figure 9**, which is a scan of the weld interface of the sample produced at a rotational speed of 2000 min^{-1} and a traverse speed of 100 mm/min.

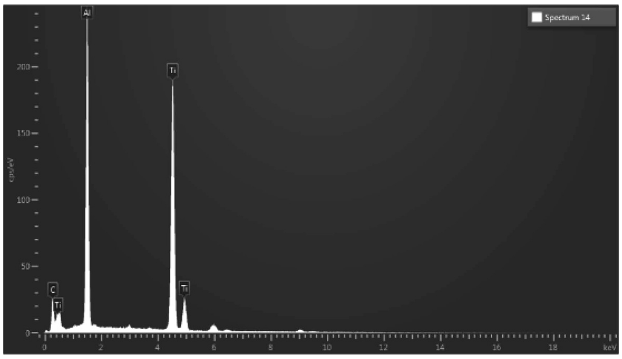

Figure 9: EDS from the weld interface at a rotational speed of 2000 min^{-1} and a traverse speed of 100 mm/min
Slika 9: EDS iz stika z zvarom pri hitrosti vrtenja 2000 min^{-1} in prečni hitrosti 100 mm/min

The elemental composition by atomic weight at the stir zone is confirmed to be 72.04 % of aluminium, 23.71 % of carbon and 4.34 % of titanium.

3.3 Microhardness Profiling

The Vickers hardness distribution is illustrated in **Figure 10**. The shape of the hardness distribution is a "W-sinusoidal". The lowest hardness value was found at the HAZ and the highest hardness value at the SZ. The hardness value of the SZ increased by 58 % when compared to the base metal for sample C1. Thangarasu[21] suggested four methods of hardening in FSW MMC:

- Orowan strengthening.
- Grain and substructure strengthening.
- Quench hardening resulting from the dislocations generated to accommodate the differential thermal contraction between the reinforcing particles and the matrix.
- Work hardening due to the strain misfit between the elastic reinforcing particles and the plastic matrix.

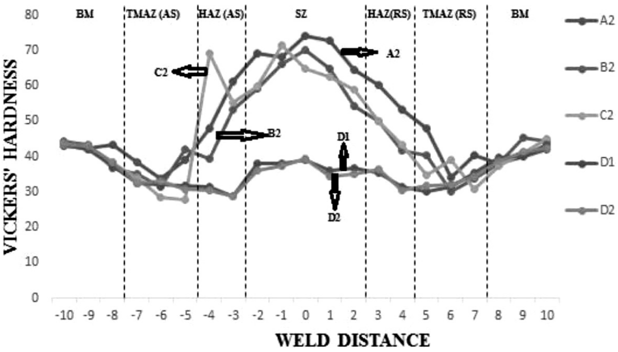

Figure 10: Hardness profile of the FSL welds
Slika 10: Profil trdote preko FSL-zvarov

Table 3: Shear strength and joint efficiency of the welds
Tabela 3: Strižna trdnost in skupna učinkovitost različnih zvarov

Weld number	Rotational speed (min^{-1})	Traverse speed (mm/min)	Weld pitch (mm/ min)	Average shear fracture load per unit width (N/mm)	Joint efficiency (%)
A1	1600	100	0.063	**159**	79.4
A2	1600	200	0.125	**150**	60.8
A3	1600	300	0.188	**132**	52.97
B1	1800	100	0.056	**185**	90.51
B2	1800	200	0.111	**178**	77.53
B3	1800	300	0.167	**170**	68.60
C1	2000	100	0.050	**218**	92.14
C2	2000	200	0.100	**213**	85.96
C3	2000	300	0.150	**175**	69.44
D1	1600	200	0.125	**201**	81.67
D2	1800	200	0.111	**187**	81.45
D3	2000	200	0.100	**173**	69.81

The increment in the hardness value at the SZ is attributed to grain refinement and the presence of reinforcement particles. The fragmentation of larger TiC particles gave rise to dislocation density and dynamic recrystallization during welding, thereby producing a finer grain size in the stir zone. These factors are responsible for higher hardness values in the stir zone of welds with the reinforcement particles. The minimum hardness value appeared at the HAZ. This is due to the thermal history experienced at this zone, which resulted in the coarsening of the precipitates.

Because of the distribution and the deposition of the TiC particles around the AS of the welded zone, the AS size shows higher hardness values than the RS due to the fact that materials on the RS have a shorter time to rotate since the current flow of material is directly proportional to the time of flow on this side.

3.4 Tensile behaviour

In order to quantify the mechanical resistance of the FSWed joints, the ratio between the maximum transferred load by the specimens in shear test to the width of the specimen itself was considered. In this way, the values are shown for all the considered cases. The average results of the three replica samples carried out are reported. Every sample was tested to failure. The shear fracture load per unit width of the FSWed Al with and without the TiC composite for different process parameters are presented in **Table 3**.

From the results obtained, it was found that the maximum shear strength was observed at a rotational speed of 2000 min^{-1} and a traverse speed of 100 mm/min, and the minimum was observed at a rotational speed of 1600 min^{-1} and a traverse speed of 300 mm/min. Both the maximum and the minimum shear strengths were observed when the TiC reinforcement particles were added, but at different rotational and traverse speeds, respectively. It can be concluded from the results that the relationship between the fracture load and the traverse speed is inversely proportional. An increase in the traverse speed causes the fracture load to decrease. A shorter reaction time and a lower reaction temperature are associated with a higher traverse speed and this led to a decrease in the stirring period and the vertical movement of the material with the reinforcement, thereby affecting the strength of the bonding at the interface. It is obvious that the fracture load increases with an increase in the rotational speed for all the samples with reinforcement. As the rotational speed increased from 1600 min^{-1} to 2000 min^{-1}, a substantial increase in the fracture load was observed. A higher rotational speed generated a higher heat input because of the higher friction heating, which resulted in more intense stirring and mixing of the material.

It should be noted that the fracture load behaviour that occurred in the samples without reinforcement is the reciprocal of results obtained from the samples with reinforcement. The absence of the ceramic particle along the path of the weld seam exposed the weld interface to a higher degree of thermal reaction, thereby making it sensitive to temperature changes. As the rotational speed increases, the temperature around the weld zone in-

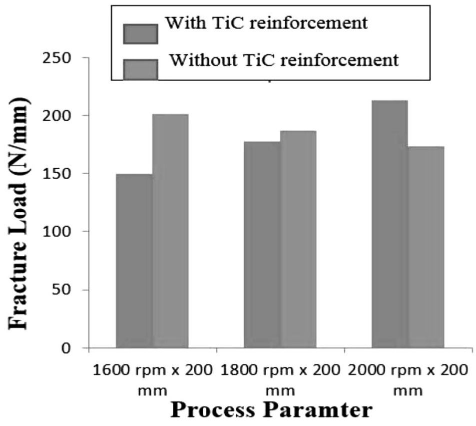

Figure 11: Fracture load against the process parameters
Slika 11: Odvisnost obremenitve pri porušitvi od parametrov procesa

creases, causing a highly turbulent mixture and stirring of the materials. Since there is no intermediate particle to balance the temperature change, the strength of the bonding will be compromised. However, once a sufficient rotational speed is achieved, a further increase is not beneficial to the mechanical properties for welds produced without reinforcement particles.

Figure 11 shows the effect of the reinforcement particles on the fracture load. As can be seen, the presence of the TiC reinforcement particles contributed an appreciable strength change to the fracture load at a higher rotating speed of 2000 min^{-1} and does not show a remarkable improvement in the fracture load at rotational speeds of 1600 min^{-1} and 1800 min^{-1}, respectively, instead, it had an inverse effect on the strength.

At a rotational speed of 2000 min^{-1}, the TiC homogenously mixed with the Al alloy properly, thereby forming a well-bonded matrix that yielded a higher fracture strength. The presence of the ceramic particles constrained the easy failure of the material when under loading, thereby improving the mechanical strength of the matrix.

Joint efficiency

To estimate the joint efficiency of the FS welds, the ratios of the tensile strength of the lap shear specimens were compared to the tensile strength of the base metals. According to studies,[27] the tensile strength of the lap shear specimen is derived from the fracture load per unit width to the effective sheet thickness (EST) as shown in Equation (1):

$$\begin{array}{l}\text{Tensile strenth of}\\ \text{lap shear specimen}\end{array} = \frac{\text{Fracture load per unit width}}{\text{EST}} \qquad (1)$$

The EST is defined as the minimum sheet thickness determined by measuring the smallest distance between any un-bonded interface and the top surface of the upper sheet or the bottom surface of the lower sheet and it varies with the process parameter, depending on the degree of bonding that exists between the weld interfaces. These phenomena should have apparent influences on the bearing load of FSW lap-welded joints. Also presented in **Table 3** is the joint efficiency of the processed samples for different process parameters. From the result, the joint efficiency ranges from 52 % to 92 %. The highest was found at a rotational speed of 2000 min^{-1} and a traverse speed of 100 mm/min.

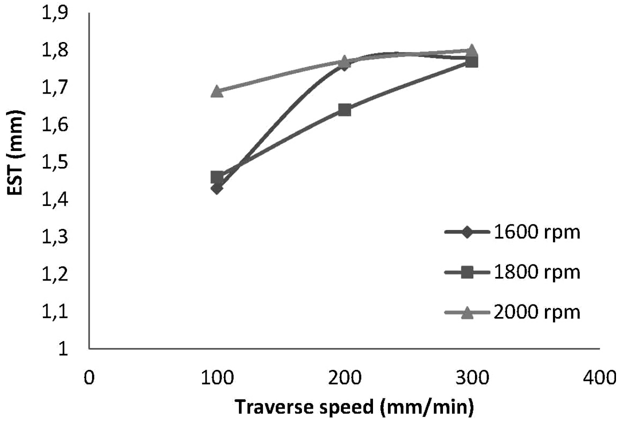

Figure 12: EST against the traverse speed
Slika 12: Odvisnost med EST in prečno hitrostjo

The effect of the traverse speed on the EST was studied. **Figure 12** shows the graphical relationship between the EST versus traverse speed. The traverse speed exhibits a linear relationship with the EST. As the traverse speed increased, the dimension of the EST also increased, thereby reducing the area of the metallurgical bond that exists at the processed interface. Since the strength of the weld interface depends on the area of the metallurgical bond during the welding process, it is apparent that the relationship between the EST and the overall strength of the processed zone is exponential.

Fracture behaviour

Four different modes of failure were observed at the joint interfaces, as illustrated in **Figure 13**. They are the fracture mode (FM) 1, the shear fracture that occurred due to a lack of joint formation along the original inter-

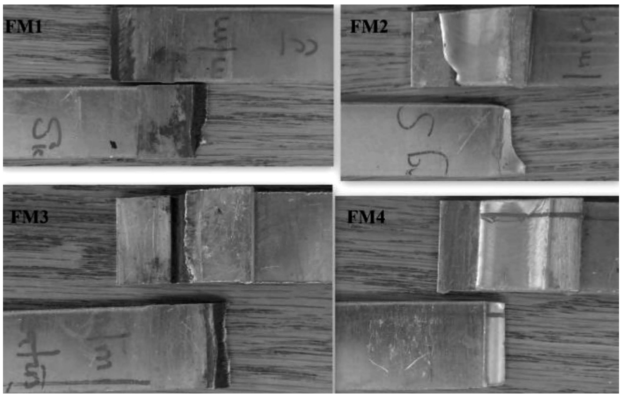

Figure 13: Fracture mode of the welded samples for different process parameters
Slika 13: Način zloma vzorcev, zvarjenih pri različnih procesnih parametrih

Table 4: Mode of fracture for different process parameters
Tabela 4: Način zloma pri različnih procesnih parametrih

Weld number	Rotational speed (min^{-1})	Traverse speed (mm/min)	Fracture mode
A1	1600	100	FM 1/FM 2
A2	1600	200	FM 2
A3	1600	300	FM 1
B1	1800	100	FM 3
B2	1800	200	FM 3
B3	1800	300	FM 4
C1	2000	100	FM 3/FM 4
C2	2000	200	FM 3
C3	2000	300	FM 4
D1	1600	200	FM 3
D2	1800	200	FM 4
D3	2000	200	FM 4

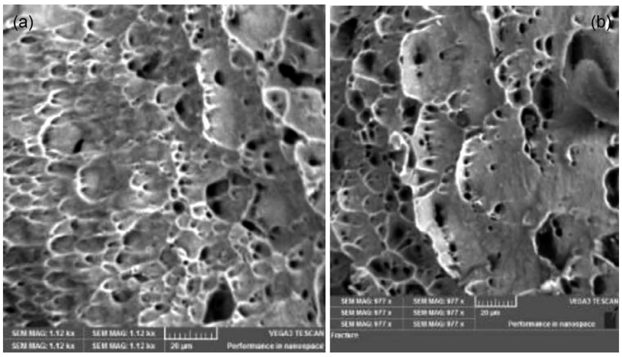

Figure 14: SEM images of the fracture surface for the weld produced at a rotational speed of 2000 min^{-1} and a traverse speed of 100 mm/min
Slika 14: SEM-posnetek površine preloma zvara, izdelanega pri hitrosti vrtenja 2000 min^{-1} in prečni hitrosti 100 mm/min

face of the two sheets. This led to a pseudo metallurgical bond between the two sheets and the bond shear under tensile loading. Fracture mode 2 occurred on the advancing size hooking in which the crack initiates from the tip of the hook on the AS, propagates upward along the SZ/TMAZ interface and finally, the fracture at the SZ. Fracture mode 3 was noticed on the retreating side softening initiated from the hook and then linked to the pores on the bottom plates caused by the diffusion of the bottom plate with the backing plate. The crack follows the sharp end of the grove to the other end. Fracture mode 4 failure took place close to the base metal, but the weld actually failed at the HAZ on the advancing side of the weld. **Table 4** lists the failure modes observed for each process parameter combination.

FM 1 was found at a low rotational speed of 1600 min^{-1} and a high traverse speed of 300 mm/min. The dominant fracture modes are FM 3 and FM 4.

FM 1 is observed at a a low rotational speed and high traverse speed. This process condition is associated with the low heat input that resulted in insufficient deformation and a flow of the material forming the pseudo weld. The crack initiation occurs through the gap tip of the unwelded area and went through the stir zone, making the weld shear into two at the welded area. This usually occurs when an insufficient metallurgical bond is formed between the sheets.

FM 2 and FM 3 are the most dominating failure modes. The fracture mode is similar to the normal tensile behaviour of the aluminium alloy. The material went through necking for a period before eventually fracturing at the weakest zone.

The SEM images of the fracture surfaces were taken to determine the mode of fracture. Figure 14 illustrates the typical fractography features of the failure surfaces.

The morphology of the failure mode shows a large number of fine dimples, which confirms the amount of plastic flow prior to the failure under tensile loading. The fine dimple features observed indicate that the behaviour of the fracture is ductile, which implies that the lap joints exhibited ductile fracture during the lap shear tests.

4 CONCLUSION

Based on the observations from the results, the followings conclusions can be drawn:

- The microstructural evolution correlates with the process parameters employed to produce the welds in this study. It was found that as the traverse speed increases, the evolving microstructure changed from elliptical to a basin-like shape at the interface.
- The microstructure revealed that the majority of the TiC particles were transported from the weld interface and deposited in the bottom sheet.
- The highest tensile value of 218 N/mm and the joint efficiency of 92 % were recorded for a weld produced at a high rotational speed of 2000 min^{-1} and a low traverse speed of 100 mm/min. This parameter combination setting can be recommended.
- The maximum hardness occurred at the stir zone and the minimum at the HAZ. The advancing side exhibited a higher hardness distribution compared to the retreating side of the welds.

Acknowledgements

Mr Abegunde (co-author) would like to acknowledge the University of Johannesburg under the Global Excellence Stature (GES) award scholarship of the Postgraduate Research Centre for their financial support, Prof Esther Akinlabi (co-author) acknowledges the Johannesburg Institute of Advanced Study (JIAS) for the writing fellowship award during which she was able to contribute to this manuscript and finally, the eNtsa Research Group of Nelson Mandela Metropolitan University (NMMU), Port Elizabeth, South Africa is acknowledged for allowing us to use their facility to produce the welds.

5 REFERENCES

[1] R. Mishra, Z. Ma, Friction stir welding and processing. Materials Science and Engineering: R: Reports 50 (**2005**) 1, 1–78, doi:10.1016/j.mser.2005.07.001

[2] K. Kainer, Metal matrix composites: Custom-made materials for automotive and aerospace engineering. John Wiley & Sons, 2006

[3] Fabrication of near-net shape graphite/magnesium composites for large mirrors, Orlando'90, International Society for Optics and Photonics, 1990, 16–20

[4] D. Miracle, Metal matrix composites–from science to technological significance, Composites Sci. Technol. 65 (**2005**) 15, 2526–40, doi:10.1016/j.compscitech.2005.05.027

[5] S. Rawal, Metal-matrix composites for space applications, Journal of Minerals, Metals and Materials Society, 53 (**2001**) 4, 14–7, doi:10.1007/s11837-001-0139-z

[6] L. Santo, D. Paulo, Surface engineering techniques and applications: Research Advancements, 2014, 1–347

[7] P. Babalola, C. Bolu, A. Inegbenebor, K. Odunfa, Development of aluminium matrix composite, International Journal of Engineering and Technology Research, 2 (**2014**) 1, 1–11

[8] W. Thomas, E. Nicholas, J. Needham, M. Murch, P. Temple Smith, C. Dawes, Inventors, Friction stir welding, UK Patent Office, London patent, December 6, 1991.

[9] D. Klobcar, L. Kosec, A. Pietras, A. Smolej, Friction-stir welding of aluminium alloy 5083, Mater. Tehnol., 46 (**2012**) 5, 483–488

[10] S. Kastelic, J. Tušek, D. Klobčar, J. Medved, P. Mrvar, AA4130 and AA1050 Joined with friction-stir welding, Mater. Tehnol., 47 (**2013**) 2, 195–198

[11] R. Palanivel, P. Mathews, The tensile behaviour of friction-stir-welded dissimilar aluminium alloys, Mater. Tehnol., 45 (**2011**) 6, 623–626

[12] E. Akinlabi, Characterisation of dissimilar friction stir welds between 5754 aluminium alloy and C11000 copper, Dissertation submitted to Nelson Mandela Metropolitan University, Port Elizabeth, South Africa 2011

[13] D. Sanders, Development of friction stir welding combined with superplastic forming processes for the fabrication of titanium structures. Dissertation submitted to University of Washington, Washington, United States 2008

[14] A. Elrefaey, M. Gouda, M. Takahashi, K. Ikeuchi, Characterization of aluminum/steel lap joint by friction stir welding, 2004

[15] R. Mishra, Z. Ma, I. Charit, Friction stir processing: A novel technique for fabrication of surface composite. Materials Science and Engineering, 341 (**2003**) 1, 307–310, doi:10.1016/S0921-5093(02)00199-5

[16] Z. Ma, Friction stir processing technology: A review. Metallurgical and Materials Transactions, 39 (**2008**) 3, 642–658, doi:10.1007/s11661-007-9459-0

[17] A. Smolej, D. Klobčar, B. Skaza, A. Nagode, E. Slaček, V. Dragojević, S. Smolej, The superplasticity of friction stir processed al-5Mg alloy with additions of scandium and zirconium, International Journal of Materials Research, 105 (**2014**) 12, 1218–1226, doi:10.3139/146.111141

[18] A. Smolej, Superplastic behaviour of AA5083 aluminium alloy with scandium and zirconium, Materials Science ForumTrans Tech Publ, 2012, doi:10.4028/www.scientific.net/MSF.706-709.395

[19] V. Sharma, U. Prakash, B. Kumar, Surface composites by friction stir processing: A review, J Mater Process Technology, vol. 706–709, 2015,395

[20] E. Akinlabi, R. Mahamood, S. Akinlabi, E. Ogunmuyiwa, Processing parameters influence on wear resistance behaviour of friction stir processed al-TiC composites, Advances in Materials Science and Engineering, 2014, doi:10.1155/2014/724590

[21] A. Thangarasu, N. Murugan, I. Dinaharan, S. Vijay, Microstructure and microhardness of AA1050/TiC surface composite fabricated using friction stir processing, Sadhana 37 (**2012**) 5, 579–586, doi:10.1007/s12046-012-0097-x

[22] S. Jerome, S. Bhalchandra, S. Babu, B. Ravisankar, Influence of microstructure and experimental parameters on mechanical and wear properties of al-TiC surface composite by FSP route, Journal of Minerals and Materials Characterization and Engineering, 11 (**2012**) 05, 488–493, doi:10.4236/jmmce.2012.115035

[23] Standard A. E3, standard guide for preparation of metallographic specimens, ASTM International, West Conshohocken, PA 2001

[24] Standard A. E92-82 E3. 1997: Standard test method for vickers hardness of metallic materials, Annual Book of ASTM Standards, ASTM International, West Conshohocken, PA ASTM

[25] Standard A. D1002-01, 2001, Standard Test Method for Apparent Shear Strength of Single-Lap-Joint Adhesively Bonded Metal Specimens by Tension Loading (Metal-to-Metal), ASTM International, West Conshohocken, PA, 2001, doi:10.1520/D1002-10.

[26] Standard A. E8/E8M-13a, standard test method for determining volume fraction by systematic manual point, ASTM International, West Conshohocken, PA 2013

[27] X. Xu, X. Yang, G. Zhou, J. Tong, Microstructures and fatigue properties of friction stir lap welds in aluminum alloy AA6061-T6, Journal of Materials and Design 35 (**2012**) 5, 175–83, doi:10.1016/j.matdes.2011.09.064

UDK 620.193.95:621.793.8:669.058
Original scientific article/Izvirni znanstveni članek

ISSN 1580-2949
MTAEC9, 51(2)307(2017)

EVALUATION OF THE WEAR BEHAVIOR OF NITRIDE-BASED PVD COATINGS USING DIFFERENT MULTI-CRITERIA DECISION-MAKING METHODS

OCENA OBRABE NITRIDNEGA PVD NANOSA Z UPORABO RAZLIČNIH METOD VEČKRITERIJSKIH POSTOPKOV ODLOČANJA

Yılmaz Küçük[1], Ahmet Öztel[2], Mehmet Yavuz Balalı[3], Mecit Öge[1], Mustafa Sabri Gök[1]

[1]Bartin University, Faculty of Engineering, Department of Mechanical Engineering, 74100 Bartin, Turkey
[2]Bartın University, Faculty of Economics and Administrative Sciences, Department of Management, 74100 Bartın, Turkey
[3]Turkish Military Academy, 06654 Ankara,Turkey
mecitoge@bartin.edu.tr, mecitoge@yahoo.com

Prejem rokopisa – received: 2016-03-02; sprejem za objavo – accepted for publication: 2016-05-05

doi:10.17222/mit.2016.041

In this study, AISI 7131 (16MnCr5) case-hardened steel specimens were prepared in two groups, carbonitrided and without heat treatment, and the specimen surfaces were coated with three different coating materials (CrN, TiAlN and TiN) as a single layer using the physical vapor deposition (PVD) cathodic arc method. The wear behaviors of the coated specimens were tested with the micro-abrasion method. The test results of the micro-abrasion wear tests were analyzed with Multi-Criteria Decision Making (MCDM) techniques to determine the combination of coating and heat treatment that yields the lowest wear rate. According to the analyses conducted with the Technique for Order Preference by Similarity to Ideal Solution (TOPSIS), Multiple Attribute Utility Theory (MAUT) and Compromise Programming (CP) MDCM techniques, the TiAlN coating exhibited the best wear performance. The MAUT and CP methods produced an identical ranking of the alternatives, whereas a slight deviation was found in the ranking with the TOPSIS method. Uncoated and CrN-coated specimens exhibited the worst wear performance of all the MCDM methods.

Keywords: wear, micro-abrasion, multi-criteria decision making, PVD coating

V študiji sta bili pripravljeni dve skupini jekla za cementacijo AISI 7131 (16MnCr5), karbonitrirana jekla in jekla brez toplotne obdelave, katerih površina vzorcev je bila prekrita s tremi različnimi nanosi (CrN, TiAlN in TiN) v enem sloju, s pomočjo fizikalne depozicije preko plinske faze (angl. PVD) z metodo obloka. Obnašanje vzorcev z nanosom pri obrabi je bilo preizkušeno z mikroabrazijsko metodo. Rezultati preizkusov mikroabrazijske obrabe so bili analizirani z uporabo večkriterijske tehnike odločanja (angl. MCDM), za določitev kombinacije nanos – toplotna obdelava, ki kaže najmanjšo hitrost obrabe. Glede na analize, ki so bile izvedene s pomočjo tehnike, ki je najbližja idealni rešitvi (angl. TOPSIS), s teorijo večkratne prednosti (angl. MAUT) in s programsko tehniko (angl. CP) MDCM-kompromisov, je najboljšo odpornost na obrabo pokazal TiAlN. MAUT- in CP-metodi dajeta enakovredne alternative, medtem ko je bilo manjše odstopanje ugotovljeno pri TOPSIS-metodi. Vzorci brez nanosa in s CrN nanosom so pokazali najslabšo odpornost na obrabo od vseh MCDM-metod.

Ključne besede: obraba, mikroabrazija, večkriterijsko odločanje, PVD-nanos

1 INTRODUCTION

Many of the machine parts used in automotive, aircraft and machine tools are exposed to mechanical loads under certain conditions in which they are in contact with their counterparts. Hence, many researches are conducted to understand the tribological properties of such parts to improve their service life and reduce the maintenance costs. One of the methods used to solve this problem is the thin-film coating application. In the thin-film coating process, the adhesive characteristics and hardness of the coatings are improved through optimization of the coating parameters using various deposition techniques.

In this work, the coatings (TiN, CrN and TiAlN) widely employed in actual industrial applications were selected and deposited by the cathodic arc-evaporation PVD technique in order to make a comparative analysis of their tribological performances. In general, TiN and CrN coatings are known to be the most commonly employed thin hard coatings,[1,2] whereas TiAlN is generally used for the coating of cutting tools in special machining operations.[3]

TiN, CrN and TiAlN thin hard coatings exhibit different wear behaviors due to their differing characteristic properties, such as friction coefficient, hardness, abrasive wear and corrosion resistance under various service conditions.[3,4] Abrasive wear is one of the most commonly known wear mechanisms and it is of great importance in terms of the evaluation of the wear performance of coatings and the selection of abrasive wear-resistant coatings suitable for specific applications.[5]

The micro-abrasion wear-testing method is widely used to determine the abrasive wear resistance of thin hard coatings.[6–11] In the micro-abrasion wear test, the most effective test parameters that affect the test results can be classified as the rotational speed of the ball,[12,13] the normal load,[12] the ball sliding distance,[13–14] the ball surface condition[15], the size[6,16–19] and the type of abrasive particle in the slurry.[20]

The coating materials may exhibit different wear performances depending on various test conditions. Therefore, it is necessary to determine the optimum test parameters that simulate the best service conditions. To select the most suitable material for a specific application, the criteria affecting the material selection should be properly identified.[21,22] The selection of suitable thin hard coatings having the best wear performance among several choices for a specific application can be considered as a MCDM problem.[23–24] The selection of the best method for a given problem is yet another important issue with no definite answer.[25] A. Abrishamchi et al.[26] state that the selection of an appropriate MCDM from a long list of available MCDM methods is a multi-criteria problem itself. There is no single MCDM technique that can be deemed superior for all decision-making problems.[27] TOPSIS, EXPROM2 (Preference Ranking Organization Method for Enrichment Evaluation), VIKOR (Višekriterijumsko Kompromisno Rangiranje – Multicriteria Optimization and Compromise Solution), ELECTRE (Elimination and Choice Expressing the Reality), Linear Assignment Method, and COPRAS (Complex Proportional Assessment)[24] are among the MCDM methods used by researchers for optimum selection among a variety of options in industrial problems.

A determination of the effects of the coating material and the nitriding processes on the wear behaviour of coating is a complex, multi-factorial problem and a limited number of studies are available in the literature on the use of MCDM techniques in the selection of coating materials. The TOPSIS method was used by A. Chauhan and R. Vaish[27] for the selection of the best alternative among hard coatings based on their hardness, Young's modulus, thermal expansion coefficient, H/E and H^3/E^2 ratios. H. Çalışkan et al.[24] used EXPROM2, TOPSIS and VIKOR methods to select the best coating material among a variety of multicomponent nanostructured boron-based hard coatings deposited using magnetron-sputtering and ion-implementation-assisted magnetron-sputtering methods in consideration of their hardness, Young's modulus, elastic recovery, friction coefficient, and critical load. Again, the EXPROM II, TOPSIS and VIKOR methods were used by H. Çalışkan et al.[24] to determine the best selection among a variety of materials for tool holders used in hard milling.

TOPSIS was developed by Hwang and Yoon (1981)[28] as a value-based compensatory method in conception and application,[29] which attempts to choose alternatives that are both closest to the positive-ideal solution and farthest from the negative-ideal solution.[30] The benefit criteria are maximized and the cost criteria are minimized by a positive-ideal solution, and the opposite applies for the negative-ideal solution.[31] TOPSIS provides a cardinal ranking of alternatives through the full use of the attribute information without a requirement for independent attribute preferences.[32,33] The main strengths of the TOPSIS method can be listed as its understandable principle and easy implementation, its applicability, which requires a collection of precise and overall information,[34] a consideration of both positive and negative ideal solutions, the provision of a well-structured analytical framework for ranking of alternatives, and the use of fuzzy number to deal with alternatives.[35] The requirement of vector normalization for multidimensional problems can be regarded as a weakness of the method.

MAUT is a systematic method for the analysis and identification of multiple variables for obtaining a decision on a common basis.[36] In this method, a multi-attribute utility function is derived, which requires single utility functions and related weighting factors.[37,38] For an evaluation of the performance criteria individually in the same units, single utility functions are used as a means to render their aggregation possible in the multi-attribute utility function. In this procedure an objective is set and attributes are established for the goal; a range of attributes are set; single utility functions are derived for each attribute; weighting factors are estimated for each attribute; and a multi-attribute utility function is derived.[39]

The MAUT strategy allows the decision maker to make more objective decisions based on their experience and the result of the analysis.

The CP method was first developed by M. Zeleny[40] and later extended by A. Bárdossy, I. Bogárdi, L. Duckstein[41] as composite programming for dealing with problems of a hierarchical nature. CP is within the class of distance-based, multi-criteria analytical methods, designed to identify non-dominated solutions, closest to an ideal solution by some distance measure.[42] Its simple structure is one of the main advantages of this method. This is a simple and easily understandable method that provides good performance when compared with complicated and time-consuming methods.[43]

In this study the micro-abrasion wear behaviour of single-layer CrN, TiN and TiAlN coatings was investigated using the fixed-ball micro-scale abrasion test. Afterwards, some of MCDM techniques such as TOPSIS, MAUT and CP, were implemented to compare their outputs as a means to determine the thin hard coating having the highest wear resistance. As indicated, there are studies[23–24,28] available in the literature on the use of the TOPSIS method for the selection of the best alternative among a variety of coating applications. In this study the MAUT and CP methods are used to make a comparative analysis between TOPSIS and these methods. Also, among the other MCDM methods, the TOPSIS, MAUT and CP methods were chosen for their widespread usage,[44] easy computation and for being within the same class of unique synthesis criterion approaches in which different points of view are merged into a unique functional structure for further optimization, which in turn facilitates the solution of material selection problems.[45]

2 MATERIALS AND METHODS

2.1 Substrate and coating

Test samples made of AISI 7131 (16MnCr5) steel with a diameter of 40 mm and a thickness of 10 mm were used as a substrate for the deposition of TiN, TiAlN and CrN thin hard coatings. After the sample polishing process, all the test samples were subjected to a carburizing process performed in accordance with the heat treatment procedure given in **Figure 1**.

The substrate surface is hardened through a duplex surface treatment, a combination of nitriding and carburizing, since most of the applied forces must be supported by the substrate due to the thin structure of the PVD coatings.[46–48] The nitriding process can provide a significantly high wear and adhesion resistance for TiAlN coatings.[49]

Therefore, in this study, in addition to carburizing, a nitriding process was also applied to some samples to determine its synergistic effect on the abrasive wear behaviour of thin hard coatings. The nitriding process parameters are given in **Table 1**. The list of prepared samples is given in **Table 2**. After the carburizing and/or nitriding surface-hardening processes, polishing was performed as the last operation before the deposition process to remove the white layer (oxide or nitride layer) emerging during the heat treatment and having an adverse effect on the coating's adhesion.[50] The average surface roughness of the polished samples was measured as R_a = 0.02 μm after measurements conducted with a Mitutoyo SJ 201 profilometer. Before the coating process, the sample surfaces were washed 2 times with an alkaline detergent using an ultrasonic washing device. Then, the samples were washed 3 times with distilled water, each time for a period of 30 s, and then dried with hot air.

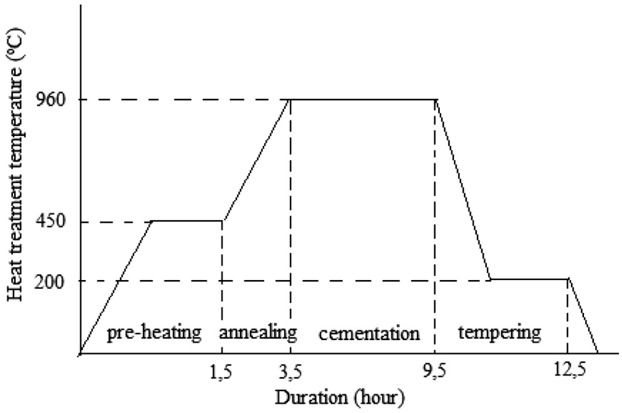

Figure 1: Process diagram of carburizing
Slika 1: Diagram poteka naogljičenja

Table 1: Nitriding parameters
Tabela 1: Parametri nitriranja

Process type	Plasma nitriding
Temperature	480 °C
Duration	10 h
Gas mixture/ratio	Nitrogen-Hydrogen / 3:1
Pressure	2.5 mbar (in vacuum)

Table 2: Test sample classification
Tabela 2: Razvrstitev preizkusnih vzorcev

Coating material	Carburizing	Nitriding	Notation
CrN	+	-	CrN
CrN	+	+	CrN+N
TiN	+	-	TiN
TiN	+	+	TiN+N
TiAlN	+	-	TiAlN
TiAlN	+	+	TiAlN+N

Table 3: PVD deposition parameters
Tabela 3: Parametri PVD-depozicije

Parameter	Coating material		
	TiN	CrN	TiAlN
Cathode current	70 A	70 A	60 A
Bias voltage (DC)	50–60 V	50–60 V	50–60 V
Number of cathode	6	6	8
Duration	1 h	1 h 30 min	1 h 10 min

Following the ion bombardment on the coated sample surface, thin hard coatings were deposited on the sample surfaces using the parameters given in **Table 3** by the cathodic arc PVD technique.

2.2 Micro-abrasion test

The micro-abrasion wear test is a widely used method in the determination of the abrasive wear performance of thin hard coatings. In this study, micro-abrasion wear tests were carried out using a fixed-ball-cratering device shown in **Figure 2**. In micro-abrasion tests, an

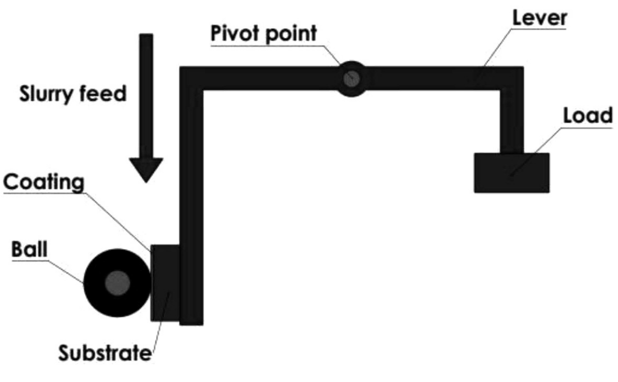

Figure 2: Scheme of the fixed-ball micro-abrasion test set up
Slika 2: Shema postavitve mikro-abrazijskega preizkusa s fiksno kroglo

abrasive slurry composed of 25 g of SiC in 75 mL distilled water for each abrasive mesh size (800, 1000 and 1200) mesh, was applied as 3 drops per minute, onto an AISI 52100 steel polished ball with a diameter of 25.4 mm.

2.3 Multi-criteria decision making method

2.3.1 Definition of the problem and setting up

Coating materials may yield differing wear results under different test conditions. In such situations a determination of the best choice for a coating material may be addressed as a multi-criteria decision making (MCDM) problem.[23,24] In this study, implementation of MCDM methods is based on the assumption that each wear value obtained under different conditions is a criterion. The alternatives for the coating material are shown in **Table 4**.

Table 4: Alternatives for coating material
Tabela 4: Izbire materiala za nanašanje

Alternative	Material
A1	CrN
A2	N+CrN
A3	N+TiAlN
A4	N+TiN
A5	TiAlN
A6	TiN
A7	Uncoated

Table 5: Wear test factors
Tabela 5: Faktorji preizkusa obrabe

Abrasive (mesh)	Load (N)	Speed (r/min)
800	0,5	45
1000	1	90
1200	1,5	140

The factors for the wear test and their levels are shown in **Table 5**. 27 tests were conducted with these coating materials for three different factors. On the assumption that the wear rate found in each test is a criterion for a decision, our criteria can be organized as C(Abrasive, Load, Speed). Our criteria and the test parameters are shown in **Table 6**.

2.3.2 Entropy method for criteria weighting

In MCDM problems, the significance level of each criteria cannot be the same. A weighting value must be specified for each criterion to evaluate this significance level. Several objective weighting methods are proposed by researchers. One of the most prominent of them is the entropy method. This method is based on the concept of *Entropy,* which is defined as a measure of uncertainty by Shannon.[51] In the information theory, entropy is a criterion for the level of uncertainty given by discrete probability distribution, such that, the ones with significantly high values exhibit higher levels of uncertainty.[52] If the decision matrix with sufficient information for the alternatives is available, then the entropy method can be used as a tool to determine the significance rankings, i.e., the weighting values of the criteria.[28,53–55] The method can be summarized as follows:[56–57]

Let the decision matrix for a multi-criteria decision making problem with *m* alternatives and *n* criteria be Equation (1):

$$D=\begin{array}{cc} & \begin{array}{cccccc} X_1 & X_2 & \dots & X_j & \dots & X_n \end{array} \\ \begin{array}{c} A_1 \\ A_2 \\ \vdots \\ A_i \\ \vdots \\ A_m \end{array} & \begin{bmatrix} x_{11} & x_{12} & \dots & x_{1j} & \dots & x_{1n} \\ x_{21} & x_{21} & \dots & x_{2j} & \dots & x_{2n} \\ \vdots & \vdots & \vdots & \vdots & \vdots & \vdots \\ x_{i1} & x_{i2} & \dots & x_{ij} & \dots & x_{in} \\ \vdots & \vdots & \vdots & \vdots & \vdots & \vdots \\ x_{m1} & x_{m2} & \dots & x_{mj} & \dots & x_{mn} \end{bmatrix} \end{array} \qquad (1)$$

Here, x_{ij}: is the success value of *i*-th alternative according to *j*-th criterion. $i = 1,2,...,m$ and $j = 1,2,...,n$.

Here, *A* and *X* stand for the alternative and the criterion, respectively.

Step 1:
With the following Equation (2):

$$r_{ij}=\frac{x_{ij}}{\sum_{p=1}^{m} x_{pj}} \quad i = 1,2,...,m \text{ and } j = 1,2,...,n \qquad (2)$$

$R=\left[r_{ij}\right]_{m\times n}$ normalized decision matrix is obtained.

Table 6: Criteria parameters
Tabela 6: Merila parametrov

Criterion	Abrasive (mesh)	Load (N)	Speed (r/min)	Criterion	Abrasive (mesh)	Load (N)	Speed (r/min)	Criterion	Abrasive (mesh)	Load (N)	Speed (r/min)
C_1	800	0.5	45	C_{10}	1000	0.5	45	C_{19}	1200	0.5	45
C_2	800	0.5	90	C_{11}	1000	0.5	90	C_{20}	1200	0.5	90
C_3	800	0.5	140	C_{12}	1000	0.5	140	C_{21}	1200	0.5	140
C_4	800	1	45	C_{13}	1000	1	45	C_{22}	1200	1	45
C_5	800	1	90	C_{14}	1000	1	90	C_{23}	1200	1	90
C_6	800	1	140	C_{15}	1000	1	140	C_{24}	1200	1	140
C_7	800	1.5	45	C_{16}	1000	1.5	45	C_{25}	1200	1.5	45
C_8	800	1.5	90	C_{17}	1000	1.5	90	C_{26}	1200	1.5	90
C_9	800	1.5	140	C_{18}	1000	1.5	140	C_{27}	1200	1.5	140

Step 2:

With the following Equation (3):

$$e_j = -\frac{1}{\ln m}\sum_{i=1}^{m} r_{ij} \ln r_{ij} \quad j = 1,2,...,n \tag{3}$$

entropy value of each criterion is found. Here, e_j is the entropy value of the *j* the criterion.

Step 3:

The weighting values of the criteria are assigned with Equation (4):

$$W_j = \frac{1-e_j}{\sum_{p=1}^{n}(1-e_p)} \quad j = 1,2,...,n \tag{4}$$

It is apparent that $\sum_{j=1}^{n} W_j = 1$

3 RESULTS AND DISCUSSION

In this study, TOPSIS, MAUT and CP methods among the MDCM methods are used with the wear results obtained from the conducted micro-abrasion tests for the selection of the most suitable coating material, and afterwards the solutions proposed by each method are compared.

First, the criteria were weighted through the implementation of the Entropy method on the decision matrix (**Table 7**) consisting of the test results obtained from the micro-abrasion tests conducted in accordance with the test parameters given in **Table 3**, and then the analyses were carried out for each of the TOPSIS, MAUT and CP methods, as a means for the selection of the most suitable coating material. The resulting solutions were listed in descending order (from the most to the least suitable) by a comparative evaluation.

The criterion weights obtained with the Entropy method are given in **Table 8**.

The criteria weights were objectively determined with the Entropy method. The criteria weights calculated using the Entropy method are given in **Table 8**. According to these results, the criterion weights of the 26th, 22nd, 25th and 19th criteria were found to be higher than the other criteria. This arises from the fact that the 7th alternative Uncoated sample and 1st alternative CrN coating result in relatively higher wear rates, whereas N+CrN,TiAlN and TiN coatings result in lower wear rates. Consequently, the coatings providing lower wear rates under these criteria are favored over the other coatings. Other criterion weights generally had approximate values.

3.1 Analysis using TOPSIS method

The Technique for order preference by similarity to ideal solution (TOPSIS) method developed by C. - L. Hwang and K. Yoon[28] is based on the basic concept of

Table 7: The decision matrix for coating-material selection
Tabela 7: Matrica odločitev pri izbiri materiala nanosa

Material	C1	C2	C3	C4	C5	C6	C7	C8	C9	C10	C11	C12	C13	
CrN	0.0097	0.0134	0.0135	0.0149	0.0195	0.0221	0.0169	0.0226	0.0267	0.0071	0.0047	0.0044	0.0050	
N+CrN	0.0047	0.0061	0.0066	0.0073	0.0099	0.0106	0.0104	0.0096	0.0094	0.0016	0.0013	0.0055	0.0078	
N+TiAlN	0.0060	0.0071	0.0074	0.0055	0.0067	0.0077	0.0043	0.0067	0.0123	0.0031	0.0079	0.0020	0.0054	
N+TiN	0.0042	0.0060	0.0093	0.0085	0.0129	0.0161	0.0088	0.0185	0.0189	0.0015	0.0037	0.0059	0.0026	
TiAlN	0.0030	0.0050	0.0073	0.0059	0.0119	0.0111	0.0073	0.0130	0.0190	0.0013	0.0024	0.0075	0.0019	
TiN	0.0041	0.0059	0.0083	0.0070	0.0093	0.0130	0.0074	0.0156	0.0108	0.0042	0.0061	0.0065	0.0039	
Uncoated	0.0094	0.0147	0.0147	0.0220	0.0214	0.0228	0.0196	0.0220	0.0267	0.0081	0.0102	0.0122	0.0117	
Material	C14	C15	C16	C17	C18	C19	C20	C21	C22	C23	C24	C25	C26	C27
CrN	0.0055	0.0072	0.0100	0.0064	0.0118	0.0021	0.0024	0.0013	0.0020	0.0021	0.0022	0.0024	0.0021	0.0029
N+CrN	0.0058	0.0093	0.0051	0.0036	0.0094	0.0005	0.0006	0.0009	0.0008	0.0006	0.0006	0.0005	0.0003	0.0004
N+TiAlN	0.0092	0.0026	0.0054	0.0068	0.0050	0.0003	0.0008	0.0005	0.0004	0.0015	0.0007	0.0009	0.0010	0.0005
N+TiN	0.0018	0.0117	0.0065	0.0016	0.0064	0.0009	0.0011	0.0015	0.0011	0.0014	0.0009	0.0012	0.0017	0.0012
TiAlN	0.0056	0.0054	0.0012	0.0028	0.0034	0.0015	0.0006	0.0006	0.0004	0.0004	0.0007	0.0004	0.0004	0.0007
TiN	0.0045	0.0011	0.0072	0.0092	0.0090	0.0004	0.0009	0.0012	0.0005	0.0007	0.0006	0.0006	0.0007	0.0008
Uncoated	0.0139	0.0246	0.0164	0.0166	0.0255	0.0048	0.0049	0.0024	0.0053	0.0030	0.0040	0.0055	0.0067	0.0027

Table 8: The criterion weights obtained using the entropy method
Tabela 8: Kriterijske uteži, dobljene z metodo entropije

Criterion	C1	C2	C3	C4	C5	C6	C7	C8	C9
Weight	0.0158	0.0163	0.0082	0.0245	0.0131	0.0120	0.0203	0.0126	0.0131
Criterion	C10	C11	C12	C13	C14	C15	C16	C17	C18
Weight	0.0403	0.0297	0.0196	0.0279	0.0259	0.0571	0.0321	0.0414	0.0357
Criterion	C19	C20	C21	C22	C23	C24	C25	C26	C27
Weight	0.0758	0.0616	0.0219	0.0866	0.0353	0.0540	0.0790	0.0922	0.0482

the selection of the alternative closest to ideal solution and the farthest to anti-ideal solution. The consecutive stages of this method are as follows:[28,56]

Step 1: Constructing the normalized decision matrix: with the following Equation (5):

$$r_{ij} = \frac{x_{ij}}{\sqrt{\sum_{p=1}^{m} (x_{pj})^2}} \quad i = 1,2,...,m \text{ and } j = 1,2,...,n \tag{5}$$

Normalized decision matrix $R = \left[r_{ij} \right]$ is obtained.

Step 2: Constructing the weighted normalized decision matrix, with the following Equation (6):

$$v_{ij} = w_j r_{ij} \quad i = 1,2,...,m \text{ and } j = 1,2,...,n \tag{6}$$

Normalized decision matrix $V = \left[v_{ij} \right]_{m \times n}$ is obtained.

Here, w_j : j-th criterion's weight value obtained with the entropy method.

Step 3: Determination of ideal and negative-ideal solutions:

If the two artificial solutions A^* (ideal solution) and A^- (negative-ideal solution) are defined as follows:

$$\begin{aligned} A^* &= \left\{ (\max_i v_{ij} \middle| j \in J), (\min_i v_{ij} \middle| j \in J') \middle| i = 1,2,\dots,m \right\} \\ &= \left\{ v_1^*, v_2^*, \dots, v_j^*, \dots v_n^*, \right\} \end{aligned} \tag{7}$$

$$\begin{aligned} A^- &= \left\{ (\min_i v_{ij} \middle| j \in J), (\max_i v_{ij} \middle| j \in J') \middle| i = 1,2,\dots,m \right\} \\ &= \left\{ v_1^-, v_2^-, \dots, v_j^-, \dots v_n^-, \right\} \end{aligned} \tag{8}$$

here,

$J = \left\{ j = 1,2,\dots,n \middle| \text{in case of benefit criterion} \right\}$

$J' = \left\{ j = 1,2,\dots,n \middle| \text{in case of cost criterion} \right\}$

Step 4: Calculation of the separation measure:

Each alternative's measure of separation from the ideal solution S_{i^*} and from the negative-ideal solution S_{i^-}, is given as follows:

$$S_{i^*} = \sqrt{\sum_{j=1}^{n} (v_{ij} - v_j^*)^2}, i = 1,2,\dots,m \tag{9}$$

$$S_{i^-} = \sqrt{\sum_{j=1}^{n} (v_{ij} - v_j^-)^2}, i = 1,2,\dots,m \tag{10}$$

Step 5: Calculation of the relative proximity to the ideal solution:

The relative proximity to the i-th alternative to the ideal solution (A^*) is defined as follows:

$$C_{i^*} = S_{i^-}(S_{i^*} - S_{i^-}), 0 < C_{i^*} < 1, \ i = 1,2,\dots,m \tag{11}$$

Step 6: Performing the decision ranking: The decision ranking of the alternatives is performed in accordance with the descending order of C_{i^*} values.

The weighted and normalized decision matrix, related to the analysis conducted in accordance with the steps defined in the TOPSIS method, is given in **Table 9**. Ideal and anti-ideal solutions obtained using Equations (7) and (8), are given in **Table 10**. As indicated in the table, the highest C_{i^*} valued alternative stands for the best selection in the TOPSIS method.

Positive and negative separation measures given in **Table 11** and relative proximities to the ideal solution are calculated respectively with Equations (9), (10) and (11). Also, the ranking of the coating materials based on the relative proximities to ideal solution are given in **Table 11**. According to this ranking, TiAlN is qualified as the best coating material owing to its excellent performance, which is followed by N+CrN, TiN and N+TiAlN with similar performance values. N+TiN and CrN resulted in low performance values, whereas the uncoated material resulted in the worst performance value.

Table 9: Weighted normalized decision matrix
Tabela 9: Pretehtana normalizirana matrica odločitev

Material	C1	C2	C3	C4	C5	C6	C7	C8	C9	C10	C11	C12	C13	
CrN	0.0091	0.0091	0.0042	0.0118	0.0069	0.0063	0.0109	0.0066	0.0070	0.0235	0.0089	0.0047	0.0083	
N+CrN	0.0044	0.0041	0.0020	0.0058	0.0035	0.0030	0.0067	0.0028	0.0024	0.0053	0.0024	0.0059	0.0130	
N+TiAlN	0.0056	0.0048	0.0023	0.0044	0.0024	0.0022	0.0028	0.0020	0.0032	0.0102	0.0150	0.0021	0.0091	
N+TiN	0.0039	0.0041	0.0029	0.0068	0.0045	0.0046	0.0057	0.0054	0.0049	0.0048	0.0069	0.0063	0.0044	
TiAlN	0.0028	0.0034	0.0023	0.0047	0.0042	0.0032	0.0047	0.0038	0.0050	0.0042	0.0045	0.0080	0.0032	
TiN	0.0038	0.0040	0.0026	0.0056	0.0033	0.0037	0.0048	0.0045	0.0028	0.0137	0.0116	0.0070	0.0065	
Uncoated	0.0088	0.0100	0.0046	0.0175	0.0075	0.0066	0.0127	0.0064	0.0070	0.0267	0.0192	0.0131	0.0196	
Material	C14	C15	C16	C17	C18	C19	C20	C21	C22	C23	C24	C25	C26	C27
CrN	0.0072	0.0135	0.0141	0.0121	0.0132	0.0289	0.0257	0.0080	0.0292	0.0171	0.0244	0.0304	0.0259	0.0325
N+CrN	0.0076	0.0175	0.0072	0.0069	0.0105	0.0065	0.0062	0.0053	0.0115	0.0046	0.0069	0.0058	0.0037	0.0044
N+TiAlN	0.0119	0.0048	0.0075	0.0130	0.0055	0.0038	0.0082	0.0032	0.0055	0.0127	0.0073	0.0111	0.0122	0.0051
N+TiN	0.0023	0.0220	0.0092	0.0030	0.0070	0.0128	0.0112	0.0093	0.0159	0.0114	0.0104	0.0155	0.0209	0.0133
TiAlN	0.0073	0.0101	0.0017	0.0053	0.0037	0.0206	0.0062	0.0036	0.0055	0.0030	0.0082	0.0051	0.0044	0.0073
TiN	0.0058	0.0020	0.0102	0.0176	0.0100	0.0048	0.0096	0.0073	0.0069	0.0059	0.0066	0.0070	0.0088	0.0089
Uncoated	0.0181	0.0464	0.0231	0.0316	0.0283	0.0651	0.0526	0.0149	0.0784	0.0243	0.0447	0.0696	0.0845	0.0302

Table 10: Ideal and anti-ideal solutions
Tabela 10: Idealne in neidealne rešitve

Criterion	C1	C2	C3	C4	C5	C6	C7	C8	C9
A^*	0.0028	0.0034	0.0020	0.0044	0.0024	0.0022	0.0028	0.0020	0.0024
A^-	0.0091	0.0100	0.0046	0.0175	0.0075	0.0066	0.0127	0.0066	0.0070
Criterion	C10	C11	C12	C13	C14	C15	C16	C17	C18
A^*	0.0042	0.0024	0.0021	0.0032	0.0023	0.0020	0.0017	0.0030	0.0037
A^-	0.0267	0.0192	0.0131	0.0196	0.0181	0.0464	0.0231	0.0316	0.0283
Criterion	C19	C20	C21	C22	C23	C24	C25	C26	C27
A^*	0.0038	0.0062	0.0032	0.0055	0.0030	0.0066	0.0051	0.0037	0.0044
A^-	0.0651	0.0526	0.0149	0.0784	0.0243	0.0447	0.0696	0.0845	0.0325

Table 11: Positive and negative separation measures, relative proximities to the ideal solution and the ranking
Tabela 11: Pozitivni in negativni ukrepi ločevanja, relativni približki idealni rešitvi in razvrstitev

Material	S+	S-	C+	Sýra
CrN	0.0724	0.1104	0.6039	6
N+CrN	0.0234	0.1632	0.8747	2
N+TiAlN	0.0262	0.1610	0.8602	4
N+TiN	0.0371	0.1433	0.7946	5
TiAlN	0.0212	0.1648	0.8861	1
TiN	0.0255	0.1620	0.8640	3
Uncoated	0.1742	0.0023	0.0132	7

3.2 Analysis using MAUT method

According to the basic principle of MAUT (Multiple Attribute Utility Theory) method, there is an *U* utility function with a real value, defined over the set of suitable alternatives, and the decision maker maximizes this.[58] The procedure followed in the MAUT method is defined in 4 steps:[59–60]

Step 1: Utility values are determined according to the benefit criteria and the normalized values r_{ij} are calculated using these values:

$$r_{ij}=\frac{x_{ij}-l_l^-}{u_j^+-l_l^-},\quad u_j^+=\max_i x_{ij},\quad l_j^-=\min_i x_{ij} \tag{12}$$

Similarly, the utility values are also determined based on the cost criterion, and normalized values r_{ij} are calculated accordingly:

$$r_{ij}=\frac{u_l^+-x_{ij}}{u_j^+-l_l^-},\quad u_j^+=\max_i x_{ij},\quad l_j^-=\min_i x_{ij} \tag{13}$$

Step 2: Weighted sum of r_{ij} values gives the total utility value.

$$U_i=\sum_{j=1}^{n} w_j r_{ij} \tag{14}$$

Step 3: Decision ranking is performed. The alternative with the highest total utility value is deemed the best alternative.

The single-attribute utility function values of the alternatives calculated with MAUT method based on the criteria, are given in **Table 12**.

MAUT multi-attribute utility function values and their ranking are given in **Table 13**. As shown in Table

Table 12: MAUT single-attribute utility function values
Tabela 12: Posamezni MAUT-atributi vrednosti funkcije koristnosti

Material	C1	C2	C3	C4	C5	C6	C7	C8	C9	C10	C11	C12	C13	
CrN	0.0000	0.1299	0.1556	0.4352	0.1283	0.0498	0.1777	0.0000	0.0000	0.1428	0.6139	0.7683	0.6856	
N+CrN	0.7483	0.8835	1.0000	0.8920	0.7841	0.8094	0.6014	0.8183	1.0000	0.9493	1.0000	0.6587	0.3997	
N+TiAlN	0.5519	0.7813	0.8990	1.0000	1.0000	1.0000	1.0000	1.0000	0.8310	0.7342	0.2495	1.0000	0.6384	
N+TiN	0.8212	0.8924	0.6653	0.8215	0.5769	0.4445	0.7070	0.2588	0.4521	0.9742	0.7299	0.6205	0.9282	
TiAlN	1.0000	1.0000	0.9083	0.9812	0.6450	0.7784	0.8047	0.6033	0.4462	1.0000	0.8771	0.4622	1.0000	
TiN	0.8332	0.9034	0.7956	0.9099	0.8235	0.6514	0.7982	0.4395	0.9160	0.5800	0.4557	0.5562	0.7969	
Uncoated	0.0450	0.0000	0.0000	0.0000	0.0000	0.0000	0.0000	0.0399	0.0000	0.0000	0.0000	0.0000	0.0000	
Material	C14	C15	C16	C17	C18	C19	C20	C21	C22	C23	C24	C25	C26	C27
CrN	0.6906	0.7401	0.4203	0.6811	0.6160	0.5904	0.5791	0.5917	0.6755	0.3393	0.5349	0.6074	0.7250	0.0000
N+CrN	0.6669	0.6501	0.7451	0.8653	0.7248	0.9560	0.9991	0.8200	0.9174	0.9229	0.9944	0.9889	1.0000	1.0000
N+TiAlN	0.3921	0.9361	0.7284	0.6518	0.9275	1.0000	0.9580	1.0000	1.0000	0.5444	0.9827	0.9071	0.8948	0.9741
N+TiN	1.0000	0.5491	0.6526	1.0000	0.8645	0.8520	0.8925	0.4780	0.8575	0.6050	0.9001	0.8378	0.7873	0.6851
TiAlN	0.6856	0.8163	1.0000	0.9198	1.0000	0.7259	1.0000	0.9622	1.0000	1.0000	0.9589	1.0000	0.9915	0.8953
TiN	0.7755	1.0000	0.6055	0.4903	0.7436	0.9834	0.9266	0.6537	0.9804	0.8625	1.0000	0.9698	0.9372	0.8410
Uncoated	0.0000	0.0000	0.0000	0.0000	0.0000	0.0000	0.0000	0.0000	0.0000	0.0000	0.0000	0.0000	0.0000	0.0822

13, TiAlN takes the first place with its superior performance, followed by N+CrN, N+TiAlN and TiN with similar performance values. N+TiN, CrN and especially uncoated material exhibited significantly low performances, as the highest total utility valued alternative stands for the best selection.

Table 13: MAUT Multi-utility function and the ranking
Tabela 13: MAUT Večvrednostna funkcija in razvrstitev

Material	Multi utility values	Ranking
CrN	0.509431	6
N+CrN	0.879946	2
N+TiAlN	0.860277	3
N+TiN	0.784909	5
TiAlN	0.909513	1
TiN	0.841247	4
Uncoated	0.005178	7

3.3. Analysis using CP method

CP (Compromise Programming) is a MCDM method developed in the 1970s by M. Zelen[61] and P. – L. Yu.[62] This method is based on minimization of the distance to the ideal point f^*. The L_p metric is used for the calculation of distance. The method can be summarized as follows:[63–66]

Step 1: Ideal point f^* and anti-ideal point f_* are established.

$$f^* \equiv f_1^*, f_2^*, \ldots, f_n^*,\; f_* \equiv f_{1*}, f_{2*}, \ldots, f_{n*} \quad (15)$$

here,

$$f_j^* = \begin{cases} \max_{i=1,2,\ldots,m} \{x_{ij}\} & j.\text{criterion utility} \\ \min_{i=1,2,\ldots,m} \{x_{ij}\} & j.\text{criterion cost} \end{cases} \quad (16)$$

$$f_{j*} = \begin{cases} \min_{i=1,2,\ldots,m} \{x_{ij}\} & j.\text{criterion utility} \\ \max_{i=1,2,\ldots,m} \{x_{ij}\} & j.\text{criterion cost} \end{cases} \quad (17)$$

here, x_{ij}: is the success value of the i-th alternative according to the j-th criterion. $i = 1,2,\ldots,m$, $j = 1,2,\ldots,n$.

Step 2: The distance to the ideal point is minimized:

$$\min L_p = \left[\sum_{j=1}^{n} W_j \left(\frac{f_j^* - f_j(x_i)}{f_j^* - f_{j*}} \right)^p \right]^{1/p},\; i = 1,2,\ldots,m \quad (18)$$

Step 3: The alternative giving the minimal value is the best alternative.

L_1, L_2 and L_∞ are, respectively, named as the Manhattan, Euclidean and Tchebycheff metrics.

The optimal values obtained using the CP method and the ranking are shown in **Table 14**. Given that in the CP method the alternative giving the lowest optimal value is the best alternative; TiAlN may be considered to have shown the best performance by far, as the highest total utility valued alternative stands for the best selection. N+CrN, N+TiAlN and TiN materials underperformed compared to the performance values of TiAlN. The performance values of N+TiN, CrN and the uncoated materials lined up at the bottom of the performance list.

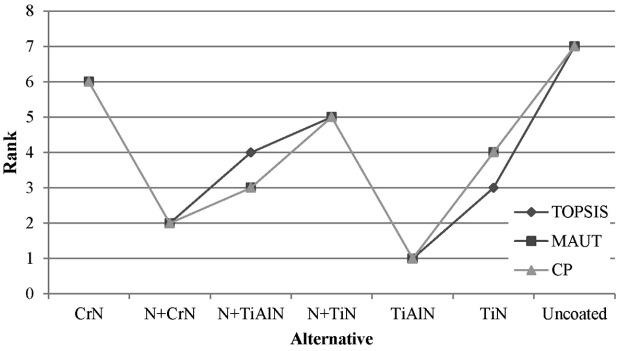

Figure 3: Ranking of the alternatives obtained with MCDM methods
Slika 3: Razvrstitev alternativnih variant, dobljenih z MCDM metodami

Table 14: CP optimal values and the ranking
Tabela 14: CP optimalne vrednosti in razvrstitev

Material	Optimal value	Rank
CrN	0.269379	6
N+CrN	0.070013	2
N+TiAlN	0.080999	3
N+TiN	0.120416	5
TiAlN	0.055632	1
TiN	0.089914	4
Uncoated	0.543521	7

The rankings obtained using the TOPSIS, MAUT and CP methods are shown in **Figure 3**. As seen in the figure, the MAUT and CP methods produced the identical ranking of the alternatives, whereas there is a slight deviation in the ranking obtained with the TOPSIS method. However, all the methods indicate that TiAlN is the best material, followed by N+CrN. CrN and the uncoated materials displayed the best performances, according to all the MCDM methods implemented in the study.

4 CONCLUSIONS

In this study, abrasive wear tests were conducted using the micro-abrasion wear technique on TiN, CrN and AlTiN coatings, which were deposited on nitrided and non-nitrided substrates with the PVD technique, then the measured wear values were used so as to determine the best coating selection through analyses with each of the TOPSIS, MAUT and CP methods among the MCDM techniques. The most suitable coating types, according to each method, were determined and comparatively evaluated. The obtained results are summarized as follows:

- According to the TOPSIS method TiAlN was determined to be the coating with the best performance; which was followed by N+CrN, TiN and N+TiAlN, respectively. The N+TiN and CrN coatings underperformed compared to other coatings; however, the uncoated material displayed the worst performance, with a dramatic decline compared to all the coated materials.

- According to the MAUT method, TiAlN exhibited the best performance. Other coatings were ranked as N+CrN, N+TiAlN and TiN, respecively. N+TiN, CrN and especially the uncoated material displayed remarkable underperformances.
- The CP and MAUT methods produced the same ranking of alternatives. In the TOPSIS method only N+TiAlN and TiN shifted places in the ranking differently from the CP and MAUT methods. However, all the methods indicate that TiAlN is the best material, which is followed by N+CrN. Again, the CrN and uncoated materials became the alternatives with worse performances according to all the MCDM methods.
- The highest C_{i*} valued alternative is deemed the best selection in the TOPSIS method. While the highest total utility valued alternative is the best selection for MAUT, in the CP method the shortest distance is favored.
- Increasing the number of MCDM methods could be useful for a comparative analysis of the obtained results in further studies.

Acknowledgements

The authors would like to acknowledgement the funding support of the Scientific Research Project (BAP) no 2013.1.85. provided by Bartin University Scientific Research Projects Unit. All other support provided by the Engineering Faculty of Bartin University and its staff is also acknowledged.

5 REFERENCES

[1] J. Vetter, Vacuum arc coatings for tools: potential and application. Surface and Coatings Technology, 76–77 (**1995**), 719–724, doi:10.1016/0257-8972(95)02499-9

[2] R. J. Rodriguez, J. A. Garcia, A. Medrano, M. Rico, R. Sanchez, R. Martinez, Tribological behaviour of hard coatings deposited by arc-evaporation PVD, Vacuum, 67 (**2002**), 559–566, doi:10.1016/s0042-207x(02)00248-8

[3] H. Çalışkan, P. Panjan, S. Paskvale, Monitoring of wear characteristics of TiN and TiAlN coatings at long sliding distances, Tribology Transactions, 57 (**2014**), 496–502, doi:10.1080/10402004.2014.884254

[4] M. Vite, M. Moreno-Rios, E. A. G. Hernandez, J. R. Laguna-Camacho, A study of the abrasive resistance of sputtered CrN coatings deposited on AISI 316 and AISI H13 steel substrates using steel particles, Wear, 271 (**2011**), 1273–1279, doi:10.1016/j.wear.2011.01.072

[5] P. Panjan, P. Cvahte, M. Čekada, B. Navinšek, I. Urankar, PVD CrN coating for protection of extrusion dies, Vacuum 61 (**2001**), 241–244, doi:10.1016/s0042-207x(01)00113-0

[6] H. Çalışkan, Effect of test parameters on the micro-abrasion behavior of PVD CrN coatings, Measurement 55 (**2014**), 444–451, doi:10.1016/j.measurement.2014.05.036

[7] M. F. C. Andrade, R. P. Martinho, F. J. G. Silva, R. J. D. Alexandre, A. P. M. Baptista, Influence of the abrasive particles size in the microabrasion wear tests of TiAlSiN thin coatings, Wear, 267 (**2009**), 12–18, doi:10.1016/j.wear.2008.12.114

[8] A. Kassman, S. Jacobson, L. Erickson, P. Hedenqvist, M. Olsson, A new test method for the intrinsic abrasion resistance of thin coatings, Surf. Coat. Technol, 50 (**1991**), 75–84, doi:10.1016/0257-8972(91)90196-4

[9] X.-Z. Ding, C. T. Bui, X. T. Zeng, Abrasive wear resistance of Ti1-xAlxN hard coatings deposited by a vacuum arc system with lateral rotating cathodes, Surf. Coat. Technol., 203 (**2008**), 680–684, doi:10.1016/j.surfcoat.2008.08.019

[10] J. C. A. Batista, C. Godoy, A. Matthews, Micro-scale abrasive wear testing of duplex and non-duplex (single-layered) PVD (Ti, Al)N, TiN and Cr–N coatings. Tribol. Int., 35 (**2002**), 363–372, doi:10.1016/s0301-679x(02)00017-8

[11] B. Kurt, Y. Kucuk, M. S. Gok, Microabrasion Wear Behavior of VC and CrC Coatings Deposited by Thermoreactive Diffusion Technique. Tribology Transactions, 57 (**2014**), 345–352, doi:10.1080/10402004.2014.880538

[12] D. N. Allsopp, I. M. Hutchings, Micro-scale abrasion and scratch response of PVD coatings at elevated temperatures. Wear, 251 (**2001**), 1308–1314, doi:10.1016/s0043-1648(01)00755-4

[13] K. Bose, R. J. K. Wood, Optimum tests conditions for attaining uniform rolling abrasion in ball cratering tests on hard coatings, Wear, 258 (**2005**), 322–332,doi:10.1016/j.wear.2004.09.018

[14] H. Çalışkan, A. Erdoğan, P. Panjan, M. S. Gök, A. C. Karaoğlanlı, Microabrasion wear testing of multilayer nanocomposite TiAlSiN/TiSiN/TiAlN hard coatings deposited on AISI H11 steel, Mater. Tehnol., 47 (**2013**), 563–568

[15] R. P. Martinho, M. F. C. Andrade, F. J. G. Silva, R. J. D. Alexandre, A. P. M. Baptista, Micro-abrasion wear behaviour of TiAlCrSiN nanostructured coatings, Wear, 267 (**2009**), 1160–1165, doi:10.1016/j.wear.2008.12.063

[16] D. N. Allsopp, R.I. Trezona, I. M. Hutchings, The effects of ball surface condition in the micro-scale abrasive wear test, Tribol. Lett., 5 (**1998**), 259–264

[17] F. J. G. Silva, R. B. Casais, R. P. Martinho, A.P.M. Baptista, Role of abrasive material on micro-abrasion wear tests, Wear, 271 (**2011**), 2632–2639, doi:10.1016/j.wear.2010.11.050

[18] A. Gunen, Y. Kucuk, Y. Er, V. V. Cay, M. Öge, M. S. Gok, Effect of the powder particle size on the wear behaviour of boronized AISI 304 stainless Steel, Materials Testing, 57–5 (**2015**), 468–473, 10.3139/120.110732

[19] M. H. Korkut, M. S. Gok, A. C. Karaoglanli, Y. Kucuk, Y. Er, A. Erdogan, Effect of Abrasive Grit Size on Wear Behavior of Ceramic Coatings by Micro-Abrasion Test, Mater.Tehnol., 47–6 (**2013**), 695–699

[20] G. B. Stachowiak, G. W. Stachowiak, J. M. Brandt, Ball-cratering abrasion tests with large abrasive particles, Tribol. Int., 39 (**2006**), 1–11, doi:10.1016/j.triboint.2004.10.010

[21] K. L. Edwards, Materials influence on design: a decade of development, Mater Des, 32 (**2011**), 1073–80, doi:10.1016/j.matdes.2010.10.009

[22] P. Chatterjee, S. Chakraborty, Material selection using preferential ranking methods, Mater. Des., 35 (**2012**), 384–93, doi:10.1016/j.matdes.2011.09.027

[23] H. Çalışkan, Selection of boron based tribological hard coatings using multi-criteria decision making methods, Materials & Design, 50 (**2013**), 742–749, doi:10.1016/j.matdes.2013.03.059

[24] H. Çalışkan, B. Kurşuncu, C. Kurbanoğlu, Ş. Y. Güven, Material selection for the tool holder working under hard milling conditions using different multi criteria decision making methods, Materials & Design, 45 (**2013**), 473–479, doi:10.1016/j.matdes.2012.09.042

[25] E. Triantaphyllou, Multi-criteria decision making methods: A Comparative Study, 2000, Springer, 5–21, doi:10.1007/978-1-4757-3157-6

[26] A. Abrishamchi, A. Ebrahimian, M. Tajrishi, M. A. Mariño, Hon. M. ASCE, Case study: application of multicriteria decision making to urban water supply, Journal of Water Resources Planning and Management, 131 (**2005**) 4, 326–335, doi:10.1061/(asce)0733-9496(2005) 131:4(326)

[27] A. Chauhan, R.Vaish, Hard coating material selection using multicriteria decision making, Mater Des 44, (**2013**), 240–245, doi:10.1016/j.matdes.2012.08.003

[28] C. - L. Hwang, K. Yoon, Lecture Notes in Economics and Mathematical Systems: Multiple Attribute Decision Making: Methods and Appllication, Springer Verlag, 1981, doi:10.1007/978-3-642-48318-9_4

[29] G. Kabir, R. Sadiq, S. Tesfamariam, A review of multi-criteria decision-making methods for infrastructure management, Structure and Infrastructure Engineering, 9 (**2014**), 1176–1210, doi:10.1080/15732479.2013.795978

[30] S. Opricovic, G. H. Tzeng, Compromise solution by MCDM methods: A comparative analysis of VIKOR and TOPSIS. European Journal of Operational Research, 2 (**2004**) 156, 445–455, doi:10.1016/s0377-2217(03)00020-1

[31] G. Kabir, R. S. Sumi, Selection of concrete production facility location integrating fuzzy AHP with TOPSIS method. International Journal of Productivity Management and Assessment Technologies, 1 (**2012**) 1, 40–59, doi:10.4018/ijfsa.2013070104

[32] S. J. Chen, C. L. Hwang, Fuzzy multiple attribute decision making, methods and application. Berlin: SpringerVerlag, (1992), doi:10.1007/978-3-642-46768-4_5

[33] K. P. Yoon, C. L. Hwang, Multiple attribute decision making, Thousand Oaks, CA: Sage Publication, (1995), doi:10.4135/9781412985161

[34] A. Pires, N. B. Chang, G. Martinho, An AHP-based fuzzy interval TOPSIS assessment for sustainable expansion of the solid waste management system in Setubal Peninsula, Portuga. Resources, Conservation and Recycling, 56 (2011) 1, 7–21, doi:10.1016/j.resconrec.2011.08.004

[35] G. Kabir, M. A. A. Hasin, Integrating fuzzy AHP with TOPSIS method for optimal power substation location selection, International Journal of Enterprise Network Management, Advance online publication, (2012b), doi:10.1504/ijleg.2013.059166

[36] B. Benyahia, M. A. Latifi, C. Fonteix, F. Pla, Multicriteria dynamic optimization of an emulsion copolymerization reactor. Computers & Chemical Engineering, 35 (**2011**) 12, 2886–2895, doi:10.1016/s1570-7946(10)28077-x

[37] R. L. Keeny, H. Raiffa, Decision with multiple objectives John Wiley, NY (1976)

[38] R. L. Keeny, H. Raiffa, Decision with multiple objectives: Preferences and value trade-offs, Cambridge University Press (1993), doi:10.1017/cbo9781139174084

[39] S. K. Kim, O. Song, A MAUT approach for selecting a dismantling scenario for the thermal column in KRR-1 Annals of Nuclear Energy, 36 (**2009**), 145–150, doi:10.1016/j.anucene.2008.11.034

[40] M. Zeleny, Multiple criteria decision making, New York 1982

[41] A. Bárdossy, I. Bogárdi, L. Duckstein, Composite programming as an extension of compromise programming. Mathematics of Multi Objective Optimization (375–408). Wien: Springer Verlag, doi:10.1007/978-3-7091-2822-0_15

[42] A. Elmahdi, K. Kheireldin, A. Hamdy, GIS and multi-criteria evaluation: Robust tools for integrated water resources management, Water International, 31 (**2006**) 4, 440–447, doi:10.1080/02508060608691948

[43] G. Kabir, R. Sadiq, S. Tesfamariam, A review of multi-criteria decision-making methods for infrastructure management, Structure and Infrastructure Engineering, 10 (**2014**) 9, 1176–1210, doi:10.1080/15732479.2013.795978

[44] N. H. Zardari et al., Weighting Methods and Their Effects on Multi-Criteria Decision Making Model Outcomes in Water Resources Management, 2014, Springer, doi:10.1007/978-3-319-12586-2

[45] E. De Las Heras, D. A. Egidi, P. Corengia, D. Gonzalez-Santamaria, A. Garcia-Luis, M. Brizuela et al., Duplex surface treatment of an AISI 316L stainless steel; microstructure and tribological behavior, Surf Coat Technol, 202 (**2008**), 2945–2954, doi:10.1016/j.surfcoat.2007.10.037

[46] L. C. Gontijo, R. Machado, S .E. Kuri, L. C. Casteletti, P. A. P. Nascente, Corrosion resistance of the layers formed on the surface of plasma-nitrided AISI 304L steel. Thin Solid Films, 515 (**2006**), 1093–6, doi:10.1016/j.tsf.2006.07.075

[47] T., Wierzchon Structure and properties of multicomponent and composite layers produced by combined surface engineering methods. Surf Coat Technol, 180, 181 (**2003**), 458–64, doi:10.1016/j.surfcoat.2003.10.090

[48] P. Novak, D. Vojtch, J. Serak, V. Knotek, B. Bartova, Duplex surface treatment of the Nb-alloyed PM tool steel. Surf Coat Technol, 201 (**2006**), 3342–3349, doi:10.1016/j.surfcoat.2006.07.101

[49] P. L. Ge, M. D. Bao, H. J. Zhang, K. You, X. P. Liu, Effect of plasma nitriding on adhesion strength of CrTiAlN coatings on H13 steels by closed field unbalanced magnetron sputter ion plating. Surface & Coatings Technology, 229 (**2013**), 146–150, doi:10.1016/j.surfcoat.2012.08.002

[50] C. E. Shannon, W. Weaver The Mathematical Theory of Communication: University of Illinois Press., Urbana, III; 1949

[51] H. J. Gold, B. S. No, Application of Maximum Entropy and Minimum Cross-entropy Formalisms to Stochastic Modeling of Complex Dynamic Systems: Formulation of the Problem, Citeseer ;1983

[52] P. Nijkamp, Reflections on gravity and entropy models, Regional Science and Urban Economics, 5 (**1975**) 2, 203–225, doi:10.1016/0166-0462(75)90004-6

[53] A. Van Delft, P. Nijkamp, Multi-criteria analysis and regional decision-making. Springer Science & Business Media 8 (**1975**), doi:10.3828/tpr.49.4.352126u26l581260

[54] M. Zeleny, Linear multiobjective programming. Berlin: Springer-Verlag; 1974, doi:10.1007/978-3-642-80808-1

[55] M. Islamoglu, M. Apan, A. Oztel, An Evaluation of the Financial Performance of REITs in Borsa Istanbul: A Case Study Using the Entropy-Based TOPSIS Method. International Journal of Financial Research 6 (**2015**) 2, 124, doi:10.5430/ijfr.v6n2p124

[56] T.-C. Wang, J.-C. Hsu, Evaluation of the business operation performance of the listing companies by applying TOPSIS method. Paper presented at the Systems, Man and Cybernetics. 2004 IEEE International Conference, doi:10.1109/icsmc.2004.1399802

[57] D. L. Olson Decision aids for selection problems. Springer Science & Business Media 1995, doi:10.1007/978-1-4612-3982-6

[58] I. Erol, S. Sencer, R. Sari, A new fuzzy multi-criteria framework for measuring sustainability performance of a supply chain. Ecological Economics, 70 (**2011**) 6, 1088-1100, doi:10.1016/j.ecolecon.2011.01.001

[59] J. Zietsman, L. R. Rilett, S.-J. Kim, Transportation corridor decision-making with multi-attribute utility theory. International Journal of Management and decision making, 7 (**2006**) 2, 254-266, doi:10.1504/ijmdm.2006.009147

[60] M. Zeleny, Compromise programming. Multiple criteria decision making, MANJKA !!! 1973, 286

[61] P. L. Yu, Multiple-criteria decision making, Springer 1985, doi:10.1007/978-1-4684-8395-6

[62] I. Erol, S. Sencer, A. Özmen, C. Searcy, Fuzzy MCDM framework for locating a nuclear power plant in Turkey.Energy Policy 67 (**2014**), 186–197, doi:10.1016/j.enpol.2013.11.056

[63] F. J. André, C. Romero, Computing compromise solutions: on the connections between compromise programming and composite programming. Applied Mathematics and Computation 195 (**2008**) 1, 1–10,doi:10.1016/j.amc.2007.04.064

[64] E. Ballestero, C. Romero, Portfolio selection: A compromise programming solution. Journal of the Operational Research Society 1996: 1377–1386, doi:10.1057/jors.1996.173

[65] Öztel A, M. S. Köse, İ.Aytekin, Kurumsal Sürdürülebilirlik Performansının Ölçümü İçin Çok Kriterli Bir Çerçeve: Henkel Örneği. Tarih Kültür ve Sanat Araştırmaları Dergisi 1 (**2012**) 4, 32–44, doi:10.7596/taksad.v1i4.85

MATERIALI IN TEHNOLOGIJE/MATERIALS AND TECHNOLOGY (1967–2017) – 50 LET/50 YEARS

UDK 669.018.25:669.13:621.79
Professional article/Strokovni članek

ISSN 1580-2949
MTAEC9, 51(2)317(2017)

IN-SITU SYNTHESIS OF TITANIUM CARBIDE PARTICLES IN AN IRON MATRIX DURING DIODE-LASER SURFACE ALLOYING OF DUCTILE CAST IRON

IN SITU SINTEZA DELCEV TITANOVEGA KARBIDA V OSNOVI ŽELEZA MED POVRŠINSKIM LEGIRANJEM LITEGA ŽELEZA Z DIODNIM LASERJEM

Damian Janicki
Silesian University of Technology, Faculty of Mechanical Engineering, Welding Department, 18a Konarskiego Street,
44-100 Gliwice, Poland
damian.janicki@polsl.pl

Prejem rokopisa – received: 2015-07-02; sprejem za objavo – accepted for publication: 2016-05-03

doi:10.17222/mit.2015.198

An in-situ formation of titanium carbide (TiC) particles in an iron matrix during diode-laser surface alloying of ductile cast iron (DCI) with direct injection of titanium powder into a molten pool was investigated. The microstructure of the in-situ TiC-reinforced surface alloying layers (SALs) was assessed with scanning electron microscopy (SEM), energy-dispersive spectroscopy (EDS) and X-ray diffraction (XRD). Comparative erosion tests of the as-received DCI and the SALs were performed following the ASTM G 76 standard test method. It was found that the morphology and volume fraction of the TiC particles directly depend on the amount of the titanium powder introduced into the molten pool, which, in turn, is strongly affected by the laser-power level. An increase in the titanium concentration in the molten pool results in a change in the TiC morphology, form cubic (> 2 µm in size) to dendritic (up to 10 µm in size). The maximum volume fraction of the TiC particles in the SALs was 12 %. The SALs exhibited a noticeable increase in the erosion resistance in comparison to the as-received DCI, especially at steep angles.

Keywords: in-situ composite, composite surface layer, TiC, laser surface alloying, ductile cast iron, erosive wear

Preiskovan je bil in situ nastanek delcev titanovega karbida (TiC) v osnovi železa med legiranjem površine duktilnega litega čeleza (DCI) z diodnim laserjem, z vpihovanjem titanovega prahu v staljeno kopel. Mikrostruktura površinskega legiranega sloja (SAL), ojačanega z in situ nastalim TiC je bila ocenjena z vrstičnim elektronskim mikroskopom (SEM), z energijsko disperzijsko spektroskopijo (EDS) in z rentgensko difrakcijo (XRD). Primerjalni erozijski preizkusi med dobavljenim DCI in SAL so bili izvedeni po ASTM G 76 standardni preizkusni metodi. Ugotovljeno je, da sta morfologija in volumski delež TiC delcev neposredno odvisna od količine prahu titana, ki je doveden v talino, kar je posledično močno odvisno od moči laserja. Povečanje koncentracije titana v staljeni kopeli se odraža na spremembi morfologije TiC iz kubične (pri velikosti > 2 µm) v dendritno (do velikosti 10 µm). Največji volumski delež delcev TiC v SAL je bil 12 %. SAL je pokazal občutno povečanje odpornosti na erozijo v primerjavi z dobavljenim DCI, še posebno pri večjih kotih.

Ključne besede: in situ kompozit, kompozitna površinska plast. TiC, legiranje površine z laserjem, duktilno lito železo, erozijska obraba

1 INTRODUCTION

Ductile cast iron (DCI) is extensively used for manufacturing machine parts in many industries such as automotive, power generation, mining, military and agricultural industry.[1,2] However, in some applications, there is a need to increase the durability of machine parts by improving their resistance to erosion.[3–7] The enhancement of erosion resistance of DCI can be achieved by reinforcing its surface layer with ceramic particles (the reinforcing phase), in particular, with an in-situ synthesis of titanium carbide (TiC). During the in-situ fabrication of composite surface layers (CSLs), reinforcing phases (RPs) are formed throughout the matrix (from the melt) due to a chemical reaction.[8] As a result, the RPs are free of contaminants and have a high coherency and a strong interface with the metal matrix. The difficulty with the in-situ fabrication of CSLs is related to the fact that the distribution homogeneity and the average particle size of an RP depend on the solidification conditions and the fluid flow in the molten pool, so they are difficult to control.[8–10]

Laser surface alloying is particularly well suited to the needs of the in-situ fabrication of the CSLs, mainly due to an accurate control of the molten-pool solidification.[11] Moreover, the molten pool generated during laser processing undergoes a rapid solidification, which provides a unique opportunity to synthesize non-equilibrium phases.[10] To date, a number of studies have focused on the laser surface alloying of both grey and ductile cast irons in order to improve the wear resistance. Some studies also attempted to investigate the in-situ formation of CSLs on a cast-iron substrate.[8,9] Most of the research, however, have been conducted using CO_2 and various types of Nd:YAG lasers. A high-power direct-diode laser (HPDDL) with a uniform intensity distri-

Table 1: Chemical composition of the investigated ductile cast iron
Tabela 1: Kemijska sestava preiskovanega duktilnega litega železa

C	Si	Mn	Cu	Cr	Ni	Ti	Al	Mg	P	S	Fe
3.21	2.58	0.23	0.83	0.07	0.05	0.03	0.01	0.04	0.017	0.008	bal.

bution over the rectangular beam spot (called a flat-top beam) is especially suited for the surface-alloying process with direct injection of alloying powder into the molten pool. In the above-mentioned surface-alloying process, the flat-top beam of HPDDL and the powder shape (the powder spot size) match the laser-beam spot result in reducing the heat input and providing a better control of the molten-pool solidification.[12,13]

The present study investigated an in-situ formation of TiC particles during laser surface alloying of DCI with direct injection of titanium powder into the molten pool, using a high-power direct-diode laser (HPDDL) with a rectangular laser beam spot and a uniform distribution of the laser power (the flat-top beam). This study was specifically concerned with establishing the effect of processing parameters on the precipitation morphology of TiC particles and its distribution throughout the iron matrix.

2 EXPERIMENTAL PROCEDURE

The substrate material used in this investigation was a ductile cast iron (DCI) with its chemical composition shown in **Table 1**. Microstructurally, the DCI consisted of graphite spheres with the average diameter of 35 µm in a pearlite matrix. The substrate specimens, in the form of 10-mm discs with a diameter of 50 mm, were ground to a surface finish of 0.5 µm R_a and cleaned with acetone prior to the alloying process. A commercially available titanium powder (99.6 % purity) having a particle size range of 45–75 µm was used as the alloying material.

The laser surface alloying (LSA) was carried out using a high-power direct-diode laser (HPDDL) Rofin-Sinar DL020 with the maximum output power of 2.0 kW. The rectangular HPDDL beam spot with a size of 1.8 × 6.8 mm and a focal length of 82 mm was focused on the top surface of the substrate and the long beam axis was set transversely to the traverse direction (6.8 mm wide). The titanium powder was injected into the molten pool using an off-axis powder injection nozzle. The powder feed-rate accuracy of the used feeder was within 1 %. The molten pool was protected by a shielding gas – argon – at a flow rate of 10 L/min. The cylindrical shielding-gas nozzle with a diameter of 20 mm was set coaxially with the powder feeding nozzle.

The investigation of the LSA process was performed based on the amount of titanium powder (the powder feed rate) provided per unit length of a single-pass alloy bead (SAB) in a range of 0.0010–0.0050 g/mm. To study the impact of the laser-power level and the traverse speed on the SAB geometry, microstructure and hardness, the experiments were conducted at three laser-power levels, 1000 W, 1200 W and 1400 W, and different traverse speeds, ranging from 0.1 m/min to 0.25 m/min. The surface-alloyed layers (SALs) were produced with the multi-pass overlapping alloying with an overlap ratio of 40 %. The experiments were performed without preheating the substrate.

Fluorescent dry penetrant testing was used to detect cracks of the SABs and SALs. The structure and morphology of the SALs were investigated with scanning electron microscopy (SEM) and energy-dispersive spectroscopy (EDS). The volume fraction of TiC was measured using a Nikon NIS-Elements quantitative image analysis system. The measurements were conducted on cross-sections from under the surface and in the middle areas of the SALs, over a total area of 10 mm^2 for each SAL. Geometrical parameters of the SABs were measured using an optical microscope and the Image Analyzer software. The cross-sectional microhardness distribution of the SALs was measured by means of a Wilson Wolpert 401 MVD Vickers hardness tester at a load of 200 g for a dwell time of 10 s. The X-ray diffraction analysis of the as-received DCI and the SALs was conducted using a PANalytical X'Pert PRO MPD X-ray diffractometer equipped with an X'Celerator detector and a Co-K_α (λ = 0.179 nm) source. The X-ray tube was operated at 40 kV and 30 mA.

Erosion-resistance tests of the as-received DCI and SALs were performed at impact angles of 30° and 90° in accordance with standard ASTM G76-95. Angular alumina powder (Al_2O_3) with the average particle size of 50 µm was used as the abrasive material. The impact velocity of the abrasive particles was kept in a range of 30±2 m/s. The abrasive-particle flow rate and test period were 2.0±0.5 g/min and 10 min, respectively. After the erosive wear tests, the mass loss of the specimens was measured with an accuracy of 0.01 mg.

3 RESULTS AND DISCUSSION

Cross-sectional macrographs of the single-pass alloyed beads (SABs) produced at a traverse speed of 0.2 m/min, a powder feed rate of 0.0016 g/mm and two levels of laser power are presented in **Figure 1.** Fusion-zone cross-sectional shapes indicate that, during the investigated LSA process, the surface-tension temperature coefficient on the molten-pool surface was positive. In this case, the surface tension is highest at the center of the molten pool, producing an inward fluid flow along the surface of the molten pool.[14] As a result, the SABs have a hemispherical shape in their cross-sections. Fur-

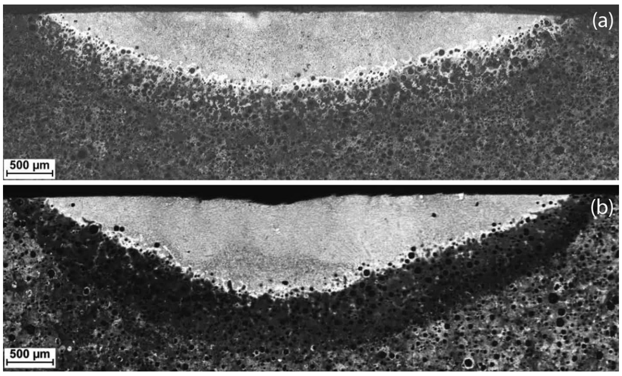

Figure 1: Macrographs of SABs produced at a traverse speed of 0.2 m/min, powder feed rate of 0.0016 g/mm and laser-power levels of: a) 1000 W, b) 1200 W

Slika 1: Makroposnetek SAB-ov, nastalih pri prečni hitrosti 0,2 m/min, hitrosti dodajanja prahu 0,0016 g/mm in pri moči laserja: a) 1000 W, b) 1200 W

thermore, an increase in the laser-power level, leading to a higher fluid-flow velocity in the molten pool driven by the surface-tension gradient, results in a concave bead profile and deeper fusion at the center. Typical dimensions of a SAB were a width of approx. 5.5 mm and a depth of fusion in a range of 0.7–1.2 mm. The fluid-flow velocity and its pattern are also the major factors, which determine the transfer of the alloying material in the molten pool and thus directly affect the TiC distribution in the alloyed layers.

Figure 2 presents the EDS line-scan analysis made at the cross-section of a SAB produced at a laser power of 1400 W, traverse speed of 0.25 m/min and powder feed rate of 0.0042 g/mm. The composition profiles, taken at the mid-depth of the bead along the line parallel to the bead surface (**Figure 2a**), indicated a slight titanium (Ti) enrichment in the centre of the alloyed bead, whereas the depth profile revealed an almost homogeneous distribution of Ti (**Figure 2b**). It follows that this fluid-flow pattern transfers the alloying elements quite efficiently throughout the fusion zone, leading only to a slightly

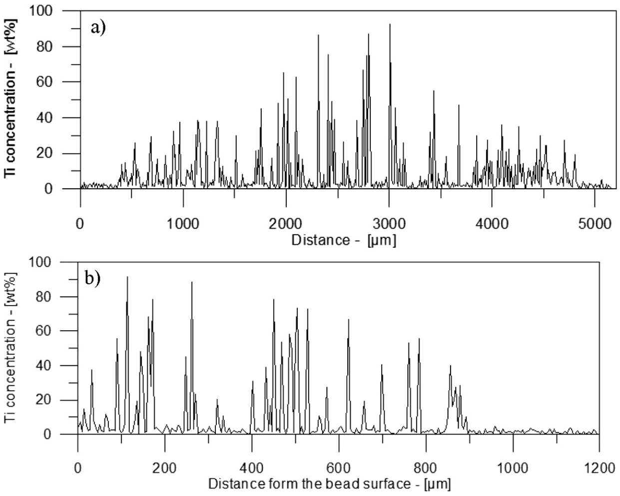

Figure 2: EDS line-scan analysis of the cross-section of a SAB produced at a laser power of 1400 W, traverse speed of 0.25 m/min and powder feed rate of 0.0042 g/mm: a) profile taken at the mid-depth of the bead along the line parallel to the bead surface, b) depth profile in the centre of the bead

Slika 2: EDS-linijska analiza na preseku SAB nastalem pri laserju moči 1400 W, prečni hitrosti 0,25 m/min in hitrosti dodajanja prahu 0,0042 g/mm: a) profil, posnet na srednji globini kopeli, vzdolž linije vzporedne s površino kopeli, b) profil v globino na sredini kopeli

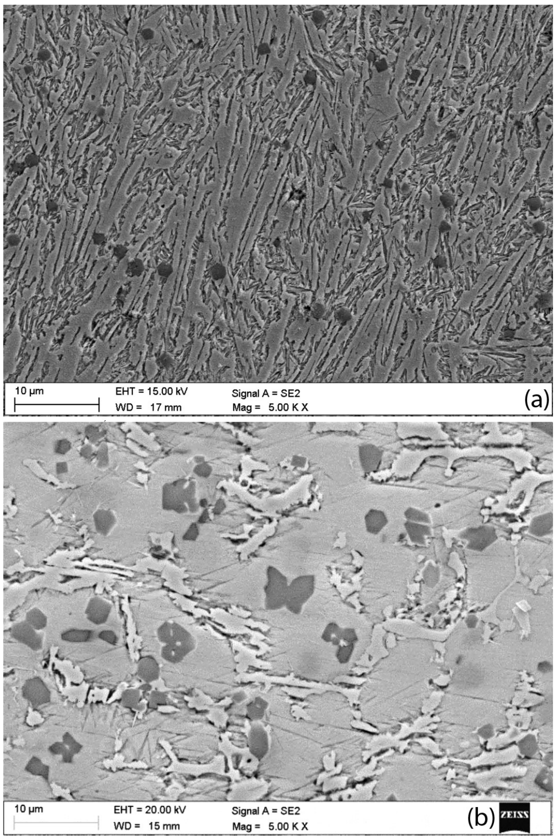

Figure: 3: SEM micrographs taken at the mid-sections of the SALs produced at a laser power of 1400 W, traverse speed of 0.15 m/min and powder feed rates of: a) 0.0010 g/mm, b) 0.0046 g/mm

Slika 3: SEM-posnetek iz sredine preseka SAL, nastalega pri moči laserja 1400 W, prečni hitrosti 0,15 m/min in hitrosti dodajanja prahu: a) 0,0010 g/mm, b) 0,0046 g/mm

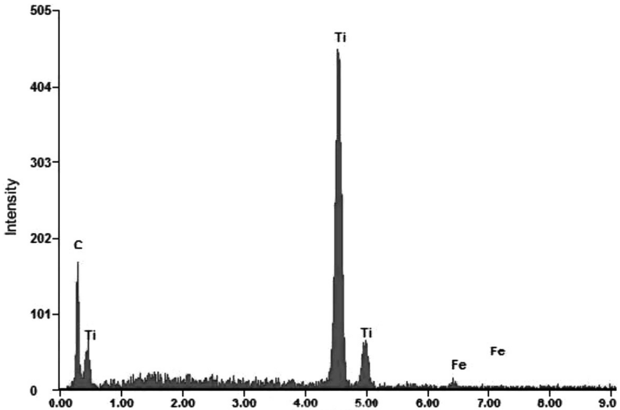

Figure 4: Typical EDS spectrum of a TiC particle

Slika 4: Značilen EDS-spekter delcev TiC

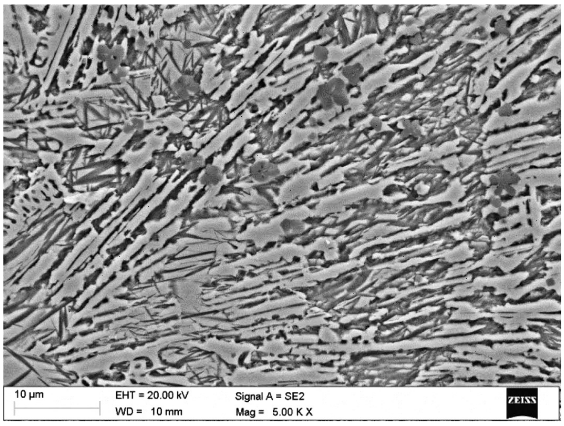

Figure 5: SEM micrograph of the fusion boundary area of a SAL produced at a laser power of 1400 W, traverse speed of 0.15 m/min and powder feed rate of 0.0046 g/mm

Slika 5: SEM-posnetek meje zlivanja področja SAL, nastalega pri laserju moči 1400 W, prečni hitrosti 0,15 m/min in hitrosti dodajanja prahu 0,0046 g/mm

higher fraction of the TiC precipitation in the central area of the alloyed bead.

Generally, the laser-power level determines the maximum amount of titanium powder that can be introduced to a SAB, thus the concentration of titanium in the molten pool and, in consequence, the morphology and fraction of TiC particles. In the cases of laser-power levels of 1000 and 1400 W, the maximum powder feed rate, which allows the production of SABs with no internal defects, such as porosity or microvoids, was 0.0016 and 0.0046 g/mm, respectively.

Figure 3 shows SEM micrographs of the surface alloyed layers (SALs) produced at powder feed rates of 0.0010 and 0.0046 g/mm. Based on the EDS analysis, the approximate concentration of Ti in these SALs was estimated to be 3 % and 7 % of the mass fractions, respectively. In turn, a quantitative analysis of the micrographs of the above-mentioned SALs indicated that the volume fraction of the TiC particles was approx. 4 % and 12 %, respectively.

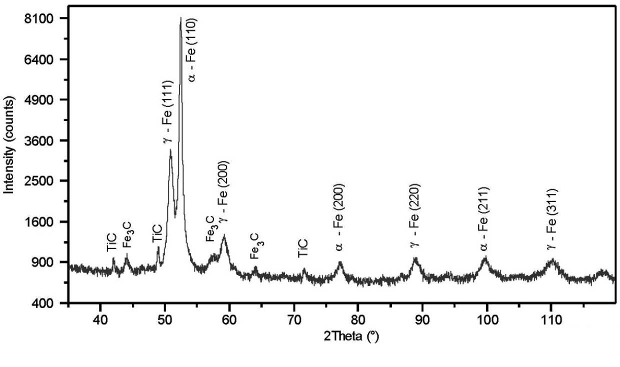

Figure: 6: XRD pattern of a SAL produced at a laser power of 1400 W, traverse speed of 0.15 m/min and powder feed rate of 0.0046 g/mm

Slika 6: Rentgenogram SAL, nastalega pri laserju moči 1400 W, prečni hitrosti 0,15 m/min in hitrosti dodajanja prahu 0,0046 g/min

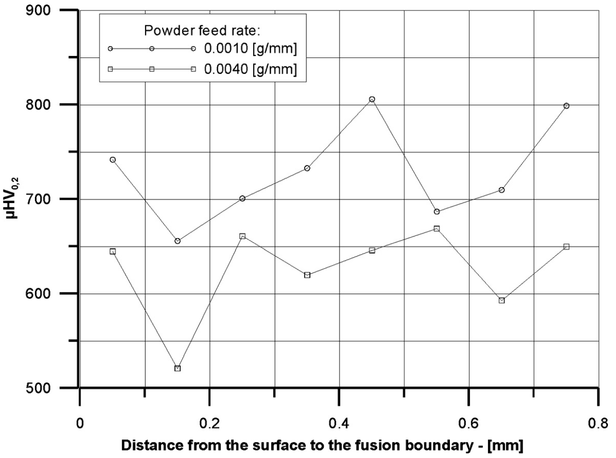

Figure 7: Microhardness distribution on the cross-sections of the SALs produced at a laser power of 1400 W, traverse speed of 0.2 m/min and different powder feed rates

Slika 7: Razporeditev mikrotrdote na preseku SAL, nastalega pri moči laserja 1400 W, prečni hitrosti 0,2 m/min in pri različni hitrosti dodajanja prahu

Figure 4 presents a typical EDS spectrum of the TiC particles (dark grey particles). As can be seen in **Figure 3**, the concentration of Ti strongly affects the shape and size of TiC particles. With an increasing Ti concentration, the morphology of TiC changes form cubic (>2 µm in size) to dendritic (up to 10 µm in size). Furthermore, the size of the TiC particles varies from the fusion boundary to the surface of a SAL, due to the changes in the local solidification conditions. The smaller TiC particles observed in the fusion boundary area (**Figure 5**) result primarily from the highest cooling rate; however, as indicated by the EDS line-scan analysis (**Figure 2b**), they can also be attributed to a lower concentration of Ti in this area.

The presence of TiC particles in the SALs was confirmed with the X-ray diffraction analysis (**Figure 6**). The X-ray diffraction pattern of a SAL, containing the highest volume fraction of TiC, indicated that martensite is the dominant phase. Apart from martensite, austenite and cementite were also detected. Furthermore, a metallographic examination and X-ray analysis revealed that an increasing titanium concentration in the SALs increases both the volume fractions of TiC and austenite, leading simultaneously to a lower fraction of cementite. All the SALs were free of porosity and microcracks.

The results of fluorescent dry penetrant testing showed that the SABs were free of cracks; however, transverse cracks were revealed in all the SALs. The cracks propagate mainly perpendicularly to the fusion boundary and do not affect the integrity of the SALs.

Figure 7 shows the microhardness distribution on the cross-sections of the SALs produced at a laser power of 1400 W, traverse speed of 0.2 m/min and different powder feed rates. As can be seen, the increase in the powder feed rate slightly reduced the hardness of the SAL, which is connected with the above-mentioned change in the volume fractions of austenite and cementite.

The solid-particle erosion-test results showed that the HPDD laser surface alloying of DCI, involving an in-situ synthesis of TiC, provides a significant improvement in the erosion resistance of the investigated DCI for both 30° and 90° impact angles. Erosion values of the SALs at an impact angle of 90° were approx. 40 % lower than those of the as-received DCI. In turn, for the impact angle of 30°, the SALs exhibited a three-time higher erosion resistance than for the as-received DCI. A detailed analysis of the erosion-degradation mechanism of the investigated in-situ composite layers is still in progress.

4 CONCLUSIONS

The HPDD laser surface alloying of DCI with direct injection of the titanium powder into the molten pool enables us to produce in-situ TiC-reinforced surface alloying layers with quite a uniform distribution of TiC throughout the matrix and the TiC volume fraction of up to 12 %. The morphology and fraction of TiC particles depend directly on the amount of the titanium powder introduced into the molten pool, which, in turn, is strongly affected by the laser-power level. With an increasing titanium (Ti) concentration in the molten pool, the morphology of the TiC particles changes form cubic (> 2 μm in size) to dendritic (up to 10 μm in size). Moreover, the increase in the Ti concentration increases the volume fraction of both TiC and austenite and, simultaneously, results in a lower fraction of cementite. The SALs exhibited a noticeable increase in the erosion resistance in comparison to the as-received DCI, especially at steep angles.

5 REFERENCES

[1] R. Elliott, Cast Iron Technology, Butterworth-Heinemann, 1988

[2] R. Burdzik, Ł. Konieczny, Z. Stanik, P. Folega, A. Smalcerz, A. Lisiecki, Analysis of impact of chosen parameters on the wear of camshaft, Archives of Metallurgy and Materials, 59 (**2014**) 3, 957–963, doi:10.2478/amm-2014-0161

[3] C. H. Chen, C. J. Altstetter, J. M. Rigsbee, Laser processing of cast iron for enhanced erosion resistance, Metallurgical Transactions A, 15A (**1984**), 719–728

[4] J. H. Abbud, Microstructure and erosion resistance enhancement of nodular cast iron modified by tungsten inert gas, Materials and Design, 35 (**2012**), 677–684, doi:10.1016/j.matdes.2011.09.029

[5] K. F. Alabeedi, J. H. Abboud, K. Y. Bnounis, Microstructure and erosion resistance enhancement of nodular cast iron by laser melting, Wear, 266 (**2009**), 925–933, doi:10.1016/j.wear.2008.12.015

[6] A. Kurc-Lisiecka, W. Ozgowicz, W. Ratuszek, J. Kowalska, Analysis of Deformation Texture in AISI 304 Steel Sheets, Solid State Phenomena, 203–204 (**2013**), 105–110, doi:10.4028/www.scientific.net/SSP.203-204.105

[7] M. Staszuk, L. A. Dobrzanski, T. Tanski, W. Kwasny, M. Musztyfaga-Staszuk, The effect of PVD and CVD coating structures on the durability of sintered cutting edges, Archives of Metallurgy and Materials, 59 (**2014**), 269–274, doi:10.2478/amm-2014-0044

[8] H. I. Park, K. Nakata, S. Tomida, In situ formation of TiC particles composite layer on cast iron by laser alloying of thermal sprayed titanium coating, Journal of Materials Science, 35 (**2000**) 747–755, doi:10.1023/A:1004717603612

[9] K. Das, T. K. Bandyopadhyay, S. Das, A Review on the various synthesis routes of TiC reinforced ferrous based composites, Journal of Material Science, 37 (**2002**), 3881–3892, doi:10.1023/A:1019699205003

[10] A. Singh, N. B. Dahotre, Phase evolution during laser in-situ carbide coating, Metallurgical and Materials Transactions A, 36A (**2005**), 797–803, doi:10.1007/s11661-005-1010-6

[11] A. Lisiecki, Welding of thermomechanically rolled fine-grain steel by different types of lasers, Archives of Metallurgy and Materials, 59 (**2014**) 4, 1625–1631, doi:10.2478/amm-2014-027

[12] D. M. Janicki, High power diode laser cladding of wear resistant metal matrix composite coatings, Solid State Phenomena, 199 (**2012**), 587–594, doi:10.4028/www.scientific.net/SSP.199.587

[13] A. Lisiecki, Titanium matrix composite Ti/TiN produced by diode laser gas nitriding, Metals, 5 (**2015**), 54–69, doi:10.3390/met5010054

[14] C. R. Heiple, J. R. Rop, R. T. Stanger, J. Aden, Surface active element effect on the shape of GTA, Laser and electron beam welds, Welding Journal, 62 (**1983**), 72–77

UDK 67.017:621.793/.795:669.715
Professional article/Strokovni članek

ISSN 1580-2949
MTAEC9, 51(2)323(2017)

MECHANICAL PROPERTIES OF PLASMA-SPRAYED LAYERS OF ALUMINIUM AND ALUMINIUM ALLOY ON AZ 91

MEHANSKE LASTNOSTI S PLAZMO NANEŠENIH PLASTI ALUMINIJA IN ALUMINIJEVE ZLITINE NA AZ 91

Tomáš František Kubatík, Pavel Ctibor, Radek Mušálek, Marek Janata
Institute of Plasma Physics CAS, v.v.i., Za Slovankou 1782/3, 182 00 Prague, Czech Republic
kubatik@ipp.cas.cz

Prejem rokopisa – received: 2015-10-29; sprejem za objavo – accepted for publication: 2016-02-09

doi:10.17222/mit.2015.326

Magnesium alloys are promising materials thanks to their high specific strength and stiffness. However, their wide application is discouraged by their low resistance to wear and very low resistance to corrosion. Plasma-spraying technology makes it possible to prepare protective metal and non-metal coatings. In this work, 450 μm thick and 490 μm thick plasma-spray coatings of commercially pure (CP) aluminium and aluminium alloy AlCr6Fe2 were prepared on magnesium alloy AZ91. The adhesion strength of plasma-sprayed aluminium was about 19 MPa, while the aluminium alloy showed an adhesion strength of about 12 MPa. Plasma-sprayed coatings improved the wear resistance of the AZ91 surface up to four times.

Keywords: plasma spraying of aluminum, adhesion of coating, wear, magnesium alloy AZ91

Magnezijeve zlitine so obetajoč material, zahvaljujoč njihovi veliki specifični trdnosti in togosti. Vendar pa njihovo široko uporabo zavira majhna odpornost na obrabo in zelo slaba korozijska odpornost. Tehnologija plazemskega nabrizgavanja omogoča izdelavo zaščitnih kovinskih in nekovinskih nanosov. V tem delu so bili pripravljeni plazemsko nabrizgani, 450 μm in 490 μm debeli nanosi komercialno čistega (CP) aluminija in aluminijeve zlitine AlCr6Fe2 na magnezijevi zlitini AZ91. Adhezijska trdnost plazemsko nabrizganega aluminija je bila okrog 19 MPa, aluminijeva zlitina je pokazala adhezijsko trdnost okrog 12 MPa. Plazemsko nabrizgani nanosi so izboljšali obrabno odpornost zlitine AZ91 za 4×.

Ključne besede: plazemsko nabrizgavanje aluminija, adhezija nanosa, obraba, magnezijeva zlitina AZ91

1 INTRODUCTION

Magnesium and its alloys have an excellent ratio of density and strength; they are suitable for lightweight construction in the automotive and aerospace industries, and also for bio-medical applications due to their high specific strength and stiffness.[1,2] Magnesium and magnesium alloys are very susceptible to galvanic corrosion, which can result in severe pitting, especially in a wet and salty environment. This disadvantage can be utilized in biomedicine for endoprosthetics, which may dissolve at a controlled speed.[3] Alloying of magnesium with aluminium or manganese can improve not only its mechanical properties but also the corrosion resistance. Aluminium in the contents of 4–9 % by weight can rapidly improve the corrosion resistance thanks to the formation of the intermetallic phase $Mg_{17}Al_{12}$, which precipitates along the grain boundaries and serves as a corrosion barrier.[4] Magnesium and its alloys can be also protected by a deposition of surface-protective coatings. There are several technologies for producing protective coatings, metal and non-metal ones (in particular the technology of plasma spraying) making it possible to prepare anticorrosion coatings, improving the surface abrasive resistance as well as the hardness. In references[5–8] the authors devote their studies to the plasma-sprayed coatings of aluminium, NiAl5 and Al_2O_3 on the magnesium alloy AZ91.[8] Plasma spraying of pure Al on the AZ 91 alloy provided coating adhesion strengths of 6–12 MPa, and when spraying NiAl5 on the AZ91 alloy, the adhesion strengths of 17–25 MPa were reported.[8] This work deals with the study of mechanical properties, the adhesion strength and the resistance to wear of the coatings made of commercially pure (CP) aluminium and an alloy thermally stable up to 300 °C, i.e., AlCr6Fe2[9] on the magnesium alloy AZ 91 using a hybrid water-stabilized plasma torch WSP-H 500© which potentially provides a rather high throughput for spraying large areas.

2 EXPERIMENTAL PART

Two powders were used as a feedstock for plasma spraying using a hybrid water-stabilized torch WSP-H 500© (Institute of Plasma Physics CAS, v.v.i, CZ) operated at the power of 160 kW, namely, a commercially pure (CP) aluminium powder with grain sizes from 45 μm to 90 μm and aluminium alloy AlCr6Fe2 (ICT-Prague, CZ) with grain sizes from 80 μm to 180 μm. The aluminium alloy powder was prepared with the atomization of the melted aluminium alloy AlCr6Fe2 using compressed Ar and the subsequent sieving to achieve the proper fraction. During plasma spraying, the powder in the quantity of 110 g/min was injected with compressed air into the plasma jet, and the spraying distance was 330 mm. The substrates of (70 × 20 × 5) mm were manufactured from magnesium alloy AZ91. Prior to plasma spraying, the substrates were grit blasted with alumina grit and degreased in acetone. The original feedstock powder as well as both the free surface and the metallographic cross-sections of the sprayed layers were observed with a scanning electron microscope EVO MA 15 (Carl Zeiss SMT, D). The cylindrical specimens (the substrate of magnesium alloy AZ91) with a diameter of 25 mm, a height of 50 mm and with an impassable tapped screw M10 were prepared for the evaluation of the coating adhesion strength, which was conducted in accordance with the ASTM C 633 standard. The coating deposition was carried out on the blasted cylinder ends with a roughness of approximately Ra 9.5 μm, pre-heated to 180 °C and with a target thicknesses of approximately 500 μm. This thickness guaranteed that the coating-adhesion test was not influenced by the glue penetrating into the coating microstructure.[10] The counterpart, i.e., a steel cylinder of the same dimensions, was glued with the heat-hardenable one-component epoxy adhesive E1100S (Gupex, UK) on the plasma-coated surface. After the heat hardening of the adhesive, tension tests were conducted using an Instron 1362 (Instron, UK) electro-mechanical tensile testing machine. The presented adhesion-strength result is the average of six measurements.

Table 1: Average values of the adhesion strength for CP-Al and aluminium alloy

Tabela 1: Povprečna vrednost adhezijske trdnosti za CP – Al in aluminijevo zlitino

Sample	Adhesion strength
CP-aluminium coating	18.94 ± 1.29 MPa
Aluminium-alloy coating	12.15 ± 1.22 MPa

In order to obtain a compact reference sample for abrasive-wear testing, the feedstock powders, used for plasma spraying, were sintered by means of the spark-plasma-sintering (SPS) technique.[11] The sintering began with evacuation of the chamber. Afterwards, the sample was pre-loaded to 20 MPa, followed by heating with a rate of 100 °C/min. After reaching the desired sintering temperature of 550 °C, the sample was loaded with the final compression pressure of 80 MPa. The dwell time at this temperature and pressure was 5 min. After the dwell time, the DC pulse source was turned off and the sample was cooled down to the room temperature by free cooling. After aeration of the chamber, the sample was removed from the graphite tool.

The wear resistance of the samples was evaluated by the slurry abrasion response (SAR) test following the ASTM standard.[12] The test was carried out in four increments (runs) with the mass loss being measured at the end of each run. The applied force was 22 N per specimen. In the case of the studied materials, the runs were shortened to one quarter of the standard duration because of the relatively low thickness and resistance of the coatings. After each run, the specimens were ultrasonically cleaned, dried and weighted. The slurry consisted of 150 g of organic oil (the water recommended in the ASTM standard had to be avoided because of its reactivity with the studied materials) and 150 g of alumina powder with a size of 40–50 μm. The accuracy of the measurement is typically ± 5 %.[12]

Microhardness was measured using a Hanemann microhardness head (Zeiss, Germany) mounted on an optical microscope with a fixed load of 0.5 N and a Vickers indenter. Twenty indentations made at randomly selected spots on the cross-section of each sample were analyzed.

3 RESULTS AND DISCUSSION

3.1 Microstructure

Figure 1 depicts the microstructures of the used powders: a) CP aluminium and b) aluminium alloy

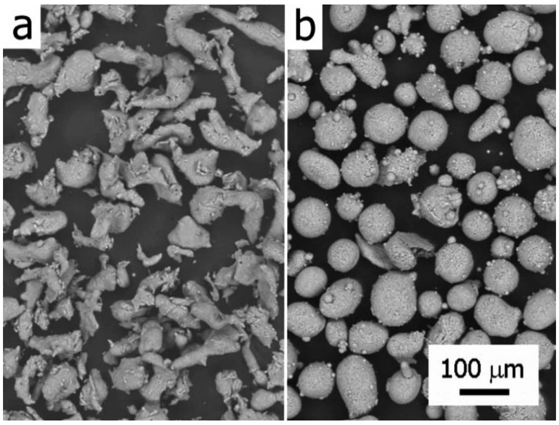

Figure 1: Feedstock powder: a) aluminium CP-Al, fraction 90 + 45 μm, b) aluminium alloy AlCr6Fe2, fraction 180 + 80 μm (SEM – BSE)

Slika 1: Izhodni prah: a) aluminij CP-Al – 90 + 45 μm frakcija, b) aluminijeva zlitina AlCr6Fe2, frakcija 180 + 80 μm (SEM – BSE)

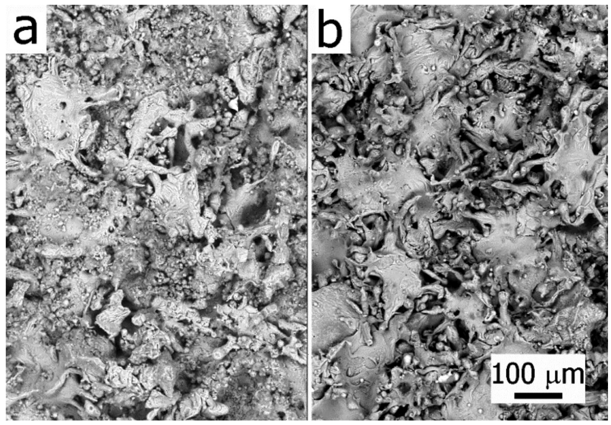

Figure 2: Free surface of the layer prepared with plasma spraying: a) aluminium powder CP-Al and b) aluminium alloy (SEM – BSE)

Slika 2: Prosta površina nanosa, izdelanega s plazemskim naprševanjem: a) aluminija v prahu CP-Al in b) aluminijeva zlitina (SEM – BSE)

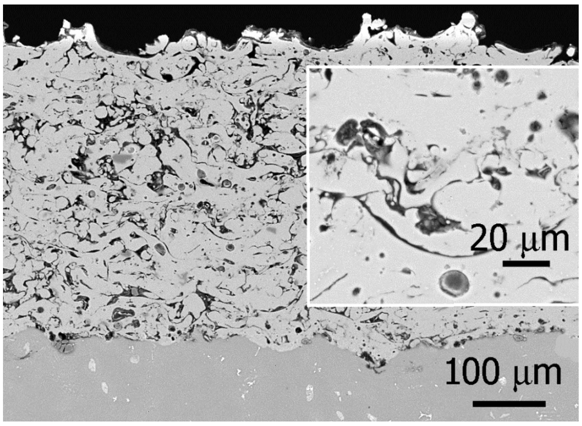

Figure 3: Microstructure of the cross-section of CP-Al sprayed on magnesium alloy AZ 91 (SEM – BSE)

Slika 3: Mikrostruktura prereza nabrizganega CP-Al na magnezijeve zlitine AZ91 (SEM – BSE)

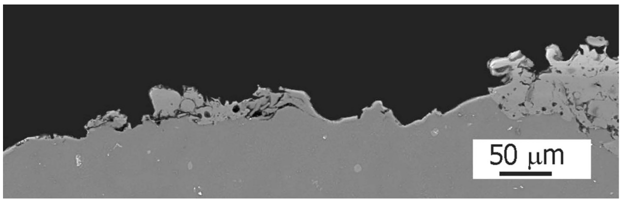

Figure 5: Residue of CP-Al coating on AZ 91 after the adhesion test (SEM – BSE)

Slika 5: Ostanki CP-Al nanosa na AZ91 po preizkusu adhezije (SEM-BSE)

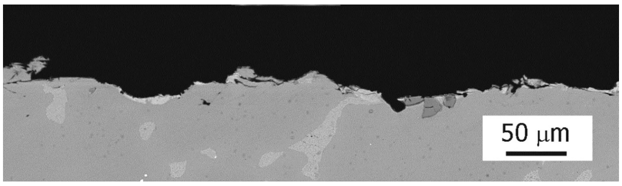

Figure 6: Residue of aluminium alloy coating on AZ 91 after the adhesion test (SEM – BSE)

Slika 6: Ostanki aluminijeve zlitine na AZ91 po preizkusu adhezije (SEM – BSE)

AlCr6Fe2. It can be seen that the used aluminium powder on **Figure 1a** was of an irregular shape, most often consisting of elongated straight or twisted particles. The aluminium alloy from **Figure 1b** consisted of regular spherical particles with the mean size of about 100 micrometers. It is also visible on **Figure 2a** that the surface of the sprayed coatings is mainly composed of irregular splats and small spherical particles. In the case of the aluminium alloy from **Figure 2b** the surface is dominantly composed of irregular splats.

Figure 3 shows the cross-sectional microstructure of the plasma coating of CP aluminium on magnesium alloy AZ 91. The microstructure is typical for plasma-sprayed metallic coating sprayed in an open-air atmosphere, containing splats, spherical particles and pores. The layer was prepared using plasma spraying with the average thickness of 448±31 µm. The plasma-sprayed layer of the aluminium alloy on magnesium alloy AZ-91 is shown in **Figure 4**. The layer contains large particles and splats because almost a double grain size of the powder was used. The prepared layer has an average thickness of 489±26 µm.

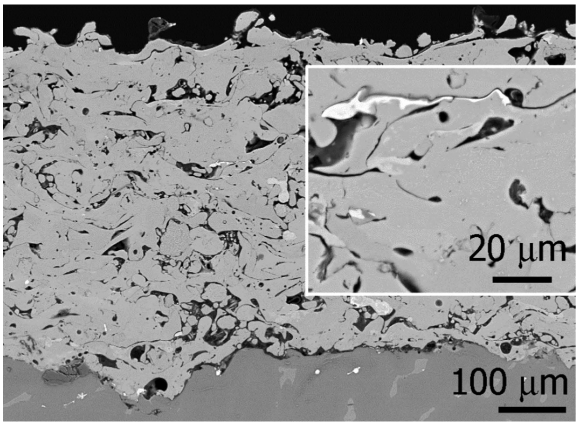

Figure 4: Microstructure of the cross-section of the aluminium alloy sprayed on magnesium alloy AZ 91 (SEM – BSE)

Slika 4: Mikrostruktura prereza aluminijeve zlitine nabrizgane na magnezijevo zlitino AZ91 (SEM – BSE)

3.2 Adhesion testing

The average value of the tensile adhesion strength of CP Al coating is 18.94±1.29 MPa, and the one of the aluminum alloy is 12.15±1.22 MPa. In the case of CP Al coatings, all samples were fractured near the coating-substrate (**Figure 5**) interface in combined cohesion/adhesion failure. In the case of Al alloy coating on AZ91, the whole layer was detached from the surface at the substrate-coating interface in all six measured samples (adhesion failure of Al alloy coating, cross-section, **Figure 6**). The values of adhesion strength for CP aluminium coating ranging from 17 to 20.5 MPa are significantly higher than in the case of the strength of Al

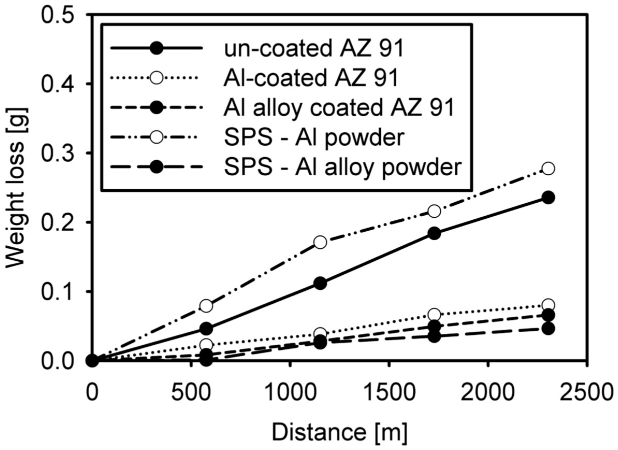

Figure 7: SAR test result, weight-loss dependence on the travel distance

Slika 7: Rezultati SAR-preizkusa, odvisnost izgube teže od dolžine poti alloy coatings, and also higher than published by Maria Parco et al.,[8] who published values ranged from 6 MPa to 12 MPa for the substrate without pre-heating, and adhesion strength of 15 MPa for the substrate preheated to 160 °C and with a blasted surface.

The results of the wear-resistance measurement, namely, the dependence of mass losses for path lengths (576, 1152, 1728 and 2304) m, are plotted in the graph in **Figure 7**. The results of the wear-resistance measurement are in line with the expectations, i.e., the SPS-sintered pure aluminium showed the highest wear loss followed by the uncoated magnesium alloy AZ 91. It is clearly visible in the graph that both plasma coatings have an improved wear resistance of the substrate material (AZ 91). The best results are achieved when aluminium alloy is used as a coating, and the wear values within the distance of 1152 m are similar to those of the sintered aluminium alloy. The sintered aluminium alloy, followed by the aluminium-alloy coating, are the most resistant to wear for the whole path. The measured roughness is listed in **Table 2**. The roughness is rather high for the as-sprayed coatings but after 576 m of the wear test, it is greatly reduced and not changed significantly during the further wear testing. The compact sintered aluminium alloy is tougher and more resistant to abrasion and there is a similar effect of the plasma spraying technology when used for improving the abrasion resistance.

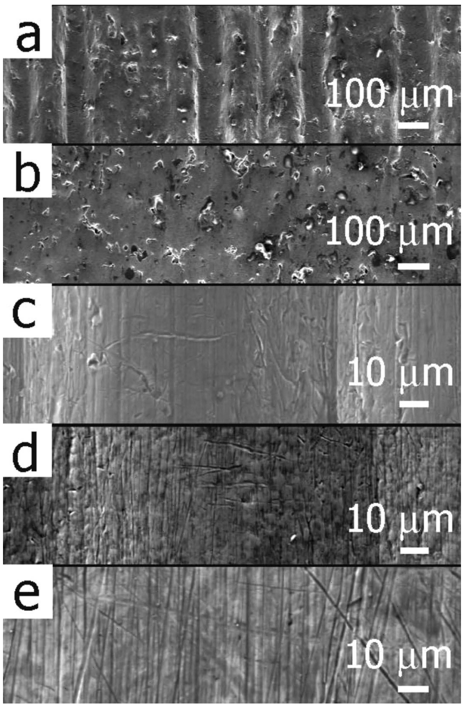

Figure 8: Free surfaces of the samples after the measurement of abrasion resistance: a) plasma-sprayed CP-Al, b) plasma-sprayed aluminium alloy, c) SPS-sintered CP-Al, d) SPS-sintered aluminium alloy, e) uncoated AZ-91 (SEM – SE)

Slika 8: Prosta površina vzorcev po merjenju odpornosti na abrazijo: a) plazemsko nabrizgan CP-Al, b) plazemsko nabrizgana aluminijeva zlitina, c) SPS sintran CP-al, d9 SPS sintrana aluminijeva zlitina, e) AZ-91 brez nanosa (SEM – SE)

Table 2: Roughness R_a (µm) of the free surfaces of test samples before and during the wear test

Tabela 2: Hrapavost R_a (µm) treh prostih površin na preizkušancih, pred in po preizkusu obrabe

Sample	0	576 m	1728 m	2304 m
uncoated AZ-91	2.3	1.9	2.0	2.4
CP Al-coated AZ-91	14.8	5.9	5.0	7.0
Al-alloy coated AZ-91	20.2	10.6	9.0	8.2

Table 3: Microhardness of plasma-sprayed layers

Tabela 3: Mikrotrdota plazemsko nabrizganih plasti

Sample	Microhardness (HVm)
CP Al coating	65±11
Al-alloy coating	223±48
Substrate	120±42

Plasma-sprayed CP-Al, **Figure 8a**, has the surface textured in the direction of the movement of the test (deep vertical grooves). The plasma-sprayed aluminium alloy, **Figure 8b**, has, thanks to its higher hardness (**Table 3**), very homogeneous wear damage concentrated only in small areas. The highest weight loss during the wear test was shown on sintered pure aluminium and the uncoated magnesium alloy AZ 91. Their surfaces are displayed in **Figures 8c** and **8e**. The surfaces are scratched by the abrasive medium but the damage is very homogeneous. The appearance of the surface of the SPS-sintered aluminum alloy, **Figure 8d**, is similar.

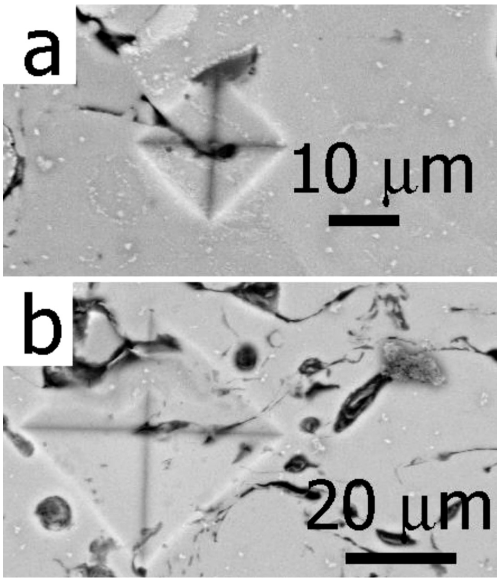

Figure 9: Details of the microstructures of plasma-sprayed layers with indenter imprint after the measurement of microhardness (SEM – BSE): a) aluminium alloy, b) CP-aluminium

Slika 9: Detajl mikrostrukture s plazmo nabrizganega sloja, z odtiskom trdote po merjenju mikrotrdote (SEM – BSE): a) aluminijeva zlitina, b) CP-aluminium

3.3 Hardness

The hardness-measurement results are listed in **Table 3** for the plasma-sprayed layers and the substrate. The measured microhardness values are comparable with the microhardness of the Al coatings deposited with the cold-spray technique.[13] The average microhardness of the plasma-sprayed aluminium alloy (223 HVm) is nearly four times higher than that of the sprayed CP aluminium (65 HVm). In reference[9] dealing with the thermal stability of a similar alloy, a hardness of 160–195 HV is listed. **Figure 9** shows micrographs of the indents. In both cases, the coatings are very plastic, without any cracks (in the case of a small load) initiating from the indent corners and also without any distortion of the adjacent pores.

4 CONCLUSION

In this work, plasma-sprayed coatings of commercially pure (CP) aluminium and aluminium alloy AlCr6Fe2 were applied on the magnesium alloy AZ 91 by means of a hybrid water-stabilized torch WSP-H 500©. Layers with a thickness of 450 µm for CP aluminium and 490 µm for the aluminium alloy were prepared. Both obtained plasma-sprayed coatings are relatively inhomogeneous and porous. The micrographs (**Figures 3** and **4**) show incomplete metallurgical bonds between individual powder particles and molten droplets (splats), respectively. The prepared plasma coatings have a relatively good adhesion, microhardness and abrasion resistance in comparison with the relevant literature. Plasma coating of CP aluminium showed the average adhesion strength of 19 MPa, and the aluminium alloy showed an adhesive strength of 12 MPa. During the pull-off test, combined adhesive-cohesive fracture of the CP-aluminum coating occurred. In the case of the aluminium-alloy coating, the whole layer was pulled off, leading to the adhesion mode of failure. The results also clearly show that the abrasion resistance of the plasma-sprayed CP-aluminum coating is better than that of the sintered CP aluminum. In case of the aluminium alloy, the plasma-sprayed coating and the sintered material have a similar abrasion resistance.

Acknowledgements

This work was supported by the Czech Science Foundation through the project with number 14-31538P "Evaluation of bonding interface during and after plasma spraying of metallic materials on magnesium and magnesium alloy."

4 REFERENCES

[1] D. Votěch, V. Knotek, Magnesium alloys for hydrogen storage, Mater. Tehnol., 46 (**2012**) 3, 247–250

[2] E. Altuncu, H. Alanyali, The applicability of sol-gel oxide films and their characterisation on a magnesium alloy, Mater. Technol., 48 (**2014**) 2, 289–292

[3] J. Kubásek, I. Pospíšilová, D. Vojtěch, E. Jablonská, T. Ruml, Structural, mechanical and Cytotoxicity characterization of as-cast biodegradable Zn-xmg (x = 0.8– 8.3 %) alloys, Mater. Tehnol., 48 (**2014**) 5, 623–629

[4] M. Horynová, Fatigue Characteristics of AZ31 magnesium alloy after corrosion degradation, Master's thesis, Brno 2011, 95

[5] M. Qian, D. Li, S.B. Liu, S.L. Gong, Corrosion performance of laser-remelted Al–Si coating on magnesium alloy AZ91D, Corr. Sci., 52 (**2010**) 10, 3554–3560, doi.org/10.1016/j.corsci.2010.07.010

[6] E. Altuncu, S. Iric, F. Ustel, Wear-resistant intermetallic arc spray coatings, Mater. Tehnol., 46 (**2012**) 2, 181–183

[7] B. Zou, S. Tao, W. Huang, Z. S. Khan, X. Fan, L. Gu, Y. Wang, J. Xu, X. Cai, H. Ma, X. Cao, Synthesis and characterization of in situ TiC–TiB_2 composite coatings by reactive plasma spraying on a magnesium alloy, Appl. Surf. Sci., 264 (**2014**), 879–885, doi.org/10.1016/j.apsusc.2012.10.177

[8] M. Parco, L. Zhao, J. Zwick, K. Bobzin, E. Lugscheider, Investigation of particle flattening behaviour and bonding mechanisms of APS sprayed coatings on magnesium alloys, Surf. Coat. Technol., 201 (**2007**) 14, 6290–6296, doi.org/10.1016/j.surfcoat.2006.11.034

[9] B. Bártová, D. Vojtěch, J. Verner, A. Gemperle, V. Studnička, Structure and properties of rapidly solidified Al–Cr–Fe–Ti–Si powder alloys, J. Alloy Compd., 387 (**2005**) 1–2, 193–200

[10] R. Mušálek, M. Vilémová, J. Matějíček, V. Pejchal: Multiple-Approach Evaluation of WSP Coatings Adhesion/Cohesion Strength, Proc. from the Int. Thermal Spray Conference and Exposition, Houston, 2012, 746–751

[11] T. F. Kubatík, Z. Pala, P. Novák, Compacting the powder of Al-Cr-Mn alloy with SPS**,** Mater. Tehnol., 49 (**2015**) 1, 129–132

[12] US Standard ASTM G 75-95: Standard Test Method for Determination of Slurry Abrasivity (Miller number) and Slurry Abrasion Response of Materials (SAR number), ASTM International, West Conshohocken, PA, United States, 1995

[13] B.T. Sofyan, D. Satiti, E. Pereloma, Characteristics of Cold Spray Aluminium Coating on ZE41A-T5 Magnesium, AA7075 Aluminium, and 4130 Steel Substrates: Proc. Int. Conf. Materials and Metallurgical Tech., Surabaya, 2009, 99–103

UDK 621.78:66.017:669.14.018.298
Professional article/Strokovni članek

ISSN 1580-2949
MTAEC9, 51(2)329(2017)

HEAT TREATMENT OF RAILS

TOPLOTNA OBDELAVA TIRNIC

Milan Hnizdil, Petr Kotrbacek

Brno University of Technology, Faculty of Mechanical Engineering, Heat transfer and fluid flow laboratory,
Technicka 2896/2, 616 69, Brno, Czech Republic
hnizdil@fme.vutbr.cz

Prejem rokopisa – received: 2015-12-23; sprejem za objavo – accepted for publication: 2016-03-31

doi:10.17222/mit.2015.357

Heat treatment is increasingly used in the heavy industry. The main advantage of this method is the achievement of the required material and mechanical properties. Heat treatment allows for a manufacturing process, which can improve product performance by increasing the steel strength, hardness and other desirable characteristics. The microstructure, grain size and chemical composition of steel affect its overall mechanical behavior. Heat treatment is an efficient way to manipulate the properties of a steel product by controlling the cooling rate. It can be expressed using the heat-transfer coefficient (HTC). The controllability of the cooling process is very important. Mist and water nozzles may provide good controllability of the HTC. An experimental stand was designed and built. The stand consists of a movable trolley with a test sample, which moves under a spray at a given velocity. Sensors record the temperature history of the tested material. This experimental stand enables simulations of a variety of cooling regimes and evaluations of the final structures of tested samples. The same experimental stand is also used for designing cooling sections in order to determine the required heat-treatment procedures and the final structures. This paper describes a cooling-section design procedure for obtaining the required structure and mechanical properties of rails.

Keywords: heat transfer, heat treatment, cooling, heat-transfer coefficient, spray cooling

Uporaba toplotne obdelave se v težki industriji povečuje. Glavna prednost te metode je, da se doseže zahtevane mehanske lastnosti materiala. Toplotna obdelava omogoča postopke izdelave, ki lahko izboljšajo lastnosti proizvodov s tem, da povečajo trdnost jekla, trdoto in druge zaželjene značilnosti. Mikrostruktura, velikost zrn in kemijska sestava jekla vplivajo na mehanske lastnosti. Toplotna obdelava je učinkovita pot za vplivanje na lastnosti jeklenega proizvoda s kontroliranjem hitrosti ohlajanja. Lahko se jo izrazi z uporabo koeficienta prenosa toplote. Možnost kontrole postopka ohlajanja je zelo pomembna. Obvladanje procesa ohlajanja je zelo pomembno. Vodna para in vodne šobe omogočajo dobro kontrolo koeficienta prenosa toplote (angl. HTC). Načrtovano in postavljeno je bilo eksperimentalno stojalo. Stojalo sestoji iz vozička z vzorcem, ki se pomika pod šobe z dano hitrostjo. Senzorji beležijo temperaturno zgodovino vzorca. Eksperimentalno stojalo omogoča simulacijo različnih režimov ohlajanja in oceno končne mikrostrukture preizkušenega vzorca. Isto stojalo je uporabno tudi kot orodje pri načrtovanju hladilnih odsekov za določanje postopka toplotne obdelave in končne mikrostrukture. Članek opisuje postopek načrtovanja odseka za izvajanje hlajenja, za zagotavljanje željene mikrostrukture in mehanskih lastnosti železniških tirnic.

Ključne besede: prenos toplote, toplotna obdelava, ohlajanje, koeficient prenosa toplote, ohlajanje s pršenjem

1 INTRODUCTION

Heat treatment of rolled materials by hot rolling plants has become frequent. Alloying elements are typically used to improve material properties. Heat treatment is a different approach applied to achieve the required material properties using fewer alloys in the steel. Heat treatment enables the manufacture of modern steels with a higher ratio of yield strength and elongation. The controllability of the cooling process is the most important aspect for achieving the required mechanical properties. An appropriate cooling intensity and its duration are chosen with respect to the continuous cooling transformation diagram (CCT) for the selected material. Numerical simulation of the cooling follows. One task is to determine the boundary condition (HTC – heat transfer coefficient) for the simulation because various parameters such as nozzle type, spray distance, water impingement density, nozzle position, nozzle overlap, movement velocity and scales have significant influences on the cooling intensity.[1–3] Additionally, accurate thermo-physical material properties are needed for simulations.[4] The Heat Transfer and Fluid Flow Laboratory developed a methodology for predicting the temperature field of heat-treated rails. This methodology is described in this article.

2 DESIGN STRATEGY FOR THE COOLING SECTION

Three different types of experiments were done to predict the required cooling regime defined by the CCT diagram. A special hardening-capacity test bench (**Figure 1**) was developed to find the limits of a quenched rail. The test bench consists of a heater, a trolley with a tested sample, a water nozzle holder and a pneumatically driven deflector.

Each test starts with heating a rail-head sample to the initial temperature. This temperature is held for more than 10 min to attain the austenite structure of the entire body. The sample is protected with an inert atmosphere in the furnace to prevent the development of scales. Next, the sample is moved from the heater to a position

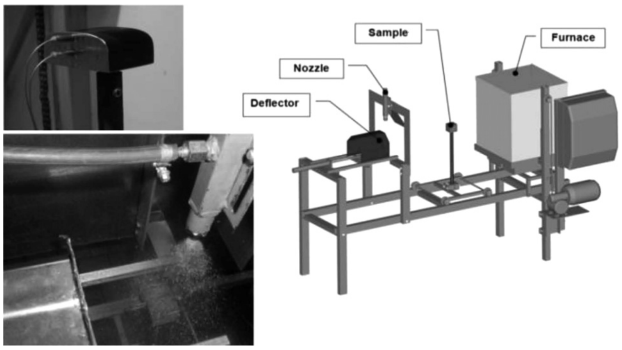

Figure 1: Hardening-capacity test bench
Slika 1: Preizkušanje zmogljivosti utrjevanja

under the nozzle. The pneumatically driven deflector, positioned between the nozzle and the sample, is moved and the water sprays the top of the rail head. Each sample is equipped with thermocouples under the surface to detect the temperature gradient in the material. The material hardness and its structure are observed. The hardness values of the original (base) material and the heat-treated material are compared because the heat-treatment process is dependent on the quality of the steel-making process (chemical composition, enclosures, casting speed, etc.).[5–8]

If these tests are sufficient, heat-transfer tests are then performed. A special testing bench called a linear stand (**Figure 2**) was developed by the Heat Transfer and Fluid Flow Laboratory. This bench is a six-meter long girder with a trolley which can move the tested rail sample, plate, etc., through the cooling section. A 25 mm thick, flat austenitic steel plate is used for the heat-transfer tests. It is embedded with four thermocouples positioned 0.5 mm under the sprayed surface. This plate is moved through the spray-cooling system (2 m long) in two directions, forward and backward.

The dependences of the heat-transfer coefficient on the surface temperature are evaluated for various cooling parameters (spray distance, type of nozzle, water impingement density, etc.). The obtained boundary conditions are used for simulations to predict the temperature field in the rail head. The shape of the rail also has a significant influence on the cooling intensity. Therefore, an authentically shaped austenitic steel sample is made and embedded with several thermocouples, positioned 2 mm under the rail surface. The length of this sample is around 300 mm. Simulations of the rail cooling are compared with the temperatures measured during the austenitic rail cooling. The boundary conditions obtained from the flat austenitic steel plate are adjusted and the model is verified with measurements. The last step is the verification including a full-scale, carbon-rail sample. A sample is fixed on the trolley (the linear stand) and moved through the cooling section. The measured and simulated temperatures are compared and the cooling model is verified. Finally, the hardness is measured again. This is the most important result that shows if the cooling regime works optimally.

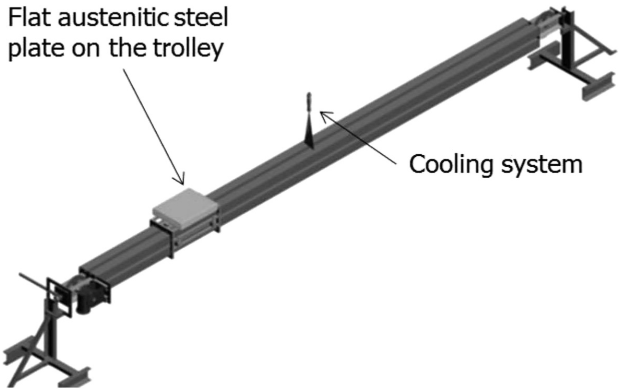

Figure 2: Linear-stand scheme
Slika 2: Shema linearnega stojala

3 RESULTS

The cooling strategy was described in Section 2. The experimental steps began with the study of CCT diagrams. Material R260 was chosen for the heat-treatment tests. The hardness-capacity tests were performed first to find the limit of the quenched material and to choose the appropriate nozzle size with respect to the required cooling regime. All the tested samples were embedded with thermocouples to verify the cooling regime. These samples were sawed after quenching and hardness was measured along the center line of the rail head (from the top of the surface down to the center – the red line). An example of the cooling regime (for a successful test) is shown in **Figure 3**.

The measured hardness for this sample was around 400 HV0.3 (**Figure 4**). The required fine pearlite structure was found using a microstructure analysis (**Figure 5**).

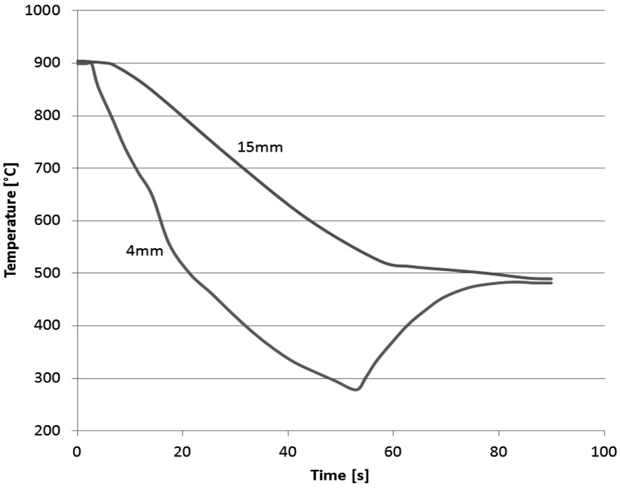

Figure 3: Temperature record for the rail head during a successful static-hardness-capacity test
Slika 3: Zapis temperature glave tirnice med uspešnim preizkusom zmogljivosti trdote

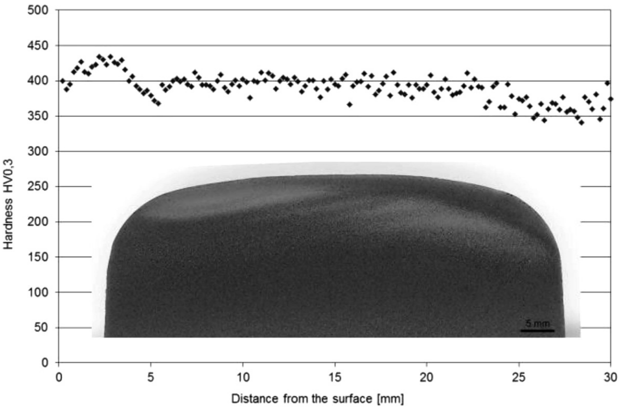

Figure 4: Measured hardness of the rail head after the static-hardness-capacity test
Slika 4: Izmerjena trdota v glavi tirnice med statičnim preizkusom trdote

An appropriate choice of the nozzle and the verification of the cooling regime using the CCT diagram were confirmed with a static-hardening-capacity test. The next step was to find the cooling parameters for the moving samples (transient boundary conditions). The linear stand was used for these tests. A 25 mm thick, flat austenitic steel plate was used and several parameters such as water pressure, spray distance, spray angle and movement velocity were tested. The boundary conditions obtained from the experiment were used to simulate the cooling regime for a real moving rail. A full-scale rail sample (material R260) was built and embedded with six thermocouples positioned 2 mm under the surface (**Figure 6**).

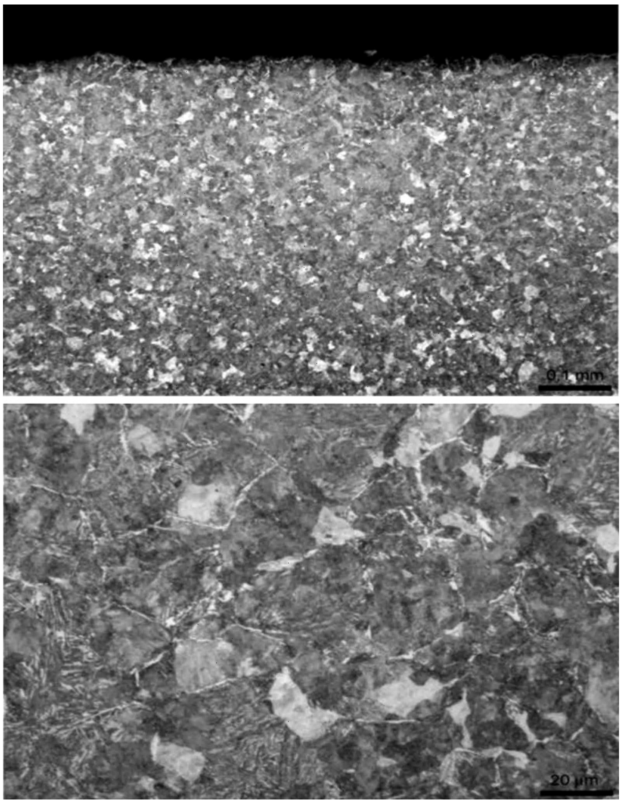

Figure 5: Microstructure – close to the sprayed surface – center of the rail-head surface
Slika 5: Mikrostruktura – blizu poškropljene površine – sredina površine glave tirnice

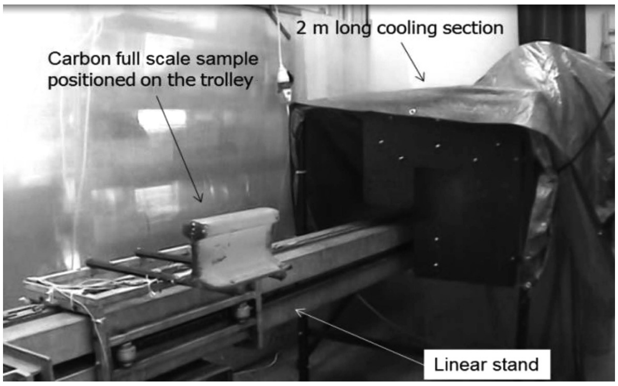

Figure 6: Full-scale carbon sample heated to the initial temperature before entering the cooling section
Slika 6: Realen vzorec ogret do začetne temperature pred vstopom v področje ohlajanja

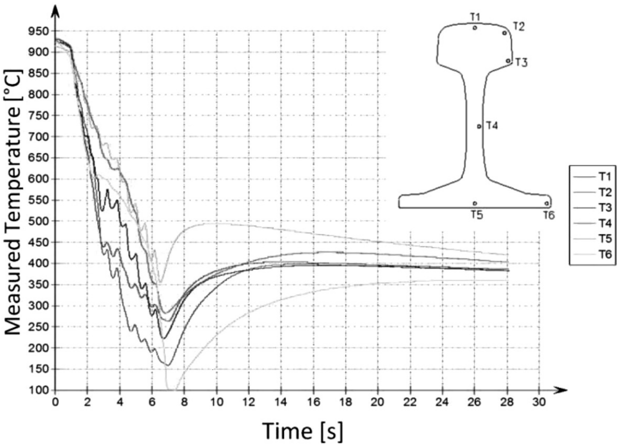

Figure 7: Temperature record for the heat-treated full-scale sample
Slika 7: Temperatura zabeležena na toplotno obdelanem realnem vzorcu

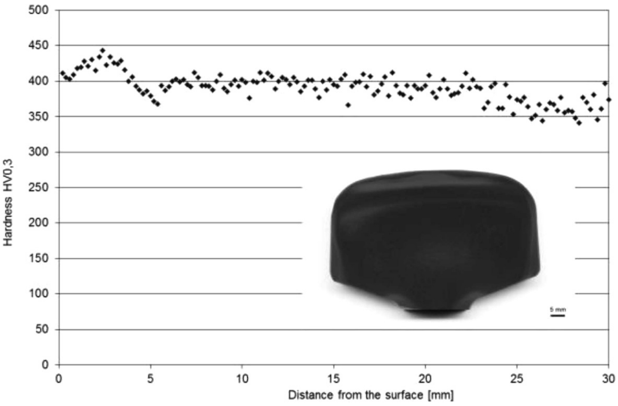

Figure 8: Measured hardness at the center line of the rail head
Slika 8: Trdota izmerjena na sredini glave tirnice

The first full-scale test showed that the rail shape has a significant influence on the cooling intensity, so additional experiments with a full-scale austenitic sample and temperature-field prediction-model tuning were necessary to obtain the required material structure. Finally, a full-scale, carbon-rail sample was made and it too was embedded with thermocouples. Simulated temperatures were compared to measured temperatures and the model was verified. An example of the cooling regime of a successful full-scale test is shown in **Figure 7**.

The measured hardness of this sample was around 400 HV0.3 (**Figure 8**). This corresponded to the results from the static-hardening-capacity test.

4 CONCLUSION

The goal of this article was to illustrate a verified methodology for rail heat treatment. The first step was to compute a CCT diagram and determine the settings for the optimum cooling regime to achieve the required material structure. The accuracy of the CCT diagram was verified with a hardening-capacity test (Jominy test). The next step was to measure the dependence of the heat-transfer coefficient on the surface temperature using a flat austenitic steel plate with thermal sensors. Various cooling parameters were tested: water pressure, spray distance, spray angle, movement velocity and others. These boundary conditions were used to predict the temperature-field evolution in the rail. It was found that the rail shape has a significant influence on the cooling intensity. A full-scale austenitic steel rail sample (300 mm long) was made and the cooling model was tuned using simulation data and the temperatures measured during the experiments with a full-scale sample. The final design of the cooling section was made and the cooling model was verified by measuring an authentic full-scale carbon sample in the laboratory. The final hardness of the heat-treated rail sample was measured and compared with the data obtained during the hardening-capacity test. Both of these results were around 400 HV0.3. A fine perlite structure was found along the center line of the heat-treated rail-head sample.

Acknowledgement

The research leading to these results received funding from the MEYS under the National Sustainability Programme I (Project LO1202).

5 REFERENCES

[1] M. Chabicovsky, M. Raudensky, Experimental Investigation of a Heat Transfer Coefficient, Mater. Tehnol., 47 (**2013**) 3, 395–398

[2] M. Raudensky, M. Chabicovsky, J. Hrabovsky, Impact of Oxide Scale on Heat Treatment of Steels, Proc. of the 23rd International Conference on Metallurgy and Materials, Brno, 2014, 553–558

[3] M. Chabicovsky, M. Hnizdil, A. A. Tseng, M. Raudensky, Effects of Oxide Layer on Leidenfrost Temperature during Spray Cooling of Steel at High Temperatures, International Journal of Heat and Mass Transfer, 88 (**2015**), 236–246, doi:10.1016/j.ijheatmasstransfer.2015.04.067

[4] T. Mauder, C. Sandera, J. Stetina, Optimal Control Algorithm for Continuous Casting Process by Using Fuzzy Logic, Steel Research International, 86 (**2015**) 7, 785–798, doi:10.1002/srin.201400213

[5] K. Gryc, K. Stransky, K. Michalek, A Study of the High-Temperature Interaction between Synthetic Slags and Steel, Mater. Tehnol., 46 (**2012**) 4, 403–406

[6] K. R. Santanu, Surface Quality of Steel Products, Role of Chemistry, Steelmaking & Continuous Casting, New Delhi 2006

[7] L. Klimes, J. Stetina, L. Parilak, P. Bucek, Influence of Chemical Composition of Cast Steel on Temperature Field of Continuously Cast Billets, Proc. of the 21st International Conference on Metallurgy and Materials, Brno, 2012, 135–141

[8] T. Mauder, J. Stetina, Improvement of the Casting of Special Steel with a Wide Solid-Liquid Interface, Mater. Tehnol., 50 (**2016**) 1, 3–6, doi:10.17222/mit.2014.122

MATERIALI IN TEHNOLOGIJE/MATERIALS AND TECHNOLOGY (1967–2017) – 50 LET/50 YEARS

UDK 620.17:539.4:669.715
Professional article/Strokovni članek

ISSN 1580-2949
MTAEC9, 51(2)333(2017)

STRAIN-RATE-DEPENDENT TENSILE CHARACTERISTICS OF AA2139-T351 ALUMINUM ALLOY

NATEZNA TRDNOST ALUMINIJEVE ZLITINE AA2139-T351 V ODVISNOSTI OD HITROSTI OBREMENJEVANJA

Onur Çavuşoğlu[1], Alan Gordon Leacock[2], Hakan Gürün[1], Ahmet Güral[3]

[1]Gazi University, Faculty of Technology, Department of Manufacturing Engineering, 06500 Teknikokullar-Ankara, Turkey
[2]University of Ulster, Nanotechnology and Advanced Materials Research Institute, Advanced Metal Forming Research Group, School of Engineering, Co. Antrim, Northern Ireland BT37 0QB, United Kingdom
[3]Gazi University, Faculty of Technology, Department of Metallurgical and Materials Engineering, 06500 Teknikokullar-Ankara, Turkey
onurcavusoglu@gazi.edu.tr

Prejem rokopisa – received: 2016-01-05; sprejem za objavo – accepted for publication: 2016-02-22

doi:10.17222/mit.2016.009

Mechanical properties of sheet materials are affected by the strain conditions. In this study, the influence of the strain rate on the mechanical properties of AA2139-T351 aluminium-alloy sheet materials was studied, by applying uniaxial tensile tests on these materials at four different strain rates (0.03, 0.003, 0.0003, 0.00003) s^{-1}. Upon analysing the obtained results, it was seen that the elongation, anisotropy value and the load-carrying ability during the necking were reduced, while the AA2139-T351 yield strength, tensile strength, work-hardening coefficient and work-hardening rate were not significantly affected by the increasing strain rate.

Keywords: strain rate, tensile strength, aluminium alloys, AA2139-T351

Na mehanske lastnosti pločevin vplivajo pogoji obremenjevanja. V študiji je proučevan vpliv hitrosti obremenjevanja na mehanske lastnosti pločevine iz aluminijeve zlitine AA2139-T351, z uporabo enoosnega nateznega preizkusa tega materiala pri štirih različnih hitrostih obremenjevanja (0,03, 0,003, 0,0003, 0,00003) s^{-1}. Iz analize dobljenih rezultatov sledi; raztezek, vrednost anizotropije in nosilna sposobnost na kontrakcijo so se zmanjšali, medtem ko se meja tečenja AA2139-T351, natezna trdnost, koeficient utrjevanja in hitrost utrjevanja niso spreminjale pri povečani hitrosti obremenjevanja.

Ključne besede: hitrost obremenjevanja, nateznost, aluminijeve zlitine, AA2139-T351

1 INTRODUCTION

The main purpose of the current studies conducted on the materials used in vehicles, is to observe the fuel consumption when using light materials such as aluminium and magnesium alloys and, as a result, the reduction of the CO_2 fingerprint.[1] Aluminium alloys are widely preferred in the automotive and aerospace industries because these materials have superior characteristics such as low density, high strength and formability capabilities, resource availability, high corrosion resistance, good thermal and electrical conductivity.[1–2]

Tensile testing is a widely used method in order to determine a number of mechanical properties of materials and their deformation behaviours. Many parameters obtained from a tensile test may differ depending on the deformation conditions of the material.[3] The strain rate is known to affect the mechanical properties of many metallic materials by affecting the stress/strain relationship.[2] When the studies on the effect of the strain rate on the mechanical properties of aluminium alloys were examined, T. Ohwue et al.[4] determined, by examining the mechanical properties depending on the temperature and strain rate of aluminium/magnesium alloys, that the tensile strength is not affected by an increase in the strain rate at room temperature and that the amount of elongation shows very little tendency to decrease.[4] In the study of Y. Chen et al.[5] it was seen that the strain rate had no significant effect on the tensile behaviour of the AA6xxx and AA7xxx aluminium alloy series, that a strain-rate increase had no significant effect on the yield strength and that this increase only slightly improved the tensile strength.[5] In the study of O. – G. Lodema et al.[6] they determined, by examining the strain rate sensitivity of the AA1200 and 3103 aluminium alloys, that a slight increase in the tensile strength and elongation amount occurred depending on the increase of the strain rate although the yield strength was not affected. M. J. Hadianfard et al.[7] determined, at different strain rates of the AA5182 and AA5754 alloys, that the tensile strength and the elongation amount decreased with an increase in the strain rate while the yield strength was not affected due to the increase in the strain rate. F. Ozturk et al.[8] determined in their study that there is a decrease in the increase in the strain rate, the elongation amount and the work-hardening coefficient of the 5052 aluminium alloy at room temperature. A. L. Noradila et al.[9] studied the tensile properties and work-hardening behaviour of aluminium/magnesium alloys. F. Ozturk et al.[10] also studied the work-hardening and strain-sensitivity behaviour of the high-strength steel sheet in their other study.

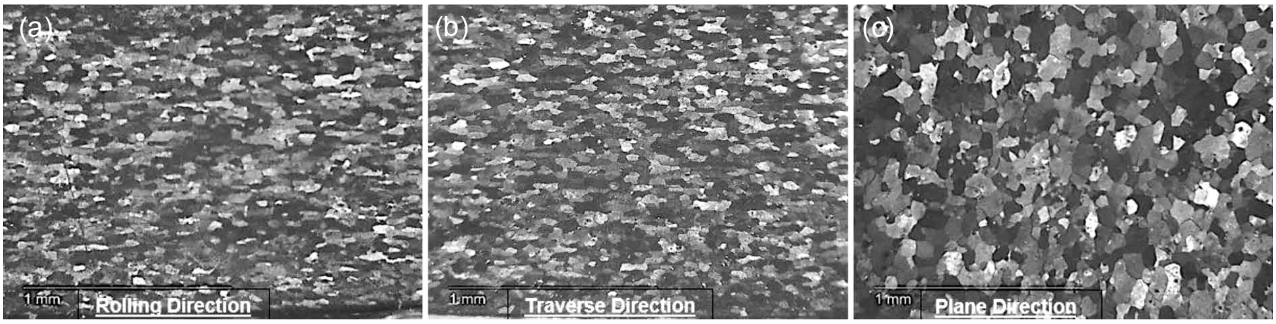

Figure 1: Microstructure of the AA2139-T351 alloy
Slika 1: Mikrostruktura zlitine AA2139-T351

Table 1: Chemical composition of AA2139-T351 sheet-metal material, in mass fractions (*w*/%)
Tabela 1: Kemijska sestava materiala pločevine AA2139-T351, v masnih odstotkih (*w*/%)

Material	Cu	Mg	Ag	Mn	Si	Fe	Ti	Zr	Sn	Ni	Cr	Al
2139-T351	4.80	0.43	0.31	0.27	0.06	0.06	0.06	0.03	<0.01	<0.01	< 0.01	Bal

Upon considering the studies in the literature, it is seen that researches were conducted to specify the mechanical properties of various aluminium alloys.

A determination of the mechanical properties of AA2139-T351 has a great importance for the aerospace industry. In this study, the mechanical properties of the AA2139-T351 aluminium-alloy sheet material were studied in detail at different strain rates and the obtained data was intended to be included into the literature.

2 MATERIAL AND EXPERIMENTAL PART

2.1 Material

In this study, the mechanical properties of the AA2139-T351 aluminium-alloy sheet material were examined depending on the strain rate. The chemical composition of this material is presented in **Table 1**. Moreover, microstructure photographs taken in the rolling direction, plane direction and traverse direction are also shown in **Figure 1**.

Tensile-test specimens in line with the ASTM E517 standard were used in the uniaxial tensile tests performed in order to determine of the mechanical properties. The cutting process was carried out on a water-jet machine to minimize the thermal effects that could have occurred in the sheet material during the preparation of the test specimens. Also, the notch effect that could have occurred during the strain was eliminated by polishing the side surfaces of the test specimens.

2.2 Experimental study

The mechanical properties of the AA2139-T351 aluminium-alloy sheet material depending on the strain rate at room temperature were determined by using a mechanical strain meter and an Instron 5500 tensile meter. According to the standard ASTM E517, the tension tests at four different strain rates (0.03, 0.003, 0.0003, 0.00003) s^{-1} were performed on the specimens with a sheet thickness of 1.6 mm in two different rolling directions (rolling direction, traverse direction). The average values were determined by repeating the tests three times for each parameter in order to reduce the margin of error. The yield strength, the tensile strength, the work-hardening coefficient, the total elongation and the anisotropy values were determined as a result of these tests, by obtaining true stress/true strain curves depending on the strain rate. In addition, the strain-rate sensitivity, work-hardening rate and load capacity on necking were examined.

3 RESULTS AND DISCUSSION

3.1 Tensile-test results

The change in the mechanical properties of the sheet material was determined by performing the tensile tests at the (0.03, 0.003, 0.0003, 0.00003) s^{-1} strain rates. The data obtained from the tensile test are given in **Table 2**.

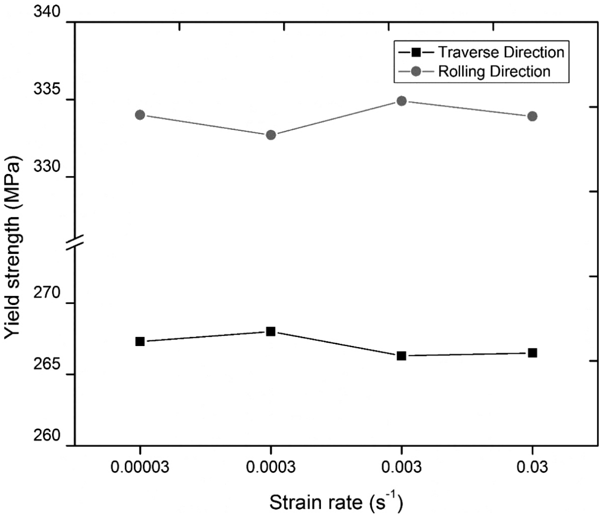

Figure 2: Yield strength – strain rate relation
Slika 2: Odvisnost meja plastičnosti – hitrost obremenjevanja

The strain rate/yield strength relationship of the AA2139-T351 aluminium alloy is shown in **Figure 2**. When **Figure 2** is examined, the yield strength between the minimum (0.00003 s^{-1}) and the maximum (0.03 s^{-1}) strain ratios is determined to be approximately between 332 MPa and 334 MPa in the rolling direction and between 265 and 268 MPa in the traverse direction. The strain rate and the yield strength are shown to vary to a very small extent. Therefore, the yield strength of the AA2139-T351 aluminium alloy is not affected by the increase in the strain rate. This outcome is found to be in compliance with the results from the studies conducted by Y. Chen et al.,[5] O. – G. Lodema et al.[6] and M. J. Hadianfard et al.[5–7]

Table 2: AA2139-T351 tensile-test results
Tabela 2: Rezultati nateznih preizkusov AA2139-T351

Direction	Strain rate	Yield strength	Tensile strength	*R* value	Elongation	Hardening coefficient
Rolling	0.03	333.9	502.4	0.730	16.3	0.156
Rolling	0.003	334.9	499.5	1.078	16.2	0.170
Rolling	0.0003	332.7	497.1	1.097	17.2	0.168
Rolling	0.00003	334.0	498.2	1.116	17.3	0.169
Traverse	0.03	266.5	473.4	0.990	15.5	0.179
Traverse	0.003	266.3	475.0	1.052	15.8	0.189
Traverse	0.0003	268.0	476.2	1.198	16.7	0.189
Traverse	0.00003	267.3	480.1	1.219	16.5	0.188

The amount of the tensile strength of a material is an extremely important parameter for the selection of the materials in engineering applications. The strain rate/tensile strength relationship is given in **Figure 3**. The tensile strength was determined to be 497–502 MPa in the rolling direction and 473–480 MPa in the traverse direction in the quasi-static strain-rate tests. The tensile strength was seen to be effected by the strain rate in a very small range. While the tensile strength was not affected by an increase in the strain rate in the study of T. Ohwue et al.,[4] a small increase in the tensile strength was found to occur in the studies of Y. Chen et al.[5] and O. – G. Lodemo et al.[6] Upon increasing the strain rate, the tensile strength of the material was found to reduce slightly depending on the occurring failure mechanisms in the study of M. J. Hadianfard et al.[7] The shift mechanisms may be delayed, especially in the soft matrix phase (α), due to an increase in the strain rate. In this case, the tensile strength of the material is thought not to significantly increase with the increasing strain rate because it may cause a premature rupture of the precipitates when the occurring tensile stress directly affects the precipitates.

The amount of elongation of the sheet-metal materials is extremely important in terms of sheet-metal forming processes. The elongation behaviour of a material under a desired amount leads to tear formation on the sheet metal before the sheet metal is formed as desired. The amount of elongation is known to decrease with an increase in the strain rate.[7–8] **Figure 4** shows the elongation behaviour of the AA2139-T351 aluminium alloy depending on the strain rate. The maximum elongation occurred at the two lowest strain rates (0.00003 s^{-1} and 0.0003 s^{-1}) in the rolling direction. The elongation capability of the material was reduced with the increase in strain rate.

The material gains strength through the hardening occurring depending on the dislocation pile-up in the internal structure of the material during the strain of the sheet-metal materials. The strain rate may affect the dislocation pile-up and, consequently, the material strength. Upon examining the relationship between the work-hardening coefficient and the strain rate in **Figure 5**, a slight reduction in the work-hardening coefficient is observed in the results obtained from the maximum strain-rate parameter (0.03 s^{-1}), while no change in the low strain rates is observed. When the overall results are examined,

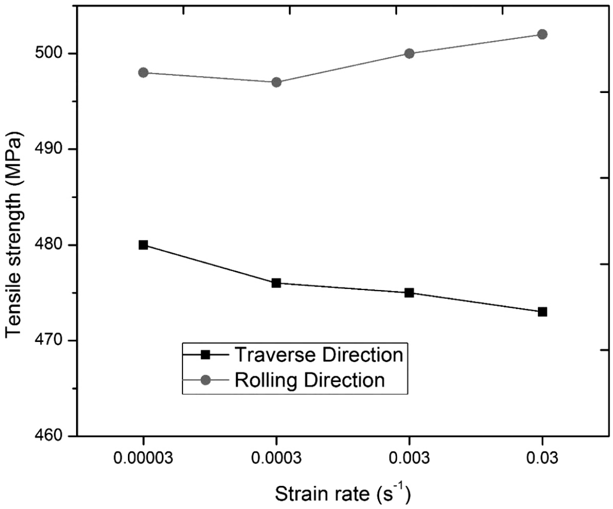

Figure 3: Tensile strength – strain rate relation
Slika 3: Odvisnost natezna trdnost – hitrost obremenjevanja

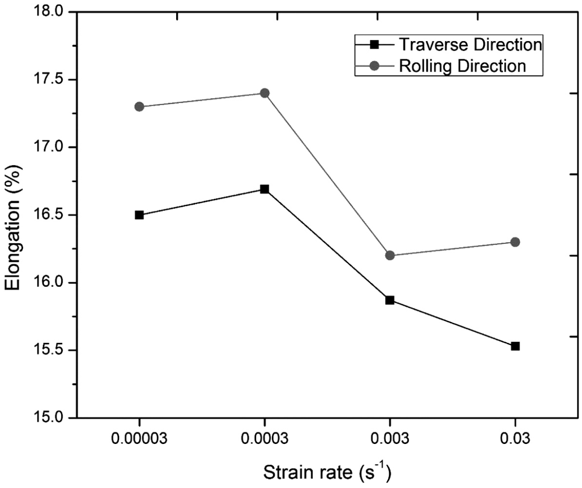

Figure 4: Elongation – strain rate relation
Slika 4: Odvisnost raztezek – hitrost obremenjevanja

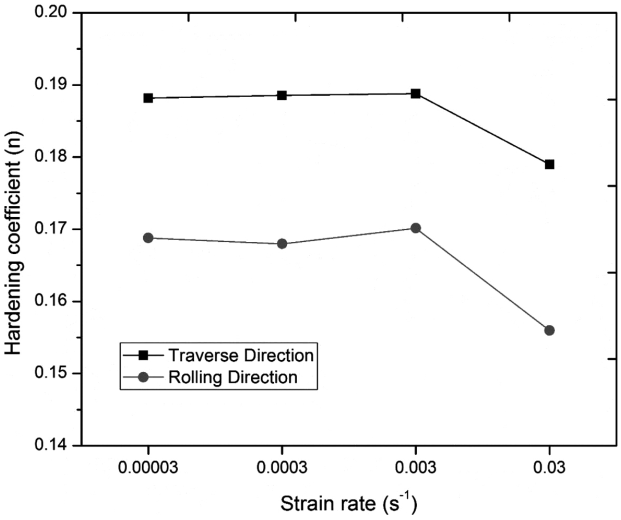

Figure 5: Hardening coefficient – strain rate relation

Slika 5: Odvisnost med koeficientom utrjevanja in hitrostjo obremenjevanja

the work-hardening coefficients obtained in the traverse direction are seen to be higher than the results obtained in the rolling direction. In the study of F. Ozturk et al.,[8] a very slight reduction in the coefficient of work hardening was seen to occur with an increase in the strain rate and the work-hardening coefficient was determined to change in a very small range depending on the strain rate.[8–9]

When the planar anisotropy value in **Figure 6** was examined, the anisotropy value was found to decrease with an increase in the strain rate. The decrease in the amount of elongation due to an increase in the strain rate supports this conclusion.

In the scope of the study, the sensitivity rate between the strain-rate values used in the tests for the AA2139-T351 aluminium-alloy sheet material was determined. For this purpose, the lowest strain rate of 0.00003 s^{-1} was selected as the reference value and it was calculated according to the formulas shown in Equation (1). When **Figure 7** was examined, it was seen that the strain-rate sensitivity was reduced as long as the rate range was decreased. When the maximum strain rate is applied, the decrease in the strain-rate sensitivity is thought to adversely affect the plastic deformation since the decrease in the strain-rate sensitivity adversely affects the plastic deformation in Equation (1):

$$\overline{m}(\dot{\varepsilon})=\frac{\mathrm{d}(\ln(\sigma))}{\mathrm{d}(\ln(\varepsilon))} \tag{1}$$

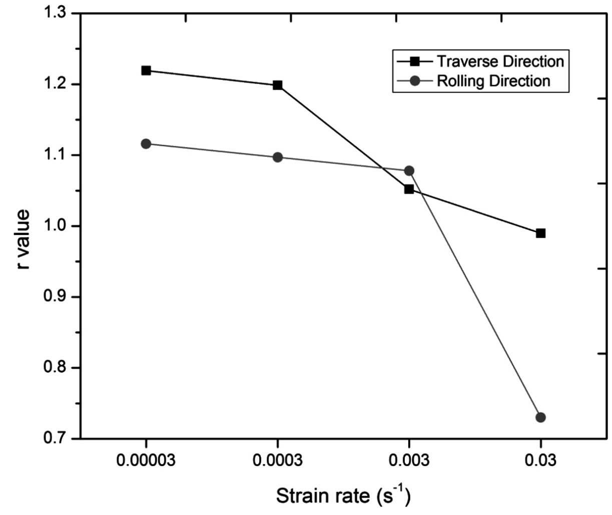

Figure 6: Anisotropy – strain rate relation

Slika 6: Odvisnost: anizotropija – hitrost obremenjevanja

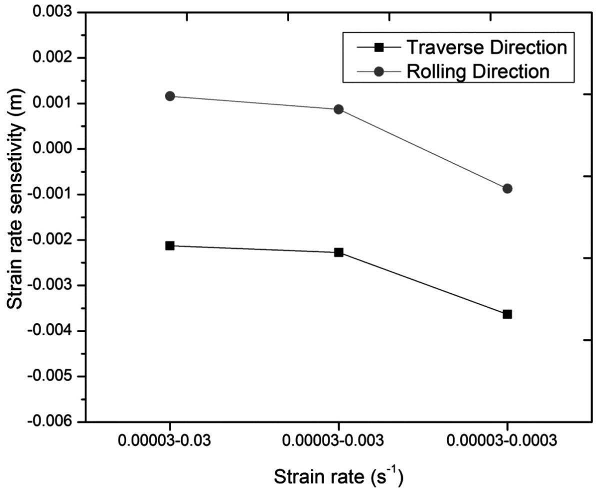

Figure 7: Strain rate sensitivity – strain rate relation

Slika 7: Odvisnost: občutljivost na hitrost obremenjevanja – hitrost obremenjevanja

In this study, the work-hardening rate was used to show the ability of the AA2139-T351 aluminium alloys for work hardens after the occurrence of plastic deformation. Work hardening occurs due to the dislocation movements and dislocation generation against the crystal

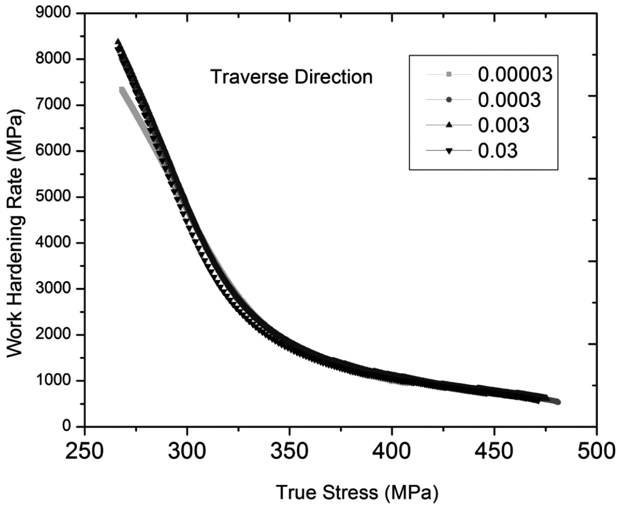

Figure 8: Work hardening rate – true stress relation in the transverse direction

Slika 8: Odvisnost: hitrost deformacijskega utrjevanja – prava napetost v prečni smeri

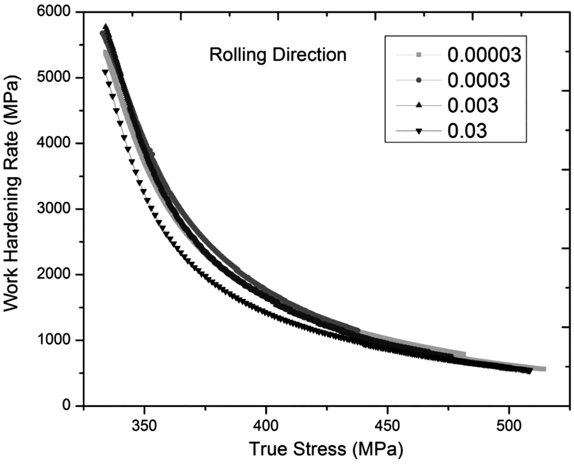

Figure 9: Work hardening rate – true stress relation in the rolling direction
Slika 9: Odvisnost: hitrost utrjevanja – prava napetost v smeri valjanja

structures of alloys.[9] The change in the work-hardening rate due to the strain rate is shown **Figures 8** and **9**. The work-hardening rate was determined to decrease with the increasing stress in the rolling direction. It is possible to interpret this case as a decrease in the work-hardening rate with the increase in the amount of strain. When the work-hardening-rate values obtained in the traverse direction and the rolling direction are compared, a higher amount of the work-hardening rate is found in the traverse direction than in the rolling direction. The reason for this is thought to be the fact that the work-hardening-coefficient result obtained for the traverse direction is higher than that obtained for the rolling direction although very close tensile-strength values are obtained.

The behaviour of the material strain due to reaching the maximum tensile strength up to fracture is referred to as the necking.[10]

The load-carrying capacity of a material during its necking behaviour depending on the strain rate was studied in the current study. Upon analysing the relationship between the load-carrying capacity and the strain rate in **Figures 10** and **11**, the fracture behaviour of the material was found to occur early with the increasing strain rate in the direction of rolling, and the load capacity of the material during the necking was determined to decrease with the increasing strain rate. The materials with a high tensile strength were seen to show their fracture behaviour earlier in the study of F. Ozturk et al.[8] When the traverse-direction and rolling-direction losses of the load-carrying ability during the necking were compared, the earlier fracture was determined to occur in the rolling direction having a higher tensile strength.

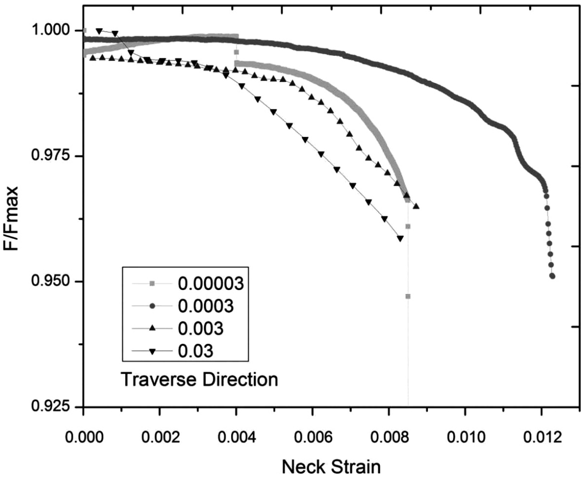

Figure 10: Transverse-direction loss of the load-carrying ability of the neck strain
Slika 10: Zmanjšanje nosilnosti v prečni smeri od napetosti v vratu

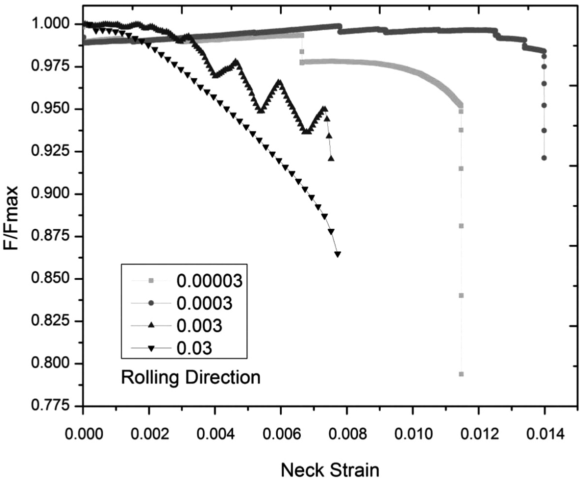

Figure 11: Rolling-direction loss of the load-carrying ability during the necking
Slika 11: Zmanjšanje nosilnosti v smeri valjanja od napetosti v vratu

4 CONCLUSIONS

It was found that the semi-static strain rates, the yield strength, the tensile strength and the work-hardening coefficient of the AA2139-T351 aluminium alloy are not significantly affected by the strain rate. The amounts of the elongation and anisotropy (*r*) tend to decrease with an increase in the strain rate. The material shows a negative strain-rate sensitivity. The work-hardening rate was found not to be significantly influenced by the strain rate. The load-carrying ability during the necking decreased slightly with the increase in the strain rate.

Acknowledgement

The authors would like to thank the Turkish Council of Higher Education for the research grant and the University of Ulster, Advanced Metal Forming Research Group (AMFOR) for the necessary equipment and material support.

5 REFERENCES

[1] S. Toros, F. Ozturk, I. Kacar, Review of warm forming of aluminum–magnesium alloys, Journal of Materials Processing Technology, 207 (**2008**), 1–12, doi:10.1016/j.jmatprotec.2008.03.057

[2] B. M. Dariani, H. G. Liaghat, M. Gerdooei, Experimental investigation of sheet metal formability under various strain rates, Proc. IMechE Part B: J. Engineering Manufacture, 223 (**2009**), 703–712, doi:10.1243/09544054JEM1430

[3] C. Kubat, A. Kiraz, The modeling of tensile test in virtual laboratory design using artificial intelligence, Journal of the Faculty of Engineering and Architecture of Gazi University, 27 (**2012**) 1, 205–209, doi:10.17341/gummfd.04550

[4] T. Ohwue, K. Takata, M. Saga, M. Kikuchi, Temperature and Strain Rate Dependence of Mechanical Properties and Square Shell Deep Drawability of Al–Mg Alloy Sheets in Warm Working Condition, Materials Transactions, 43 (**2002**) 12, 3184–3188, doi:10.2320/matertrans.43.3184

[5] Y. Chen, A. H. Clausen, O. S. Hopperstad, M. Langseth, Stress-strain behaviour of aluminium alloys at a wide range of strain rates, International Journal of Solids and Structures, 46 (**2009**), 3825–3835, doi:10.1016/j.ijsolstr.2009.07.013

[6] O. G. Lademo, O. Engler, J. Aegerter, T. Berstad, A. Benallal, O. S. Hopperstad, Strain-Rate Sensitivity of Aluminum Alloys AA1200 and AA3103, Strain-Rate Sensitivity of Aluminum Alloys AA1200 and AA3103, J. Eng. Mater. Technol., 132 (**2010**) 4, 041007, doi:10.1115/1.4002160

[7] M. J. Hadianfard, R. Smerd, S. Winkler, M. Worswick, Effects of strain rate on mechanical properties and failure mechanism of structural Al–Mg alloys, Materials Science and Engineering A, 492 (**2008**), 283–292, doi:10.1016/j.msea.2008.03.037

[8] F. Ozturk, S. Toros, S. Kilic, Evaluation of tensile properties of 5052 type aluminum-magnesium alloy at warm temperatures, Archives of Materials Science and Engineering, 34 (**2008**) 2, 95–98

[9] A. L. Noradila, Z. Sajuri, J. Syarif, Y. Miyashita,Y. Mutoh, Effect of strain rates on tensile and work hardening properties for Al-Zn magnesium alloys, Materials Science and Engineering, 46 (**2013**), 012031, doi:10.1088/1757-899X/46/1/012031

[10] F. Ozturk, A. Polat, S. Toros, R. C. Picu, Strain Hardening and Strain Rate Sensitivity Behaviors of Advanced High Strength Steels, Journal of Iron and Steel Research, Internatıonal, 20 (**2013**) 6, 68–74, doi:10.1016/S1006-706X(13)60114-4

UDK 621.1.016.4:621.18.06:669-5
Professional article/Strokovni članek

ISSN 1580-2949
MTAEC9, 51(2)339(2017)

DETERMINING THE HEAT-TRANSFER COEFFICIENT IN AN ISOTHERMAL MODEL OF A SHAFT FURNACE

DOLOČITEV KOEFICIENTA PRENOSA TOPLOTE V IZOTERMNEM MODELU JAŠKOVNE PEČI

Mária Čarnogurská[1], Romana Dobáková[1], Tomáš Brestovič[1], Miroslav Příhoda[2]
[1]Technical University of Košice, Faculty of Mechanical Engineering, Vysokoškolská 4, 042 00 Košice, Slovakia
[2]VŠB – Technical University of Ostrava, Faculty of Metallurgy and Materials Engineering, Ostrava-Poruba, Czech Republic
maria.carnogurska@tuke.sk

Prejem rokopisa – received: 2016-03-03; sprejem za objavo – accepted for publication: 2016-04-01

doi:10.17222/mit.2016.042

The paper addresses an analysis of the influence of the batch grain size and air flow through a shaft furnace on the transfer coefficient from the air to the batch and the time for heating the batch to the required temperature. The stated influence was experimentally investigated on a reduced shaft-furnace model at three air-flow amounts, 48.8 $m^3 h^{-1}$, 56.3 $m^3 h^{-1}$ and 72 $m^3 h^{-1}$, and three varying grain sizes of the used batch: 4–8 mm, 8–10 mm and 10–12 mm. The influence of the stated parameters upon the evenness of the velocity field of the air along the cross-section of the furnace was also monitored in two selected horizontal planes in order to obtain information about the air velocity in the vicinity of the wall of the model furnace and at distances of 1.5 cm, 3.5 cm and 5.0 cm from it.

Keywords: batch grain size, heat-transfer coefficient, velocity field

Članek obravnava analizo vpliva zrnatosti vložka in pretoka zraka skozi jaškasto peč na koeficient prenosa iz zraka na vložek in na čas segrevanja vložka na potrebno temperaturo. Navedeni vpliv je bil eksperimentalno preiskovan na pomanjšanem modelu jaškaste peči, pri treh pretokih zraka 48,8 $m^3 h^{-1}$, 56,3 $m^3 h^{-1}$ in 72 $m^3 h^{-1}$ ter pri treh različnih zrnatostih vložka: med 4–8 mm, med 8–10 mm in med 10-12 mm. Opazovan je bil tudi vpliv omenjenih parametrov na enakomernost hitrostnega polja zraka po preseku peči v dveh izbranih horizontalnih ravninah z namenom, da bi dobili informacijo o hitrosti zraka blizu stene modelne peči in na razdaljah: 1,5 cm, 3,5 cm in 5,0 cm od nje.

Ključne besede: zrnatost vsipa, koeficient prenosa toplote, hitrostno polje

1 INTRODUCTION

Using various technical devices, it is necessary to examine the intensity of the heat exchange between two substances – most often between a gas and a solid substance. The heat-exchange intensity is represented by a heat-transfer coefficient and it takes place via conduction, convection, flow and radiation.[1–2]

Metallurgical furnaces currently represent a complicated mechanised and automated equipment and equally complicated procedures taking place within. The thermal regime of such industrial aggregates is very complicated and it therefore requires appropriate attention.

Several authors focus upon the heat transfer in varying metallurgical furnaces and compare their results obtained experimentally with the results from numeric simulations.[3–5]

2 EXPERIMENTAL PART

2.1 Description of the heat exchange in a layer of a shaft-furnace batch

The heat exchange in a batch layer of shaft furnaces and similar furnace aggregates is provided by direct contact between the gas medium and the batch. The heat in the batch layer is mainly transferred via radiation and convection.[6–8] The radiation component is present to a lesser extent than the convection component. When heating a batch, gas radiation is influenced by the small dimensions of the channels created between individual grains of the batch material and the low concentration of heteropolar gases. In practice, heat exchange via radiation only takes place at high batch temperatures.

Heat exchange via conduction also takes place between individual pieces of the batch. However, this heat exchange is negligible.

The gas-flow velocity has a decisive effect during the heat exchange between a flowing medium and a batch.[9] An analysis of convection during the heat transfer from the heated air to the batch was carried out on a "cold model". This means that a simulated batch formed of crushed chamotte at an ambient temperature was exposed to a flow of heated air with a known temperature and known volume. The influence of the grain size of the batch and the air flow upon the intensity of the heat exchange between the air and the batch was monitored and represented by the heat-transfer coefficient from the air to the batch.[10]

2.2 Experimental model furnace

An experiment focusing upon obtaining the information necessary to determine the heat-transfer coefficient was carried out on an equipment representing an isothermal model of a shaft furnace. A diagram of the model is on **Figure 1** and an image of the experimental equipment during the measurement is on **Figure 2**. The basic parameters of the model are given in **Table 1**. The model has a double insulation in the lower part consisting of perlite and chamotte flour. The insulation in the upper part of the model consists of just chamotte flour. The brickwork comes into direct contact with the batch and the flowing air. The bottom of the model is formed of a graduated grid, on which the batch is placed. Below the grid, there is pipework, through which the air, heated in a recuperator, is transported to the furnace model.

Table 1: Basic parameters of the model
Tabela 1: Osnovni parametri modela peči

Height of the model furnace (mm)	856		
Inner diameter of the model furnace (mm)	110		
Height of filling (mm)	488		
Gas medium	air		
Batch	crushed chamotte		
Batch density (kg m^{-3})	1900		
Batch grain size (mm)	4–8	8–10	10–12
Void fraction of the batch (1)	0.55	0.61	0.623
Air flow (m^3 h^{-1})	48.8	56.3	72

The air flow was measured using a gas meter and its pressure using a U-tube manometer. The measurement of the temperature of the batch and air was carried out using K-type (NiCr-Ni) contact thermocouples. The thermocouples were led to terminal boards from where an electric signal was transported to the data logger. Recording and storing the data was provided by computer software.

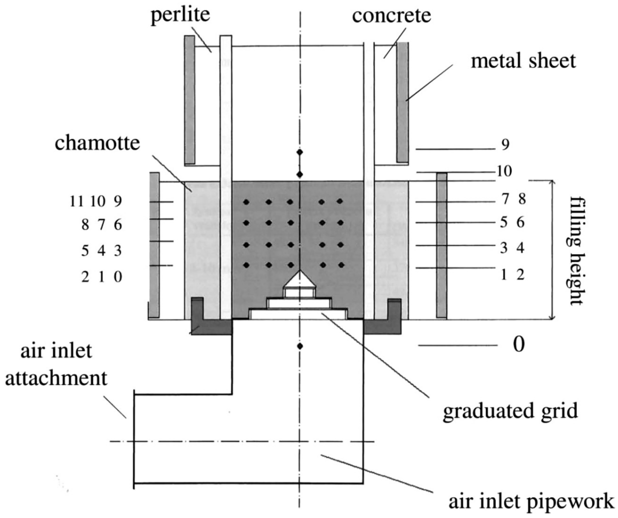

Figure 1: Furnace model with the thermocouple distribution
Slika 1: Model peči z razporeditvijo termoelementov

Figure 2: Image of the experiment equipment during the measurement
Slika 2: Pogled na eksperimentalno napravo med merjenjem

Before starting the measurement itself, air at an ambient temperature was blown into the furnace using a fan in order to stabilise the temperature in the batch. The air flow and grain size changed during the experiment. The temperature of the batch material and the temperature of the flowing air were measured along the height of the model during the experiment.

A scheme of the furnace model with the appropriate equipment and measurement devices is shown on **Figure 3**.

3 DETERMINATION OF THE HEAT-TRANSFER COEFFICIENT

Balance equations were used for determining the heat-transfer coefficient. The amount of delivered heat Q was stated using Equation (1):

$$Q = Q_V \cdot c(t'_{\mathrm{vz}} - t''_{\mathrm{vz}}) \cdot \tau = m \cdot c_{\mathrm{m}} (t''_{\mathrm{m}} - t'_{\mathrm{m}}) \tag{1}$$

The heat-transfer coefficient related to the total volume of the model furnace can be determined from

Equation (2):

$$Q = \alpha_{\mathrm{V}} \cdot V \cdot \Delta t_{\mathrm{LS}} \cdot \tau \tag{2}$$

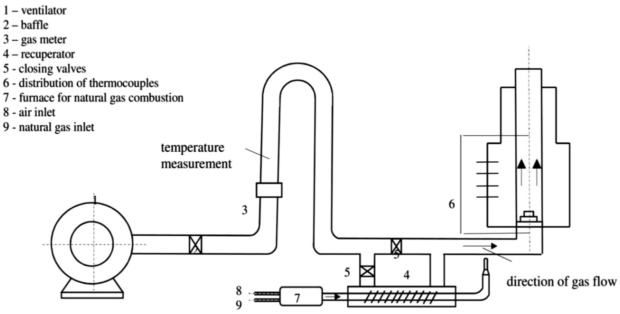

Figure 3: Scheme of a model furnace
Slika 3: Shema modela peči

For the logarithmic mean temperature difference Δt_{LS}, Equation (3) is used:

$$\Delta t_{\mathrm{LS}} = \frac{\Delta t' - \Delta t''}{\ln \dfrac{\Delta t'}{\Delta t''}} \tag{3}$$

whilst $t'_{\mathrm{vz}} - t''_{\mathrm{m}} = \Delta t'$ is the temperature difference of the air and the batch at the inlet to the model and $t''_{\mathrm{vz}} - t'_{\mathrm{m}} = \Delta t''$ is the temperature difference of the air and the batch at the outlet of the model.

By comparing Equations (1) and (2), we obtain the formula for the heat-transfer coefficient related to the volume of the furnace model:

$$\alpha_V = \frac{m \cdot c_m (t''_{\mathrm{m}} - t'_{\mathrm{m}})}{V \cdot \Delta t_{\mathrm{LS}} \cdot \tau} \tag{4}$$

3.1 Conditions for calculating the heat-transfer coefficient

For a batch grain size of 10–12 mm and the lowest air flow of 48.8 m^3 h^{-1} logarithmic mean temperature difference Δt_{LS} was determined from Equation (3) under the following conditions:

$t'_{\mathrm{vz}} = 272.1$ °C $t''_{\mathrm{m}} = 261.5$ °C

$t''_{\mathrm{vz}} = 160.9$ °C $t'_{\mathrm{m}} = 101.4$ °C

The volume of the shaft furnace model with a filling height of h = 0.488 m and an area of S = 0.0095 m^2 represents value V = 0.0046 m^3.

The weight of the batch for the monitored volume was determined using Equation (5)[4]:

$$m = V \cdot \rho \cdot (1 - \varepsilon) \tag{5}$$

The calculated weight is 3.32 kg.

The value of the volume heat-transfer coefficient is 38 963 W m^{-3} K^{-1}.

Figures 4 and **5** show the development of the heat-transfer coefficient depending upon the time with three different flows and batch grain sizes of 10–12 mm and 4–8 mm.

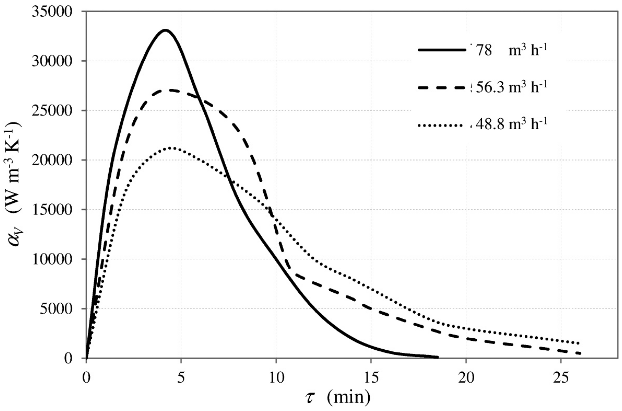

Figure 5: Development of the heat-transfer coefficient in relation to time with three varying flows and a grain size of 4–8 mm

Slika 5: Spreminjanje koeficienta prenosa toplote glede na čas, pri treh različnih pretokih in zrnatosti 4–8 mm

The air-flow velocity is related to the flow. With three different air flows (48.8 m^3 h^{-1}, 56.3 m^3 h^{-1} and 78 m^3 h^{-1}), it can be seen that the heat-transfer coefficient α_V grows with the growing flow (**Figure 5**). The higher the air flow, the higher is the value of the heat-transfer coefficient and the time necessary for heating the batch shortens.

Figure 6 shows the development of the heat-transfer coefficient for the batch grain size of 10–12 mm in relation to time, with the air flow of 48.8 m^3 h^{-1} in three places along the horizontal plane of the furnace. The distances of the places from the furnace wall were 1.5 cm, 3.5 cm and 5.5 cm. The horizontal plane was fictitiously placed at a height of 288 mm on the furnace. **Figure 7** shows the development of this coefficient along the same plane and in the same places but with a smaller batch grain size (4–8 mm). The most marked difference in the heat-transfer-coefficient value is at the distance of the measured place of 1.5 cm from the wall where, for

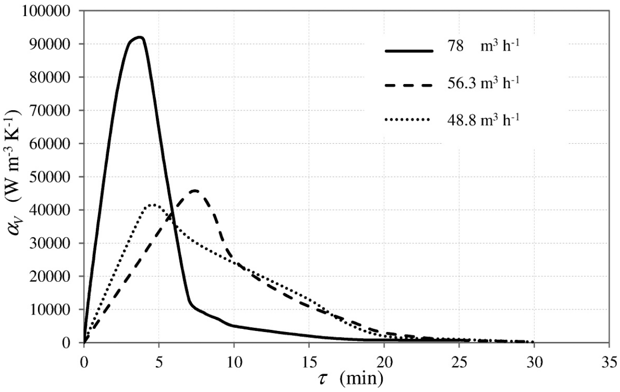

Figure 4: Development of the heat-transfer coefficient in relation to time with three varying flows and a grain size of 10–12 mm

Slika 4: Spreminjanje koeficienta prenosa toplote glede na čas, pri treh različnih pretokih zraka in zrnatosti 10–12 mm

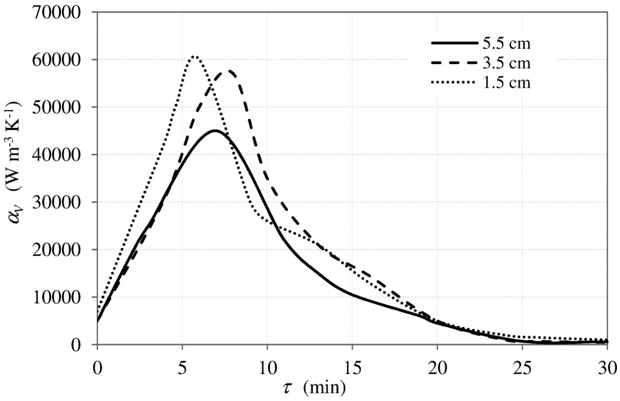

Figure 6: Development of the heat-transfer coefficient in relation to time with a grain size of 10–12 mm and air flow of 48.8 m^3 h^{-1}

Slika 6: Spreminjanje koeficienta prenosa toplote glede na čas za zrnatost vsipa 10–12 mm in pri pretoku zraka 48,8 m^3 h^{-1}

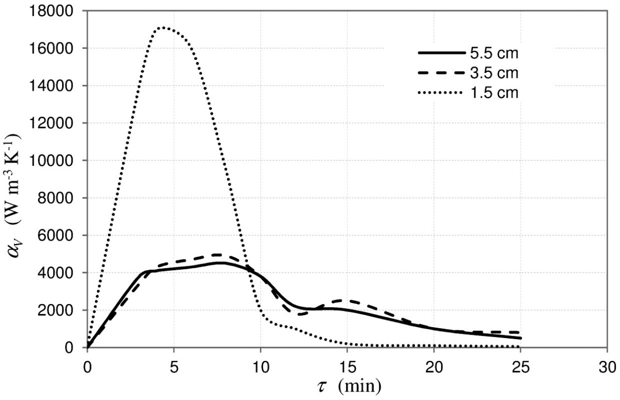

Figure 7: Development of the heat-transfer coefficient in relation to time with a grain size of 4–8 mm and air flow of 48.8 m^3 h^{-1}

Slika 7: Spreminjanje koeficienta prenosa toplote glede na čas pri zrnatosti vsipa 4–8 mm in pretoku zraka 48,8 m^3 h^{-1}

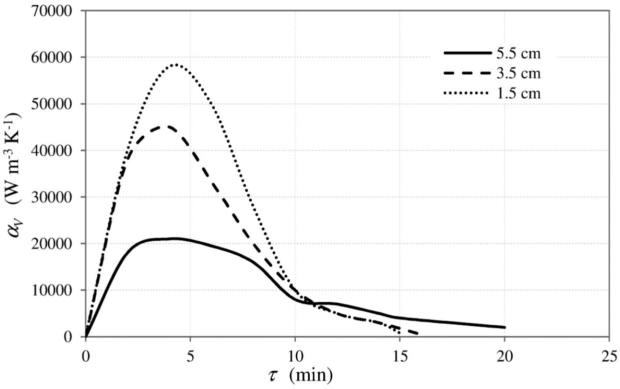

Figure 9: Development of the heat-transfer coefficient in relation to time with a grain size of 4–8 mm and air flow of 72 m^3 h^{-1}

Slika 9: Gibanje koeficienta prenosa toplote glede na časa pri zrnatost vsipa 4–8 mm in pretoku zraka 72 m^3 h^{-1}

example, with the flow of 48.8 m^3 h^{-1} and the batch grain size of 4–8 mm (**Figure 7**), the heat-transfer coefficient is 17000 W m^{-3} K^{-1}. With the same flow and the same distance from the wall, this coefficient increases with an increase of the batch grain size to 10–12 mm (**Figure 6**), by about 62 %. At the distance of 5.5 cm from the wall and under the same conditions (the grain size of 4–8 mm, the flow of 48.8 m^3 h^{-1}) the coefficient is 4200 W m^{-3} K^{-1} and with the grain size of 10–12 mm, it is almost 46000 W m^{-3} K^{-1}. This represents an approximately 9-fold increase in the value of this coefficient.

It can be seen from **Figures 6** and **7** that the smaller the batch grain size, the greater is the hydraulic resistance of the batch, and the air in the direction of the flow only partially passes through the centre of the model. For this reason, the flow is more intensive in the very close vicinity of the wall of the furnace model. The flowing air therefore delivers less heat to the batch than in the case of a lower hydraulic resistance, where the air passes through the cross-section of the furnace more evenly – this is the case with a larger batch grain size.

With a greater air flow and the largest batch grain size used in the experiment (10–12 mm), there was a more even distribution of the air flow along the cross-section of the model furnace (**Figure 8**). With the grain size of 4–8 mm, the air flow was again more intensive close to the wall (**Figure 9**).

In order to verify the air-flow conditions along the cross-section of the batch in the model furnace, a calculation was carried out using the numeric method in the ANSYS_CFX program. The solution was expected to confirm or deny the nature of the flow and the distribution of the air-velocity field along the cross-section of the furnace. The used edge conditions of the solution were identical to the conditions in the real experiment.

Figure 10 shows the distribution of the velocity along the cross-section of the model furnace with the air flow of 48.8 m^3 h^{-1}, grain sizes of 4–8 mm and 10–12 mm, and with the batch height of 280 mm. **Figure 11** shows the distribution of the velocity along the

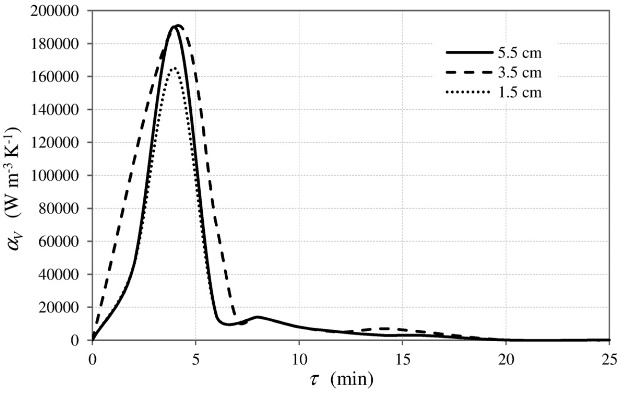

Figure 8: Development of the heat-transfer coefficient in relation to time with a grain size of 10–12 mm and air flow of 72 m^3 h^{-1}

Slika 8: Spreminjanje koeficienta prenosa toplote glede na čas pri zrnatosti vsipa 10–12 mm in pretoku zraka 72 m^3 h^{-1}

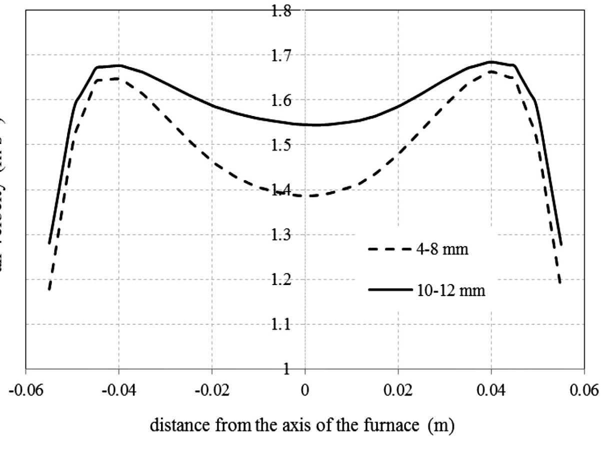

Figure 10: Air-velocity profile along the cross-section at a height of batch of 280 mm and air flow of 48.8 m^3 h^{-1}

Slika 10: Hitrostni profil zraka po prečnem prerezu peči, pri višini vsipa 280 mm in pretoku zraka 48,8 m^3 h^{-1}

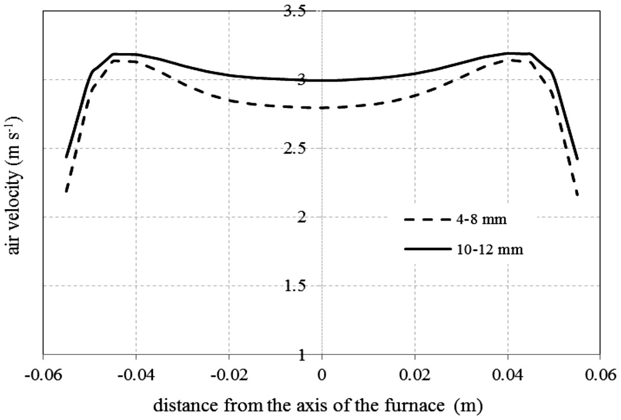

Figure 11: Air-velocity profile along the cross-section at a height of batch of 280 mm and air flow of 72 m^3 h^{-1}

Slika 11: Hitrostni profil zraka po prečnem prerezu peči, pri višini vsipa 280 mm in pretoku zraka 72 m^3 h^{-1}

cross-section of the furnace, at the same batch height, the selected grain sizes and at the higher air flow (78 m^3 h^{-1}).

At the air flow of 72 m3·h-1 and the batch grain size of 4–8 mm, the air-velocity field is displayed in the vector shape on **Figure 12a**. **Figure 12b** shows the velocity field at the same flow and the grain size of 10–12 mm. **Figure 12b** documents a more even distribution of the air-velocity field than in the case of using a smaller batch grain size.

4 RESULTS AND DISCUSSION

The influence of the flow upon the heat-exchange intensity is shown on **Figures 4** and **5**. With the grain size of 10–12 mm and air flow of 78 m^3 h^{-1}, the heat-transfer coefficient was about 50 % higher compared to the flow of 48.8 m^3 h^{-1}. With the grain size decreased to 4–8 mm and the same flow of 78 m^3 h^{-1}, this coefficient decreased by about 63 %. The maximum value of the heat-transfer coefficient for both flows was reached in approximately the same time of heating the batch which was about 4 min.

The heat exchange in the batch along the cross-section of the model furnace has a varying intensity. This is related to the structure of the batch and the amount of the air flow. For example, at the distance of 1.5 cm from the wall, the flow of 48.8 m^3 h^{-1} and the batch grain size of 4–8 mm (**Figure 7**), the heat-transfer coefficient is about 17000 W m^{-3} K^{-1}. At the same flow and the same distance from the wall, this coefficient increases with an increased batch grain size of 10–12 mm (**Figure 6**) to a value of 60000 W m^{-3} K^{-1}, i.e., by about 2.5 times.

Higher air flows influence heat exchange more intensively. With the same distance from the wall (1.5 mm), the air flow of 72 m^3 h^{-1} and batch grain size of 4–8 cm (**Figure 9**), the heat-transfer coefficient is circa 58000 W m^{-3} K^{-1}. With the same air flow and at the same distance from the wall, the heat-transfer coefficient increases more than threefold with the batch grain size increased to 10–12 mm (**Figure 8**), i.e., to a value of 192000 W m^{-3} K^{-1}.

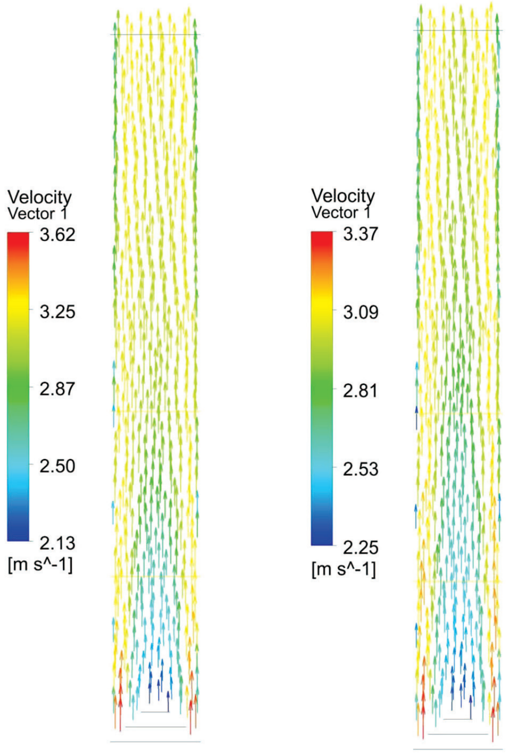

Figure 12: Air flow along the whole cross-section of the furnace with an air flow of 72 m^3 h^{-1}

Slika 12: Kroženje zraka po celotnem prečnem prerezu peči, pri pretoku zraka 72 m^3 h^{-1}

The influence of the distance of the investigated location of the batch upon the heat-transfer coefficient is more pronounced with a lower batch grain size. For example, for the air flow of 72 m^3 h^{-1} and grain size of 4–8 mm, the heat-transfer coefficient has a value of 21000 W m^{-3} K^{-1} if the distance from the furnace wall is 5.5 cm. At the same distance from the wall and the grain size of 10–12 mm, the value of the coefficient remains the same as for the distance of 1.5 cm, i.e., 192000 W m^{-3} K^{-1}. It is clear from the above that the air velocity along the cross-section of the furnace is distributed more evenly with a greater batch grain size. The same result was confirmed by calculating the flow conditions using the numeric simulation.

5 CONCLUSION

The value of the coefficient of the heat transferred from the flowing air into a batch depends upon several factors. Important roles are played by the batch grain size, the fact of how evenly it is distributed, the input temperature of the flowing air and the amount of the air flowing through the batch layer. Most of the heat transferred to the batch at a given temperature of the flowing air was reached with the largest grain size. In order to achieve an intensive heat transfer with a lower batch grain size, it is necessary to ensure a higher flow of the heated air and an even distribution of the batch. With a smaller grain size, it is very complicated, or even impossible, to ensure that the hydraulic resistance of the batch does not increase. This always results in the changes in the direction of the input air flow to the batch layer and the flow is directed towards the furnace wall, where it leaves the model furnace without any significant transfer of heat to the batch. This is documented with the outputs of the numeric simulation.

Acknowledgments

This paper was written with the financial support of project KEGA č. 003TUKE-4/2016, project EU operational programme ITMS 26220220044 and SP2017/37-FMMI VŠB TUO.

Nomenclature

α_V	heat-transfer coefficient related to the volume of the model	$W\ m^{-3}\ K^{-1}$
c	specific heat capacity of the air	$J\ m^{-3}\ K^{-1}$
c_m	specific heat capacity of the batch	$J\ kg^{-1}\ K^{-1}$
ε	void fraction	1
Δt_{LS}	logarithmic mean temperature difference	°C
m	batch weight	kg
Q	amount of heat delivered	J
Q_V	air flow	$m^3\ s^{-1}$
ρ	chamotte density	$kg\ m^{-3}$
t_{vz}'	air temperature at the inlet to the furnace	°C
t_{vz}'	air temperature at the outlet from the furnace	°C
t_m'	batch temperature at input	°C
t_m''	batch temperature at output	°C
τ	time	s
V	volume of the model shaft furnace	m^3

6 REFERENCES

[1] M. Čarnogurská, M. Příhoda, Z. Hajkr, Z. R. Pyszko, Z. Toman, Thermal effects of a high-pressure spray descaling process, Mater. Tehnol., 48 (**2014**) 3, 389–394

[2] M. Rédr, M., Příhoda, Heat Transfer and Fluid Mechanics, VŠB-TU Ostrava, 1998

[3] P. Zhou, H. Li, P. Shi, C. Zhou, Simulation of the transfer process in the blast furnace shaft with layered burden, Applied Thermal Engineering, 95 (**2016**), 296–302, doi:10.1016/j.applthermaleng.2015.11.004

[4] S. Natsui, H. Takai, R. Nashimoto, T. Kikuchi, R. Suzuki, Model study of the effect of particles structure on the heat and mass transfer through the packed bed in ironmaking blast furnace, International Journal of Heat and Mass Transfer, 91 (**2015**) 1176–1186, doi:10.1016/j.ijheatmasstransfer.2015.08.033

[5] P. Mullinger, B. Jenkins, Furnace Design Methods, Industrial and Process Furnaces, 2nd Ed., 2013, 457–506, doi:10.1016/B978-0-7506-8692-1.00012-0

[6] K. Stopar, M. Kovačič, P. Kitak, J. Pihler, Electric-arc-furnace productivity optimization, Mater. Tehnol., 48 (**2014**) 1, 3–7

[7] S. Matsuzaki, T. Nishimura, A. Shinotake, K. Kumito, M. Naito, T. Sugiyama, Development of Mathematical Model of Blast Furnace, Nippon Steel Technical Report, 94 (**2006**), 87–95

[8] McGraw-Hill Dictionary of Scientific & Technical Terms, 6E, 2003, The McGraw-Hill Companies Inc., http://encyclopedia2.thefreedictionary.com/Shaft+Furnace

[9] The Great Soviet Encyclopedia, 3rd Ed., 1970–1979, The Gale Group, Inc., http://encyclopedia2.thefreedictionary.com/Shaft+Furnace

[10] J. Beňo, J. Vontorová, V. Matějka, K. Gál, Evaluation of the thermal resistance of selected bentonite binders, Mater. Tehnol., 49 (**2014**) 3, 465–469

[11] R. Nosek, M. Holubčík, Š. Papučík, Emission Controls Using Different Temperatures of Combustion Air, The Scientific World Journal, 2014, doi:10.1155/2014/487549

UDK 621.762:621.6.04:669.295
Professional article/Strokovni članek

ISSN 1580-2949
MTAEC9, 51(2)345(2017)

THE INFLUENCE OF SCANNING SPEED ON THE LASER METAL DEPOSITION OF Ti/TiC POWDERS

VPLIV HITROSTI SKENIRANJA NA LASERSKO DEPOZICIJO Ti/TiC PRAHU NA KOVINO

Kehinde Sobiyi, Esther Akinlabi, Stephen Akinlabi
University of Johannesburg, Department of Mechanical Engineering Science, Auckland Park Campus, 2006 Johannesburg, South Africa
kk_sob@yahoo.com

Prejem rokopisa – received: 2016-04-07; sprejem za objavo – accepted for publication: 2016-05-10

doi:10.17222/mit.2016.062

The paper describes experimental work performed on the laser metal deposition (LMD) of titanium carbide powders on a pure titanium substrate. The understanding the effect of LMD processing parameters is vital in controlling the properties of the final product fabricated from the LMD process. The objective of the study is to characterize the influence of the laser scanning speed of the metal deposition of titanium and titanium carbide powders on a pure titanium substrate. Microstructural results showed that the substrate is characterized by two-phase morphology; alpha and beta phases. The deposit zone microstructures showed that the grains are of continuous columnar in nature. The heat-affected zone region grain areas appear to decrease with increasing in scanning speed for different samples at different scanning speeds. The height of samples was observed to decrease with an increase in the scanning speed. The microhardness results showed that the hardness of the deposits is greater than the hardness of the substrate. Wear-resistance performance results showed that the coefficient of friction of the substrate is greater than the coefficient of friction of the deposit samples. Similarly, the wear volume loss of material of the substrate is higher than the deposits. The deposit contains titanium carbide and, as such, this powder has improved the wear resistance performance of the substrate.

Keywords: titanium, lasers, metal deposition, scanning speed

Članek opisuje eksperimentalno delo pri laserskem nanašanju (angl. LMD) prahu titanovega karbida na podlago iz čistega titana. Upoštevanje učinkov LMD procesnih parametrov je ključno za kontrolo lastnosti končnega proizvoda, izdelanega z LMD postopkom. Namen študije je določiti vpliv hitrosti skeniranja laserja na nanašanje prahu kovinskega titana in titanovega karbida na podlago iz čistega titana. Rezultati mikrostrukturne karakterizacije so pokazali, da je za podlago značilna dvofazna morfologija; alfa- in beta faza. Mikrostruktura nanešene plasti je pokazala, da so zrna običajno stebraste strukture. Zrna v področju toplotno vplivane cone se zmanjšujejo z naraščanjem hitrosti skeniranja, pri različnih vzorcih in različnih hitrostih skeniranja. Višina vzorcev pri različnih hitrostih skeniranja, se je zmanjševala z naraščanjem hitrosti skeniranja. Rezultati mikrotrdote so pokazali, da je trdota nanosa večja od trdote podlage. Obnašanje pri obrabi je pokazalo, da je koeficient trenja podlage večji kot pa koeficient trenja nanosa. Izguba materiala zaradi obrabe je večja pri podlagi kot pa pri nanosu. Nanos vsebuje titanov karbid, zato je ta prah povečal obrabno odpornost podlage.

Ključne besede: titan, laserji, nanašanje kovine, hitrost skeniranja

1 INTRODUCTION

Titanium and its alloys are becoming widely used engineering materials, most especially in the aerospace, biomedical and chemical industries, due to its impressive mechanical properties such as, high-strength-to-weight ratio, high-temperature strength and excellent corrosion resistance.[1,2] However, the use of titanium in severe wear applications is limited due to its poor tribological properties.[3,4] Titanium alloys are very expensive to replace when damaged during their service life as a result of their high cost.

The Laser Metal Deposition (LMD) technique is efficient, cost effective, and environmentally friendly used for repairing or modifying components that were worn during service by improving its surface properties.[3] The technique can be used for modifying the surfaces of titanium alloys using powder metals such as, ceramics, metals and alloys, composites and intermetallics, for improving its wear resistance, medical biocompatibility, corrosion and oxidation resistance.[5]

Several processing parameters such as laser power, scanning speed, powder rate, or gas flow rate are important during LMD.[6,7] However, the efficiency of the LMD process is affected by the processing parameters which, in turn, affect the physical, microstructural, and microhardness profiling properties. Understanding the effects of these processing parameters during the LMD process, assist on controlling the resulting material properties. Although several studies have been performed to understand the effect of laser process parameters on the LMD process, only few attempts have been made to improve the wear properties of commercially pure titanium.

This study presents the effect of scanning speed on the microstructure and the wear of the resulting deposit using the LMD technique.

2 EXPERIMENTAL PART

LMD of titanium (average particle size of 60 µm) and titanium carbide (average particle size of 200 µm) powders on the surface of 99.6 % pure titanium substrate (75 mm × 75 mm) was achieved using a Kuka robot, 4.4 KW Nd-YAG laser deposition machine. The experimental setup consisted of the following subsystems operating in a control system: the laser beam attached to the robot arm, dual powder feeding system hoppers (for the titanium and titanium carbide powders), and the control unit. The deposition was performed using a laser focal length of 195 mm and a beam diameter of 2 mm. **Figure 1** is a schematic diagram of the Kuka robot system used in the LMD process.

At the beginning of the experiment, a pre-test inspection is performed to eliminate factors that might affect the results. The substrate was sand blasted and then rinsed in acetone to clean the surface before the deposition process. After sand blasting, the powders were deposited on the surface of the substrate.

Six samples were prepared, each at a different laser scanning speed. The scanning speeds were varied from 0.3 m/min and increased with an increment of 0.2 m/min until 1.3 m/min. The experimental matrix is presented in **Table 1**. The laser power and powder volume flow rate for the powders were kept constant at 1200 W and 0.3 min^{-1}, respectively.

The cladding powders were shielded by argon gas at a flow rate of 2 L/min while depositing on the surface of the substrate. The oxygen level was kept in the 10 min^{-1} level using a glove box. The deposition process was achieved by feeding the powders onto the melting pool on the surface of the substrate.

Table 1: Experimental matrix
Tabela 1: Matrika preizkusov

Samples	Scanning speed (m/min)	Ti powder flow rate (min^{-1})	TiC powder flow rate (min^{-1})
A	0.3	1.7	0.3
B	0.5	1.7	0.3
C	0.7	1.7	0.3
D	0.9	1.7	0.3
E	1.1	1.7	0.3
F	1.3	1.7	0.3

Microscopic examination was performed on the laser deposit, to examine the defects that might affect the properties of the materials. Characterization was performed in accordance with the ASTM E3-11 standards for preparing the samples.

Small pieces of samples for each scanning speed were cut from the substrate, cleaned, mounted using polyfast resin. The substrate was grinded to achieve a smooth surface, using silicon carbide paper (320 grit), MD-largo and DiaPro. Polishing was done using MD-Chem cloth with OP-S mixture as the suspension. Each sample was etched for 25 s using Nital solution.

The microstructure and the surface topography of the substrate were observed using an optical microscope (Olympus BX51M). Microhardness was performed using a Vickers testing machine (EMCOTEST®), and a test load of 500 g/f was used. Ten indentations were applied per sample and the average diagonal values of the samples were recorded. The micrograph of the wear scars was observed under the TESCAN scanning electron

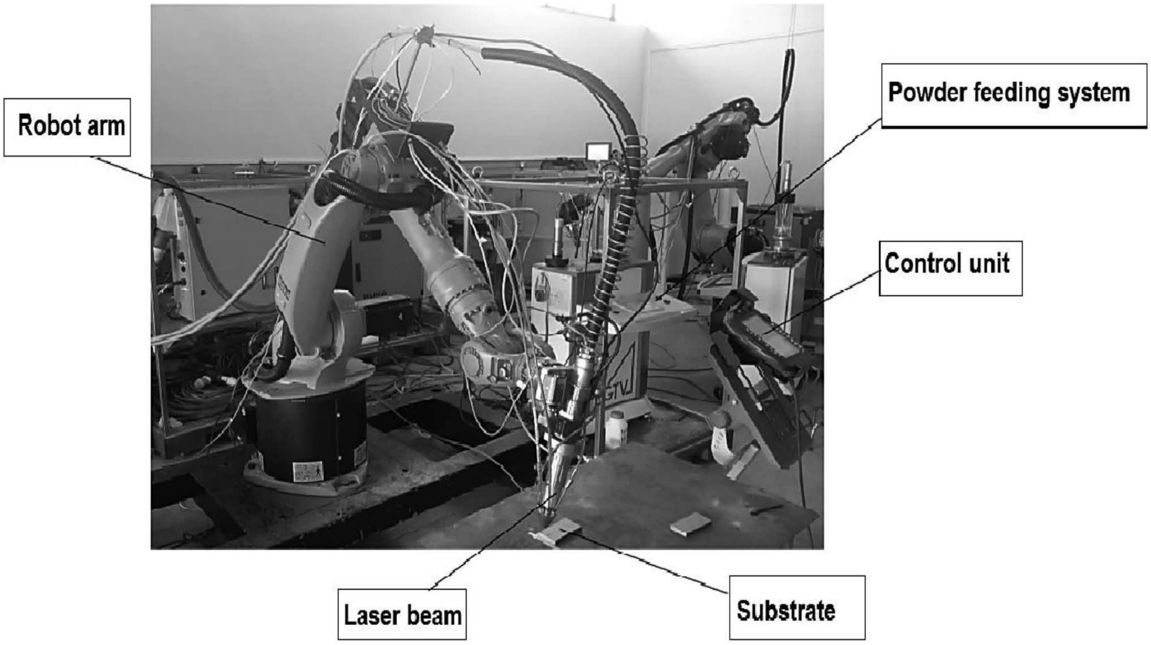

Figure 1: Kuka robot system used for laser deposition process
Slika 1: Kuka robotski sistem, uporabljen pri postopku nanašanja z laserjem

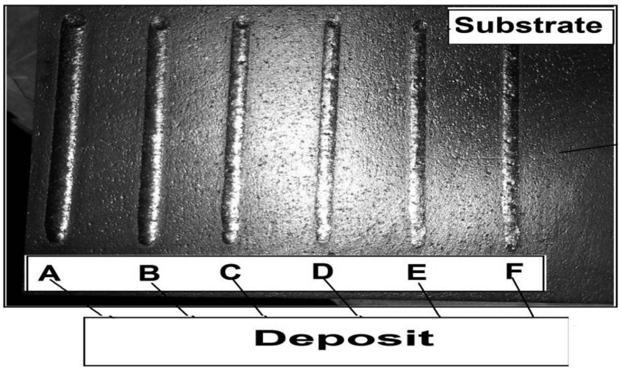

Figure 2: Physical appearance of the deposits
Slika 2: Fizični izgled nanosov

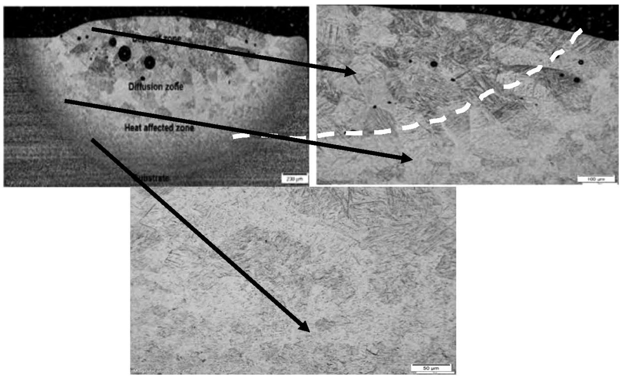

Figure 3: a) Morphology of sample A, b) enlarged deposit zone and diffusion zone, c) enlarged heat-affected zone
Slika 3: a) Morfologija vzorca A, b) povečano področje nanašanja in področje difuzije ter c) povečano toplotno vplivano področje

microscope (SESCAN) equipped with an Oxford Instruments energy-dispersive X-ray spectrometer (EDS).

A dry sliding wear test was performed on the deposited surfaces to investigate the wear resistance of the substrate at different laser scanning speeds, according to ASTM G133-05 standard using a pin-on-disk tribometer (by Cert). The sample was preloaded with a tungsten carbide ball of diameter 10 mm at 25 N force for the 10 s, and then loaded with the same force 25 N for 1000 m. The coefficient of friction, lateral force, horizontal force and carriage position were plotted against time for 1000 seconds. The wear volume loss of material on the substrate is calculated from Equation 1:

$$V_{total} = V_A + V_B = L\left\{ r^2 \sin^{-1}\left(\frac{W}{2r}\right) - \frac{W}{2}\left(r^2 - \frac{W^2}{4}\right)^{1/2} \right\} + \\ + \frac{\pi}{3}\left\{ 2r^3 - 2r^2\left(r^2 - \frac{W^2}{4}\right)^{1/2} - \frac{W^2}{4}\left(r^2 - \frac{W^2}{4}\right)^{1/2} \right\} \quad (1)$$

3 RESULTS AND DISCUSSION

3.1 Effect of speed on laser metal deposition

Figure 2 shows the physical appearance of the deposits on the substrate after LMD of the titanium carbide powders. The thicknesses of the layers varies with scanning speeds. At a low scanning speed the thickness appears to be bigger and wider than the thickness at a high scanning speed. Observed the texture of the surface at lower scanning speed appears more rough compared to the surface texture at higher scanning speeds. This is probably due to more powders were melted on the surface of the substrate, thus enhancing the surface texture. The microstructure of the laser deposit was observed to be relatively homogeneous. The deposits were generally free from cracks but pores were

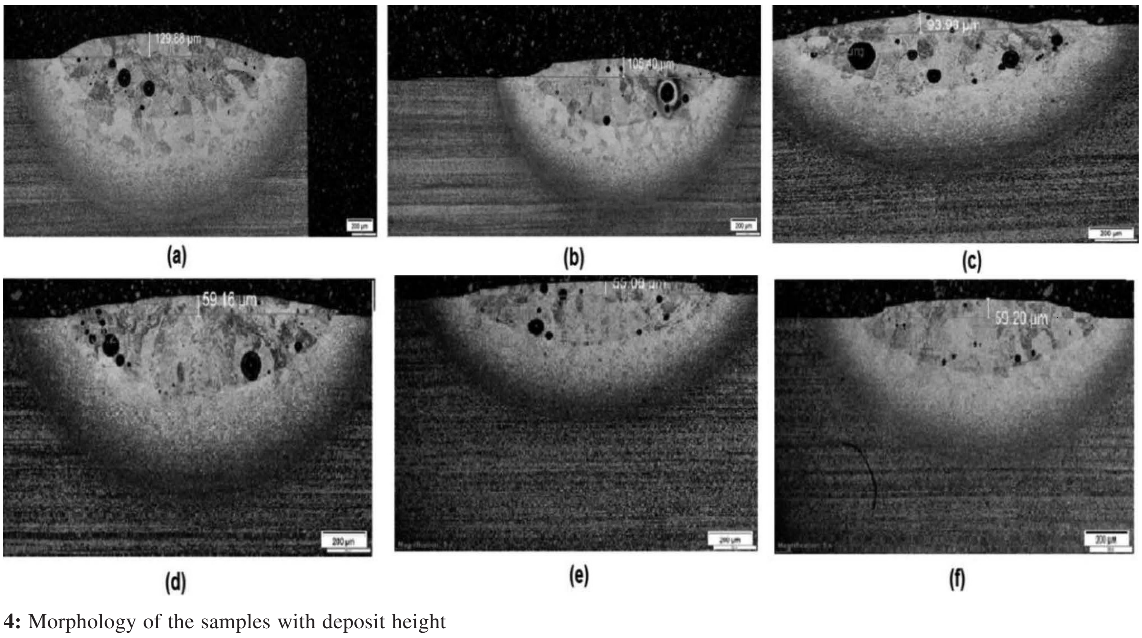

Figure 4: Morphology of the samples with deposit height
Slika 4: Morfologija vzorcev z višino nanosa

observed (**Figure 4**), caused by gas produced from the in situ, entrapped within the molten pool during the deposition process.[4,8]

Figure 3a shows the morphology of sample A and **Figure 3b** the enlarged view of the deposit zone and diffusion zone, at scanning speed of 0.3 m/min. The deposit zone, diffusion zone and heat-affected zone (HAZ) were observed in **Figure 3**. The deposit zone is the layer of powder deposited on the substrate. The diffusion zone is the mixture of the deposition powder and the substrate material resulting after the laser metal deposition process. The HAZ is the portion on the surface of the substrate altered by heat during the deposition process. The deposit zone and diffusion zone appear to have a similar grains structure characterized by the grains of the beta phase. The deposit zone and the diffusion zone are all characterized by the grains of the beta phase. From the microstructure, it can be noticed that the deposit zone grains are of a continuous columnar nature, confirming the beta phase. As the laser scanning speed increases the alpha phase is noticed to be developing.

With the other samples, the deposit zone region is noticed to be decreasing with an increase in the scanning speed. This is a result of heat received by the region during deposition, which cause microstructural changes in that region. As the scanning speed increases the time it takes for the laser to complete the deposit decreases. It can also be observed that as the scanning speed increases the grains appear to be decreasing and more regions of alpha phase are appearing on the microstructures of the samples.

The grains on the heat-affected region appear to be characterized by beta phase, similar to that observed by R. M. Mahamood et al.[9] Generally, at a low laser scanning speed, there is a good bonding between the substrate material and the deposit powder.[9] The material of sample A is fully dense compared to material of the sample scanned at a high laser scanning speed. The optical micrograph of the other five samples is shown in **Figures 4b** to **4f**). Comparing Sample A and sample F in **Figure 4f**, it can be noticed that areas of HAZ are different. For sample F the area is very small and for sample A the area is large.

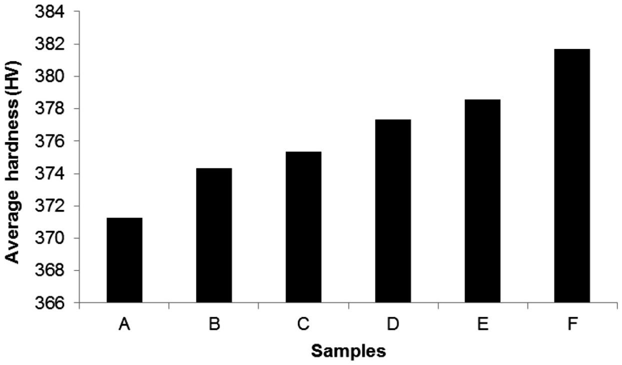

Figure 6: Graphical representation of average hardness for all the samples

Slika 6: Grafična predstavitev povprečne trdote za vse vzorce

The area of the HAZ appears to decrease as the scanning speed increases. The HAZ region of sample B is characterized by a microstructure with grains less that the grains of sample A. As the scanning speed increases the melt pool gets bigger and the solidification becomes slower, causing the materials of the substrate to melt deeper, causing the substrate to mix more of its material with the deposit material, thus, the deposit height decreases.[10]

The HAZ area of sample F where the scanning speed is 1.3 m/min is characterized with fewer refined grains formed in that area compared to the HAZ of sample A where the scanning speed is 0.3m/min. This is caused by heat received by the area, which cause microstructural changes in that area.

The deposit zone of sample A was measured to be 129.88 µm. The heights of the other samples (B–F) were 105.4 µm, 93.96 µm, 59.16 µm, 55.08 µm and 59.20 µm respectively. Comparing measured heights of all samples and height of sample A it can be seen that the height decreases with increase in scanning speed.

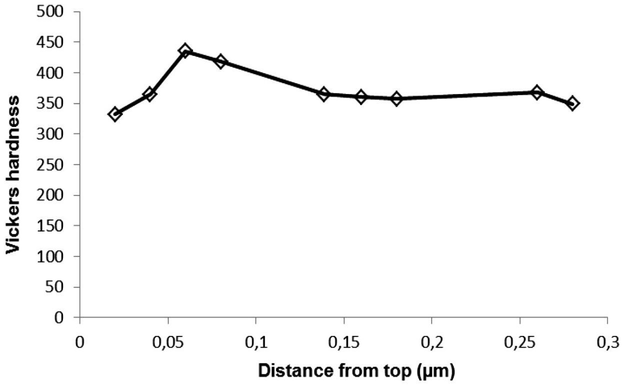

Figure 5: Microhardness profile of sample A at a scanning speed of 0.3 m/min

Slika 5: Profil mikrotrdote vzorca A pri hitrosti skeniranja 0,3 m/min

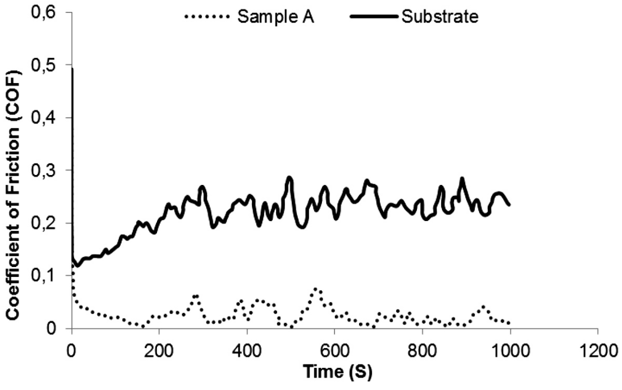

Figure 7: Graphical representation of coefficient of friction (*COF*) with time

Slika 7: Grafična predstavitev koeficienta trenja v odvisnosti od časa

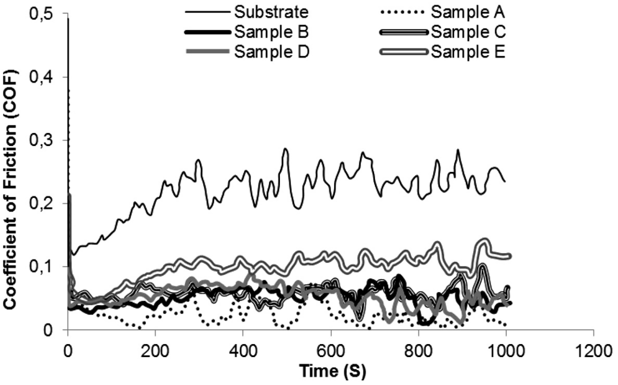

Figure 8: Graphical representation of average coefficient of friction
Slika 8: Grafična predstavitev povprečja koeficienta trenja v odvisnosti od časa

Figure 5 shows a graphical representation of the microhardness profile measured across the section of the sample A from top to bottom. The first three hardness measurements were taken on the deposit zone region, the next three measurements were taken on the HAZ region and the last three measurements were taken on the substrate material region. From the graphical representation of the microhardness profile results, it can be observed that the hardness increases initially and then later decreases towards the substrate. The higher hardness experienced at the transition between the deposit and HAZ zone can be attributed to possibly better crystallization of the grains in this zone. Similar was observed with the other five samples. This shows that the addition of titanium carbide powder improves the mechanical properties of the substrate, and the heat generated by the laser affects the mechanical properties of the substrate.

Figure 6 shows the experimental average microhardness for all six samples. From the graphical representation of the results it can be noticed that the average hardness increased with an increase in the scanning speed. At a higher scanning speed there is rapid solidification of the deposit, which reduces the time taken for the melt pool to solidify, thus promoting higher hardness.

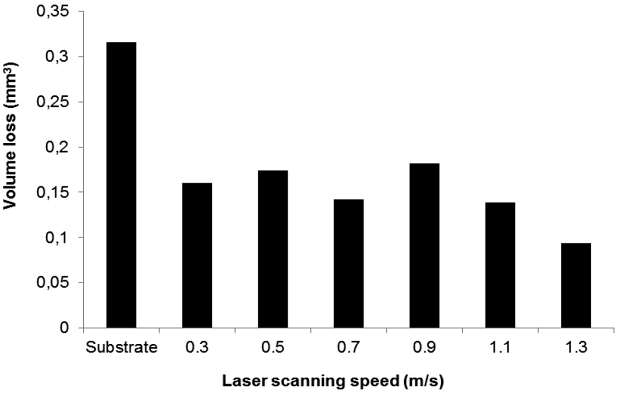

Figure 9: Graphical representation of wear volume loss
Slika 9: Grafična predstavitev volumske izgube pri obrabi

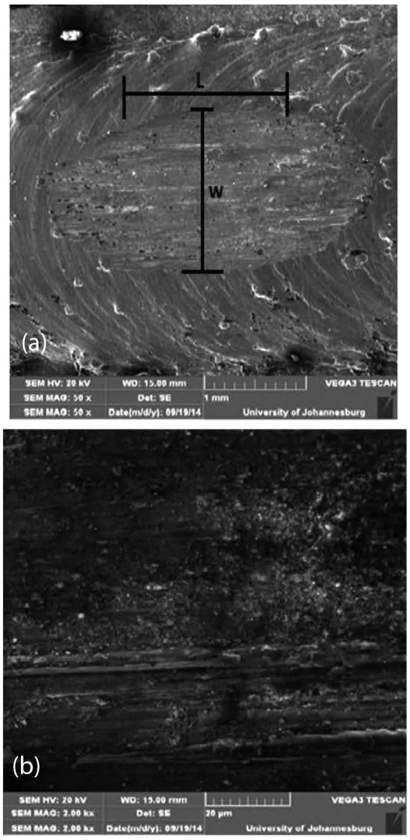

Figure 10: SEM morphology of sample A wear scar: a) low magnification, b) high magnification
Slika 10: SEM-morfologija področja obrabe vzorca A: a) pri majhni povečavi, b) pri večji povečavi

3.2 Wear resistance behaviour

In **Figure 7**, the experimental coefficient of friction for sample A and the substrate are shown for the dry sliding wear resistance tests. From the graphical representation of the results it can be noticed that the coefficient of friction of the substrate is higher than the coefficient of friction. Similar result was obtained for all the other samples investigated.

The titanium wear resistance is found to be very poor compared to the deposit layer as a result of its high coefficient of friction and higher chemical affinity with the tungsten carbide ball used for the wear test thus it is expected for the substrate material to have a high wear volume loss of material.[10,11] The coefficient of friction of the deposits of all other samples is lower than the one of the substrate resulting from the melted TiC particles on the surface. Titanium carbide powder was used as a reinforcement in this study.

In **Figure 8**, the average coefficient of friction at increasing scanning speed corresponding to the individual samples is shown for the dry sliding wear performance testing. The graphical representation of the results shows that the coefficient of friction increases with an increase in the scanning speed; as a result, sample A has a smaller

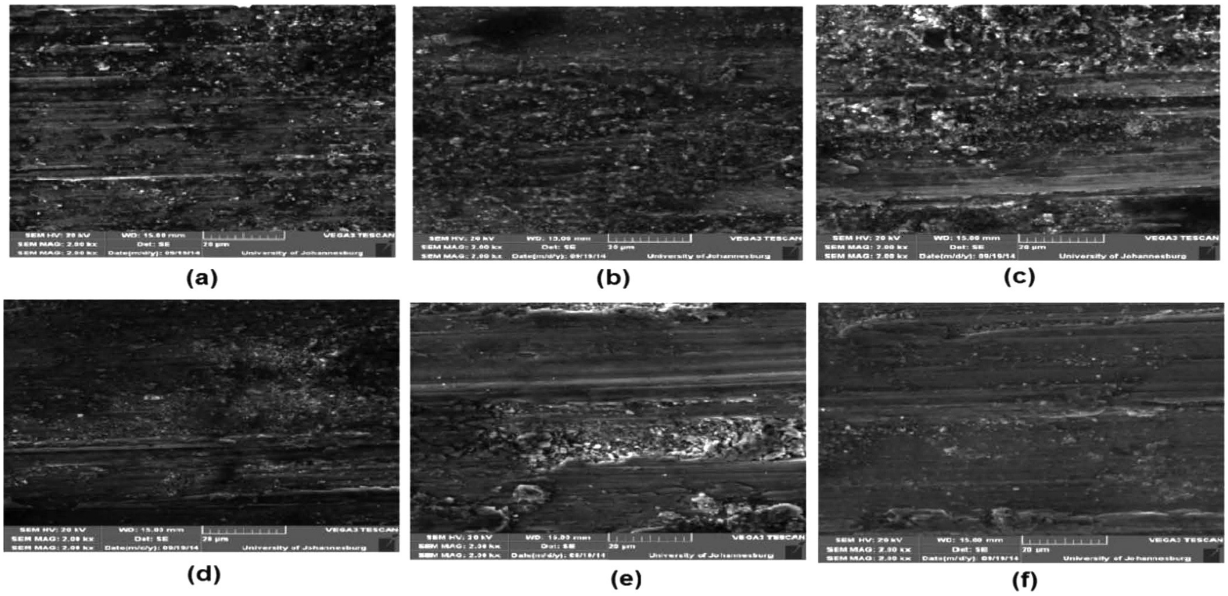

Figure 11: SEM images of wear tracks at 2000×: a) sample A at 0.3 m/min, b) sample B at 0.5 m/min, c) sample C at 0.7 m/min, d) sample D at 0.9 m/min, e) sample E at 1.1 m/min, f) sample F at 1.3 m/min

Slika 11: SEM-posnetki sledov obrabe pri 2000× povečavi: a) vzorec A pri 0,3 m/min, b) vzorec B pri 0,5 m/min, c) vzorec C pri 0,7 m/min, d) vzorec D pri 0,9 m/min, e) vzorec E pri 1,1 m/min in f) vzorec F pri 1,3 m/min

coefficient compared to sample F. Consequently, the substrate is observed to have the highest coefficient of friction.

Figure 9 shows the experimental wear volume loss at different scanning speeds. The figure shows a higher volume of material removal from the surface of the substrate compared to the volume loss of material of the samples at different scanning speeds. The titanium wear resistance is very poor, so it is expected that the substrate material will have a high wear volume loss of material. On the deposit the wear volume loss will be at a minimum level as the deposit layers contain titanium carbide powder melted on the surface of the substrate. The presence of titanium carbide reinforced composite layer improved the wear resistance of the substrate.

Figure 10 shows the SEM micrograph of sample A at low and high magnifications. From the figure, a large scar was observed, with the appearance of large width and long length, which is an indication of wear on the surface of the sample. Un-melted particles of titanium carbide powder were also observed on the surface of the substrate, as shown in **Figure 10a**.

The morphology of wear scars for all other five samples are at higher magnification is shown in **Figure 11**. Surface defects such as pits and wear debris were observed along the wear tracks; an indicating abrasive and adhesive wear mechanism which is coupled with severe plastic deformation around the edges of the wear scars.

4 CONCLUSION

The study investigated the characterization of the influence of the laser scanning speed of LMD for titanium and titanium carbide powders on a titanium alloy substrate.

The results obtained through the characterization of the influence of the laser scanning speed of the laser deposition for titanium and titanium carbide powders has shown that the laser process parameters have an effect on the material properties of components subjected to the LMD process. The microstructure of each sample of different laser deposition scanning speeds showed that the HAZ region increased with an increase in the scanning speed and the heights of the deposits were observed to be different for different laser scanning speeds of the powder particles.

The microhardness results showed that different zones on the substrate have different hardness properties. The hardness decreases from the deposit zone, HAZ and from the HAZ to the substrate. The microhardness was found to increase with an increase in the scanning speed for all the samples investigated. This was a result of the time taken by the laser to interact with the substrate material. These results showed that at a lower scanning speed the laser interacts with the material for a long period of time, which takes longer to solidify the deposits, which in turn affects the results of hardness. This shows that at a lower laser scanning speed the degree of mixing for the substrate material with the deposited powder is proper.

The results of the wear resistance performance behavior of the samples at different scanning speeds and the substrate indicates that the wear volume of material removed from the surface of the substrate is higher than the wear volume of the material removed from the deposit surface. The coefficient of friction of the substrate was observed to be higher than the coefficient of friction of the samples at different scanning speeds. The deposition of titanium carbide showed that the volume loss of material from the substrate could be reduced. Titanium carbide improved the wear resistance of the component. The SEM analysis showed that at a low laser scanning speed some powder particles are completely melted on the surface of the substrate.

Acknowledgments

The authors would like to thank NLC Council for Science and Industrial Research for the use of their Nd: YAG laser deposition machine and Tshwane University of Technology for their wear resistance testing apparatus.

5 REFERENCES

[1] F. H. Froes, The titanium image: Facing the realities of life, The Journal of The Minerals, Metals & Materials Society (JOM), 52 (**2000**) 5, 12, doi:10.1007/s11837-000-0023-2

[2] K. K. Sobiyi, D. C. Blaine, Initial Studies in Powder Metallurgy processing of titanium, Proceedings of The Southern African Institute of Mining and Metallurgy, Advanced Metals Initiative (AMI), **2010**, 105–119

[3] B. Graf, A. Gumenyuk, M. Rethmeier, Laser metal deposition as repair technology for stainless steel and titanium alloys, Physics Procedia, 39 (**2012**), 376–38, doi:10.1016/j.phpro.2012.10.051

[4] Y. S. Tian, C. Z. Chen, S. T. Li, Q. H. Huo, Research progress on laser surface modification of titanium alloys, Applied Surface Science, 242 (**2005**) 1–2, 177–184, doi:10.1016/j.apsusc.2004.08.011

[5] F. Weng, C. Chen, H. Yu, Research status of laser cladding on titanium and its alloys: A review, Materials and Design, 58 (**2014**), 412–425, doi:10.1016/j.matdes.2014.01.077

[6] R. M. Mahamood, E. T. Akinlabi, M. Shukla, S. Pityana, Effect of scanning speed on material efficiency of laser metal deposition of Ti6Al4V, Proceedings of World Academy of Science, Engineering and Technology, 71 (**2012**), 1531–1535

[7] Y. Sun, M. Hao, Statistical analysis and optimization of the process parameters in Ti6Al4V laser cladding using Nd:YAG laser, Optics and lasers in Engineering, 50 (**2012**) 7, 985–995, doi:10.1016/j.optlaseng.2012.01.018

[8] J. Sampedro, I. Perez, B. Carcel, J.A. Ramos, V. Amigo, Laser cladding of TiC for better titanium components, Physics Procedia, 12 (**2011**), 313–322, doi:10.1016/j.phpro.2011.03.040

[9] R. M. Mahamood, E. T. Akinlabi, M. Shukla, S. Pityana, Scanning velocity influence on microstructure, microhardness and wear resistance performance on laser deposited Ti6Al4V/TiC composite, Materials and Design., 50 (**2013**), 656–666, doi:10.1016/j.matdes.2013.03.049

[10] R. M. Mahamood, E.T. Akinlabi, M. Shukla, S. Pityana, Laser Metal Deposition of Ti6Al4V: study on the effect of laser power on microstructure and Microhardness, Proceedings of the International Multi Conference of Engineers and Computer Scientist, Vol. II, 2013

[11] C. Guo, J. Zhou, J. Chen, J. Zhao, Y. Yu, H. Zhou, Improvement of the oxidation and wear resistance of pure Ti by laser cladding at elevated temperature, Surface Coating Technology, 205, (**2010**) 7, 2142–2151, doi:10.1016/j.surfcoat.2010.08.125

ICM&T

25TH INTERNATIONAL CONFERENCE ON MATERIALS AND TECHNOLOGY

OCTOBER 16–19 2017
GRAND HOTEL BERNARDIN
PORTOROŽ, SLOVENIA

ICMT25@IMT.SI / ICMT25.COM

IJS
University of Maribor
IMT Inštitut za kovinske materiale in tehnologije

design **Ajda Schmidt**

ELECTRONIC
ACCESS

http://mit.imt.si

ISSN 1580-2949

9 771580 294004